DISSERTATION

GAS PHASE CLUSTER STUDIES USING A DESK-TOP SIZE SOFT X-RAY LASER FOR SINGLE PHOTON IONIZATION

Submitted by

Scott Heinbuch

Department of Electrical and Computer Engineering

In partial fulfillment of the requirements

For the Degree of Doctor of Philosophy

Colorado State University

Fort Collins, Colorado

Spring 2009

UMI Number: 3374651

INFORMATION TO USERS

The quality of this reproduction is dependent upon the quality of the copy submitted. Broken or indistinct print, colored or poor quality illustrations and photographs, print bleed-through, substandard margins, and improper alignment can adversely affect reproduction.
In the unlikely event that the author did not send a complete manuscript and there are missing pages, these will be noted. Also, if unauthorized copyright material had to be removed, a note will indicate the deletion.

UMI®

UMI Microform 3374651
Copyright 2009 by ProQuest LLC
All rights reserved. This microform edition is protected against unauthorized copying under Title 17, United States Code.

ProQuest LLC
789 East Eisenhower Parkway
P.O. Box 1346
Ann Arbor, MI 48106-1346

COLORADO STATE UNIVERSITY

April 6, 2009

WE HEREBY RECOMMEND THAT THE DISSERTATION PREPARED UNDER OUR SUPERVISION BY SCOTT HEINBUCH ENTITLED GAS PHASE CLUSTER STUDIES USING A DESK-TOP SIZE SOFT X-RAY LASER FOR SINGLE PHOTON IONIZATION BE ACCEPTED AS FULFILLING IN PART REQUIREMENTS FOR THE DEGREE OF DOCTOR OF PHILOSOPHY.

Committee on Graduate Work

Adviser

Co-Adviser

Department Head/Director

ABSTRACT OF DISSERTATION

GAS PHASE CLUSTER STUDIES USING A DESK-TOP SIZE SOFT X-RAY LASER FOR SINGLE PHOTON IONIZATION

This dissertation reports the study of the structure and reactivity of clusters using a new mass spectrometry approach in which the ionization is produced by high energy photons generated by a desk-top size soft x-ray (SXR) laser. The work was motivated by the importance that catalytic processes have in enhancing the rate of gas phase chemical reactions such as the manufacture of hydrocarbons, polymers, drugs, sulfuric acid, fertilizers, pesticides, etc., many forms of pollution control, development of robust mirror coatings for extreme ultraviolet (EUV) lithography, and hydrogen storage for clean energy applications. Extensive mass spectrometry studies have shown that gas phase nanoclusters are effective model systems to study surface reactions in the bulk phase. However, the use of multi-photon ionization or electron impact ionization sources results in cluster fragmentation, limiting the information gained about the neutral cluster parent.

Our approach uses the 26.5 eV photons of a compact capillary discharge driven laser to ionize clusters by single photon events, avoiding the cluster fragmentation associated with multi-photon ionization. The high photon energy also allows the detection of neutral clusters and small molecule reaction products with high ionization energies.

Experiments were conducted for several types of clusters including van der Waals clusters, metal oxides, and metal oxide reactions. Density Functional Theory (DFT) calculations were employed to elucidate cluster geometries, properties, and reaction mechanisms. For hydrogen/van der Waals clusters, the unimolecular dissociation rate

constants for reactions involving loss of one neutral molecule were calculated and neutral cluster temperature were estimated.

The results of metal oxide clusters experiments and calculations suggest that SO_2 can be reduced and oxidized by oxygen deficient and oxygen rich vanadium oxide clusters, respectively. Three SO_3 formation mechanisms are proposed, and several condensed phase catalytic cycles are suggested based on SO_3 formation mechanisms. Other experiments showed that C=C bonds of alkenes can be broken on neutral vanadium oxide oxygen rich clusters with the general structure $VO_3(V_2O_5)_{n=0,1,2...}$. DFT calculations provide a mechanistic explanation for the general reaction in which the C=C double bond of alkenes are broken. New results also help to elucidate the selective catalytic reduction of NO using NH_3 on a vanadium oxide catalyst. A separate set of experiments to identify capping layer materials for extreme EUV optical coatings that are resistive to carbon contamination. Results show that oxidized Hf and Zr are much less reactive than Ti or Si oxide, and might lead to capping layers that might extend lifetimes of EUV mirror coating upon EUV irradiation. Zr oxide was found to be less reactive than Hf oxide.

The set of results demonstrate the potential of compact soft-ray lasers as new tools for chemistry and photo-physics studies with intense soft x-ray light in small laboratory environments.

Scott Heinbuch
Electrical and Computer Engineering Department
Colorado State University
Fort Collins, CO 80523
Spring 2009

Chapter 1

Introduction

The experiments discussed in this dissertation are designed with the objective of studying the structure and reactivity of nanoclusters, with emphasis in metal-oxide species that play an important role in the industrial production of economically important chemicals. The enhancement of the rate of gas phase chemical reactions by condensed phase surface and bulk systems is an essential ingredient in our current economic and environmental health. The long term goal of the project is to develop a quantum mechanical (potential energy surface), mechanistic, atomic level understanding of heterogeneous reaction rate enhancement of gas phase reactions by the bulk and surface condensed phase. In conventional nanocluster spectroscopy systems that make use of visible or UV wavelength lasers, multi-photon absorptions cause undesirable fragmentation of the clusters; a soft x-ray (SXR) laser source drastically changes the ionization process so that multi-photon effects are eliminated.

This introductory chapter gives an overview of clusters and their potential uses. A few sample studies are examined to exemplify the vast collection of theoretical and experimental data available over the past half century. Chapter 2 will discuss the experimental setup in detail. The remaining chapters are reserved for the presentation

of experimental data collected for many systems that include hydrogen bonded and van der Waals clusters, metal oxide clusters, and reactions.

1.1 CLUSTERS: AN OVERVIEW

To physicists and chemists, the word cluster has come to mean a group of atoms or molecules formed by interactions ranging from very weak van der Waals contacts to strong ionic bonds. Although reference to the formation of aggregates and related nucleation phenomena can be found in literature dating from the 1930s and earlier, studies of clusters in mass spectrometer ion sources and later in molecular beams[1.1] began to emerge in the 1950s and developed rapidly as a subject of considerable interest in the 1970s and 1980s. The advent of the laser vaporization technique[1.2] enabled researchers to produce clusters of virtually any element in the periodic table and spawned wide-ranging interest in the studies of clusters of various compositions. In the past 30 years clusters have come to symbolize a new form of matter that is an intermediate between atoms and their bulk counterpart. Clusters bridge phases as well as disciplines.

An enormous amount of work in the past three decades has made it clear not only that clusters are an intermediate form of matter, but also that their properties can often be changed by adding a single atom or electron.[1.3–1.10] Some of these clusters, with their unique stability and properties, can be thought of as super atoms and serve as building blocks for a new class of materials with tailored properties.[1.11-1.12] Equally important, the properties of these clusters can help us understand problems that exist in many areas of science. In addition to being a bridge between these disciplines, clusters also serve as a bridge within disciplines by combining ideas among atomic,

molecular, condensed matter, and nuclear physics as well as among physical, organic, and analytical chemistry. Because of the huge amount of literature on clusters, we are forced to illustrate the excitement that studies of clusters have brought to many disciplines with only a few examples.

We begin by defining what constitutes a cluster. For example, what distinguishes a cluster from a molecule when both can be thought of as groups of atoms? There are many different subtle views on the definition; this is an attempt to give a general view. Note that molecules made by nature are stable under ambient conditions, whereas clusters tailored in a laboratory often are metastable. Molecules are relatively stubborn with respect to stoichiometry, whereas the cluster's composition can usually be altered by a change of production conditions. Generally, clusters tend to coalesce when brought close together, and oftentimes they may react with ambient gases. Thus, although all molecules can in principle be identified as clusters, very few clusters can be called molecules, some exceptions being fullerenes[1.13] and Met-Cars[1.14].

Another interesting question is raised when speaking of the relative size of a cluster, namely, how large must the aggregate be to cease being a cluster? An answer to this question comes from realizing that the properties of a cluster evolve nonmonotonically with size, where, in general, every atom counts. Beyond a certain limit, the properties would smoothly vary, eventually reaching the bulk limit. The size at which the transition to bulk happens depends not only on the kind of atoms or molecules that form the cluster but also on the property being investigated. Thus, by

definition, a cluster is intrinsically an ''artificial molecule'' that is metastable and whose properties depend on the exact number and kinds of atoms that compose it.

Clusters are frequently formed by supersonic expansion through nozzles.[1.15-1.16] The intensity of their mass spectra carries information on the relative stability of the clusters, that is, barring any fragmentation or ionization crossection anomalies. The relative stability also can be studied by reacting the clusters with various reagent gases and reexamining the intensity of their mass peaks. The electronic, optical, and magnetic properties of mass selected, isolated clusters are studied by using a number of experimental techniques, including resonant ionization and electric and magnetic deflection methods. The ionization potential, electron affinity, dissociation energies, gap between highest occupied molecular orbitals (HOMO) and lowest unoccupied molecular orbitals (LUMO), and reactivity provide a wealth of information that can be used to characterize a cluster and study the evolution of its properties with size and composition.

Current theoretical techniques based on ab initio quantum chemical approaches and density functional theory are able to provide accurate and often quantitative information on the structure and properties of clusters, whereas simpler techniques based on phenomenological models describe the systematic evolution of clusters from atoms to bulk. The geometry of clusters is difficult to probe directly with available experimental techniques, and theory plays an indispensable role in elucidating the atomic structure of this intermediate form of matter. This combined effort between theory and experiment has been critical in the development of the field of clusters.

Clusters have played an important role in understanding some of the key issues in physics[1.17-1.19], biology[1.20-1.30], materials science[1.13,1.31-1.46], and a very broad range of issues in chemistry from salvation, energetics and reaction dynamics[1.57-1.62] to organometalics[1.63-1.70] to catalytic processes involving fuels, fertilizers, plastics, and the environment.[1.71-1.79] The role of clusters in chemical catalytic processes is the most closely related field to the work of this dissertation.

1.2 CATALYSIS

A catalyst is a substance that can facilitate a chemical reaction by lowering the reaction energy barrier, enhancing the reaction kinetics, and/or changing the mechanism of the reaction. A catalyst does not change the overall reaction thermodynamics (ΔE, ΔH, or ΔG). Catalytic technology affects our everyday lives in many ways: it provides a range of products from fuels and fertilizers to plastics and pharmaceuticals. It is also used to clean emissions from cars, power plants, and industrial production. The technology is essential to our economy. It has been estimated that 20%–30% of production in the industrialized world is dependent on catalysis.[1.71,1.80] We are facing enormous new challenges that call for an even larger focus on catalysis. The realization that the way we produce energy may jeopardize the Earth's climate points to accelerated investments in alternative energy production technologies, and catalysis is central to most scenarios being discussed. Catalysts are often used solely because of their activity, that is, their ability to enhance the rate of a chemical reaction, often by many orders of magnitude. In other cases, catalysts are desirable because of their selectivity, i.e., their ability to specifically increase the rate of formation of one particular reaction product relative to that of other possible but

unwanted by-products. Control of the absolute rate and the product distribution of chemical reactions is a major challenge of great importance.

Traditionally, the field of catalysis is subdivided into the three areas of heterogeneous, homogeneous, and enzyme catalysis.[1.71] Heterogeneous catalysts are present in a phase different from that of the reactants; usually, the catalyst is a solid surface. Homogeneous catalysts operate in the same phase as the reactants. Enzyme catalysts are specialized proteins. For both homogeneous and enzyme catalysis, it has been possible to reach molecular-scale insight into the structure of the active site (or species) and the reaction mechanism for a multitude of catalysts and reactions. This has been achieved by combining various structural characterization techniques, kinetic investigations, and computational studies for each system.

1.3 CLUSTERS IN CATALYSIS

While the impact that catalysis has on the economy and technology of industrialized countries is well know, current knowledge of how to design catalysts that will lead to the formation of desired products with high selectivity is still lacking.[1.84-1.86] Catalyst development often relies on studies of the influence of various materials on the overall course of reactions. A promising complementary approach to conventional surface science involves the use of clusters as model systems to unravel basic mechanisms of selected classes of reactions effected by heterogeneous catalysts and elucidate the physical and chemical properties of condensed-phase catalysts.[1.87-1.93] Notably, through advances in recent years, it is now possible to produce clusters of nearly any composition, size, stoichiometry, and oxidation and charge state and to

investigate reactions of selected classes of molecules that are influenced by interactions with them.

Already some years ago, findings suggested that a metal oxide surface may be envisioned as a collection of clusters[1.94,1.95], and subsequent experiments revealed that the identification of the reactive sites in heterogeneous catalysis can be aided by gas-phase studies of neutral and ionic clusters[1.96], in addition to studies of these materials in solids or solutions.

In keeping with the ideas outlined above, there are numerous examples showing a direct similarity between reaction mechanisms involving clusters and similar ones affected by industrial catalysts.

1.3.1 Example: V_mO_n Clusters

A notable example that shows a direct correspondence between gas-phase reactions and those known to function in condensed-phase heterogeneous processes include gas-phase studies of the reactions between V_mO_n clusters. Although this is a specific example, the experimental techniques and data analysis and extraction can be applied to virtually any other cluster system that one would desire.

Vanadium oxides are very important industrial heterogeneous catalysts.[1.97-1.100] V_2O_5 catalysis has been employed for oxidation of SO_2 to SO_3 (sulfuric acid production, SO_2 removal), selective reduction of NO_x with NH_3, oxidation of hydrocarbons (butene, benzene, *o*-xylene, naphthalene) to anhydrides, and for other reactions. In order to improve efficiency of industrial catalysts and to find new catalysts for these important processes, fundamental studies of catalytic mechanisms are essential, especially with regard to microscopic or molecular level reaction

dynamics and kinetics.[1.101] With the development of spectroscopic catalyst characterization techniques (x-ray absorption, infrared and Raman spectroscopy, solid-state NMR, ...), the understanding of catalytic mechanisms involving condensed phase transition metal oxide systems[1.102] has increased. Nevertheless, only very limited observations for complex heterogeneous catalytic system are presently available and microscopic reaction mechanisms are sometimes proposed based on incompletely supported models, ideas, and concepts.

Oxidation of SO_2 over supported vanadia catalysts has been carefully studied[1.103-1.105] and conclusive mechanisms have been drawn based heavily on O=V-(O-*support*) structural models.[1.99,1.100,1.102] Very recent theoretical and experimental studies,[1.106,1.107] however, strongly suggest that the catalyst should possess an O_2O=V-O-*support* structure.

Gas phase vanadium oxide clusters (V_mO_n) are excellent model systems to help elucidate and understand molecular level processes occurring in the above mentioned reactions using vanadia catalysts. Catalytically active sites can be simulated/modeled by clusters with particular *m* and *n*: the difficulty is to find proper values from *m* and *n* that represent an active site.[1.94-1.96,1.108] One obvious advantage of using clusters to simulate catalytically active sites is that modern quantum chemistry calculations can be applied to obtain reliable information that is hard to access by direct observations.[1.102]

1.3.1.1 Ion studies vs. Neutral studies of V_mO_n

Successful joint experimental and theoretical studies of the reactivity of cationic V_mO_n toward hydrocarbons have been reported.[1.109-1.113] Many other experimental

and theoretical investigations of vanadium oxide clusters are reported; brief reviews can be found in Refs. 1.112 and 1.114. Because electric and magnetic forces can be used to control and manipulate charged particles and charged particles can be detected very efficiently, most of the experimental studies are on cationic and anionic vanadium oxide clusters. To date, no report can be found for experimental reactivity studies of *neutral* vanadium (and other transition metal) oxide clusters, other than ours.[119]

The major difficulty for such studies of the reactivity of neutral metal oxide clusters lies in finding a valid method to ionize neutral species with typical ionization energies in the range of 8-10 eV or higher (e.g., VO_3, SO_3, N_2, V_3O_8,...), and in detecting them without loss of information (neutral cluster mass and abundance distributions). Typical multi-photon and electron impact ionization almost always cause severe cluster fragmentation, and thus loss of original neutral cluster information.

Recently, single-photon ionization (SPI) through vacuum ultra-violet (VUV) and soft x-ray (SXR) laser radiation have been successfully used by us to study a series of neutral metal oxide cluster distributions without fragmentation.[1.114-1.119] The 118 nm single photon energy is 10.5 eV and the SXR single photon energy is 26.5 eV; for most transition metal oxide clusters (M_mO_n, M = Ti, V, Co, Nb, Fe...), the ionization energy is around 10 eV. Therefore, clusters ionized by SXR laser radiation may have more excess energy than those ionized by 118 nm laser radiation. Thus, for SXR laser ionization, the relative signal intensities of weakly bound products, such as association products, $V_mO_nSO_2$, can be smaller than those observed by 118 nm

ionization, because more excess energy can remain in the clusters and the clusters can fragment. We have found that SXR ionization produces nearly identical spectra to near threshold ionization techniques and therefore without significant fragmentation. The ejected photoelectron must take away most of the energy above the vertical ionization energy. The SXR laser is clearly essential to detect all the neutral clusters and their products. The adoption of SXR laser ionization for our studies is important for detection of products with high ionization energy (IE), such as SO_3 and V_mO_n clusters that are oxygen rich. The photoionization process is discussed in detail in sections 2.3.1.6 – 2.3.1.8.

1.4 INTRODUCTION TO DENSITY FUNCTIONAL THEORY (DFT)

As mentioned above, the combined effort between theory and experiment has been critical in the development of the field of clusters. Quantum chemical calculations have been developed over the last decade and are now a tool capable of realistically addressing the stability of intermediates as well as reaction energy barriers for surface reactions. This development is largely based on density functional theory (DFT[1.120]) which has reached the accuracy and efficiency needed to treat the complex problems of catalysis. Theoretically, a chemical reaction is described by the potential energy surface (PES) diagram for the reaction. The PES diagram shows the stability of all the intermediates in the process and the activation barriers separating them. The PES diagram therefore contains all the information necessary to calculate the rates of the individual elementary steps in the catalytic reaction and the coverage of all the intermediates.

Traditional methods in electronic structure theory, in particular Hartree-Fock theory (HF) and its descendants (configuration interaction (CI), coupled cluster (CC), Moller-Plesset perturbation theory (MP2,3,4, etc.)) are based on a complicated many-electron wavefunction; electron correlation is treated in an average sense or in a perturbation approach. The main objective of DFT is to replace the many-body electronic wavefunction with the electronic density as the basic quantity. The many-body wavefunction is dependent on $4N$ variables, three spatial variables and one spin variable for each of the N electrons. The density is only a function of three variables and is a simpler quantity to deal with both conceptually and practically.

Within the framework of Kohn-Sham DFT[1.121], the intractable many-body problem of interacting electrons in a static external potential is reduced to a tractable problem of non-interacting electrons moving in an effective potential using the Hohenberg-Kohn theorems.[1.122] The electronic energy of a system can then be partitioned into several terms:

$$E = E^T + E^V + E^J + E^{XC} \tag{1.1}$$

where E^T is the kinetic energy term of the motion of the electrons, E^V includes terms of the potential energy of the nuclear-electron attraction and the repulsion between pairs of nuclei, E^J is the electron-electron repulsion term (Coulomb self-interaction of the electron density), and E^{XC} is the exchange-correlation term and includes the remaining part of the electron-electron interactions.[1.123] All terms except the nuclear-nuclear repulsion are functions of the electron density $\rho(r)$. E^J can be expressed as:

$$E^J = \frac{1}{2}\iint \rho(\vec{r}_1)(\Delta r_{12})^{-1}\rho(\vec{r}_2)d\vec{r}_1 d\vec{r}_2 \tag{1.2}$$

$E^T + E^V + E^J$ is the classical energy of the charge distribution $\rho(r)$. The E^{XC} term (eq. 1.1) accounts for any remaining terms for the energy: (1) the exchange energy from the antisymmetry of the quantum mechanical wave function, (2) dynamic correlation in the motions of individual electrons.

E^{XC} can be divided into separate parts for the exchange and correlation to become:

$$E^{XC}(\rho) = E^X(\rho) + E^C(\rho) \tag{1.3}$$

The simplest approximation is the local-density approximation (LDA), which is based upon exact exchange energy for a uniform electron gas, which can be obtained from the Thomas-Fermi model, and from fits to the correlation energy for a uniform electron gas.

DFT has been very popular for calculations in solid state physics since the 1970s. In many cases DFT with the local-density approximation gives quite satisfactory results for solid-state calculations at relatively low computational costs compared to other ways of solving the quantum mechanical many-body problem. However, it was not considered accurate enough for calculations in quantum chemistry until the 1990s, when the approximations used in the theory were greatly refined to better model the exchange and correlation interactions. DFT methods are defined by pairing an exchange functional with a correlation functional. For example, in most of our calculations we use a hybrid functional formulated by Becke[1.124] (B) who combined

his exchange functional with the correlation functional of Lee, Yang and Parr[1.125] (LYP) and defined the exchange energy as:

$$E_{B3LYP}^{XC} = E_{LDA}^{X} + c_0\left(E_{HF}^{X} - E_{LDA}^{X}\right) + c_X \Delta E_{B88}^{X} + E_{VWN3}^{C} + c_C\left(E_{LYP}^{C} - E_{VWN3}^{C}\right) \quad (1.4)$$

This form includes a mixture of HF and DFT exchange along with DFT correlation. The c's in eq. (1.4) are constants. c_0 allows any mixture of HF and LDA local exchange to be used. Also, Becke's gradient correction to LDA exchange is included, scaled by c_X. The VWN3 local correlation functional is used and can be corrected by the LYP correlation by c_C. Becke determined these parameter values by fitting to the atomization energies, ionization potentials, proton affinities, and first-row atomic energies in the G1 molecule set.[1.123] This DFT method is know as B3LYP.[1.126]

DFT is now a leading method for electronic structure calculations of large many electron systems. Despite the improvements in DFT, there are still difficulties in using density functional theory to describe intermolecular interactions properly, especially van der Waals (dispersion) and charge transfer interactions. DFT calculation of transition states, global potential energy surfaces and other strongly correlated systems, and band gaps in semiconductors are also difficult and can be inaccurate. The development of new DFT methods designed to overcome these problems by alterations to the functional or by the inclusion of additive terms, is a current research topic.

1.5 SUMMARY AND ORGANIZATION OF DISSERTATION

We have employed 26.5 eV single photon ionization to detect many cluster systems and products. Our motivation is to understand possible molecular level mechanisms

for condensed phase (catalytic) reactions, as well as discover cluster geometries and properties by way of DFT calculations.

The procedure is discussed in great detail in Chapter 2. In order to gain insight into neutral cluster systems, we developed a spectrometric setup, comprising a Time-of-Flight mass spectrometer (ToF-MS), and single-photon ionization (SPI) through vacuum ultra-violet (VUV) and soft x-ray (SXR) laser radiation. This dissertation will focus mainly on our work with SXR radiation. The setup allows us to characterize cluster species produced under "cold conditions" without significant fragmentation. A molecular beam is coupled with a flow tube reactor to study the reactivity of neutral clusters. The very cold conditions that are usually obtained at the entrance of the mass spectrometer help stabilizing the species formed in the molecular beam. Most of the clusters produced, which have their thermal energy reduced and converted to kinetic energy along a specific direction, can reach the detector before they dissociate. If a cluster does dissociate, we use the reflectron mode of the mass spectrometer to determine metastable dissociation rates, and even estimate temperatures of the clusters.

For hydrogen bonded and van der Waals clusters, neutral clusters are generated in a supersonic expansion of desired gases from a pulsed nozzle. In the case of a liquid, the saturated liquid vapor is formed by flowing He through a reservoir containing the desired liquid at room temperature. For generation of clusters from a gas, the gas is seeded into the He carrier gas. The molecular beam is collimated by a skimmer. Chapter 2 is designed to give a detailed description of our experimental set up and procedure used in our study.

The remaining chapters will be reserved for an in depth discussion of many cluster systems that we have studied and will be divided as follows: Chapter 3 is reserved for hydrogen bonded and van der Waals clusters, Chapter 4 is based on metal/metal oxide clusters, Chapters 5-11 will discuss reactions with various cluster systems including reduction of emissions and hydrogen storage materials, and finally Chapter 12 will summarize and conclude the results for this dissertation.

Note: The following chapters may use the terms extreme ultraviolet (EUV), and soft x-ray (SXR) interchangeably. Different scientific communities use one term or the other. Depending on the audience, EUV or SXR may be used.

REFERENCES

[1.1] E.W. Becker, F. Trager, and G. Putlitz, "Metal Clusters," (Springer, Berlin, 1986).

[1.2] T.G. Dietz, M.A. Duncan, D.E. Powers, and R.E. Smalley, J. Chem. Phys. **74,** 6511 (1981).

[1.3] P. Jena, S.N. Khanna, and B.K. Rao, "Physics and Chemistry of Small Metal Clusters," (Plenum, New York, eds. 1987).

[1.4] S. Sugano, "Microcluster Physics," (Springer, Berlin 1991).

[1.5] H. Haberland, "Clusters of Atoms and Molecules," (Springer, Berlin, ed. (1994).

[1.6] S.N. Khanna, and A.W. Castleman, Jr., "Quantum Phenomena in Clusters and Nanostructures," (Springer, Berlin, eds. 2003).

[1.7] T. D. Mark, and A.W. Castleman, Jr., "Experimental Studies of Cluster Ions," Adv. Atomic Mol. Phys. **20,** 65 (1984).

[1.8] A.W.Castleman, Jr. and R.G. Keesee, "Clusters: Bridging the Gas and Condensed Phases," Acc. Chem. Res. **19,** 413 (1986).

[1.9] A.W.Castleman, Jr. and R.G. Keesee, "Gas Phase Clusters: Spanning the States of Matter," Science **241,** 36 (1988).

[1.10] A.W.Castleman, Jr. and R.G. Keesee, "Ionic Clusters," Chem. Rev. **86,** 589 (1986).

[1.11] S.N. Khanna, and P. Jena, "Assembling Crystals from Clusters," Phys. Rev. Lett. **69,** 1664 (1992).

[1.12] S.N. Khanna, and P. Jena, "Atomic Clusters- Building Blocks for a new class of solid," Phys. Rev. B **51,** 13705 (1995).

[1.13] H.W. Kroto, J.R. Heath, S.C. O'Brein, R.F. Curl, and R.E. Smalley, "C-60 Buckminsterfullerene," Nature **318,** 162 (1985).

[1.14] B.C. Guo, K.P. Kerns, and A.W. Castleman, Jr., "$Ti_8C_{12}^+$ - Metallo-Carbohedrenes: A New Class of Molecular Clusters?," Science **255,** 1411 (1992).

[1.15] A.W. Castleman, Jr., R.G. Keesee, "Clusters: Properties and Formation," Annu. Rev. Phys. Chem. **37,** 525 (1986).

[1.16] A.W. Castleman, Jr. and S. Wei, "Cluster Reactions," Annu. Rev. Phys. Chem. **45,** 685 (1994).

[1.17] A. Heidenreich, J. Jortner, and I. Last, "Cluster Chemistry And Dynamics Special Feature: Cluster dynamics transcending chemical dynamics toward nuclear fusion," PNAS USA **103**, 10589 (2006).

[1.18] I. Last, Y. Levy, and J. Jortner, "Fragmentation channels of large multicharged clusters," J. Chem. Phys. **123**, 154301 (2005).

[1.19] A. McPherson, B.D. Thompson, A.B. Borisov, K. Boyer, and C.K. Rhodes, "Multiphoton-induced X-ray emission at 4–5 keV from Xe atoms with multiple core vacancies," Nature **370**, 631 (1994).

[1.20] D.E. Bergeron, A.W. Castleman, Jr., T. Morisato, and S.N. Khanna, "Formation and properties of halogenated aluminum clusters," J. Chem. Phys. **121,** 10456 (2004).

[1.21] L.R. Hirsch, R.J. Stafford, J.A. Bankson, S.R. Sershen, B. Rivera, R.E. Price, J.D. Hazle, N.J. Halas, and J.L. West., Proc. Natl. Acad. Sci. USA **100,** 13549 (2003).

[1.22] Q. Sun, Q. Wang, B.K. Rao, and P. Jena, "Electronic Structure and Bonding of Au on a SiO_2 Cluster: A Nanobullet for Tumors," Phys. Rev. Lett. **93,** 186803 (2004).

[1.23] Q.A. Pankhurst, J. Connolly, and J. Dobson, "Applications of magnetic nanoparticles in biomedicine," J. Phys. D Appl. Phys. **36,** R167 (2003).

[1.24] T. Kinoshita, S. Satoshi, Y. Mizukoshi, Y. Otome, T. Nakagawa, K. Okitsu, and T.A. Yamamoto, "Magnetic separation of amino acids by gold/iron-oxide composite nanoparticles synthesized by gamma-ray irradiation," J. Magn. Magn. Mater. **293,** 106 (2005).

[1.25] K.C. Buschbeck, "Gmelin Handbook of Inorganic Chemistry," (Springer, Berlin), Vol. XIII, Suppl. 2 (1981). "

[1.26] I. Boutsani, "Systematic investigation on cationic boron clusters: $B_n^+(n$ =2-14)," Int. J. Quantum Chem. **52,** 1081 (1994).

[1.27] H.J. Zhai, B. Kiran, J. Li, and L.S. Wang, ""Hydrocarbon Analogs of Boron Clusters: Planarity, Aromaticity, and Antiar-omaticity" Nat. Mater. **2,** 827 (2003).

[1.28] A.H. Soloway, W. Tjarks, B.A. Barnum, F.G. Rong, R. Barth, I.M. Codogni, and J.G. Wilson, "The Chemistry of Neutron Capture Therapy," Chem. Rev. **98,** 1515 (1998).

[1.29] M.F. Hawthorne, "The Role of Chemistry in the Development of Boron Neutron Capture Therapy of Cancer (p 950-984)," Angew. Chem. Int. Ed. Engl. **32,** 950 (1993).

[1.30] V.P. Zharov, R.R. Letfullin and E. Galitovskaya, "Microbubbles-overlapping mode for laser killing of cancer cells with absorbing nanoparticle clusters," J. Phys. D. Appl. Phys. **38,** 2571 (2005).

[1.31] A. W. Castleman, Jr. and Puru Jena, "Clusters: A bridge across the disciplines of environment, materials science, and biology," PNAS **103**, 10552 (2006).

[1.32] S.N. Khanna and P. Jena, "Assembling crystals from clusters," Phys. Rev. Lett. **69**, 1664 (1992).

[1.33] W. Kratachmer, L.D. Lamb, K. Fostiropoulos, D.R. Huffman, "Solid C_{60}: a new form of carbon," Nature **347**, 354 (1990).

[1.34] Q. Sun, Q. Wang, P. Jena, B. Rao, and Y. Kawazoe, "Stabilization of Si_{60} Cage Structure," Phys. Rev. Lett. **90**, 135503 (2003).

[1.35] H. Hiura, T. Miyazaki, and T. Kanayama, "Formation of Metal-Encapsulating Si Cage Clusters," Phys. Rev. Lett. **86**, 1733 (2001).

[1.36] S. Khanna, B.K. Rao, and P. Jena, "Magic Numbers in Metallo-Inorganic Clusters: Chromium Encapsulated in Silicon Cages," Phys. Rev. Lett. **89**, 016803 (2002).

[1.37] W. Zheng, J.M. Nilles, D. Radisic, and K. Bowen, "Photoelectron spectroscopy of chromium-doped silicon cluster anions," J. Chem. Phys. **122**, 071101 (2005).

[1.38] K. Koyasu, M. Akutsu, M. Mitsui, and A. Nakajima, "Selective Formation of MSi_{16} (M = Sc, Ti, and V)," J. Am. Chem. Soc. **127**, 4998 (2005).

[1.39] Q. Sun, Q. Wang, Y. Kawazoe, and P. Jena, "Design of a heterostructure peapod using magic silicon clusters," Phys. Rev. B **66**, 245425 (2002).

[1.40] B.C. Guo, S. Wei, J. Purnell, S. Buzza, and A.W. Castleman, Jr., "Metallo-Carbohedrenes [$M_8C_{12}^+$ (M=V, Zr, Hf and Ti)]: A Class of Stable Molecular Cluster Ions," Science **256,** 515 (1992).

[1.41] J.S. Pilgrim, and M.A. Duncan, "Metallo-carbohedrenes: chromium, iron, and molybdenum analogs," J. Am. Chem. Soc. **115,** 6958 (1993).

[1.42] B.D. May, S.F. Cartier, and A.W. Castleman, Jr., ""Delayed Ionization and Delayed Atomic Ion Emission of Ti and V Metallocarbohedrenes: Evidence for Collective Electronic Effects," Chem. Phys. Lett. **242,** 265 (1995).

[1.43] D.E. Bergeron, A.W. Castleman, Jr., T. Morisato, and S.N. Khanna, "Formation of $Al_{13}I^-$: Evidence for the Superhalogen Character of Al_{13}," Science **304,** 84 (2004).

[1.44] D.E. Bergeron, P.J. Roach, A.W. Castleman, Jr., N.O. Jones, and S.N. Khanna, "Al Cluster Superatoms as Halogens in Polyhalides and as Alkaline Earths in Iodide Salts," Science **307,** 231 (2005).

[1.45] O.C. Thomas, W.J. Zheng, T.P. Lippa, S.J. Xu, S.A. Lyapustina, and K.H. Bowen, "In search of theoretically predicted magic clusters: Lithium-doped aluminum cluster anions," J. Chem. Phys. **114,** 9895 (2001).

[1.46] D.E. Bergeron, A.W. Castleman, Jr., "Formation and properties of halogenated aluminum clusters," T. Morisato, and S.N. Khanna, J. Chem. Phys. **121,** 10456 (2004).

[1.47] A. W. Castleman, Jr. and Puru Jena, "Clusters: A bridge between disciplines," PNAS **103**, 10552 (2006).

[1.48] R.E. Smalley, D.H. Levy, and L. Wharton, "Fluorescence excitation spectrum of Hel-2 van der Waals complex," J. Chem. Phys. **64,** 3266 (1976).

[1.49] R.E. Smalley, L. Wharton, and D.H. Levy, "Molecular optical spectroscopy with supersonic beams and jets," Acc. Chem. Res. **10,** 139 (1977).

[1.50] J.E. Kenny, K.E. Johnson, W. Sharfin, and D.H. Levy, "The photodissociation of van der Waals molecules: Complexes of iodine, neon, and helium," J. Chem. Phys. **72,** 1109 (1980).

[1.51] S. Rudic, J.M. Merritt, and R.E. Miller, "Infrared laser spectroscopy of the CH_3–HCN radical complex stabilized in helium nanodroplets," J. Chem. Phys. **124,** 1043051 (2006).

[1.52] J.P. Toennies, and A.F. Vilesov, "Superfluid Helium Droplets: A Uniquely Cold Nanomatrix for Molecules and Molecular Complexes," Angew. Chem. Int. Ed. **43,** 2622 (2004).

[1.53] P. Ayotte, and M.A. Johnson, "Electronic absorption spectra of size-selected hydrated electron clusters: $(H_2O)^{n-}$, n=6–50," J. Chem. Phys. **106,** 811 (1997).

[1.54] J.V. Coe, G.H. Lee, J.G. Eaton, S.T. Arnold, H.W. Sarkas, K.H. Bowen, C. Ludewigt, H. Haberland, and D.R. Worsnop, "Photoelectron spectroscopy of

hydrated electron cluster anions, $(H_2O)^-_{n=2-69}$," J. Chem. Phys. **92,** 3980 (1990).

[1.55] J.R.R. Verlet, A.E. Bragg, A. Kammrath, O. Cheshnovsky, and D.E. Neumark, "Observation of Large Water-Cluster Anions with Surface-Bound Excess Electrons," Science **307,** 93 (2005).

[1.56] L. Turi, W.S. Sheu, and P.J. Rossky, "Characterization of Excess Electrons in Water-Cluster Anions by Quantum Simulations," Science **309,** 914 (2005).

[1.57] A.L. Sobolewski, and W. Domcke, "Hydrated hydronium: a cluster model of the solvated electron?," Phys. Chem. Chem. Phys. 4, 4 (2002).

[1.58] P. Kebarle, "Interaction Between Ions and Molecules," ed. Ausloos, P. (Plenum, New York), pp. 459–487 (1974).

[1.59] M.T. Bowers, "Gas Phase Ion Chemistry," (Academic, New York), pp. 84–119 (1979).

[1.60] T.B. McMahon, "Fundamentals and Applications at Gas Phase Ion Chemistry," ed. Jennings, K. R. (Kluwer Academic, Dordrecht, The Netherlands), pp. 202–222 (1999).

[1.61] P. Kebarle, "Ion thermochemistry and salvation from gas phase ion equilibrium," Annu. Rev. Phys. Chem. **28,** 445 (1977).

[1.62] P. Kebarle, "Ion-Molecule Reactions," ed. Franklin, J. L. (Plenum, New York), pp. 315–362 (1972).

[1.63] M. Sodupe, and C.W. Bauschlicher, "Theoretical study of the bonding of the first- and second-row transition-metal positive ions to acetylene." J. Phys. Chem. **95,** 8640 (1991).

[1.64] M. Sodupe, C.W. Bauschlicher, S.R. Langhoff, and H. Partridge, "Theoretical study of the bonding of the first-row transition-metal positive ions to ethylene," J. Phys. Chem. **96,** 2118 (1992).

[1.65] C.W. Bauschlicher, H. Partridge, and S.R. Langhoff, "Theoretical study of transition-metal ions bound to benzene," J. Phys. Chem. **96,** 3273 (1992).

[1.66] M. Sodupe, and C.W. Bauschlicher, "A study of the ground and low-lying states of $MgC_2H_2^+$ and $MgC_2H_4^+$," Chem. Phys. **185,** 163 (1994).

[1.67] R. Pandey, B.K. Rao, P. Jena, and J.M. Newsam, "Unique magnetic signature of transition metal atoms supported on benzene," Chem. Phys. Lett. **321,** 142 (2000).

[1.68] R. Pandey, B.K. Rao, P. Jena, and M.A. Blanco, "Electronic Structure and Properties of Transition Metal-Benzene Complexes," J. Am. Chem. Soc. **123,** 3799 (2001).

[1.69] B.K. Rao, and P. Jena, "Caging of Ni clusters by benzene molecules and its effect on the magnetism of Ni clusters," J. Chem. Phys. **116,** 1343 (2002).

[1.70] A.K. Kandalam, B.K. Rao, and P. Jena, "Geometry and electronic structure of $V_n(Bz)_m$ complexes," J. Chem. Phys. **120,** 10414 (2004).

[1.71] C.H. Christensen and J.K. Nørskov, "A molecular view of heterogeneous catalysis," J. Chem. Phys. **128**, 182503 (2008).

[1.72] G.A. Samoraj and J.Y. Park, "Evolution of the surface science of catalysis from single crystals to metal nanoparticles under pressure," J. Chem. Phys. **128**, 182504 (2008).

[1.73] S. Heinbuch, F. Dong, J.J. Rocca, and E.R. Bernstein, "Gas phase study of the reactivity of optical coating materials with hydrocarbons using a desk-top size EUV laser," JOSA B **25**, B85 (2008).

[1.74] F. Dong, S. Heinbuch, Y. Xie, J.J. Rocca, Z. Wang, K. Deng, S. He, and E.R. Bernstein, "C=C bond cleavage on neutral $VO_3(V_2O_5)_n$ clusters," JACS (submitted Aug. 2008).

[1.75] F. Dong, S. Heinbuch, Y. Xie, J. J. Rocca, and E. R. Bernstein, "Reaction of Neutral Vanadium Oxide Clusters With methanol and Ethanol", J. Chem. Phys. submitted.

[1.76] F. Dong, S. Heinbuch, Y. Xie, J.J. Rocca, Z. Wang, K. Deng, S. He, and E.R. Bernstein, "Experimental and theoretical study of the reactions between neutral vanadium oxide clusters and ethane, ethylene, and acetylene," J. Am. Chem. Soc. **130(6)**, 1932 (2008).

[1.77] Z. Wang, W. Xue, Y. Ma, X. Ding, S. He, F. Dong, S. Heinbuch, J.J. Rocca, and E.R. Bernstein, "Partial Oxidation of Propylene Catalyzed by VO_3 Clusters: A DFT Study," J. Phys. Chem. **112,** 5984 (2008).

[1.78] S.-G. He, Y. Xie, F. Dong, S. Heinbuch, E. Jakubikova, J.J. Rocca, and E.R. Bernstein, "Reactions of Sulfur Dioxide with Neutral Vanadium Oxide Clusters in the Gas Phase. I. Experimental Study Employing Single Photon Ionization," Journal of Physical Chemistry A (Submitted).

[1.79] M. Calatayud, B. Mguig, and C. Minot, "Modeling catalytic reduction of NO by ammonia over V_2O_5," Surf. Sci. Rep. **55**, 169 (2004).

[1.80] I. Maxwell, "Driving forces for innovation in applied catalysis," Stud. Surf. Sci. Catal. **101**, 1 (1996).

[1.81] K. N. Ferreira, T. M. Iverson, K. Maghlaoui, J. Barder, and S. Iwata, "Architecture of the Photosynthetic Oxygen-Evolving Center," Science **303**, 1831 (2004).

[1.82] A. Gao, J. Garcia-Viloca, M. Karplus, and D. G. Truhlar, "How Enzymes Work: Analysis by Modern Rate Theory and Computer Simulations," Science **303**, 186 (2004).

[1.83] P.E.M. Siegbahn, J.W. Tye, and M.B. Hall, "Computational Studies of [NiFe] and [FeFe] Hydrogenases," Chem. Rev. **107**, 4414 (2007).

[1.84] J. Haggin, Chem. Eng. News. **72,** 22 (1994).

[1.85] J. Sauer, "Molecular models in ab initio studies of solids and surfaces: from ionic crystals and semiconductors to catalysts," Chem. Rev. **89,** 199 (1989).

[1.86] K.A. Zemski, D.R. Justes, and A.W. Castleman, Jr., "Studies of Metal Oxide Clusters: Elucidating Reactive Sites Responsible for the Activity of Transition Metal Oxide Catalysts," J. Phys. Chem B **106,** 6136 (2002).

[1.87] P.S. Kirlin, H. Knozinger, and B.C. Gates, "Mononuclear, trinuclear, and metallic rhenium catalysts supported on magnesia: effects of structure on catalyst performance," J. Phys. Chem. **94,** 8451 (1990).

[1.88] M.D. Morse, M.E. Geusic, J.R. Heath, and R.E. Smalley, "Surface reactions of metal clusters. II. Reactivity surveys with D_2, N_2, and CO," J. Chem. Phys. **83,** 2293 (1985).

[1.89] Q.L. Zhang, S.C. O'Brien, J.R. Heath, Y. Liu, R.F. Curl, H.W. Kroto, and R.E. Smalley, "Reactivity of large carbon clusters: spheroidal carbon shells and their possible relevance to the formation and morphology of soot," J. Phys. Chem. **90,** 525 (1986).

[1.90] R.L. Whetten, D.M. Cox, D.J. Trevor, and A. Kaldor, "Advances in research on clusters of transition metal atoms," Surf. Sci. **156,** 8 (1985).

[1.91] P. Fayet, A. Kaldor, and D.M. Cox, "Palladium clusters: H_2, D_2, N_2, CH_4, CD_4, C_2H_4, and C_2H_6 reactivity and D_2 saturation studies," J. Chem. Phys. **92,** 254 (1990).

[1.92] A. Kaldor, D.M. Cox, D.J. Trevor, and M.R. Zakin, "The chemistry and physics of molecular surfaces," Z. Phys. D **3,** 195 (1986).

[1.93] M.R. Zakin, R.O. Brickman, D.M. Cox, and A. Kaldor, "Size-selective dehydrogenation of benzene by gas-phase niobium cluster ions (Nb_n^+)," J. Chem. Phys. **88,** 5943 (1988).

[1.94] M. Witko, K. Hermann, and R. Tokarz, "Ab initio and semiempirical cluster studies on the reactivity of the vanadium pentoxide (010) surface," J. Electron Spectrosc. Rel. Phenom. **69,** 89 (1994).

[1.95] E.L. Muetterties, "Molecular Metal Clusters," Science **196**, 839 (1977).

[1.96] X. Lai and D.W. Goodman, "Structure-reactivity correlations for oxide-supported metal catalysts: new perspectives from STM," J. Mol. Catal. A **162**, 33 (2000).

[1.97] G. Ertl, H. Knozinger, and J. Weikamp, "Handbook of Heterogeneous Catalysis," (Wiley-VCH, 1997).

[1.98] I.T. Horvath, "Encyclopedia of Catalysis," (Wiley International, 2003).

[1.99] B.M. Weckhuysen, and D.E. Keller, "Chemistry, spectroscopy and the role of supported vanadium oxides in heterogeneous catalysis," Catal. Today **78**, 25 (2003).

[1.100] J.L G. Fierro, "Metal Oxides," (Taylor & Francis Group, LLC, 2006)

[1.101] R.A. van Santen and M. Neurock, "Molecular Heterogeneous Catalysis," (Wiley-VCH, 2006).

[1.102] I.E. Wachs, "Recent conceptual advances in the catalysis science of mixed metal oxide catalytic materials," Catal. Today **100**, 79 (2005).

[1.103] J.P. Dunn, H.G. Stenger, Jr., and I.E. Wachs, "Oxidation of SO_2 over Supported Metal Oxide Catalysts," J. Catal. **181**, 233 (1999)

[1.104] J.P. Dunn, H.G. Stenger, Jr., and I.E. Wachs, "Oxidation of sulfur dioxide over supported vanadia catalysts: molecular structure – reactivity relationships and reaction kinetics," Catal. Today **51**, 301 (1999)

[1.105] I. Giakoumelou, V. Parvulescu, and S. Boghosian, "Vanadia-silica and vanadia-cesium-silica catalysts for oxidation of SO_2," J. Catal. **225**, 337 (2004)

[1.106] J.N.J. van Lingen, O.L.J. Gijzeman, B. M. Weckhuysen, and J.H. van Lenthe, "On the umbrella model for supported vanadium oxide catalysts," J. Catal. **239**, 34 (2006).

[1.107] D.E. Keller, D.C. Koningsberger, and B.M. Weckhuysen, "Molecular Structure of a Supported VO_4 Cluster and Its Interfacial Geometry as a

Function of the SiO_2, Nb_2O_5, and ZrO_2 Support," J. Phys. Chem. B **110**, 14313 (2006).

[1.108] J. M. Thomas, "The tortuous tale of the catalytically active site," Topics in Catalysis 38, 3 (2006).

[1.109] D. R. Justes, R. Mitric, N. A. Moore, V. Bonacic-Koutecky, and A. W. Castleman, Jr., "Theoretical and Experimental Consideration of the Reactions between $V_xO_y^+$ and Ethylene," J. Am. Chem. Soc. **125**, 6289 (2003).

[1.110] A. Fielicke, R. Mitric, G. Meijer, V. Bonacic-Koutecky, and G. van Helden, "The Structures of Vanadium Oxide Cluster-Ethene Complexes. A Combined IR Multiple Photon Dissociation Spectroscopy and DFT Calculation Study," J. Am. Chem. Soc. **125**, 15716 (2003).

[1.111] N. A. Moore, R. Mitric, D. R. Justes, V. Bonacic-Koutecky, and A. W. Castleman, Jr., "Kinetic Analysis of the Reaction between $(V_2O_5)_{n=1,2}^+$ and Ethylene," J. Phys. Chem. B. **110**, 3015 (2006).

[1.112] S. Feyel, D. Schroder, X. Rozanska, J. Sauer, and H. Schwarz, "Gas-Phase Oxidation of Propane and 1-Butene with $[V_3O_7]^+$: Experiment and Theory in Concert," Angew. Chem. Int. Ed. **45**, 4677 (2006).

[1.113] S. Feyel, D. Schroder, X. Rozanska, J. Sauer, and H. Schwarz, "Thermal Activation of Methane by Tetranuclear $[V_4O_{10}]^+$," Angew. Chem. Int. Ed. **45**, 4681 (2006).

[1.114] Y. Matsuda and E. R. Bernstein, "Identification, Structure, and Spectroscopy of Neutral Vanadium Oxide Clusters," J. Phys. Chem. A **109**, 3803 (2005).

[1.115] Y. Matsuda and E. R. Bernstein, "On the Titanium Oxide Neutral Cluster Distribution in the Gas Phase: Detection through 118 nm Single-Photon and 193 nm Multiphoton Ionization," J. Phys. Chem. A **109**, 314 (2005).

[1.116] Y. Matsuda, D. N. Shin, and E. R. Bernstein, "On the zirconium oxide neutral cluster distribution in the gas phase: Detection through 118 nm single photon, and 193 and 355 nm multiphoton, ionization," J. Chem. Phys. **120**, 4142 (2004).

[1.117] D. N. Shin, Y. Matsuda, and E. R. Bernstein, "On the iron oxide neutral cluster distribution in the gas phase. II. Detection through 118 nm single photon ionization," J. Chem. Phys. **120**, 4157 (2004).

[1.118] Y. Matsuda, D. N. Shin, and E. R. Bernstein, " On the copper oxide neutral cluster distribution in the gas phase: Detection through 355 nm and 193 nm multiphoton and 118 nm single photon ionization," J. Chem. Phys. **120**, 4165 (2004).

[1.119] F. Dong, S. Heinbuch, S.-G. He, Y. Xie, J. J. Rocca, and E. R. Bernstein, "Formation and distribution of neutral vanadium, niobium, and tantalum oxide clusters: Single photon ionization at 26.5 eV," J. Chem. Phys. **125**, 164318 (2006).

[1.120] W. Kohn, "Nobel Lecture: Electronic structure of matter—wave functions and density functionals," Rev. Mod. Phys. **71**, 1253 (1999).

[1.121] W. Kohn, L.J. Sham, "Self-consistent equations including exchange and correlation effects," Phys. Rev. **140**, A1133 (1965).

[1.122] P. Hohenberg, W. Kohn, "Inhomogeneous electron gas," *Phys. Rev.* **136,** B864 (1964).

[1.123] J.B. Foresman and A. Frisch, "Exploring Chemistry with Electronic Structure Methods," (Gaussian Inc., 1996).

[1.124] A. D. Becke, "Density-functional exchange-energy approximation with correct asymptotic behavior," Phys. Rev. A **38**, 3098 (1988).

[1.125] C. Lee, W. Yang, and R. G. Parr, "Development of the Colle-Salvetti correlation-energy formula into a functional of the electron density," Phys. Rev. B **37**, 785 (1988).

[1.126] A. D. Becke, "Density-functional thermochemistry. III. The role of exact exchange," J. Chem. Phys. **98**, 5648 (1993).

Chapter 2

Experimental setup

This chapter is designed to give a detailed description of our experimental set up and all of its components. To avoid the redundancy of describing the apparatus for metal oxide (M_mO_n) clusters and van der Waals/hydrogen bonded clusters, this chapter discusses the more complicated set up used in the study of metal-oxide clusters, including a laser ablation step. The reader needs only to understand that the experiment for hydrogen bonded and van der Waals clusters is exactly the same as what is described here, with the exception of the laser ablation step. Hydrogen bonded and van der Waals clusters neutral clusters are simply generated in a supersonic expansion of desired gases from the pulsed nozzle.

2.1 SETUP FUNCTION AND COMPONENTS

Laser vaporization sources have been successfully employed to investigate various metal oxides.[2.1-2.5] They are often used in combination with a supersonic expansion technique to provide intense molecular/cluster beams with practically all metals. The target material is laser ablated from a solid target and seeded into a flowing stream of inert gas expanding into vacuum from a small nozzle. Rarefaction and the adiabatic cooling of the gas mixture steeply reduce the collision rate experienced by beam components as a

function of distance from the expansion source. A simple model, which describes the molecular beams produced by a supersonic expansion of a binary gas mixture with one component diluted, was presented in 1993 by DePaul et al.[2.6]

Weakly bound complexes and clusters are formed if sufficient collisions occur before the beam becomes too diffuse and further interactions among the contained chemical species are virtually impossible. Molecules produced initially are entrained with the expanding gas. They lose internal energy by collisions during the expansion.[2.7] Depending on how much internal energy the molecules lose, they either stabilize or dissociate. At the same time, the probability of further collisions drops off.

A schematic drawing of the experimental apparatus realized for our experiments is shown in Figure 2.1. A gas mixture containing a small addition of an oxygen donor to He gas is introduced with high (up to 100 psi) backing pressure into a vacuum chamber by a pulsed valve. The repetition rate is set by the repetition rate of the ionization laser (1-10 Hz). If a continuous nozzle is used, maintenance of a high vacuum into which the gases can expand requires very large pumping rates. Pulsing the valve reduces the size of the vacuum pumping system required, by limiting the total gas throughput. Still, during the gas pulse, high densities can be established close to the valve nozzle enabling high reaction rates.

Before expansion, metal vapor is added to the gas stream. Metal vapor can be produced by heating up a solid sample to a temperature providing an adequate vapor pressure or by ablating material from a surface. Ablation of the target material from a solid body is most elegantly performed with laser light focused to a small spot. The laser beam impinges on the material surface which gets hot and evaporates. The laser ablation

process produces dense vapors at very high temperatures in an expanding plasma plume that crosses the gas stream perpendicularly. High vapor

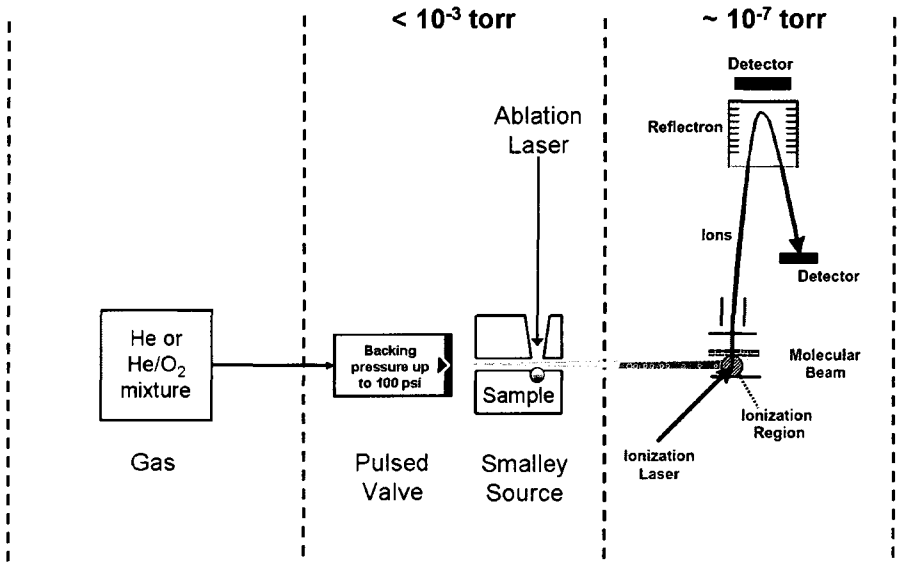


Figure 2.1: Schematic of experimental setup

temperatures are adverse to molecule formation. However, the hot metal plume rapidly mixes with the carrier gas resulting in colder temperatures at which chemical species may associate. The buffer gas density and type can be varied to maximize the cooling efficiency of the plume and achieve an optimal cooling and stabilization effect on expansion.

A vaporization source based on a Smalley design[2.8-2.10] is realized and used to evaporate metals into the He gas stream. The metal vapor, entrained in the gas flow, expands into vacuum through a nozzle. The length of the source exit channel, also called mixing region or "waiting room", could be chosen long enough so that many three-body collisions can occur that, in turn, favor cluster formation.[2.11]

The carrier gas containing clusters either proceeds downstream and rarefies on expansion up to a point where no more collisions occur, or is expanded and reacted with

a reactant gas in a flow tube reactor (Φ6 mm × 76 mm). The reactant gases are pulsed into the tube 20 mm downstream from the exit of the narrow cluster formation channel by a pulsed valve (General Valve). Reactions in the flow tube reactor are believed to occur at near room temperature due to the large number of collisions between M_mO_n clusters and the bath gas (He) and/or reactants.

At this point, the molecular beam is skimmed from the expansion cloud by a skimmer (Φ5 mm or Φ2 mm). This collimated beam of molecules then enters the interaction (ionization) region of a time of flight mass spectrometer (ToF-MS) for single photon ionization by radiation of one of three different lasers: a 193 nm (6.4 eV) Excimer laser, a 118 nm (10.5 eV) VUV laser or a 46.9 nm (26.5 eV) soft x-ray (SXR) laser. Ions formed are guided to a detector by electric fields along the mass spectrometer.

The ToF-MS experiment in its present configuration is contained in three chambers. As depicted in Fig. 2.2 we refer to these chambers as "source", "detection", and "optics" chambers respectively, since both vaporization and ionization occur in the "source", charged molecules are detected in the "detection" chamber, and the z-fold mirrors used to focus and direct the ionization beam, are contained in the "optics" chamber.

2.1.1 Source Chamber

The source chamber has 10 ports of access with various sizes. Two pairs of ports with 2¾" Conflat (CF) metal-seal flanges on opposite sides are available. One of these ports is closed with a 2¾" CF flange having a 40 mm diameter fused silica window. The ablation laser (532 nm from Nd:YAG) passes through this window. The remaining three 2¾" CF flanges are fitted with electrical and gas feedthroughs for control of (1) a motor to rotate and translate the metal target, and general gas valve for reactions, (2) voltage for grids to

remove ions from the molecular beam created by the ablation process and (3) a gas feedthrough for the reaction cell.

Two more ports on the source chamber are fitted with ANSI ASA-9 flanges. The SXR ionization laser passes through these two ports that are on axis with the ionization

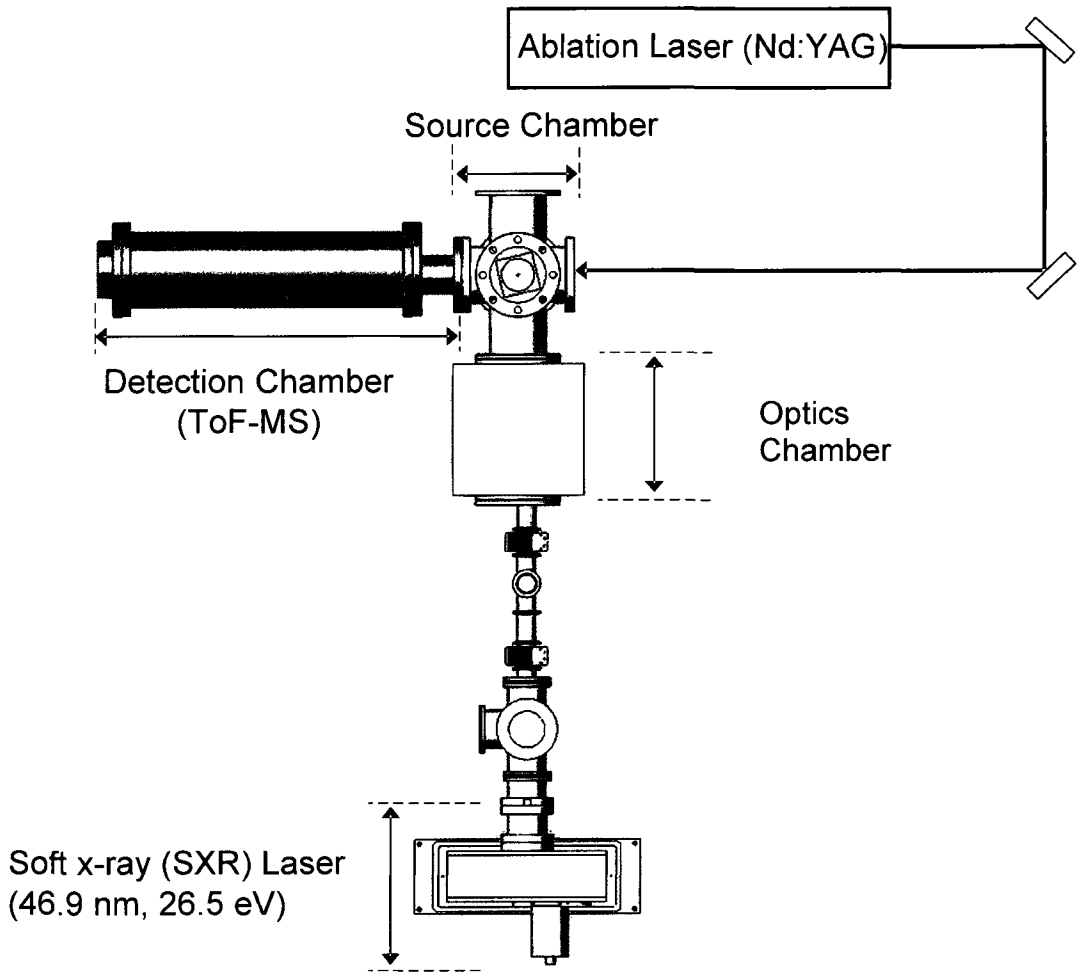


Figure 2.2: Schematic top view of the experimental setup. It comprises a source , detection, and a z-fold chamber. The ablation laser light path is also sketched. The 2nd harmonic output beam generated by a Nd-YAG laser is used for material ablation. In all measurements the output beam of the SXR laser system ionizes the molecules for the mass spectrometric detection.

region of the ToF-MS. The ablation laser beam propagates perpendicular to the ionization beam. In the top port (ASA-9), the vaporization source is connected to the pulsed gas nozzle, leaving the bottom port (ASA-11) to mount a 1000 L/min Seiko Seiki

turbomolecular pump to evacuate the chamber. The remaining two ports are both 8" CF flanges. One is left blank for future use as either another electrical or gas feedthrough, or to mount a photoelectron spectrometer and the remaining 8" CF connects the "detection" chamber or the ToF-MS.

2.1.2 Detection Chamber

The detection chamber has 3-ports other than the one connected to the source chamber. The smallest port, with a 2¾" CF flange, is located at the top side of the chamber and hosts a vacuum gauge. Located at the opposing side a second port ends with an 8" CF flange and is used to support another 1000 L/min Seiko Seiki turbomolecular pump. The remaining port is terminated with a 6" CF flange. It is used to fasten the detection chamber to a mass gate for removing unwanted ions from the mass spectrum. The detection chamber also houses a reflectron and two micro-channel plate (MCP) ion detectors, as described below.

2.1.3 Optics Chamber

The optics chamber is a 14" cube that has only two ports that are placed coaxially on opposite walls. One side connects the SXR laser via an ASA-9 flange to the input of the z-fold mirror setup while the output is connected to the source chamber. This chamber contains a gold-coated torodial mirror and planar mirror that are placed in a grazing incidence, Z-fold configuration just before the ionization region of the ToF-MS to provide alignment and focusing capabilities for the SXR laser with respect to the molecular beam at the ionization region. The mirrors are controlled using picomotors that may be moved while under vacuum with an external controller to allow us to adjust the ionization laser alignment while observing the mass spectrum. The transmissivity of the

mirror system is about 60%. The SXR laser light is loosely focused in the ionization region to avoid multiphoton ionization and a space charge Coulomb effect due to He^+ ions. The top and bottom of the chamber may be removed for easy access to the mirrors and motors for maintenance.

2.2 THE MOLECULAR BEAM APPARATUS

Since the 1920's[2.12] atomic and molecular beams have been used in spectroscopic investigations. These beams are also termed "effusive" beams[2.13] when the constituent particles act as individuals with the number of collisions reduced almost to zero. A collision-less beam of molecules is obtained if the orifice size is small enough such that $D << \lambda_0$, where D is the diameter of the circular orifice and λ_0 is the collision mean free path of the gas at pressure P_b, which is the backing pressure of the gas reservoir.[2.14] In 1951 Kantrowitz and Grey published a theoretical description of a proposed supersonic jet as a molecular beam source.[2.15] While their original goal was to increase the beam intensity, they noted that their source would produce a cooling of the translational and internal degrees of freedom of the molecules in the beam. The main feature of Kantrowitz and Grey's proposal was the reversal of the inequality noted above with respect to the nozzle diameter and the mean free path. If $D >> \lambda_0$, there could be many collisions as the gas flows through the orifice and through the expansion region downstream from the orifice. When a gas expands from a high-pressure tank through a properly designed orifice into a low-pressure chamber, a supersonic jet emerges in which most of the thermal energy has been converted into directed mass flow. Most of the random molecular motion is lost, the gas is cooled and one can define a temperature T to describe the remaining "randomness" in the translational temperature. Collisions within the jet

also convert energy from rotation and vibrational degrees of freedom, thereby cooling them. Generally this cooling is less than the translational cooling. Eventually the gas collides with the walls of the chamber or room temperature background gas molecules and warms up. In the brief period before this happens, we have a gas phase sample supercooled far below the condensation temperature.

Other thermodynamic quantities are affected by this process, for example, the classical speed of sound, c, defined as

$$c = \left(\frac{\gamma \cdot K_B \cdot T}{m} \right)^{1/2} \tag{2.1}$$

where $\gamma = C_p/C_v$ is the heat capacity ratio, K_B is the Boltzmann constant, T is temperature, and m is the particle mass. Since c is proportional to $T^{1/2}$, the local speed of sound decreases during the expansion process, and the Mach number (M = u/c, u is the molecular velocity) increases. In an ideal expansion M=1 for the most constricted point in the nozzle, but with additional expansion M can become greater than one.[2.14] If M > 1, the supersonic flow regime is reached, and it is this regime in which our present apparatus functions. The gas behaves as a continuous liquid in which its molecular characteristics are suppressed because no significant changes in its properties occur over a mean free path. By definition a flowing gas is in thermodynamic equilibrium, or quasi-equilibrium if its instantaneous properties deviate only slightly, or slowly from what one would expect if it were actually in equilibrium. [2.16]

A supersonic jet expansion consists of four stages: (1) continuum flow near the nozzle, (2) transition between continuum and molecular flow, (3) molecular flow, and (4) rewarming in the chamber via collisions with background gas or chamber walls.

During continuum flow, the behavior of the jet is governed by the laws of hydrodynamics, and almost all of the cooling occurs in this stage. Molecules upstream collide with and accelerate those downstream. A good analogy is to imagine a piston being pushed by the gas molecules. Through collisions, the piston travels downstream and is accelerated. The random molecular motion that determines the temperature decreases continuously as the piston moves downstream. The piston is accelerated at the expense of random motion in a reversible, adiabatic, and hence, isentropic expansion. An isentropic flow is a flow that is both adiabatic and reversible. That is, no energy is added to the flow, and no energy losses occur due to friction or dissipative effects. At first, the idea of an isentropic expansion may seem incorrect. This idea only holds true in the region of continuum flow. When the continuum flow transitions to molecular flow, the density becomes so low that collisions are infrequent and free expansion (irreversible) occurs. For an isentropic flow of a perfect gas, several relations can be derived to define the pressure, density and temperature along a streamline.

In practice, a jet of a carrier (buffer) gas is seeded with vapor of a substance under study. Cooling of the sample occurs by way of collisions with the carrier. In the continuum flow stage, the work done by the gas equals the decrease in gas enthalpy, H, as derived from an isentropic expansion. Thus,

$$\frac{1}{2}u^2 = \Delta H = \left[\frac{\gamma r}{(\gamma - 1)}\right](T_0 - T) \tag{2.2}$$

where H is the enthalpy per unit mass and r is the gas constant per unit mass, and u is molecular flow velocity. This can easily be rearranged with the help of equation 2.1 to derive expression for temperature, pressure, and particle density as a function of the Mach number M at any point in the continuum region:

$$\frac{T}{T_0} = \left(1 + \left[\left(\frac{\gamma - 1}{2}\right)M^2\right]\right)^{-1} \tag{2.3a}$$

$$\frac{P}{P_0} = \left(1 + \left[\left(\frac{\gamma - 1}{2}\right)M^2\right]\right)^{-\gamma(\gamma-1)} \tag{2.3b}$$

$$\frac{n}{n_0} = \left(1 + \left[\left(\frac{\gamma - 1}{2}\right)M^2\right]\right)^{-\frac{1}{(\gamma-1)}} \quad \text{(n is particle density)} \tag{2.3c}$$

In 1964, Ashkenas and Sherman developed an expression for M as a function of the distance X downstream from the nozzle.[2.17] It can be shown that for a monatomic gas (γ = 5/3) in the continuum region that:

$$M = 3.26X^{2/3} \tag{2.4}$$

X is measured in units of the nozzle diameter. Equations 2.3 and 2.4 can be used to profile the expansion throughout the continuum region.

Following the work of Anderson and Fenn[2.18], it can be shown that the transition point from continuum to molecular flow is determined by,

$$X_{tr} = 0.238(\varepsilon / Kn_0)^{3/5} \tag{2.5}$$

where ε is a collision effectiveness parameter and the Knudsen number Kn_0 is given by,

$$Kn_0 = \frac{\lambda_0}{D} = \frac{(3.07 \times 10^{-23})T_0}{d^2 P_0 D} \tag{2.6}$$

in which d is the gas collision diameter. Continuum flow terminates abruptly in a shockwave (Mach disk) whose thickness corresponds to several mean free paths at pressure P_D in the chamber. The Mach disk is found at a distance,

$$X_{MD} = 0.77(P_0 / P_D)^{1/2} \tag{2.7}$$

from the nozzle. In our experiments, we evacuate the chamber with high speed pumps to reduce P_D and thereby move the Mach disk as far downstream as possible.

Cooling continues in the molecular flow stage, but at a much slower rate since the gas now consists of individual atoms, not a continuous fluid. The Mach number reaches a limiting value of,

$$M_{\lim} = 2.05(\varepsilon/Kn_0)^{2/5} \tag{2.8}$$

Using this quantity, the limiting flow velocity can be found from equation 2.2 and a corresponding limiting temperature is found from equation 2.1.

The core of the expansion (the so-called "zone of silence") is the active region for downstream experiments. Skimmers are frequently employed to separate the cold core of the beam from the hot shock wave which defines the outer envelope of the expansion. In our case a conical skimmer with a 2-5 mm diameter orifice separates the ionization region of the ToF-MS and detection chambers, where the ionization region remains at a hundred times lower pressure than the detection chamber. In a conically skimmed beam, the molecular flow regime dominates, thereby minimizing multi-body collisions.[2.19]

2.2.1 Pulsed Valve

A pulsed molecular beam source (C-12 PSV Pulsed Supersonic Valve from R.M. Jordan Company) which is capable of providing a 55 microsecond pulse of gas at choked flow at 10 Hz repetition rate is the basis of our source setup.[2.20] This is defined as the condition in which beam pressure is limited only by the conductance of the nozzle, maximum flow is occurring, and the full theoretical cooling has been obtained. This condition is evidenced by a flat topped pulse when measured with the FIG (fast ion gage, Fig. 2.3).

Pulse widths as narrow as 20 microseconds can be obtained if maximum flow is not required.

The PSV Pulsed Supersonic Molecular Beam Valve operates on the magnetic beam repulsion principle, first applied to molecular beam valves by Dimov.[2.21] The PSV design passes a current pulse of up to 5000 Amps and 20 microseconds pulse duration

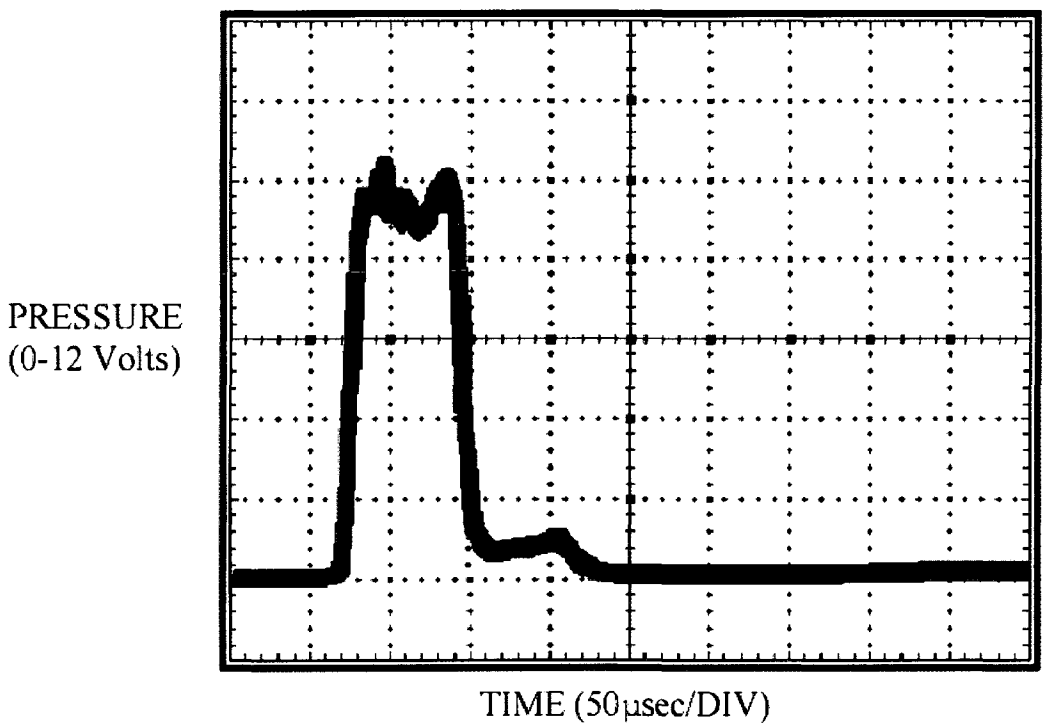


Figure 2.3: Fast Ionization Gage Pressure-Time Curve Sample Pressure: 1.0 Atm. He, Nozzle Diameter: 0.5mm Valve Current: 5,000 Amps (well above choke flow) Gage Distance From Nozzle: 5.0 cm. (This figure is reproduced from the R.M. Jordan product manual in reference 2.17.)

through two parallel beam conductors in a hairpin configuration. The high current passing in opposite directions in adjacent conductors generates a magnetic force which lifts the top beam from an O-ring seal over the nozzle and opens the valve. This admits carrier gas to a supersonic free expansion nozzle which injects molecular beam pulses of approximately 60 μs pulse length into the sample vacuum chamber.

A pulse driver system (PSV Power Supply[2.20]) controls the valve opening and shut off. This unit can be triggered both internally and externally (also in single shot mode) via a TTL pulse that is +2.5-12 V with a pulse width of 1-100 μs. The delay between triggering and effective opening of the valve can be adjusted.

2.2.2 Laser Vaporization

2.2.2.1 Ablation and plume characteristics

According to Smalley[2.21], a metal vapor stream for cluster studies can be created by vaporizing a solid material sample with a laser. Laser irradiation initiates a sequence of events which extend up to a few microseconds after the short laser pulse. During the interaction between an incident laser beam pulse and a metal target, part of the laser beam energy is reflected back and part is absorbed within a short penetration depth, by the metal (see Fig. 2.4(A-B). As a result of the surface absorption, the metal heats and transiently changes phase to both liquid (melting) and vapor (sublimation/evaporation), as illustrated in Fig. 2.4(B-C). The generated vapor may consist of neutrals, excited species, and dissociated and ionized atoms or molecules and free electrons, thus creating a high density plasma which absorbs part of the energy of the incident laser beam by inverse Bremsstrahlung (Fig. 2.4(C-D)). This causes the plasma temperature to rise with the free electrons acquiring sufficient energy to efficiently ionize atoms and ions by collisional ionization. Thereby the degree of ionization of the vapor is also increased, with further absorption of the trailing part of the laser beam. The plasma behaves like a thick medium providing a progressive shielding of the target surface from the laser beam. Once the high temperature plasma is formed above the target surface, its energy is transferred away via radiative exchanges with the target material/ambient surroundings

and by the acceleration of the vapor to hypersonic velocities by pressure gradients. The hot plasma transfers energy to the target via electron heat conduction, in addition to a combination of the following two mechanisms:[2.22]

- Short-wavelength thermal plasma radiation absorbed by the target surface;
- Phase change of the vapor which condenses due to the plasma pressure at the interface with the target where the plasma becomes sufficiently cold.

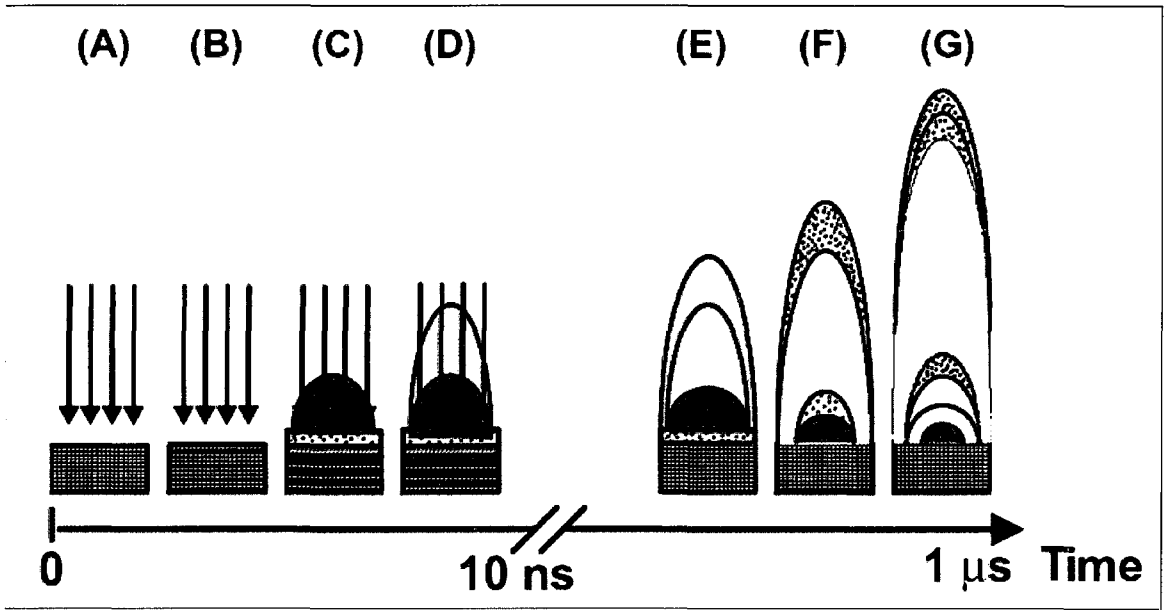


Figure 2.4: Plasma plume development and material detachment produced by a nanosecond laser pulse. The process extends well after the short time during which the laser beam illuminates the material surface.

This underlines the plasma's key role in the context of this thermal coupling, when its inner mechanisms are not yet fully unveiled. The complexity of the laser-plasma-target interactions accounts for additional heat flux contributions to the target surface which, at specific moments, might exceed the laser light due to the plasma absorption (see Fig. 2.4(D-E)). Thus, the combination of the adiabatic expansion of the saturated gas and the heat transfer at the contact surface between the plume and ambient leads to a very rapid cooling (as shown in Fig. 2.4(F-G)).

The ablation process in general can be described as a combination of thermal and non-thermal effects. For thermal ablation one assumes that all energy is transferred into heat and that the material cannot dissipate the absorbed energy by heat conductivity because of the short pulse duration (~ 10 ns) and local heating occurs. The non-thermal contribution would include photo-absorption in the ablated material and fragmentation via dissociative channels. Reaching several hundreds of MW/cm^2 of ablation energy, ionization of the ablated material becomes dominant and a plasma plume is generated above the ablated surface.[2.25] Ionization of the plume additionally results from a combination of laser induced ionization and secondary ionization from highly energetic electrons in the plasma. The electrons gain kinetic energy due to the inverse Bremsstrahlung effect and therefore increase their ionizing cross section. This means that as long as the ion density of the plasma increases, the plasma plume absorption of the ablation laser light is enhanced.

Finally, no direct radiation reaches the material surface and only secondary radiation hits the metal surface; however, the optimal laser intensity used in our experiment is below the plasma breakdown threshold of most gases, and the ionization degree of the plume is expected to be sufficiently characterized by taking into account the thermal balance.[2.26] The ionization state of a *sufficiently dense* plasma may be approximated by using the density corrected 'Saha' equation:[2.27]

$$\frac{n^{i+}}{n^{(i-1)+}} \approx 2\frac{\sqrt{(2\pi m_e k)^3}}{h^3}\frac{T_e^{3/2}}{n_e}e^{\left(\frac{-E_{ion}^{i+}}{kT_e}\right)} \tag{2.9}$$

where n^{i+} is the number density of i'th ionization state of the ablated material, n_e is the number density of electrons, T_e is the temperature of the plasma, and E_{ion}^{i+} is the

ionization energy for the i'th ion state of the ablated material. The highest ionization degree is expected at the highest plasma temperature, which is expected to be at the end of the laser pulse.[2.23] At low density and high temperatures, one can determine the ionization state using the corona model where radiative processes dominate. Similarly, one can use a collisional radiative model to bridge the gap between the conditions in which the Saha approximation holds, and the conditions where the corona model can be used.

We have favorable conditions for the homogeneous nucleation of the vapor, according to classical condensation theory, if the time for the cooling process is much shorter then the time needed for the condensation.

The saturation ratio $S= p_v/p_s$, namely the ratio between the actual vapor pressure and the saturation pressure for a given temperature, tends to assume high values with the cooling. The free energy of formation of a condensate is determined from a balance between bulk solid cohesive forces, liquid cohesive energy, and surface energy (tension). Its impact on the proceeding of the homogeneous nucleation can be noticed in the equation for the free energy, ΔG, of a spherical condensed cluster of radius r:[2.23]

$$\Delta G = -\frac{4}{3}\pi r^3 N\Delta\mu + 4\pi r^2\sigma \qquad (2.10)$$

in which $\Delta\mu = k_b T \ln(S)$ is the chemical potential difference between condensed and uncondensed atoms, k_b and T being the Boltzmann constant and the vapor temperature, respectively, N is the atom density, and σ is the surface tension. The velocity distributions of ablated particles are expressed in terms of a Maxwell-Boltzmann distribution function for a stream velocity, u, directed along the z axis:[2.24]

$$dN(\vec{v},T,u)=\left(\frac{m}{2\pi k_b T}\right)e^{\left(-\frac{m\left(v_x^2+v_y^2+(v_z-u)^2\right)}{2k_bT}\right)dv_x dv_y dv_z} \tag{2.11}$$

where m denotes the particle mass, and υ_x, υ_y and υ_z are the components of the velocity $\vec{v}$ in the corresponding Cartesian directions.

This section presents a general description of the ablation process and formation of ablated particles (clusters). More detail can be found in the literature.

2.2.2.2 Ablation Laser

The 2nd harmonic output beam of a Spectra Physics Nd:YAG laser, DCR-11, operating at a repetition rate matched to the SXR laser (usually 1-3 Hz, but has been run up to 10 Hz), is used for the material ablation. When used in Q-switched mode, the rep. rate of the Nd:YAG laser is driven externally via positive TTL pulsed signals given as input to the flash lamp, and the Q-switch high voltage pulser. The delay between the rising edge of the lamp and Q-switch pulses must be ~ 260 ns to obtain the maximum output power.

While the DCR-11 is capable of producing over 150 mJ per 8-10 ns pulse at 532 nm, the pulse energy required to start the detachment of the material via ablation is typically smaller. Excess energy may manifest itself in an increased kinetic energy of the ablated atoms. The formation of weakly bonded molecules is then hampered. For extra control of the ablation pulse energy for different metal targets, a beam attenuator may be used. With the attenuator, the laser pulse energy impinging on the rod could be varied below 30% of the maximum output energy per pulse. The laser beam exhibits a uniform round shape with diameter of roughly 8 - 9 mm diameter.

2.2.2.3 Ablation Setup

A schematic of a laser ablation setup that produces metal vapor plumes with acceptable reproducibility is illustrated in Fig. 2.5. To avoid the crater, formed by laser interaction, digging deeper into the material from shot to shot, thereby changing the shape of the plume of ejected material, a fresh portion of the surface has to be used for every laser light pulse. This can be achieved using a disc of the material under investigation that rotates and translates up or down along a threaded rod. A schematic drawing of the design we adopted for the vaporization source is shown in Fig. 2.6. Our goal was to realize a versatile source that could be easily modified. The source is placed

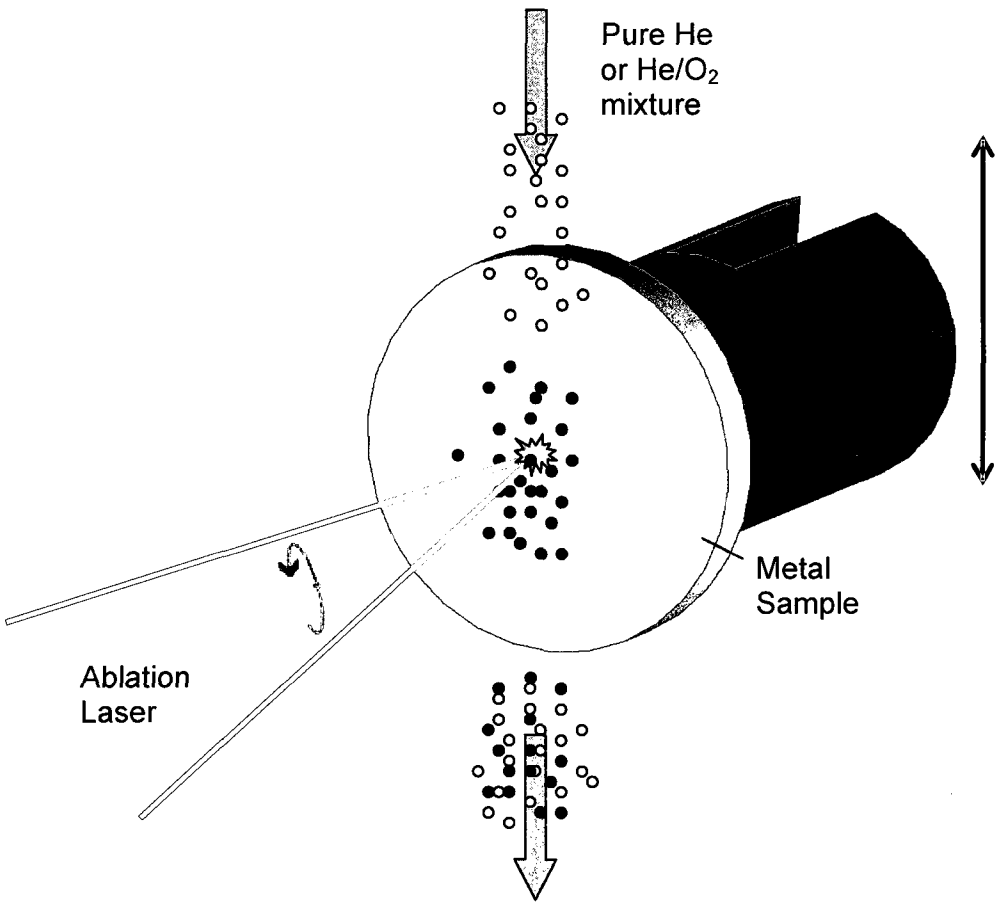


Figure 2.5: A focused laser beam impinges on a metal disc that revolves around its cylindrical symmetry axis and translates up and down perpendicular to this axis. The plume formed is entrained in a noble gas pulse, optionally mixed with oxygen donor molecules.

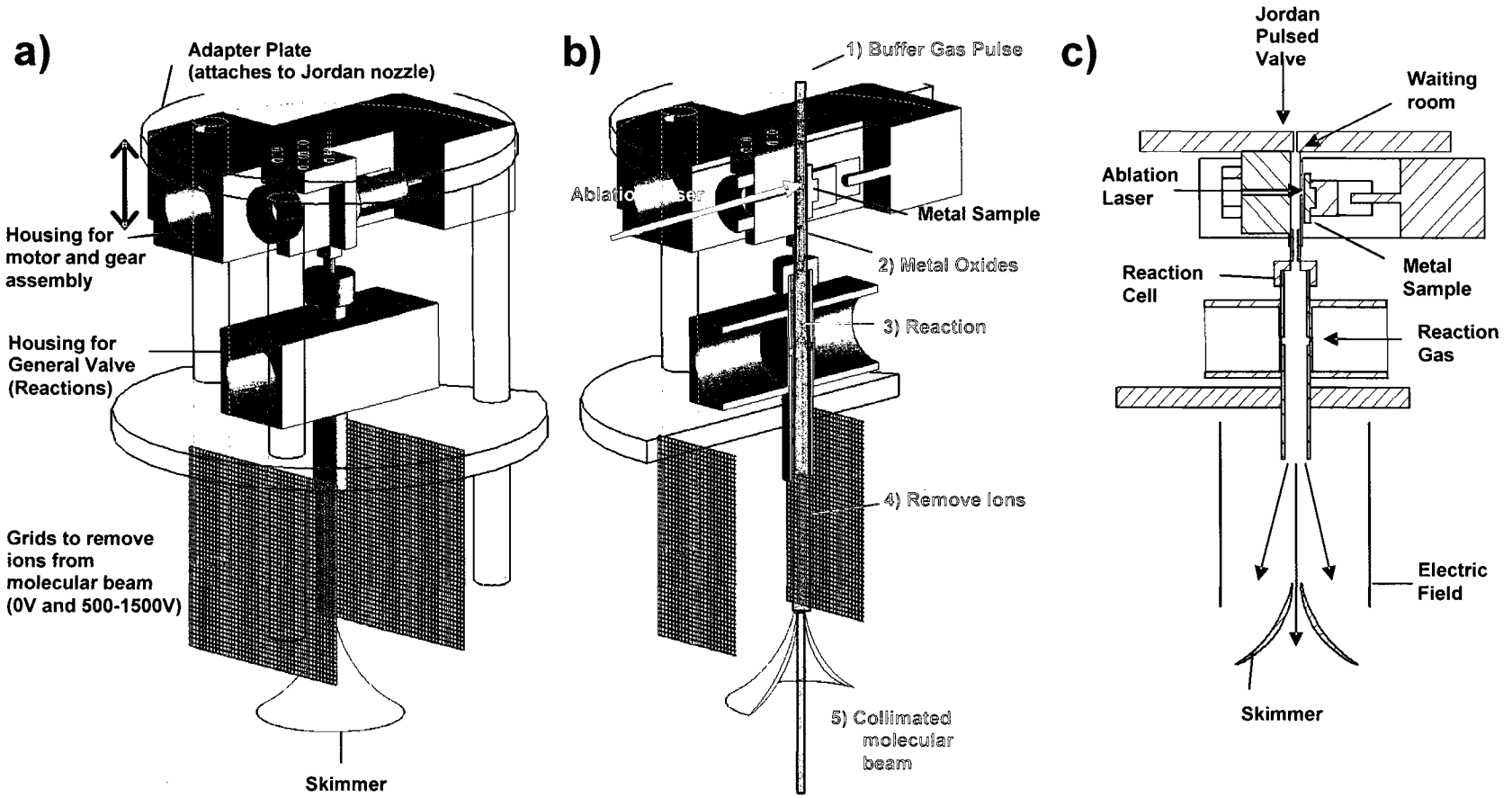


Figure 2.6: (a) Full view of nozzle apparatus. (b) Cutaway of the nozzle apparatus to show how the molecular beam evolves from the buffer gas pulse of the Jordan valve, to a collimated molecular beam after the skimmer. (c) Crossection view of the nozzle apparatus. The gas pulse starts in the Jordan valve and then passes into the vaporization source gas channel. Upon entering the vaporization source, the buffer gas jet (He or He/O_2 mixture), immediately encounters the material that has been ablated from the metal sample in the system, and the buffer and metal vapor are mixed in a waiting room. The metal oxide sample now passes into the reaction cell. The experimenter has the option to input a reaction gas or study the metal oxide distribution. The beam passes through an electric field that is intended to remove the unwanted ions from the molecular beam and is finally collimated by the skimmer.

within a vacuum chamber where a pulsed laser is used to ablate material from the target surface of a disc. The disc moves in vacuum and is pressed against a stainless steel block containing bores in a way that the plume of ablated material is confined within a 2 mm diameter bore from where it is blown out into vacuum by a carrier gas.

In typical operation the disc movements are continuous so that the laser light impinging on its surface hits a different spot on every shot. The disc is actuated by a DC motor (Maxon) that has negligible outgassing. It is installed within the vacuum environment, with a tubular motor holder and gear assembly that both rotates the target and moves the assembly up and down, as shown in Fig. 2.6. We wanted to avoid an external motor and a rotary feedthrough to move the metal target inside the vacuum vessel. The mini-motor is coaxially mounted with the sample rod.

A three dimensional drawing, with a cutaway showing the cross section of the source, is depicted in Fig. 2.6(a-c). The adapter plate of the vaporization source, the motor holder, the reaction cell, the electric field grids to remove ions, and the skimmer, all marked in the sketch. In sketches (b) and (c) of Fig. 2.6, an isometric cutaway and a side crossection view of the vaporization source mid sections are shown respectively. Figure 2.6(a) shows the source in a full view with no cuts taken. A block is fastened to the adapter plate that contains a channel for the ablation laser. Perpendicular to this channel, a hole is collinear with the one of the Jordan valve. This bore extends the path of the gas introduced by the valve, and we sometimes refer to it as the "gas channel". The 0.5 mm diameter output of the Jordan valve is surrounded by a 3 mm hole that connects the vaporization source and the valve. Hence the gas expanding from the valve can only flow into vacuum through the gas channel of the vaporization source with negligible

escape. Upon entering the vaporization source, the buffer gas jet (He or He/O_2 mixture), immediately encounters the material that has been ablated from the metal sample in the system, and the buffer and metal vapor are mixed in a so-called "waiting room". The gas jet now contains the metal oxide or pure metal sample that the experimenter would like to study.

The metal oxide sample now passes through a 2 mm passageway into the reaction cell. The experimenter has the option to input a reaction gas or study the metal oxide distribution. The reaction gas may be input through a 1 mm hole by way of a General Valve whose pulse strength, length and timing are adjusted manually by an external trigger. Following the reaction cell the beam passes through an electric field that is intended to remove the unwanted ions from the molecular beam. The electric field is realized between two stainless steel grids, one is held at ground potential while the other is varied between ~ 300-1500 V depending on how many ions are being produced. The voltage is adjusted while monitoring the signal on an oscilloscope until the ion signal becomes very week or disappears completely. The remaining neutral cluster beam is then skimmed by a 2-5 mm diameter skimmer.

The assembled ablation source is placed on the front of the pulsed nozzle of the valve as shown in Fig. 2.6. The valve is fastened to a metal assembly protruding into the vacuum chamber from its top flange. The assembly comprises several parts forming a vacuum tight "arm" of adjustable-length. The vaporization source, positioned at one extremity of the arm, is introduced into the vacuum chamber to fit the geometry defined by the ablation laser beam and the mass spectrometer. The top flange contains many bolts and adjustable parameters that provide a way to change the vaporization source

placement within the chamber. The length of the assembly is chosen according to the required distance between the output of the ablation source and the skimmer. When the source chamber is open for servicing the apparatus, one can temporarily remove the metal disc to adjust the ablation laser. The focused laser light of the laser then entered the chamber from one side port to exit from an opposing opening, after having passed through the laser channel in the vaporization source.

2.3 TIME-OF-FLIGHT MASS SPECTROMETRY

Time-of-flight mass spectrometry (ToF-MS) is a well established technique for determining ions masses and their relative concentrations. Introduced by Cameron and Eggers in 1948[2.28], ToF-MS begins with gas-phase ion formation and then involves ion acceleration through an electric field into a field-free drift region. The acceleration voltage, giving all ions the same kinetic energy, propels the ions at different velocities based on their specific mass-to-charge (normally singly charged species are produced) ratios. Subsequently, the ions are allowed to drift in a field free region where they separate spatially as a function of their individual kinetic energies. Lighter ions move faster than heavier ions. Following ion detection, "peaks" representing ion-packets each having the same mass comprise the mass spectrum, and the time needed to travel the length of the drift region (the "time-of flight") can be related to the mass of the ion.

2.3.1 Jordan Re-ToF-MS: Dimensions and arrangement

Measurements are performed on a Jordan angular reflectron ToF-MS (model D-850[2.29]), assembled with a laser ionization chamber. The Re-ToF-MS, oriented orthogonally to the molecular beam from the vaporization source, is operated in positive-ion detection mode, with polarities chosen accordingly for ion extraction (positive extraction voltage),

acceleration and detection (negative bias). The mass spectrometer design allows for either linear mode or reflectron mode operation. In the first case, detection occurs through the inactive reflectron with a Microchannel Plate (MCP) detector placed behind it.

The second operation mode, with the reflectron on, is characterized by ions flying back (refocusing) in the flight tube toward their starting position, where they are detected by a MCP mounted slightly off-axis in order not to obstruct the path of incoming ions. Overall, the instrument can be considered a system of several regions, the ionization stage, the focusing ion lens and mass gate, the free field flight tube, the reflectron, and ion detectors. The Jordan Re-ToF-MS is schematically represented in Fig. 2.7 with the electrode voltages and relative distances indicated. The actual values for electrode distances are noted in Table 2.1. A ion flight length of ~ 1.8 m is expected[2.30] for this type of mass spectrometer in reflectron mode.

The design employed by R.M. Jordan Co. is based on the original suggestions of Wiley and McLaren.[2.31] In this design, the ion flight time is relatively insensitive to the exact point of ion formation in the extraction region. This technique, called "space focusing" allows high mass resolution and relative simplicity of construction.[2.32] The readers, interested in the mathematics behind the space-focusing criterion, are referred to the review by Guilhaus.[2.33]The optimum operating voltages for the experiments were provided and designed by R.M. Jordan company. In our experience, these voltages could be used in all of our ion detection experiments with only small tweaks. The voltages themselves were provided by an AREF Time of Flight Power Supply also provided by Jordan. The (AREF) Angular Reflectron Power Supply is designed to be a single compact source for the voltages used in a typical angular reflectron spectrometer. Choice

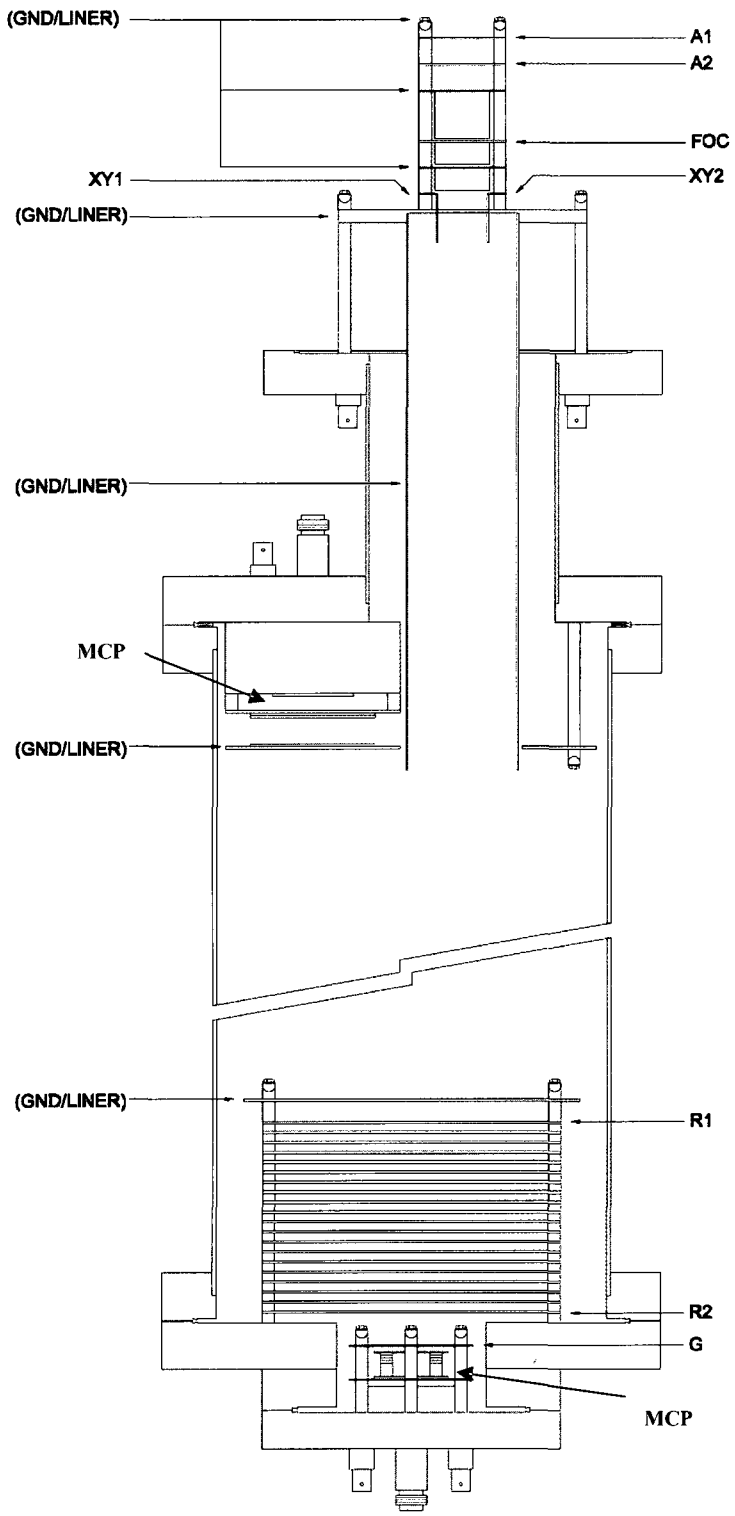


Figure 2.7: A sketch of the ToF-MS (Jordan D-850 AREF assembly). Schematic taken from the manual of the Jordan model we used. The associated potentials are designated by symbols used in the text.

of this unit reduces instrument clutter in the immediate vicinity of the experiment. All voltages are monitored by the same meter. A voltage is only displayed while its monitor button is held down. Each end of every cable is labeled to match the receptacle to which it connects. Note that FOC (Einsel Lens) is not equipped in our ToF-MS.

Table 2.1: Mass spectrometer potentials. Nomenclature refers to Figure 2.7

Parameter	VA_1	VA_2	Vxy	VR_1	VR_2
Linear Voltage	4000 V	3750 V	Adjusted for max signal (50-200V)	GND	GND
Reflectron Voltage	1000 V	700 V	Adjusted for max signal (50-200V)	700 V	1200 V

2.3.1.1 Vacuum System

A vacuum of ~10^{-7} mTorr, and that of ~10^{-5} mTorr while operating the molecular beam source, is achieved by a two-pump system. A Seiko Seiki turbo-molecular pump (STP-H1000C, 1000 l/s pumping speed), connected to the main source chamber through its bottom port (ASA-11), is used in conjunction with a Leybold Trivac D25-BCS fore pump. The rotor of the pump is separated from the volume of the source chamber by a gasket and a metallic grid. The second turbo pump (Seiko Seiki, STP-H1000C) is attached to a port devised in the drift tube of the mass spectrometer (Jordan, Sideport Tee C-687). The turbo pump is connected to another mechanical Leybold Trivac D25-BCS fore-pump. Flexible metal tubes KF40 and KF25 are used to connect the turbo pumps and their mechanical roughing pumps. Both fore pumps are provided with an oil mist eliminator stage to trap exhausted oil from the pump and return it back. Each turbo pump is driven by a Seiko Seiki STP controller that can adjust the turning speed of the pump rotor according to the torque it experiences. Vacuum pressure is monitored in detection

chamber by a combination of TC and ionization gauges which provide full range coverage which covers the entire range from 10^{-3} mTorr down to 10^{-8} mTorr. During measurements, the flight tube pressure is maintained between $1x10^{-6}$ mTorr and $1.5x10^{-5}$ mTorr. The base pressure with no gas load is typically 10^{-7} mTorr for the detection chamber.

The ionization or interaction region of the Jordan mass spectrometer is defined by two plates, a "repeller" and an extraction grid. After extraction, an ion is accelerated by a field established between the extraction grid and another electrode, the accelerator plate.

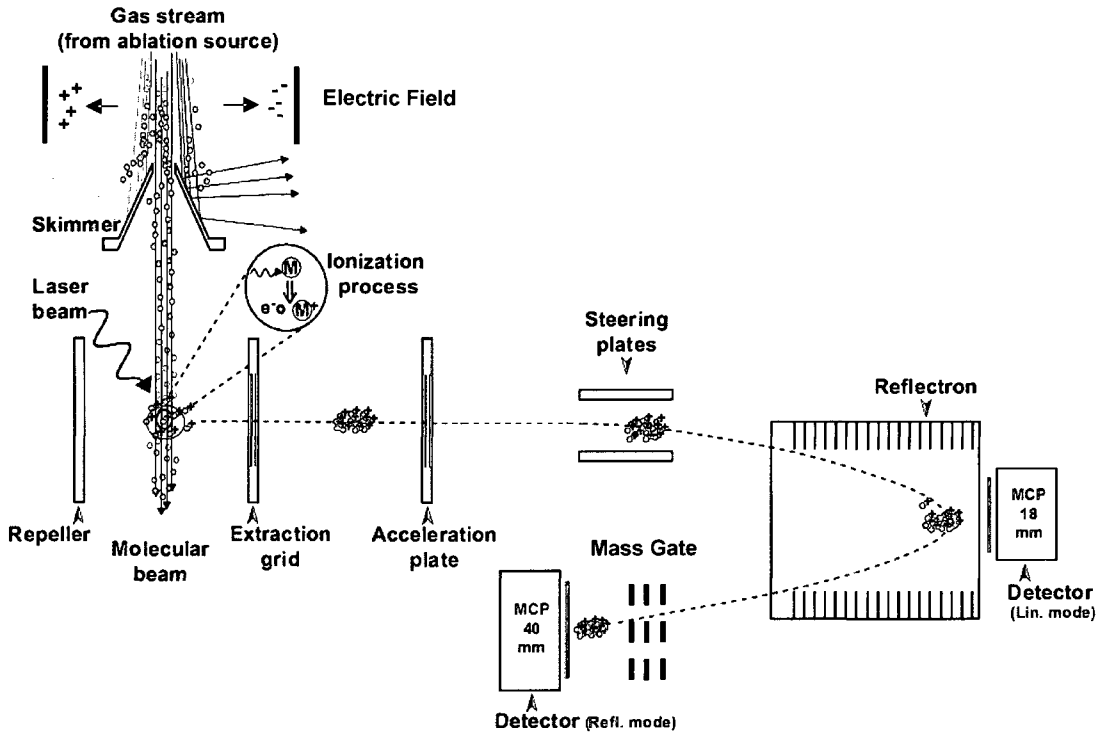


Figure 2.8: The molecular beam produced by the ablation source is skimmed to select the central part within a small solid angle. Finally the remaining beam reaches the ionization stage of the mass spectrometer where it crosses, transversely, a focused laser beam. The laser ionizes the molecules dispersed in the molecular beam. Emerging ions are accelerated by the DC voltage difference applied across the repeller and extraction grid. A second stage (acceleration stage), where another field is applied and propels the ions further away towards the drift region, where no field is present. Ions with higher masses take more time to reach the detector.

A sketch which illustrates all stages of ion mass detection, from ion formation and extraction to its detection, is shown in Fig. 2.8.

A thick gold-plated copper shroud encloses the ionization space (see Fig. 2.9), which allows an efficient differential pumping. The molecular beam enters through a skimmer between the ion extraction plates where the ionization laser beam strikes the molecules orthogonally. After ion formation, the static positive extraction voltage difference propels ions out of the ionization region and transmits them through the extraction grid (Ni mesh) into the acceleration region. The acceleration plate is set to a constant bias (0 V) which accelerates ions into the drift tube and maintains the field free requirement of the drift tube.

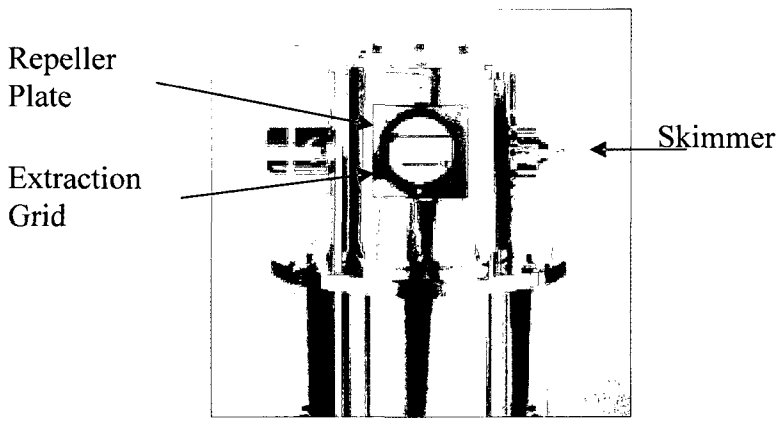


Figure 2.9: Photograph of the ionization region of the mass spectrometer from Jordan. A Ni skimmer is installed on a shroud enclosing the dual-stage ionization and acceleration section of the ToF-MS.

2.3.1.2 Ion deflection and mass cutoff

Steering plates are located at the entrance of the field free flight tube. They are used to reject a range of ion masses from the mass spectrum by deflecting their trajectories. They can also be used to compensate for transversal speed components that could cause the ions to drift away from the axis of the flight tube. The presence of ions with low masses potentially represents an obstacle in detecting higher masses with less abundance. In

particular, if the electrical pulse generated at the MCP exceeds the maximum current sustainable from the MCP (nominally 400 μA), the signal saturates the device and makes it relatively insensitive to subsequent masses arriving within a short time interval. Potentially, mass selection among the detectable ions is achieved by applying a pulsed voltage across the steering plates. The steering plate can be switched on for the time during which unwanted masses pass along it, and they are then kicked off the trajectories reaching the detector. However, this technique only allows for a range of masses to effectively be removed from the mass spectrum. To achieve single mass unit removal, a different technique must be used. Note too that all the ions are bundled together at the entrance to the flight tube where the steering plates are placed.

Alternatively, the detector itself, the MCP, can be switched on and off. This option works well enough with the one drawback being that the ions still impinge on the surface of the detector, even if it is not on. This raises questions of whether or not disturbances viewed in the mass spectrum are a result of the response of the MCP's when a large amount of ions are present on the surface (creating a large current) and then the detector is pulsed on. In order to answer these questions, we retrofitted our ToF-MS with a home made mass gate that allows us to apply a stopping potential that blocks ions from reaching the detector with single mass resolution.

A driver, providing a 1500 V pulse with a rise and fall time of < 25 ns and minimum pulse width of 60 ns, is used to set the mass gate off. The pulse generator is commercially available from DEI (PVM-4140) and can provide switching voltages adjustable between -3000 V and +3000 V. The 1500 V pulse is used to overcome the kinetic energy of the ions coming from the reflectron grid set at 1200 V. Voltage is applied to the middle grid

of a stack of three. The outside two grids are held at ground potential in order to respect the field free region of the mass spectrometer. The pulse width can be adjusted to exclude a single mass, up to the entire mass spectrum if so desired. A schematic of the device is shown in Fig. 2.10.

2.3.1.3 Reflectron

The Jordan ToF spectrometer comprises a dual stage reflectron which is shown schematically in Fig. 2.7. This is composed of an entry grid which is normally at ground

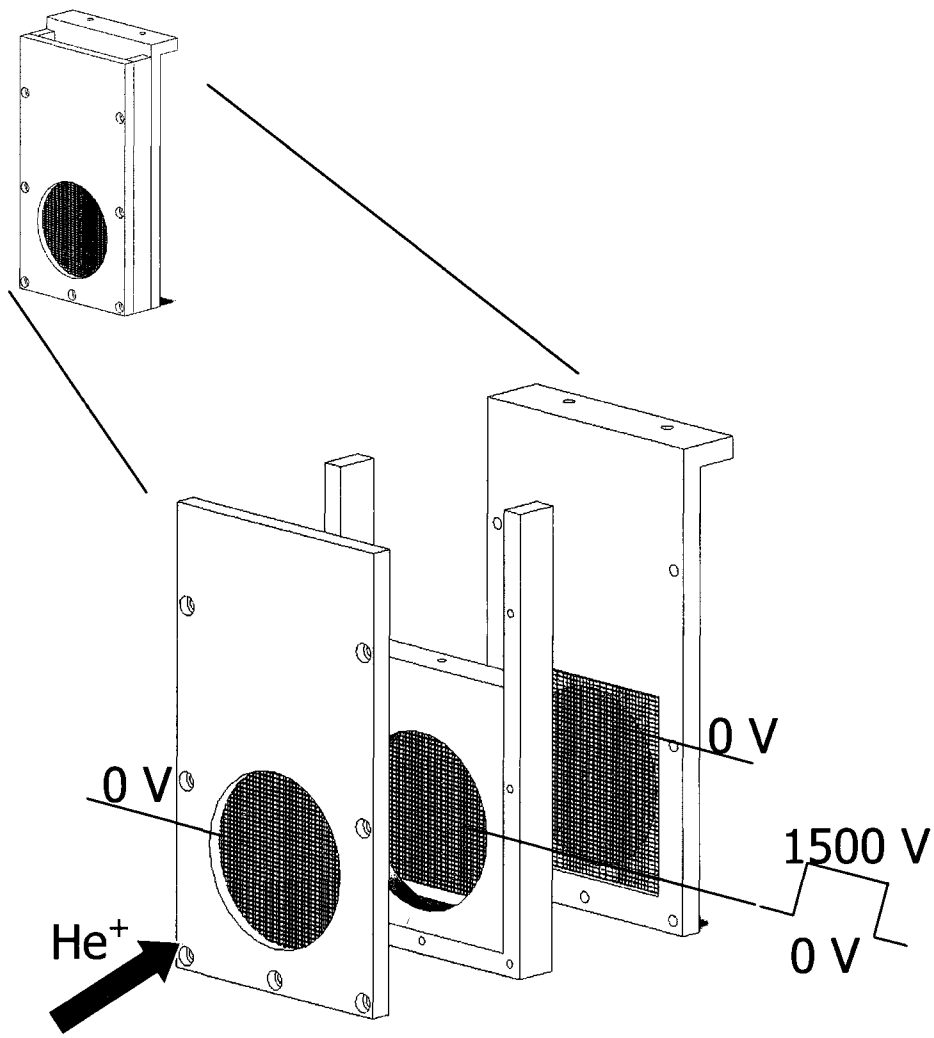


Figure 2.10: Schematic representation of our home made mass gate. A voltage pulse of 1500 V is applied to middle grid in a stack of three. The voltage, when applied, stops ions from passing through to the detector and can be selected to block a single mass or a range of masses.

or flight tube potential. Behind is a grid, followed by a set of several plates equally spaced. Contiguous plates are not isolated but a high impedance of 1MΩ between each pair of them exists (due to this high resistance, the reflectron stack may not be pulsed). Only the voltages of the entrance and exit plates of the reflectron must be set to give a uniform repelling field. In Fig. 2.7 the reflectron voltages are indicated as R1 and R2). When they are set equal to ground potential, the ions can pass through the reflectron plates and be detected, in linear mode, by a MCP.

The reflectron was introduced by Mamyrin[2.34] in 1973. After traversing the flight tube, ions enter a retarding field defined by a series of grids (reflectron), and are turned around and sent back through the flight tube. The principle of the reflectron (or ion mirror) is that an ion with higher energy will penetrate the retarding field more deeply, will spend more time turning around, and will just catch up with a slower ion (of the same mass) at the time they both reach the detector.

The reflectron results in some loss of the reflected ion signal. In part this is due to the introduction of additional grids that are not 100% transmissive. However, the loss in the reflected ion signal (particularly that due to molecular ions) is also due to the fate of metastable ions, which decompose in the field-free region prior to entering the reflectron.

2.3.1.4 Ion detectors

Two dual micro-channel plate detectors (Burle Electro-Optics, Inc., Part#30220-30392) with active diameters of 18 and 40 mm respectively, are used in combination with the Jordan Re-ToF-MS. Both MCPs are characterized by a gain of 10^6 and sub-nanosecond rise time.[2.35] A grid, 1 cm in front of each MCP stack, is held at ground potential to allow a field-free drift region for ions in the flight tube. Details, on how two MCP plates

can be placed in series (chevron configuration) to increase MCP stack gain and to suppress ion feedback effects, could be found in the article by O. Almen et al.[2.36]

When in linear operation mode, the ions focus at an 18 mm detector at the end of the flight tube, and the 40 mm detector is reached after reflection, back through the flight tube, when in reflectron mode (See Fig. 2.7). The electronic configuration does not preclude simultaneous use of both detectors. Each of the MCP detectors is operated for positive-ion detection. A divider box (schematic shown in Figure 2.11) provides the three

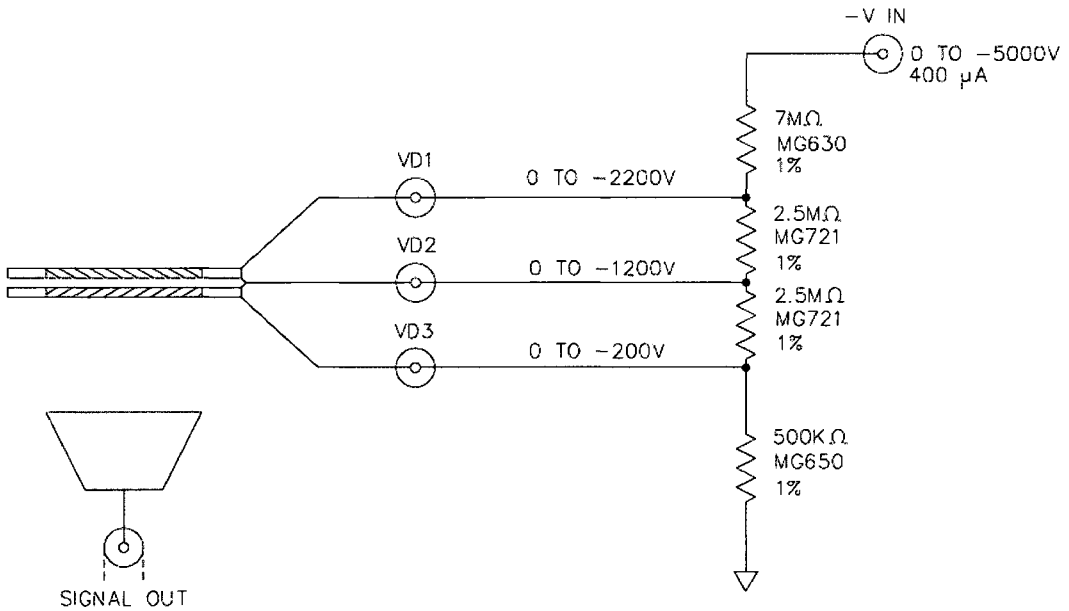


Figure 2.11: Schematic of divider circuit used to supply bias voltage's for MCP's.

voltages necessary for a dual MCP detector. Following impact by the positive ion, the first plate produces an electron output which is subsequently amplified by more electron collisions to provide a gain on the ion signal.

The detector gain is governed by the potential applied to the plates (0 kV to 3 kV). For detector potentials of 1000 V to 2000 V, the nonlinear gain profile is between 104

and 105.[2.35] Considerable signal ringing and poor signal quality are characteristics of operating voltages close to 3000 V on the detector. Therefore, with most experiments we employed potentials between 1600 V and 2200 V. The gain selected is determined by the intensity of the ion signal observed on the oscilloscope, and signal saturation is avoided by lowering the detector voltage. The output of the detectors is an electron current that is transmitted to the oscilloscope and terminated in a 50 Ω resistance.

2.3.1.5 Interlocks

An electronic interlock system utilizing voltage relays was designed to prevent, or at least minimize the danger of jeopardizing the apparatus and its auxiliary equipment in case of a catastrophic failure. An upper limit for the pressure is set to 5.0×10^{-5} Torr. If, during the experiment, the pressure were to rise above this pressure (e.g. broken capillary, power outage), pneumatic valves will seal the vacuum system from the pumps to maintain low pressure in the vacuum chambers, mainly to allow time to lower the voltage on the MCP's. This also allows the turbo pumps to slow down at a reasonable rate to avoid damage.

2.3.1.6 Photoionization

In time of flight mass spectrometry, ion masses are marked as different according to the time the ions need to reach a detector placed at a fixed distance. Neutral species cannot be detected unless they are previously ionized.

In our experiment in particular, we concentrate our attention on the neutrals that might originate from the combination of ions and neutrals in the plasma plume with oxidizing molecules seeded in the noble gas. Ionization can be brought about by electrical discharge, laser light, electrons, or other charged particles, but it usually leads to

fragmentation of the molecules. In this work we restrict our attention to laser light ionization. Under this broad category, we shall distinguish between single photon ionization (photo-ionization processes) and double or multi-photon ionization.

A tabletop SXR laser is used as an ionization source for the mass analyzer. The laser emits pulses of about 1.5 ns duration with an energy of about 10 μJ at a repetition rate of up to 12 Hz, and occupies a smaller table area than most UV gas lasers (approximately 0.4 x 0.4 m^2, 0.4 x 0.8 m^2 including a turbomolecular pump).[2.37] The small size of this capillary discharge device is achieved by making use of a very low inductance coaxial discharge configuration illustrated in Fig. 2.12. Laser amplification is obtained for the

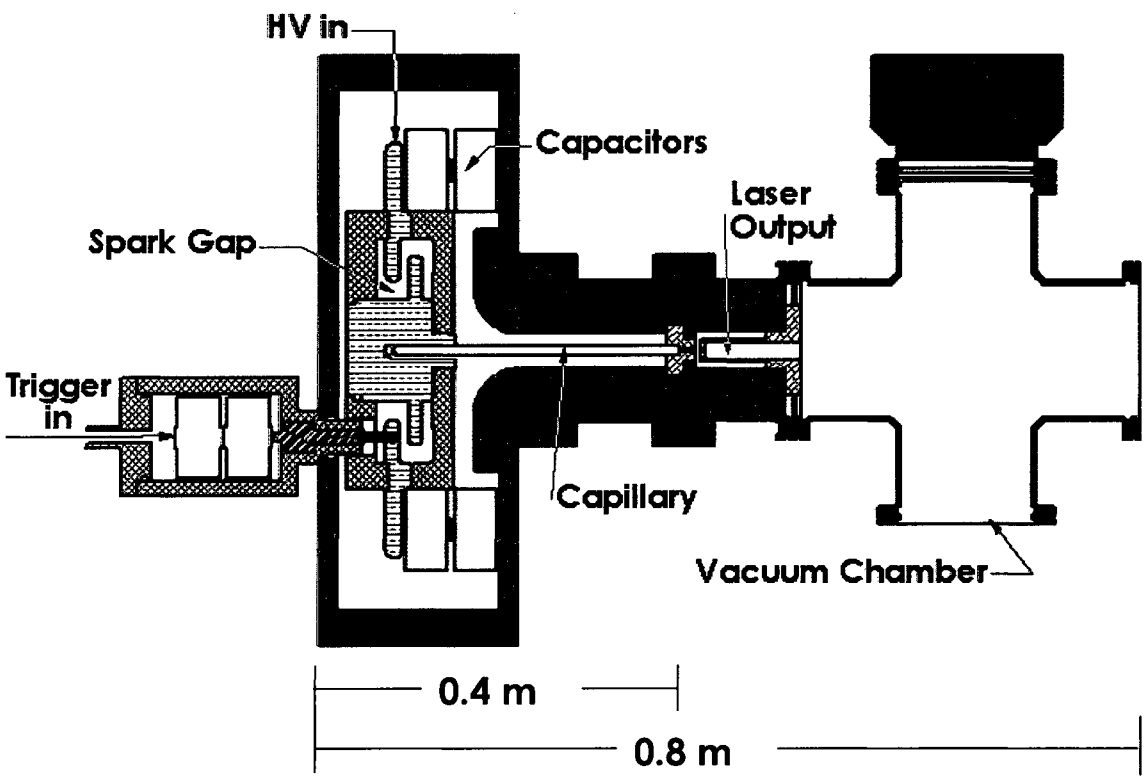


Figure 2.12: Schematic representation of the 46.9 nm capillary discharge, soft x-ray laser.

$3p(^1S_0)$–$3s(^1P_1)$ line of Ne-like Ar.[2.38] The plasma column is generated in an Al_2O_3 capillary 3.2 mm inside diameter (i.d.) and 21 cm long, filled with preionized Ar gas at an optimized pressure of 450-800 mTorr depending on the rep rate. The plasma column is excited by a current pulse of about 22 kA peak amplitude with a 10%–90% rise time of approximately 60 ns. The excitation current pulse is produced by discharging a set of ceramic capacitors through a pressurized spark gap switch connected in series with the capillary load. The main current pulse through the capillary is initiated by triggering the spark gap with an ~ 50 kV pulse to allow synchronization of the laser pulse with external events with a jitter of several nanoseconds, as is required for the application of this laser as the ionization source for ToF-MS experiments. The magnetic force of the current pulse and large thermal pressure gradients near the capillary wall rapidly compress the plasma to form a dense, hot column with a high density of Ne-like Ar ions, with high axial uniformity.[2.39] Collisional electron impact excitation of the ground state Ne-like Ar ions produces a population inversion between the $3p\ ^1S_0$ and $3s\ ^1P_1$ levels in Ar^{+8}, resulting in the amplification of light at 46.9 nm (26.5 eV). The laser is described in greater detail in Appendix B. The pulses intersect the supersonic molecular beam containing the ablated material seeded in He with some oxidizer and provide single photon ionization of any species.

When molecules are irradiated with high-energy photons, processes such as photoexcitation, photoionization, or some combination of the two may occur simultaneously to produce a multitude of final states.

In the process of photoexcitation a molecule is transferred from its initial state to a bound excited state by absorption of a photon. The energy absorbed is,

$$h\upsilon_{ij} = E_i - E_j \tag{2.12}$$

where υ_{ij} is the frequency of the incident radiation and E_i and E_j are the energies of the state involved in the transition. If the exciting radiation is of sufficiently high energy, the molecule can be excited to a region of continuous states lying above the bound states, corresponding to dissociation and ionization processes of the molecule. In our experiment, we use high energy (26.5 eV), monochromatic radiation for excitation and photoionization where the incident photon energy is used to ionize the molecule, thereby releasing an electron. Any energy in excess of the ionization energy (IE) appears as kinetic energy (KE) of the photoelectron. Only ionization processes for which the IE $\leq h\upsilon$ can occur.

Direct photoionization is the process where an electron is ejected from a molecule in its ground electronic and vibrational level to form a corresponding molecular ion. The probability of such a transition between the molecular ground state given by the eigenfunction Ψ'' and the final state (ion + photoelectron) given by Ψ' is determined by the square of the transition moment integral[2.40,2.41],

$$M = \left\langle \Psi'' \middle| \sum p \middle| \Psi' \right\rangle \tag{2.13}$$

where p is the dipole moment operator and the sum extends over all electrons i and nuclei j. Ψ'' and Ψ' are functions of the electron r and nuclear R coordinates.

This is a simplified expression that relies on the assumption that photoionization is a single step one-electron process in which the interaction between a neutral molecule and a photon is described by a one-electron operator. If the wavefunctions for the neutral and ionized states are constructed from the same set of molecular orbitals and a one-electron operator is used, only states characterized by an electronic configuration differing from

that of the neutral molecule by one molecular orbital will normally be predicted. In this simple description, some electronic states of a molecular ion have to be described by a configuration that differs from that of the ground state of the neutral molecule by two molecular orbitals or more. That is, ejection of one electron and simultaneous excitation of another electron into an unoccupied orbital.[2.42-2.46]

To describe such two-electron processes, replace the simple molecular orbital description by a more correct configuration interaction expansion of wavefunctions. The wavefunction Ψ_j of the jth electronic state can be expressed as a configuration interaction expansion over all electronic configurations Φ_i belonging to a certain spin and symmetry species.

$$\Psi_j = \sum_{i=1}^{\infty} c_{ij}\Phi_i \tag{2.15}$$

The configurations Φ_i may be singly and/or doubly excited. Substituting this into the transition moment integral one can obtain,

$$M = \left\langle \Psi'' \middle| p \middle| \sum_{i=1}^{\infty} c_{ij}\Phi_i \right\rangle = \sum_{i=1}^{\infty} c_{ij} \langle \Psi'' | p | \Phi_i \rangle \tag{2.16}$$

Transitions to the state described by Ψ_j are allowed if any of the components in the summation of eq. 2.16 are nonzero. Therefore, a transition to a state described mainly by a doubly excited configuration can be allowed by the mixing of singly excited configurations into the expansion of Ψ_j.[2.41] The intensities of such transitions are determined by the square of the configuration interaction coefficients and the transition moment integral of eq. 2.16. The intensities of these two electron transitions are dependant on the photon energy of the ionization source. The intensities are negligible for

the ejection of an electron from the valence shell by He I radiation for example. But, these transitions do become important in the presence of He II radiation, evidently due to the increased photon energy making transitions to more highly excited states of molecular ions possible.[2.41,2.45] The two electron processes may even confuse the analysis of simple spectra in some regions where band intensities become comparable to single electron conditions.[2.41]

2.3.1.7 Autoionization

Another possible ionization mechanism is probable when the radiation used is of sufficiently high energy to excite electrons, other than the most loosely bound, to discrete neutral states above the ionization threshold. An atom or molecule in such a state can produce radiationless transitions from the discrete state to the ionization region. This is called autoionization and can be represented by,

$$M + h\upsilon \rightarrow M^* \rightarrow M^+ + e^- \qquad (2.17)$$

where M^* si the atom or molecule in a highly excited state. When a molecule is excited by photons whose energy coincides with that of an autoionized resonance, there is a high probability of exciting the molecule to this autoionizing state with a well defined vibrational quantum number. More on autoionization can be found in reference 2.41.

2.3.1.8 Advantages of single photon ionization

One of the more serious problems encountered in the investigation of neutral clusters is fragmentation. Due to high ionization energy, clusters often require multiphoton absorption in order to be detected by most mass spectroscopy techniques. Electron Impact (EI) usually suffers considerably from the fragmentation of parent cluster ions due to the large excess (above the vertical ionization energy, VIE) energy present during the

ionization process. A nanosecond MPI process results in predissociation of neutral clusters prior to the ionization step. Even multiphoton ionization is typically thought to be gentler than electron ionization. Multiphoton absorption by clusters is often difficult to control due to the neutral or ionic cluster ability to absorb many photons. Neutral clusters can thereby ionize at high, super-excited, un-relaxed electronic states or by thermionic emission through rapid electronic relaxation and heating of the neutral cluster. In either event cluster fragmentation, and thus loss of neutral cluster distribution information, is often the end result.[2.3,2.47] On the other hand, single photon near threshold ionization at low laser fluence yields little fragmentation and thus maximum neutral cluster information.[2.4,2.48-2.51]

In general, single photon ionization is a good way to study clusters since less fragmentation of the parent cluster ions occurs compared to EI and MPI. We have previously demonstrated that, if 10.5 eV is sufficient energy for the ionization of a cluster,[2.3,2.50] a 118 nm VUV laser provides a nonresonant soft ionization for metal oxide and methanol clusters,[2.3,2.50] as fragmentation is minimized during the ionization process. The 10.5 eV photon, however, is not energetic enough to meet the VIE of all clusters.[2.52]

A 26.5 eV tabletop, SXR laser with a 10 μJ/pulse, and 10 Hz output energy is used as the ionization source in our laboratory. To the best of our knowledge, this is the first soft x-ray laser source employed to study clusters and chemical dynamics. A single photon of this laser has sufficient energy to ionize any cluster, molecule, or atom. The experimental results in the upcoming sections demonstrate that the 26.5 eV laser is a very good ionization source for many systems, including van der Waals clusters, hydrogen bonded,

metal, metal oxide, and cluster reaction. Little photon energy remains in the cluster above the VIE following ionization, since this excess energy is removed by the ejected electron. The problem of predissociation of neutral clusters caused by MPI processes is thereby avoided.

2.4 TIME DELAY SCHEMES FOR TRIGGERING

The frequency of data acquisition cannot exceed 10 Hz because of the maximum repetition rates of our DCR-11 YAG laser and the SXR laser. During experiments several events must be synchronized:

- Opening of pulsed gas valves (Jordan and General valves);
- Laser firing for photo-ablation;
- Laser firing for ionization;
- Start of oscilloscope signal recording (data acquisition);
- Extraction pulse for ion masses to be rejected (mass gate).

The master timing diagram in Fig. 2.13 summarizes the events occurring for the triggering scheme we exploited. The timing of the events are controlled by two programmable delay generators (Stanford Research Systems model DG 535). These devices play a key role for the experiments. In Fig. 2.14 a schematic block diagram shows the connections between the delay generators and the other parts of the experimental setup. Arrow directions show whether a signal is used to trigger (inward arrow) a device or originates from it (outward arrow) to drive other equipment. A 1-10 Hz TTL pulsed signal is generated by the DG 535 that controls the timing for firing the

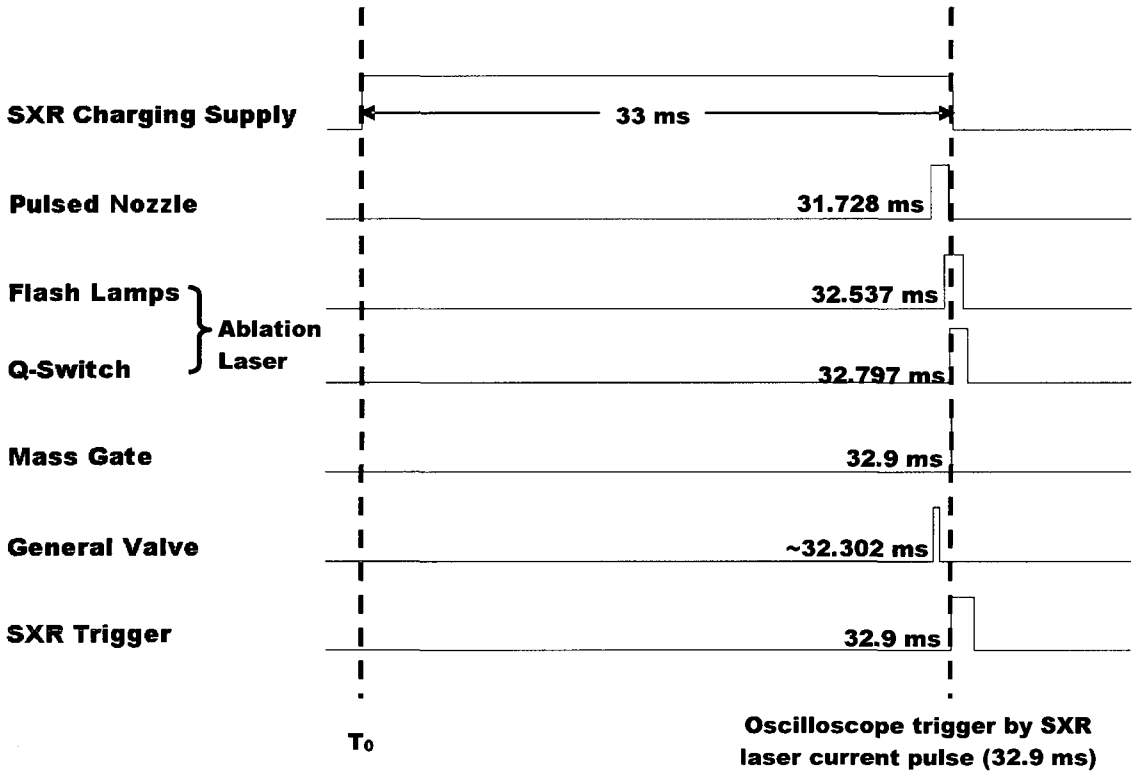


Figure 2.13: Timing diagram through one complete cycle (up to 10 Hz). T_0 is the beginning of the timing sequence for the DG 535 delay generator. The timing of all signals can be optimized during the experiment to maximize the mass spectrum intensity. The timing for the General valve is optional and varies greatly from experiment to experiment. The oscilloscope is triggered by the current pulse from the SXR laser at 32.9 ms.

SXR laser.

The TTL signal also triggers the second DG 535 unit. Output signals, opportunely delayed from the trigger, are generated by the Stanford device to:

- Open the Jordan valve (the closing time is regulated by the controller described in section 2.2.1);
- Trigger the oscilloscope to start a data acquisition (which lasts for the oscilloscope capture time typically hundreds of μs);
- Make the ablation laser fire and intersect the gas stream let in by the valve;
- Pulse voltage on the middle grid of the mass gate;

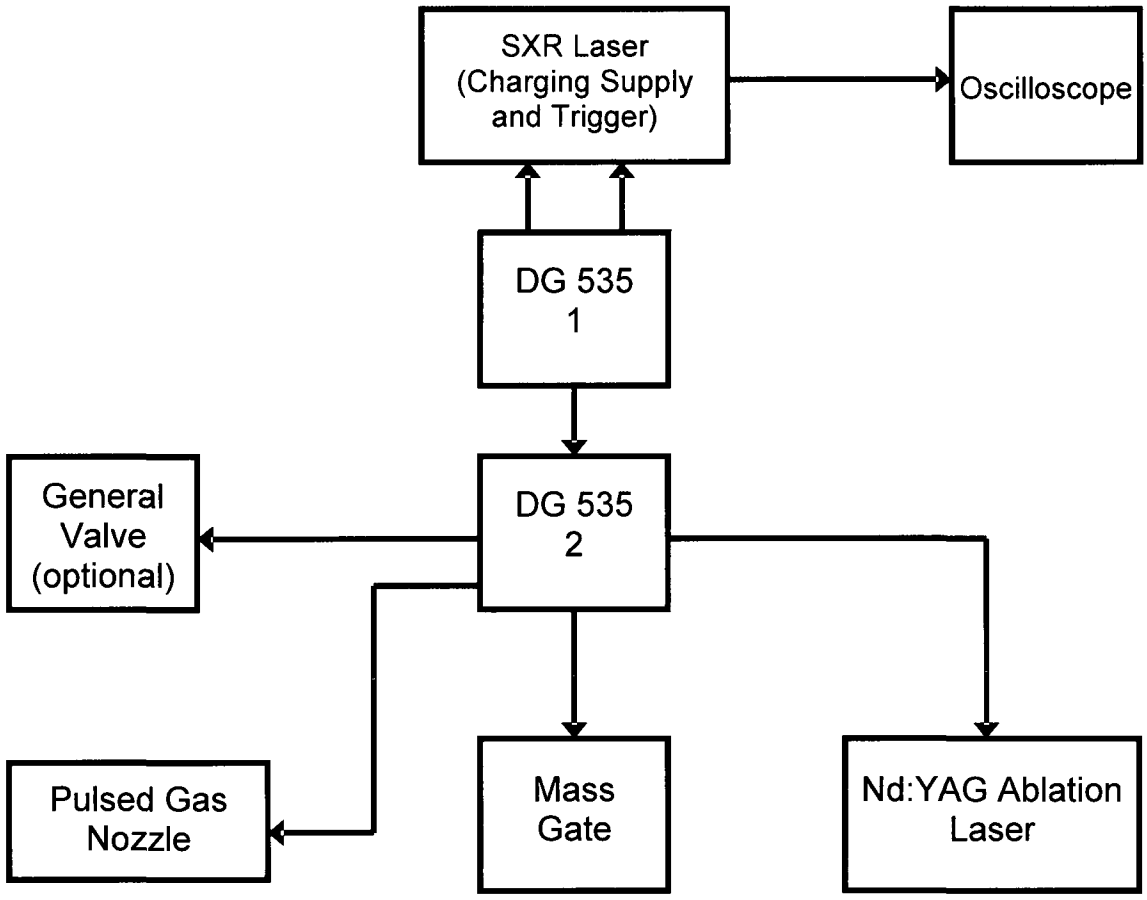


Figure 2.14: Schematic block diagram of the connections for event synchronization in the experimental setup. Directions of arrows show whether trigger signals are given in input or are generated by a device.

- (Optional) Open the General valve that is connected to the reaction cell for reaction experiments.

The timing sequence of the experiment is started with the SXR laser. A TTL pulse initiates a CCDS Power Supply (General Atomics) that charges a capacitor bank to 60 kV for 33 ms. A second 12V TTL pulse at 32.9 ms sets off a high voltage trigger that discharges the 60 kV capacitor bank through a high voltage spark gap switch and fires the SXR laser (more details in Appendix A). It is this second pulse at 32.9 ms (SXR laser firing) to which all of the other timings are related.

Since the laser fires at 32.9 ms, the gas pulse and molecular beam must be formed before this time. At 31.728 ms, the pulsed gas nozzle is fired using another TTL pulse from the second DG 535. This is the earliest pulse, and the gas pulse remains for up to 1 ms. Shortly after the gas pulse, the ablation laser is triggered. The ablation flash-lamp signal represents the trigger for the flash lamp of the ablation laser. Its timing is set, by way of another external delay box, accordingly with the occurrence of the Q-switch in order to keep the interval between their pulses constant at 260 μs. This condition, required to obtain the best stability for the ablation laser throughput, is achieved by adjusting the two delay generators generating the required pulses. The mass gate signal, whose delay is manually adjusted, controls the switching of a high voltage pulser (see section 2.3.1.2) that does not allow unwanted ions (usually He^+) to reach the MCP detectors after being refocused by the Re-ToF-MS. The optional General valve operation is manually adjusted to maximize collisions when the reaction cell is being used for experiments. Usually we adjust the timing while monitoring the mass spectra until a condition is reached at which the signal intensity is decreased by about 50%. All timings can be manually adjusted in order to maximize the output signal from the Re-ToF-MS.

The output signal from the MCP assembly (see section 2.3.1.4) at the end of the Tof-MS is monitored by a 350 MHz, 5 Gs/s digital oscilloscope (Tektronix model TDS5032B). The data are visualized on the oscilloscope display to guide fine tuning of the signals delays, averaged for 200-300 shots to reduce random background noise seen in the spectrum, and logged for off-line data analysis. Data are imported into the Origin6.0 Pro software for labeling and analysis.

2.5 INSTRUMENT CHARACTERIZATION

In a ToF-MS instrument the signal measured represents the intensities of the detected ions vs. time. An approximate correspondence between mass-to-charge ratio and detection time (time-of-flight) of ions could be determined directly in an "External Calibration" fashion from equations required for instrument design[2.37] if the exact drift lengths, acceleration and reflectron potentials are known. In practice this approach for the calibration of the mass spectrometer is rarely used.

In most cases, calibration for ToF-MS is performed from empirical determination of the times-of-flight of several known masses. In our case, if the spectrum is not well known, the background may be used for calibration of peaks that are ionized by the SXR laser such as He, H_2O, N_2, O_2, and Ar. Subsequently, a calibration line is drawn, according to equation,

$$\frac{M}{Z} = (at + b)^2 \tag{2.18}$$

where M is the ion mass (in a.m.u.), Z represents the ion charge (in electron charge units), a and b are the calibration constants, and t is the experimental time-of-flight. The calibration constants a and b are determined through a least-squares regression which fits the equation 2.18 with the known pairs of times-of-flight and masses. After calibration, any experimental time-of-flight can be converted to a M/Z value to identify the unknown ions.

Mass calibration with most samples was straightforward, since they provide an appreciable signal with the characteristic patterns shown in the data in the later sections. In addition, impurities still present in vacuum, such as H_2O, O_2, Ar, and N_2 can be identified in the signal from the mass spectrometer.

2.5.1 Re-ToF-MS Resolution

Broadly defined, resolution is the ability to distinguish two ions of different masses, and is usually scaled to the mass range under consideration, such that

$$R = \frac{M}{\Delta M} \tag{2.19}$$

where R is the resolution, ΔM is the difference in mass of the species, and M is the average mass of the two ions. Referring specifically to (Re)Tof-MS and assuming a single charge on the ion, the resolution equation can be rearranged to yield the equation:

$$R = \frac{T}{\Delta t_{FWHM}} \tag{2.20}$$

where the Full Width at the Half-Maximum (FWHM) of the signal peak, Δt_{FWHM}, has replaced the masses of the two separate ions. This enables resolution estimates for any given mass based solely on the time-of-flight and peak width.

From equation 2.20, it is clear that an increased time-of-flight, t, (long drift length and/or low acceleration potential) or narrowed peak width (Δt_{FWHM}) maximizes resolution. Ideally, this could be done simultaneously, but system parameters usually affect t and Δt_{FWHM} in opposite manners, and all peak-widening factors must be considered to select the parameters for Tof-MS operation. If a lot of time is spent on realizing a signal with the smallest FWHM possible, we can reach resolutions of 700-1000. Typically, we run the experiments in a way that we can still realize mass detection of 1 mass unit and have resolutions of ~ 200.

2.5.2 Ablation laser energies

The employed ablation laser energies per pulse were chosen based on the ease of ablation for the particular samples. Care is taken to avoid signal saturation effects and damage to

the multi-channel plate detectors. To measure the pulse laser energy, a power-meter with a detection head intercepts the laser beam at the entrance of the vacuum chamber.

The observed pulse energy at this location is reduced to account for the ~ 8% attenuation of the quartz window on the vacuum chamber. For most analysis, the pulse energy ranged between 0.25 mJ and 5 mJ, after the laser attenuation. To control the beam focused on the sample, an adjustable lens is installed to maximize the ion yield (proportional to the observed signal on the oscilloscope). The beam size can be viewed on a white card and measured with a caliper at the position of the 40 cm focal length lens. The beam radius depends on the laser energy used, as higher laser energies produce a larger beam radius (~ 0.95 cm) and lower energies yield a smaller radius (~ 0.80 cm). For typical analysis with an energy setting of ~ 2 mJ, the radius is approximately 0.85 cm to 0.90 cm. The measured radius at the lens can be used to approximate the beam spot size at the focal point assuming Gaussian beams:

$$d = \frac{4f\lambda}{\pi d_0} \tag{2.21}$$

where d represents the beam diameter at the focal point of the lens, f represents the lens focal length, λ is the wavelength of the laser light, and d_0 is the beam diameter as measured at the lens. The beam size at the sample surface thus translates to a diameter of 13 μm to 14 μm, yielding an area of 136 μm^2 to 153 μm^2. Laser energy densities when using 2 mJ are then calculated to vary between 13 and 15 J/mm^2.

2.5.3 Number of ions detected

Peak area data obtained after integration experimentally estimates the number of ions detected. The output from the multichannel plate detectors, an electrical current, is directly related to the number of ions that strike the multichannel plate. By knowing the

termination resistance (R) and the gain of the detector (G), the following relation estimates the number of ions associated to a given peak:[2.53]

$$V_p = R \times i_p = R\frac{G \cdot N \cdot q}{\Delta t} \qquad (2.22)$$

where V_p and i_p are the peak voltage and current respectively, Δt is the peak width (FWHM), q is the charge of an ion, and N represents the number of ions detected. Integration of the area under the peak gives therefore V_p x Δt which is proportional to N. In our experiments G varied between 10^5 and 10^6 while peaks of few hundreds of mV (V_p) were observed on the oscilloscope with R = 50 Ω. Their widths were typically of 20 ns (Δt). Using these values in eq. 2.22, N is found to range between 500 and 5000 ions. Similarly, one ion gives about a 4 mV signal.

2.5.4 Yield versus experimental parameters

The collected spectra using our experimental setup are dependent on several experimental parameters. The effect of these parameters vary depending on the sample used. The buffer gas back pressure and oxygen percentage, valve opening time, detector sensitivity, ablation energy and alignment, and reaction gas can be changed. A multivariate analysis could be done to determine how each parameter affects the spectral features, but is not very useful when one can monitor the effect of any one parameter from the output from the ToF-MS while adjusting it during the experiment. Each parameter is said to be optimal when it is adjusted and causes a maximum in the spectral signal.

References

[2.1] L.S. Andrews, A. Rohrbacher, C.M. Laperle, and R.E. Continetti, "Laser desorption/ionization of transition metal atoms and oxides from solid argon," J. Phys. Chem. A **104**, 8173 (2000).

[2.2] A. Pramann, K. Koyasu, A. Nakajima, and K. Kaya, "Photoelectron spectroscopy of cobalt oxide cluster anions. J. Phys. Chem. A **106**, 4891 (2002).

[2.3] D.N. Shin, Y. Matsuda, and E.R. Bernstein, "On the iron oxide neutral cluster distribution in the gas phase. I. Detection through 193 nm multiphoton ionization," J. Chem. Phys. **120**, 4150 (2004).

[2.4] Y. Matsuda, D.N. Shin, and E.R. Bernstein, "On the zirconium oxide neutral cluster distribution in the gas phase: Detection through 118 nm single photon, and 193 and 355 nm multiphoton, ionization," J. Chem. Phys. **120**, 4142 (2004).

[2.5] W.J. Balfour, J. Cao, R.H. Jensen, and R. Li, "The spectrum of nickel monoxide between 410 and 510 nm: laser-induced fluorescence and dispersed fluorescence measurements," Chem. Phys. Lett. **385**, 239 (2004).

[2.6] S. DePaul, D. Pullman, and B. Friedrich, "A pocket model of seeded supersonic beams," J. Phys. Chem. **97**, 2167 (1993).

[2.7] J. Westergren and H. Grobeck, "Noble gas temperature control of metal clusters: a molecular dynamics study," J. Chem. Phys. **107**, 3071 (1997).

[2.8] Laser Applications to Chemical Dynamics, volume 742 of Proceedings of the SPIE - The International Society for Optical Engineering, 13-14 Jan 1987. Los Angeles, CA, USA.

[2.9] P.Milani and W.A. deHeer, "Improved pulsed laser vaporization source for production of intense beamof neutral and ionized clusters," Rev. Sci. Instru. **61**, 1835 (1990).

[2.10] W.A. deHeer and P. Milani, "An improved laser vaporization cluster source and time of- flight mass spectrometer," Z. Phys. D - Atoms, Molecules and Clusters **20**, 437 (1991).

[2.11] F.K. Urban III, S.W. Feng, and J.J. Nainaparampi, "Determination of zinc cluster size in ionized cluster beam film deposition," J. Appl. Phys. **74**, 1335 (1993).

[2.12] A.R. Skinner and D.W. Chandler, "Spectroscopy with supersonic jets," Am. J. Phys. **48**, 8 (1980).

[2.13] C.C. Jr. Leiby and A.L. Besse, "Molecular beams and effusive flows" Am. J. Phys. **47**, 791 (1979).

[2.14] R.E. Smalley, L. Wharton, and D.H. Levy, "Molecular optical spectroscopy with supersonic beams and jets," Acnts. Chem. Res. **10,** 139 (1977).

[2.15] A. Kantrowitz and J. Grey, "A high intensity source for the molecular beam. Part I. Theoretical," Rev. Sci. Instru. **22**, 328 (1951).

[2.16] M. Rudin, "Criteria for thermodynamic equilibrium in gas flow," Phys. Fluids **1**, 384 (1958).

[2.17] H. Ashkenas and F.S. Sherman, *Fourth Symposium on Rarefied Gas Dynamics* (Academic, New York, 1966, Vol. 2)

[2.18] J.B. Anderson and J.B. Fenn, Phys. Fluids **8**, 780 (1965).

[2.19] M.D. Morse. Supersonic beam sources. In F. Dunning and R. Hulet, editors, Atomic, molecular, and optical physics: Atoms and molecules, volume 29B, pages 21–46. 1996.

[2.20] Jordan TOF Products Inc., "PSV and Power Supply Manual," (http://www.rmjordan.com/c211-451.html). (Jordan TOF Products Inc., Grass Valley, Ca).

[2.21] G.I. Dimov, "Quick Acting Valves for admitting Short Gas Pulses into Vacuum Devices," Prib. Tekh. Eksp. **5**, 168 (1968).

[2.22] S.S. Harilal, C.V. Bindhu, M.S. Tillack, F. Najmabadi, and A.C. Gaeris, "Internal structure and expansion dynamics of laser ablation plumes into ambient gases," J. Appl. Phys. **93**, 2380 (2003).

[2.23] M.S. Tillack, D.W. Blair, and S.S. Harilal, "The effect of ionization on cluster formation in laser ablation plumes," Nanotechnology **15**, 390 (2004).

[2.24] L.V. Zhigilei and B.J. Garrison, "Velocity distributions of molecules ejected in laser ablation," Appl. Phys. Lett. **71**, 551 (1997).

[2.25] R.W. Dreyfus. Laser Ablation of Electronic Materials: Basic Mechanisms and Applications, volume 4, chapter Comparison of the Ablation of Dielectrics and Metals at High and Low Laser Powers, pages 61–72. European Materials Research Society Monographs, North-Holland, Amsterdam, 1992.

[2.26] I.C.E. Turcu, M.C. Gower, and P. Huntington, "Measurement of KrF laser breakdown threshold in gases," Opt. Comm. **134**, 66 (1997).

[2.27] H.R. Griem, "High-density corrections in plasma spectroscopy," Phys. Rev., **128**, 997 (1962).

[2.28] A.E. Cameron and D.F. Jr. Eggers, "An ion 'velocitron'," Rev. Sci. Instru. **19**, 605 (1948).

[2.29] R.E. Steiner, C.L. Lewis, and V. Majidi, "Consideration of a millisecond pulsed glow discharge time-of-flight mass spectrometer for concurrent elemental and molecular analysis," J. Anal. At. Spec. **14**, 1537 (1999).

[2.30] A. Zelenyuk and D. Imre, "Single particle laser ablation time-of-flight mass spectrometer: An introduction to SPLAT," Aerosol Sci. and Tech. **39**, 1 (2005).

[2.31] W.C. Wiley and I.H. McLaren, "Time-of-flight mass spectrometer with improved resolution," Rev. Sci. Instru. **26**, 1150 (1955).

[2.32] D.M. Lubman and R.M. Jordan, "Design for improved resolution in a time-of-flight mass spectrometer using a supersonic beam and laser ionization source," Rev. Sci. Instru. **56**, 373 (1985).

[2.33] M Guilhaus, "Principles and instrumentation in Time-of-Flight Mass Spectrometry," J. Mass Spec. **30**, 1519 (1995).

[2.34] B.A.Mamyrin, V.I. Karataev, D.V. Shmikk, and V.A. Zagulin, "The mass-reflectron, a new nonmagnetic time-of-flight massspectrometer with high resolution," Sov. Phys.-JETP **37**, 45 (1973).

[2.35] BURLE optics Inc, "Burle long-life MCP selection guide," (http://www.burle.com). (Burle Electro-optics Inc., Sturbridge, Ma, 2003).

[2.36] O. Almen, W. Hartmann, K. Frank, and J. Christiansen, "Fast rise time, high sensitivity MCP ion detector for low-energy ion spectroscopy." J. Phys. E, **22**, 382 (1989).

[2.37] S. Heinbuch, M. Grisham, D. Martz, and J. J. Rocca, "Demonstration of a desk-top size high repetition rate soft x-ray laser," Opt. Express **13**, 4050 (2005).

[2.38] J. Rocca, V. N. Shlyaptsev, F. G. Tomasel, O. D. Cortazar, D. Hartshorn, and J. L. A. Chilla, "Demonstration of a Discharge Pumped Table-Top Soft-X-Ray Laser," Phys. Rev. Lett. 73, 2192 (1994).

[2.39] J. J. Rocca, "Table-top soft x-ray lasers," Rev. Sci. Instrum. **70**, 3799 (1999).

[2.40] H. Eyring, J. Walter, and G.E. Kimball, "Quantum Chemistry," (Wiley, New York, 1944).

[2.41] J.W. Rabalais, "Principles of ultraviolet photoelectron spectroscopy," (Wiley-Interscience monographs in chemical physics, 1977).

[2.42] J.C. Lorquet and C. Cadet, Chem. Phys. Lett. **6**, 198 (1970).

[2.43] J.C. Lorquet and M. Desouter, Chem. Phys. Lett. **16**, 136 (1972).

[2.44] R.N. Dixon and S.E. Hull, Chem. Phys. Lett. **3**, 367 (1969).

[2.45] A.W. Potts and T.A. Williams, J. Electron Spectrosc. **3**, 3 (1974).

[2.46] M. Okuda and N. Jonathan, J. Electron Spectrosc. **3**, 19 (1974).

[2.47] M. Foltin, G. J. Stueber, and E. R. Berstein, "On the growth dynamics of neutral vanadium oxide and titanium oxide clusters," J. Chem. Phys. **111**, 9577 (1999).

[2.48] D. N. Shin, Y. Matsuda, and E. R. Bernstein, "On the iron oxide neutral cluster distribution in the gas phase. II. Detection through 118 nm single photon ionization," J. Chem. Phys. **120**, 4157 (2004).

[2.49] Y. Matsuda, D. N. Shin, and E. R. Bernstein, " On the copper oxide neutral cluster distribution in the gas phase: Detection through 355 nm and 193 nm

multiphoton and 118 nm single photon ionization," J. Chem. Phys. **120**, 4165 (2004).

[2.50] Y. Matsuda, and E. R. Bernstein, "On the Titanium Oxide Neutral Cluster Distribution in the Gas Phase: Detection through 118 nm Single-Photon and 193 nm Multiphoton Ionization," J. Phys. Chem. A **109**, 314 (2005).

[2.51] E. R. Bernstein, and Y. Matsuda, Environmental Catalysis, (Marcel Dekker, New York, 2005).

[2.52] S. Tomoda and K. Kimura, "Ionization energies and hydrogen-bond strength of the water clusters," Chem. Phys. Lett. **102**, 560 (1983).

[2.53] R. Odom and B. Schueler, "Lasers and Mass Spectrometry," chapter 5. Oxford University Press, 1990.

Chapter 3

Hydrogen bonded and van der Waals Clusters

Chapters 3-5 are a collection of papers that have been published on the experiment outlined in Chapters 1 and 2. Each section represents one publication in a peer reviewed journal. Chapter 3 discusses our results on hydrogen bonded and van der Waals clusters. Chapter 4 reviews our work on metal oxide clusters followed by discussion of reactions in Chapter 5.

3.1 DYNAMICS AND FRAGMENTATION OF van der WAALS CLUSTERS: $(H_2O)_n$, $(CH_3OH)_n$, and $(NH_3)_n$ UPON IONIZATION BY A 26.5 eV SOFT X-RAY LASER

The study of van der Waals cluster formation and growth in the gas phase can contribute to the understanding of solvation processes, solvation dynamics, and the nucleation and growth of small clusters. The investigation of water, methanol, and ammonia clusters together is of particular importance because these clusters demonstrate a wide range of van der Waals interactions and hydrogen bonding: water clusters are very strongly and dominantly hydrogen bonded; methanol clusters somewhat less so; and ammonia clusters perhaps not at all.[3.1,3.2]

Water clusters are one of the most important van der Waals/hydrogen bonded clusters because of their unique role in both fundamental research and a wide range of

applied fields, including atmospheric science,[3.3,3.4] astrophysics,[3.5], and biology.[3.6] Neutral water clusters have been studied by electron impact (EI) ionization,[3.7,3.8] corona discharge ionization,[3.9,3.10] chemical ionization (CI),[3.11] VUV resonance lamp ionization,[3.12] and fs photoionization.[3.13] These approaches generate mass spectra of water clusters that are typically dominated by the protonated cluster ions $(H_2O)_nH^+$: these species are produced by a fast proton transfer reaction and loss of OH from the cluster following the ionization process. The two cluster ions $(H_2O)_{21}H^+$ and $(H_2O)_{28}H^+$ are identified as "magic number" clusters in this mass spectrum since intensity anonomalies of the 21- mer and 28- mer are observed under numerous experimental conditions.[3.14-3.19] The structures of medium sized protonated water clusters have been reviewed by Chang et al. recently.[3.20] Shinohara and co-workers[3.12] observed unprotonated $(H_2O)_n^+$ clusters ($2 \leq n \leq 10$) for the first time by applying near threshold photoionization with an Ar resonance lamp (11.83 eV) for a molecular beam expansion of H_2O and Ar. They suggest that unprotonated water cluster ions are generated because the mixed cluster ions $(H_2O)_n Ar_m^+$ are created and give rise to $(H_2O)_n^+$, without sufficient excess energy needed to drive the proton transfer reaction, through evaporative loss of mAr. Binding energies and metastable dissociation rate constants for protonated water clusters have been measured by Castleman's group.[3.11,3.13] Water cluster mass spectra cannot be observed through ns multiphoton ionization (MPI) processes because water clusters are dissociated in the MPI process.

Methanol clusters represent an important complementary class of hydrogen bonded van der Waals clusters to water clusters, as their van der Waals interaction energy should be larger and their hydrogen bonded interaction energy should be smaller than those

found for water clusters. Many ionization techniques have also been employed to investigate methanol clusters (e.g., EI,[3.21,3.22] MPI,[3.23-3.25] and IR/VUV excitation[3.26]). As found for water clusters, protonated methanol clusters dominate the mass spectra of $(CH_3OH)_n$: unprotonated $(CH_3OH)_n^+$ ($n \leq 7$) are only observable in an Ar expansion.[3.21] The possible relationship between methanol cluster ion distributions and methanol cluster distributions has been addressed by Lipson et al.[3.27] and Fu et al.[26] based on single photon VUV (118 nm) laser ionization. Formation of $H^+(H_2O)(CH_3OH)_n$ and $(CH_3OH)_n\left[(CH_3)_2O\right]H^+$ clusters via two kinds of intramolecular ion-molecule reactions are observed for EI ionization[3.21,3.22] but not for single photon (118 nm) ionization.[3.26,3.27]

Ammonia is another important solvent species: it is characterized by van der Waals, but not hydrogen bonding, interactions, as it is a very poor proton donor, albeit a very good proton acceptor (ammonia proton affinity $PA(NH_3) \sim 204$ kcal/mol[3.28] vs. $PA(H_2O) \sim 160$ kcal/mol[3.29]). Ammonia clusters are investigated by EI,[3.30,3.31] MPI,[3.30,3.33] fs laser,[3.34,3.35] and single photoionization[3.36] techniques. Like water and methanol clusters, protonated ammonia clusters somewhat surprisingly dominate its mass spectra. Nonetheless, unprotonated ammonia clusters are observed by various ionization techniques.[3.31,3.35,3.36] Shinohara and co-workers[3.36] detect unprotonated ammonia cluster ions $(NH_3)_n^+$ for n up to 25 employing single photon ionization with atomic resonance lamps.

One of the more serious problems encountered in the investigation of the neutral cluster distribution of van der Waals and hydrogen bonded clusters is fragmentation of the ionizing cluster due to intra-cluster ion molecule reactions that generate protonated cluster ions. EI usually suffers considerably from fragmentation of parent cluster ions due

to the large excess (above the vertical ionization energy - VIE) energy present during the ionization process. A ns MPI process results in predissociation of neutral water clusters prior to the ionization step. In general, single photon ionization is a good way to study van der Waals and hydrogen bonded clusters since less fragmentation of the parent cluster ions occurs compared to EI and MPI. We have previously demonstrated that, if 10.5 eV is sufficient energy for ionization of a cluster,[3.37,3.38] a 118 nm VUV laser provides a nonresonant soft ionization for metal oxide and methanol clusters, [3.37,3.38] as fragmentation is minimized during the ionization process. The 10.5 eV photon, however, is not energetic enough to meet the VIE of $(H_2O)_n$.[3.39]

Recently, we have developed a 26.5 eV table-top, soft x-ray laser with a 10 μJ/pulse, 10 Hz output energy that is now operational in our laboratory.[3.40] To the best of our knowledge this is the first soft x-ray laser source employed to study clusters and chemical dynamics. A single photon of this laser has sufficient energy to ionize any cluster, molecule, or atom. The experimental results demonstrate that the 26.5 eV laser is a very good ionization source for many systems, including van der Waals clusters. Little photon energy remains in the cluster above the VIE following ionization, since this excess energy is removed by the ejected electron. The problem of predissociation of neutral clusters caused by MPI processes is thereby avoided.

The present study of water, methanol, and ammonia clusters is the first application of a soft x-ray laser in chemistry. Distributions of water, methanol, and ammonia clusters are compared to those found by other single photon, near threshold, photoionization techniques. Dissociation rate constants for metastable protonated water, methanol, and ammonia clusters are obtained. Temperatures of neutral clusters are estimated for water

and methanol, while temperatures for ammonia clusters cannot be estimated accurately due to inconsistencies in the extant ammonia cluster data set.

3.1.1 Experimental Procedures

The apparatus used in this experiment is shown in Figure 3.1. It includes a time of flight (linear/reflectron) mass spectrometer (TOFMS) and a table-top soft x-ray laser as

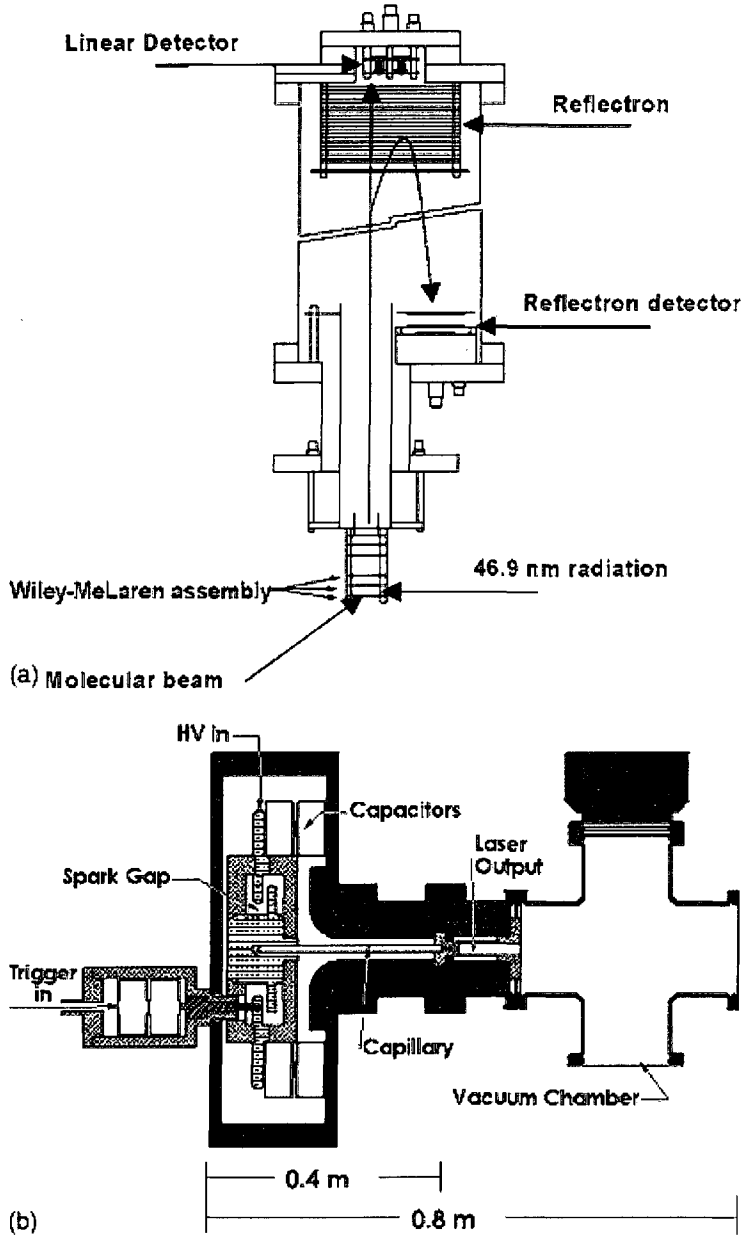


Figure 3.1: (a) Schematic of the experimental setup of the reflectron time of flight mass spectrometer. (b) Schematic representation of the 46.9 nm capillary discharge, soft x-ray laser.

an ionization source for the mass analyzer. The laser emits pulses of about 1.5 ns duration with an energy of about 10 μJ at a repetition rate of up to 12 Hz, and occupies a smaller table area than most UV gas lasers, approximately 0.4 x 0.4 m^2 (0.4 x 0.8 m^2 including a turbomolecular pump).[3.40a] The small size of this capillary discharge device is achieved making use of a very low inductance co-axial discharge configuration illustrated in Figure 3.1b. Laser amplification is obtained for the 3p ($^1S_0$) -3s ($^1P_1$) line of Ne like Ar.[3.40b] The plasma column is generated in an Al_2O_3 capillary 3.2 mm I.D. and 21 cm long, filled with pre-ionized Ar gas at an optimized pressure of 700 mTorr. The plasma column is excited by a current pulse of about 22 kA peak amplitude with a 10% to 90% rise time of approximately 60 ns. The excitation current pulse is produced by discharging a set of ceramic capacitors through a pressurized spark gap switch connected in series with the capillary load. The main current pulse through the capillary is initiated by triggering the spark gap with a ~50 kV pulse to allow synchronization of the laser pulse with external events with a jitter of several ns, as is required for the application of this laser as the ionization source for TOFMS experiments. The magnetic force of the current pulse and large thermal pressure gradients near the capillary wall rapidly compress the plasma to form a dense, hot column with a high density of Ne like Ar ions, with high axial uniformity.[3.40c] Collisional electron impact excitation of the ground state Ne like Ar ions produces a population inversion between the 3p $^1S_0$ and 3s $^1P_1$ levels of Ar^{+8}, resulting in amplification of light at 46.9 nm (26.5 eV). The laser is described in greater detail in ref. 3.40a.

A pair of mirrors placed in a Z fold configuration just before the ionization region of the TOFMS (Figure 1a.) provides alignment capability and focus for the laser beam with

respect to the molecular cluster beam at the ionization source. The Z-fold mirror set consists of two 1 inch diameter Sc/Si multilayer mirrors with about 40% reflectivity each;[3.41] a planar mirror, placed 30.5 cm from a f = 50 cm concave mirror, focuses the incoming laser beam to the ionization region of the TOFMS. The use of these optics improves the experimental set up in three ways: 1. the two mirrors allow full directional control of the ionizing 46.9 nm bright beam in order to improve alignment (motor controls for the mirrors are external to the vacuum system); 2. improved intensity of the light beam at the ion source region by using a focusing mirror for a tight focal spot; and 3. a tight focal spot that results in sharp (ca. 10 ns) TOFMS features. The mirror Z-fold has a transmissivity of about 10 percent, that reduces the soft x-ray laser pulse energy from ~10 μJ/pulse at the output of the laser to ~1 μJ/pulse at the entrance of the ionization region.

Neutral clusters are generated in a supersonic expansion of desired gases from a pulsed nozzle (200 μm diameter opening). During operation, saturated water or methanol vapor in He is formed by flowing He (99.9% General Air) at a pressure of 25 psi through a reservoir containing liquid distilled water or methanol (spectroscopic grade) at room temperature. The molecular beam is collimated by a 2.0 mm diameter skimmer, located approximately 2 cm downstream from the nozzle. For generation of ammonia clusters, 15% ammonia is seeded into the He carrier gas. Neutral clusters are ionized by the soft x-ray laser at 26.5 eV. For the linear TOF detection mode, the positive ions formed by a single photon ionization process are accelerated to 4000 eV of total kinetic energy by a three-plate Wiley-McLaren assembly (0, 3750, 4000 V), as shown in Figure 3.1a. The accelerated ions travel 110 cm in a field free flight tube and arrive at a microchannel plate

(MCP) detector at the end of the tube. For the reflectron mode of operation ions are accelerated by three plates (0, 700, 1000 V) after ionization and pass through the first field free region toward the reflection voltage grid. Ions are then reflected to travel another ~65 cm in a field free region to another MCP detector (see Figure 3.1a). Metastable fragmentation of the ions leaving the acceleration/source region and entering the first field free region can occur in the latter region of the TOFMS. Daughter ions generated in the first field free region by metastable (slow, 1 – 100 μs) dissociation have lower kinetic energy than their parent ions but the same speed. Parents and daughters arrive at the linear TOFMS mode detector at the same flight time but can be separated in time, by adjusting the reflectron grid voltages, at the reflectron detector. Pressure in the field free and detector regions is maintained at 2×10^{-6} Torr during the experiment. Experiments are conducted to ensure that collision induced dissociation of cluster ions is negligible.

Since the 26.5 eV photons from the soft x-ray laser are able to ionize the He carrier gas employed in the expansion, the MCP detector voltage is gated to reduce the gain of the plates when He^+ arrives at the detector in order to prevent detector circuit overload and saturation. Signals from the detector are analyzed by a 350 MHz, 5 Gs/s digitizing oscillioscope through a 50 Ω MHV connector. Time delays between valve opening, ionization laser firing, and MCP gating are generated by two programmable Stanford Research System digital delay generators (DG 535). All timings are adjusted to maximize the spectral signal strengths.

3.1.2 Results and Discussion

3.1.3.1 Water Clusters

Distribution of Water Clusters Ionized by 26.5 eV Photons

Figure 3.2 displays a reflectron TOF mass spectrum of water clusters ionized by the 26.5 eV soft x-ray laser. All of the cluster features in this spectrum (except $(H_2O)_2^+$) arise from protonated water clusters of the general formula $(H_2O)_nH^+$. The parent cluster ions $(H_2O)_nH^+$ labeled by P_n in the figure are generated from the neutral species $(H_2O)_{n+1}$, ionized by the soft x-ray laser; following this event, the intracluster proton transfer reaction,

$$(H_2O)_{n+1} + h\nu \rightarrow \left[(H_2O)_{n+1}^+\right]^* + e^- \rightarrow (H_2O)_n H^+ + OH + e^-, \qquad (3.1a)$$

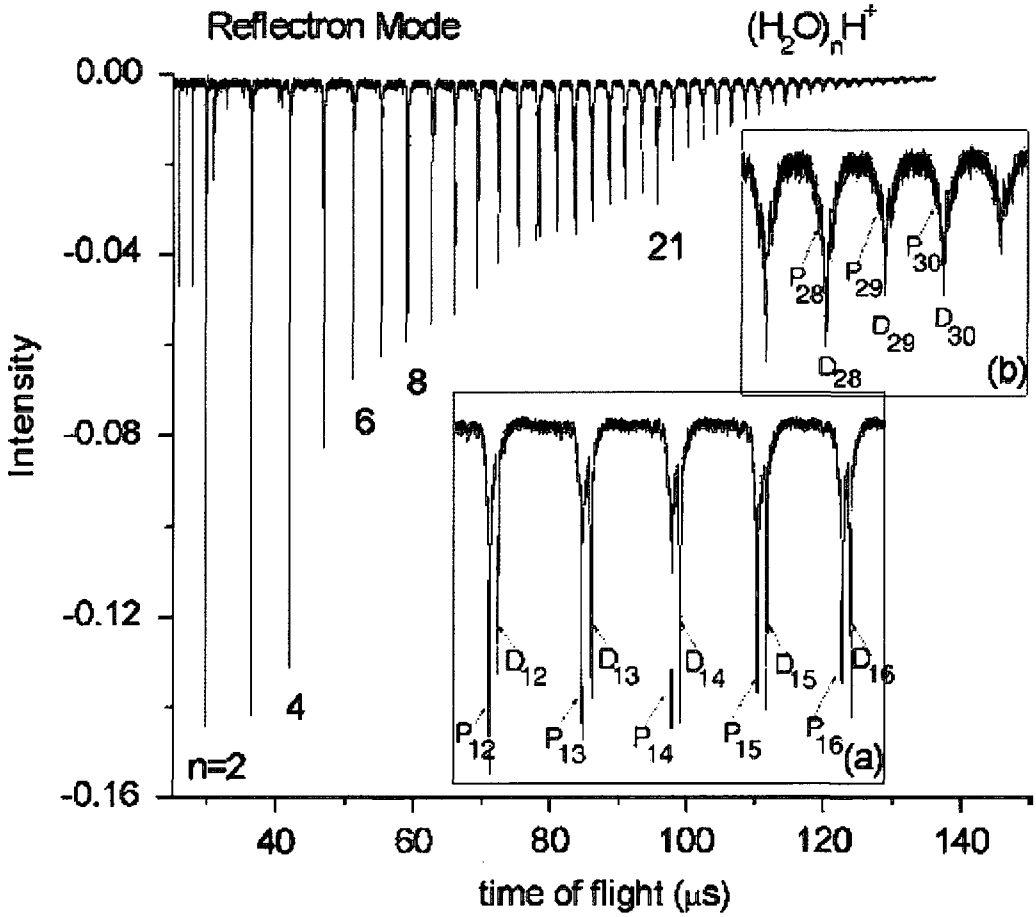


Figure 3.2: A reflection TOF mass spectrum of water clusters ionized by a 26.5 eV soft x-ray laser. P_n stands for the parent ion $(H_2O)_nH$; D_n represents the daughter ion formed from P_{n+1} via losing a single water molecule in the first field-free region.

is initiated. These parent ion signals dominate the mass spectrum of water clusters for small clusters up to n=14. This is shown clearly in the insert spectra of Figure 3.2. Daughter ions labeled D_n are created from parent ions P_{n+1} by unimolecular dissociation in the first field free region of the reflectron TOFMS by the reaction,

$$(H_2O)_{n+1}\,H^+ \rightarrow (H_2O)_n\,H^+ + H_2O. \qquad (3.1b)$$

In linear mode operation, D_n and P_{n+1} appear at the same mass channel but these two features can be separated by adjusting the reflectron grid potentials in the reflectron mode for the TOFMS. Daughter ion signals appear and dominate the mass spectral peaks in the region of larger clusters. Note that unimolecular dissociation of cluster ions is more rapid for larger clusters than smaller ones, as the D_n daughter features become larger than the P_n parent features in the spectrum. This apparent anomaly (i.e., non-RRKM behavior for clusters of a constant amount of internal energy), and the correctness of the above implicit assumption that the reaction,

$$(H_2O)_n + h\nu \rightarrow (H_2O)_n^+ + e^- \rightarrow (H_2O)_{n-1-m}\,H^+ + OH + e^- + m\,H_2O, \quad (3.2)$$

does not occur rapidly (< 1 ns) in the ionization region will be discussed later in this section after more of the data is presented and discussed.

For the 9-mer cluster ion (from the 10-mer neutral cluster), the ratio of daughter ion to parent ion intensity is about 0.34. This ratio increases to about 1.0 at n=14. This result is in agreement with those of $(H_2O)_n$ by fs multiphoton ionization (MPI).[3.13] A distinct intensity drop occurs between peaks $(H_2O)_{21}H^+$ and $(H_2O)_{22}H^+$, as can be seen in Figure 3.2, for the reflectron mode of operation of the TOFMS. The $(H_2O)_{21}H^+$ feature exhibits an enhanced intensity compared to its neighbor features. The overall $(H_2O)_nH^+$ intensity distribution also exhibits less distinct irregularities at the $(H_2O)_{28}H^+$ and $(H_2O)_{29}H^+$

features. Both $(H_2O)_{21}H^+$ and $(H_2O)_{28}H^+$ are typically suggested as "magic numbers" and have especially stable structures according to calculations.[3.42-3.46] These irregular intensity patterns have been supported for several different types of experiments.[3.14-3.20] Although the 26.5 eV photon energy is absorbed by a water cluster, no doubly charged species are apparent in the mass spectrum. Doubly charged water cluster ions are reported for large clusters (n >, 37) using a multiphoton (800 nm) fs ionization technique.[3.13]

Spectra obtained by the two TOFMS modes of operation are compared in Figure 3.3. The upper spectrum is obtained in the linear TOFMS mode: it records the size distribution for cluster ions created in the acceleration region, approximately within less than 1 μs following single photon 26.5 eV ionization. Note that this ion intensity decreases roughly exponentially and smoothly as a function of cluster size n. No obvious intensity anomaly at $(H_2O)_{20}H^+$ generated from $(H_2O)_{21}$ ionization is observed. This indicates that the neutral cluster $(H_2O)_{21}$ does not enhance the intensity of its "daughter" protonated $(H_2O)_{20}H^+$ cluster in the distribution of protonated cluster ions. Thus the neutral cluster distribution in the beam is roughly exponentially decreasing as a function of cluster size n. The lower spectrum in Figure 3.3 is obtained with the TOFMS operated in the reflectron mode. This spectrum indicates the population distribution of cluster ions formed in the first field free region within the time range 1-80 μs. A strong intensity decrease for the parent cluster ion P_{22}, $(H_2O)_{22}H^+$, and an obvious intensity enhancement at daughter ion D_{21}, $(H_2O)_{21}H^+$, which derives from the reaction,

$$(H_2O)_{22}H^+ (P_{22}) \rightarrow (H_2O)_{21}H^+ (D_{21}) + H_2O$$

can be readily discerned. Note that P_{21} is not significantly more intense than P_{20} in Figure 3.3. Similarly, the daughter ion of P_{21}, D_{20}, is not significantly smaller than other

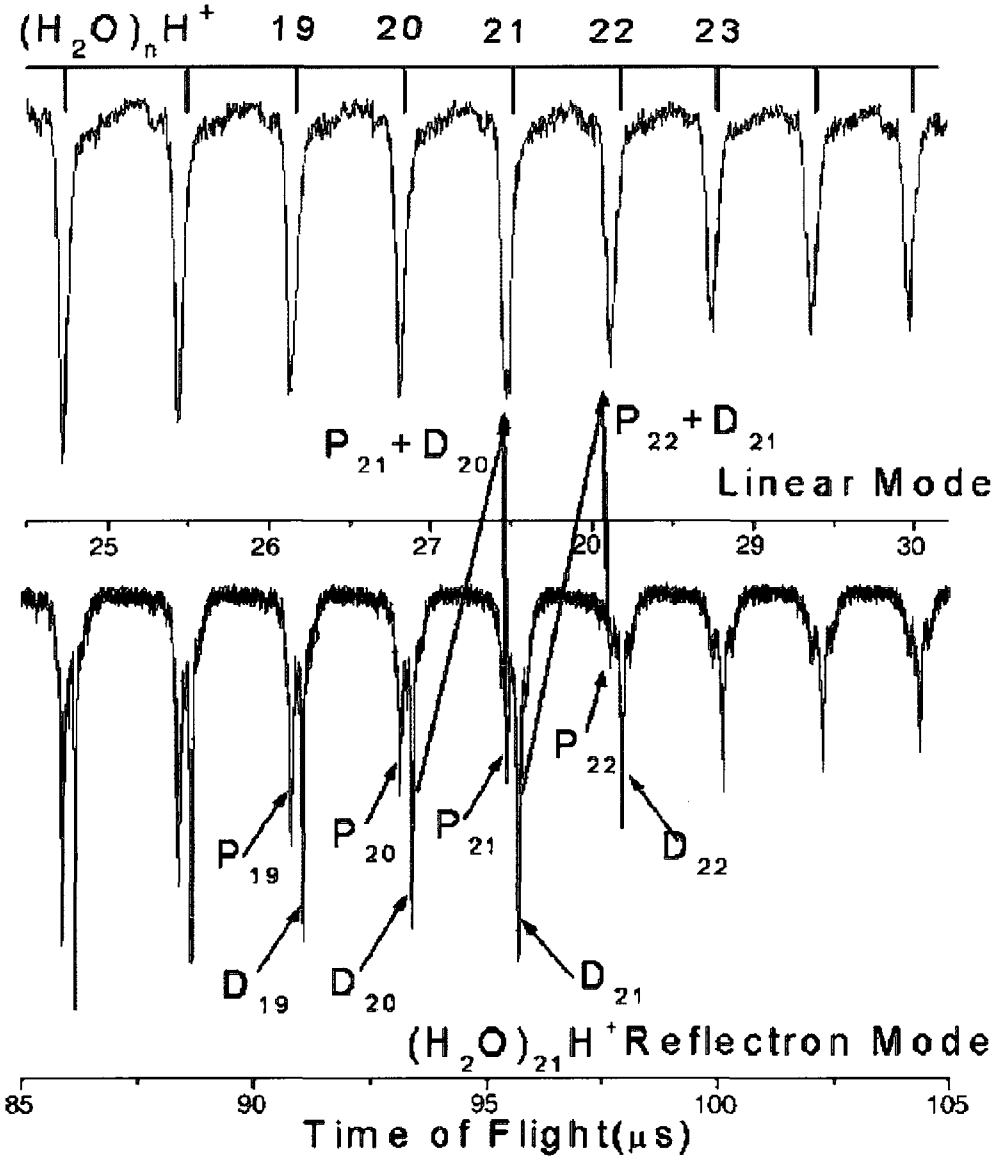


Figure 3.3: Mass spectrum of size distribution of water cluster ions around the region of n=21. The upper spectrum is obtained by a linear mode. It reflects the distribution of the water cluster ions generated in ionization region. The lower spectrum is obtained by a reflectron mode. It shows the distribution of water cluster ions after the metastable decay in the first field-free region.

neighbor daughter ions, such as D_{19}. D_{21} appears to be the most intense feature in this mass region. This set of intensities indicates that the parent ion P_{21} (created from $(H_2O)_{22}$ ionized by 26.5 eV photon) does not evidence an especially stable structure even though calculations suggest enhanced stability for P_{21}.[3.42-3.46] Collecting and organizing all these facts leads one to the conclusion that the intensity anomalies ca. n=21 are due to the

unstable behavior of the metastable parent ion P_{22}, $(H_2O)_{22}H^+$, which arises from the neutral cluster $(H_2O)_{23}$ in the molecular beam. The parent ion P_{22}, $(H_2O)_{22}H^+$, dissociates rapidly in the field free region yielding an enhanced signal intensity for D_{21}, its daughter species.

Echt and co-workers[3.7] also observed similar behavior employing electron impact (EI) ionization at 40 eV in a linear mode TOFMS. In their experiment, a positive voltage was applied to a barrier grid in front of the detector to block daughters from reaching the detector. This was accomplished because, while daughter ions have nearly the same velocity as parent ions in the field free region between the acceleration region and the linear mass detector, they have lower kinetic energy. They found that the parent P_{22} ion intensity is much lower than its neighbors $(H_2O)_{21}H^+$ (P_{21}) and $(H_2O)_{23}H^+$ (P_{23}). The conclusion is that the parent ion P_{22} dissociates rapidly after leaving the acceleration region of the TOFMS. On the other hand, if no positive potential barrier is placed in front of the mass detector (that is, parent and daughter ions are simultaneously detected at the same mass channel-time), the distribution of protonated cluster ions decreases roughly exponentially with increasing cluster size. The implication of these results is that the neutral cluster distribution evidences no anomalies. Thus both the present data and those of ref. 3.7 reach the same conclusions, implying that 40 eV EI and 26.5 eV single photon ionization yield the same cluster ion distribution based on the same neutral cluster distribution.

Observation of Neutral Water Dimer.

As shown in Figure 3.4a, a small signal for $(H_2O)_2^+$ is observed on the low mass side of $(H_2O)_2H^+$, the daughter ion for $(H_2O)_3$. In general, unprotonated water clusters are not

observed in our experiments in which He is employed as the backing/expansion gas. Most of the neutral dimers in the beam generate $(H_2O)H^+$ ions following single photon ionization by 26.5 eV photons. If 5% Ar is mixed into the He expansion gas, the $(H_2O)_2^+$ signal increases and the H_3O^+ signal decreases (see Figure 3.4b). For a 20% Ar/80% He expansion, the $(H_2O)_2^+$ mass feature is much larger than that for H_3O^+ (Figure 3.4c).

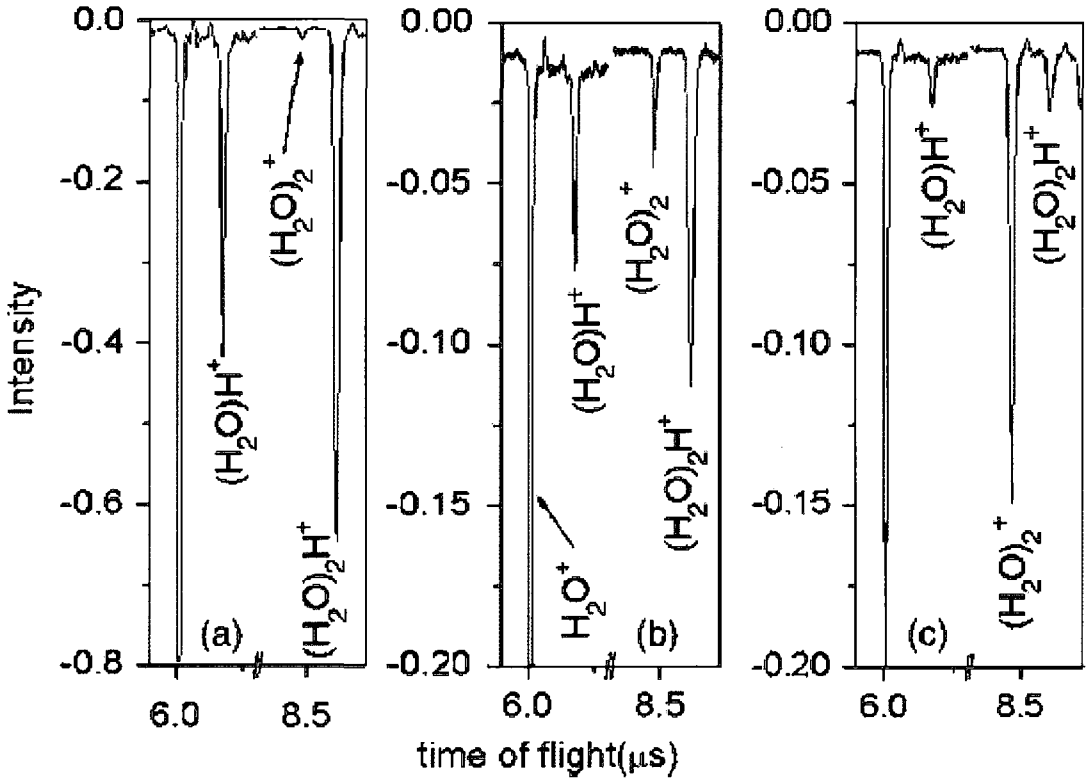


Figure 3.4: TOF mass spectra of unprotonated water dimer ion formed in different carrier gases: (a) pure He gas, (b) 5% Ar mixed in He gas, and (c) 20% Ar mixed in He gas, respectively.

Intensity of the protonated cluster ion $(H_2O)_2H^+$ also decreases as Ar concentration in the binding gas is increased.

Ng et al.[3.29] measured appearance potentials for H_3O^+ and $(H_2O)_2^+$ as 11.73 and 11.21 eV respectively. Shinohara et al[3.12] observed various unprotonated water cluster ions $(H_2O)_n^+$ $(2 \leq n \leq 10)$ by photoionization of neutral $(H_2O)_n$ with atomic VUV resonance lines at 11.83 and 11.63 eV. They explain that unprotonated ions are produced

from mixed $Ar_n (H_2O)_m^+$ cluster ions followed by loss of Ar through evaporation. They also observe that 40 eV EI ionization does not yield $(H_2O)_n^+$ signals. Nonetheless, Shiromaru and co-workers[3.47] observe $(H_2O)_n^+$ ($1 \leq n \leq 6$) cluster ions ionized by synchrotron radiation at 85 nm (14.6 eV) for the $Ar/H_2O/He$ system. This photon energy is ca. 3 eV larger than that employed with Ar resonance lamps and certainly enough excess energy above the VIE of $(H_2O)_n^+$ to induce intra cluster proton transfer and form $(H_2O)_{m-1}H^+$. They suggest that the unprotonated water clusters are generated because most of the excess energy following single photon ionization is removed from the cluster by the exiting electron.

Single photon ionization by a 26.5 eV photon is also much more energy (ca. 15 eV) than that required for ionization of all the water clusters. If this energy were to remain in the clusters, we would observe only H_2O^+ and its fragments in our TOFMS. Nonetheless, $(H_2O)_2^+$ is observed in this experiment even with no Ar present in the expansion. Again this suggests that almost all of the excess energy in these clusters (ca. 15 eV) is removed by the exiting electron. Single photon ionization of water clusters thus seems to be very gentle in terms of fragmentation even with a 26.5 eV photon.

In the preceding presentation of results and discussion, dissociation of protonated water cluster ions, directly following the ionization of neutrals in the ion source/extraction region of the TOFMS, is assumed not to occur. The loss of at most only one water molecule for each cluster $(H_2O)_nH^+$ (created by ionization, rapid proton transfer, and loss of OH) through metastable dissociation occurs only in the flight tube (1 to 2 μs after ionization). While this assumption cannot be proved by our data or that of others, the following four observations can be collected to support this assumption. First,

the linear mode TOFMS reflects the size distribution of cluster ions formed within the acceleration/extraction region of the TOFMS, approximately less than 1 μs following ionization (see Figure 3.3). The individual features of cluster ions $(H_2O)_nH^+$ $17 \leq n \leq 25$ can be fit to a Gaussian curve. If metastable dissociation of cluster ions $(H_2O)_nH^+$ were to occur in less than 1 μs, a long tail should be observed on each cluster feature in the linear mass spectrum to the high mass, long time side of each peak. Second, one knows that the intensity of the mass peak for $(H_2O)_{21}H^+$ is due to the fast metastable dissociation of the $(H_2O)_{22}H^+$ cluster ion. If metastable dissociation of $(H_2O)_{22}H^+$ occurs in the acceleration/extraction region of the TOFMS, an enhanced intensity of $(H_2O)_{21}H^+$ should be observed in the linear mode TOFMS, as the linear spectrum reflects the cluster ion distribution formed within this region. As shown in Figure 3.3, this is not the case. Nonetheless, an enhanced intensity is clearly observed for $(H_2O)_{21}H^+$ in the reflectron TOFMS (Figure 3.3), proving the metastable fragmentation of $(H_2O)_{22}H^+$ to generate $(H_2O)_{21}H^+$ occurs in the flight tube at times between ~1 and ~100 μs. Only the loss of one monomer is observed in the reflectron TOFMS of water clusters. Third, based on studies of cluster ion metastability, the unimolecular decay occurs within a time window 1 to 15 μs for these cluster ions.[3.11,3.48] This additionally holds true for methanol,[3.23] ammonia,[3.49] and acetone[3.50] cluster ions. Fourth, if very rapid cluster ion fragmentation was to occur in the ionization/acceleration/extraction region of the TOFMS for all the clusters, at least some of the cluster ions should show such behavior as a function of size, and more complex line shapes and cluster populations should be apparent in either linear or reflectron TOFMS operation.

Dissociation Rate Constants for Metastable Water Cluster Ions.

Unimolecular dissociation of metastable protonated water clusters can be observed during the time window ~1 to ~80 μs, corresponding to the flight time in the first field free region of the reflectron TOFMS. The decay fractions, $I_D/(I_D + Ip)$, for clusters have been obtained (Figure 3.5) in which I_D and Ip are the integrated intensities of the daughter and parent ions, respectively. An obvious increase in the decay fractions occurs at n = 22, and this fraction decreases slightly at n = 21. These results show good agreement with observations reported by Shi et al.[3.11] using chemical ionization. Both our results and those of Shi et al. are plotted in Figure 3.5.

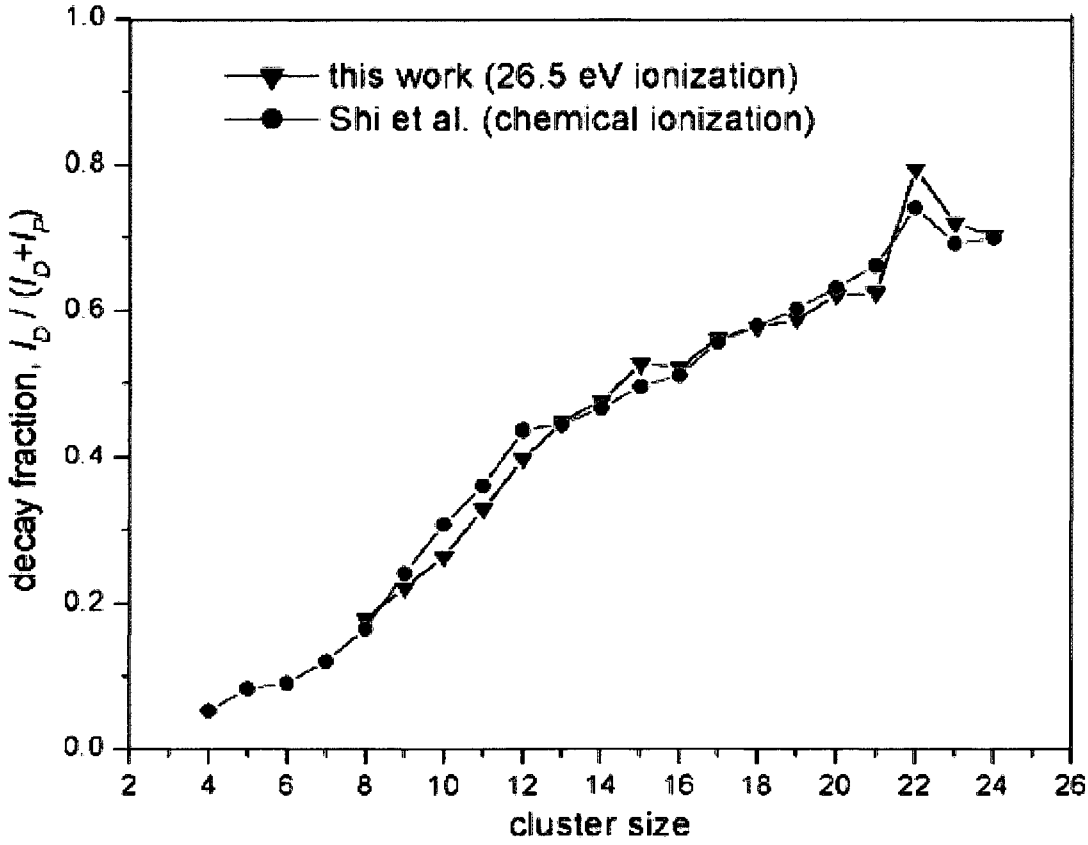


Figure 3.5: Decay fractions of protonated water clusters $(H_2O)_nH^+$, as a function of cluster size *n* (Ref. 3.11).

The unimolecular dissociation rate constant for protonated water cluster ions can be obtained from these decay fractions. The rate constant k can be represented as

$$k = -\left(\frac{1}{t}\right) \ln\left[1 - \frac{I_D}{I_D + I_P}\right]$$

$$= -\frac{1}{t} \ln\left[\frac{I_P}{I_D + I_P}\right], \qquad (3.3)$$

in which t is the flight time of the parent ion in the first field free region of the reflectron TOFMS. For the present apparatus, this flight time is about 60% of the total reflectron flight time shown in the reflectron TOFMS of Figure 3.2. Rate constants for the metastable dissociation of parent cluster ions to daughter cluster ions are found to be in the range from 0.6 to 2.7 x 10^4 s^{-1} within cluster ion size range $9 \leq n \leq 24$, as plotted in Figure 3.6. An obvious increase in dissociation rate constant occurs for k_{22}. These rate constants are in agreement with those reported using fs ionization:[3.13] for $8 \leq n \leq 18$, k_n falls in the range 0.8 to 1.3 x 10^4 s^{-1}. This correspondence further suggests that the assumed fragmentation behavior (loss of only one water molecule following the proton transfer reaction to generate $(H_2O)_nH^+$ cluster ions, which occurs slowly in the first field free region of the reflection TOFMS) is correct.

An obvious decrease in cluster ion intensity occurs at P_{22} in the parent ion distribution and an increase in cluster intensity occurs at D_{21} in the daughter ion distribution (see Figure 3.3). This behavior is caused by the fast dissociation of protonated water clusters at P_{22}, $(H_2O)_{22}H^+$: thus the n = 21 cluster ion has been termed a "magic number." Suggestions have been made that this enhanced cluster stability at n =

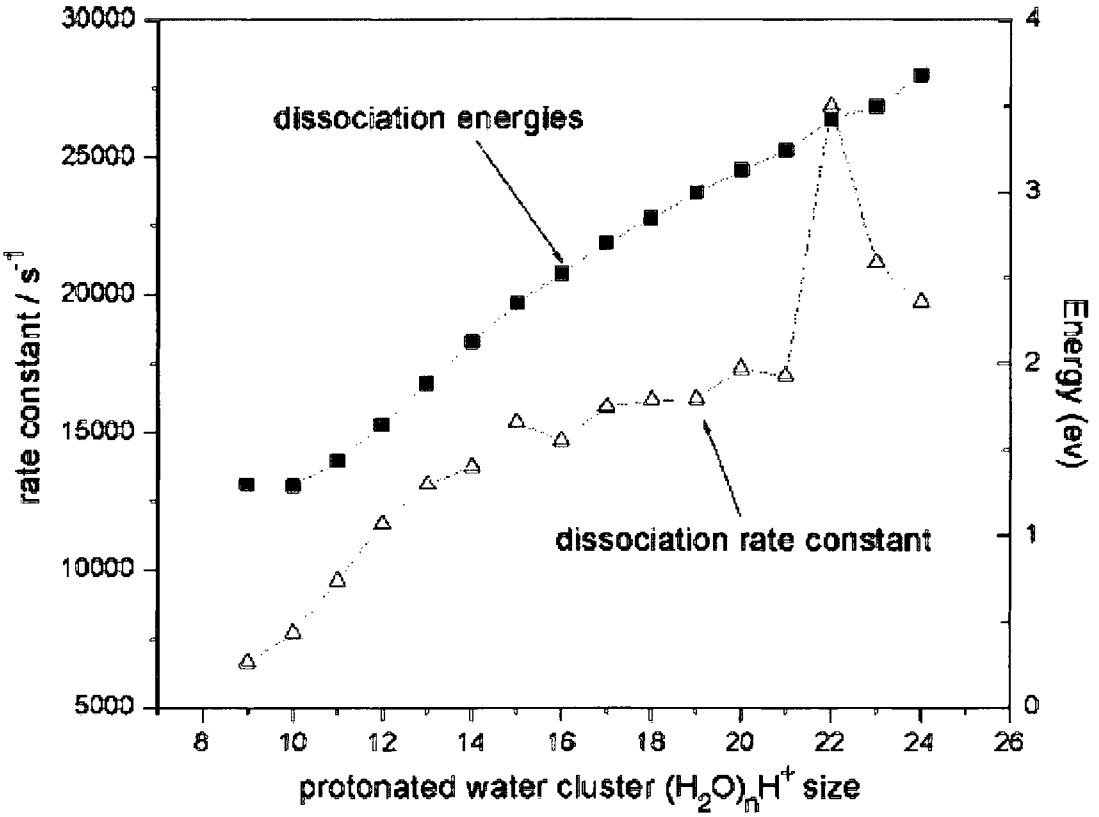


Figure 3.6: Metastable dissociation rate constants and dissociation energies for protonated water clusters.

21 is due to a stable dodecahedral cage structure of the protonated $(H_2O)_{21}H^+$.[3.42-3.46] An anomalously small dissociation rate of parent $(H_2O)_{21}H^+$ compared to its neighbor parent cluster ions is not observed, however. We find no clear evidence in our experiments to document that $(H_2O)_{21}H^+$ is more stable than other cluster ions. Based on our observations we conclude that the "magic number" at n = 21 is due to the enhanced dissociation rate of parent ion $(H_2O)_{22}H^+$ to its daughter ion $(H_2O)_{21}H^+$ (i.e., $P_{22} \rightarrow D_{21} + H_2O$). The energy required for metastable unimolecular dissociation of parent ion clusters in the field free drift tube can be calculated employing classical RRK theory,[3.51]

$$k = \nu(1 - E_{bind}/E_{dissoc})^{s-1}, \qquad (3.4)$$

in which $E_{activation}$ is replaced by E_{bind} of protonated water clusters. One assumes here no barriers to dissociation exist for this process; that is, $E_{activation} \sim E_{bind}$. Values of E_{bind} are taken from ref. 3.11. The ensuing rate constants k are illustrated in Figure 3.6. A value of $\nu = 10^{13}$ s^{-1} is taken for the intermolecular vibrational coordinate frequency for the dissociative reaction coordinate. Assuming that only intermolecular degrees of freedom participate in the dissociation of $(H_2O)_nH^+$ to $(H_2O)_{n-1}H^+ + H_2O$ in the field free region, S = 6n – 6. Water has three internal vibrational modes 3675, 3756, and 1595 cm^{-1}.[3.66] For large clusters these molecular modes also make a contribution to dissociation due to fast internal transfer of vibrational energy. Based on the heat capacity of water clusters, ref. 3.11 suggests that $C_n = (6.6\ n - 6)\ k_B$ for $6 \leq n \leq 29$, and thus with $E = C_nT$, $S = (6.6\ n - 6)$ is reasonable for RRK calculations of k for water clusters. Similar results obtain for ammonia clusters.[3.52] E_{dissoc} for the unimolecular reaction $P_n \rightarrow D_{n-1} + H_2O$ is also given in Figure 3.6 and Table 3.1. The dissociation energy does not change much at n = 22 (P_{22}), although the k_{22} rate constant for loss of H_2O at n = 22 is much larger than that of other clusters, due to the exponential relation for $k \propto E^S$ given in eq (3.4).

Vibrational Temperature of Water Clusters.

Neutral water clusters are ionized by absorption of a 26.5 eV single photon. If all the photon energy is used to ionize and subsequently dissociate the clusters, they will, however for large n, fragment in single H_2O molecules. This point is, in fact, the main reason we explore the behavior of van der Waals and hydrogen bonded clusters with respect to 26.5 eV single photon ionization. Nonetheless, the water cluster ion distribution appears in the TOFMS, and even the unprotonated dimer is observed (see Figure 3.4). One can thus reasonably assume that almost all the photon energy above the

Table 1. Data used to calculate the temperature of neutral water clusters in the molecule beam.

n	E_{disso} (ev)[a] $(H_2O)_{n-1}H^+$	$-\Delta_aH_{n-1,n}$ (ev)[b]	$-\Delta_bH_{n,n+1}$ (ev)[c]	ΔH_n (eV)[d] $(H_2O)_n$	E_{excess} (eV)[e] $(H_2O)_{n-1}H^+$	E_{therm} (eV)[f] $(H_2O)_n$	Temp. (K) $(H_2O)_n$
2		1.409	0.456	11.73			
3		0.872	0.529	10.777			
4		0.759	0.383	10.435			
5		0.581	0.356	10.059			
6		0.520	0.454	9.834			
7		0.464	0.697	9.768			
8		0.522	0.391	10.002			
9		0.424	0.497	9.871			
10	1.298	0.381	0.259	9.943	1.057	0.242	47
11	1.290	0.386	0.622	9.822	1.178	0.112	20
12	1.441	0.404	0.445	10.058	0.940	0.500	79
13	1.647	0.426	0.495	10.099	0.898	0.749	109
14	1.886	0.447	0.369	10.168	0.830	1.056	142
15	2.126	0.460	0.466	10.090	0.907	1.219	152
16	2.347	0.465	0.439	10.096	0.901	1.446	169
17	2.519	0.470	0.540	10.070	0.927	1.592	174
18	2.705	0.467	0.368	10.140	0.856	1.848	190
19	2.843	0.467	0.529	10.040	0.955	1.888	184
20	2.992	0.457	0.446	10.103	0.892	2.100	193.
21	3.127	0.458		10.092	0.908	2.219	194

[a] E_{dissoc}, calculated based on dissociation rate constant obtained in present experiment.
[b] $\Delta_aH_{n-1,n}$, taken from experimental data of reference [3.11] and webbook.nist.gov.
[c] $\Delta_bH_{n,n+1}$, taken from theoretical calculations of references [3.53,3.54].
[d] ΔH_n, calculated from the thermodynamic cycles displayed in Figure 3.8.
[e] E_{excess} = VIP(11.0 eV) - ΔH_n.
[f] $E_{therm} = E_{dissoc} - E_{excess}$.

vertical ionization energy (VIE) is removed from the cluster by the exiting photoelectron. This assumption is also suggested by ref. 3.12 based on observed unprotonated water clusters ($2 \leq n \leq 6$) in an Ar carrier gas using 85 nm (14.6 eV) ionization. Ab initio calculation of the VIEs of water clusters (n = 2-8) show that VIEs decrease with increasing cluster size n and appear to converge ca. 11.0 eV. We thereby suggest that for neutral cluster ionization by 26.5 eV photons, photon energy above ~11.0 eV is removed by the exiting photoelectron for clusters $9 \leq n \leq 24$. Part of the deposited photon energy

in the neutral cluster $(H_2O)_n$ must be used to initiate the proton transfer reaction $\left[(H_2O)_{n+1} \rightarrow (H_2O)_n H^+(P_n) + OH\right]$ and the following unimolecular dissociation of the protonated cluster $\left[(H_2O)_n H^+(P_n) \rightarrow (H_2O)_{n-1} H^+ (D_{n-1}) + H_2O\right]$. If we neglect the transitional energy release of the fragments, the excess energy (E_{excess}) that comes from a soft x-ray laser photon and is used for metastable dissociation of $(H_2O)_n H^+$, can be determined.

As shown in Figure 3.7, the excess energy is the difference between VIE (~11.0 eV) of a water cluster and the reaction energy (ΔH_n) of $(H_2O)_n \rightarrow (H_2O)_{n-1}H^+ + OH + e^-$. Thus E_{excess} = (VIE (11.0 eV) - ΔH_n) with ΔH_n for cluster sizes $9 \leq n \leq 22$ calculated based on the thermodynamic cycle shown in Figure 3.8. $\Delta_a H_{n-1,n}$ is the reaction energy of a protonated cluster $(H_2O)_{n-1} H^+$ combined with a water molecule to generate $(H_2O)_n H^+$. This value can be obtained from the experimental data of ref. 3.11. $\Delta_b H_{n,n+1}$ is the reaction energy of the neutral cluster $(H_2O)_n$ combined with another water molecule. This value is obtained from calculations.[3.53,3.54] Thus the following relation can be obtained:

$$\Delta H_{n+1} = \Delta H_n + \Delta_a H_{n,\,n-1} - \Delta_b H_{n,\,n+1}. \qquad (3.5)$$

Appearance energy of H_3O^+ is measured as 11.73 eV[3.29] and the ΔH_2 of the dimer reaction is known as

$$(H_2O)_2 \rightarrow (H_2O)H^+ + OH \quad \Delta H_2 = 11.73 \text{ eV}. \qquad (3.6)$$

Given eq. (3.6) ΔH_3, ΔH_4, ... can be calculated. ΔH_n is the minimum energy required for initiation of the reaction $(H_2O)_n \rightarrow (H_2O)_{n-1}H^+ + OH + e^-$ without excess energy used for metastable dissociation of the protonated cluster, $(H_2O)_{n-1}H^+$. These ΔH_n values are listed in Table 3.1.

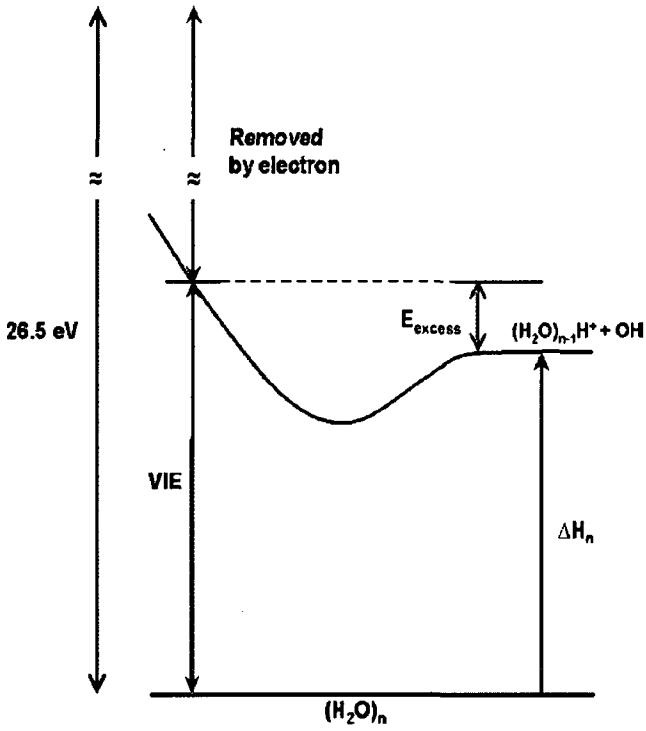


Figure 3.7: Schematic of the potential energy diagram for ionization of water clusters. 26.5 eV photon energy is absorbed by a neutral water cluster, $(H_2O)_n$. The photon energy above VIE is removed by an electron. H_n is the minimum energy to initiate the reaction of $(H_2O)_n \rightarrow (H_2O)_{n-1}H^+ + OH$. Excess energy ($E_{excess}$)comes from a soft x-ray laser photon to be used for metastable dissociation of $(H_2O)_{n-1}H^+$.

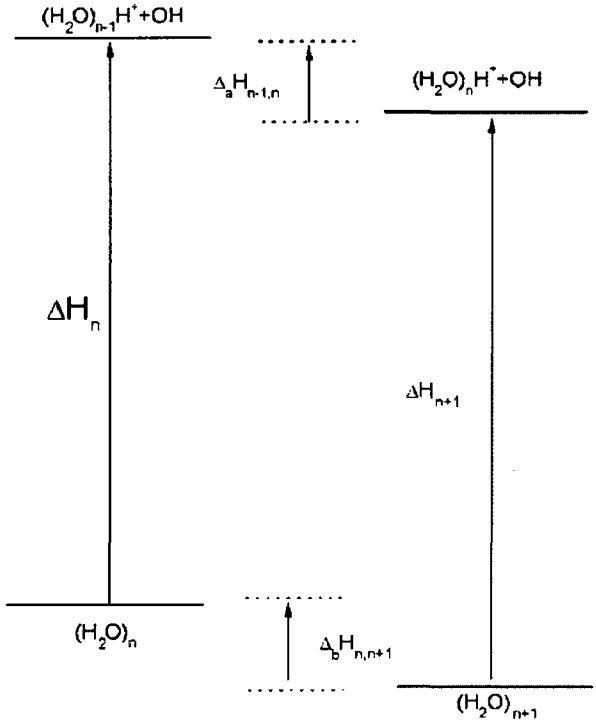


Figure 3.8: Thermodynamic energy diagram for water clusters.

Through comparison of the dissociation energy (E_{dissoc}) calculated based on experimental data and the excess energy (E_{excess}) that is deposited by the soft x-ray laser photon upon ionization, one finds that $E_{excess} < E_{dissoc}$, implying that just E_{excess} is insufficient to dissociate the metastable cluster ion at the experimentally determined rate. The required E_{dissoc} for the metastable cluster ion can come from two sources. One source is E_{excess} from the ionization photon (listed in Table 3.1). Another source is the internal thermal vibrational energy of the neutral cluster, which depends on cluster temperature in the molecular beam. The cluster thermal energy can thus be calculated by the relation $E_{therm} = E_{dissoc} - E_{excess}$, as listed in Table 3.1. Based on a thermodynamic mechanism, k_BT is the thermal (statistical) energy associated with each degree of freedom for the cluster. The vibrational energy contribution to the total cluster available energy is $E_{therm} = k_BT$ (6.6n – 6). The temperatures of neutral water clusters can thus be estimated within this classical approximation. As shown in Table 3.1 they are in the range 40-200 K for clusters $10 \leq n \leq 21$. The higher temperatures of larger clusters with respect to smaller ones are due to the exothermic reaction of added water molecules to the neutral clusters. This must be true if the RRK calculated dissociation rate constant k_n increases rather than decreases with increasing cluster size. The results in Table 3.1 for T_n give $T_{11} < T_{10}$ because the reaction energy for n = 10 ($\Delta_b H_{10,11} = 0.259$ eV) is lower than that for n = 11: this result gives $\Delta H_{10} > \Delta H_{11}$. Additionally, perhaps the VIEs of all water clusters ($9 \leq n \leq 21$) are not truly constant at 11.0 eV, especially near the small cluster end of this range.

3.1.1.2 Methanol clusters

Distribution of Methanol Clusters Ionized at 26.5 eV.

The reflectron TOFMS of methanol clusters ionized by 26.5 eV photons is shown in Figure 3.9. Two major series of ion peaks are observed: the protonated $(CH_3OH)_nH^+$ (P_n parent ions) and their daughter ion peaks $(CH_3OH)_{n-1}H^+$ (D_{n-1}). The protonated parent ions are generated from the neutrals by a rapid internal ion-molecule reaction as follows:

$$(CH_3OH)_n + h\nu \rightarrow \left[(CH_3OH)_n^+\right]^* + e^- \rightarrow (CH_3OH)_{n-1}\,H^+ + CH_3O + e^-. \quad (3.7)$$

Daughter ions are generated in the field free flight tube at longer times (ca. 1-80 μs) by the loss of one CH_3OH molecule,

$$(CH_3OH)_{n-1}\,H^+ \rightarrow (CH_3OH)_{n-2}\,H^+ + CH_3OH. \quad (3.8)$$

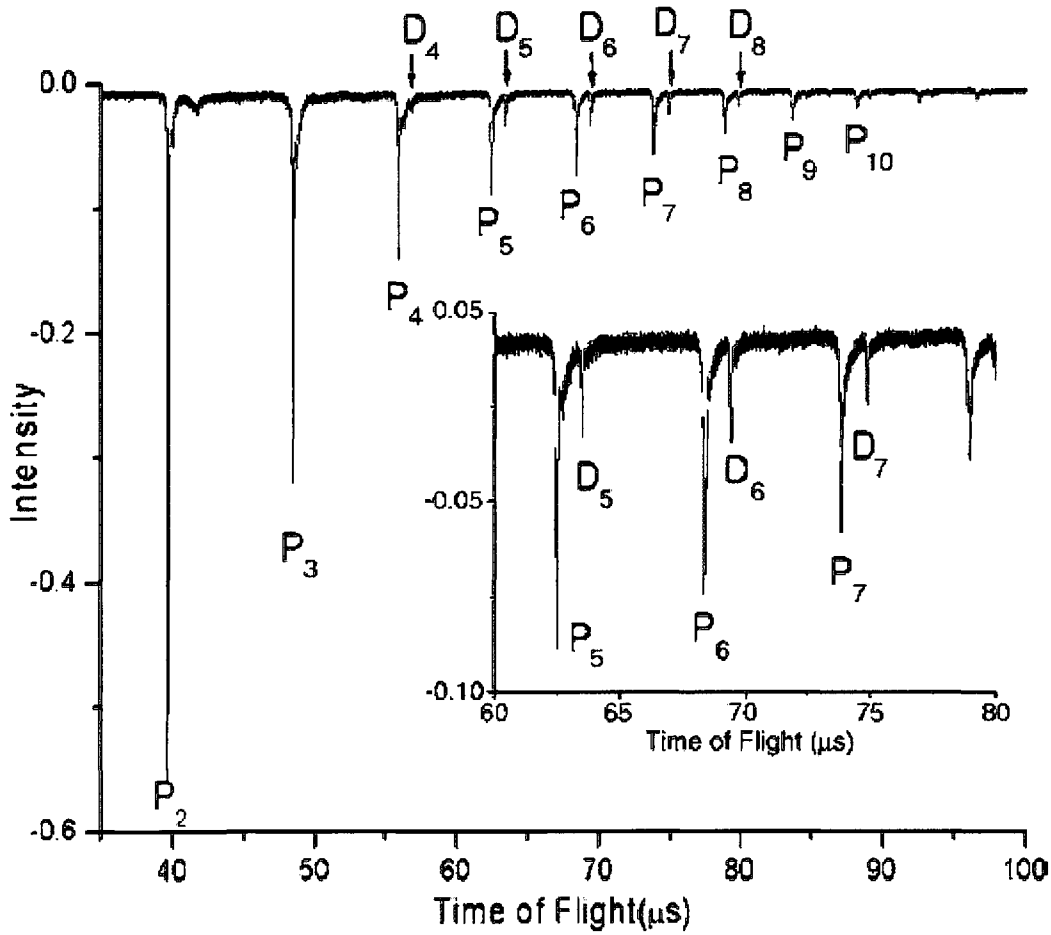


Figure 3.9: A reflectron TOF mass spectrum of methanol clusters photoionized by a 26.5 eV soft x-ray laser. The peaks labeled P_n correspond to parent ion series. The peaks labeled D_n belong to the daughter ion series, which is formed via loss of CH_3OH from parent ions P_{n+1}.

In our single photon 26.5 eV ionization approach, only one (CH_3OH) is lost by the parent cluster ion [See the discussion for the water clusters concerning this point]. In MPI experiments,[3.23,3.25] loss of up to five methanol monomers from the protonated octomer is observed. Ions corresponding to unprotonated clusters, $(CH_3OH)_n^+$ (n>2), are not generally detected employing a pure He expansion. Garvey and co-workers[3.21] observed unprotonated cluster ions ($n \leq 7$) in an Ar expansion, as has been observed for water clusters (see above and ref. 3.12). They suggest that in this instance and with ionization by low energy electron impact ($\leq$ 20 eV), such species can be attributed to indirect ionization of neutral heteroclusters of the form $Ar_m(CH_3OH)_n$ via intracluster Penning ionization. A similar behavior is also observed by Shinohara et al.[3.12,3.65] for water and ammonia clusters. The soft x-ray laser generated mass spectrum shows no intensity peak anomalies and the intensity of $(CH_3OH)_nH^+$ features is smoothly decreasing with increasing n. Similar results obtain for EI,[3.21,3.22] 118 nm,[3.26,3.27] and MPI[3.23-3.25] studies of the methanol cluster system.

Some studies[3.22,3.26,3.27] have found that the protonated trimer ion $(CH_3OH)_3H^+$ is more intense than the protonated dimer feature while others[3.21,3.23-3.25] have not. The present results show $(CH_3OH)_2H^+$ more intense than $(CH_3OH)_3H^+$ by roughly 60% (see Figure 3.9). This is not due to fragmentation of larger clusters by 26.5 eV ionization in the ionization/acceleration region as the protonated dimer feature is narrower than the larger cluster features including the protonated trimer. In these experiments $(CH_3OH)_2H^+$ is not fragmented from larger clusters and we suggest that the observed intensity distribution represents (but clearly is not identical to) the neutral methanol cluster distribution in the molecular beam. Arguments against rapid wholesale fragmentation of

neutrals in the ionization region have been offered for water clusters and a similar set of reasons can be offered in this instance against such an occurrence. The 118 nm ionization results,[3.26,3.27] which give the protonated dimer ion signal smaller than the protonated trimer ion signal, can be explained as due to a near threshold ionization of the neutral trimer leading to a reduced cross section for ionization. The reduced ionization cross section near threshold can be associated with a poor Franck-Condon overlap between the neutral and ionic methanol trimer.

Another series of cluster ions is observed in EI[3.21,3.22] and MPI[3.23,3.24] experiments. These clusters are identified by the empirical formula $(CH_3OH)_nH_3O^+$ for $n \geq 7$. The suggested product generation mechanism is

$$(CH_3OH)_nH^+ \rightarrow (CH_3OH)_{n-2}(H_2O)H^+ + (CH_3)_2O. \qquad (3.9)$$

This series of clusters is not observed by either 10.5 eV[3.26] or 26.5 eV single photon ionization. Reaction (3.9) requires roughly 2 kcal/mol more activation energy than reaction (3.8) in order to occur[3.22] for $(CH_3OH)_nH^+$, $n \geq 3$. For near threshold 118 nm (10.5 eV) ionization one can assume that the $(CH_3OH)_nH^+$ cluster ions do not have sufficient activation energy for the reaction (3.9) channel to be open. The reason that 26.5 eV ionization does not generate reaction (3.9) is most probably the same: excess energy above the VIE for those clusters is removed by the exiting electron, as is found above for water clusters.

A weak feature is observed (Figure 10) at m/z = 47 and is assigned as $(CH_3)_2OH^+$. This feature probably arises from the methanol dimer as follows:[3.55]

$$(CH_3OH)_2H^+ \rightarrow (CH_3)_2OH^+ + H_2O, \quad \Delta H = 22.7 \text{ kcal/mol}. \qquad (3.10)$$

The $(CH_3)_2OH^+$ ion is also observed by MPI[3.23,3.24] and EI,[3.21,3.22] but not by 118 nm ionization.[3.26,3.27] Again the suggestion is that near threshold ionization (118 nm) and, in general, single photon (46.9 nm) ionization does not leave sufficient energy in the protonated dimer ion (neutral timer) to open reaction channel (3.10). Reaction (3.8) has a lower activation energy than either (3.9) or (3.10).

Photolysis of Methanol Monomer and Dimer.

Figure 3.10 depicts the mass spectrum of the methanol monomer and dimer ionized by 26.5 eV photons. The products CH_3^+, CHO^+, CH_2O^+, CH_2OH^+/CH_3O^+ and CH_3OH^+

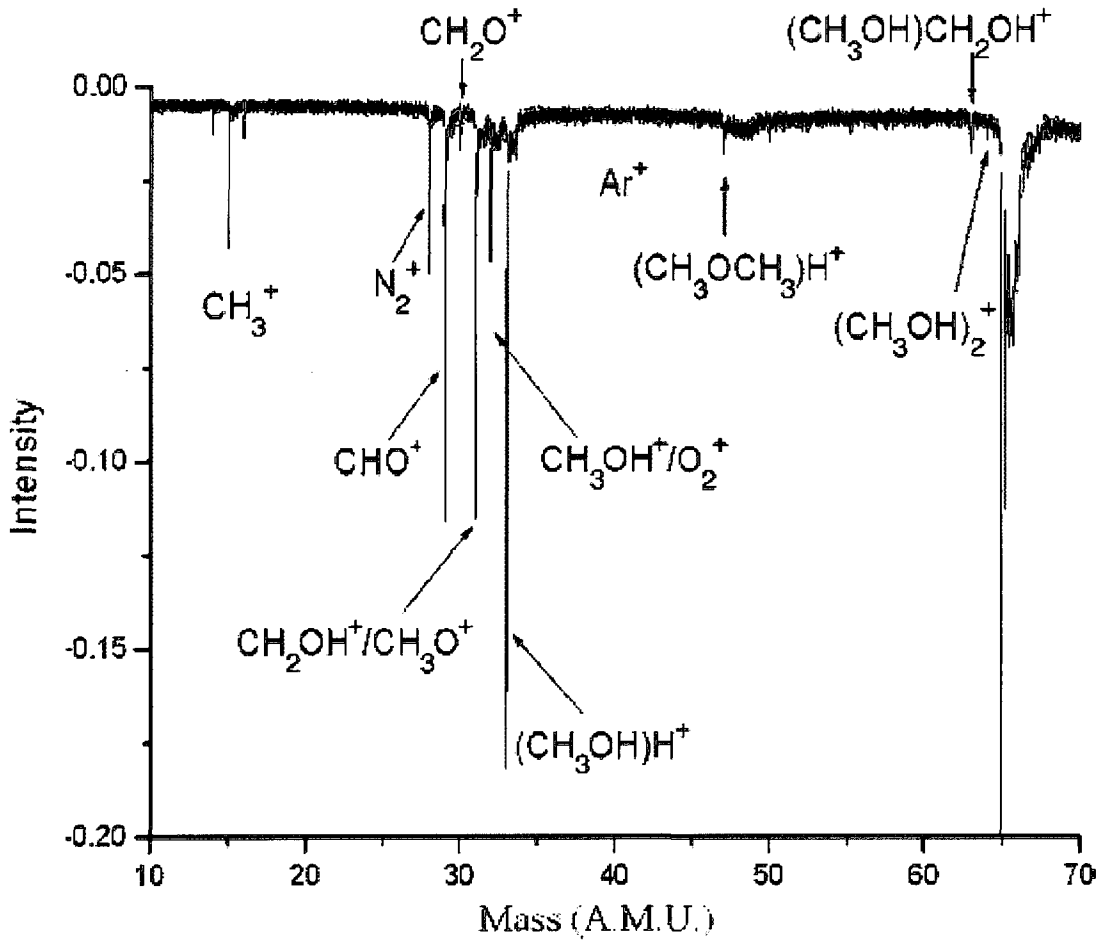


Figure 3.10: Mass spectrum of methanol monomer and dimer ionized by a 26.5 eV soft x-ray laser.

are observed from photolysis of the CH_3OH molecule. The product channels are thus,

$$CH_3OH + h\nu \rightarrow CH_3OH^+ \qquad 20.2 \qquad (3.11a)$$

$$\rightarrow CH_3^+ + OH \qquad 12.5\% \qquad (3.11b)$$

$$\rightarrow CHO^+ + H_2 + H \qquad 31.5\% \qquad (3.11c)$$

$$\rightarrow CH_2OH^+/CH_3O^+ + H \qquad 31.2\% \qquad (3.11d)$$

$$\rightarrow CH_2O^+ + H_2 \qquad 4.6\% \qquad (3.11e)$$

The CHO^+ and CH_2OH^+/CH_3O^+ are the major photolysis channels, with the undissociated methanol ion channel yielding about 20% of the product species. CH_3OH^+ is not observed for MPI,[3.23,3.24] as either predissociation occurs before ionization or ionization occurs at very high internal methanol excess energy.

An additional minor feature associated with the methanol dimer appears at the $(CH_3OH)CH_2OH^+$ mass channel, as shown in Figure 3.10. Similar ions are not observed for larger clusters. One possible reason for the rich ion chemistry for CH_3OH and $(CH_3OH)_2$, but not $(CH_3OH)_n$, $n > 2$, is that for these two species the VIE can be much larger than the adiabatic ionization energy (AIE) and thus the ionization process generates more excess energy in these two small species than it does for larger clusters.

Dissociation Rate Constant of Metastable Methanol Cluster Ions.

The unimolecular dissociation rate constant for the loss of one CH_3OH from the cluster $(CH_3OH)_nH^+$ can be obtained from the decay fraction of the parent cluster P_n. The approach employed here is the same as that employed to analyze the decay rate of water cluster ions. As shown in Figure 3.11, the dissociation rate constants are in the range 3.6 to 6.0×10^3 s^{-1} for methanol cluster ion sizes $5 \leq n \leq 11$. Compared with the results of MPI experiments,[3.25] the rate constants obtained are ~ 2-3 times smaller. These rates

again suggest that MPI deposits more energy into the neutral methanol clusters than does single photon ionization, even at 26.5 eV, which is ca. 15 eV above the cluster VIE. This point is also documented by the absence of product cluster ions such as $(CH_3OH)_n\ H_3O^+$ (observed by MPI and EI studies).

Based on the dissociation rate constant for $(CH_3OH)_nH^+ \rightarrow (CH_3OH)_{n-1}H^+ + CH_3OH$, the dissociation energy (E_{dissoc}) required for the unimolecular (statistical –

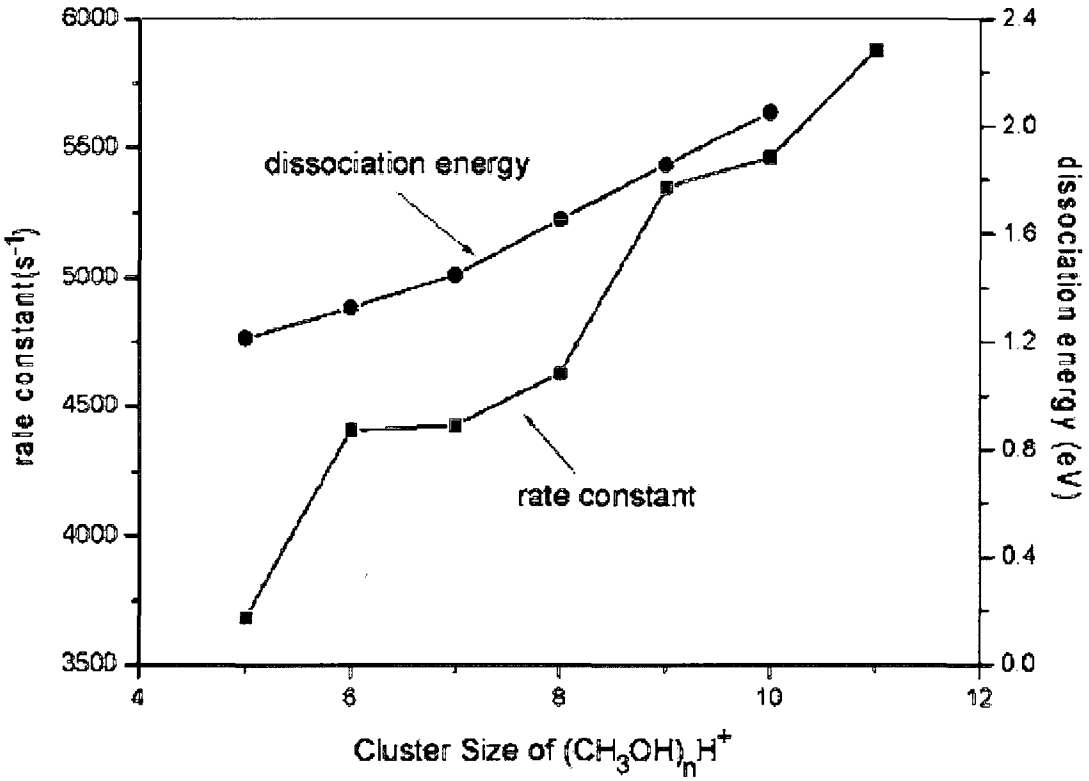


Figure 3.11: Metastable dissociation rate constants and dissociation energies for protonated methanol clusters.

RRK) dissociation of protonated methanol cluster ions can be calculated. The values for $E_{bind,n}$ are taken from ref. 3.56. The rate constants are shown in Figure 3.11. The methanol molecule has two vibrational modes whose energies (295 and 200 cm^{-1})[3.66] are very close to those for the cluster van der Waals modes: we thus let S = 8n – 6, and $E_{dissoc,n}$ can be obtained as listed in Table 3.2 and plotted in Figure 3.11. More energy is

required for unimolecular dissociation of larger clusters, since these clusters have a larger number of vibrational states in which to store energy than do smaller ones. Note that the larger clusters dissociate faster than the smaller ones: this is not a statistical (ergodic) result if the clusters are considered to have a constant amount of energy based on VIE and reaction energies. This is, of course, the same trend as found for water clusters above.

Vibrational Temperature of Neutral Methanol Clusters.

The distribution of protonated methanol cluster ions obtained by 26.5 eV ionization is about the same as that observed for 10.5 eV ionization except for the protonated dimer ion intensity. Apparently all the energy above the VIE of methanol clusters is removed by the photo-ejected electron. This point has also been documented above for water clusters. If product translational energy release is neglected, the excess energy (E_{excess}) due to x-ray laser photon absorption by the cluster that is used for the metastable dissociation of $(CH_3OH)_nH^+$ can be calculated (as discussed above for the water cluster system) as,

$$E_{excess} = VIE - \Delta H_n,$$

with ΔH_n for

$$(CH_3OH)_n \rightarrow (CH_3OH)_{n-1}H^+ + CH_3O$$

calculated based on the same thermodynamic cycle employed for water clusters (see Figures 3.7 and 3.8). The $\Delta_a H_{n-1,n}$ is the reaction energy of a protonated methanol cluster ion $(CH_3OH)_{n-1}H^+$ combining with a methanol molecule. $\Delta_b H_{n,n+1}$ is the reaction energy of the neutral cluster $(CH_3OH)_n$ combining with a methanol molecule, and can be generated from theoretical calculations.[3.57] The appearance energy of the $CH_3OH_2^+$ product has been measured as 10.5 eV:[3.21]

$$(CH_3OH)_2 \rightarrow (CH_3OH)H^+ + CH_3O, \quad \Delta H_2 = 10.5 \text{ eV}. \qquad (3.12)$$

Thus ΔH_3, ΔH_4, ..., ΔH_{10} can be calculated and are listed in Table 3.2. ΔH_n is the minimum energy required for the initiation of the reaction (3.12) without excess energy used for metastable dissociation of protonated methanol cluster ions.

The VIE for larger methanol clusters is not known, but it should not change much with increasing cluster size. Based on a study by Cooke et al.,[3.58] the VIE of $(CH_3OH)_5$ is about 9.9 eV; the VIE for $5 \leq n \leq 10$ is thereby taken as 9.9 eV. The calculated results for E_{excess} for these clusters are given in Table 3.2. Comparing the cluster ion dissociation energies $E_{dissoc,n}$, to their excess energies, $E_{excess,n}$, thus obtained, one finds that $E_{excess,n} < E_{dissoc,n}$. In other words, the energy deposited in the cluster upon ionization is not enough to dissociate the metastable clusters as rapidly as is observed experimentally. The extra (thermal) energy must come from the neutral cluster and the difference between E_{dissoc} and E_{excess} must be E_{therm}. $E_{therm,n}$ then generates a temperature for each neutral cluster in the supersonic beam.

Neutral cluster temperatures are presented in Table 3.2. These vary from 50 to 100 K for neutral clusters $6 \leq n \leq 11$. These temperatures appear reasonable when compared to those obtained for neutral water clusters (Table 3.1). The temperatures of neutral water are about 40 to 100 K for the sizes n = 10 to 15. According to theoretical calculations, the binding energy of neutral water clusters and methanol clusters is similar (ca. 1800 – 2000 cm^{-1} for the dimers). Since the exact VIE is not known experimentally for methanol clusters, the temperatures reported here should be thought of as an estimate of the internal energy of the neutral clusters.

Table 2. Data used to calculate the vibrational temperature of neutral methanol clusters in the molecule beam.

n	E_{dissoc} (eV)[a] $(H_2O)_{n-1}H^+$	$\Delta_aH_{n-1,n}$ (eV)[b]	$\Delta_bH_{n,n+1}$ (eV)[c]	ΔH_n (eV)[d] $(H_2O)_n$	E_{excess} (eV)[e] $(H_2O)_{n-1}H^+$	$E_{thermal}$ (eV)[f] $(H_2O)_n$	Temp (K) $(H_2O)_n$
2		1.435	0.416	10.58			
3		1.14	0.674	9.56			
4		0.698	0.567	9.09			
5		0.585	0.532	8.96	0.94		
6	1.213	0.542	0.442	8.91	0.99	0.223	62
7	1.326	0.516	0.468	8.81	1.09	0.236	55
8	1.451	0.52	0.473	8.76	1.14	0.311	62
9	1.655	0.52	0.492	8.71	1.19	0.465	82
10	1.857			8.69	1.21	0.647	102
11	2.052						

[a] E_{dissoc}, calculated based on dissociation rate constant obtained in present experiment.
[b] $\Delta_aH_{n-1,n}$, taken from experimental data of reference [3.56].
[c] $\Delta_bH_{n,n+1}$, taken from theoretical calculations of references [3.57].
[d] ΔH_n, calculated based on the same thermodynamic cycles employed for water cluster in Figure 8.
[e] E_{excess} = VIP(9.9 eV) - ΔH_n.
[f] $E_{therm} = E_{dissoc} - E_{excess}$.

3.1.2.3 Ammonia Clusters

Distribution of Ammonia Clusters Ionized by a Soft x-ray Laser.

Figure 3.12 presents a typical reflectron TOFMS of ammonia clusters ionized at 26.5 eV by single photon ionization. Most of the prominent features in the spectrum are identified as protonated ammonia cluster ions with the general formula $(NH_3)_nH^+$. They are generated, as by now expected, from intracluster ion-molecule reactions upon ionization of the neutral clusters in the molecular beam. For single photon ionization this reaction has been proposed as an absorption-ionization-dissociation mechanism,

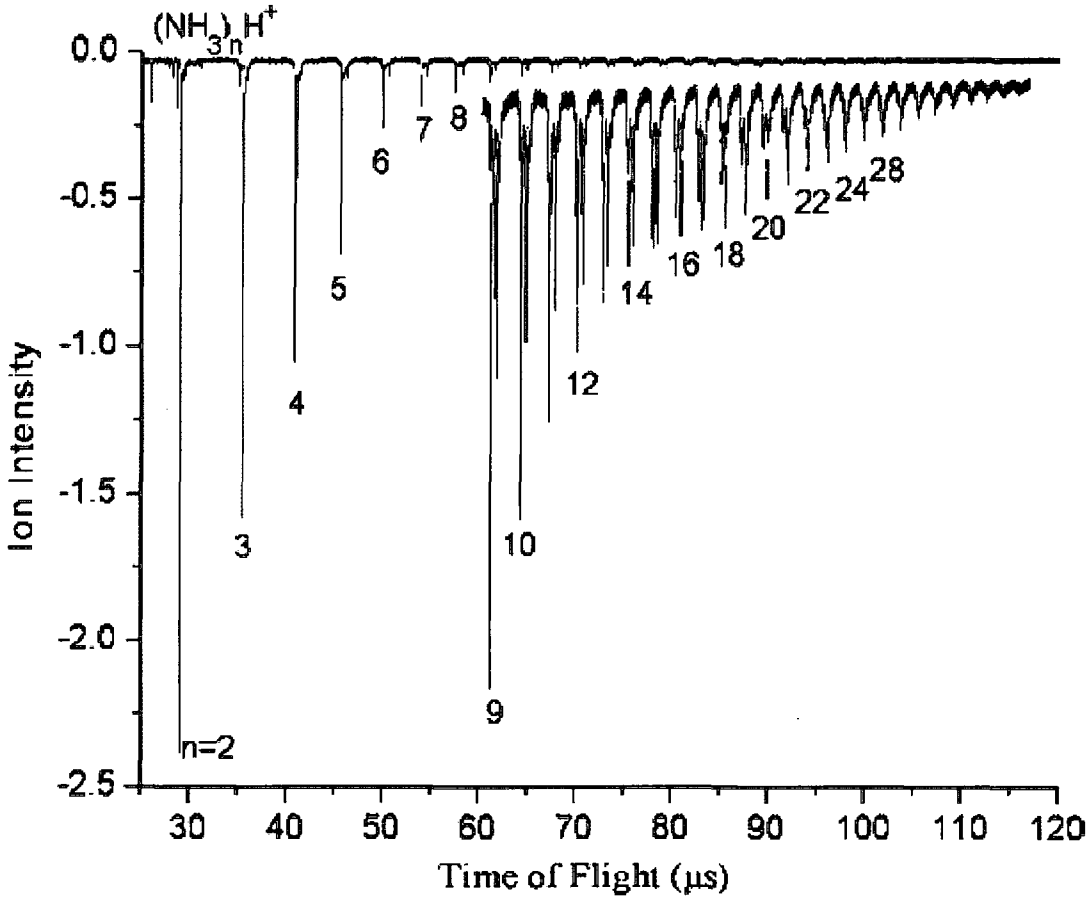


Figure 3.12: A reflectron TOF mass spectrum of ammonia clusters ionized by a 26.5 eV soft x-ray laser.

$$(NH_3)_n + h\nu \rightarrow \left[(NH_3)_n^+\right]^* + e^- \rightarrow (NH_3)_{n-1}H^+ + NH_2 + e^- . \qquad (3.13)$$

Intensities of protonated ammonia cluster ions decrease roughly exponentially with increasing cluster size n. A significant drop in intensity occurs at n = 6 and special cluster ion sizes are not observed in the spectrum. Similar behavior for this system has been observed by other ionization techniques such as EI,[3.30,3.31] ns laser MPI,[3.32,3.33] fs laser MPI,[3.34,3.35] and single photon ionization.[3.36] A high resolution spectrum for small clusters is presented in Figure 3.13. Five different series of cluster ions are identified in this mass range. These are labeled A_n, B_n, P_n, D_n, E_n in Figure 3.13. The peaks labeled P_n represent parent ions of the protonated ammonia cluster series. P_n are generated from the

neutral clusters $(NH_3)_{n+1}$ by intracluster ion-molecule reaction upon ionization. They dominate the spectrum at small cluster sizes up to n = 14. Peaks marked D_n are daughter ions of the parent protonated ammonia clusters. They are created by the unimolecular dissociation of P_{n+1}, $(NH_3)_{n+1}H^+ \rightarrow (NH_3)_nH^+ + NH_3$, in the first field free region of the reflectron TOFMS. In the absence of collision induced dissociation processes, only one ammonia molecule is lost for each parent protonated cluster ion for all observed clusters $5 \leq n \leq 22$. Daughter ion signals dominate the spectrum for larger ammonia clusters, $n \geq 14$.

The cluster ion series labeled B_n can also be observed in the mass spectrum presented in Figure 3.13: these species can be identified for $5 \leq n \leq 12$ in our experiments. This series of clusters is observed for $n \sim 25$ by EI[3.59] ionization. These clusters have been suggested to have the formula $(NH_3)_nH_2^+$. Series B_n features can be generated from an intracluster ion-molecule reaction as follows:

$$(NH_3)_{n+1}^+ \rightarrow (NH_3)_nH_2^+ + NH \qquad (3.14)$$

Some part of the intensity of these features could arise from the presence of water in the clusters as $(NH_3)_{n-2}(H_2O)NH_4^+$ and $(NH_3)_{n-1}H_2^+$ have the same mass.

Another series of cluster ions labeled E_n is identified as $(NH_3)_{n-1}NH_2^+$ in Figure 3.13. This series is generated from neutral cluster $(NH_3)_n$ by loss of one H atom during the ionization process,

$$(NH_3)_n + h\nu \rightarrow \left[(NH_3)_n^+\right]^* + e^- \rightarrow (NH_3)_{n-1}NH_2^+ + H + e^- \qquad (3.15)$$

The remaining (fifth) series as shown in Figure 3.13 is discussed in the next subsection and is labeled A_n ($(NH_3)_n^+$).

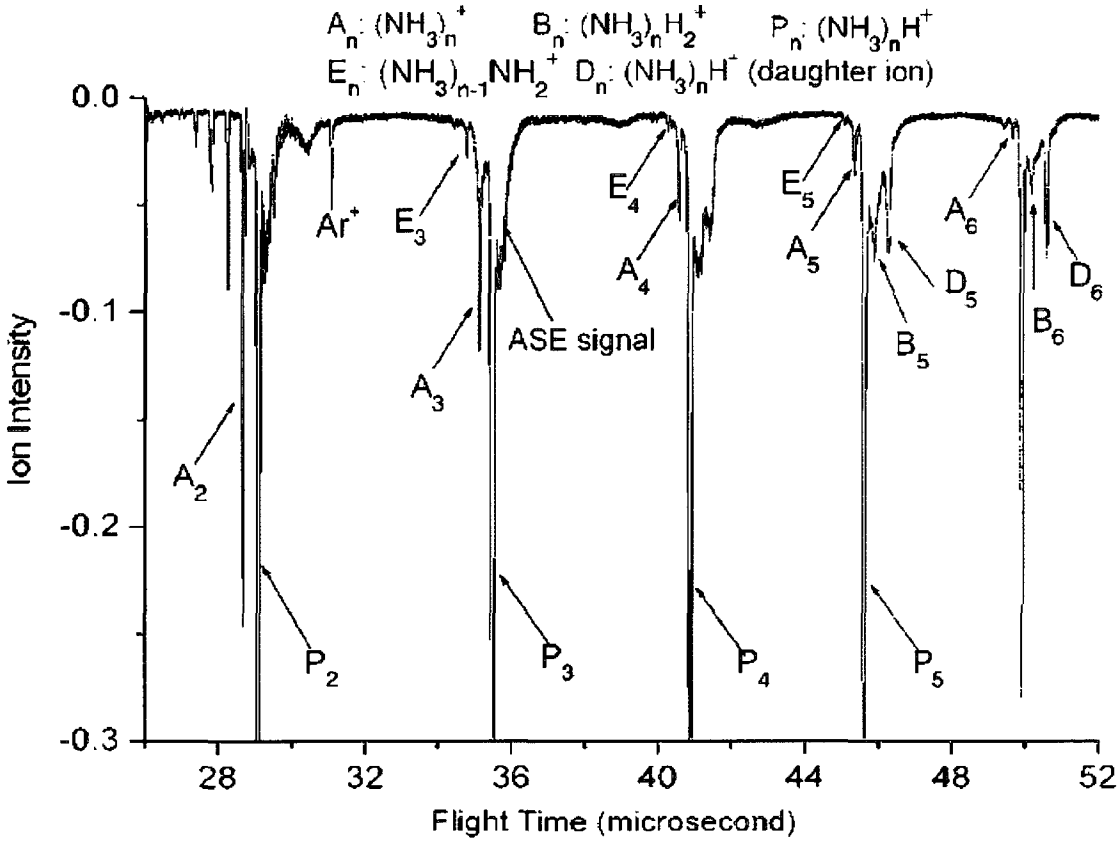


Figure 3.13: A high-resolution reflectron TOF mass spectrum of small ammonia clusters ionized by a 26.5 eV soft x-ray laser. A_n: unprotonated cluster ions generated directly from the ionization of neutral ammonia clusters $(NH_3)_n$. P_n: parent protonated ammonia ions generated from a neutral cluster $(NH_3)_{n+1}$. D_n: daughter ions formed from parent ions P_{n+1} via loss of one NH_3 molecule. B_n: one mass larger than protonated ammonia ions. They are generated from $(NH_3)_{n+1}$ via losing NH after ionization. E_n: one mass smaller than $(NH_3)^+$ ions. they are generated from $(NH_3)_n$ via loss of one H atom during the ionization process.

Unprotonated ammonia cluster Ions $(NH_3)_n^+$.

Figure 3.13 also shows unprotonated ammonia cluster ions labeled A_n (observed for $2 \leq n \leq 20$). They are formed by direct ionization of $(NH_3)_n$ neutral clusters that do not undergo a proton transfer reaction or a fragmentation reaction following ionization with a single photon of 26.5 eV. A plot of the unprotonated cluster ion intensity as a function of cluster size n is presented in Figure 3.14. The intensity distribution of $(NH_3)_n^+$ exhibits a sharp decrease at n = 6, increases slowly to n = 10, and then decreases again with

increasing n. Also plotted in Figure 3.14 is the intensity ratio $(NH_3)_n^+/(NH_3)_{n-1}H^+$, both components of which come from the same neutral parent clusters $(NH_3)_n$. This ratio

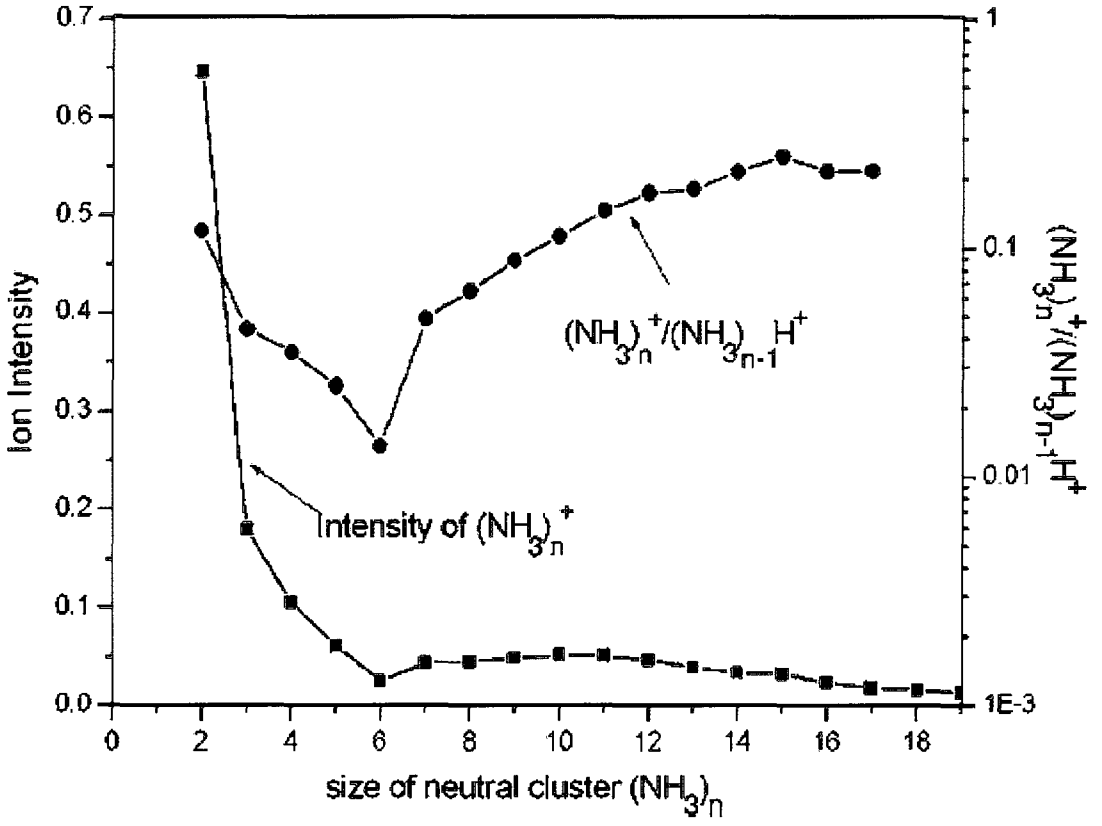


Figure 3.14: Plots of the intensity distributions of unprotonated ammonia clusters and intensity ratio distributions of $(NH_3)_n/(NH_3)_{n-1}H^+$ as a function of cluster size *n*.

has a distinct minimum at n = 6 and a maximum at n = 15. These patterns imply that proton transfer reactions proceed more rapidly for n = 6, which in turn seems to suggest an enhanced structured stability for $(NH_3)_5H^+$. Note the reduction in relative intensity for $(NH_3)_6H^+$ in Figure 3.12.

A comparison of these results with those generated with atomic resonance lamp radiation [Ar (11.83 and 11.62 eV), Kr (10.64 and 10.03 eV), and Xe (9.57 eV)] employed for ionization,[3.36] proves interesting. In both experiments a single photon is absorbed by a neutral ammonia cluster for ionization but the photon energies are quite

different; nonetheless, similar trends are observed in the distribution of unprotonated ammonia clusters in all instances. For resonance lamp ionization, unprotonated ammonia cluster ions are observed for n = 2 to 25, and the intensity ratios $(NH_3)_n^+/(NH_3)_{n-1}H^+$ have a minimum at n = 6. The largest intensity for the $(NH_3)_2^+$ is observed with Xe (9.57 eV) ionization and the $(NH_3)_2^+$ intensity decreases for Kr and Ar lamp ionization. This behavior is not observed for $(NH_3)_n^+$ with $n \geq 3$. The 26.5 eV ionization intensities resemble those for Kr lamp ionization. EI ionization finds $(NH_3)_n^+$ features only for $n \geq 10$ and these signals depend on the electron energy.[3.36] Again these comparisons relate the usefulness of single photon ionization and demonstrate the fact that the ionized electron carries with it most, if not all, of the excess photon energy above the VIE of the neutral cluster.

Photolysis of NH_3, $(NH_3)_2$ and $(NH_3)_3$.

As shown in Figure 3.15A, product species NH_3^+, NH_2^+ and NH^+ are observed from the ionization of NH_3 by a 26.5 eV photon. The main product from this ionization is NH_2^+. The appearance energy for NH_2^+ from NH_3 is 15.8 eV.[3.60] Intensity of the NH_2^+ ion feature is about 1.7 times larger than that of the NH_3^+ ion. Only a small intensity is detected for the NH^+ ion, whose threshold is 17.1 eV.[3.61] Three channels are identified for the photolysis/ionization of NH_3 by a 26.5 eV photon:

$$NH_3 + h\nu(26.5\,eV) \rightarrow NH_3^+ + e^- \qquad 36\% \qquad (3.16a)$$

$$\rightarrow NH_2^+ + H + e^- \qquad 62.6\% \qquad (3.16b)$$

$$\rightarrow NH^+ + 2H + e^-. \qquad 1.3\% \qquad (3.16c)$$

The percentage values in the eq. (3.13) are the branching ratio for these reactions.

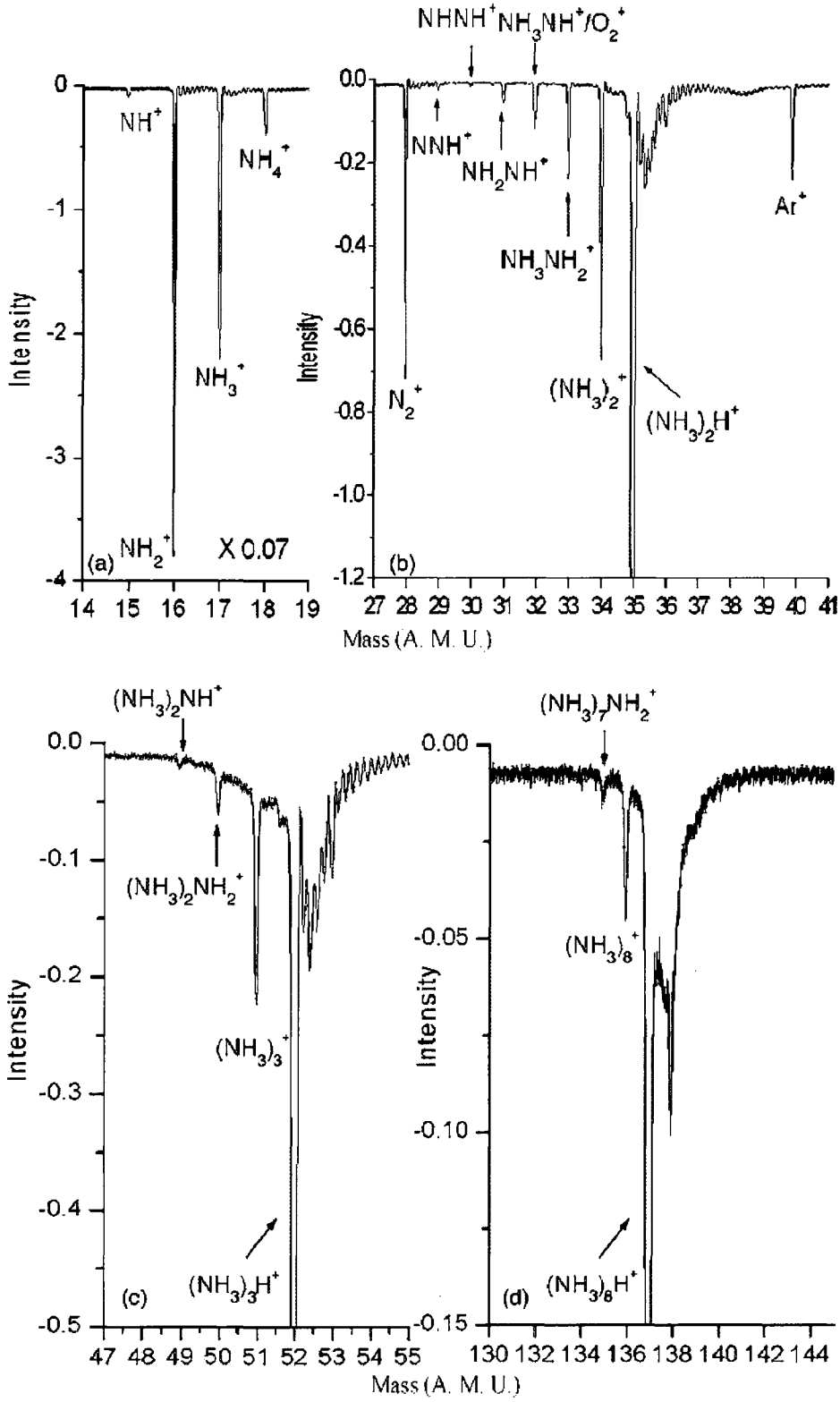


Figure 3.15: Mass spectra of (A) NH_3, (B) $(NH_3)_2$, (C) $(NH_3)_3$, and (D) $(NH_3)_8$ ionized by a 26.5 eV soft x-ray laser, respectively.

The $(NH_3)_2$ photolysis/ionization products are shown in Figures 3.15B and 3.15A $\left(NH_4^+\right)$. Product channels can be identified as follows:

$$(NH_3)_2 + h\nu(26.5\,eV) \rightarrow NH_4^+ + NH_2 + e^- \qquad 84\% \qquad (17a)$$

$$\rightarrow (NH_3)_2^+ + e^- \qquad 9.9\% \qquad (17b)$$

$$\rightarrow NH_3\,NH_2^+ + H + e^- \qquad 3.6\% \qquad (17c)$$

$$\rightarrow (NH_3)NH^+/\,(NH_2)_2^+ + 2H + e^- \qquad \leq 1.7\% \qquad (17d)$$

$$\rightarrow NH_2\,NH^+ + 3H + e^- \qquad < 1\% \qquad (17e)$$

$$\rightarrow NHNH^+ + 4H + e^- \qquad < 1\% \qquad (17f)$$

$$\rightarrow NNH^+ + 5H + e^-. \qquad < 1\% \qquad (17g)$$

The main product $\left(NH_4^+\right)$ from the dimer photoionization is generated by an intracluster ion-molecular reaction as found for the other clusters discussed in this report. The product $(NH_2)_2^+$ is observed in an argon expansion ionized by an ArF excimer at 193 nm (6.42 eV).[3.67] Mass features at 28 and 32 amu could also have contamination by N_2 and O_2, respectively, which exist in the background gas (~ 10^{-6} Torr) in the vacuum chamber, and perhaps in the expansion He gas as well. The fact that $(NH_3)_2$ displays different ionization properties than water and methanol dimers may be related to its different cluster structure and (dipole-dipole) bonding arrangement.[3.1,3.2] The weaker intermolecular interactions for $(NH_3)_2$ vs $(H_2O)_2$ and $(CH_3OH)_2$ may also account for its different products that can arise by a greater localization of the absorbed photon energy.

Products $(NH_3)_2H^+$ (P_2), $(NH_3)_3^+$, $(NH_3)_2^+$, and $(NH_3)_2NH^+$ are observed from photodissociation/ionization of the neutral ammonia trimer $(NH_3)_3$ as shown in Figure 3.15B, C. They are generated in the following reaction channels:

$$(NH_3)_3 + h\nu(26.5\,eV) \rightarrow (NH_3)_2H^+ + NH_2 + e^-, \quad 94.8\% \quad (18a)$$

$$\rightarrow (NH_3)_3^+ + e^-, \quad 4.2\% \quad (18b)$$

$$\rightarrow (NH_3)_2\,NH_2^+ + H + e^-, \quad < 1.0\% \quad (18c)$$

$$\rightarrow (NH_3)_2\,NH^+ + 2H + e^-. \quad < 0.2\% \quad (18d)$$

The $(NH_3)_2\,H^+$ ion (Figure 3.15B) is the main product as usual, and $(NH_3)_3^+$ is generated by direct ionization of the trimer without the subsequent proton transfer reaction.

The mechanism of photolysis/ionization of neutral $(NH_3)_3$ is apparently different from that of the dimer. Products with loss of more than three H atoms are not observed in the spectrum of the neutral trimer but are observed in the dimer spectrum. As shown in Figure 3.15D, only the loss of one H atom is observed for larger clusters. Clusters of the form $(NH_3)_nNH_2^+$ are also observed by EI ionization[3.59] and MPI;[3.62] these latter species are not observed, however, with VUV resonance lamp ionization[3.36] for which only $(NH_3)_nH^+$ and $(NH_3)_n^+$ cluster ions are detected. This implies that the loss of one H atom to generate $(NH_3)_{n-1}\,NH_2^+$ cluster ions requires more energy than the proton transfer reaction to generate $(NH_3)_{n-1}H^+$, and that the proton transfer reaction is more favorable for larger clusters. The larger $(NH_3)_n$ clusters have a greater proton affinity than do smaller ones.[3.49,3.63]

As noted above, the structure of $(NH_3)_n$ and $(CH_3OH)_n$ and $(H_2O)_n$ are very different due to the dominance of dipole-dipole interactions for $(NH_3)_n$ and hydrogen bonding

interactions for $(CH_3OH)_n$ and $(H_2O)_n$ clusters. Such structural and potential differences may also be related to the difference in small cluster (n = 2, 3) chemistry for these species. The photon energy absorbed by the cluster following ionization may remain localized longer in the weakly bonded (~ 1000 cm^{-1}/dimer) ammonia system than in the more strongly bonded (~ 1800 – 2200 cm^{-1}/dimer) water and methanol systems, and thus may be responsible for the more varied "molecular" chemistry found for the ammonia cluster system.

Dissociation Rate Constants of Metastable Ammonia Cluster Ions.

The unimolecular dissociation rate constant of protonated ammonia cluster ions can be obtained from the decay fraction of the parent ion in much the same way as described above for $(H_2O)_nH^+$ and $(CH_3OH)_nH^+$ clusters. As shown in Figure 3.16, the rate

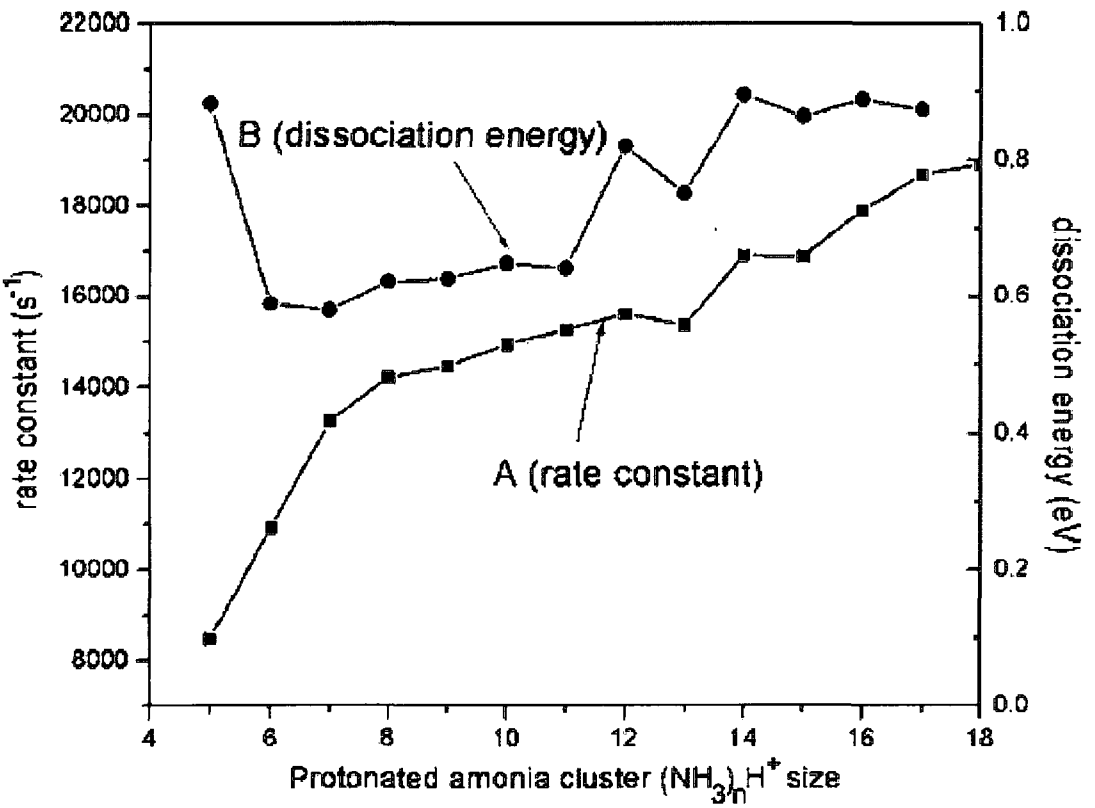


Figure 3.16: Metastable dissociation rate constants (A) and dissociation energies (B) for protonated ammonia clusters generated from the experimental data for 26.5 eV ionization.

constant for the unimolecular reaction $(NH_3)_nH^+ \rightarrow (NH_3)_{n-1}H^+ + NH_3$ is about 0.8 to 2 x 10^4 s^{-1} and increases with increasing n in the cluster ion range $5 \leq n \leq 18$. In the experiment of Wei et al.,[3.64] unimolecular dissociation rate constants are observed for this cluster series and a value of $k_{17} = 1.7 \times 10^4$ s^{-1} is found: our values for k_{17} is 1.9 x 10^4 s^{-1}.

If a rate constant is obtained for a unimolecular reaction, a value for E_{dissoc} can be obtained based on classical RRK calculations (see eq. (3.4)). Values of E_{bind} are taken from ref. 3.49 and k_n are taken from our experimental data. Ammonia has two low energy vibrational modes (932 and 968 cm^{-1}). For large clusters these modes can contribute to the cluster vibrational degrees of freedom required for statistical ergodic calculations of rate constants: we thus, following the lead for water clusters, use S = 6.6 n – 6. Values of E_{dissoc} for the metastable dissociation of loss of one NH_3 molecule from $(NH_3)_nH^+$ $(P_n \rightarrow D_{n-1})$ in the first field free region of the reflectron TOFMS are shown in Figure 3.16 and listed in Table 3.3. Note that at n = 5, much more energy is required for dissociation of $(NH_3)_5H^+$ than for the other cluster ions; the reason for this increased dissociation energy $E_{dissoc,5}$ is that the binding energy for this cluster ion $E_{bind,5}$ is much larger than $E_{bind,n}$ and other larger clusters (see Table 3.3) for n up to ~ 15.

Ammonia Cluster Temperature.

In the present experiments, the ammonia cluster ion distribution is observed in the mass spectrum and even unprotonated cluster ions ($2 \leq n \leq 20$) can be observed (see Figures 3.12, 3.13, 3.14). One can assume that energy above the VIE is removed by the ejected electron, as done previously for $(H_2O)_n$ and $(CH_3OH)_n$ clusters. Neglecting translational energy release for the products, residual energy (E_{excess}) needed to dissociate

the $(NH_3)_nH^+$ cluster ions can be calculated: E_{excess} = VIE - ΔH_n according to eq. (3.6), and $\Delta H_{n+1} = \Delta H_n + \Delta_a H_{n-1,\ n} - \Delta_b H_{n,n+1}$. Thus ΔH_n for ammonia cluster ions can be calculated as has been done above for the water and methanol species. Here, $\Delta_a H_{n-1,n}$ is the reaction energy for the protonated cluster ion $(NH_3)_{n-1}H^+$ and an ammonia monomer,[3.49] and $\Delta_b H_{n,n+1}$ is the reaction energy for neutral $(NH_3)_n$ and an ammonia monomer.[3.63] Lee and co-workers[3.28] have measured ΔH_3 for $(NH_3)_3H^+$ generation from $(NH_3)_4$

Table 3. Data used to calculate the vibrational temperature of neutral ammonia clusters in the molecule beam.

n	$E_{dissociation}$ (eV)[a] $(H_2O)_nH^+$	$\Delta_a H_{n-1,n}$ (ev)[b]	$\Delta_b H_{n,n-1}$ (ev)[c]	ΔH_n (eV)[d] $(H_2O)_n$
5	0.954	0.53	0.260	8.689
6	0.640	0.30	0.240	8.362
7	0.632	0.26	0.256	8.361
8	0.678	0.24	0.232	8.350
9	0.683	0.22	0.265	8.396
10	0.709	0.21	0.245	8.433
11	0.701	0.19	0.312	8.559
12	0.898	0.22	0.198	8.537
13	0.822	0.19	0.265	8.615
14	0.981	0.21	0.254	8.663
15	0.947	0.19	0.286	8.762
16	0.9742	0.18	0.259	8.841
17	0.9586	0.17	0.273	8.948

[a] E_{dissoc}, calculated based on dissociation rate constant obtained in present experiment.
[b] $\Delta_a H_{n-1,n}$, taken from experimental data of reference [3.49].
[c] $\Delta_b H_{n,n+1}$, taken from theoretical calculations of references [3.63].
[d] ΔH_n, calculated based on the same thermodynamic cycles employed for water cluster in Figure 3.8.

$$(NH_3)_4 \rightarrow (NH_3)_3H^+ + NH_2 + e^- \quad \Delta H_4 = 9.03\ eV, \qquad (3.19)$$

and thereby ΔH_5, ΔH_6,... ΔH_n can be calculated. This ΔH_n value represents the minimum energy required for the reaction $(NH_3)_n \rightarrow (NH_3)_{n-1}H^+ + NH_2$ to occur without excess energy remaining in the cluster ion for metastable dissociation of the protonated ammonia cluster to occur in the first field free region of the TOFMS drift tube. Values of ΔH_n for ammonia clusters ($10 \leq n \leq 21$) are listed in Table 3.3. Unlike the situation found for water and methanol cluster ions (Tables 3.1 and 3.2), ΔH_n for ammonia cluster ions increases with increasing n, since $\Delta_a H_{n-1,n}$ is smaller than $\Delta_b H_{n,n+1}$. But, this trend is different than that observed for water and methanol cluster ions: for these other clusters, ΔH_n decreases with increasing n and then tends to a constant value for large cluster sizes (see Tables 3.1 and 3.2). For ammonia clusters, cluster binding energy ($\Delta_a H_{n-1,n}$) of protonated cluster ions and cluster binding energy ($\Delta_b H_{n,n+1}$) of neutral clusters do not match well for the calculation of ΔH_n. So the thermal properties and temperature of neutral ammonia clusters cannot be estimated as is done above for water and methanol clusters, even though the qualitative interaction and data set appear the same for all these species. This difficulty could be due to a real difference for $(NH_3)_n$ vs $(H_2O)_n$ and $(CH_3OH)_n$ or it could be due to an inconsistency in the required thermodynamic $(NH_3)_n$ data set for this procedure. While at this time we cannot be certain which of these possibilities is correct, we favor the second explanation for the inability to generate a consistent and small set of temperatures for the ammonia cluster system.

If we accept that the cause of our inability to assign a set of temperatures to ammonia clusters has to do with an inconsistent data set for these species, the three cluster system present an impressively similar set of quantitative properties and behaviors with regard to

species and trends (see Figure 3.6, 3.11, 3.16). Note too that the three systems have considerably different structures, bonding patterns, and bonding energies. In other words statistical, ergodic, RRK/RRKM dynamics hold for all cases and the structural details and different limiting potentials for these three systems play a relatively minor role in their chemistry.

3.1.3 Summary and Conclusions

The very compact 26.5 eV soft x-ray laser is a near ideal ionization source with which to investigate weakly bound (hydrogen bonded and van der Waals) clusters in the gas phase. In this work, water, methanol, and ammonia clusters are ionized by a single 26.5 eV laser photon. The advantage of single photon ionization is that it prevents or hinders cluster fragmentation after ionization. This is typically not the case for ns multiphoton ionization. Although 26.5 eV energy is initially absorbed by the neutral cluster, almost all the energy above the VIE is removed by the ejected photoelectron. Metastable dissociation of cluster ions can thereby be understood and characterized through the internal intracluster reaction energies and neutral cluster temperature.

Protonated water clusters up to n = 60 are observed in mass spectra. Intensity of these cluster ions decreases roughly exponentially with increasing cluster size. The parent water cluster ion does not show any special signal ("magic number") intensity at $(H_2O)_{21}H^+$, and the enhanced intensity at n = 21 is due to the fast dissociated of $(H_2O)_{22}H^+$ in the drift tube. A small signal of unprotonated water dimer ion is observed if pure He is used as the carrier gas for the supersonic expansion. This unprotonated dimer signal intensity increases if the concentration of Ar in the carrier gas is increased, due to the formation of binary clusters Ar_m $(H_2O)_n$. These mixed clusters undergo rapid

dissociation of Ar_m during the ionization/fragmentation process and this dissociation removes enough energy from the cluster to impede the proton transfer/fragmentation reaction. The unimolecular dissociation rate constant for protonated water cluster ions is 0.6 to 2.7 x 10^4 s^{-1} for clusters of $8 \leq n \leq 24$. The vibrational temperatures of neutral water clusters are in the range 40 to 200 K for the clusters $10 \leq n \leq 21$, based on the rate constants, excess energies, and calculated thermodynamics for $(H_2O)_n$.

The major series of protonated methanol clusters is observed in the mass spectrum with no abnormal or "magic number" signals. The cluster ion signal intensity decreases roughly exponentially with increasing cluster size. The only unprotonated methanol cluster observed is the dimer. Cluster ions of the form $(CH_3OH)_n$ H_3O^+, generated from an intracluster ion-molecule reaction and loss of $(CH_3)_2O$, are not observed in the mass spectrum because only a small amount of excess energy is deposited in neutral clusters employing single photon 26.5 eV ionization. Products CH_3^+, CHO^+, CH_2O^+, CH_2OH^+, and CH_3OH^+ are observed in the photolysis/ionization of CH_3OH monomer. At this energy, rate constants for metastable dissociation of protonated methanol cluster ions are obtained in the range 3.6 to 6.0 x 10^{+3} s^{-1} for cluster sizes $5 \leq n \leq 10$. Vibrational temperatures of neutral methanol clusters are about 50 to 100 K for the cluster range $6 \leq n \leq 10$.

Protonated ammonia cluster ions dominate the ammonia cluster mass spectrum, as usual for the other two systems discussed, and signal intensity decreases roughly exponentially with increasing cluster size. Unprotonated clusters are observed in the range $2 \leq n \leq 22$. The intensity distribution for unprotonated cluster ions exhibits a distinct minimum at $n = 6$. This intensity decrease implies a more rapid proton transfer

reaction process for the $(NH_3)_6^+$ cluster and enhanced structural stability of the $(NH_3)_5H^+$ cluster ion. Products for loss of up to five H atoms in the photolysis/ionization process for the neutral ammonia dimer are observed. Loss of more than three H atoms is not observed in the mass spectrum of larger ($n \geq 3$) cluster ions. The unimolecular metastable dissociation rate constants for protonated ammonia cluster ions are found to be between 0.8 and 2.0 x 10^4 s^{-1} for $5 \leq n \leq 18$. A cluster temperature range for $(NH_3)_n$ neutral clusters could not at present be characterized (as accomplished for (H_2O) and $(CH_3OH)_n$) most probably due to inconsistencies within the existing thermodynamic data set for this system.

3.2 SINGLE PHOTON IONIZATION OF HYDROGEN BONDED CLUSTERS WITH A SOFT X-RAY LASER: $(HCOOH)_x$ and $(HCOOH)_y(H_2O)_z$

Formic acid is the first organic acid that has been detected in interstellar ice and also plays a role in Earth's atmospheric chemistry. More recently it has been detected in the coma of comets.[3.68] It may be key in the formation of molecules such as glycine (NH_2CH_2COOH) and acetic acid (CH_3COOH) in the interstellar media.[3.69] Formic acid is the simplest of the carboxylic acids of the form RCOOH, in which R can be replaced by a number of substituents, and can serve as a model system for the properties of larger, more complex molecules. It has been analyzed thoroughly through theoretical calculations, mainly due to the abundance of available experimental data. Many of the experiments on formic acid involve electron impact (EI) ionization studies. EI causes substantial fragmentation, and neutral parent cluster information is thereby lost. Our soft x-ray laser (26.5 eV photons) has proven itself in the past to be a gentle, single photon

ionization source[3.70-3.73] and we confirm that to be the case as well in the present study of formic acid.

Clusters are said to bridge the gap between gas and condensed phase behavior; extensive experiments have been conducted on formic acid clusters revealing the protonated cluster ion series of the form $(HCOOH)_nH^+$, generated from a proton transfer reaction in the parent ion $(HCOOH)_{n+1}^+$ directly following ionization of $(HCOOH)_{n+1}$ at 26.5 eV. Experiments are reported by Lifshitz and co-workers using EI ionization and unimolecular dissociation of the cluster series $(HCOOH)_nH^+$ is observed and characterized.[3.74,3.75] To accompany their experiments, the same group has performed ab initio calculations for the cluster ion series at the HF/4-31G# level.[3.76] The optimized structures generated seem to agree well with experimental results, revealing that open chain structures are favored for cluster values $n \leq 5$, and chain structures terminated by cyclic dimer units are favored for $n \geq 6$. The infrared photodissociation spectra of protonated formic acid clusters were studied by Inokuchi and Nishi.[3.77] Their studies reveal two free OH stretching vibrations for the n = 2,3 species indicating a chain structure open on both ends. The n = 4 and 5 ions reveal only one free OH stretching vibration, signifying that the chain may be terminated on one end by a cyclic dimer while the other end remains open. The n = 7 ion species does not possess a free OH vibrational band, implying that both ends of the chain structure are terminated by cyclic dimers.[3.77] They too provide Density Functional Theory (DFT) calculations that corroborate their experimental data.

The aqueous protonated cluster ion series denoted as, $(HCOOH)_n(H_2O)_mH^+$, has also been extensively researched. Lifshitz and co-workers have reported formic acid/water

cluster series studies in which they observe a particularly abundant protonated cluster ion of the form $(HCOOH)_5(H_2O)H^+$.[3.64] This cluster size may be referred to as a "magic number". Employing collisionally activated dissociation, they observe that clusters with smaller n values favor water molecule loss and those with larger n values favor formic acid molecule loss. The data suggests that a critical cluster size, n, exists below which an $(HCOOH)H^+$ ion core is preferred rather than an $(H_2O)H^+$ ion core. Above this value the opposite is true. On the basis of ab initio molecular orbital calculations at the HF-/4-31G# level,[3.78] they conclude that the proton switch occurs between the values n = 3 and 4. Inokuchi and Nishi report infrared photodissociation spectroscopy data for protonated formic acid water clusters $(HCOOH)_n(H_2O)_mH^+$.[3.77,3.79] In the m = 1 series, they find a water asymmetric OH stretch vibration for clusters n = 1-3, which disappears for the n = 4 and 5 clusters. Their results imply that the ion core switches from $(HCOOH)H^+$, for n = 1-3, to $(H_2O)H^+$ for n = 4 and 5. They also suggest that the n = 5, m = 1 cluster ion has a stable cyclic type structure in which the $(H_2O)H^+$ ion is fully surrounded and secured by 5 formic acid molecules. This is the reason for the magic number at n = 5, m = 1, according to reference 3.79.

In the present study, formic acid and mixed formic acid/water clusters are accessed by single photon ionization with a 26.5 eV (46.9 nm) soft x-ray laser. The distributions of neutral $(HCOOH)_{n+1}$ and $(HCOOH)/(H_2O)$ clusters are detected. Metastable dissociation rate constants for $(HCOOH)_nH^+$ cluster ions are measured in the range of $4 \leq n \leq 9$. The rate constants display an odd/even alternating behavior between monomer and dimer loss that can be attributed to the structure of the cluster. After proton transfer, $(HCOOH)_nH^+$ cluster ions are the dominant products in the photoionization of neutral $(HCOOH)_{n+1}$

clusters using a single photon of 26.5 eV energy for ionization. Compared with electron impact techniques, $(HCOOH)_nH^+$ clusters suffer only a small dissociation by the present single photon ionization and thus a nearly accurate neutral cluster distribution is detected by time of flight mass spectroscopy (TOFMS). Similar results, with regard to soft x-ray laser single photon ionization, are found for other van der Waals and hydrogen bonded clusters, as well as metal and metal oxide clusters.[3.70-3.73] The neutral cluster distribution $(HCOOH)_{n+1}$, as observed through $(HCOOH)_nH^+$ ions, shows an anomalous relative intensity peak ("magic number") at n = 5 (for certain conditions). For the neutral $HCOOH/H_2O$ cluster series, the protonated mixed cluster series $(HCOOH)_n(H_2O)_mH^+$ for n = 1-8 and m = 0-4 is observed. A magic number in the cluster series n = 5, at m = 1 is observed. The mechanism for mixed cluster formation is discussed in detail in this report.

3.2.1 Experimental Procedures

A general outline of the experimental scheme pertaining to formic acid will be presented in this section. A table-top soft x-ray laser (26.5 eV photons) is used as the single photon ionization source.[3.80] The laser emits pulses of ca. 1 ns duration with an energy of ca. 10 μJ/pulse at a repetition rate of up to 12 Hz. Laser action is produced by electron impact ionization to generate Ne-like argon ions in the plasma of a fast capillary discharge.[3.81,3.82] A time of flight (linear/reflectron) mass spectrometer (TOFMS) is used as a mass analyzer. A pair of mirrors placed in Z-fold configuration just before the ionization region of the TOFMS provides alignment capability and focus for the laser beam with respect to the molecular beam at the ionization source. The Z-fold transmissivity is about 10% and thus the ionization point in the TOFMS receives about 1 μJ/pulse laser energy. Since the 26.5 eV photons from the soft x-ray laser are able to

ionize the He carrier gas employed in the supersonic expansion discussed below, the microchannel plate mass detector voltage is gated to reduce the gain of the plates when He^+ ions arrive at the MCP in order to prevent detector circuit overload and saturation.

Pure neutral $(HCOOH)_{n+1}$ clusters are generated in a supersonic expansion of HCOOH/He mixed gas created by flowing helium through a formic acid reservoir at a backing pressure up to 150 psi. The mixture expands into vacuum from a pulsed nozzle (200 μm diameter opening). A mixed $HCOOH/H_2O$ gas is obtained by flowing He at pressures of 40 or 150 psi through a reservoir containing a 2% or 98% liquid formic acid/water mixture at room temperature. Mixed $HCOOH/H_2O$ clusters are generated in a molecular beam by expanding the gas mixture into a vacuum chamber. The molecular beam is collimated by a skimmer with a 2.0 mm diameter aperture at its apex, located approximately 2 cm downstream from the nozzle. Chamber pressure in the field free and detector regions of the TOFMS is on the order of 10^{-6} Torr during the experiment. Experiments are conducted to ensure that collision induced dissociation of cluster ions is negligible. The pressure in the beam at the ionization region (ca. 10^{-5} Torr) is too low to cause collision induced ionization of $(HCOOH)_{n+1}$.

3.2.2 Results

3.2.2.1 Photoionization of formic acid monomer, dimer and clusters

Figure 3.17 depicts the mass spectrum of the formic acid monomer ionized by 26.5 eV photons. The products $HCOOH^+$, HCO_2^+, CO_2^+, HCO^+, and H_2CO^+ are observed from the photolysis of the HCOOH molecule. The product channels are thus:

$$HCOOH + h\nu \rightarrow HCOOH^+ \qquad 9.2\% \quad (7.7\%) \qquad (3.19a)$$

$$\rightarrow HCO_2^+ + H \qquad 18.9\% \quad (17.9\%) \qquad (3.19b)$$

$\rightarrow CO_2^+ + H_2$	6.8%	(15.6%)	(3.19c)
$\rightarrow HCO^+ + OH$	60.2%	(52.3%)	(3.19d)
$\rightarrow H_2CO^+ + O$	4.9%	(6.5%)	(3.19e)
$\rightarrow CO^+ + H_2O$			(3.19f)

The HCO^+ ion is the major photoionization channel in which the HCOOH molecule loses an OH radical. The undissociated formic acid ion channel yields about 9.2% of the product species. The product CO^+ can not be assigned since a big background signal of N_2 is detected at the same mass number of 28. If the clusters are formed at a condition of 2% HCOOH and 98% H_2O, the distribution of formic acid clusters changes so that only the formic acid dimer is present, and $(H_2O)_n$ and mixed $(H_2O)_n(HCOOC)_m$ clusters

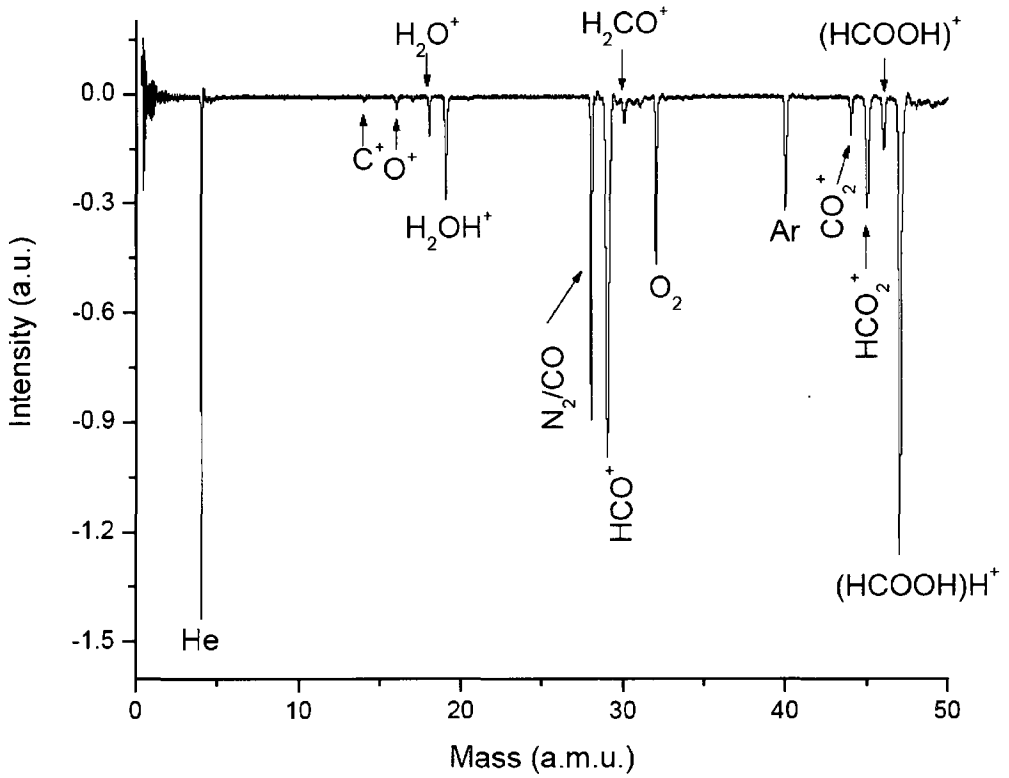


Figure 3.17: Mass spectrum of formic acid monomer ionized by a 26.5 eV soft x-ray laser. The feature at 47 a.m.u. is due to proton transfer generated fragmentation of the formic acid dimer cation.

dominate the mass spectrum, as discussed below. These latter branching ratios, shown in parentheses, do not change significantly with the exception of the CO_2^+ channel. This may be caused by variable residual CO_2 in the vacuum chamber or in the H_2O/HCOOH mixture. Under the two conditions, the ratios of $HCOOH^+/HCO_2^+$ and $HCOOH^+/HCO^+$ are similar. This comparison emphasizes that the observed monomer fragments are not derived from large $(HCOOH)_n$ cluster fragmentation.

Figure 3.18 depicts the mass spectrum of the formic dimer for which the products $(HCOOH)_2^+$, $(HCOOH)COOH^+$, $(HCOOH)H_2O^+$, $(HCOOH)CH_2^+$, $(HCOOH)H_2^+$, and $(HCOOH)H^+$ are observed from the photoionization of the neutral $(HCOOH)_2$ dimer. The product channels are identified as:

$$(HCOOH)_2 + h\nu \rightarrow (HCOOH)_2^+ \qquad 3.3\% \qquad (3.20a)$$

$$\rightarrow (HCOOH)H^+ + COOH \qquad 48.1\% \qquad (3.20b)$$

$$\rightarrow (HCOOH)COOH^+ + H \qquad 38.2\% \qquad (3.20c)$$

$$\rightarrow (HCOOH)H_2O^+ + CO \qquad 4.3\% \qquad (3.20d)$$

$$\rightarrow (HCOOH)CH_2^+ + O_2 \qquad 3.2\% \qquad (3.20e)$$

$$\rightarrow (HCOOH)H_2^+ + CO_2 \qquad 2.9\% \qquad (3.20f)$$

The $(HCOOH)H^+$ species is the major photoionization product and stems from the proton transfer reaction of the dimer ion $(HCOOH)_2^+$ following ionization. The undissociated formic acid dimer ion product, generated directly from ionization of the neutral dimer, yields about 3.3% of the product species. Channel 3.20d, loss of a CO molecule to produce $(HCOOH)H_2O^+$, is found to be an actual dissociation channel and not the result of excess water in the system. This fact is tested during experiments of mixed formic

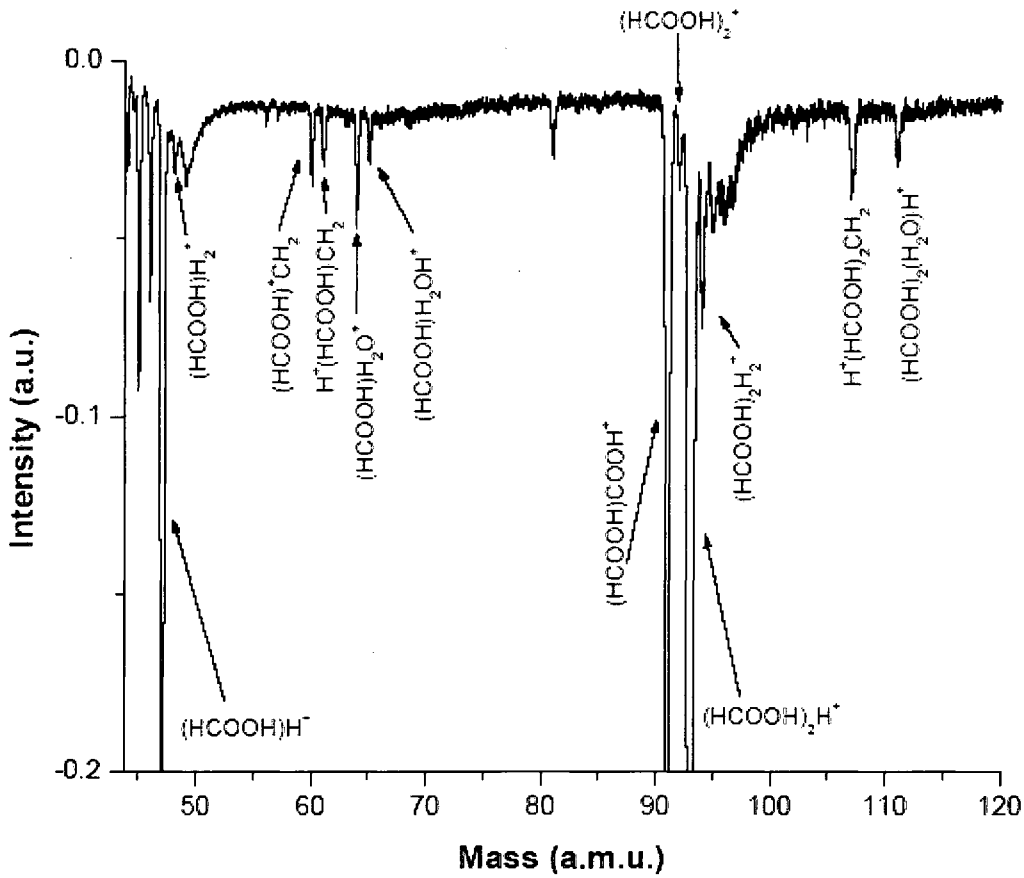


Figure 3.18: Mass spectrum of formic acid dimer ionized by a 26.5 eV soft x-ray laser. The $(HCOOH)_2H^+$ features arise from the proton transfer reaction in the $(HCOOH)_3^+$ cluster.

acid/water clusters. If excess water is added to the system, the relative ratio of dissociation channel 3.20d does not increase, signifying that it is an actual channel of dissociation following photoionization of the formic acid dimer. An additional minor feature associated with the formic acid dimer appears at the $(HCOOH)CH_2^+$ mass channel (eq. 3.20e), as shown in Fig. 3.18.

Besides proton transfer,

$$(HCOOH)_{n+1} + h\nu \rightarrow (HCOOH)_{n+1}^+ + e^-, \quad (3.21a)$$

$$(HCOOH)_{n+1}^+ \rightarrow (HCOOH)_nH^+ + COOH, \quad (3.21b)$$

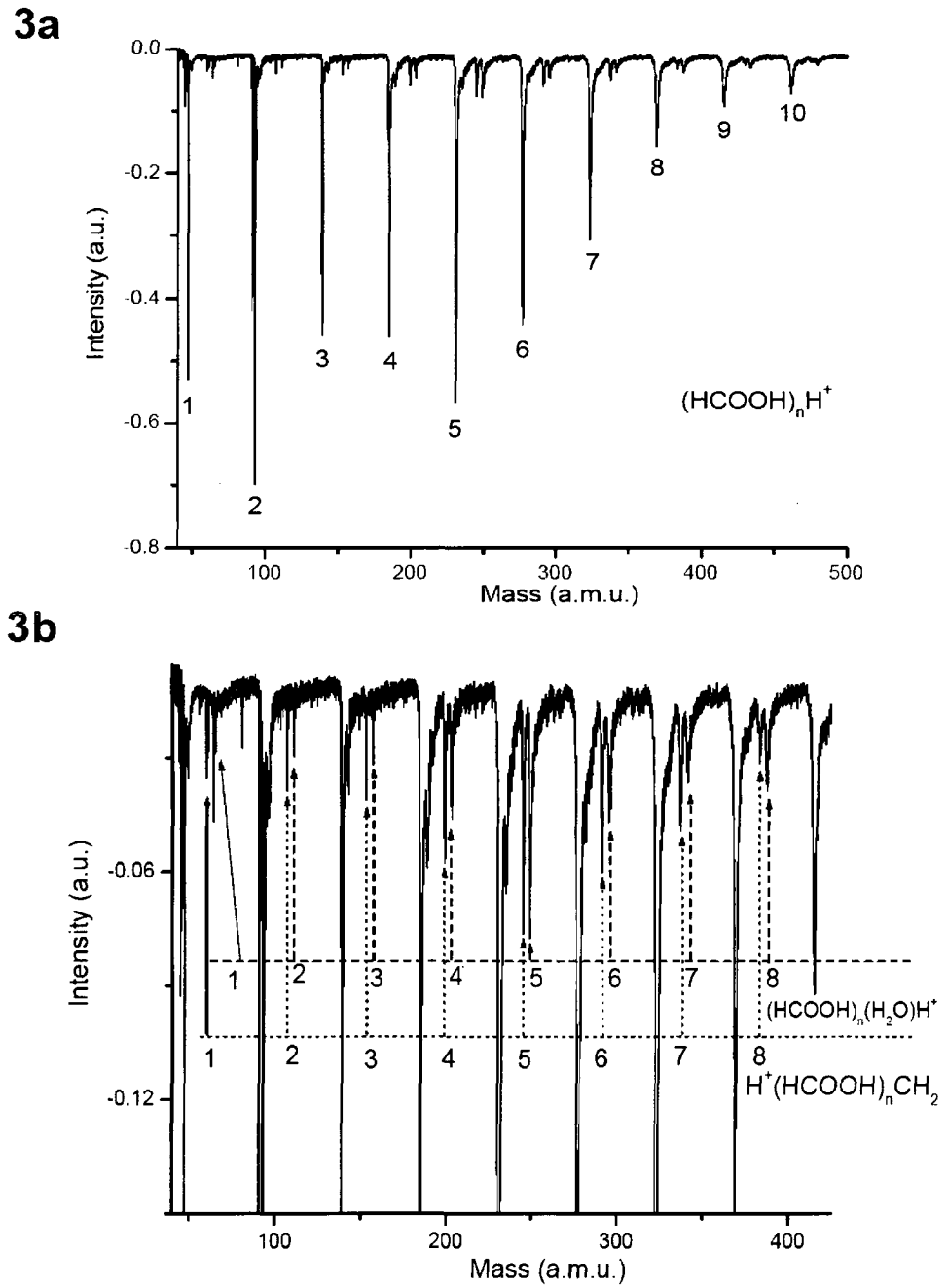


Figure 3.19: (a) Mass spectrum showing the dominant protonated formic acid cluster series $(HCOOH)_nH^+$. Note that the intensity of the $(HCOOH)H^+$ signal is reduced by MCP gating because it saturates the detection system at the normal high voltage, gain setting. (b) An expanded scale view of Figure 3a revealing the cluster ion series $(HCOOH)_n(H_2O)H^+$ and $(HCOOH)_nCH_2H^+$.

which is the dominant product channel for clusters $n \geq 2$ as displayed in Figure 3.19a, this minor photoionization feature (eq. 3.20e) is the only other channel for dissociation

following photoionization observed for larger clusters as shown in Figure 3.19b. The product channels for clusters $n \geq 3$ are thus:

$$(HCOOH)_{n+1} + h\nu \rightarrow (HCOOH)_nH^+ + COOH \qquad > 90\% \qquad (3.22a)$$

$$\rightarrow H^+(HCOOH)_{n-1}CH_2 + O_2 \qquad < 10\% \qquad (3.22b)$$

One also notes a series of mixed formic acid-water clusters, $(HCOOH)_nH_2O^+$, due to residual water in the expansion gases, nozzle, or vacuum system. We do not observe the same fragment channels for larger clusters as the monomer or dimer except for the case in which the loss of COOH is present. In fact, the intensity of $(HCOOH)H^+$ is large enough to saturate the MCP detector, and we reduce the intensity of this mass channel by gating the MCP timing. Therefore, in Figure 3.19a, the $(HCOOH)H^+$ signal is smaller than the $(HCOOH)_2H^+$. In addition, the intensities of $(HCOOH)_nCH_2^+$ and $(HCOOH)_nH_2O^+$ signals obviously follow the change of the cluster distribution as shown in Figures 3.19a and b.

3.2.2.2 Distribution of neutral $(HCOOH)_{n+1}$ clusters and mixed $(HCOOH)/(H_2O)$ clusters

Figure 3.20 displays a sequence of linear TOF mass spectra of $(HCOOH)_nH^+$ clusters photoionized by a single photon of 26.5 eV energy from the soft x-ray laser. The spectra reveal the size distribution of the cluster ions as they are generated in the ionization/extraction region of the TOFMS on a time scale of less than 1μs after ionization, as the laser/nozzle time separation is varied. The spectra, as viewed from top to bottom of Fig. 3.20, differ by an increased timing delay between the soft x-ray laser and pulsed gas nozzle. At 170 μs delay time, the intensity of clusters decreases approximately exponentially as a function of increasing cluster ion size n. As the timing

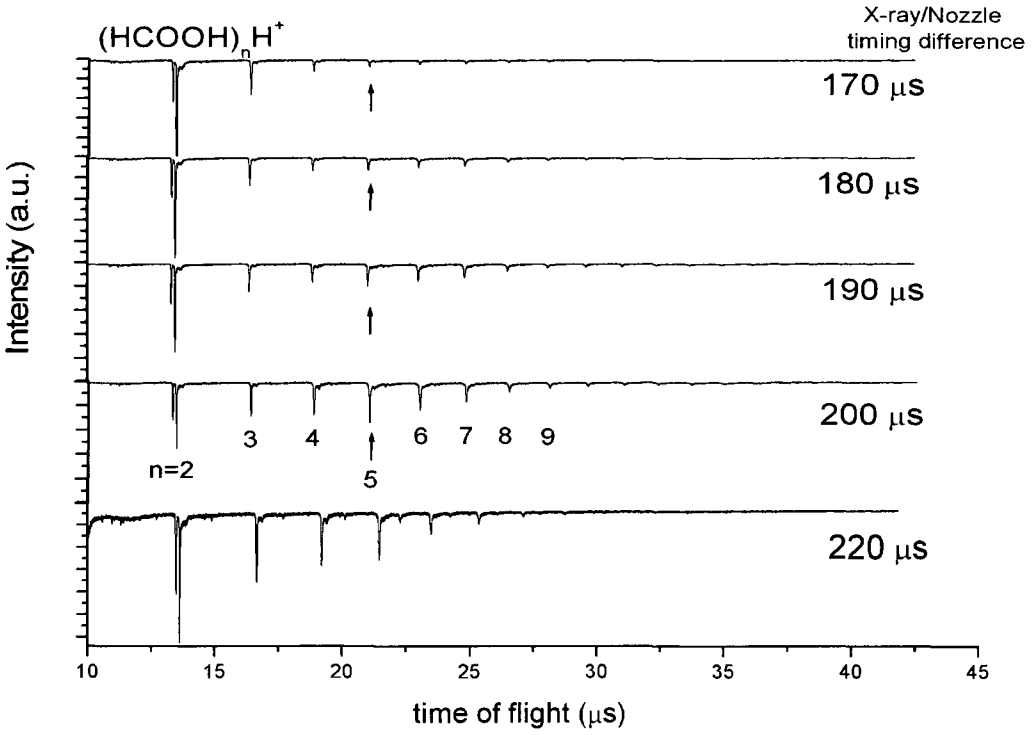


Figure 3.20: High resolution mass spectra sequence of HCOOH clusters that are generated by expansion of mixed gas HCOOH/He at 150 psi backing pressure. Cluster ions $(HCOOH)_nH^+$ dominate the mass spectrum. A magic number at n = 5 develops as conditions are changed. The time axis refers to the delay between nozzle opening and laser firing.

delay is increased, one witnesses the emergence of a magic number in the cluster distribution. The distribution is dominated by protonated cluster ions of the form $(HCOOH)_nH^+$ ($2 \leq n \leq 15$) with an intensity anomaly at n = 5. After 200 μs, the magic number at n = 5 decreases until the cluster distribution resembles the distribution at 170 μs; it decreases approximately exponentially with no intensity anomalies. Such a result could not arise if major cluster fragmentation were associated with 26.5 eV ionization.

Mixed $HCOOH/H_2O$ clusters are generated by expanding He gas and formic acid/water into the vacuum chamber at room temperature under two different experimental conditions: 1. 2% H_2O mixed with 98% HCOOH at 150 psi backing pressure; and 2. 2% HCOOH mixed with 98% H_2O at 40 psi backing pressure. Figure

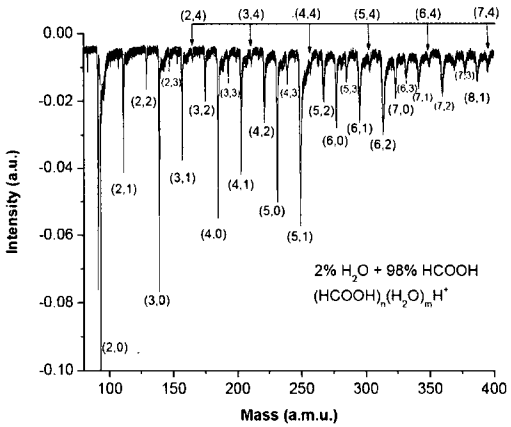


Figure 3.21: A high resolution mass spectrum of mixed HCOOH/H_2O clusters that is generated by flowing He gas at 150 psi through a 2% H_2O 98% HCOOH liquid mixture. Cluster ions $(HCOOH)_n(H_2O)_mH^+$ are observed for n = 1-8 and m = 1-4. The development of a magic number at n = 5, m = 1 is observed.

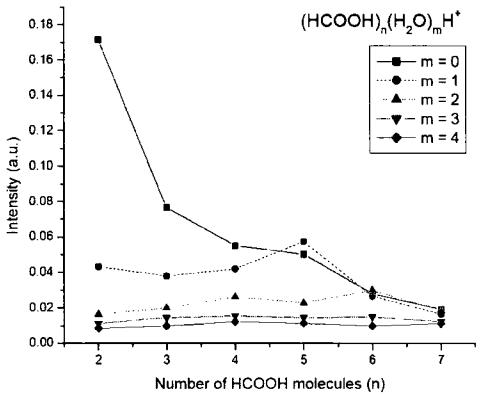


Figure 3.22: A plot of the intensity as a function of the number of HCOOH molecules (n) for the series $(HCOOH)_n(H_2O)_mH^+$ for a constant number of water molecules (m). m is increased from 0-4. A magic number for n = 5, m = 1 is observed as well as a slight increase in intensity for n = 6, m = 2.

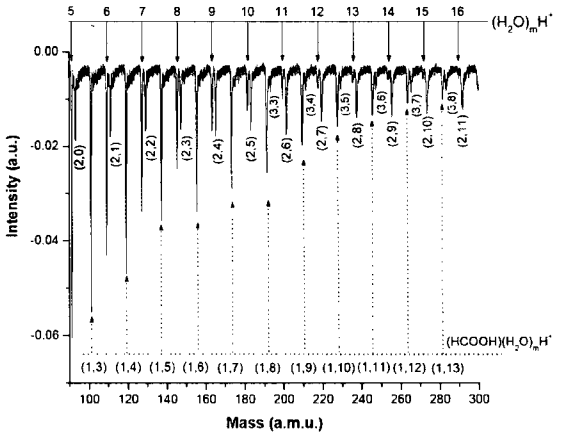


Figure 3.23: A high resolution mass spectrum of mixed HCOOH/H_2O clusters that is generated by flowing He gas at 40 psi through a 2% HCOOH, 98% H_2O liquid mixture. Cluster ions $(HCOOH)_n(H_2O)_mH^+$ are observed for n = 0-3 and m = 0-16.

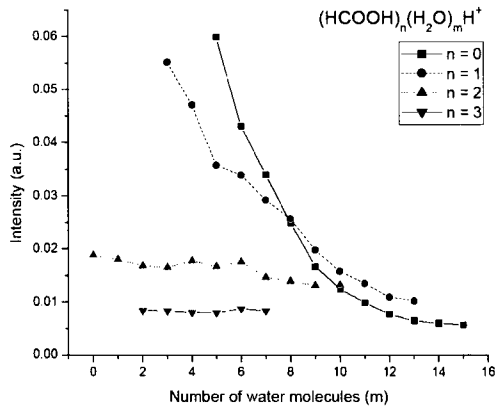


Figure 3.24: A plot of intensity as a function of the number of H_2O molecules (m) for the series $(HCOOH)_n(H_2O)_mH^+$ for a constant number of formic acid molecules (n). n is increased from 0-3. No intensity anomalies are observed.

3.21 show a mass spectrum of mixed HCOOH/H_2O clusters formed under condition 1. At this high backing pressure, high HCOOH content condition, $(HCOOH)_nH^+$ cluster ions dominate the spectrum, and pure water clusters are not observed. Also produced in the mass spectrum are the protonated series $(HCOOH)_n(H_2O)_mH^+$ for n = 1-8, and m = 0-4. The unprotonated series are not observed. Figure 3.22 displays a plot of the intensity of the mixed cluster as a function of the number of HCOOH molecules, n, for $0 \leq m \leq 4$. In the cluster series with m = 0, the intensity decreases roughly exponentially with increasing cluster size. At m=1, however, we observe a magic number at n = 5. In the series m = 2, the intensity for n = 6 is slightly larger than its neighbors and for m > 2, the intensity is nearly constant for all n.

If the concentration of HCOOH and the backing pressure are reduced to that of condition 2 (low concentration and pressure), the dominant signal in the mass spectrum changes from $(HCOOH)_nH^+$ to $(HCOOH)(H_2O)_mH^+$ (m = 0-16), and pure water clusters are observed, as illustrated in Figure 3.23. The series $(HCOOH)_n(H_2O)_mH^+$ for n = 0-3, and m = 0-16 are also observed. Figure 3.24 displays a plot of the intensity of the clusters as a function of the number of H_2O molecules, m, for n = 0-3 HCOOH molecules. In the cluster series with m = 0, the intensity decreases roughly exponentially with increasing cluster size. No mixed clusters are observed to have relative intensity anomalies; magic numbers in any of the cluster series for low concentration and pressures of HCOOH are not found.

3.2.2.3 Metastable Dissociation Rate constants for $(HCOOH)_nH^+$ cluster ions

Figure 3.25 presents a reflectron TOF mass spectrum indicating the population distribution of cluster ions formed in the first field free region of the TOFMS. Daughter

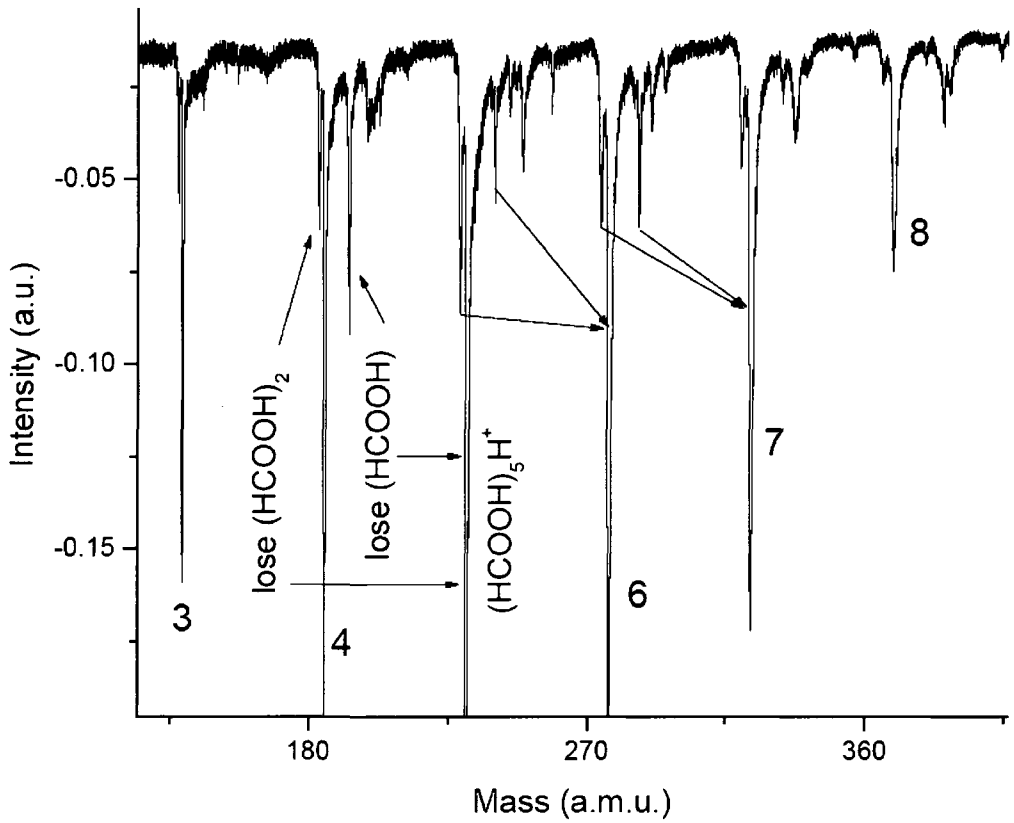


Figure: 3.25: High resolution reflectron TOF mass spectrum of $(HCOOH)_nH^+$ clusters. Metastable dissociation of $(HCOOH)_nH^+$ cluster ions in the field free region is observed. The loss of monomer and dimer units from the parent ion $(HCOOH)_nH^+$ is displayed.

ions are produced from their parent ions by metastable dissociation reactions in the drift tube. Both the loss of a monomer and a dimer from the parent cluster ion to generate the daughter ion are evident,

$$(HCOOH)_nH^+ \rightarrow (HCOOH)_{n-1}H^+ + HCOOH \quad (3.23a)$$

$$\rightarrow (HCOOH)_{n-2}H^+ + (HCOOH)_2 \quad (3.23b)$$

The metastable dissociation process of losing one dimer to obtain reaction 5b, may also be identified as a process of losing two monomers; however, it has been demonstrated in our previous work[3.70,3.73] that the loss of only one neutral molecule from a metastable cluster ion by unimolecular dissociation can occur on a microsecond time scale using

single photon ionization of our 26.5 eV laser. So in this case, losing one dimer unit, not two monomers, from the parent ion is probably correct.

The unimolecular metastable dissociation rate constants for the $(HCOOH)_nH^+$ cluster ion dissociation to generate $(HCOOH)_{n-1,2}H^+$ can be calculated as

$$k = -(1/t)\ln[1-I_D/(I_D + I_P)], \tag{3.24}$$

in which I_D and I_P are the intensities of the dissociated daughter ion and the undissociated parent ions, respectively, and t is the time of flight of the parent ion in the first field free region of the reflectron TOFMS. For the present apparatus this is about 60% of the total flight time for the reflectron mode TOFMS. Figure 3.26 shows that these rate constants, for cluster ions $4 \leq n \leq 9$, fall between 0.1 to 0.8×10^4 s^{-1}. For the cluster value n = 4, the

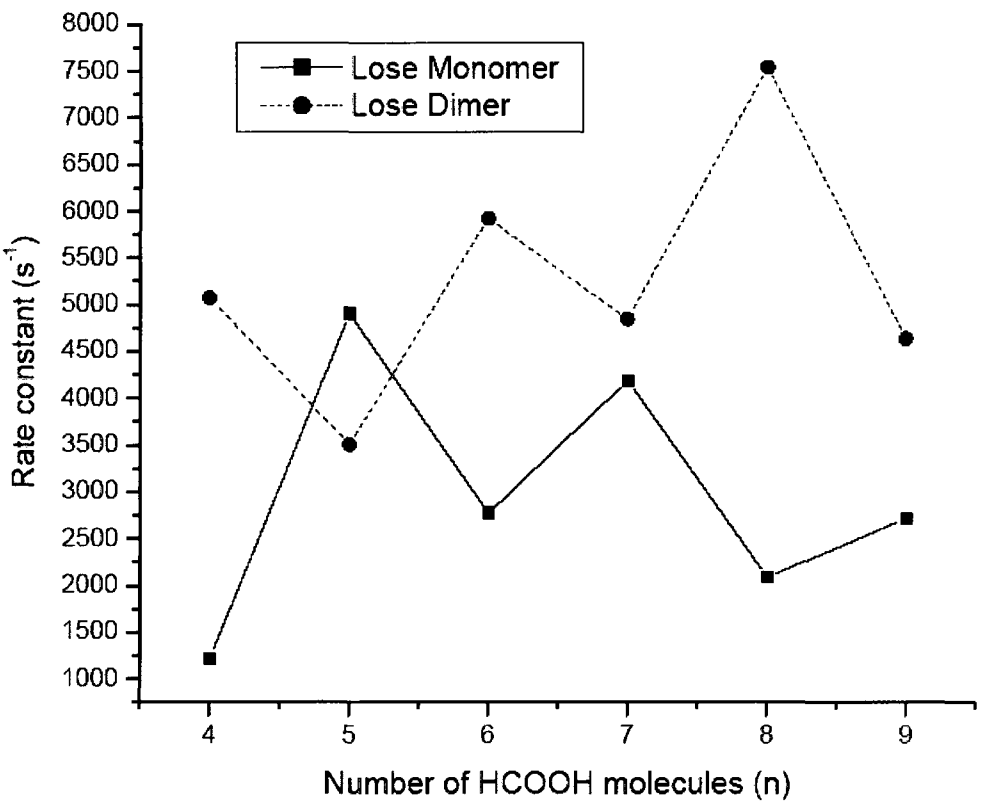


Figure 3.26: A plot of metastable dissociation rate constants for $(HCOOH)_n^+$ cluster ions as a function of the cluster size, n.

k value for the loss of a dimer is favored over loss of a monomer by a factor of 5. For the cluster n = 5, the loss of a monomer is favored over that of dimer. For n = 6-9, dimer loss is favored over monomer loss but an oscillating behavior in the rate constant for odd and even clusters is observed. The rate constant for loss of a monomer is larger for odd numbered clusters (n = 5, 7, 9), and the rate constant for loss of a dimer is larger for even numbered clusters (n = 4 ,6 ,8).

3.2.3 Discussion

3.2.3.1 Photolysis of formic acid monomer and clusters

Photodissociation of formic acid in the gas phase has been studied extensively at 220-193 nm.[3.83] A direct dissociation to HCO + OH at the S_1 state was found to be a dominant pathway with a quantum yield of 0.7-0.8. A small amount of CO and CO_2 was also observed as a result of internal conversion to the ground state. Similar photolysis pathways are observed when 26.5 eV light is employed to ionize the formic acid monomer. The HCO^+, CO_2^+ are observed in the mass spectrum of Figure 3.17. The channel HCO^+ + OH is identified as the main photodissociation channel with quantum yield of 0.62. A minor channel of H_2CO^+ + O is identified experimentally for the first time. Based on theoretical calculation,[3.84] this path needs 180 kcal/mol energy above ground state to enable this reaction occur. Our 26.5 eV, soft x-ray laser has enough energy to excite a formic acid molecule to this high excited state during the ionization process.

Dissociation following photoionization of the formic acid dimer is studied for the first time. $(HCOOH)H^+$ is the main product generated from the neutral dimer by a proton transfer reaction after ionization by 26.5 eV radiation. A second dissociation product,

$(HCOOH)COOH^+$, generated by loss of an H atom, has a high quantum yield, 0.38. The minor pathways to produce CO and CO_2 are also identified by observation of fragments $(HCOOH)H_2O^+$ and $(HCOOH)H_2^+$, respectively. An interesting feature in the dissociation of the dimer is the absence of a channel containing the loss of an OH, which is the main channel for dissociation following photoionization of the monomer HCOOH. This dissociation suggests that the neutral formic acid dimer contains a double hydrogen bond, with no free OH available for dissociation, and not an open chain structure. Neutral formic acid clusters are hydrogen bonded in nature, and the dimer has been experimentally established to posses a cyclic C_{2h} structure in the gas phase with two hydrogen bonds of 29.3 kJ/mol each;[3.84] these bonds are nearly linear and are of the form O-H···O.

The dissociation channel losing O_2 to produce $H^+(HCOOH)_{n-1}CH_2$, is observed for larger clusters with small quantum yields, about 0.1; however, the dissociation channels for losing OH (yield, 0.62) and H (yield, 0.38), which are the main channels for the monomer and dimer, are not observed for larger clusters. The absence of these channels for larger clusters ($n > 2$) indicates that no free OH moiety exists in the structure of neutral formic acid clusters. Based on DFT[3.86,3.88] calculations, the trimer structure with the lowest energy consists of the cyclic dimer bonded to a monomer by an O-H···O and a C-H···O. Also, the lowest energy structure of the tetramer contains a pair of dimers held together by two weak C-H···O bonds[3.87,3.88]. For neutral formic acid clusters, the general trend for $n \leq 5$ seems to be that the lowest energy structures favor rings or chains made up of the lowest energy dimers, and trimers in combination with monomers. Thus the DFT calculated structures are in agreement with the observed

photoionization/dissociation chemistry. Additionally, larger clusters posses many more vibrational degrees of freedom that can absorb any excess energy deposited in the cluster, rendering fragmentation a slow process in general, and closing certain low probability channels. Similar behavior is observed in the study of $(SO_2)_n$[3.71] and $(CO_2)_n$[3.72] clusters.

The dissociation channels given in equations 3.19 and 3.20 discussed above occur for higher excited electronic states of the monomer and clusters pumped by 26.5 eV radiation; however, these channels are apparently very minor features for larger clusters. In our previous studies of $(SO_2)_n$ clusters,[3.71] a large dissociation to ionization ratio at electronically excited states of the ion is observed for the SO_2 monomer, $I[SO^+]/I[SO_2^+]$ =1.1. This ratio decreases to $I[(SO_2)_{n\geq 5}SO^+]/I[(SO_2)_{n\geq 5}^+] < 0.1$ as cluster size increases. This behavior is also observed in the studies of other clusters.[3.70,3.72] Compared with EI, dissociation by 26.5 eV single photon ionization is much smaller. For example, the dissociation branching ratios of $(CO_2)_n$ clusters is up to 0.5 for EI ionization, but < 0.1 for 26.5 eV ionization.[3.72] The mechanism for this behavior may be that as the excited ion states become more delocalized due to interactions in the cluster (charge delocalization), their absorption cross section for the reaction $I + h\upsilon \rightarrow I^{+*} + e^-$ decreases. Such behavior is found for charge transfer transitions in extended systems, in general.

Another issue that can be argued is that these observed dissociation channels could arise from the fragmentation of larger clusters. Three pieces of evidence arise from our data that can help address this issue. First, the branching ratios for HCO_2^+, HCO^+, and H_2CO^+ do not change under two different experimental conditions of cluster formation. For the pure formic acid/He expansion, the $(HCOOH)_nH^+$ cluster distribution can be observed for n~1-10, while only the formic acid dimer is observed if water is added to the

formic acid liquid generating a concentration of 2% HCOOH/98% H_2O for the He carrier gas expansion. If fragmentation occurs for larger clusters, the branching ratios of HCO_2^+, HCO^+, and H_2CO^+ should increase for the pure formic acid expansion, since large clusters are present in this instance only. Nonetheless, the fragment branching ratios remain the same for both cases. Second, the dissociation product signals $H^+(HCOOH)CH_2$ and $(HCOOH)H_2O^+$ are smaller than dissociation product signals $H^+(HCOOH)_nCH_2$ and $(HCOOH)_nH_2O^+$ for n > 2, indicating that fragmentation from larger clusters does not contribute greatly to the $H^+(HCOOH)CH_2$ and $(HCOOH)H_2O^+$ signal intensities. Also the intensity of the $H^+(HCOOH)_nCH_2$ and $(HCOOH)_nH_2O^+$ fragment signals obviously follow the change in intensity for the parent signal, as shown in Figure 3.19: that is, the fragment intensity increases for n=2-5 and then decreases for n>5. Thus, $H^+(HCOOH)CH_2$ and $(HCOOH)H_2O^+$ must be generated from the formic acid dimer. Another main dissociation product, $(HCOOH)COOH^+$, can also only result from the dimer since dissociation products $(HCOOH)_nCOOH^+$ for n>2 are not observed in our experiment. If large clusters generate the fragment $(HCOOH)COOH^+$, one should observe a distribution of $(HCOOH)_nCOOH^+$ (n>2) in the cluster distribution. This is not the case. Third, the distribution of cluster ions is dependant on the neutral cluster structures. As shown in Figure 3.19, the intensities of $(HCOOH)H^+$ and $(HCOOH)_5H^+$ clusters are larger than their neighbors. This is due to the stable structure of $(HCOOH)_2$ and $(HCOOH)_6$. The formic acid dimer mainly consists of a double hydrogen bonded structure in formic acid vapor.[3.86] If one assumes that the large clusters fragment to the smaller clusters during the 26.5 eV ionization process, one should observe the cluster distribution intensity decrease with increasing cluster size. One should not observe the

"magic number" at $(HCOOH)_5H^+$ in the cluster distribution since a 26.5 eV photon has enough energy to fragment any large cluster to the monomer after ionization. Since we do observe a magic number, we consider that formic acid clusters do not suffer serious fragmentation during 26.5 eV ionization.

3.2.3.2 Distribution of $(HCOOH)_n$ clusters and mixed $HCOOH/H_2O$ clusters

We have learned from studies of H_2O, CH_3OH, NH_3,[3.70] SO_2,[3.71] CO_2,[3.72] and metal oxide clusters,[3.73] as well as this study of HCOOH, that 26.5 eV photons ionize van der Waals and hydrogen bonded clusters such that very little energy above the vertical ionization energy (VIE) remains in the cluster. Cluster fragmentation in the ionization region of the mass spectrometer (less than 1 μs following ionization) is driven in most instances by the energy difference between cluster VIE and AIE or the energy difference between VIE and the barrier to the proton transfer/dissociation reaction following ionization. The proton transfer/dissociation reaction is typically quite exothermic and this energy can also be used in part to fragment (metastable fragmentation, typically) the cluster. The protonated cluster $(HCOOH)_nH^+$ signal is dominant in the mass spectra as the VIE minus the AIE is always enough energy to drive a proton transfer reaction following ionization. The proton transfer reaction can not be avoided for hydrogen bonded clusters even if ionization takes place at the VIE threshold, and is not a result of a 26.5 eV photon inputting excess energy (above the cluster VIE) into the cluster. The only additional fragmentation beyond that driven by proton transfer in the reaction $(HA)_{n+1}^+ \rightarrow (HA)_nH^+ + A$ is metastable fragmentation[3.70-3.73] after the ion has traveled out of the ionization region and gone into the flight tube of the TOFMS. This

fragmentation occurs at times greater than 1 μs following the laser ionization pulse and is detected by reflectron TOFMS. We will discuss this latter issue in Section 3.2.3.3 below.

As illustrated in Figure 3.20, signals for $(HCOOH)_nH^+$ cluster ions dominate the mass spectrum for all n due to a proton transfer reaction following ionization. The signal for the fragmentation series $H^+(HCOOH)_{n-1}CH_2$ becomes increasingly weak over the range n = 1-8. For 26.5 eV single photon ionization, the summed relative intensity ratios for fragment ions with respect to the $(HCOOH)_nH^+$ main feature is < 0.1 for all values of n. These results, in conjunction with linear TOFMS data, strongly suggest that the neutral cluster distribution, $(HCOOH)_{n+1}$, is quite similar to the observed $(HCOOH)_nH^+$ distribution. In the experiment, the cluster distribution is related to the timing delay between the ionization laser pulse and pulsed gas nozzle trigger. Under certain conditions, the $(HCOOH)_5H^+$ cluster displays an intensity anomaly (see Figure 3.20). The $(HCOOH)_5H^+$ cluster is generated from the neutral cluster $(HCOOH)_6$ in the molecular beam by a proton transfer reaction following ionization, $(HCOOH)_6 + h\upsilon \rightarrow [(HCOOH)_6]^+ + e^- \rightarrow (HCOOH)_5H^+ + HCOO + e^-$. With the timing delay changes presented in 3.20, the mass spectrum of cluster ions indicates that the neutral cluster distribution is different in different parts of the pulsed molecular beam. For example, at a delay time of 170 μs, the neutral cluster distribution at the first part of the molecular beam is detected, and at 200 μs, the distribution at the middle part of the beam pulse is detected. At the beginning and end of molecular beam, the temperature is higher and expansion pressure is lower than that of the middle part. This means that the neutral cluster $(HCOOH)_6$ is a stable structure in the molecular beam at a relatively low temperature. The $(HCOOH)_5H^+$ signal also increases with increased backing pressure. A

similar behavior is also observed in Feng and Lifshitz's experiments.[3.75,3.75] They found that the intensity of $(HCOOH)_5H^+$ can be identified as a "magic number" for low temperature clusters. Thus, the $(HCOOH)_5H^+$ cluster intensity anomaly is due to the stability of the neutral $(HCOOH)_6$ cluster. This result is different than the intensity anomaly found in water cluster experiments. The relative abundance of cluster $(H_2O)_{21}H^+$ is due to the fast metastable fragmentation of $(H_2O)_{22}H^+$, not the stability of its parent neutral cluster $(H_2O)_{22}$, in the molecular beam.[3.70]

In the cluster distribution for mixed formic acid/water clusters (Figure 3.21), the $H_2O(HCOOH)_5H^+$ cluster is particularly abundant in the mass spectrum, with formic acid serving as a solvent. Based on ab initio calculations,[3.79] the $H_2O(HCOOH)_5H^+$ cluster has a cyclic-type structure, and the H_3O^+ ion core is fully surrounded and stabilized by five formic acid molecules. Additionally, formic acid and water can solvate each other with any ratio of the two species as shown in Fig. 3.22 and Fig. 3.23.

3.2.3.3 Unimolecular metastable dissociation reactions

Metastable decay (loss of $(HCOOH)_{1,2}$) rate constants for protonated formic acid clusters (outside the ionization/extraction region of the TOFMS, $t > 1$ μs following ionization), are measured to be about 0.1 to 0.8×10^4 s^{-1}. The rates are similar to those of all van der Waals ($0.6\text{-}1.5 \times 10^4$) and hydrogen bonded ($0.1\text{-}2.0 \times 10^4$) cluster ions studied by 26.5 eV single photon photoionization.[3.70-3.72] This coincidence implies a loose relation between cluster binding energy, (VIE-AIE), ΔH for proton transfer, and the barriers to the proton transfer reactions in the appropriate clusters. While this is not a quantitative relationship, it is qualitatively implied by the similar rate constants.

An oscillating behavior in the rate constant for odd and even n clusters $(HCOOH)_nH^+$ is observed, as shown in Fig. 3.26. The loss of a monomer is more probable for odd number (n odd) clusters and loss of a dimer is more probable for even number (n even) clusters. The observation implies certain structural information for protonated formic acid ion clusters. Note too that these observations imply a slow unimolecular dissociation of the clusters based on only little residual excess energy. The protonated cluster ion series $(HCOOH)_nH^+$ has been studied through EI.[3.74] Following cluster ion generation by EI, unimolecular dissociation is observed. $(HCOOH)_nH^+$ clusters with $n \leq 5$ are shown to release mainly a monomer. Dimer evaporation is favored for $n \geq 6$ with monomer evaporation effectively disappearing at n = 9. Metastable rate constants are calculated to be in the range $k = 10^4\text{-}10^6\ s^{-1}$. Structure for the protonated ion series $(HCOOH)_nH^+$ is also supported with infrared photodissociation spectroscopy experiments.[3.77] Ref. 3.77 finds that for clusters $n \leq 6$, the photodissociation spectra show one (n = 2,3) or two sharp bands (n = 4,5,6) in the free OH stretching vibration region, implying that at least one free OH group is present in each member of the protonated cluster ion series. At n = 7, the band disappears indicating that the chain is terminated on both ends by cyclic dimers with no free OH moieties in the clusters. Based on ab initio calculations of cluster structure, [3.76] optimized structures for $n \leq 5$ are found to be open ended chains with one or two free OH group(s) on the ends. Chain structures terminated by cyclic dimer units are favored for $n \geq 6$. The same behavior is found for protonated acetic acid clusters using IR plus vacuum ultraviolet spectroscopy.[3.89]

Neutral cluster ($(HCOOH)_{n+1}$) structure calculations[3.85-3.88,3.90] and experiments[3.91] have shown much different results than for the protonated ion series $(HCOOH)_nH^+$.

Neutral clusters form a cyclic structure, with all OH groups involved in the cluster hydrogen bonding network. DFT[3.86,3.88] calculations have yielded trimer structure with the lowest energy structure consisting of the cyclic dimer bonded to a monomer by an O-H···O and a C-H···O bond. The tetramer has seen more variety in the lowest energy structure for different computational schemes. It is argued that the lowest energy of the tetramer contains a pair of dimers held together by two weak C-H···O bonds[3.87,3.88], with several other structures lying within 0.4 kcal/mol. Limited attention has been paid to the neutral pentamer for which the Gibbs free energy suggests that the most stable structure is a planar ring that consists of the lowest energy trimer bound to the lowest energy dimer by two C-H···O bonds.[3.88] The general trend, for neutral formic acid clusters $n \leq 5$, seems to be that the lowest energy structures favor rings or chains made up of the lowest energy dimers and trimers, in combination with monomers, not open ended monomer chains, or monomer chains terminated by cyclic dimers, as suggested for the protonated ion cluster series $(HCOOH)_nH^+$.

Figures 3.25, and 3.26 present results of metastable fragmentation of protonated formic acid clusters after ionization by the 26.5 eV soft x-ray laser. In the range of $5 \leq n \leq 9$, our results follow closely those generated by the EI experiments;[3.74] that is, loss of a dimer is favored over a monomer. A more obvious alternating behavior corresponding to odd and even clusters is observed in our experiments. Additionally, at cluster size $n = 4$, our results differ from those generated by EI. 26.5 eV single photon ionization for $(HCOOH)_4H^+$ yields dimer evaporation as nearly the only open channel. Conversely, EI demonstrates only monomer evaporation for $(HCOOH)_4H^+$. These different metastable dissociation reactions indicate a different structure for the parent ion of the protonated

formic acid cluster $(HCOOH)_4H^+$. This could be caused by different ionization processes and different generation conditions for the clusters.

One can also note this structural difference in values of metastable dissociation rate constants for EI and single photon ionization generated species. Metastable decay rates are calculated to be in the range of 0.1-0.8 x 10^4 s^{-1} for ionization upon a single 26.5 eV photon, whereas EI rate constants are almost three orders of magnitude faster in the range $k = 10^4$-10^6 s^{-1}. This distinction could arise from the difference in energy deposited into the cluster from a 26.5 eV photon and an electron beam. A single 26.5 eV photon deposits very little (excess) energy in the cluster after ionization for fragmentation. Since clusters under ionization by EI have much faster metastable decay rates, these clusters must be hotter with more energy deposited in the cluster for metastable fragmentation than those created by 26.5 eV single photon ionization.

If the EI generated cluster ion is hotter and has more energy than the single photon generated cluster ion, its structural properties and its position on its potential energy surface can be different. For example, the most stable structure of neutral cluster $(HCOOH)_5$ as suggested by calculations,[3.88] is a ring structure consisting of two dimers and one monomer. During the ionization process, the excess energy deposited in the cluster may cause it to break apart into an open chain structure. After EI ionization, the protonated cluster ion $(HCOOH)_4H^+$, generated from the neutral cluster $(HCOOH)_5$ by a proton transfer reaction following ionization, may have an open chain structure without any dimer rings;[3.76] evaporation of single monomer is thus a favorable process for the metastable dissociation of EI generated $(HCOOH)_4H^+$. After ionization by a single 26.5 eV photon, however, the photoelectron takes away almost all of the energy above the

vertical ionization energy leaving little excess energy in the cluster. The structure of this cluster ion generated by photoionization, may be much different than the structure of the ion generated by EI, and indeed may still have the structure of its neutral parent. Neutral formic acid clusters are of the general form of rings or chains consisting of lowest energy dimers, and trimers. Thus, under appropriate experimental conditions, the metastable loss of a dimer following ionization and the proton transfer reaction is not unreasonable, even for $(HCOOH)_4H^+$.

Another reason for the difference between EI vs. photoionization generated ions is that a number of isomers exist for protonated clusters, which depend on the neutral cluster generation conditions and ionization method. The internal energy for cool or hot clusters generated by photoionization or EI will be used for the proton transfer reaction, structure change, and metastable fragmentation following ionization. Protonated formic acid clusters have a number of different isomeric structures with similar energies, such as open chain, and one or two dimers at the end of a cluster chain.[3.74-3.77] Feng and Lifshitz's EI experiments[3.74] show that low temperature favors dimer loss, while high temperature favors monomer loss; high temperature will supply more internal energy for cluster structural rearrangement to totally opened chains after ionization. Of course, more energy deposited by the ionization process can also generate the result that monomer loss becomes favorable for small protonated formic acid clusters.

3.2.4 Conclusions

Pure neutral $(HCOOH)_{n+1}$ clusters and $(HCOOH)/(H_2O)$ mixed clusters are investigated by TOFMS employing single photon, 26.5 eV ionization. For the pure HCOOH system, the dominant cluster series in the mass spectrum is $(HCOOH)_nH^+$ which

is directly generated from ionization of neutral clusters $(HCOOH)_{n+1}$ in the molecular beam and a proton transfer reaction. Clusters are observed for $2 < n < 15$ with an intensity anomaly at $n = 5$. We argue that the intensity anomaly at $(HCOOH)_5H^+$ is due to the enhanced stability of the $(HCOOH)_6$ neutral cluster and not an enhanced metastable fragmentation rate for $(HCOOH)_6H^+$ as found for $(H_2O)_{21}H^+$ and $(H_2O)_{22}H^+$ clusters. The neutral dimer and larger cluster structures are determined to involve cyclic dimers with the absence of any free OH bonds since the channel of OH loss, which is the main channel for dissociation following photoionization for the formic acid monomer, is not observed by 26.5 eV laser photoionization. The $H^+(HCOOH)_{n-1}CH_2$ cluster ion series is observed (weakly) as a dissociation product following photoionization of neutral $(HCOOH)_{n+1}$ clusters. This reaction channel must open for a highly excited state of the ion. This fragmentation pathway is relatively weak (< 10%) compared to the parent ion $(HCOOH)_nH^+$ signal because in most instances, all of the excess cluster energy above VIE is removed by the photoelectron during the ionization process.

Mixed $HCOOH/H_2O$ clusters are studied at two different HCOOH concentrations mixed with water and two different expansion gas pressures. The predominant signals in the mass spectra are $(HCOOH)_nH^+$ and $(HCOOH)(H_2O)_mH^+$ cluster ions for high and low parameter values, respectively. For the high concentration condition a magic number at $n = 5$, $m = 1$ for the protonated cluster ion series $(HCOOH)_n(H_2O)_mH^+$ is found.

For the hydrogen bonded protonated cluster ion series $(HCOOH)_nH^+$, metastable dissociation by loss of one or two HCOOH molecules from the cluster is observed in the reflectron TOF mass spectrum for 26.5 eV single photon ionization. The metastable dissociation rate constants are in the range of $(0.1–0.8) \times 10^4\ s^{-1}$ for $4 < n < 9$. This is the

same range as observed for the comparable dissociation of $(CO_2)_n^+$, $(SO_2)_n^+$, $(H_2O)_nH^+$, $(CH_3OH)_nH^+$, and $(NH_3)_nH^+$ clusters. This similarity between rate constants for many van der Waals and hydrogen bonded clusters implies that cluster dynamics is dependent upon cluster density of states and internal cluster temperature. An obvious oscillating behavior is observed for metastable fragmentation of protonated formic acid clusters after single photon ionization, indicating a cluster ion structure with both dimer and monomer units in the neutral cluster.

In general, $(HCOOH)_nH^+$ clusters are observed with a gentle ionization source (soft x-ray laser) that is capable of ionizing the clusters with a single photon. This gentle ionization allows us to obtain data about the protonated cluster ion series $(HCOOH)_nH^+$ distribution and we argue that it is similar to the neutral cluster distribution of formic acid.

3.3 SINGLE PHOTON IONIZATION OF VAN DER WAALS CLUSTERS WITH A SOFT X-RAY LASER: $(CO_2)_n$ and $(CO_2)_n(H_2O)_m$

Carbon dioxide is the major gas phase pollutant responsible for the "green house effect" of the atmosphere.[3.92] Many experiments employing supersonic expansion coupled with mass spectroscopic detection have been conducted in order to study monomeric and clustered CO_2 structure and behavior.[3.93-3.112] Spectroscopic and photochemical properties of $(CO_2)_n$ should be related to cluster structure.

Small CO_2 clusters have been studied by Linn and Ng[3.97a] employing a discharge lamp source in the wavelength range 65 to 69 nm to measure the photoionization efficiency curves for $(CO_2)_2$, $(CO_2)_3$, and $(CO_2)_4$. They obtained ionization energy (IE) values of 13.32 $\pm$ 0.02, 13.24 $\pm$ 0.02, 13.18 $\pm$ 0.01 eV, respectively, for these cluster species. The IE of the CO_2 monomer had previously been determined at 13.77 $\pm$ 0.01

eV.[3.97b] The structure of $(CO_2)_n^+$ clusters has been explored through electron diffraction experiments[3.98-3.100] and molecular dynamics simulations.[3.101] Clusters of size $n \geq 100$ apparently have a cubic structure.[3.98] Clusters with $n \leq 100$ undergo a cubic (large) to octahedral (small) structure change in the range $n \sim 20$-55. IR and Raman spectroscopy have demonstrated crystalline structures in even larger clusters.[3.102-3.104] Scanning electron microscope experiments have shown octahedral forms for CO_2 crystals of ~0.1 μm diameter.[3.105]

While few reports of photoionization studies of CO_2 clusters are available, many experiments employing electron impact ionization of $(CO_2)_n$ clusters have appeared. This is probably due to the high ionization energy for CO_2. Size dependent fragmentation electron impact experiments have recently been reported for $(CO_2)_n$ clusters. Three series of fragment ions are observed: $(CO_2)_nO^+$, $(CO_2)_nCO^+$, and $(CO_2)_nO_2^+$. The fragment (daughter) cluster ions are formed from the loss of CO and O from parent ions. The ions corresponding to $(CO_2)_nO_2^+$ daughters may arise from $(CO_2)_{n+1}O^+$ losing one CO molecule.[3.107] Relative intensity anomalies are also observed at n=4,5 and n=15,16 at multiple stagnation pressures. The increased cluster ion intensity at n=4,5 can be attributed to a stable symmetrical structure for the $(CO_2)_n^+$ ion.[3.108] The intensity anomaly at cluster sizes n=15,16 is attributed to a "magic number," the first assigned to a van der Waals cluster. Unfortunately, as in most electron impact cluster studies, fragmentation effects from larger clusters tend to blur the true relative intensities of the neutral cluster size distribution.[3.107] With this technique, one does not observe the true neutral cluster distribution.

A few studies have been conducted involving mixed CO_2/H_2O clusters and these agree that the CO_2/H_2O bond is not a hydrogen bond. The neutral CO_2H_2O cluster has a T-shaped structure in which the hydrogens point away from the CO_2 molecule. These latter results are based on IR spectroscopy[3.113] and ab initio calculations.[3.113,3.114] Theoretical studies of larger cluster ions suggest that the CO_2-H_2O bond is no longer a van der Waals bond but a weak hydrogen bond that is susceptible to cleavage.[3.115] These details will be reexamined in the Discussion Section on the mixed cluster ion $(CO_2)_n(H_2O)_m$ series.

In the present study, carbon dioxide and mixed carbon dioxide-water clusters are accessed by single photon ionization with a 26.5 eV (46.9 nm) soft X-ray laser. The distributions of neutral $(CO_2)_n$ and $(CO_2)_n(H_2O)_m$ clusters are detected and metastable dissociation rate constants for $(CO_2)_n^+$ cluster ions are measured in the range $5 \leq n \leq 16$ and for $(CO_2)_nH_2O$ in the range $5 \leq n \leq 9$. $(CO_2)_n^+$ cluster ions are the dominant products in the photoionization of neutral $(CO_2)_n$ clusters using a single photon of 26.5 eV energy for ionization. Compared with electron impact techniques, $(CO_2)_n$ clusters suffer only a small dissociation by this present single photon ionization and a nearly accurate neutral cluster distribution is observed by time of flight mass spectroscopy (TOFMS). The neutral cluster distribution $(CO_2)_n$, as observed through $(CO_2)_n^+$ ions, shows no sign of anomalous relative intensity peaks that could be termed "magic numbers" associated with van der Waals clusters. For the neutral CO_2-H_2O cluster series, both $(CO_2)_n(H_2O)^+$ and $(CO_2)(H_2O)_nH^+$ cluster ions are observed under different experimental conditions. Also observed is the unprotonated water cluster ion series that is not observed for pure neutral

water clusters ionized by 26.5 eV photons.[3.116] The mechanism for mixed cluster formation is discussed in detail in this report.

3.3.1 Experimental Procedures

The experimental apparatus and soft X-ray laser have been described in previous publications from this laboratory[3.116,3.117] and therefore only a general outline of the experimental scheme will be presented in this report. A table-top soft X-ray laser (26.5 eV photons) is used as the single photon ionization source.[3.118] The laser emits pulses of ca. 1 ns duration with an energy of ca. 10 μJ/pulse at a repetition rate of 12 Hz. A time of flight (linear/reflectron) mass spectrometer (TOFMS) is used as a mass analyzer. A pair of mirrors placed in Z-fold configuration just before the ionization region of the TOFMS provides alignment capability and focus for the laser beam with respect to the molecular beam at the ionization source. The Z-fold transmissivity is about 10% and thus the ionization point in the TOFMS receives about 1 μJ/pulse laser energy. Since the 26.5 eV photons from the soft X-ray laser are able to ionize the He carrier gas employed in the supersonic expansion discussed below, the microchannel plate mass detector voltage is gated to reduce the gain of the plates when He^+ ions arrive at the MCP in order to prevent detector circuit overload and saturation.

Pure neutral $(CO_2)_n$ clusters are generated in a supersonic expansion of 20% CO_2/He or Ar mixed gases from a pulsed nozzle (200 μm diameter opening) at 80 psi backing pressure. A mixed CO_2-H_2O gas is obtained by flowing 5% or 20% CO_2/He at pressures of 30 or 80 psi through a reservoir containing liquid water at room temperature. Mixed CO_2/H_2O clusters are generated in the molecular beam by expanding the gas mixture into a vacuum chamber. CO_2 and gases used in these experiments are 99.9% pure from

General Air. The molecular beam is collimated by a skimmer with a 2.0 mm diameter hole at its apex, located approximately 2 cm downstream from the nozzle. Chamber pressure in the field free and detector regions of the TOFMS is 2 x 10^{-6} Torr during the experiment. Experiments are conducted to ensure that collision induced dissociation of cluster ions is negligible. The pressure in the beam at the ionization region (ca. 10^{-5} Torr) is too low to cause collision induced ionization of $(CO_2)_n$.

3.3.2 Results

3.3.2.1 Distribution of CO_2 Clusters Ionized by a 26.5 eV Soft X-ray Laser.

Figure 3.27 displays a linear TOF mass spectrum of CO_2 clusters photoionized by a single photon of 26.5 eV energy. The spectrum reveals the size distribution of the clusters as they are generated in the ionization/extraction region of the TOFMS on a time scale of less than 1 μs after ionization. The distribution of $(CO_2)_n^+$ ($2 \leq n \leq 20$) clusters that dominate the spectrum decreases approximately exponentially as a function of increasing cluster size n. If the intensity scale is expanded, as shown in Figure 3.28, one can observe other cluster series in the mass spectrum: in particular, the series $(CO_2)_nO_2^+$ and $(CO_2)_nCO^+$ are fragment features. They arise within the time frame of the ca. 1 ns laser pulse, as the features are sharp (~10 ns for an Ar expansion) and do not tail off to the high mass side of the spectrum, as would be expected for slow fragmentation (1 μs > τ_{frag} > 10 ns) in the extraction region. One also notes a series of mixed water-carbon dioxide clusters $(CO_2)_nH_2O^+$, due to residual water in the expansion gases, nozzle, or vacuum system. The three pure CO_2 cluster ion series arise as follows:

$$(CO_2)_n + h\nu \rightarrow (CO_2)_n^+ + e^- \quad (3.25)$$

$$\rightarrow (CO_2)_{n-1} CO^+ + O + e^- \quad (3.26)$$

$$\rightarrow (CO_2)_{n-1}O^+ + CO + e^- \rightarrow \quad (3.27a)$$

$$(CO_2)_{n-2}O_2^+ + CO + O + e^-. \quad (3.27b)$$

To be certain that the $(CO_2)_{n-2}O_2^+$ cluster ion series does not originate from residual O_2 in the system, a test is conducted in which 10% O_2/He is employed as the backing gas and the signal intensity of $(CO_2)_{n-2}O_2^+$ cluster ions is monitored. No enhancement of the signals in these mass channels is observed, indicating that reaction (3.27) is the actual mechanism for the appearance of the $(CO_2)_{n-2}O_2^+$ series of cluster ions. If these results are compared to those for electron impact ionization,[3.107] as expected, one finds significantly less cluster fragmentation generated by 26.5 eV photoionization.

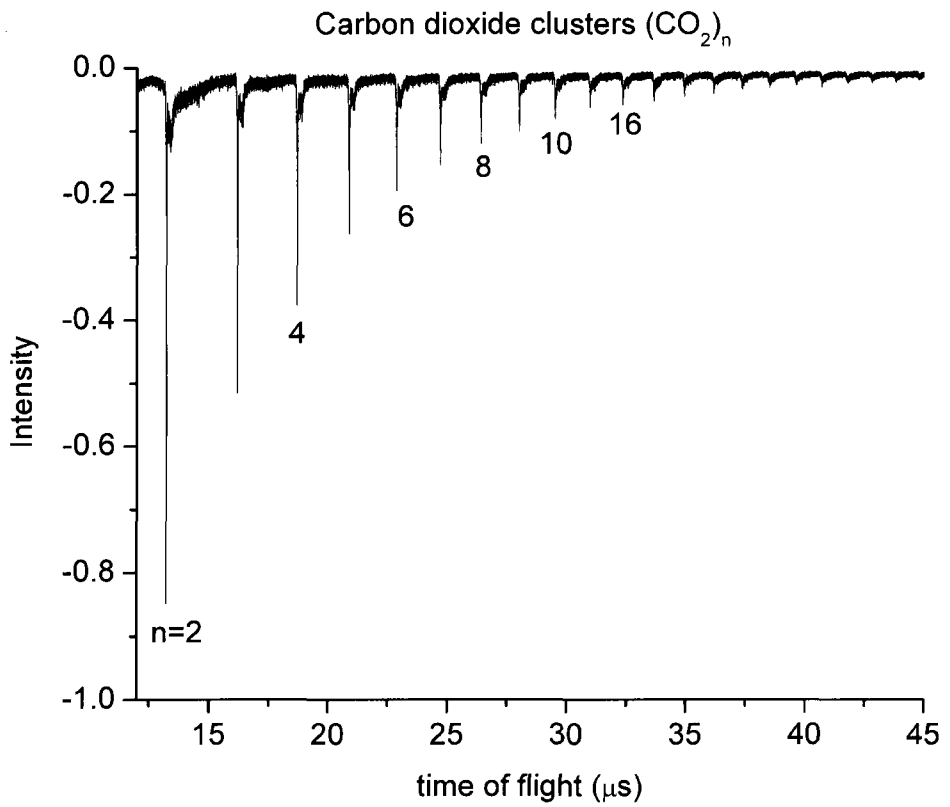


Figure 3.27: A linear TOF mass spectrum of CO_2 clusters ionized by a 26.5 eV soft X-ray laser. The CO_2 clusters are generated by expansion of 20% CO_2/Ar mixed gas at 80 psi.

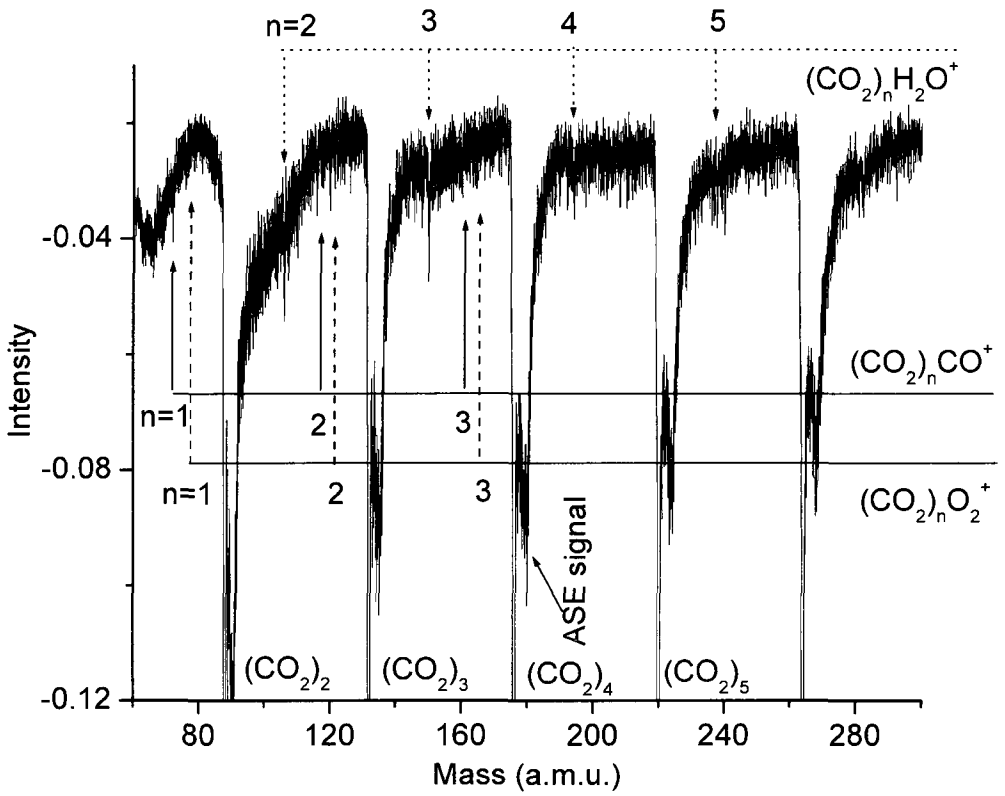


Figure 3.28: An expansion of the scale in Figure 3.327 showing the weak intensity dissociated cluster ion series $(CO_2)_nO_2^+$, and $(CO_2)_nCO^+$. ASE is the Amplified Spontaneous Emission from the creation of the laser plasma. For more information see reference [3.118] and the references therein.

3.3.2.2 Mixed Carbon Dioxide-Water Clusters.

Mixed CO_2-H_2O clusters are generated by expanding a mixed gas of CO_2/He and water vapor into the vacuum chamber at room temperature. Mixed CO_2-H_2O clusters are generated under two experimental conditions: 1. 20% CO_2/He mixed with water vapor at 80 psi backing pressure; and 2. 5% CO_2/He mixed with water vapor at 30 psi backing pressure. Figure 3.29 shows a mass spectrum of mixed CO_2-H_2O clusters formed under condition 1. At this high pressure, high CO_2 content condition, $(CO_2)_n^+$ cluster ions dominate the spectrum, and pure water clusters are not observed. The same exponential decrease in the cluster ion distribution is noticed relative to the distribution without water

in the beam. Again if the scale of Figure 3.29 is expanded, as in Figure 3.30, new pure and mixed cluster ion series are observed. In addition to the pure cluster series $(CO_2)_n^+$ and $(CO_2)_nCO^+$, the two mixed cluster series $(CO_2)_n(H_2O)_2$ and $(CO_2)_nH_2O$ can be observed: note that all of these clusters are unprotonated. The signal intensities for the cluster ions $(CO_2)_nH_2O^+$ are approximately 10% of the intensities for the cluster ions $(CO_2)_n^+$ for n = 2-5. Additionally, some small signals of $(CO_2)_{2,3}H_2OH^+$ cluster ions are observed. Figure 3.31 illustrates metastable dissociation for cluster ions $(CO_2)_n^+$, and for the mixed cluster ions $(CO_2)_nH_2O^+$ for n = 5-8 at condition 1. The spectrum of Figure 3.31 is observed with the TOFMS operating in reflectron mode and indicates the population of cluster ions as found in the first field free region of the TOFMS within the time window 1-100 μs. The peaks labeled $(CO_2)_{n+1}$ are the parent ion clusters of the daughter ion peaks labeled D_n. The daughter ions are generated by loss of one CO_2 molecule from the parent ion. Similarly, the peaks labeled $(CO_2)_{n+1}H_2O^+$ are the parent cluster ions of the daughter peaks labeled B_n produced by loss of one CO_2 molecule from the parent ion.

If the concentration of CO_2 in the backing gas and the backing pressure are reduced to that of condition 2 (low concentration and pressure), the dominant signal in the mass spectrum changes from $(CO_2)_n^+$ to $(H_2O)_nH^+$ (n = 3-22) as illustrated in Figure 3.32. The $(CO_2)_n^+$ signal is less intense but still observable. Expanding the scale as shown in Figure 3.33, displays three more cluster ion series. The protonated mixed cluster ions $(CO_2)(H_2O)_nH^+$ appear in the mass spectrum and are generated from the mixed neutral cluster $(CO_2)(H_2O)_{n+1}$ by a proton transfer reaction following ionization:

$$(CO_2)(H_2O)_{n+1} + h\nu \rightarrow \{(CO_2)(H_2O)^+_{n+1}\}^* + e^- \rightarrow (CO_2)(H_2O)_nH^+ + OH + e^- . \quad (3.28)$$

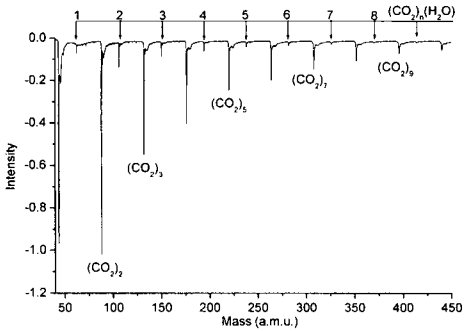


Figure 3.29: A high resolution spectrum of mixed CO_2-H_2O clusters that are generated by expansion of mixed gas 20% CO_2/water vapor/He at 80 psi backing pressure. Cluster ions $(CO_2)_n^+$ dominate mass spectrum. The signal intensity of cluster ions $(CO_2)_n(H_2O)^+$ is about 10% of the intensity of the cluster ions $(CO_2)_n^+$, for values of $n \leq 10$.

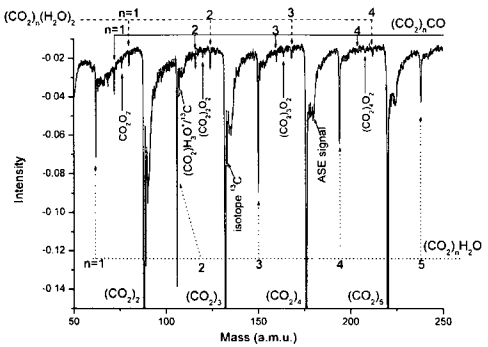


Figure 3.30: An expanded scale view of Figure 3.29 revealing the cluster ion series $(CO_2)_n(H_2O)^+$ and $(CO_2)_n(H_2O)_2^+$. ASE is the Amplified Spontaneous Emission from the creation of the laser plasma. For more details see reference [3.118] and the references therein.

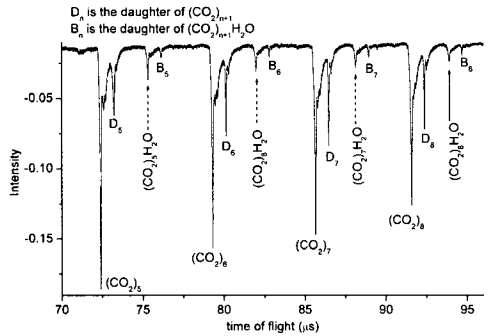


Figure 3.31: A high resolution reflectron TOF mass spectrum of $(CO_2)_n$ clusters Metastable dissociation of $(CO_2)_n^+$ and $(CO_2)_nHO^+$ cluster ions in the field free region is observed. B_n $(CO_2)_nH_2O$ is the daughter peak of $(CO_2)_{n+1}H_2O$ and D_n $(CO_2)_n$ is the daughter peak of $(CO_2)_{n+1}$. See text for a discussion of the metastable fragmentation.

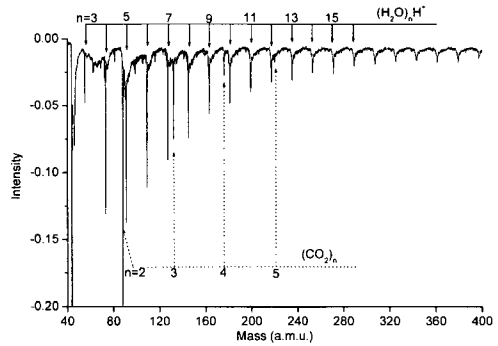


Figure 3.32: Spectrum of mixed CO_2-H_2O clusters that are generated by expansion of mixed gas 5% CO_2/water vapor/He at 30 psi backing pressure. Protonated water cluster ions $(H_2O)_nH^+$ dominate mass spectrum while $(CO_2)_n^+$ cluster ions are still observed.

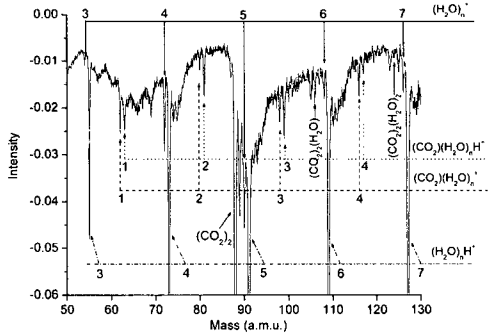


Figure 3.33: An expanded scale view of Figure 6 revealing the protonated cluster ion series $(CO_2)(H_2O)_nH^+$, and the unprotonated series $(CO_2)(H_2O)_n^+$, $(CO_2)_2(H_2O)_n^+$, and $(H_2O)_n^+$.

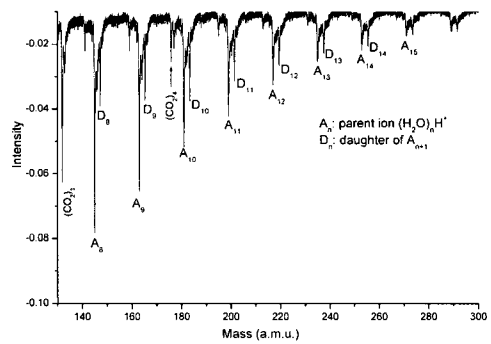


Figure 3.34: A high resolution reflectron TOF mass spectrum of the CO_2-H_2O mixed cluster system for low pressure flow concentration CO_2 conditions. Metastable dissociation of $(H_2O)_nH^+$ cluster ions in the field free region is observed.

Unprotonated cluster ions $(CO_2)(H_2O)_n^+$ and $(H_2O)_n^+$ appear in the mass spectrum as well and may be generated by the reactions:

$$(CO_2)_m(H_2O)_{n+1} + h\nu \rightarrow \{(CO_2)_m(H_2O)_{n+1}^+\}^* + e^-$$

$$\rightarrow (CO_2)(H_2O)_n^+ + (m-1)\,CO_2 + e^-, \quad (3.29)$$

$$\rightarrow (H_2O)_n^+ + m\,CO_2 + e^-. \quad (3.30)$$

Mixed cluster ions containing more than one CO_2 molecule are not observed except for $(CO_2)_2\,(H_2O)_n^+$ n=1,2. The generation of mixed CO_2-H_2O cluster ions will be discussed in more detail in the next section.

Figure 3.34 presents metastable dissociation of cluster $(H_2O)_nH+^+$ for n=8-16 at condition 2. The peaks labeled A_n are the parent ion clusters of the daughter peaks labeled D_{n-1} produced by the loss of one H_2O molecule from the parent ion A_n. The relative signal intensities of the parent and daughter ions switch dominance at n~14.

3.3.2.3 Metastable Dissociation Rate Constants for $(CO_2)_n^+$ and $(CO_2)_nH_2O^+$ Cluster Ions.

Figure 3.31 presents a reflectron TOF mass spectrum indicating the population distribution of cluster ions formed in the first field free region of the TOFMS. Daughter ions are produced from their parent ions by metastable dissociation reactions in the drift tube. Based on our previous studies of weakly bound cluster ions with both van der Waals and hydrogen bonding structures (e.g., $(H_2O)_n$, $(CH_3OH)_n$, $(NH_3)_n$, $(SO_2)_n$), we can assume that only one CO_2 molecule is lost from each $(CO_2)_n^+$ and $(CO_2)_nH_2O^+$ parent cluster ion to generate the daughter ions. The unimolecular metastable dissociation rate constants for $(CO_2)_n^+$ and $(CO_2)_nH_2O^+$ cluster ion dissociation can be calculated as

$$k = -\left(\frac{1}{t}\right) \ln\left[1 - I_D/(I_D + I_P)\right], \quad (3.31)$$

in which I_D and I_P are the intensities of the dissociated daughter ion and the undissociated parent ions, respectively. t is time of flight of the parent ion in the first field free region of the reflectron TOFMS. For the present apparatus this is about 60% of the total flight time for the reflectron mode TOFMS. Figure 3.35 shows that these rate constants, for cluster ions $5 \leq n \leq 12$, fall between 0.1 to 1.0 x 10^4 s^{-1}. The k values for $(CO_2)_nH_2O^+$ are similar to those for $(CO_2)_n^+$ for the same n values. These values are also very similar to those found in our previous studies of van der Waals and hydrogen bonded clusters.[3.116]

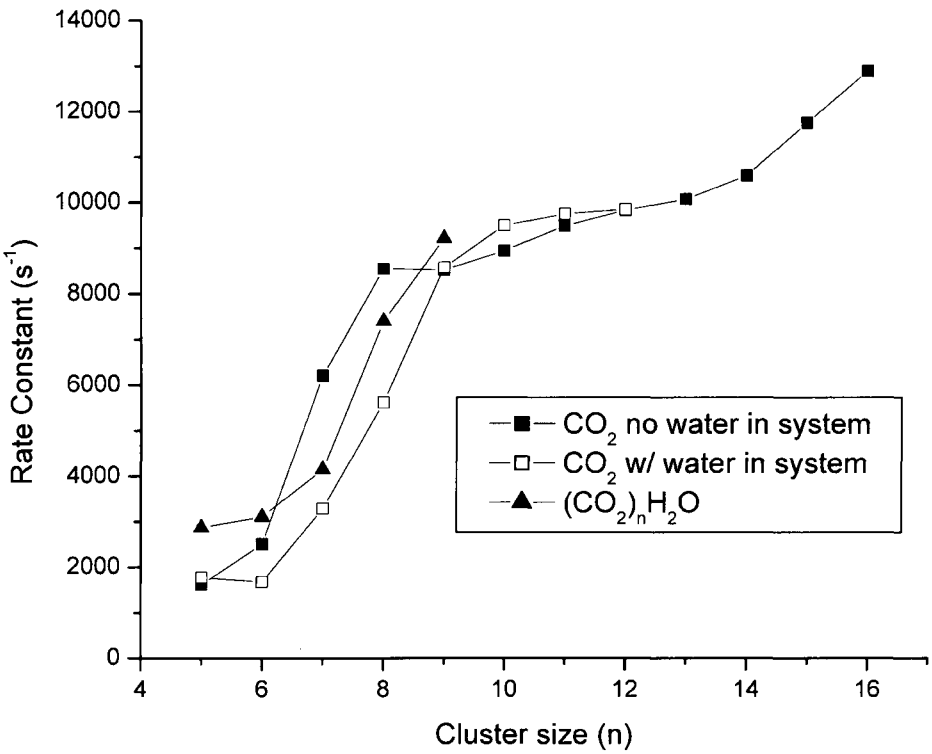


Figure 3.35: A plot of metastable dissociation rate constants for $(CO_2)_n^+$ (with and without water experimentally added to the system), and $(CO_2)_nH_2O^+$ cluster ions as a function of the cluster size, n.

We hypothesize that the $(CO_2)_nH_2O^+$ daughter cluster ion series is formed through a process in which the parent ion loses one CO_2 molecule, not water. This conclusion is drawn from an analysis of the flight time difference between the parent and its respective

daughter ion in each series. For the $(CO_2)_n^+$ cluster ion series, the parent/daughter flight time difference $\Delta(t_p - t_D)$ = 6.11, 5.49 and 5.12 μs for n = 6,7,8, respectively. For the $(CO_2)_nH_2O^+$ cluster ion series, $\Delta(t_p - t_D)$ = 5.95, 5.38, and 4.99 μs for m = 6,7,8, respectively. The similarity between these series timing differences implies that the $(CO_2)_nH_2O^+$ cluster ion series loses one CO_2 unit in the drift tube. Moreover, the overall rate constant similarities for all these metastable dissociations strongly favor the conclusion that all these cluster ions lose the same number of components to metastable dissociation in the drift. The mass spectral peak shapes and widths for the TOF mass spectral features also imply that rapid dissociation following ionization within the ion extraction region of the TOFMS (10 ns to 1 μs) does not occur for any of these van der Waals and hydrogen bonded clusters. The results plotted in Figure 3.35 are consistent with the the conclusion that CO_2 cluster ions generated in the mixed system also come from neutral $(CO_2)_n$ clusters and not the mixed clusters $(CO_2)_n(H_2O)_n^+$.

3.3.3 Discussion

3.3.3.1 Distribution of $(CO_2)_n$ Clusters.

We have learned from both this study of CO_2 clusters and previous studies of H_2O, CH_3OH, NH_3, and SO_2 clusters that 26.5 eV photons ionize van der Waals and hydrogen bonded clusters such that very little energy above the vertical ionization energy (VIE) of the clusters remains in the cluster. Cluster metastable fragmentation is driven in most instances by the energy difference between cluster VIE and adiabatic ionization energy (AIE) or the energy difference between VIE and the barrier to the proton transfer/dissociation reaction following ionization (e.g., $(H_2O)_2 \rightarrow (H_2O)_2^+ + e^- \rightarrow (H_2O)H^+ + OH + e^-$).

Carbon dioxide clusters are van der Waals in nature with a $(CO_2)_2$ pair bonding energy of ca. 1.3 kcal/mol compared to $(H_2O)_2$ pair bonding energy of ca. 5 kcal/mol.[3.120] As illustrated in Figure 3.27, signals for $(CO_2)_n^+$ cluster ions dominate the spectrum for all n. Signals for $(CO_2)_{n-1}CO^+$ and $(CO_2)_{n-2}O_2^+$ become increasingly weak in the range n = 1-4. These results are in stark contrast with electron impact results[3.117] for $(CO_2)_n$ clusters, in which such fragmentation yields nearly 50% of the cluster ion intensity for n = 5, 16. For 26.5 eV single photon ionization the summed relative intensities for fragment ions have a ratio < 0.01 for all values of n. These results, in conjunction with linear TOFMS data, strongly suggest that the neutral cluster $(CO_2)_n$ distribution is quite similar to the observed $(CO_2)_n^+$ distribution.

Metastable fragmentation (outside the ionization/extraction region of the TOFMS, t > 1 μs) occurs with nearly the same rate constant for all van der Waals and hydrogen bonded cluster ions studied with 26.5 eV single photon photoionization.[3.116,3.117] This coincidence implies a loose relation between cluster binding energy, (VIE-AIE), ΔH for proton transfer and binding energy for OH and NH_2 in their respective clusters, and the barriers to proton transfer reactions in the appropriate clusters. While this is far from a quantitative relationship, such a connection is qualitatively implied by the similar rate constants. What is implied by these metastable rate constant similarities is that the details of cluster structure and limiting potential energy models is less important than the overall cluster density of states and statistical or ergodic behavior. Since the metastable dissociation rate constants increase with increasing cluster size (see Figure 3.35), the cluster vibrational temperature must increase with cluster size, as well.

Based on our results, we consider that most neutral carbon dioxide clusters $(CO_2)_n$ are free of fragmentation directly following the single photon ionization of the soft x-ray laser. This claim can be supported by three main observations. First, the peaks observed in the mass spectra are sharp and symmetrical, implying that cluster fragmentation does not occur in the first < 1 μs following ionization. Second, the loss of only one carbon dioxide molecule is observed in the field free region after ionization. The metastable rate constants of the carbon dioxide cluster ions are similar to water, ammonia, and methanol.[3.116] Ref. 3.116 presents many arguments that support almost no fragmentation for van der Waals clusters. Similar rate constants indicate similar behavior of the clusters following ionization. Third, we observe unprotonated mixed water-carbon dioxide clusters. This shows that during ionization, the amount of energy left in the mixed cluster is too small to drive a proton transfer reaction. This will be discussed in more detail in the following sections.

3.3.3.2 Generation of Mixed CO_2-H_2O Clusters.

Binding energies for hydrogen bonded clusters are considerably larger than those for non hydrogen bonded van der Waals clusters. Additionally the binding energy for the $(H_2O)(CO_2)$ dimer is 920 cm^{-1} or 0.114 eV.[3.114] At high backing pressure and concentration of CO_2, the $(CO_2)_n^+$ cluster ions are the dominant ones in the mass spectrum (Figure 3.29). Based on the comparison of metastable decay ratios of $(CO2)_n^+$ clusters generated in both of the pure CO_2 and mixed CO_2-H_2O systems (see Figure 3.35), one can conclude that $(CO_2)_n^+$ ions are produced from neutral $(CO_2)_n$ clusters, and not from mixed $(CO_2)_n(H_2O)$ clusters. Mixed clusters $(CO_2)_nH_2O^+$ lose one CO_2 molecule via metastable dissociation, not one water molecule, to form the daughter ion $(CO_2)_{n-1}H_2O^+$.

This latter mechanism is supported by the daughter/parent flight time difference discussed earlier in the last section. The signal intensity of the mixed cluster in $(CO_2)_nH_2O^+$ is about 10% (for n = 1-5) of that for $(CO_2)_n^+$, indicating that $(CO_2)_n$ is a reasonable solvent for H_2O.

We can understand the greater concentration of $(CO_2)_nH_2O^+$ unprotonated cluster ions with respect to $(CO_2)_nH^+$ or $(CO_2)_n(H_2O)H^+$ protonated ions in the mass spectrum based on a consideration of the proton affinity of CO_2 (5.61 eV) and OH (5.74 eV). In a hydrogen bonded cluster such as water, the proton affinity of clusters increases with increasing cluster size, so the corresponding energy required for proton transfer initiation becomes small. The protonated $(H_2O)_nH^+$ cluster ion series is always dominant in a water expansion, even for "threshold" (VIE) ionization conditions.[3.116] Under the present conditions, almost all of the excess energy above the VIE is removed by the ejected photo electron in the mixed $(CO_2)_n(H_2O)$ cluster series leaving less energy in the nascent cluster ion than required to drive a proton transfer reaction, especially in a non hydrogen bonded system. CO_2 is most likely the initially ionized moiety in the mixed cluster due to larger ionization cross section at 26.5 eV (21×10^{-18} vs 14×10^{-18} cm^2)[3.121] even though its adiabatic ionization energy is larger than that of H_2O (13.8 vs 12.6 eV).

Under the conditions of low backing pressure and concentration of CO_2, condition (2) above, protonated water cluster ions $(H_2O)_nH^+$ dominate the mass spectrum, while the $(CO_2)_n^+$ cluster ion series is detected only for $2 \leq n \leq 7$. This latter series is generated from $(CO_2)_n$ neutrals (Figure 3.32). This is documented by the metastable rate constants for $(CO_2)_n$ with and without water present in the system. From Figure 3.35 one notes that the rate constants for both conditions are very similar, suggesting that the $(CO_2)_n^+$ series

of cluster ions is generated by the same process, with and without water in the expansion, from neutral $(CO_2)_n$ clusters. Additionally, for this set of experimental parameters no $(CO_2)_nH_2O$ clusters are detected.

The distribution of $(H_2O)_nH^+$ ions generated under these low pressure, low concentration conditions for CO_2 is the same as that generated in a pure water/He expansion. For the mixed H_2O-CO_2 system, two possible channels can be identified for the generation of protonated water cluster ions:

$$(H_2O)_n + h\nu \rightarrow \{(H_2O)_n^+\}^* + e^- \rightarrow (H_2O)_{n-1} H^+ + OH + e^- \quad (3.32)$$

and

$$(CO_2)_m(H_2O)_n + h\nu \rightarrow \{(CO_2)_m(H_2O)_n^+\}^* + e^- \rightarrow (H_2O)_{n-l} H^+ + OH + e^- + m\,CO_2 \quad (3.33)$$

Assuming reaction (3.33) occurs, one could also assume that most of the excess photon energy produced by the laser would be absorbed by the ejected m CO_2 molecules, causing a decrease in the metastable dissociate rate of the protonated cluster ions $(H_2O)_nH^+$ (e.g., losing one additional H_2O molecule). The protonated water cluster parent/daughter signal intensity ratio is similar to the pure water system previously studied, in that the parent and daughter signal intensities switch dominance at the same value of n (~ 14/15) in both experiments. This indicates that the protonated water cluster ions do not form by the mixed cluster ion series $(CO_2)_m(H_2O)_nH^+$ losing the appropriate amount of CO_2 molecules, but from the neutral $(H_2O)_n$ clusters through a proton transfer reaction.

Nonetheless, evaporation of m CO_2 molecules from a mixed cluster does effect the (weak) appearance of $(CO_2)(H_2O)_n^+$ and $(H_2O)^+$ via reactions (3.29) and (3.30) as shown in Figure 3.33. Thus for these minor components of the mass spectra of mixed CO_2-H_2O

clusters, the CO_2 molecule behaves in a similar fashion to Ar with respect to removing excess energy (in this instance above the AIE) from the cluster through evaporation of the more weakly bound species.[3.122] Note that $(CO_2)_2(H_2O)_1H^+$ and $(CO_2)_2$ $(H_2O)_2H^+$ clusters are very weakly observed in the spectrum of Figure 3.33.

3.3.4 Conclusions

Pure neutral $(CO_2)_n$ clusters and $(CO_2)_n(H_2O)_m$ mixed clusters are investigated by TOFMS employing single photon 26.5 eV ionization. For the pure CO_2 system, the dominant cluster series in the mass spectrum is $(CO_2)_n^+$ which is directly generated from ionization of neutral clusters $(CO_2)_n$ in the molecular beam. The distribution of $(CO_2)_n$ neutral clusters decreases roughly exponentially with increasing cluster size n showing no anomalous signal intensities in the distribution. The $(CO_2)_{n-1}CO^+$ and $(CO_2)_{n-2}O_2^+$ cluster series are observed (weakly) as the photodissociation products of the neutral $(CO_2)_n$ clusters at a highly excited state of the ion. Compared to electron impact studies, much less dissociation is observed because in most instances all of the excess cluster energy above VIE is removed by the photoelectron during the ionization process.

For the van der Waals cluster $(CO_2)_n^+$, metastable dissociation by loss of only one CO_2 molecule from the cluster is observed in the reflectron TOF mass spectrum for 26.5 eV single photon ionization. The metastable dissociation rate constants for $(CO_2)_n^+$ loss of CO_2 are in the range 0.2 to 1.5 x 10^4 s^{-1} for $5 \leq n \leq 16$. This is the same range observed for the comparable dissociation of $(SO_2)_n^+$, $(H_2O)_n$ H^+, $(CH_3OH)_nH^+$, and $(NH_3)_n$ H^+ clusters. These rate constants imply that cluster dynamics is dependent upon cluster density of states and internal cluster temperature.

Mixed CO_2-H_2O clusters are studied at two different conditions of CO_2 concentration in the expansion gas and two different expansion gas pressures. The predominant signals in the mass spectra are $(CO_2)_n^+$ and $(H_2O)_nH^+$ cluster ions for high and low parameter values, respectively. Both cluster ion series arise from pure neutral and not mixed clusters. For the high concentration condition two more cluster series, $(CO_2)_nH_2O^+$ and $(CO_2)_n(H_2O)_2^+$ are observed. The X-ray laser photon does not deposit enough energy in the $(CO_2)_n(H_2O)_{1,2}^+$ clusters to cause proton transfer to CO_2 or H_2O. CO_2 acts as a good solvent for H_2O molecules. At low concentration and backing pressure, many additional cluster ion series are observed. The unprotonated $(H_2O)_n^+$ and $(CO_2)(H_2O)_n^+$ series are generated by the evaporation of CO_2 molecules from the mixed cluster series $(CO_2)_m(H_2O)_n^+$.

In general, the behavior of $(CO_2)_n$ and $(CO_2)_n^+$ clusters parallels that found for other van der Waals and hydrogen bonded clusters with regard to cluster distribution, cluster dissociation, and cluster vibrational temperature.

3.4 SINGLE PHOTON IONIZATION OF VAN DER WAALS CLUSTERS WITH A SOFT X-RAY LASER: $(SO_2)_n$ and $(SO_2)_n(H_2O)_m$

Sulfur dioxide emissions from combustion, coal treatment, and volcanoes can form acids in the atmosphere that return to earth in the form of acid depositions or "acid rain." Acid rain is one of the biggest environmental problems at present. Sulfur dioxide is the major contributor to acid rain and a generator of soot. The process of SO_2 and water forming acid rain has been studied for some time in order to determine the atmospheric mechanism for this environmental issue.[3.123,3.124]

The SO_2 monomer and dimer have been extensively studied. Erickson and Ng[3.125] measured the photoionization efficiency curves for SO_2 and $(SO_2)_2$ with high resolution

in the wavelength region 62.5 to 100.5 nm. The ionization energies (IE) of SO_2 and $(SO_2)_2$ are determined to be 12.35 and 11.72 eV, respectively. Kuczkowski and co-workers[3.126] investigated the microwave spectroscopy of $(SO_2)_2$. The structure of the SO_2 dimer is low symmetry in which one SO_2 unit defines a plane, and the second SO_2 unit lies above the first, with its two O atoms straddling the first SO_2. The two planes containing the SO_2 molecules are perpendicular to each other. Dissociation dynamics of $(SO_2)_n$ clusters have been explored on the fs time scale.[3.127] The lifetime of the E electronic state of $(SO_2)_n$ increases as cluster size n increases. This has been explained as due to a "cage effect" associated with the cluster. $(SO_2)_{n-1}$ SO^+ and $(SO_2)_{n-1}$ S^+ are identified as the main products for fs multiphoton ionization. To explore the neutral cluster distribution and the dynamics of cluster formation and fragmentation, single photon ionization near the ionization threshold is the best approach, but SO_2 clusters have a high ionization energy; even 118 nm (10.5 eV single photon energy) laser radiation is not sufficient to ionize SO_2 clusters.

The reaction of SO_2 solvated by water is a part of the acid rain formation process and thus clusters of H_2O/SO_2 are also an object of some scrutiny. Theoretical studies[3.128] indicate that a high barrier exists for the reaction $SO_2 \bullet H_2O \rightarrow H_2SO_3$. Li and McKee[3.129] find that the decomposition of H_2SO_3 is catalyzed by presence of additional water molecules, which lower the barrier for the reaction $H_2SO_3 \rightarrow H_2O + SO_2$. Microwave spectroscopy of $H_2O \bullet SO_2$ shows the cluster structure as non hydrogen bonded and the water and sulfur dioxide planes are tilted approximately 45° from a parallel orientation, with the O atom of H_2O lying above the S atom of SO_2.[3.130] The vibrational frequencies of each molecule in the mixed dimer are similar to those of the individual molecules.[3.131]

Theoretical calculations indicate that the interaction in the $SO_2 \bullet H_2O$ complex is not dominated by hydrogen bonding, as the two molecular planes are stacked and somewhat parallel.[3.132,3.133]

Mixed sulfur dioxide/water clusters have also been studied with multiphoton fs ionization reflectron time of flight mass spectroscopy (TOFMS).[3.134,3.135] The measured times for dissociation are independent of cluster size, indicating that the ions formed are all at the cluster surface rather than "solvated" by the other, neutral members of the cluster. SO_2 molecules are thus more likely to be weakly absorbed rather than solvated in a low water environment. All detected mixed clusters under fs multiphoton ionization are protonated ions, $(SO_2)_n\ (H_2O)_m\ H^+$ ($m \geq 0$). Based on the thermodynamic analysis of ref. 3.134 for the mixed dimer $SO_2 \bullet H_2O$, the ion-molecule reaction for the proton transfer from H_2O to SO_2 is favorable following ionization. Nonetheless, theoretical calculations indicate that the stable gas phase complex $SO_2 \bullet H_2O$ should exist with a strong bond (~3.5 kcal/mol)[3.132]: this bond is not dominated by hydrogen bonding. Thus, the dimer might have a high barrier to proton transfer. Compared to hydrogen bonded water clusters, more energy should be required to overcome the barrier to proton transfer for $SO_2 \bullet H_2O$. In the present study we observe both the $(SO_2)_n(H_2O)^+$ and the protonated $SO_2(H_2O)_nH^+$ series of cluster ions in the TOFMS following ionization by single photon, 26.5 eV soft X-ray laser light. Mechanisms for mixed cluster formation and ionization will be discussed in this report.

Previously we have shown that 26.5 eV single photon ionization of van der Waals clusters (e.g., $(H_2O)_n$, $(CH_3OH)_n$, $(NH_3)_n$) is virtually free of cluster fragmentation.[3.136] The photoelectron is suggested to carry away with it most, if not all, of the energy above

the vertical ionization energy (VIE) of the molecule or cluster. In the present study, distributions of neutral $(SO_2)_n$ and mixed $(SO_2)_n(H_2O)_m$ clusters are determined, and the metastable dissociation rate constants of $(SO_2)_n^+$ clusters are measured. We document that, during the single photon ionization process, the clusters suffer only a small fragmentation compared with multiphoton fs ionization. The photodissociation fraction for $(SO_2)_n$ clusters at 26.5 eV photon energy decreases with increasing cluster size. Unprotonated cluster ions $(SO_2)_n(H_2O)^+$ and protonated $(SO_2)\ (H_2O)_n\ H^+$ cluster ions are observed at different experimental conditions. Mechanisms for such phenomena are discussed.

3.4.1 Experimental Procedures

The experimental approach for these studies has been described in detail in previous publications from our laboratory,[3.136] and only a general outline of the experimental scheme will be given here. A table-top soft X-ray laser (26.5 eV/photon, 46.9 nm) is used as the ionization source for accessing the neutral clusters of interest. The laser emits pulses of about 1 ns duration with an energy of about 10 μJ/pulse at a repetition rate of up to 12 Hz.[3.137] A time of flight mass spectrometer (TOFMS, linear/reflectron) is employed to analyze cluster mass and fragmentation kinetics. A pair of mirrors placed in a Z-fold configuration just before the ionization region of the TOFMS provides alignment capability and focus for the X-ray laser beam with respect to the cluster beam. The Z-fold mirror system has a total transmissivity of about 10%. Since 26.5 eV photons from the soft X-ray laser are able to ionize the He carrier gas in the beam, the micro-channel plate (MCP) detector voltage is gated to reduce the gain of the MCP when He^+ arrives at the detector in order to prevent detector circuit overload and saturation.

Pure neutral clusters $(SO_2)_n$ are generated in a supersonic expansion of 20% SO_2/80% He mixed gases from a pulsed nozzle (200 μm diameter) at 80 psi backing pressure. A mixture of SO_2 and H_2O gas is obtained by flowing 5 or 20% SO_2/He at a pressure of 30 or 80 psi through a reservoir containing liquid distilled water at room temperature. Mixed $(SO_2)_n(H_2O)_m$ clusters are generated in the supersonic expansion into the vacuum system. SO_2 gas used in the experiment is 99.8% pure (Aldrich, Co.), and the He gas (99.9%) is purchased from General Air Co. The expanded supersonic molecular beam is collimated by a conical skimmer with a 2.0 mm diameter hole. The skimmer is located approximately 2 cm downstream from the nozzle. Chamber pressure in the field free and detector regions of the TOFMS is maintained at 2 x 10^{-6} torr during the experiment. Experiments are conducted to ensure that collision induced dissociation of cluster ions is negligible. Pressure in the skimmed supersonic beam is low enough in the ionization region (ca. 10^{-5} torr) that collision induced ionization of the clusters is not a likely occurrence.

3.4.2 Results

3.4.2.1 Distribution of SO_2 Clusters Ionized by 26.5 eV, Soft X-ray Laser Radiation Ionization

Figure 3.36 displays a linear TOFM spectrum of neutral SO_2 clusters ionized by 26.5 eV, soft X-ray laser radiation. The mass spectrum reflects the size distribution of cluster ions generated in the acceleration/ionization region of the TOFMS, less than 1 μs after ionization. Two series of cluster ions are identified in the spectrum. The peaks labeled A_n represent the cluster series $(SO_2)_n^+$, and the peaks labeled B_n represent the cluster series $(SO_2)_nSO^+$. The distribution of $(SO_2)_n^+$ $2 \leq n \leq 25$ clusters observed in the linear TOFMS

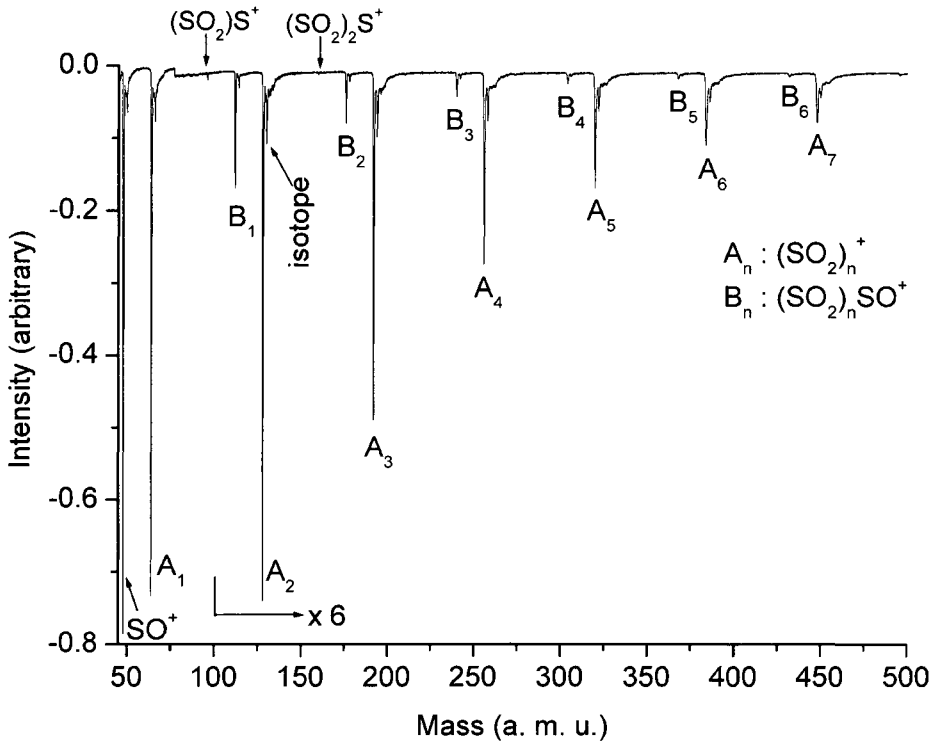


Figure 3.36: A linear TOF mass spectrum of the SO_2 clusters ionized by a 26.5 eV soft X-ray laser. The SO_2 clusters are generated by expansion of a mixed gas of 20% SO_2/80%He at 80 psi.

decreases roughly exponentially with increasing cluster size n. We will agrue in the Discussion Section following that both $(SO_2)_{n-1}SO^+$ and $(SO_2)_n^+$ cluster ions are directly generated from the same neutral parent $(SO_2)_n$ in the molecular beam by the following reactions:

$$(SO_2)_n + h\nu \rightarrow (SO_2)_n^+ + e^- \qquad (3.34)$$

$$(SO_2)_n + h\nu \rightarrow \{(SO_2)_n^*\}^+ + e^- \rightarrow (SO_2)_{n-1}SO^+ + O + e^-. \qquad (3.35)$$

The $(SO_2)_n^+$ cluster series A_n is the predominant one in the linear TOFMS following single photon ionization of neutral clusters $(SO_2)_n$ by 26.5 eV photons. The distribution in Figure 3.36 is different from that obtained by fs multiphoton ionization, which is dominated by the ionization dissociation products $(SO_2)_{n-1}SO^+$. The dissociation fraction of neutral $(SO_2)_n$ clusters at 26.5 eV ionization is shown in Figure 3.37. The intensity

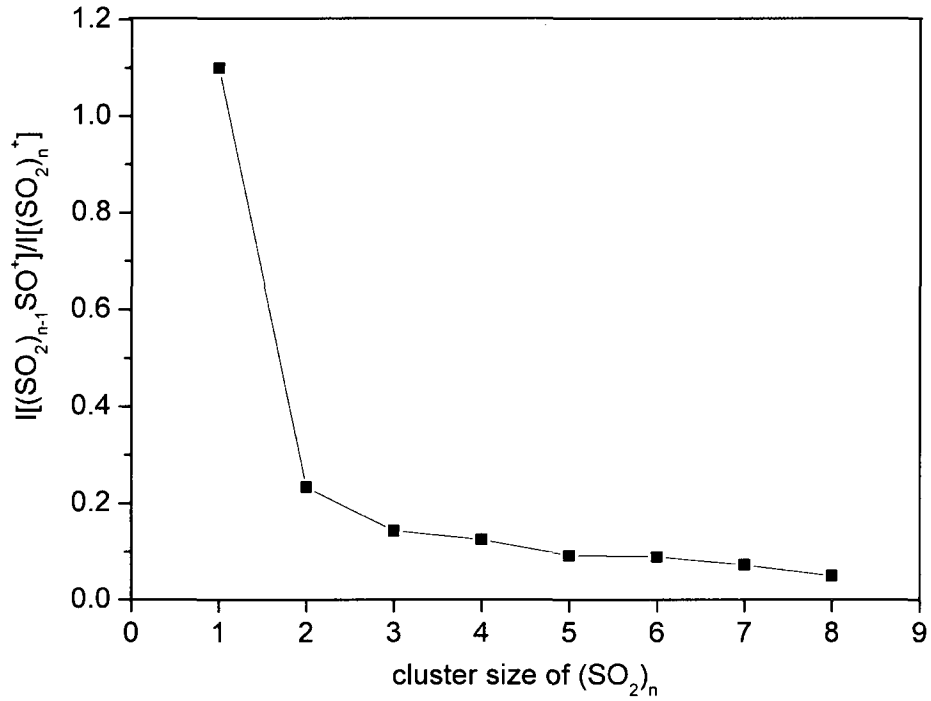


Figure 3.37: Dissociation fraction of $(SO_2)_n$ clusters at the 26.5 eV photon energy.

ratios $I\left[(SO_2)_{n-1}\ SO^+\right]/I\left[(SO_2)_n{}^+\right]$ are between 0.24 to 0.04 for cluster sizes $2 \leq n \leq 8$. These dissociation fractions decrease with increasing cluster size. The SO^+ ion is assigned as the fragment photodissociation product of SO_2 monomer: the $I\left[SO^+\right]/I\left[SO_2{}^+\right]$ is about 1.1. A number of minor fragmented species can also be identified: S^+ generated from SO_2 by loss of O_2; $(SO_2)S^+$ and $(SO_2)_2S^+$ generated by the loss of O_2 from $(SO_2)_2$ and $(SO_2)_3$, respectively. Although the mass of $^{16}O_2$ and ^{35}S overlap, the species S^+ can be identified from the background $^{16}O_2{}^+$ signal by the presence of $^{34}S^+$.

3.4.2.2 Metastable Dissociation Rate Constants for $(SO_2)_n{}^+$ Clusters.

The spectrum of Figure 3.38 is obtained in the reflectron mode of the TOFMS. It indicates the population distribution of cluster ions formed in the first field free region within the time region 1-90 μs. If the fragmentation were to happen in the acceleration region, the TOF spectrum would indicate this with mass peaks broadly dispersed in time. Since the fragmentation happens in the field free region the parent and daughter signals

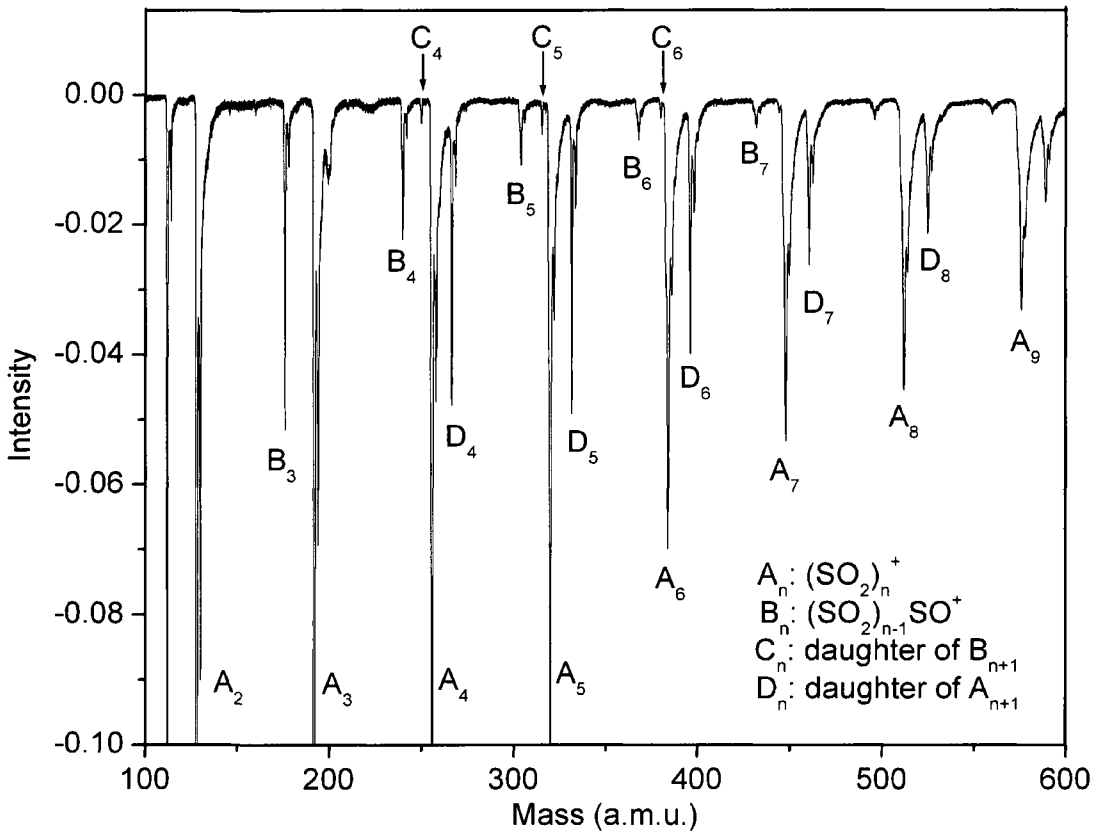


Figure 3.38: A high resolution reflectron TOF mass spectrum of the SO_2 clusters. The metastable dissociation of $(SO_2)_n^+$ and $(SO_2)_nSO^+$ cluster ions in the field free region is observed.

are separated by reflectron mass spectrometer[3.138] with good temporal resolution. Compared to the spectrum displayed in Figure 3.36, two new series of cluster ions can be identified. The peaks marked D_n are the daughter cluster ions of the parent cluster ions $(SO_2)_{n+1}^+$ (A_{n+1}), and the peaks marked C_n are the daughter cluster ions of the parent cluster ions $(SO_2)_{n+1}SO^+$ (B_{n+1}). The daughters are produced from their parents by

metastable dissociation reactions in the first field free TOFMS drift tube section. In the present experiment the loss of only one SO_2 molecule by this mechanism is observed. The unimolecular dissociation rate constant of $(SO_2)_n^+$ and $(SO_2)_nSO^+$ cluster ions can be calculated based on the following equation:[3.139]

$$k = -\left(\frac{1}{t}\right) \ln\left[1 - \frac{(I_D)}{(I_D + I_P)}\right], \tag{3.36}$$

in which I_D and I_P are the intensities of the dissociated daughter ions and the undissociated parent ions, respectively. t is the flight time of the parent ion in the first field free region of the reflectron TOFMS. For the present apparatus this time is about 60% of the total flight time. As shown in Figure 3.39, the metastable rate constants for

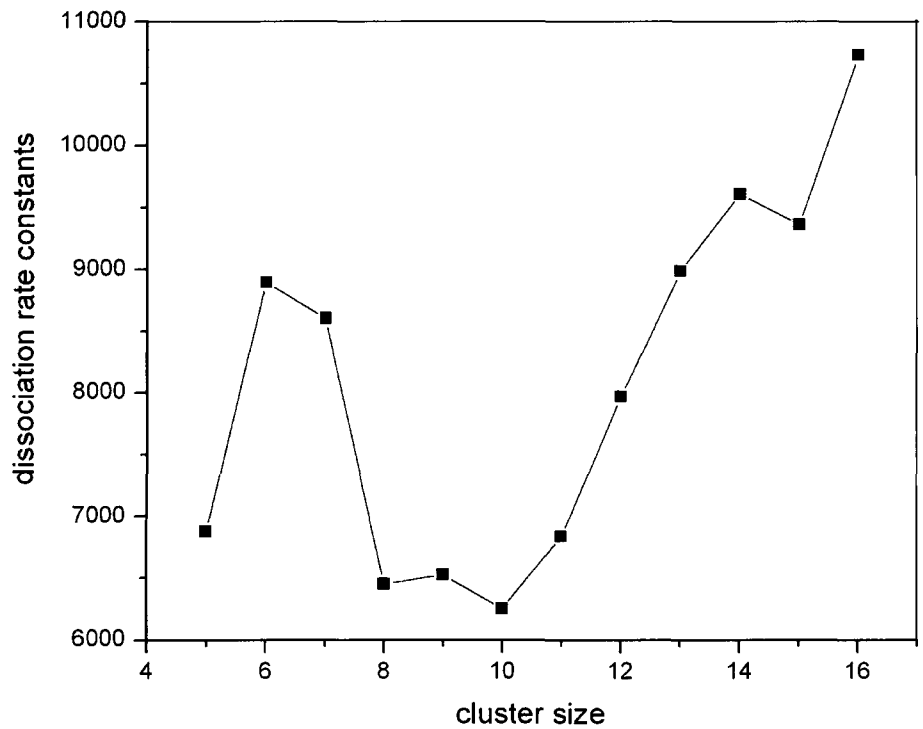


Figure 3.39: A plot of the metastable dissociation rate constants for $(SO_2)_n^+$ and $(SO_2)_nSO^+$ cluster ions as a function of the cluster size, n.

$(SO_2)_n^+$ losing SO_2 are in the range 0.6 to 1.1 x 10^4 s^{-1} for cluster sizes $5 \leq n \leq 16$. Cluster $(SO_2)_6^+$ and $(SO_2)_7^+$ show fast dissociation rates relative to their neighbors.

3.4.2.3 Mixed Sulfur Dioxide – Water Clusters

Mixed $(SO_2)_n(H_2O)_m$ clusters are generated by expanding a three component SO_2/H_2O/He gas into the vacuum chamber at room temperature. We have employed two conditions for the generation of $(SO_2)_n(H_2O)_m$ clusters: 1. 5% SO_2/He mixed with water vapor at (T ~ 300 K) and expanded at 30 psi backing pressure; and 2. 20% SO_2/He mixed with water vapor (T ~ 300 K) and expanded at 80 psi backing pressure. Figure 3.40 presents a mass spectrum of mixed $(SO_2)_n(H_2O)_m$ clusters formed at low concentration of SO_2 and low backing pressure (condition 1). The series of protonated cluster ions

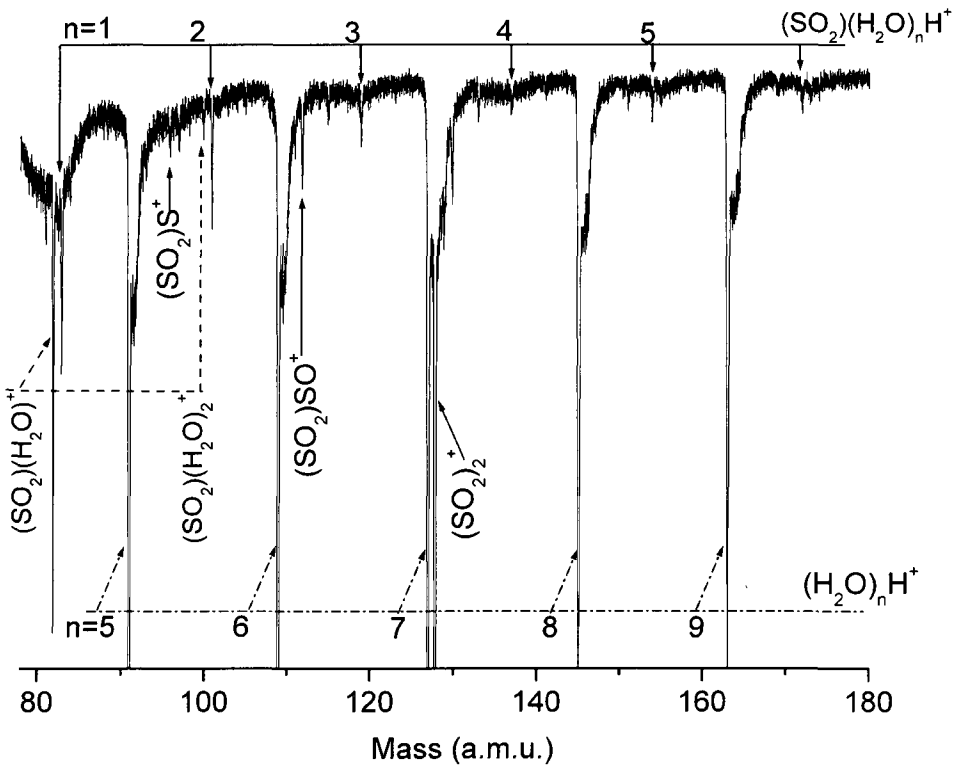


Figure 3.40: A high resolution spectrum of mixed SO_2-H_2O clusters generated by expansion of the mixed gas 5% SO_2/water vapor/He at 30 psi backing pressure. The protonated water cluster ions $(H_2O)_nH^+$ dominate mass spectrum. The signal intensity of the mixed cluster ions $(SO_2)(H_2O)_nH^+$ is about 2% of the intensity of $(H_2O)_nH^+$ at n = 5,6.

$(H_2O)_nH^+(n=1,\ldots,20)$ dominate the mass spectrum in this experiment. The $(SO_2)_n^+$ cluster ions are not observed except for the $(SO_2)_2^+$ dimer because of the lower concentration of SO_2 and low backing pressure. The protonated mixed cluster ions $(SO_2)(H_2O)_nH^+$ appear in the mass spectrum of Figure 3.40 but a very low concentration. They are generated from the neutral mixed clusters $(SO_2)(H_2O)_{n+1}$ by a proton transfer reaction following ionization:

$$(SO_2)(H_2O)_{n+1}\ h\nu \rightarrow \{(SO_2)(H_2O)_{n+1}\}^+ + e^- \rightarrow (SO_2)(H_2O)_nH^+ + OH + e^-. \quad (3.37)$$

Signal intensities of the mixed clusters $(SO_2)(H_2O)_nH^+$ are about 2% of the intensity of $(H_2O)_nH^+$ ions at n=5,6. Mixed sulfur dioxide-water clusters containing more than one SO_2 molecule are not detected. Note that at mass 82 the $(SO_2)(H_2O)^+$ signal is detected. This latter cluster can be directly generated from ionization of the neutral mixed dimer $(SO_2)(H_2O)/H_2SO_3$. No obvious HSO_2^+ signal is observed. We will discuss the generation of mixed SO_2 H_2O clusters in more detail in the Discussion Section below.

Figure 3.41 shows a comparison between metastable dissociation of protonated water clusters generated in a pure water expansion (80 psi He passed over T ~ 300 K liquid water), spectrum A, and metastable dissociation of water clusters generated in a mixed sulfur dioxide-water expansion, spectrum B. The peaks labeled P_n in this figure are parent cluster ions $(H_2O)_nH^+$, and those labeled as D_n are the daughter ions produced by loss of one H_2O from its parent ion P_{n+1} due to metastable fragmentation in the drift tube of the reflectron TOFMS. For both systems, the signal intensities of daughter and parent ions switch dominance at ca. n ~ 14/15. This means that the protonated water cluster ions generated from the two different samples have the same metastable dissociation rate constant in the field free region.

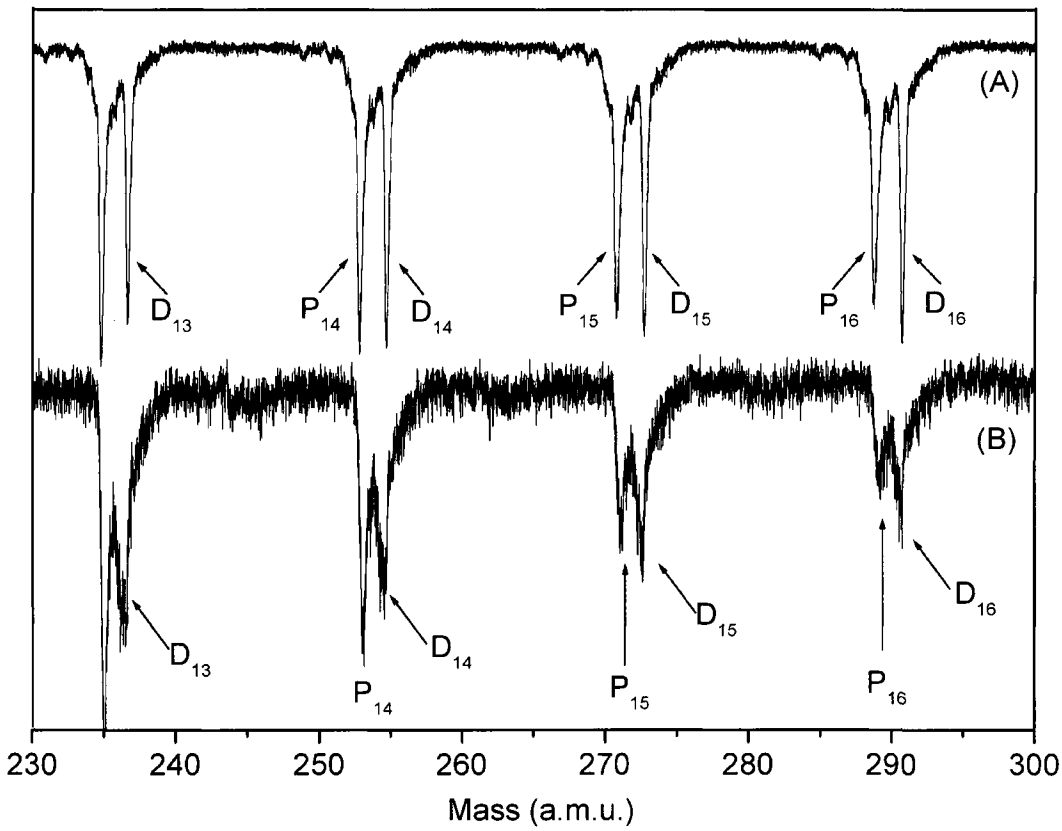


Figure 3.41: A comparison of metastable dissociation of protonated water cluster ions formed in a pure water/He expansion (curve A) and a mixed SO_2/H_2O/He expansion (curve B). The peaks labeled as P_n are the parent cluster ions $(H_2O)_nH^+$, and the peaks marked as D_n are the daughter ions generated by the loss of one H_2O from its parent ions P_{n+1} in the field free region of the reflectron TOFMS. For both systems, the signal intensities of daughter and parent ions switch at n ~ 14/15.

With the concentration of SO_2 in the backing gas is increased to 20% and the backing expansion pressure is increased to 80 psi (condition 2.), $(SO_2)_n^+$ cluster ions dominate the spectrum and the $(H_2O)_nH^+$ ion are not detected as shown in Figure 3.42. All of the mixed cluster ions that are observed in this spectrum are unprotonated $(SO_2)_n(H_2O)^+$ ($1 \leq n \leq 5$). The protonated mixed cluster ions $(SO_2)(H_2O)_nH^+$ formed under condition 1 are not observed. Signal intensities of cluster ions $(SO_2)_n(H_2O)^+$ are about 5% of the intensities of the $(SO_2)_n^+$ cluster ions, n = 2,3,4.

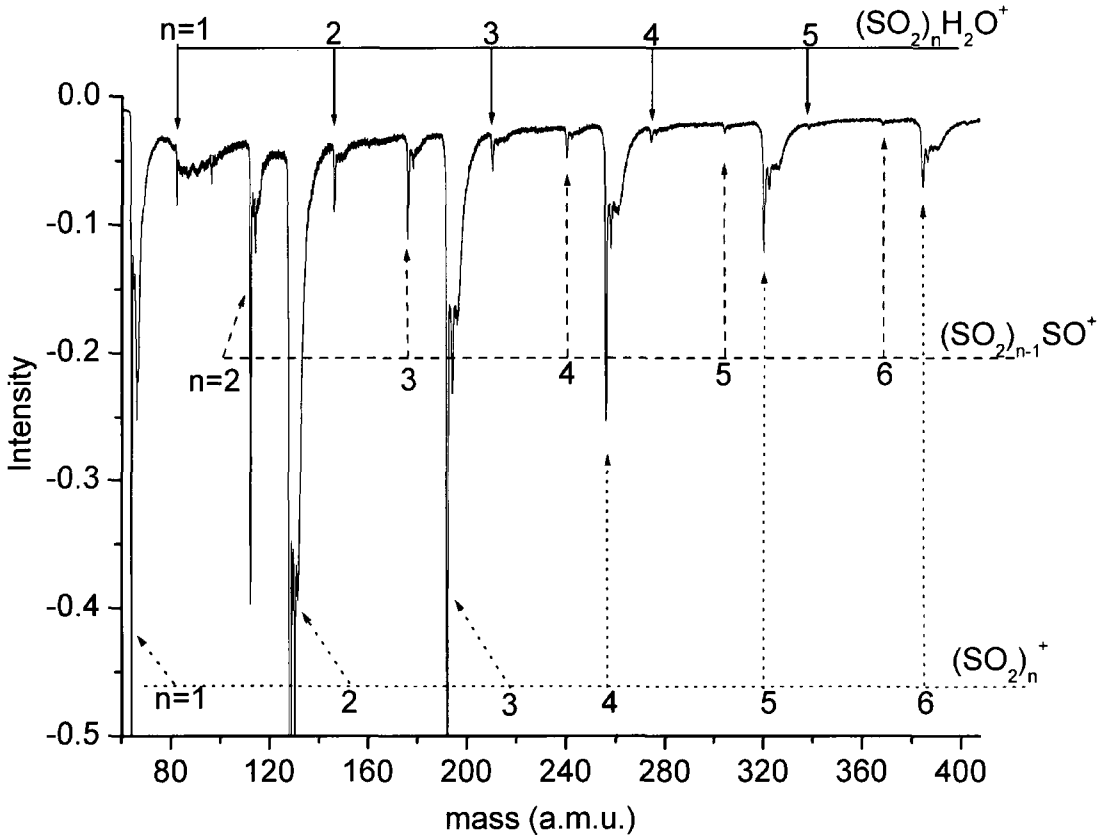


Figure 3.42: A high resolution spectrum of mixed SO_2-H_2O clusters generated by expansion of the mixed gas 20% SO_2/water vapor/He at 80 psi backing pressure. The cluster ions $(SO_2)_n^+$ dominate mass spectrum. Signal intensity of cluster ions $(SO_2)_n(H_2O)^+$ are about 5% of the intensity of the cluster ions $(SO_2)_n^+$ at n = 2, 3, 4.

3.4.3 Discussion

3.4.3.1 Distribution of $(SO_2)_n$ Clusters

Single photon, 26.5 eV ionization of water, methanol and ammonia clusters yields virtually no fragmentation of those species associated with the ionization, per se.[3.136] Although the 26.5 eV photon energy is initially absorbed by the neutral cluster, almost all the photon energy above the vertical ionization energy (VIE) of the cluster is removed by the ejected electron. The energy used by the cluster for metastable dissociation is either related to the difference between the VIE and (adiabatic) IE of the cluster or is derived from the heat of the proton transfer reaction. Thus, distribution of hydrogen bonded (or

proton transfer) clusters observed in those experiments are in good agreement with near threshold ionization experiments, such as single photon ionization by VUV resonance lamps (9.75 to 11.85 eV) and 10.5 eV VUV lasers.[3.140] In these experiments, the VIE is always greater than the energy required to drive a proton transfer reaction, and therefore protonated products are always observed. This process cannot be avoided, even using threshold ionization methods.

Sulfur dioxide clusters are bound by van der Waals interactions (dispersion) and are more weakly bound than hydrogen bonded clusters like water and methanol and even non hydrogen bonded clusters such as ammonia. As shown in Figure 3.36 the distribution of $(SO_2)_n^+$ clusters decreases roughly exponentially with increasing cluster size. $(SO_2)_n^+$ clusters dominate the mass spectrum of sulfur dioxide clusters and $(SO_2)_{n-1}SO^+$ cluster ions become very weak at n ~ 7. Multiphoton ionization of $(SO_2)_n$ by fs laser excitation shows much more extensive fragmentation, with $(SO_2)_{n-1}SO^+$ features being more intense than parent $(SO_2)_n^+$ features.[3.141-3.143] One advantage of fs vs. ns multiphoton ionization is that up pumping to the ion state typically precludes dissociation reactions for the neutral cluster during the ultrafast ionization process. Apparently single photon, even 26.5 eV, ionization imparts much less final energy ("excess energy") over that required for vertical ionization. Most $(SO_2)_n$ clusters are pumped to the ground state of the ion, and one observes that the $(SO_2)_n^+$ signal is dominant in the mass spectrum. In this case the energy required to drive the metastable reaction comes from the energy difference between the vertical and adiabatic energy levels. Very few $(SO_2)_n$ neutral clusters are excited to electronically excited states of the ion.[3.125,3.127] The few that are excited, $[(SO_2)_n^+]^*$, have sufficient excess energy above the VIE to facilitate the reaction $(SO_2)_n^+$

$\rightarrow (SO_2)_{n-1}SO^+ + O$; the ratios $I[SO_2SO^+]/I[(SO_2)_2^+]$ (Figure 3.37) depend on cluster size and decrease with increasing cluster size. In our previous $(H_2O)_n$ and $(CH_3OH)_n$ experiments,[3.136] the dissociation reactions of the monomer, are detected, such as, $H_2O \rightarrow OH^+ + H$ and $CH_3OH \rightarrow CH_3O^+ + H$; however, such dissociation does not occur for water or methanol clusters. For example, $(H_2O)_nOH^+$ and $(CH_3OH)_nCH_3O^+$ ion signals are not observed in the mass spectra. In the case of $(NH_3)_n$, molecular dissociation is observed for the dimer $(NH_3)_2$ only, which loses up to 5 H atoms. The different behavior of these clusters depends on specific characteristics of the cluster, such as photoabsorption cross section of the excited state of the cluster ion, which is sensitive to the cluster size and molecular properties.

We have measured the unimolecular (metastable) dissociation rate constants for reactions involving loss of one neutral molecule. These are 0.6 to 2.7 x 10^4 S^{-1} for water ($5 \leq n \leq 18$), 0.36 to 0.6 x 10^4 S^{-1} for methanol ($5 \leq n \leq 10$), and 0.8 to 2.0 x 10^4 S^{-1} for ammonia ($5 \leq n \leq 18$). In the present experiment, unimolecular dissociation rate constants for loss of one SO_2 molecule from $(SO_2)_n^+$ are 0.6 to 1.5 x 10^4 S^{-1} for cluster sizes $5 \leq n \leq 16$. Note that even though those clusters have a wide range of binding energies and structures, these rate constants are similar. One can extract two conclusions from these similar cluster kinetics: 1. $(SO_2)_n^+$ cluster ions do not acquire much excess energy above their VIE in single photon ionization in like manner to water, methanol and ammonia cluster ions; 2. cluster dynamics must be more related to cluster size, excess energy, degrees of freedom, densities of states, than detailed cluster structure and the approximate nature of the limiting potential interaction functions (e.g., dipole-dipole, hydrogen bonding, dispersion, etc.). The situation is actually rather complicated because the

hydrogen bonded clusters ($(H_2O)_n$ and $(CH_3OH)_n$) and donor/acceptor clusters ($(NH_3)_n$) employ the excess cluster energy (over IE) to drive the proton transfer reaction with $\Delta H < 0$, and fragment an OH, CH_3O, or NH_2 radical before undergoing metastable fragmentation of a consistent neutral molecule, while $(SO_2)_n$ clusters simply employ the VIE/IE energy difference for metastable fragmentation of SO_2.

Based on our results, we consider that most neutral sulfur dioxide clusters $(SO_2)_n$ are free of fragmentation directly following single photon ionization by the soft X-ray laser. This claim can be supported by three main observations. First, the peaks observed in the mass spectra are sharp and symmetrical, and thus fragmentation while the cluster is in the high field ionization region (< 1 μs) does not occur. Second, the loss of only one sulfur dioxide molecule is observed in the field free region after ionization. The metastable rate constants of the sulfur dioxide cluster ions are similar to those for water, ammonia, and methanol.[3.136] In ref. 3.136 many arguments are presented that support almost no fragmentation for these clusters. Similar rate constants indicate similar behavior of the clusters as they undergo ionization. Third, we observe unprotonated mixed water-sulfur dioxide clusters. This shows that during ionization, the amount of energy left in the mixed cluster is too small to drive a proton transfer reaction. This will be discussed in more detail in the following sections.

3.4.3.2 Effect of Cluster Size n on the Photodissociation of $(SO_2)_n$ Clusters

One can identify two distinct types of dissociation of the clusters following ionizaton: 1. metastable dissociation in which slow dissociation involves the breaking of a van der Waals bond between one molecule member of the cluster and the rest of the cluster; and 2. intramolecular dissociation of a cluster molecule followed by loss of a neutral atomic or

molecular radical (e.g., O, OH, NH_2, ...). In the first instance, the dissociation rate constant increases with cluster size (see Figure 3.39 and 3.41). In the second case, the rate constant for intramolecular fragmentation decreases with increasing cluster size (see Figure 3.37).

SO_2 and $(SO_2)_2$ have been studied at high resolution by photoionization spectroscopy in a molecular beam.[3.125] The IE (SO_2) = 12.35 eV and the appearance energy (AE) for the reaction $SO_2 + h\nu \rightarrow SO^+ + O + e^-$ is 15.953 eV, 3.6 eV above the ion ground state of SO_2^+. The 26.5 eV photon can access both of these processes. The IE $(SO_2)_2$ is 11.72 eV and the AE for SO_2SO^+ is 15.38 eV. At 65 nm (19.07 eV) excitation, the photoionization dissociation fraction $I[SO_2SO^+]/I[(SO_2)_2^+] \sim 0.08$ and $I[SO^+]/I[SO_2^+] \sim 0.56$. This suggests that the ionization energy and dynamics of photodissociation are different in the molecule and dimer. In our 46.9 nm (26.5 eV) excitation experiment $I[SO_2SO^+]/I[(SO_2)_2^+] \sim 0.23$ and $I[SO^+]/I[SO_2^+] \sim 1.1$. For larger clusters the dissociation fraction decreases rapidly with increasing n as reported in Figure 3.37. Under fs photodissociation and ionization, a sequential increase in lifetime associated with the SO_2 neutral E state is found and attributed to steric hindrance for the dissociation reaction.[3.127] Studies with CH_3I and H_2O have referred to a solvent cage effect for these cluster processes.[3.144-3.146]

A more general approach to these relaxation and dissociation phenomena in van der Waals clusters is through the concepts of intracluster vibrational redistribution of energy (IVR) and vibration predissociation (VP).[3.147-3.150] In this approach one need not assume or imagine a particular structure for the cluster (e.g., ion in its center, ion on the surface, etc.). The two processes IVR and VP are considered as serial phenomena in which energy

flows from the initial site of excitation following ionization to cluster modes and then the cluster can dissociate. IVR is enhanced by larger clusters (more density of states), while VP is retarded by a large density of states. For the case at hand, the 26.5 eV photon ionizes an SO_2 molecule in the cluster and the excess energy above VIE is removed by the photoelectron for most of the clusters (see Figure 3.37). The remaining energy above the IE of the cluster is redistributed to the cluster modes through IVR; this is apparently a small enough amount of energy such that VP is slow (~1-80 μs). In small clusters (e.g., $(SO_2)_2$) or the SO_2 monomer, the excess energy can stay in the excited molecule for hundreds of ps and local bond fragmentation (SO^+, SO_2SO^+, ...) can occur. In larger clusters, IVR is fast (ca. 1-10 ps) and molecular photodissociation VP would be generated, as observed.

3.4.3.3 Generation of Mixed $(SO_2)_n(H_2O)_m$ Clusters

The binding energies of van der Waals clusters can vary over a wide range, for example, 0.22 eV for $(H_2O)_2$ hydrogen bonded dimer[3.151,3.152] to 0.03 eV for the $(SO_2)_2$ dimer.[3.125] Thus water clusters are more stable and more easily formed than $(SO_2)_n$ clusters in a molecular beam. For the condition of low concentration of SO_2 (5% SO_2/He/water vapor) and low backing pressure of the expansion gas mixture, protonated water cluster ions dominate the mass spectrum, and only the $(SO_2)_2^+$ dimer ion is detected (Figure 3.40). The distribution of $(H_2O)_nH^+$ cluster ions generated in this beam condition is the same as that formed for a pure H_2O/He expansion. Two possible channels exist for the mixed SO_2/H_2O system to form $(H_2O)_nH^+$ in the expansion/ionization processes. First, they can be directly generated from the neutral water cluster

$$(H_2O)_n + h\nu \rightarrow \{(H_2O)_m^+\}^* + e^- \rightarrow (H_2O)_{n-1}H^+ + e^- + OH \qquad (3.38)$$

Second, they can be generated from a mixed cluster in a loss of one or more SO_2 molecules leading to the formation of protonated water clusters as,

$$(SO_2)_m(H_2O)_n + h\nu \rightarrow \{(SO_2)_m(H_2O)_n^+\}^* + e^- \rightarrow (H_2O)_{n-1}H^+ + OH + e^- + mSO_2\ (m\geq 1) \quad (3.39)$$

fs studies of these clusters suggest that the protonated water cluster ions $(H_2O)_nH^+$ are generated from $(SO_2)(H_2O)_n$ neutrals.[3.134,3.135,3.143] Nonetheless, results presented in the present work (Figure 3.41), lead to the conclusion that $(H_2O)_{n-1}H^+$ arise from $(H_2O)_n$ neutrals. If $SO_2(H_2O)_n$ neutral clusters were the parent of the $(H_2O)_{n-1}H^+$ cluster ion, then excess cluster energy in the ionization process would be removed from the ion by loss of SO_2 molecules as has been found for the $(H_2O)_nAr_m$ system. In this case both, $(H_2O)_n^+$ would be observed and different metastable fragmentation kinetics would be expected in the drift tube region. Neither is observed, and thus one concludes that the $(H_2O)_{n-1}H^+$ parent ions come from $(H_2O)_n$ neutrals. In a separate experiment on carbon dioxide-water clusters, the unprotonated cluster ions $(H_2O)_n^+$ are observed due to loss of several CO_2 molecules from the ionized clustered.[3.152] No unprotonated $(H_2O)_n^+$ cluster ions are observed for the SO_2/H_2O system presently under consideration.

Weak signal intensity is also observed for cluster ions $(SO_2)(H_2O)_nH^+$ as seen in Figure 3.40. Mixed SO_2/H_2O clusters containing more than one SO_2 moiety are not observed for the 5% SO_2/He low pressure expansion conditions that apply for this figure: SO_2 is not easily dissolved in water clusters. At high SO_2 concentrations in the beam and high expansion pressures (20% SO_2/H_2O/He, 80 psi), $(SO_2)_n^+$ is the dominant product (Figure 3.42). Signal intensity of the mixed cluster ion $(SO_2)_n(H_2O)^+$ is much weaker than that for the $(SO_2)_n^+$ cluster ion. The mixed cluster series containing only one H_2O

molecule, $(SO_2)_n(H_2O)^+$ is weakly observed. Thus $(SO_2)_n$ is not a good solvent for the water molecule.

3.4.3.4 Formation of Unprotonated $(SO_2)_nH_2O$ Clusters.

The photon absorption cross sections of H_2O and SO_2 are 18[3.154] and 12 x 10^{-18} cm^2,[3.155] respectively, at 26.5 eV photon energy. Both SO_2 (IE = 12.6 eV)[3] and H_2O (12.74 eV)[3.156] can function as the ionized molecular species in the cluster. Following ionization the charge can remain in either moiety and transfer between the two. The proton affinity of SO_2 and H_2O are 6.97 and 7.17 eV, respectively.[3.157] The proton affinity of water increases with increasing cluster size. For the mixed cluster $(SO_2)(H_2O)_n$ ($n \geq 2$), after ionization of H_2O, the charge will stay on one water molecule and a proton will transfer to another water molecule, generating the mixed cluster ions $(SO_2)(H_2O)_nH^+$ ($1 \leq n \leq 6$) observable in the mass spectrum for low pressure, 5% SO_2/H_2O/He expansions.

Theory and experiment give a stable $(H_2O)(SO_2)$ cluster with a binding energy of ca. 3.5 k cal/mol[3.132] and a planar SO_2 and H_2O stacked on each other in a non hydrogen bonded structure. The two molecular planes are at an angle of about 45° to one another.[3.130] Thus a barrier to proton transfer may well exist in the mixed dimer. fs ionization spectra show that the $(SO_2)H^+$ ion is detected from the ionization of the mixed neutral dimer $(SO_2)(H_2O)$.[3.134,3.135,3.143]

In the present experiment with 26.5 eV ionization, obvious signals of the unprotonated mixed dimer ion $(SO_2)(H_2O)^+$ (Figure 3.40), and mixed $(SO_2)_n(H_2O)^+$ ions $1 \leq n \leq 5$ (Figure 3.42) are observed. Two possible channels for $(SO_2)(H_2O)^+$ generation are:

Channel A: $(SO_2)(H_2O) + h\nu \rightarrow (SO_2)(H_2O)^+ + e^-$ (3.40)

Channel B: $(SO_2)_mH_2O + h\nu \rightarrow (SO_2)(H_2O)^+ + e^- + (m-1)\,SO_2$ (3.41)

$(SO_2)(H_2O)^+$ is generated directly from the mixed neutral cluster upon ionization in Channel A. $(SO_2)(H_2O)^+$ is generated from the mixed neutral cluster $(SO_2)_n(H_2O)$ in Channel B. Excess energy deposited in the cluster by the laser photon (energy above IE) is removed from the cluster by the loss of (m-1) SO_2 molecules in Channel B to generate $(SO_2)(H_2O)^+$. This behavior is observed in the study of water clusters in a 20% Ar/He expansion gas.[3.136] The signal intensity for $(H_2O)_2^+$ dimer ion is larger than that of the protonated H_3O^+ ion, generated in a He expansion by proton transfer and fragmentation of the $(H_2O)_2^+$ initial ion. Similar results obtained for $CO_2 \bullet H_2O$ clusters studied in our laboratory.[3.153] Nonetheless, no unprotonated water clusters are observed in either 5% or 20% SO_2/H_2O/He expansions at any backing pressure. As we have argued above that $(H_2O)_nH^+$ ions detected in mixed systems (5% SO_2/H_2O/He expansion) are not generated from $(SO_2)_m(H_2O)_n$ clusters by loss of SO_2 molecules. Thus we find that under our experimental conditions $(SO_2)(H_2O)^+$ is generated directly from $(SO_2)(H_2O)$.

The VIE for $(H_2O)_2$ is higher than the appearance potential of $H_3O^+ + OH$.[3.158] Thus the proton transfer reaction almost always occurs after ionization of the neutral water dimer. Protonated water clusters thereby dominate the mass spectrum for a pure H_2O/He expansion and only a very weak signal for $(H_2O)_2^+$ is observed with 26.5 eV single photon ionization.[3.143] Proton transfer can occur for the mixed dimer $(SO_2)(H_2O)$ after ionization as well, by the following reaction:

$$(SO_2)(H_2O) + h\nu \rightarrow \{(SO_2)(H_2O)^+\}^* \rightarrow SO_2H^+ + OH + e^- \quad (3.42)$$

The proton affinity of OH (5.74 eV) is clearly smaller than that of SO_2 (6.97 eV).[3.157] But the $SO_2 \bullet H_2O$ complex is a non-hydrogen bonded structure and more energy is probably required for the proton transfer reaction relative to the hydrogen bond $(H_2O)_2$ structure. In the present experiment, most if not all of the energy of the 26.5 eV ionization photon above the cluster VIE is removed by the exiting electron. Independent of the moiety in the mixed $(SO_2) \bullet (H_2O)$ dimer that is ionized, the charge probably remains on that species (for Franck-Condon reason) as the energy remaining in the cluster after ionization is insufficient to surmount the barrier to charge and proton transfer. Even as the proton affinity of the $(SO_2)_n$ moiety of the $(SO_2)_nH_2O$ cluster increases with increasing n, only unprotonated $(SO_2)_nH_2O^+$ clusters are detected (see Figure 3.42).

The mixed dimer $(SO_2)(H_2O)$ has an isomer H_2SO_3. Calculations indicate that the barrier to this isomerization is high (37 k cal/mol). Thermodynamics studies find an auto catalytic effect for the decomposition of H_2SO_3: this implies that additional water molecules can act as a catalyst to lower the reaction barrier for $H_2SO_3 \rightarrow SO_2 + H_2O$. In these experiments the mixed dimer is formed in the beam, but during the expansion process $(SO_2)(H_2O)$ does not have enough energy to convert to the H_2SO_3 molecule.

3.4.5 Conclusions

The van der Waals clusters $(SO_2)_n$ and $(SO_2)_m(H_2O)_n$ are investigated by 26.5 eV single photon ionization and TOFMS detection. The distribution of $(SO_2)_n$ clusters decreases roughly exponentially with increasing cluster size n. The loss of one SO_2 molecule from the cluster ion $(SO_2)_n^+$ is observed with a reflectron TOFMS. Metastable dissociation rate constants for $(SO_2)_n^+$ to yield $(SO_2)_{n-1}^+$ are in the range 0.6 to 1.5 x 10^4 s^{-1} for cluster sizes $5 \leq n \leq 16$. This is the same range as found for similar rate constants for

water, methanol, and ammonia cluster ions. A minor fragmentation path (loss of O atom) for the cluster ions is identified but this process is found to decrease with increasing cluster size.

Mixed $SO_2 \bullet H_2O$ clusters are studied under different cluster generation conditions and the predominant signals in the mass spectra are due to $(H_2O)_nH^+$ and $(SO_2)_n^+$ cluster ions as a function of conditions (concentration, expansion pressure). Mixed clusters of the form $(SO_2)(H_2O)_nH^+$ and $(SO_2)_nH_2O^+$ are also observed at low intensities. SO_2 and H_2O are not good solvents for one another. Unprotonated mixed cluster ions $(SO_2)_nH_2O^+$ $1 \leq n \leq 5$ are observed at high SO_2 concentration and $(SO_2)(H_2O)_nH^+$ are observed at low SO_2 concentration. Proton transfer between H_2O and SO_2 in mixed clusters has a high activation energy.

References

[3.1] D. D Nelson, Jr., G. T. Fraser, and W. Klemperer, Science, **238**, 1670 (1987).

[3.2] W. Klemperer, Science **257**, 887 (1992).

[3.3] R. G. Keesee, J. Geophys. Res. **94**, 14683 (1989).

[3.4] G. Nidener-Shatteburg and V. E. Bondybey, Chem. Rev. (Washington, D.C.) **100**, 4059 (2000).

[3.5] W. W. Duley, Astrophys. J. Lett. **471**, L57 (1996).

[3.6] A. Hansel, W. Singer, A. Wisthaler, M. Schwarzmann, and W. Lindinger, Int. J. Mass Spectrum. Ion Proc. **167/168**, 697 (1997).

[3.7] O. Echt, D. Kreisle, M. Knapp, and E. Recknagel, Chem. Phys. Lett. **108**, 401 (1984).

[3.8] U. Nagashima, H. Shinohara, N. Nishi, and H. Tanaka, J. Chem. Phys. **84**, 209 (1986).

[3.9] M. Okumura, L. I. Yeh, J. D. Myers, and Y. T. Lee, J. Phys. Chem. **94**, 3416 (1990).

[3.10] L. I. Yeh, M. Okumura, J. D. Myers, J. M. Price, and Y. T. Lee, J. Chem. Phys. **91**, 7319 (1989).

[3.11] Z. Shi, J. V. Ford, S. Wei, and A. W. Castleman, Jr., J. Chem. Phys. **99**, 8009 (1993).

[3.12] H. Shiromaru, N. Nishi, and N. Washida, J. Chem. Phys. **84**, 5561(1986).

[3.13] P. P. Radi, P. Beaud, D. Franzke, H.-M. Frey, T. Gerber, B. Mischler, and A.-P. Tzannis, J. Chem. Phys. **111**, 512 (1999).

[3.14] V. Hermann, B. D. Kay, and A. W. Castleman, Jr., Chem. Phys. **72**, 185(1982).

[3.15] X. Yang, X. Zhang and A. W. Castleman, Jr., Int. J. Mass Spectrom. Ion Processes **109**, 339 (1991).

[3.16] S. Wei, Z. Shi and A. W. Castleman, Jr., J. Chem. Phys. **94**, 3268 (1991).

[3.17] J. Stace and C. Moore, Chem. Phys. Lett. **96**, 80 (1983).

[3.18] S. K. Chowdhury and B. T. Chait, Anal. Chem. **63**, 1660 (1991).

[3.19] T. Schindler, C. Berg, G. Niedner-Schatteburg, and V. E. Bondybey, Chem. Phys. Lett. **250**, 301 (1996).

[3.20] H. Chang, C. Wu, and J.Kuo, International Reviews in Physical Chemistry **24**, 553 (2005).

[3.21] G. Vaidyanathan, M. T. Coolbaugh, W. R. Peifer, and J. F. Garvey, J. Chem. Phys. **94**, 1850 (1991).

[3.22] M. S. EI-Shall, C. Marks, L. W. Sieck, and M. Meot-Ner, J. Phys. Chem. **96**, 2045(1992).

[3.23] S. Morgan, R. G. Keesee, and A. W. Castleman, Jr, J. Am. Chem. Soc. **111**, 3841 (1989).

[3.24] S. Morgan and A. W. Castleman, Jr, J. Am. Chem. Soc. **109**, 2867 (1987).

[3.25] S. Morgan and A. W. Castleman, Jr, J. Phys. Chem. **93**, 4544 (1989).

[3.26] H. Fu, Y. J. Hu, and E. R. Bernstein, J. Chem. Phys. **124**, 024302 (2006).

[3.27] Y. J. Shi, S. Consta, A. K. Das, B. Mallik, D. Lacey, and R. H. Lipson, J. Chem. Phys. **116**, 6990 (2002).

[3.28] S. T. Ceyer, P. W. Tiedemann, B. H. Mahan, and Y. T. Lee, J. Chem. Phys. **70**, 14(1979).

[3.29] C. Y. Ng, D. J. Trevor, P. W. Tiedemann, S. T. Ceyer, P. L. Kronebusch, B. H. Mahan, and Y. T. Lee, J. Chem. Phys. **67**, 4235 (1977).

[3.30] J. A. Odutola, T. R. Dyke, B. J Howard, and Muenter, J. Chem. Phys. **70**, 4884 (1979)

[3.31] K. Stephan, J. H. Futrell, K. I. Peterson, A. N. Castleman, Jr., H. E.Wagner, N. Djuric, and T. D. Mark, Int. J. Mass Spectrom. Ion Phys. **44**, 167 (1982).

[3.32] S. Wei and A. W. Castleman, Jr, Int. J. Mass Spectrom. Ion Process **131**, 133 (1994).

[3.33] H. Shinohara and N. Nishi, Chem. Phys. Letts. **87**, 561 (1982).

[3.34] D. A. Card, D. E. Folmer, S. A. Buzza, and A. W. Castleman, Jr, J. Phys. Chem. A **101**, 3417 (1997).

[3.35] S. A. Buzza, S. Wei, J. Purnell, and A. W. Castleman, Jr., J. Chem. Phys. **102**, 4832 (1995).

[3.36] H. Shinohara and N. Nishi, J. Chem. Phys. **83**, 1939 (1985).

[3.37] D. N. Shin, Y. Matsuda, and E. R. Bernstein, J. Chem. Phys. **120**, 4150 (2004).

[3.38] Y. Matsuda and E. R. Bernstein, J. Phys. Chem. A **109**, 3803 (2005).

[3.39] S. Tomoda and K. Kimura, Chem. Phys. Lett. 102, 560 (1983).

[3.40] (a) S. Heinbuch, M. Grisham, D. Martz, and J. J. Rocca, Optics Express 13, 4050 (2005). (b) J.J. Rocca, V. N. Shlyaptsev, F.G.Tomasel, O.D.Cortazar, D. Hartshorn, J.L.A. Chilla, Physical Review Letters 73, 2192 (1994). (c) J.J. Rocca, Review Scientific Instruments 70, 3799 (1999).

[3.41] Yu. A. Uspenskii, V. E. Levashov, A. Vinogradov, A. I. Fedorenko, V. V. Kondratenko, Yu. P. Pershin, E. N. Zubarev, and V. Yu. Fedotov, Optics Letters **23**, 771 (1998).

[3.42] M. W. Jurema, K. N. Kirschner, and G. C. Shields, J. Comput. Chem. **14**, 1326 (1993).

[3.43] K. Laasonen and M. L. Klein, J. Phys. Chem. **98**, 10079 (1994).

[3.44] M. Svanberg and J. B. C. Pettersson, J. Phys. Chem. A **102**, 1865 (1998).

[3.45] I. Kusaka and D. W. Oxtoby, J. Chem. Phys. **113**, 10100 (2000).

[3.46] M. P. Hodges and D. J. Wales, Chem. Phys. Lett. **324**, 279 (2000).

[3.47] H. Shiromaru, H. Shinohara, N. Washida, H. S.Yoo, and K. Kimura, Chem. Phys. Letts. **144**, 7 (1987).

[3.48] O. Echt, P. P. S. Morgan, and A. W. Castleman, Jr., J. Chem. Phys. 82, 4076, (1985).

[3.49] S. Wei, W. B. Tzeng, and A. W Castleman, Jr, J. Chem. Phys. **93**, 2506 (1990).

[3.50] W. B. Tzeng, S. Wei, and A. W. Castleman, Jr., J. Am. Chem. Soc. 111, 6035 (1985).

[3.51] P. J. Robinson and K. A. Holbrook, Unimolecular Reaction, Wiley Interscience, New York, P53 (1971).

[3.52] S. Wei, K. Kilgore, W. B. Tzeng, and A. W. Castleman, Jr, J. Phys. Chem. **95**, 8306 (1991).

[3.53] J. T. Su, X. Xu, and W. A. Goddard III, J. Phys. Chem. A **108**, 10518 (2004).

[3.54] I. P. Buffey and W. B. Brown, Chem. Phys. Lett. **109**, 59 (1984).

[3.55] T. D. Fridgen, J. D. Keller, and T. B. McMahon, J. Phys. Chem. A **105**, 3816 (2001).

[3.56] E. P. Grimsrud and P. Kebarle, J. Am. Soc. **95**, 7939 (1973).

[3.57] U. Buck, J. G. Siebers, and R. J. Wheatley, J. Chem. Phys. **108**, 20 (1998).

[3.58] K. D. Cook, G. G. Jones, and J. W. Taylor, Int. J. Mass Spectrom. Ion Phys. **35**, 273 (1980).

[3.59] W. R. Peifer, M. T. Coolbaugh, and J. F. Garvey, J. Chem. Phys. 91, 6684 (1989).

[3.60] J. E. McCulloh, Int. J. Mass Spectrom. Ion Phys. **21**, 33 (1976).

[3.61] R. I. Reed and W. Snedden, J. Chem. Soc. (**DCE**) 4132 (1959).

[3.62] M. Farber and F. Huisken, J. Chem. Phys. **104**, 4865 (1996).

[3.63] T. A. Beu and U. Buck, J Chem. Phys. **114**, 7848 (2001).

[3.64] S. Wei, W. B. Tzeng, and A. W. Castleman, Jr, J. Chem. Phys. **92**, 332 (1990).

[3.65] H. Shinohara, N. Nishi, and N. Washida, J. Chem. Phys. **83**, 1939 (1985).

[3.66] T. Shimanouchi, Tables of Molecular Vibrational Frequencies Consolidated Volume **I**, National Bureau of Standards, 1-160 (1972).

[3.67] M. Farber and F. Huisken, J. Chem. Phys. **104**, 4865 (1996).

[3.68] S.D. Rodgers and S. Charnley, Mon. Nat. R. Astron. Soc., **320**, L61 (2001).

[3.69] I. Martin, T. Skalicky, J. Langer, H. Abdoul-Carime, G. Karwasz, E. Illengerger, M. Stano, and S. Matejcik, Phys. Chem. Chem. Phys., **7**, 2212 (2005).

[3.70] F. Dong, S. Heinbuch, J.J. Rocca, and E.R. Bernstein, J. Chem. Phys., **124**, 224319 (2006).

[3.71] F. Dong, S. Heinbuch, J.J. Rocca, and E.R. Bernstein, J. Chem. Phys., **125**, 154317 (2006).

[3.72] S. Heinbuch, F. Dong, J.J. Rocca, and E.R. Bernstein, J. Chem. Phys., **125**, 154316 (2006).

[3.73] F. Dong, S. Heinbuch, J.J. Rocca, and E.R. Bernstein, J. Chem. Phys., **125**, 164318 (2006).

[3.74] W.Y. Feng and C. Lifshitz, J. Phys. Chem., **98**, 6075 (1994).

[3.75] C. Lifshitz and W.Y. Feng, Int. J. Mass Spectrom. Ion Processes, **146**, 223 (1995).

[3.76] R. Zhang and C. Lifshitz, J. Phys. Chem., **100**, 960 (1996).

[3.77] Y. Inokuchi and N. Nishi, J. Phys. Chem., **107**, 11319 (2003).

[3.78] V. Aviyente, R. Zhang, T. Varnali, and C. Lifshitz, Int. J. Mass. Spectrom. Ion Processes, **161**, 123 (1997).

[3.79] Y. Inokuchi and N. Nishi, J. Phys. Chem. A, **106**, 4529 (2002).

[3.80] S. Heinbuch, M. Grisham, D. Martz, and J. J. Rocca, Opt. Express **13**, 4050 (2005).

[3.81] J.J. Rocca, V.N. Shlyaptsev, F.G. Tomasel, O.D. Cortazar, D. Hartshorn, and J.L.A. Chilla, , Phys. Rev. Lett. **73**, 2192, (1994).

[3.82] B.R. Benware, C.D. Macchietto, C.H. Moreno, and J.J. Rocca, Physical Review Letters **81**, 5804, (1998).

[3.83] (a) H. Su, Y. He, F. Kong, W. H. Fang, and R. Z. Liu, J. Chem. Phys., **113**, 1891, 2000; (b) R. S. Irwin, D. L. Singleton, C. Paraskevopoulos, and R. Mclaren, Int. J. Chem. Kinet. **26**, 219, 1994. (c), T. Ebata, T. Amano, and M. Ito, J. Chem. Phys.

90, 112, 1989. (d), L. Khriachtchew, E. Macoas, and M. Rasanen, J. Am. Chem. Soc. **124**, 10994, 2002.

[3.84] J. S. Francisco, J. Chem. Phys. **96**, 1167, 1992.

[3.85] A. Allouche, J. Chem. Phys., **122**, 234703 (2005).

[3.86] A.K Roy and A. J. Thakkar, Chem. Phys. Lett., **386**, 162 (2004).

[3.87] Y. Zhao and D.G. Truhlar, J. Phys. Chem. A, **109**, 6624 (2005).

[3.88] A.K Roy and A. J. Thakkar, Chem. Phys., **312**, 119 (2005).

[3.89] Y. J.Hu, H. B. Fu, and E. R. Bernstein, J. Chem. Phys. **125**, 184308, 2006.

[3.90] A. Karpfen and A.J. Thakkar, J. Chem. Phys., **124**, 224313 (2006).

[3.91] (a) J. Karle and L.O. Brockway, J. Am. Chem. Soc., **66**, 574 (1944); (b) A. Almenningen, O. Bastiansen, and T. Motzfeldt, Acta Chem, Scand., **23**, 2848 (1969); (c) A. Almenningen, O. Bastiansen, and T. Motzfeldt, Acta Chem, Scand., **24**, 747 (1970).

[3.92] (a) Rossby, C.-G. (1959). "Current Problems in Meteorology." In *The Atmosphere and the Sea in Motion*, edited by Bert Bolin, pp. 9-50. New York: Rockefeller Institute Press. (b) Wilson, Carroll L., and William H. Matthews, Eds. (1971). *Inadvertent Climate Modification. Report of Conference, Study of Man's Impact on Climate (SMIC), Stockholm.* Cambridge, MA: MIT Press.

[3.93] H. Falter, O.F. Hagena, W. Henkes, and H.V. Wedel, Int. J. Mass Spectrom. Ion Phys. **4**, 145 (1970).

[3.94] O.F. Hagena, Entropie **42**, 42 (1971).

[3.95] K. Stephan, J. H. Futrell, K. I. Peterson, A.W. Castleman, Jr., and T. D. Mark, J. Chem. Phys. **77**, 2408 (1982).

[3.96] G. Jones, and J. Taylor, J. Chem. Phys. **68**, 1768 (1978).

[3.97] S.H. Linn, and C.Y. Ng, J. Chem. Phys. **75**, 4921 (1981). (b) L. Wang, J. E. Reutt, Y. T. Lee, and D. A. Shirley, J. Electron Spectrosc. Relat. Phenon., **47**, 167 (1988).

[3.98] G. Torchet, H. Bouchier, J. Farges, M.F. de Feraudy, and B. Raoult, J. Chem. Phys. **81**, 2137 (1984).

[3.99] J.A. Barnes and T.E. Gough, J. Chem. Phys. **86**, 6012 (1987).

[3.100] G. Torchet, M.F. de Feraudy, A. Boutin, and A.H. Fuchs, J. Chem. Phys. **105**, 3671 (1996).

[3.101] G. Cardini, V. Schettino, and M.L. Klein, J. Chem. Phys. **90**, 4441 (1989).

[3.102] A. Bonnamy, R. Georges, A. Benidar, J. Boissoles, A. Canosa, and B.R. Rowe, J. Chem. Phys. **118**, 3612 (2003).

[3.103] M.A. Ovchinnikov and C.A. Wight, J. Chem. Phys. **100**, 972 (1994).

[3.104] T.E. Gough and T.Y. Wang, J. Chem. Phys. **105**, 4899 (1996).

[3.105] J.L. Foster, A.C. Chang, D.K. Hall, W.P. Wergin, E.F. Erbe, and J. Barton, J. Geophys. Res. Planets **103**, 25839 (1998).

[3.106] G. Romanowski, and K.P. Wanczek, Int. J. Mass Spectrom. Ion Processes **95**, 223 (1989).

[3.107] J. Dabek, and L. Michalak, Vacuum **63**, 555 (2001).

[3.108] G. Romanowski, and K.P. Wanczek, Int. J. Mass Spectrom. Ion Processes **62**, 277 (1984).

[3.109] G. Romanowski, and K.P. Wanczek, Int. J. Mass Spectrom. Ion Processes **70**, 247 (1986).

[3.110] Y. Negishi, T. Nagata, and T. Tsukuda, Chem. Phys. Lett. **364**, 127 (2002).

[3.111] L.W. Sieck, and R. Gorden, Jr., J. Res. Nat. Bur. Stand.:-A Phys. Chem. **78A**, 315 (1974).

[3.112] J.H. Futrell, K. Stephan, and T.D. Mark, J. Chem. Phys. **76**, 5893 (1982).

[3.113] P.A. Block, M.D. Marshall, L.G. Petersen, and R.E. Miller, J. Chem. Phys. **96**, 7321 (1992).

[3.114] J. Sadlej, J. Makarewicz, and G. Chalasinski, J. Chem. Phys. **109**, 3919 (1998).

[3.115] A. Khan, J. Molec. Struc. **665**, 237 (2003).

[3.116] F. Dong, S. Heinbuch, J.J. Rocca, and E.R. Bernstein, J. Chem. Phys. **124**, 224319 (2006).

[3.117] F. Dong, S. Heinbuch, J.J. Rocca, and E.R. Bernstein, J. Chem. Phys. submitted.

[3.118] S. Heinbuch, M. Grisham, D. Martz, and J. J. Rocca, Optics Express **13**, 4050 (2005).

[3.119] A.J. Illies, M.L. McKee, and H.B. Schlegel, J. Phys. Chem. **91**, 3489 (1987).

[3.120] J. T. Su, X. Xu, and W. A. Goddard III, J. Phys. Chem. A **108**, 10518 (2004).

[3.121] N. Wainfan, W. C. Walker, and G. L. Weissler, Phys. Rev. **99**, 542 (1955).

[3.122]H. Shiromaru, N. Nishi, and N. Washida, J. Chem. Phys. **84**, 5561(1986).

[3.123]F. Y. Leung, A. J. Colussi, and M. R. Hoffmann, J. Phys. Chem. A **105**. 8073 (2001).

[3.124]J. J. Margitan, J. Phys. Chem. A **101**, 9778 (1997).

[3.125]J. Erickson and C. Y. Ng, J. Chem. Phys. **75**, 1650 (1981).

[3.126]A. Taleb-Bendiab, K.W. Hilling II, and R. L. Kuczkowski, J. Chem. Phys. **94**, 6956 (1991).

[3.127]K. L. Knappenberger, Jr and A. W. Castleman, Jr, J. Chem. Phys. **121**, 3540 (2004).

[3.128]A. F. Voegele, C. S. Tautermann, C. Rauch, T. Loerting, and K. R. Liedl, J. Phys. Chem. A **108**, 3859 (2004).

[3.129]W. K. Li, M. L. Mckee, J. Phys. Chem. A **101**, 9778 (1997).

[3.130]K. Matsumura, K. J. Lovas, and R. D. Suenram, J. Chem. Phys. **91**, 5887 (1989).

[3.131]A. Schriver, L. Schriver, J. P. Perchard, Journal of molecular spectroscopy **127**, 125 (1988).

[3.132]W. K. Li and M. L. Mckee, J. Phys. Chem. A **101**, 9778 (1997).

[3.133]E. Bishenden and D. J. Donaldson, J. Phys. Chem. A **102**, 4638 (1998).

[3.134]K. L. Knappenberger, Jr and A. W. Castleman, Jr, J. Chem. Phys. **122**, 154306 (2005).

[3.135]T. E. Dermota, D. P. Hydutsky, N. J. Bianco, and A. W. Castleman, Jr. J. Phys. Chem. A **109**, 8254 (2005).

[3.136]F. Dong, S. Heinbuch, J. J. Rocca, E. R. Bernstein, J. Chem. Phys. **124**, 224319 (2006).

[3.137] S. Heinbuch, M. Grisham, D. Martz, and J. J. Rocca, Optics Express **13**, 4050 (2005).

[3.138] http://rmjordan.com/resources/Tutorial.pdf

[3.139] S. Wei, W. B. Tzeng, and A. W. Castleman, Jr. J. Chem. Phys. **92**, 332 (1990).

[3.140] (a) H. Shiromaru, N. Nishi, and N. Washida, J. Chem. Phys. **84**, 5561 (1986). (b) H. Shinohara and N. Nishi, J. Chem. Phys. **83**, 1939 (1985). (c) H. Fu, Y. J. Hu, and E. R. Bernstein, J. Chem. Phys. **124**, 024302 (2006).

[3.141] S. M. Hurley, T. E. Dermota, D. P. Hydutsky, and A. W. Castleman, Jr. J. Phys. Chem. A, **107**, 3497 (2003).

[3.142] T. E. Dermota, D. P. Hydutsky, N. J. Bianco, and A. W. Castleman, Jr. J. Phys. Chem. A, **109**, 8259 (2005).

[3.143] Q. Zhong, S. M. Hurley, and A. W. Castleman, Jr. Int. J. Mass Spectrom. Ion Process **185/186/187**, 905 (1999).

[3.144] D. J. Donaldson, V. Vaida, and R. Naaman, J. Phys. Chem. **92**, 1204 (1988).

[3.145] D. J. Donaldson, V. Vaida, and R. Naaman, J. Phys. Chem. **87**, 2522 (1987).

[3.146] A. Kanaev, L. Museur, F. Edery, T. Laarmann, and T. Möller, J. Chem. Phys. **117**, 9423 (2002).

[3.147] M. F. Hineman. E. R. Berstein, and D. F. Kelley, J. Chem. Phys. **94**, 2516, (1993).

[3.148] M. F. Hineman. S. K. Kim, E. R. Berstein, and D. F. Kelley, J. Chem. Phys. **92**, 4904, (1991).

[3.149] J. Yao, J. A. Fernandez, and E. R. Bernstein, J. Chem. Phys. **107**, 8813, (1997).

[3.150] P. M. Felker and A. H. Zewail, Adv. Chem. Phys. **70**, 265 (1988).

[3.151] T. S. Julius, X Xin, and A. G. William, J. Phys. Chem. A, **108**, 10518 (2004).

[3.152]I. P. Buffey and W.B. Brown, Chem. Phys. Letts. **109**, 59 (1984).

[3.153]S. Heinbuch, F. Dong, J. J. Rocca, E. R. Bernstein, J. Chem. Phys. To be submitted.

[3.154]G. N. Haddad and J. A. R. Samson, J. Chem. Phys. **84**, 6623 (1986).

[3.155]H. Hamdy, Z. X. He, and J. A. R. Samson, J. Phys. B: At. Mol. Phys. **24**, 4803 (1991).

[3.156]L. Karlsson, L. Mattsson, R. Jadrny, R. G. Albridge, S. Pinchas, T. Bergmark, K. Siegbahn, J. Chem. Phys. **62**, 4745 (1975).

[3.157]CRC Handbook of Chemistry and Physics, 81st ed., edited by D. R. Lide (CRC Press, Boca Raton, FL, 2000-2001).

[3.158]H. Shiromaru, H. Shinohara, and N. Washida, Chem. Phys. Lett. **41**, 7 (1987).

Chapter 4

Metal Oxide Clusters

4.1 FORMATION AND DISTRIBUTION OF NEUTRAL VANADIUM, NIOBIUM, AND TANTALUM OXIDE CLUSTERS: SINGLE PHOTON IONIZATION AT 26.5 eV

Transition metals, as well as their oxides, carbides, nitrides, and sulfides, are unique in their abilities to catalyze chemical reactions, primarily due to their multiplicity of low energy surface electronic states, which can readily donate and/or accept electrons in the process of making or breaking bonds at a surface.[4.1] Transition metal oxides are employed extensively as catalysts in the chemical industry, for example, vanadium oxide catalysts are used in the generation of sulfuric acid.[4.2] The microscopic properties of specific local catalytic sites and the mechanisms for catalytic activity of these metal oxide catalysts are still not elucidated. Catalytic properties of a material (activity, selectivity, and stability) are in general determined by chemical (electronic) properties of surface atoms/molecules.[4.3,4.4] Metal/metal oxide clusters generated in the gas phase are considered to be an ideal model system for the local surface of the condensed/surface phase because of their relatively well defined structures, size dependent properties, and their relative ease of accessibility by theory. To explore the reactivity and behavior of

metal and metal oxide clusters, one must first understand their neutral cluster distributions, growth patterns and pathways, structures, and electronic properties.

Neutral metal oxide clusters tend to have high ionization energies ($8 \leq IE \leq 10$ or more eV) especially for oxygen rich clusters for which most of the metal electrons are involved in bonding interactions. Due to this high ionization energy, the clusters require multiphoton absorption in order to be detected by mass spectroscopy techniques. Even multiphoton ionization is typically thought to be more gentle than electron ionization. Multiphoton absorption by clusters is often difficult to control due to the neutral or ionic cluster ability to absorb many photons. Neutral clusters can thereby ionize at high, superexcited, unrelaxed electronic states or by thermionic emission through rapid electronic relaxation and heating of the neutral cluster. In either event cluster fragmentation, and thus loss of neutral cluster distribution information, is often the end result.[4.5,4.6] On the other hand, single photon near threshold ionization at low laser fluence, yields little fragmentation and thus maximum neutral cluster information.[4.7]

Recently, mass selected metal oxide cations of vanadium, niobium, and tantalum have been studied with regard to their photodissociation properties. In order to determine the most stable cations of metal oxide clusters, selected cluster cations are exposed to 532 nm and 355 nm laser radiation and undergo multiphoton (resonant?) absorption.[4.8] Cluster cation distributions are similar for these three metal oxides. The most stable cluster cations are of the formulas MO_2^+, $M_2O_4^+$, $M_3O_7^+$, $M_4O_9^+$, $M_5O_{12}^+$, $M_6O_{14}^+$, and $M_7O_{17}^+$ (i.e., general formula $(MO_2)_x(M_2O_5)_y^+$). Collision induced dissociation of

vanadium oxide cluster cations[4.9a] and anions[4.9b] and niobium oxide[4.10] cations have also been studied. The most stable cluster ions with high dissociation energies are identified as $V_2O_4^+$, $V_3O_6^+$,7, $V_4O_8^+$,9, $V_5O^+_{11,12}$, and $V_6O^+_{13,14}$ for the vanadium cluster ion system, and $Nb_3O_7^+$, $Nb_4O_{9,10}^+$ and $Nb_5O_{12}^+$ for the niobium cluster cation system. The distribution of metal oxide ions is somewhat different than that of the neutral clusters, however. Vanadium oxide neutral clusters have been ionized by single photon absorption of near ionization threshold photon energy (10.5 eV, 118 nm).[4.11] A potential question about this ionization technique for determination of neutral cluster distributions is, of course, whether 10.5 eV is sufficient energy to ionize all, even oxygen rich neutral species. VUV photoionization at 118 nm has the best chance to ionize clusters without fragmentation and thus to be able to detect the most abundant neutral clusters found in a molecular beam. Employing 118 nm ionization and saturated oxygen growth conditions, the most abundant neutral clusters are assigned to the form $(VO_2)_x(V_2O_5)_y$. Cluster rotational and vibrational temperatures for VO_2 are determined to be 50 and 700 K, respectively. Nonetheless, species such as VO_3, VO_4, V_2O_6 have ionization energies higher than 10.5 eV[4.11] and are not detected in these experiments.

A new table top, 26.5 eV/photon, 46.9 nm extreme ultraviolet (EUV), soft X-ray laser is employed in the present study to ensure that all species in the neutral cluster metal and metal oxide distributions are detected. As we will demonstrate, the EUV laser not only ionizes all species in these experiments, but it is a very gentle ionization source that does not fragment, even metastable, slow fragmentation, any of the clusters of interest. In

the present experiment, neutral metal oxide clusters of vanadium, niobium, and tantalum are studied by single photon ionization at 26.5 eV. The neutral cluster distributions, generated under saturated oxygen conditions for metal oxide cluster growth, are determined for these three metals. The most stable neutral metal oxide clusters are determined. The structure and formation of these clusters are discussed in detail. Oxygen rich neutral clusters are detected for the first time and are found to have up to three attached hydrogen atoms.

4.2 EXPERIMENTAL PROCEDURES

Since the experimental apparatus has been described in detail elsewhere,[4.12] only a general outline of the experimental scheme will be presented in this report. Briefly, vanadium, niobium, and tantalum oxide neutral clusters are generated in a conventional laser vaporization/supersonic expansion cluster source by laser ablation of vanadium, niobium, or tantalum metal foil into a carrier gas mixed with 5% O_2 at 80 psig. Pure metal clusters can also be generated by laser ablation of the metal into a pure He (99.995%) expansion gas. A 532 nm wavelength laser (second harmonic of a Nd/YAG laser, 1064 nm) is employed to ablate the metals at 5 to 10 mJ/pulse. Ions created in the metal ablation/metal oxide growth process are removed from the supersonic expansion by an electric field outside the nozzle in the vacuum system. Neutral clusters pass through a skimmer with a 4 mm aperture into the ionization region of a time of flight mass spectrometer (Wiley-McLaren design, R.M. Jordan Co.). The clusters are ionized by three different nanosecond pulsed lasers: 193 nm (ArF), 118 nm (ninth harmonic of a seeded

Nd/YAG 1064 nm laser), and a 46.9 nm EUV soft X-ray laser.

The X-ray laser (26.5 eV/photon energy) emits pulses of about 1 ns duration with an energy/pulse of 10 μJ at a repetition rate of up to 12 Hz. A time of flight (linear/reflectron) mass spectrometer (TOFMS) is employed for mass analyzer.[4.12] A pair of mirrors placed in a Z-fold configuration just before the ionization region of the TOFMS provides alignment and focusing capabilities for the laser with respect to the molecular cluster beam at the focus of the TOFMS in the ionization region. The Z-fold mirror system has a transmissivity of about 10%. Since the 26.5 eV photons from the EUV laser are able to ionize the He carrier gas employed in the expansion, the microchannel plate (MCP) ion detector voltage is gated to reduce the gain of the MCP when He^+ arrives at the mass detector in order to prevent detector circuit overload and saturation.

4.3 RESULTS

Figure 4.1 displays a linear time of flight (TOF) mass spectrum of tantalum metal clusters (Ta_m) generated with a pure He expansion. These spectra are identical to those obtained with the TOFMS operated in reflectron mode. In the bottom spectrum, the neutral clusters are ionized through an unfocused 193 nm laser beam at a fluence of 100 $\mu J/cm^2$; the possibility of multiphoton processes from these photons is quite small. The ionization energy (IE) of Ta atom is 7.9 eV.[4.13] The vertical IE (VIE) for Ta_m clusters decreases with increasing cluster size and is measured ca. 5-6 eV for cluster sizes m=3 to 10.[4.14] Thus the single 193 nm (6.4 eV) photon has sufficient energy to ionize neutral Ta_m clusters but not enough energy to ionize the Ta atom in its ground electronic state. Thus

Ta_m ($m \geq 2$) cluster ions are observed in this experiment, and the small Ta^+ signal is detected due to

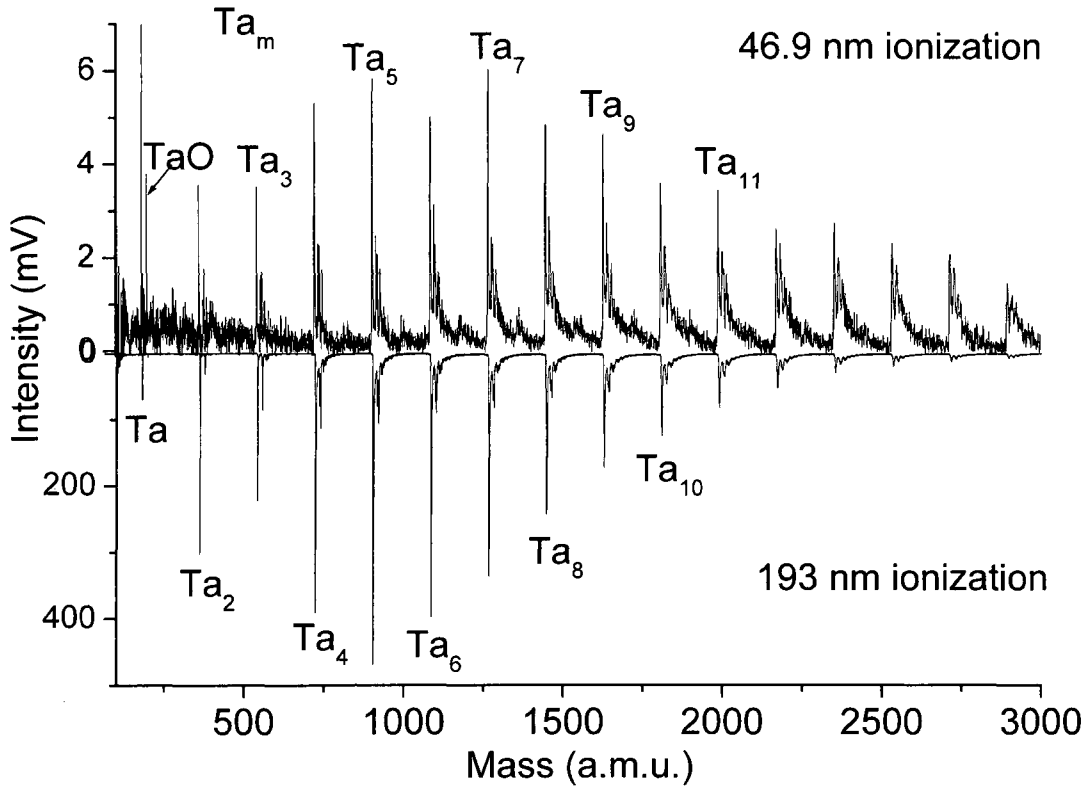


Figure 4.1: Linear TOF mass spectrum of pure tantalum metal cluster ionized by 26.5 eV laser (upper) and 193 nm laser (lower), respectively. Sharp features to the high mass side of each Ta_m peak are due to Ta_mO_x and Ta_mC_y clusters generated by impurities in the gas, vacuum and metal surfaces and bulk. Exactly the same spectra arise for reflectron mode operation of the TOFMS. Metastable (slow) fragmentation does not occur from either 193 or 46.9 nm single photon ionization.

either hot Ta atoms or a weak multiphoton component to the ionization. The upper spectrum is obtained for the same Ta_m sample employing the 26.5 eV/photon soft X-ray laser for ionization. The cluster distribution obtained through the two different single photon ionization sources is nearly identical as shown in Figure 4.1. The minor differences in peak intensities for Ta_m $m \geq 2$ are probably due to small ionization cross section differences at the different laser wavelengths. Clearly Ta and TaO species have

low cross sections for ionization at 193 nm but considerable cross sections at 46.9 nm. The pulse energy at 46.9 nm is below 1 μJ, and thus for both lasers, only single photon ionization need be considered. The bond energy of Ta_m is measured to be ca. 5 – 7 eV,[4.14-4.16] and a single photon of 6.4 eV is not energetic enough to both ionize and fragment a Ta_m cluster. In other words, the cluster ion distribution Ta_n^+ $n \geq 2$ reflects quite accurately (cross section issues aside) the neutral cluster distribution and clearly shows the 26.5 eV distribution. The 26.5 eV distribution of Ta_n^+ $n \geq 1$ reflects the total distribution of species in the supersonic expansion beam (again, cross section issues aside). Since both distributions are so similar, cross section differences as a function of wavelength must be not terribly important here. The photoelectron must remove nearly 20 eV of excess energy as it exits the cluster to avoid fragmentation of the cluster through 26.5 eV ionization. Recall that even metastable fragmentation is eliminated by the reflectron spectrum (not shown). Study of the photoelectron spectra at 26.5 eV photon energy for these metal clusters would certainly prove interesting and informative. Thus 26.5 eV causes little or no fragmentation in ionizing transition metal clusters, in general.

Figure 4.2 TOF mass spectra of Ta_mO_n clusters generated with 5% O_2/He expansion using three different wavelengths for ionization. In Figure 4.2a, only Ta^+, TaO^+, and TaO_2^+ are observed for ionization with 193 nm laser radiation. The VIE of TaO and TaO_2 is about 8 and 9 eV,[4.17,4.18] respectively. These ion signals must be generated through multiphoton ionization. The absence of larger clusters in this mass spectrum implies a great deal of fragmentation during the multiphoton ionization process(es). The large

intensities in the TaO^+ and TaO_2^+ mass channels must come from the fragmentation of large clusters. The mechanism for these fragmentations will be described in the next section. The power of

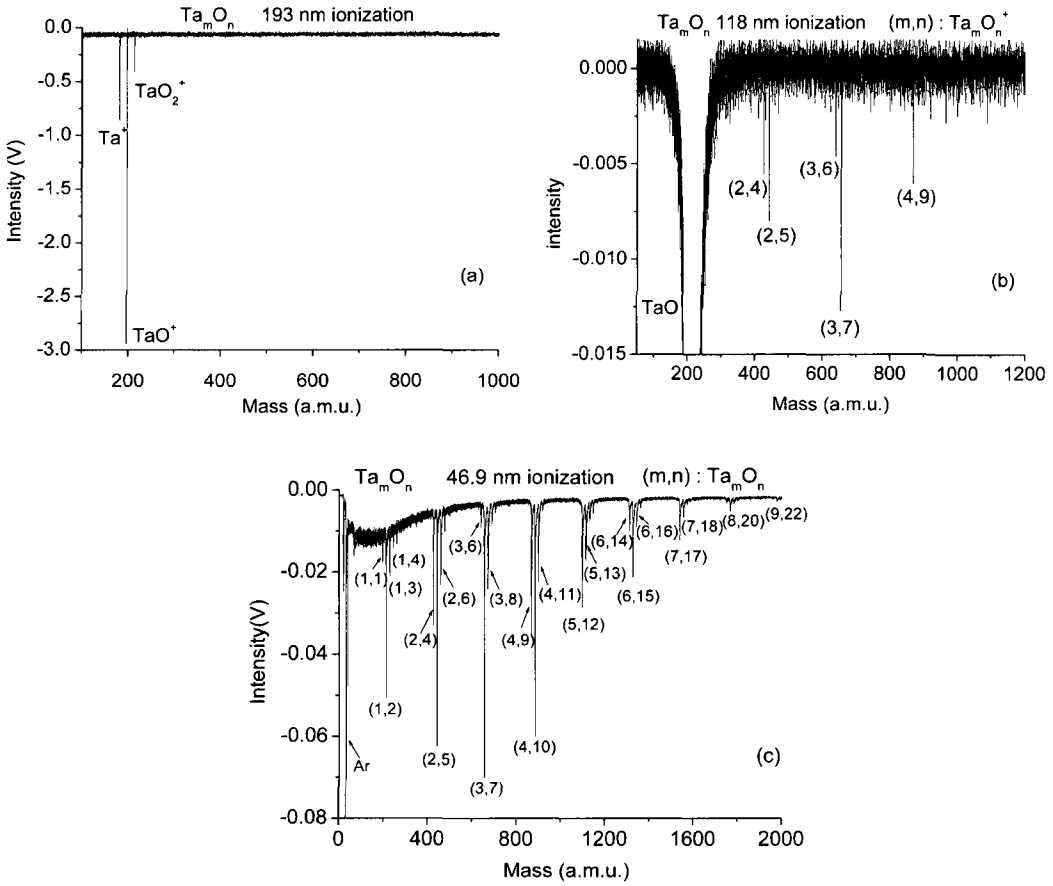


Figure 4.2: TOF mass spectra of tantalum oxide clusters ionized at three different wavelengths, (a) 193 nm multiphoton ionization at 193 nm, (b) near threshold single photon ionization at 118 nm, and (c) single photon ionization at 46.9 nm.

the 193 nm light can be decreased in order to reduce fragmentation by the absorption of too many photons, but larger clusters are still not observed.

Figure 4.2b shows the mass spectrum observed, under the same experimental conditions, upon changing the ionization source to 118 nm light. A number of larger cluster ions are observed through this ionization. Note that no oxygen rich clusters (e.g.,

Ta_2O_6, Ta_3O_8, Ta_4O_{11}, ...) are observed, however. The 10.5 eV photon energy is sufficient to ionize most Ta_mO_n clusters in the beam. The predominant detected cluster ions are TaO_2, $Ta_2O_{4,5}$, $Ta_3O_{6,7}$, Ta_4O_9 with the general formula $(TaO_2)_x$ $(Ta_2O_5)_y$. Since 118 nm light is generated by tripling 355 nm, even though the optical arrangement reduces the fluence of 355 nm light at the ionization point (focus of 118 nm light)[4.7] to less than the 118 nm fluence (ca. 10^{-6} of its original value), residual 355 nm also appears at the ionization/focal point of the TOFMS. Thus 355 + 118 nm multiphoton (perhaps resonant) excitation, ionization, fragmentation can occur for the Ta_mO_n neutral clusters: this process is probably responsible for the broad, intense signal in the TaO^+ mass channel (see Figure 4.2b).

Figure 4.2c shows a mass spectrum of Ta_mO_n clusters obtained with 26.5 eV (46.9 nm) single photon ionization from the soft X-ray laser. As shown, cluster ion signals are generated for species with up to 9 Ta atoms, TaO^+ and Ta^+ display very small signals, and the observed features are quite sharp (ca. 10 – 20 ns). Compared with the 118 nm ionization spectrum (Figure 4.2b), more stable clusters are observed, especially oxygen rich clusters such as TaO_3, Ta_2O_6, Ta_3O_8, Ta_4O_{11}, etc. with 26.5 eV ionization. Even highly oxygen rich clusters such as $TaO_{4,5}$ are detected in the low mass region. Note that Ta^+ is not observed and that only very small TaO^+ signal is observed.

The differences between Ta_mO_n mass spectra obtained with the three laser wavelengths (see Figure 4.2) in these studies can be associated with three different contributing factors. First, most of the Ta atoms generated by laser ablation of the metal

foil react with O_2 in the nozzle to form Ta_mO_n clusters. Thus the large Ta^+ and TaO^+ signals arise in the 193 and 118/355 nm generated mass spectra are generated through fragmentation of large clusters due to multiphoton ionization processes. Second, the photoionization cross section of the metal at 26.5 eV may just be much smaller than that at 193 nm. One can see from Figure 4.1 that this is at least partially correct. The signal intensity for Ta_m^+ at 26.5 eV ionization is 3 – 10 mV (Figure 4.1) while the signal intensity for $Ta_mO_n^+$ at 26.5 eV ionization is 20 – 80 mV (Figure 4.2). Third, fragmentation of large clusters does not occur for 26.5 eV ionization because of its single photon nature, as the exiting electron must remove most, if not all, of the cluster excess energy over the VIE (see Discussion Section below). Thus fragmentation of larger clusters does not contribute significantly to the small Ta^+ and TaO^+ signals to the presence of these neutrals in the expansion. These very small species have grown into the larger clusters and their presence in the beam is greatly reduced.

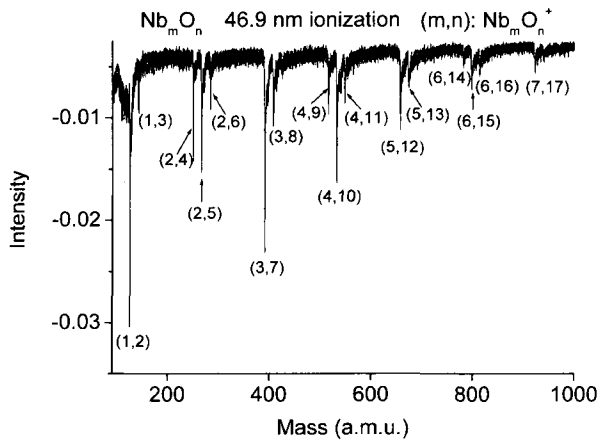


Figure 4.3: TOF mass spectrum of niobium oxide clusters ionized by 26.5 eV soft X-ray laser photons. The sample is generated by laser ablation of Nb metal into a 5% O_2/He gas mixture and 80 psi backing pressure.

The TOF mass spectrum of niobium oxide clusters ($Nb_mO_n^+$), ionized by 26.5 eV soft X-ray laser photons, is presented in Figure 4.3. The predominant ion signals are assigned as NbO_2, Nb_2O_5, Nb_3O_7, ... These stoichiometries are similar to those found for the Ta_mO_n system. The distribution of 26.5 eV ionized vanadium oxide clusters is shown in Figure 4.4. The predominant V_mO_n features in this spectrum are in agreement with those for niobium and tantalum oxide clusters with the exception of $V_2O_4^+$ which is much more intense relative to the other spectral features than that found for $Nb_2O_4^+$ and $Ta_2O_4^+$. Also the vanadium oxide spectrum shows some new stoichiometric features compared to niobium oxide and tantalum oxide spectra of Figures 4.3 and 4.2c, respectively: these new peaks include V_5O_{11} and V_7O_{16}. The formation mechanism of the neutral vanadium,

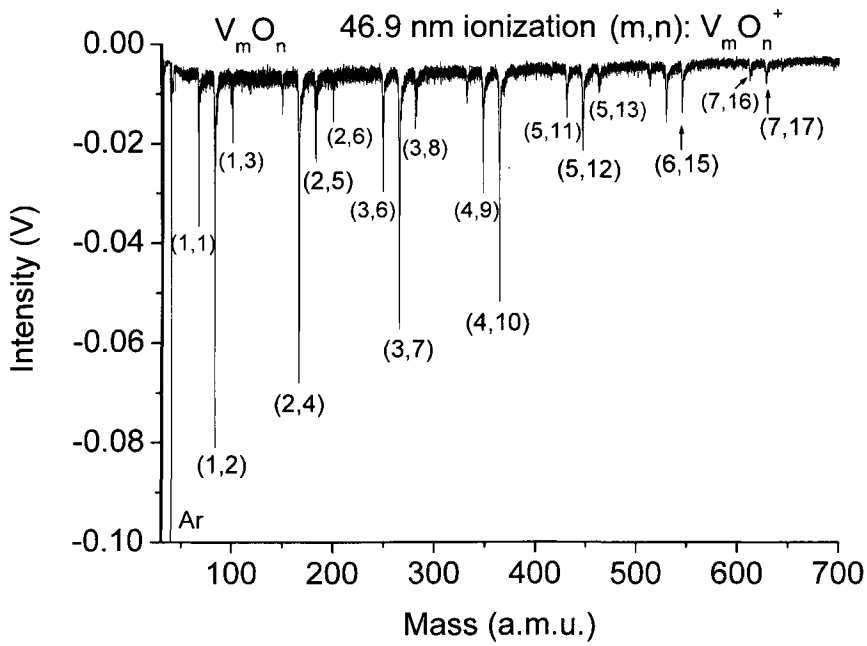


Figure 4.4: TOF mass spectrum of vanadium oxide clusters ionized by 26.5 eV soft X-ray laser photons. The sample is generated by laser ablation of V metal into a 5% O_2/He gas mixture and 80 psi backing

pressure.

niobium, and tantalum oxide clusters will be discussed below in the next section.

Figure 4.5 displays the mass spectrum of V_mO_n clusters obtained through 193 nm (multiphoton) ionization. In this mass spectrum oxygen deficient cluster ions are most intense (e.g., V_3O_4, V_4O_5, V_5O_7, ...). The signal pulses are also very broad (ca. 100 ns). This observation is in agreement with our previous report.[4.11] Additionally, intense features at mass V^+ and VO^+ are observed due to fragmentation of larger clusters; however, no V^+ and little VO^+ signals are observed for 26.5 eV ionization (Figure 4.4), as no fragmentation occurs for this ionization mode.

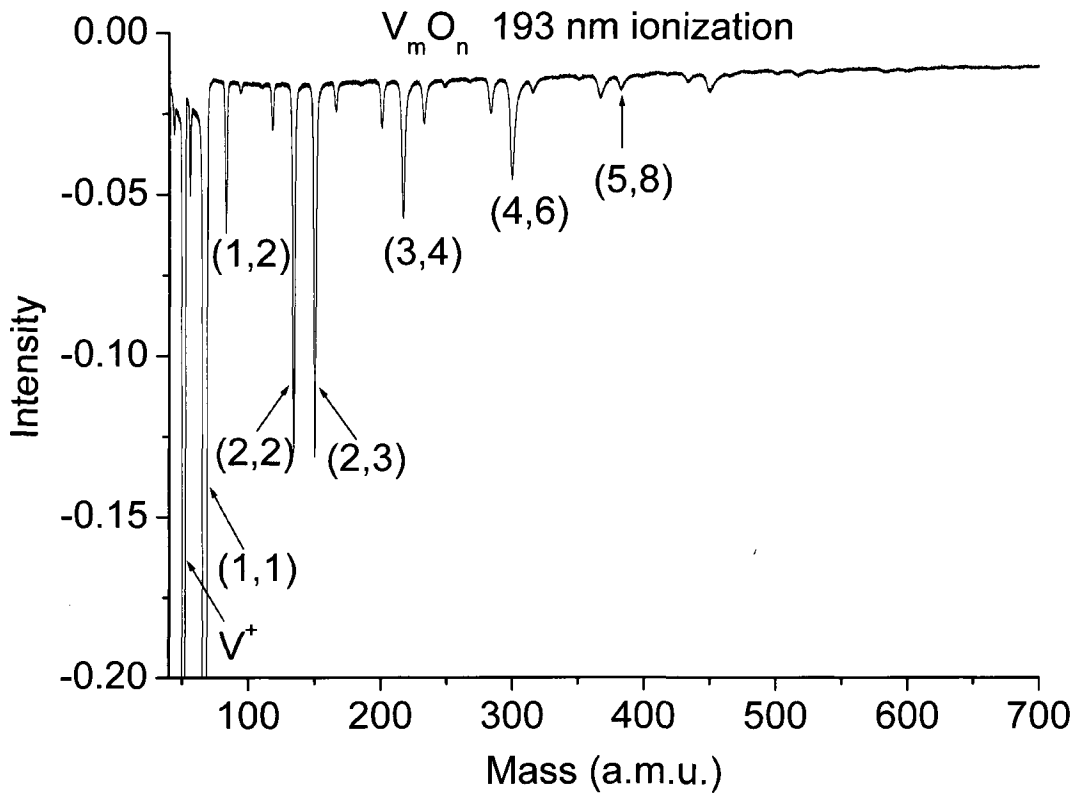


Figure 4.5: TOF mass spectrum of vanadium oxide clusters ionized by 193 nm laser photons. The sample conditions are the same as those employed for the spectrum shown in Figure 4.4.

The distribution of metal oxide clusters with the most stable (abundant) stoichiometries for the three systems are given in Figure 4.6: these are plotted based on the data of Figures 4.2c, 4.3, and 4.4. Note that MO_2 and M_2O_5 can be used as basic building blocks for the three metal oxide clusters. Systematics for oxygen deficient cluster growth are discussed below.

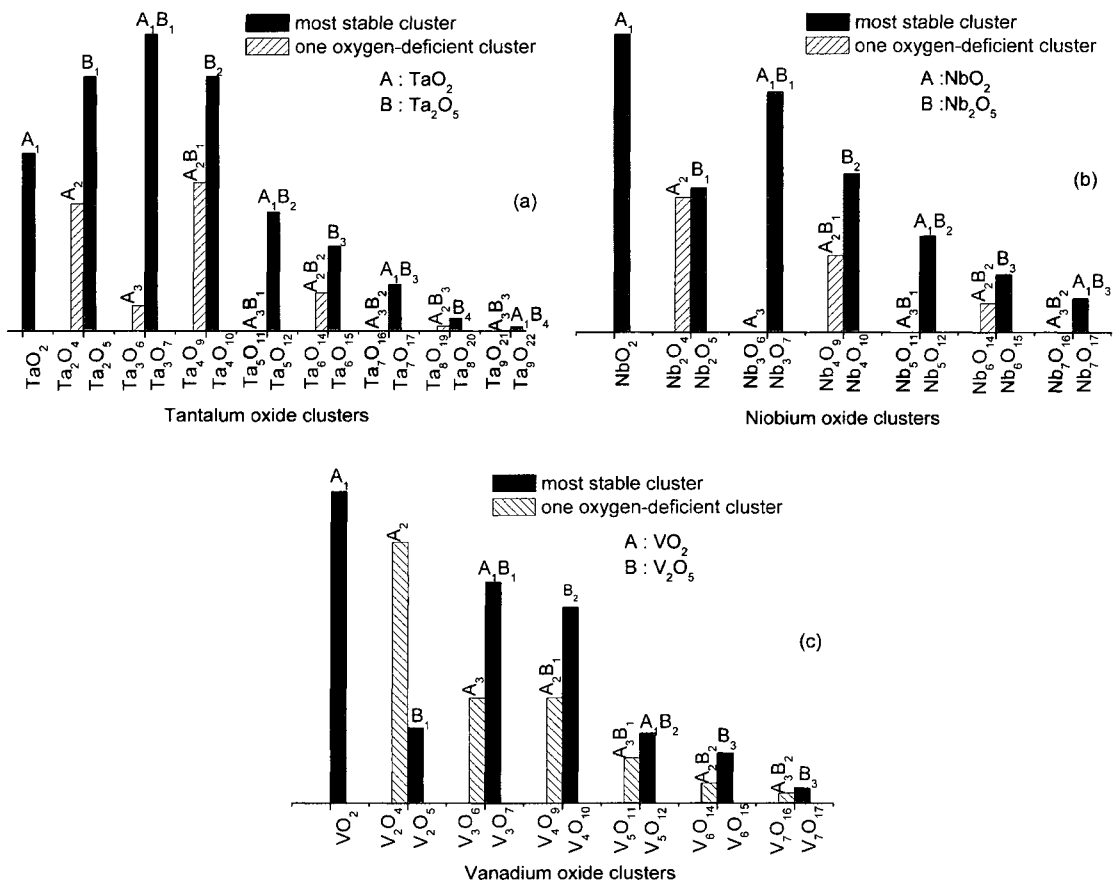


Figure 4.6: Distributions of the most stable and oxygen-deficient clusters for (a) tantalum, (b) niobium, and (c) vanadium, respectively. MO_2 and M_2O_5 are used as basic units to build the oxide clusters.

At high dispersion for 26.5 eV single photon generated mass spectra, one observes that a number of M_mO_n clusters appear to have associated peaks of 1 and 2 amu higher mass, as shown in Figure 4.7. These metals V, Nb, and Ta are all single isotope species.

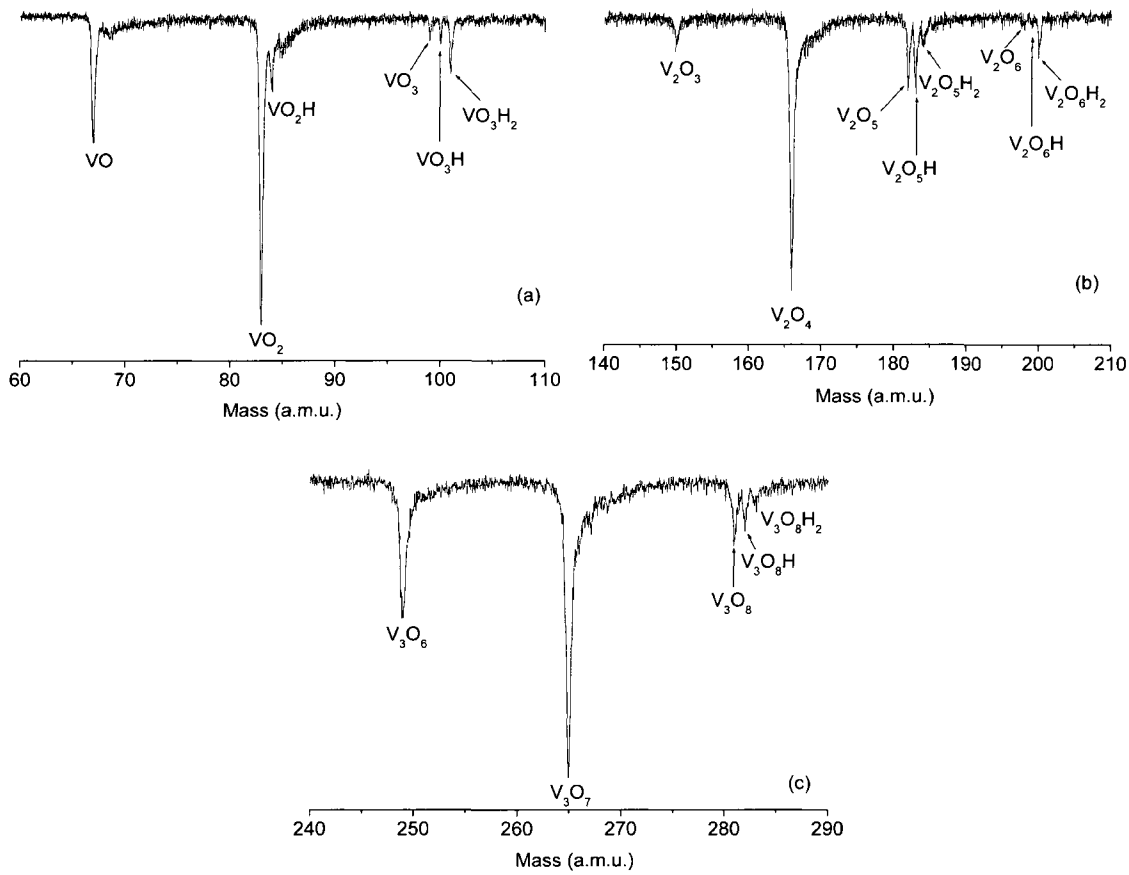


Figure 4.7: Expanded portions of the mass spectra of Fig. 4 for the regions: (a) VO, VO_2, and VO_3; (b) V_2O_3, V_2O_4, V_2O_5, and V_2O_6; and (c) V_3O_6, V_3O_7, and V_3O_8. One or two hydrogen atoms are attached to oxygen rich vanadium oxide clusters. Similar behavior also occurs for niobium and tantalum oxide clusters.

The extra features typically appear for oxygen rich or oxygen sufficient clusters. This is the first time such features have been observed because all clusters in the beam are ionized at 26.5 eV photon energy and little or no cluster fragmentation occurs upon ionization; apparently 10.5 eV photons cannot or do not ionize such species. The source of hydrogen in the clusters is not clear, but H_2O, some hydrocarbon, H_2 absorbed in the metal, or surface OH may all be possible contenders. These species will be discussed in the next section.

4.4 DISCUSSION

4.4.1 Fragmentation Mechanism for M_mO_n Clusters (M = V, Nb, Ta)

A single photon of 193 nm wavelength does not have enough energy (~ 6.4 eV) to ionize the metal oxide M_mO_n clusters of interest in this study. At least two photons of 6.4 eV energy are required to ionize TaO (VIE ~ 8.0 eV) and TaO_2 (VIE ~ 9.0 eV) and other, larger clusters. Since intracluster vibrational redistribution of energy (IVR) occurs rapidly in these clusters, a part of the absorbed photon energy before and during ionization is used to heat the clusters. These IVR dynamics lead to the predissociation (fragmentation) of metal oxide clusters. No large Ta_mO_n cluster is detected through 193 nm ionization (Figure 4.2a); these clusters are fragmented in the ionization process by multiphoton (more than two) absorption into TaO^+ and TaO_2^+. The TOFMS features at Ta^+, TaO^+, and TaO_2^+ are sharp and symmetric implying a fast predissociation of neutral clusters Ta_mO_n occurs during and/or following the 193 nm laser pulse (< ~1 ns). Additionally, this predissociation process is rapid and violent enough to dissociate large clusters into small components to form Ta^+, TaO^+, or TaO_2^+ ions only.

In like manner, Nb_mO_n neutrals yield Nb^+, NbO^+, and NbO_2^+ small fragments upon 193 nm multiphoton ionization. Thus similar fragmentation dynamics are appropriate for Ta_mO_n and Nb_mO_n neutral clusters.

The dynamical behavior for vanadium oxide clusters, upon multiphoton ionization by 193 nm photons under the same experimental conditions employed for Nb_mO_n and Ta_mO_n, is quite different. As Figure 4.5 demonstrates, a number of oxygen deficient

vanadium oxide cluster ions, such as $V_2O_3^+$, $V_3O_3^+$, $V_3O_4^+$, $V_4O_6^+$, and $V_5O_8^+$, are detected under 193 nm ionization. The two possible reasons for observation of these oxygen deficient vanadium oxide clusters under these conditions are 1. direct, single photon ionization from the neutral oxygen deficient clusters present in the supersonic beam, and 2. such clusters are formed from neutral stable clusters $(VO_2)_x(V_2O_5)_y$ by loss of several oxygen and vanadium atoms during the multiphoton ionization process. Reason 1 implies that these oxygen deficient, neutral vanadium oxide clusters V_2O_2, V_3O_3, V_3O_4, V_4O_6, and V_5O_8 have low (< 6.4 eV) VIEs. In the 26.5 eV derived mass spectrum of V_mO_n these oxygen deficient vanadium oxide clusters are not observed. We therefore conclude that through comparison with the other two systems and a knowledge the VIEs of small clusters, the V_mO_n cluster ions observed by 193 nm ionization arise due to fragmentation of larger stable clusters present in the beam prior to the ionization process. This is in fact what has happened for all three cluster systems during ionization and the different products for V_mO_n vs. Nb_mO_n and Ta_mO_n must arise from the details of the number of photons absorbed by the clusters, the cluster densities of states, and the overall cluster system ensuing dynamics.

4.4.2 Distribution of the Neutral V, Nb, Ta Oxide Clusters.

Metal oxide (and metal) clusters are bonded by chemical covalent bonds, and due to unpaired electrons, typically have a very large number of vibronic states and a very high density of states. This situation enables very rapid radiationless transitions. Multiphoton excitation is thereby quite probable for those systems and can lead to cluster

fragmentation and thereby loss of neutral cluster identity based on mass spectral data. Single photon, near threshold ionization is the best approach to the detection and identification of the true neutral cluster distribution. Metal oxide clusters such as Fe_mO_n, Ti_mO_n, V_mO_n, Cu_mO_n, etc.[4.7,4.11] have been studied by single photon ionization by 118 nm (10.5 eV) light. The distributions of neutral clusters for these systems have thus been determined; however, some neutral metal oxide clusters (e.g., highly oxidized ones, VO_3, ...) have VIEs > 10.5 eV and are thus not detected by this approach.

We have demonstrated in this work (see Figure 4.1 and in other reports from our laboratory ($(H_2O)_n$, $(CH_3OH)_n$, $(NH_3)_n$, $(SO_2)_n$, $(CO_2)_n$, metals, ...)[4.12] that 26.5 eV single photon ionization can also generate mass spectra that are not overwhelmed by fragmentation, and that can lead to a complete and quite accurate description of the neutral parent cluster distribution in the preionized, supersonic beam. Proof that these mass spectral representations of neutral cluster distributions are accurate comes from a comparison between VUV (118 nm), EUV (46.9 nm) and resonance lamp (Ar,...) generated TOFMS.[4.12] Just how the photoelectron removes the cluster excess energy (possibly ca. 15 to 20 eV for 26.5 eV ionization) is a topic of some interest which we are addressing through photoelectron spectroscopy to discover the processes and electrons involved in the ionization step. The advantage of 26.5 eV single photoionization over other, less energetic single photon photoionization sources is that the soft X-ray photon ionizes everything. Thereby, the spectra of Figures 4.1, 4.2c, 4.3 and 4.4 are an excellent

representation of the neutral clusters in the supersonic expansion prior to ionization for the respective system.

One of course must be aware that VIEs are not AIEs, and thus some excess energy will always remain in the newly formed ions and if this is enough to fragment the cluster (e.g., possibly through a reaction, like proton transfer[4.19]) one cannot expect, except through detailed analysis of the mass spectrum,[4.12] to take the single peak intensities at face value. The distribution of neutral clusters synthesized in a laser ablation source can, in principle, reflect the effects of growth kinetics in addition to thermodynamic stability of clusters. The distribution detected in these experiments tends to a stable relation at the condition of greater than 4% O_2 in the expansion gas. The same results are reported for the previous 118 nm ionization experiments.[4.11] Thus, the results support the conclusion that the neutral cluster distribution observed is not the result of growth kinetics. Additionally, single photon ionization cross sections could be wavelength dependent, and different ionization photon energies could yield different relative mass spectral intensities. Nonetheless, the data present in Figure 4.1 and our previous publications are quite compelling. Moreover, structure calculations for vanadium oxide clusters suggest that VO_2, V_2O_5, V_3O_7, V_4O_{10}, V_5O_{12}, and V_6O_{15} are the most stable clusters for V_nO_m, n = 2,3,4,5,6 in agreement with the distribution observed with 26.5 eV single photon ionization.

Upon ionization by 26.5 eV EUV light, the most stable neutral clusters are identified as MO_2, M_2O_4/M_2O_5, M_3O_7, M_4O_{10}, M_5O_{12}, M_6O_{15}, M_7O_{17}, M_8O_{20}, and M_9O_{22} for

vanadium, niobium, and tantalum oxide clusters. This determination is based on the above discussed comparisons of differently generated mass spectra.

For Ta_mO_n and Nb_mO_n clusters, the odd families (M_m, m odd) show little or no oxygen deficient cluster concentration, and for even m these species do have oxygen deficient clusters. Here we consider oxygen deficient and oxygen rich clusters as defined with respect to the most stable clusters $(MO_2)_{0,1}(M_2O_5)_y$ based on intensity for 118 nm and 46.9 nm ionization. Vanadium oxides are apparently more flexible in their stoichiometry as oxygen rich and oxygen poor clusters appear for most cluster families V_m.

One set of features for these three metal oxides, ionized by 118 and 46.9 nm radiation, do not fall into the general systematic discussed above: these peaks are for the M_2 family of clusters. For $Nb_2O_{4,5}$ and $Ta_2O_{4,5}$ the M_2O_5 feature is the most intense (stable) neutral and ion by either 118 or 46.9 nm ionization, while for V_2O_m 118 nm ionization[4.11] finds $V_2O_5^+$ more intense than $V_2O_4^+$ with the reverse true for 46.9 nm ionization. This difference does not relate to the presence of $M_2O_5H_x$ clusters in the system and is probably most readily associated with the details of wavelength dependent ionization cross sections for M_2O_4 and M_2O_5 neutral clusters.

4.4.3 Structure and Formation of Neutral Clusters.

The most common bulk stoichiometry for group 5 (V, Nb, Ta) transition metal oxides in M_2O_5, indicating that the metal has an effective oxidation state of +5 with +4 also a viable state in oxides such as VO_2 and V_2O_4. MO_2 and M_2O_5 are thereby reasonable

suggestions for the main building blocks for these metal oxide cluster series. As shown in Figure 4.6, stoichiometry of the most stable metal oxide clusters (that is, most intense mass spectral features) can be expressed as $(MO_2)_{0,1}(M_2O_5)_y$. One can conclude that an M_2O_5 unit is the basic building block for the main cluster family (M_m) feature, with only at most one MO_2 unit appearing in clusters of the most stable stoichiometry. Based on the premises that 26.5 eV photons do little in the way of cluster fragmentation and that 26.5 eV photons can ionize any species in the expansion, the TOF mass spectra at 26.5 eV ionization represents all clusters and both their neutral and cation populations.

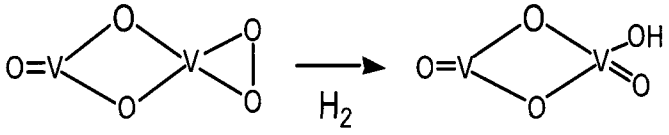
Cluster family structure and stoichiometry can be seen to be systematic for Nb_mO_n and Ta_mO_n clusters. Typically for even m, oxygen deficient, oxygen sufficient and oxygen rich clusters are observed. Thus $M_2O_{4,5,6}$, $M_4O_{9,10,11}$, $M_6O_{14,15,16}$, ... M = Nb,Ta are observed. On the other hand, for odd m families, oxygen deficient clusters are not observed. The only exception to this general rule is Ta_3O_6 which is very weak, as shown in Figure 4.2c. Oxygen deficient clusters can be represented as $(MO_2)_2(M_2O_5)_y$ and the oxygen rich clusters as $(MO_2)_{0,1}(N_2O_5)_yO_{1,2,3}$.

This odd/even family difference found for Nb/Ta_mO_n clusters is not found for V_mO_n clusters. In these species all clusters V_mO_n have oxygen deficient and oxygen rich clusters relative to the most stable one. V_nO_n clusters can be represented as $(MO_2)_x(M_2O_5)_y$ for oxygen deficient and sufficient clusters and for oxygen rich clusters as $(MO_2)_x(M_2O_5)_yO$, as appropriate. Structure calculations for these clusters[4.20] suggest that all oxygen atoms

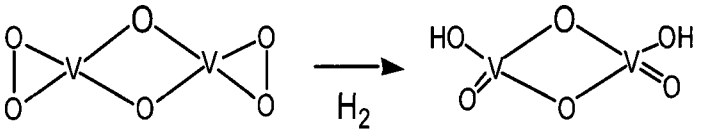
are covalently bonded to metal atoms, and metal atoms and oxygen for the lowest energy structures.

4.4.4 Hydrogen Containing, Oxygen Rich Clusters.

A number of oxygen rich clusters are found to have one or two hydrogen atoms attached to them. This makes chemical sense in that vanadium, niobium, and tantalum all have most stable stoichiometries for M^{+4} and M^{+5}. Thus MO_3, M_2O_5, M_2O_6, M_3O_8, etc. can readily form OH ligands to maintain these preferred valence states. This chemistry is consistent with, for example, a double oxygen bridged/three terminal oxygen atom structure for V_2O_5.[4.8,4.20] Added hydrogens at the terminal oxygens would maintain this chemistry as would oxo bond formation (see Scheme I).



and



Scheme I

Note that these hydrogen containing clusters do not occur for oxygen deficient species or for most oxygen sufficient (most stable) species, although they do appear for M_2O_5 M=V, Nb, Ta clusters.

4.5 CONCLUSIONS

26.5 eV single photon ionization turns out to be an excellent diagnostic for neutral cluster distribution in general for all varieties of clusters from van der Waals, to hydrogen bonded, to metal, and covalent metal oxide systems. During the ionization process(es) nearly all the excess energy above the VIE of the cluster is removed by the exiting photoelectron. Where possible a comparison between 10.5 and 26.5 eV ionization is made to show that the results of both methods of ionization are nearly identical, except that 26.5 eV ionization finds all species present in the sample. Most importantly this ionization approach has found oxygen rich clusters and oxygen rich clusters with added hydrogen that have not previously been identified for laser ablation metal oxide clusters. Systematics for Nb and Ta systems can be established while V containing clusters seem to have a more varied chemistry of oxygen rich and deficient clusters for all families (M_m) of metal containing species. Nb and Ta clusters show oxygen deficient species only for M_m m even.

The mechanism for photoelectron removal of excess ionization energy (26.5 – VIE) eV is not obvious and photoelectron spectroscopy of these processes would be very informative and useful for an understanding of the ionization mechanisms and dynamics of clusters in general at 26.5 eV.

REFERENCES

[4.1] G.A. Somorjai, Introduction to Surface Chemistry and Catalysis, (Wiley, New York, 1994) Chap 7.

[4.2] I. A Campbell, Catalysis at Surface, (Chapman and Hall, New York, 1988).

[4.3] D. W. Goodman, J. Catal., **216**, 213 (2003).

[4.4] G.A. Somorjai, J. Phys. Chem. B, **106**, 9201 (2002).

[4.5] D. N. Shin, Y. Matsuda, and E. R. Bernstein, J. Chem. Phys. **120**, 4150 (2004**).**

[4.6] M. Foltin, G. J. Stueber, and E. R. Berstein, J. Chem. Phys. **111**, 9577(1999).

[4.7] (a) Y. Matsuda, D. N. Shin, and E. R. Bernstein, J. Chem. Phys. **120,** 4142 (2004). (b) D. N. Shin, Y. Matsuda, and E. R. Bernstein, J. Chem. Phys., **120**, 4157 (2004). (c) Y. Matsuda, D. N. Shin, and E. R. Bernstein, J. Chem. Phys. **120**, 4165 (2004). (d) Y. Matsuda, and E. R. Bernstein, J. Phys. Chem. A **109**, 314 (2005). (e) E. R. Bernstein, and Y. Matsuda, Environmental Catalysis, (Marcel Dekker, New York, 2005).

[4.8] K. S. Molek, T. D. Jaeger, and M. A. Duncan, J. Chem. Phys. 123, 144313 (2005).

[4.9] (a) R. C. Bell, K. A. Zemski, D. R. Justes, and A. W. Castleman, Jr., J. Chem. Phys. **114**, 798 (2001). (b) R. C. Bell, K. A. Zemski, K. P. Kerns, H. T. Deng, and A. W. Castleman, Jr., J. Phys. Chem. A **102**, 1733 (1998).

[4.10] H. T. Deng, K. P. Kerns, and A. W. Castleman, Jr., J. Phys. Chem. **100**, 13386 (1996).

[4.11] Y. Matsuda and E. R. Bernstein, J. Phys. Chem. A 109, 3803 (2005).

[4.12] (a) F. Dong, S. Heinbuch, J. J. Rocca, and E. R. Bernstein, J. Chem. Phys. **124**, 224319 (2006). (b) S. Heinbuch, M. Grisham, D. Martz, J. J. Rocca, Optics Express **13**, 4050 (2000).

[4.13] D. R. Lide (Editor), *Ionization potentials of atoms and atomic ions*, Handbook of Chem. and Phys., 1992, 10-211 (http://webbook.nist.gov/chemistry.form-ser.html).

[4.14] B. A. Collings, D. M. Rayner, and P. A. Hackett, International Joural of Mass Spectrometry and Ion Process **125**, 207 (1993).

[4.15] A. R. Miedema, Faraday Symp. Chem. Soc. **14**, 136 (1980).

[4.16] A. R. Miedema and K. A.Gingerich, J. Phys. B **11**, 2081 (1979).

[4.17] J. M. Dyke, A. M. Ellis, M. Feher, A. Morrid, A. J. Paul, and J. C. H. Stevens, J. Chem. Soc. Faraday Trans. **83**, 1555 (1987).

[4.18] M. G. Inghram, W. A. Chupka, J. Berkowitz, J. Chem. Phys. **27**, 569 (1957).

[4.19] (a) U. Nagashima, H. Shinohara, N. Nishi, and H. Tanaka, J. Chem. Phys. **84**, 209 (1986). (b) M. Okumura, L. I. Yeh, J. D. Myers, and Y. T. Lee, J. Phys. Chem. **94**, 3416 (1990). (c) Z. Shi, J. V. Ford, S. Wei, and A. W. Castleman, Jr., J. Chem. Phys. **99**, 8009 (1993). (d) G. Vaidyanathan, M. T. Coolbaugh, W. R. Peifer, and J. F. Garvey, J. Chem. Phys. **94**, 1850 (1991). (e) J. A. Odutola, T. R. Dyke, B. J Howard, and Muenter, J. Chem. Phys. **70**, 4884 (1979).

[4.20] E. Jakubikova and E. R. Bernstein, J. Chem. Phys. to be submitted.

Chapter 5

Reactions of Sulfur Dioxide with Neutral Vanadium Oxide Clusters

5.1 REACTIONS OF SULFUR DIOXIDE WITH NEUTRAL VANADIUM OXIDE CLUSTERS IN THE GAS PHASE. EXPERIMENTAL STUDY EMPLOYING SINGLE PHOTON IONIZATION

Vanadium oxides are very important industrial heterogeneous catalysts.[5.1-5.4] V_2O_5 catalysis has been employed for oxidation of SO_2 to SO_3 (sulfuric acid production, SO_2 removal), selective reduction of NO_x with NH_3, oxidation of hydrocarbons (butene, benzene, *o*-xylene, naphthalene) to anhydrides, and for other reactions. In order to improve efficiency of industrial catalysts and to find new catalysts for these important processes, fundamental studies of catalytic mechanisms are essential, especially with regard to microscopic or molecular level reaction dynamics and kinetics.[5.5] With the development of spectroscopic catalyst characterization techniques (x-ray absorption, infrared and Raman spectroscopy, solid-state NMR, ...), the understanding of catalytic mechanisms involving condensed phase transition metal oxide systems[5.6] has increased. Nevertheless, only very limited observations for complex heterogeneous catalytic system are presently available and microscopic reaction mechanisms are sometimes proposed

based on incompletely supported models, ideas, and concepts. Oxidation of SO_2 over supported vanadia catalysts has been carefully studied[5.7-5.9] and conclusive mechanisms have been drawn based heavily on O=V-(O-*support*)$_3$ structural models.[5.3,5.4,5.6] Very recent theoretical and experimental studies,[5.10,5.11] however, strongly suggest that the catalyst should possess an O_2O=V-O-*support* structure.

Gas phase vanadium oxide clusters (V_mO_n) are excellent model systems to help elucidate and understand molecular level processes occurring in the above mentioned reactions using vanadia catalysts. Catalytically active sites can be simulated/modeled by clusters with particular *m* and *n*: the difficulty is to find proper values from *m* and *n* that represent an active site.[5.12-5.15] One obvious advantage of using clusters to simulate catalytically active sites is that modern quantum chemistry calculations can be applied to obtain reliable information that is hard to access by direct observations.[5.5]

Successful joint experimental and theoretical studies of the reactivity of cationic V_mO_n toward hydrocarbons have been reported.[5.16-5.20] Many other experimental and theoretical investigations of vanadium oxide clusters are reported; brief reviews can be found in Refs. 5.19 and 5.21. Because electric and magnetic forces can be used to control and manipulate charged particles and charged particles can be detected very efficiently, most of the experimental studies are on cationic and anionic vanadium oxide clusters. To date, no report can be found for experimental reactivity studies of *neutral* vanadium (and other transition metal) oxide clusters. The major difficulty for such studies of the reactivity of neutral metal oxide clusters lies in finding a valid method to ionize neutral

species with typical ionization energies in the range of 8-10 eV or higher (e.g., VO_3, SO_3, N_2, V_3O_8,...), and in detecting them without loss of information (neutral cluster mass and abundance distributions). Typical multi-photon and electron impact ionization almost always cause severe cluster fragmentation, and thus loss of original neutral cluster information.

Recently, single-photon ionization (SPI) through vacuum ultra-violet (VUV) and soft x-ray (EUV) laser radiation have been successfully used by us to study a series of neutral metal oxide cluster distributions without fragmentation.[5.21-5.26] The 118 nm single photon energy is 10.5 eV and the soft x-ray single photon energy is 26.5 eV; for most transition metal oxide clusters (M_mO_n, M=Ti, V, Co, Nb, Fe...), the ionization energy is around 10 eV. Therefore, clusters ionized by x-ray laser radiation may have more excess energy than those ionized by 118 nm laser radiation. Thus, for x-ray laser ionization, the relative signal intensities of weakly bound products, such as association products, $V_mO_nSO_2$, can be smaller than those observed by 118 nm ionization, because more excess energy can remain in the clusters and the clusters can fragment. Consequentially, x-ray laser ionization has both pros and cons but nonetheless, it is clearly essential to detect all the neutral clusters and their products. The adoption of soft x-ray laser ionization for this study is important for detection of some products with high ionization energy (IE), such as SO_3 and V_mO_n clusters that are oxygen rich. We have employed 26.5 eV single photon ionization to detect these clusters and products and report these results herein which are unique and essential to the demonstration of our conclusions.

In the present work, a fast flow reactor[5.27] is further employed to study the reactivity of neutral vanadium oxide clusters toward SO_2. The motivation is to understand possible molecular level mechanisms for oxidation of SO_2 in condensed phase catalytic reactions. In the present work, the experimental results are reported and discussed based on the observations and preliminary calculations. Details of the calculations are presented in the part I of this series.[5.28] Based on these results, full catalytic cycles for the condensed phase systems are suggested.

5.2 EXPERIMENTAL PROCEDURES

The experimental setup for a pulsed laser ablation/supersonic nozzle coupled with a fast flow reactor has been described in our previous study of methanol formation on metal clusters.[5.29] Only a brief outline of the experiments is given below. V_mO_n clusters are generated by laser ablation of vanadium metal foil in the presence of 1% O_2 seeded in a He carrier gas. The gas is controlled by a pulsed nozzle (called nozzle I in this work) made by the R. M. Jordan Company. The clusters formed in a gas channel (Φ2 mm × 19 mm) are expanded and reacted with SO_2 or an SO_2/O_2 mixture seeded or unseeded in He in a fast flow reactor (Φ6 mm × 76 mm). The reactant gases (SO_2, SO_2/O_2, with or without He) are pulsed into the tube 20 mm downstream from the exit of the narrow cluster formation channel by a pulsed valve (General Valve Series 9, called nozzle II in this work). Reactions in the fast flow reactor are believed to occur at near room temperature due to the large number of collisions between V_mO_n clusters and the bath gas (He) and/or reactants (SO_2, SO_2/O_2).[5.27] The instantaneous total reactant gas pressure in

the reactor is about 14 Torr in the case that the He bath gas is used. The ions are deflected from the molecular beam by an electric field located 5 mm downstream of the fast flow reactor. The gases exiting the reactor are skimmed (Φ5 mm or Φ2 mm) into the vacuum system of a time of flight mass spectrometer (TOFMS) for ionization by radiation of one of two different lasers: a 118 nm (10.5 eV) VUV laser or a 46.9 nm (26.5 eV) soft x-ray laser. Ions are detected and signals are recorded as previously described.[5.29,5.30] The 118 nm laser light is generated by focusing the third harmonic (355 nm, ~30 mJ/pulse) of a Nd:YAG laser in a tripling cell that contains about a 250 Torr argon/xenon (10/1) gas mixture. To separate the generated 118 nm laser beam from the 355 nm fundamental beam, a magnesium fluoride prism (made by Crystaltechno LTD, Russia, apex angle = 6 deg), which was not employed in our previous studies,[5.21-5.25] is inserted into the laser beams. In this case, one is quite certain that the mass signals are generated by ionization purely through the VUV laser radiation with low power (~1 μJ/pulse, pulse duration ~5 ns). The soft x-ray laser radiation (~10 μJ/pulse, pulse duration ~1.5 ns) is generated from the $3p(^1S_0)$-$3s(^1P_1)$ transition of Ne-like Ar: a detailed description of this laser can be found in the literature.[5.31,5.32] The fast flow setup employing a 118 nm laser as an ionization source is schematically shown in Fig. 5.1. The x-ray laser radiation is not focused in the TOFMS ionization region.

5.3 RESULTS

Fig. 5.2 presents low mass spectra for reactions of V_mO_n with different concentrations of SO_2 seeded in He in the fast flow reactor. Products SO and VO_2SO_2 are observed through

118 nm single photon ionization. The intensities of products (SO and VO_2SO_2) increase, while the intensities of the reactant clusters (VO and VO_2) decrease as SO_2 concentrations

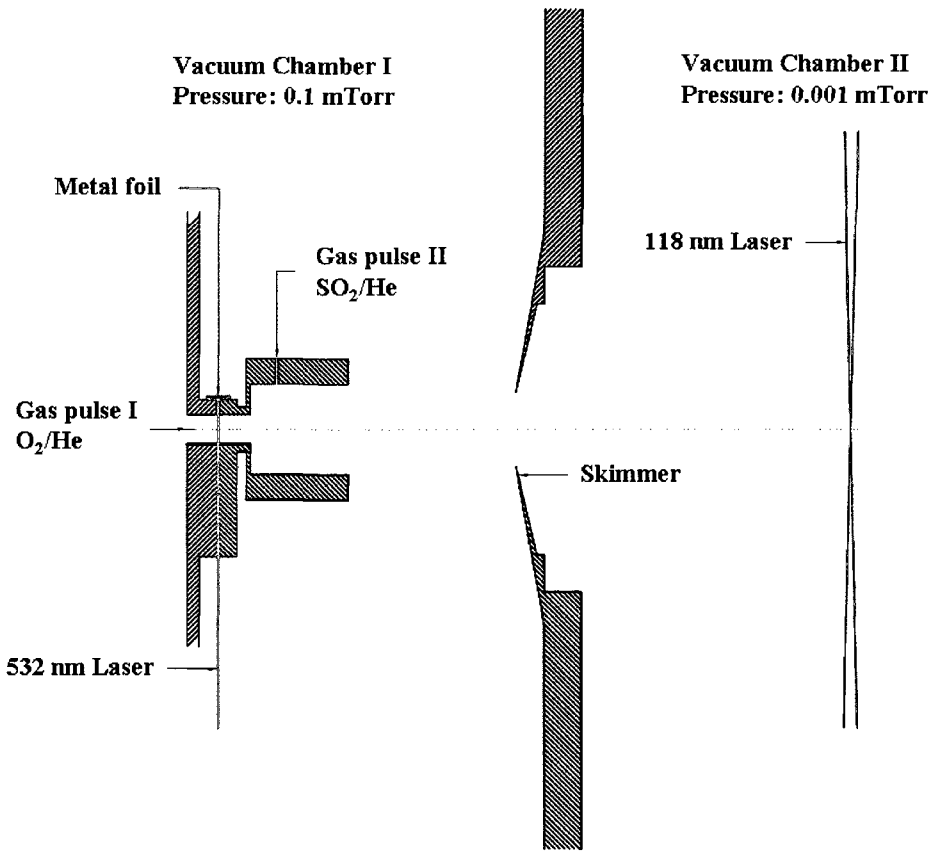


Figure 5.1: A schematic diagram of the experimental setup using 118 nm laser radiation as the ionization source.

increase. The following reactions can be derived:

$$VO + SO_2 \rightarrow VOSO_2^* \rightarrow VO_2 + SO \quad (5.1)$$

$$VO_2 + SO_2 \rightarrow VO_2SO_2^* \quad (5.2a)$$

$$VO_2SO_2^* + He \rightarrow VO_2SO_2 + He \quad (5.2b)$$

in which $VOSO_2^*$ and $VO_2SO_2^*$ (or generally $V_mO_nSO_2^*$) are initial association products that carry center of mass collision energy, reactant initial vibrational energy, and

association energy, and VO_2SO_2 (or generally $V_mO_nSO_2$) is the product stabilized by collisions with He (or reactants). Only products containing transition metal/metal oxide

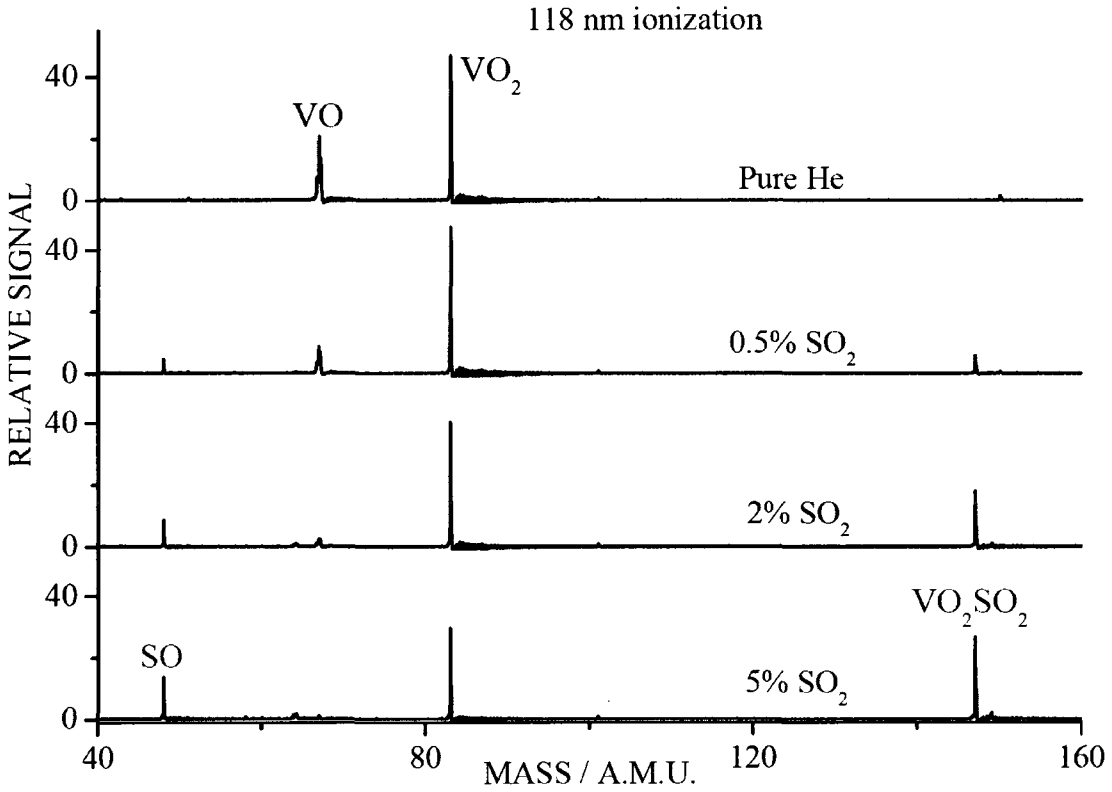


Figure 5.2: TOF mass spectra (low mass region) for reactions of V_mO_n with different concentrations of SO_2 seeded in He. The concentrations of SO_2 are 0%, 0.5%, 2%, and 5% from top to bottom traces. 1% O_2 seeded in He is used to produce V_mO_n (this condition is kept to obtain all the TOF spectra reported in the present work).

clusters are detected in the previous neutral cluster studies,[5.29,5.30] and SO as an isolated product is observed in the reactions of neutral transition metal/metal oxide clusters for the first time in these experiments. The SO signal immediately disappears if the ablation laser is blocked, which indicates SO comes from the reaction of the V_mO_n with SO_2. Signals of products and reactants are dependent on the relative delay times for opening the two pulsed nozzles (I and II). Fig. 5.3 gives the relative signal change of VO, VO_2, SO, and

VO_2SO_2 with the change of relative delay times (ΔT) between the openings of nozzles I and II. Nozzle II is always fired earlier than nozzle I to make sure the reactor is filled by

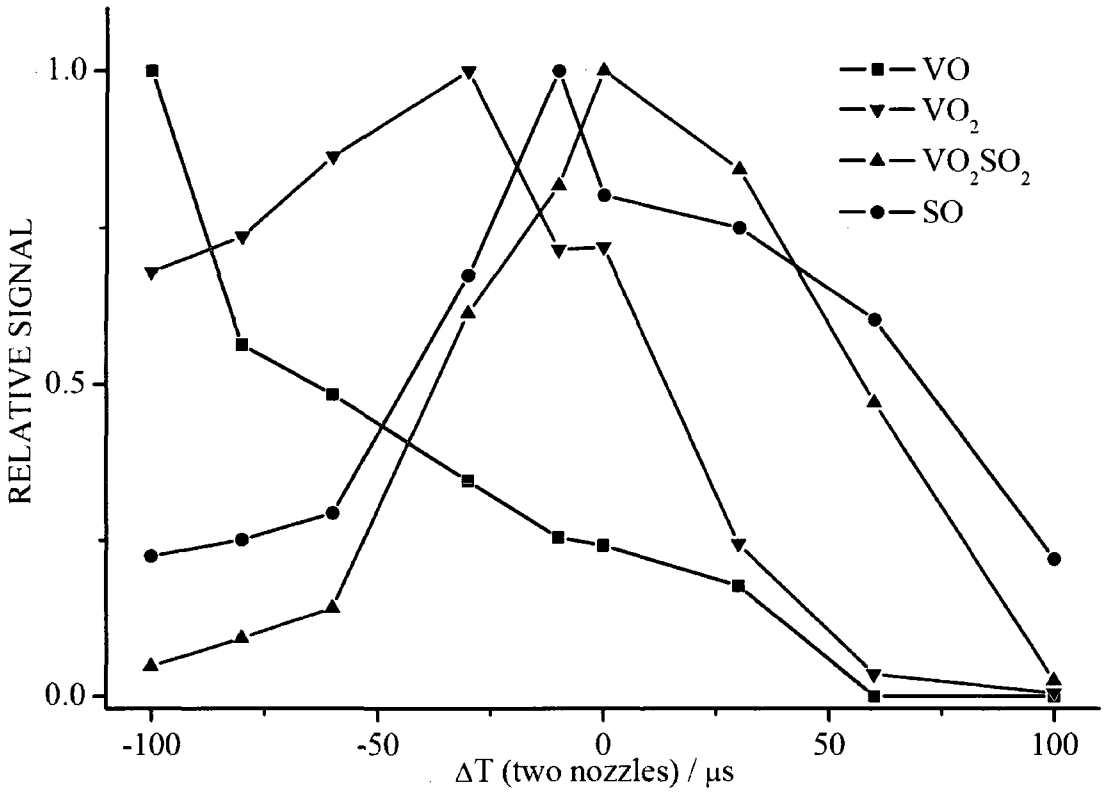


Figure 5.3: Relative signal change of VO (solid square), VO_2 (solid down triangle), VO_2SO_2 (solid up triangle), and SO (solid circle) with the change of relative delay times (ΔT) for opening two nozzles that deliver the two gas pulses discussed in the Experimental Procedures Section. 5% SO_2 seeded in He is used for the reaction of V_mO_n with SO_2. See text for details.

the reactant gases before the clusters arrive. In the experiment, $\Delta T \approx 0$ μs corresponds to the condition for the best product yield; negative ΔT values corespond to less overlap between the two gas pulses. The increase of VO_2 signal with the increase of ΔT at the beginning (ΔT < -25 μs) further verifies that reaction (5.1) happens in the reactor. The decrease of the product signal at large positive ΔT values can be understood as too much mixing of the two gas pulses so that the clusters and products are diluted in space and/or

time through collisional scattering. Note that the original laser ablation created V_mO_n clusters have a time distribution within only about 10 μs. In the present work, the mass spectra are all obtained under the condition that products have a maximum signal, which corresponds to $\Delta T \approx 0$ μs in Fig. 5.3.

Figs. 5.4 and 5.5 plot high mass spectra for reactions of V_mO_n with different concentrations of SO_2 seeded in He. Many association products ($V_mO_nSO_2$) are observed. $V_2O_4SO_2$ further reacts with SO_2 to form $V_2O_4(SO_2)_2$ if high concentrations ($\geq$ 5%) of SO_2 are used. A careful comparison between the spectra indicates that for an oxygen series (V_mO_n, m – constant, n – variable), clusters with lower n values usually have relatively higher depletion rates than clusters with higher n values (more oxygen rich clusters); for example, V_3O_6 vs. V_3O_7, V_4O_8 vs. V_4O_9, V_5O_{10} vs. V_5O_{12}, V_6O_{13} vs. V_6O_{14}, V_7O_{15} vs.

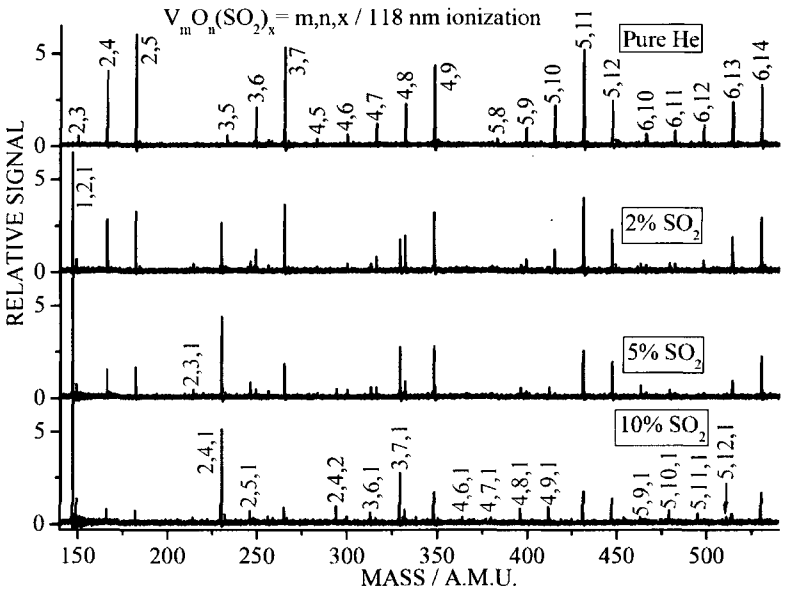


Figure 5.4: TOF mass spectra (high mass region I) for reactions of V_mO_n with different concentrations of SO_2 seeded in He. The concentrations of SO_2 are 0%, 2%, 5%, and 10% from top to bottom traces.

$V_7O_{16,17}$, and V_8O_{17} vs. $V_8O_{18,19}$. We may derive the following processes similar and parallel to reactions (5.1) and (5.2) based on such observations:

$$V_mO_n + SO_2 + He \rightarrow V_mO_nSO_2^* + He \rightarrow V_mO_nSO_2 + He \quad (5.3)$$

$$V_mO_nSO_2^* \rightarrow V_mO_{n+1} + SO \text{ (for low } n \text{ values in O-series)} \quad (5.4)$$

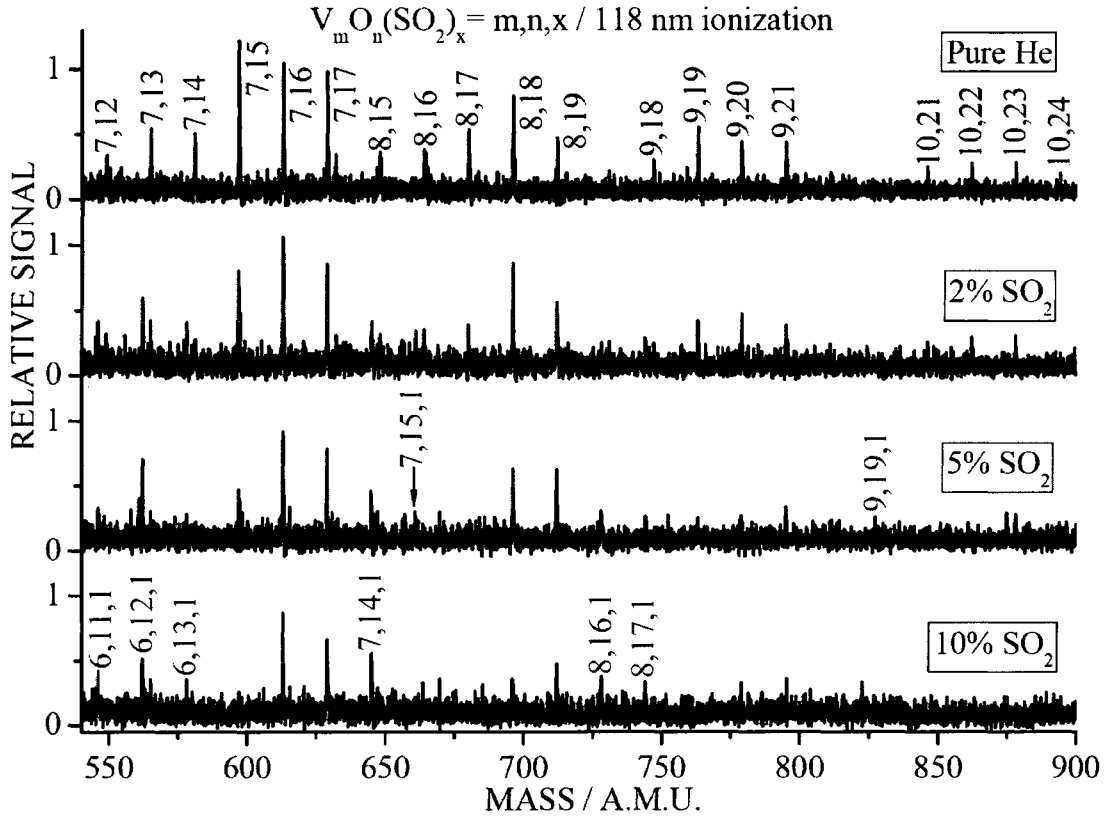


Figure 5.5: TOF mass spectra (high mass region II) for reactions of V_mO_n with different concentrations of SO_2 seeded in He. The concentrations of SO_2 are 0%, 2%, 5%, and 10% from top to bottom traces.

Fig. 5.6 presents the mass spectrum obtained for reactions of V_mO_n clusters with SO_2 employing the 26.5 eV soft x-ray laser for ionization. A mass peak 80 amu (SO_3) is detected if SO_2 is added to the fast flow reactor, as shown in the bottom spectrum. If the ablation laser is blocked to prevent the generation of V_mO_n clusters, the SO_3 signal disappears along with the cluster signals (e.g., V_2O_4), as shown in top spectrum. The

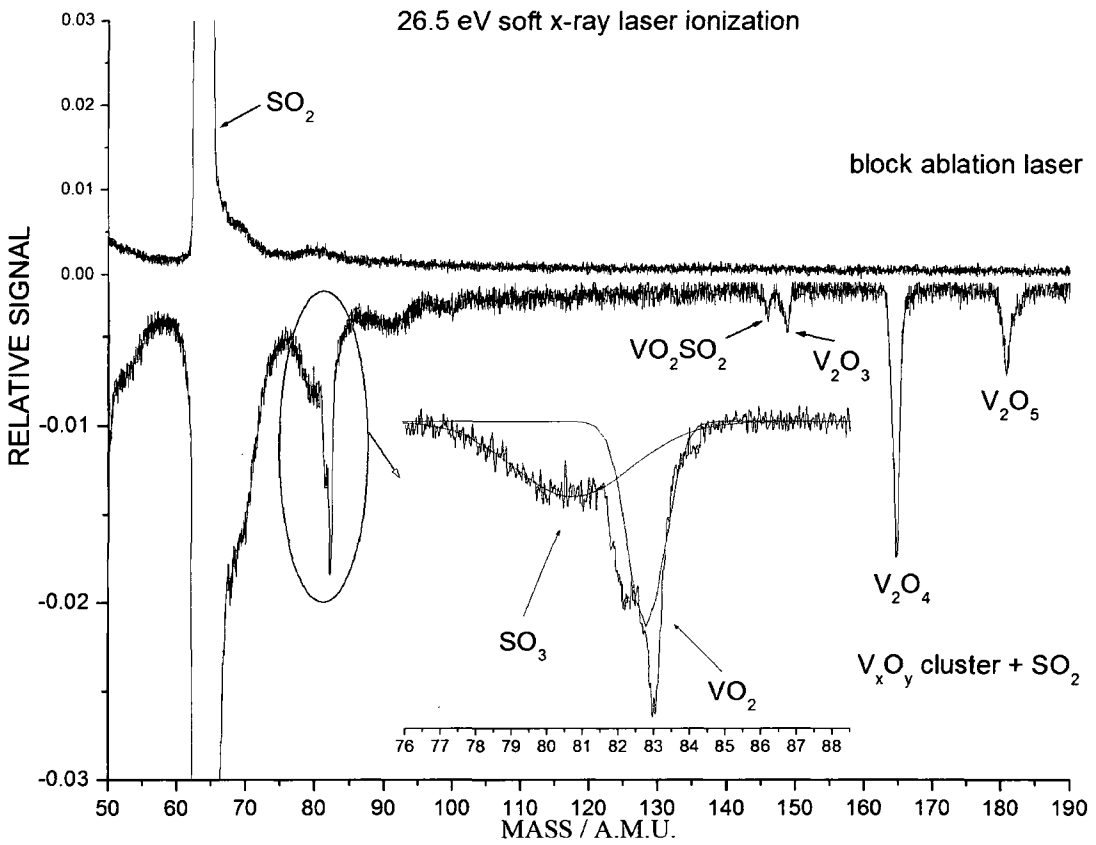


Figure 5.6: TOF mass spectra for reaction of V_mO_n with SO_2 employing a 26.5 eV soft x-ray laser for ionization. A product SO_3 is observed when SO_2 is added (bottom trace), and it disappears with the V_mO_n cluster signal when the ablation laser is blocked (top trace). SO_3 (80 amu) and VO_2 (83 amu) mass peaks are simulated by 2 gaussian curves and presented in the insert figure. Note that SO_3 mass peak is much boarder than the other mass peaks (VO_2, VO_2SO_2, V_2O_{3-5}).

ionization energy of SO_3 is measured to be 13.15 eV.[5.34] A 118nm laser is not able to ionize SO_3 through single photon ionization, and the x-ray laser is an essential tool for the detection of this product. From the bottom trace of the Fig. 5.6, two obvious bumps are observed and overlapped with the predicted SO_3 signal around 80-100 amu: the explanation for these features and their probable assignments will be presented in the Discussion section.

Results for the addition reactions of $V_mO_nSO_2$ association products with O_2 are

shown in Figs. 5.7 and 5.8 for the low and high mass regions, respectively. Interpretation of the data is complicated by reaction of V_mO_n with O_2 because a signal decrease of the oxygen deficient clusters, such as VO, V_3O_5, and V_4O_{6-8}, due to the presence of O_2 is clearly observed in comparison to VO_2, V_3O_7, and V_4O_9 features.

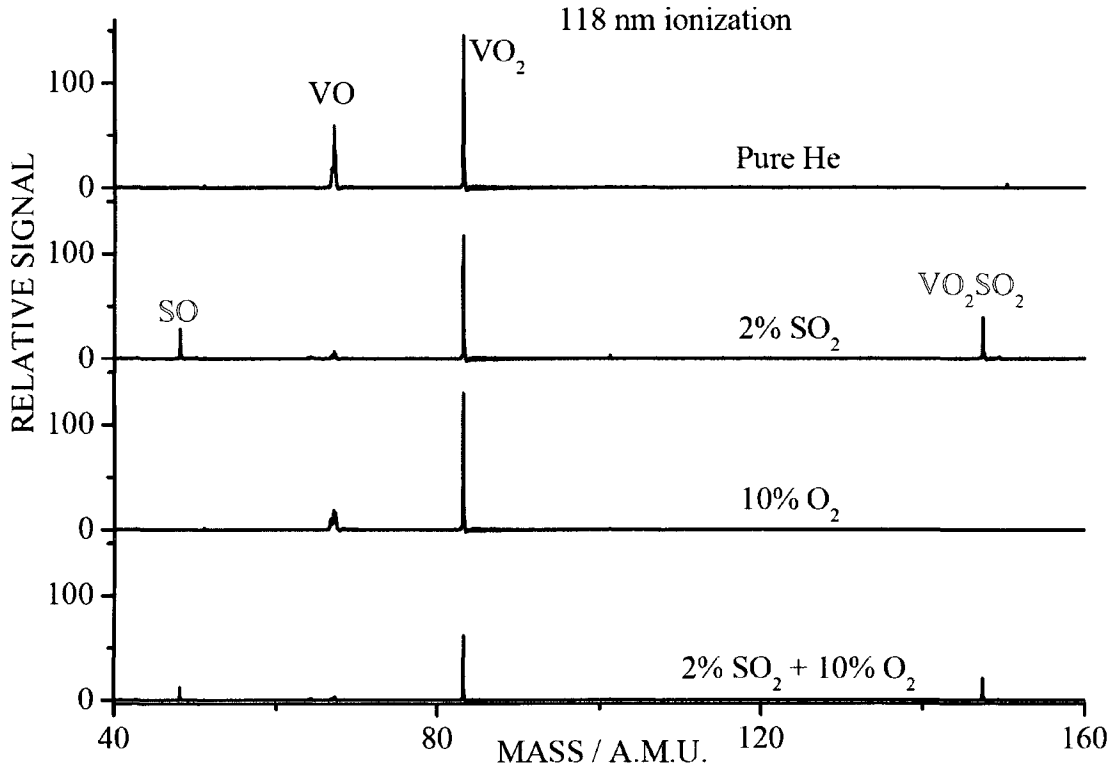


Figure 5.7: TOF mass spectra (low mass region) for reactions of V_mO_n with 2% SO_2 (top second trace), 10% O_2 (top third trace), and 2% SO_2 / 10% O_2 mixed (bottom trace) gases. A reference spectrum with no SO_2 or O_2 added in the reactant gas channel (pure He is used) is shown in the top trace.

The spectra in Fig. 5.7 show that if SO_2/O_2 mixtures rather than SO_2 are used as reactant gases, a big signal decrease of SO, VO_2, and VO_2SO_2 is observed (compare the spectrum in bottom trace with the one in top second trace). Decrease of SO signal intensity can be interpreted in terms of two processes: oxygen deficient clusters (such as VO, V_3O_5, ...) react with O_2 so that reactions (5.1) and (5.4) produce less SO; and SO

produced from reactions (5.1) and (5.4) reacts with O_2 :[5.35,5.36]

$$SO + O_2 \rightarrow SO_2 + O \quad (5.5a)$$

$$O + SO_2 + He \rightarrow SO_3 + He \quad (5.5b)$$

Decrease of VO_2 and VO_2SO_2 signal intensity can also be interpreted as due to two processes: (A) VO reacts with O_2 (to form VO_3, not detectable by 118 nm laser single photon ionization, IE (VO_3) > 10.5 eV)[5.21] so that reactions (5.1) and (5.2) produce less VO_2 and VO_2SO_2, respectively; and (B) fully or partially stabilized VO_2SO_2 from reaction (2b) reacts with O_2, to yield

$$VO_2SO_2 + O_2 \rightarrow VO_3 + SO_3 \quad (6)$$

The rate for reaction (5.2b) is dependent upon the cooling efficiency of collisions with He in the fast flow reactor; that is, $VO_2SO_2^*$ must be stabilized by collisional cooling. As seen from the third trace of Fig. 5.7, VO_2 does not react with O_2, so that the decrease of the VO_2 signal in the bottom trace of Fig. 5.7 is only due to the reaction of $VO_2 + SO_2 \rightarrow VO_2SO_2$. Based on the spectra presented in Fig. 5.7 one can suggest the reaction (5.6) is faster than reaction (5.2b).

The depletion of VO by 2% SO_2 is significantly larger than that by 10% O_2 (compare the top second and third traces in Fig. 5.7 for VO peak), indicating that the rate of reaction VO + O_2 is slower than the rate of reaction VO + SO_2. This rate difference implies that process (A) above may not be the main cause of VO_2 and VO_2SO_2 signal decrease when O_2 is further mixed with SO_2. As a result, reaction (5.6) is a possible process that occurs in the fast flow reactor. In Fig. 5.8, $V_2O_4SO_2$ (2,4,1), $V_3O_7SO_2$ (3,7,1),

and $V_5O_{10}SO_2$

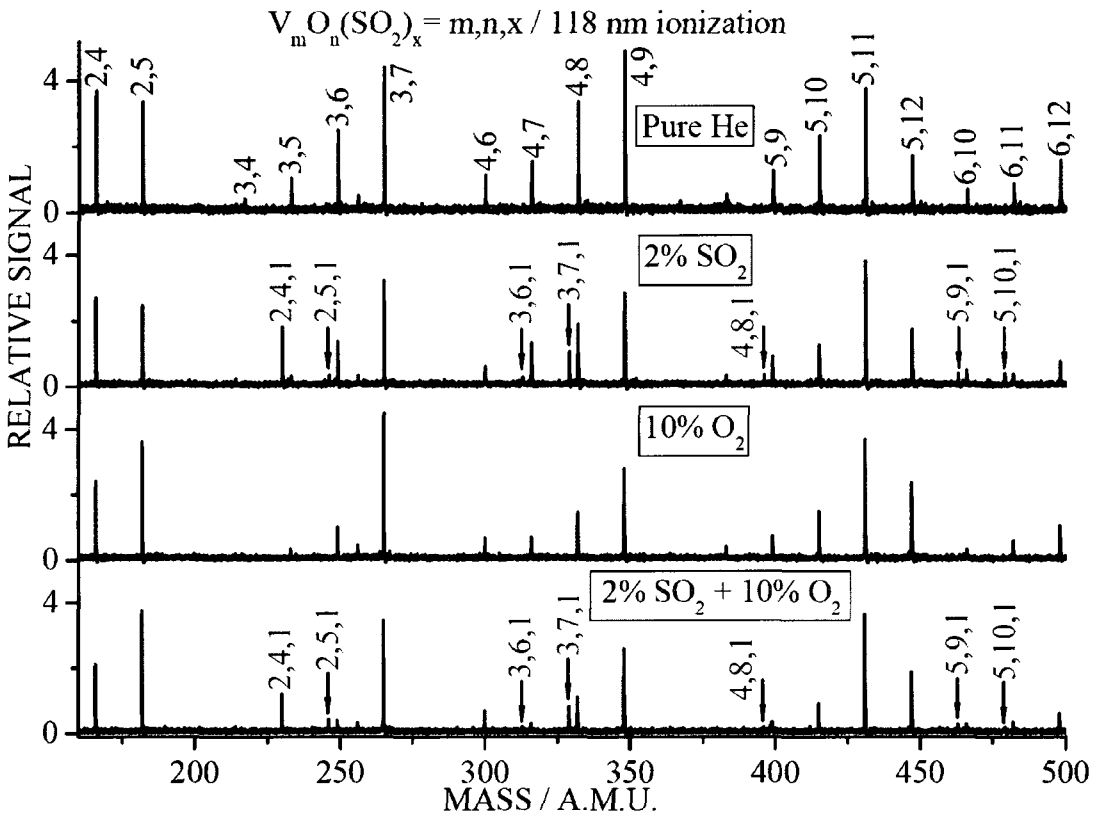


Figure 5.8: TOF mass spectra (high mass region) for reactions of V_mO_n with 2% SO_2 (top second trace), 10% O_2 (top third trace), and 2% SO_2 / 10% O_2 mixed (bottom trace) gases. A reference spectrum with no SO_2 or O_2 added in the reactant gas channel (pure He is used) is shown in the top trace.

(5,10,1) signal decreases are also evident if SO_2 is further mixed with O_2. This implies similar oxidation reactions to that given in eq. (5.6) may also occur for these association products, although O_2 itself can cause signal changes for vanadium oxide clusters (such as, V_2O_4, V_3O_7, and V_5O_{10}). The top trace of Fig. 5.9 plots simulated signal intensities for clusters and association products under conditions of cluster reactions with 2% SO_2 + 10% O_2, by using the data depicted in the top three spectra of Fig. 5.8. [i.e., (pure He spectrum) + (change made by 2% SO_2) + (change made by 10% O_2)]. In this simulation, cross reactions, such as oxidation of association products by O_2 [as in reaction (5.6)], are

not taken into account. The bottom trace re-plots the bottom spectrum in Fig. 5.8. Note that

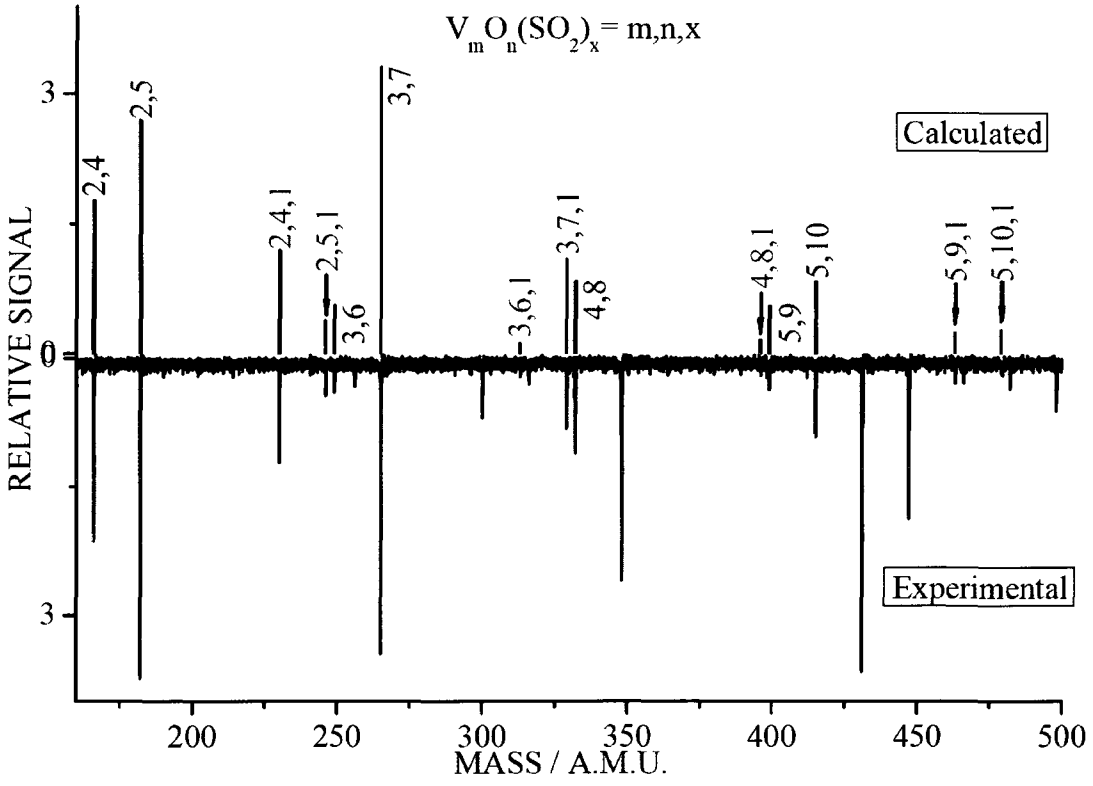


Figure 5.9: Top trace: calculated mass spectra for selected mass peaks using the top three spectra in Fig. 5.8. V_mO_n signal intensities are calculated by considering the reaction of V_mO_n with 10% O_2 followed by further reaction with 2% SO_2 (using the relative signal change for V_mO_n clusters in top second trace with respect to top trace in Fig. 5.8). $V_mO_nSO_2$ signal intensities are calculated using a fixed intensity ratio of $V_mO_nSO_2$ to V_mO_n in top second trace in Fig. 5.8. Bottom trace: re-plot of TOF spectrum shown by bottom trace in Fig. 5.8.

the simulated signals for $V_3O_7SO_2$ and $V_5O_{10}SO_2$ are significantly more intense than the observed signal, indicating that $V_3O_7SO_2$ and $V_5O_{10}SO_2$ may be further oxidized by O_2 in the fast flow reactor.

5.4 DISCUSSION

The major and new experimental and theoretical finding for these studies is the detection

and prediction of the presence of SO in the reaction of SO_2 with neutral V_mO_n clusters. As we show below in Section 5.4.1, this generation of SO from SO_2 is much more favorable for neutral V_mO_n clusters than for cationic or anionic $V_mO_n^{\pm}$ clusters. In addition, possibility of back flow of the reactant gases (SO_2, SO_2/O_2) into the cluster formation region is discussed and excluded below in Section 5.4.2. These are important points because they further support the neutral and preformed cluster origin of the reported chemistry. Possible direct detection of SO_3 is also discussed below in Section 5.4.3. The temperature issue for observing the reactivity of V_mO_n and the rate constants of V_mO_n+SO_2 reactions are discussed below in Section 5.4.4. The support of the experimental results by theoretical computations is discussed below in Section 5.4.5. The final Section 5.4.6 of this discussion presents possible correspondences between the present gas phase reactions and condensed phase reaction mechanisms for the catalytic conversion of SO_2 to SO_3 in the presence of V_2O_5 and O_2.

5.4.1 Charge transfer concern in the fast flow reactor

Neutral, cationic, and anionic particles are all generated from laser ablation and can react with the SO_2 in the fast flow reactor. An electric filed is inserted after the reactor in order to deflect ions from the molecular beam, thus, the question of charge transfer or neutralization in the reactor is addressed, since these reactions will distort the experimental results for the pure neutral cluster reactions. Exclusion of neutral product formation by ion-molecule reactions in the fast flow reactor is difficult; however, the following experimental and calculational evidence supports the neutral cluster origin of

all the observed reactions.

First, the chemistry of the neutral metal oxide clusters and anionic/cationic metal oxide clusters is obviously different. For example, the cluster distribution of cationic $V_mO_n^+$ is essentially different from the distribution of neutral V_mO_n. $V_2O_{4-8}^+$, $V_3O_{6-9}^+$, $V_4O_{8-12}^+$ species are observed as dominant in the ionic cluster distribution[5.37] while V_2O_{3-6}, V_3O_{6-8}, V_4O_{8-10} are detected in the neutral distribution.[5.26] If charge transfer occurs in the fast flow reactor, we should observe oxygen rich clusters, such as V_2O_{7-8}, V_3O_9, V_4O_{11-12}, after neutralization of cationic species in collisions with neutral clusters and other species; however, this is not the case for the present experiments.

Second, from signal decrease for reactant clusters (V_mO_n) accompanying the comparable signal increase for products ($V_mO_nSO_2$) in Figs. 5.2, 5.4 and 5.5, one can conclude that the dominant contribution to the appearance of neutral products is from neural cluster reactions. Moreover, the mass spectra presented in Fig. 5.10 show that signal intensity for V_mO_n does not decrease if C_2H_6 is seeded with the bath gas. Since $V_mO_n^+$ react with C_2H_x (x = 4, 6),[5.38] one can conclude that only little $V_mO_n^+$ is present in the ablation source relative to the neutral concentration. The ratio of ionic species to neutral species in typical ablation sources is expected to 10^{-2} to 10^{-3} based on qualitative estimates and experimental results.[5.39] Such results strongly imply that the V_mO_n/SO_2 reactions displayed in Figs. 5.2, 5.4 and 5.5 are consistent with neutral V_mO_n chemistry. Note that the reactivity of $V_mO_n^-$ is less than that of $V_mO_n^+$.[5.38]

Third, one can increase the fast flow reactor tube diameter and thereby reduce the

probability of charge transfer reactions between charged and neutral species. Such studies for $Nb_n^{0,\pm}$ and $Fe_n^{0,+}$ clusters find negligible effect for the individual cluster distributions

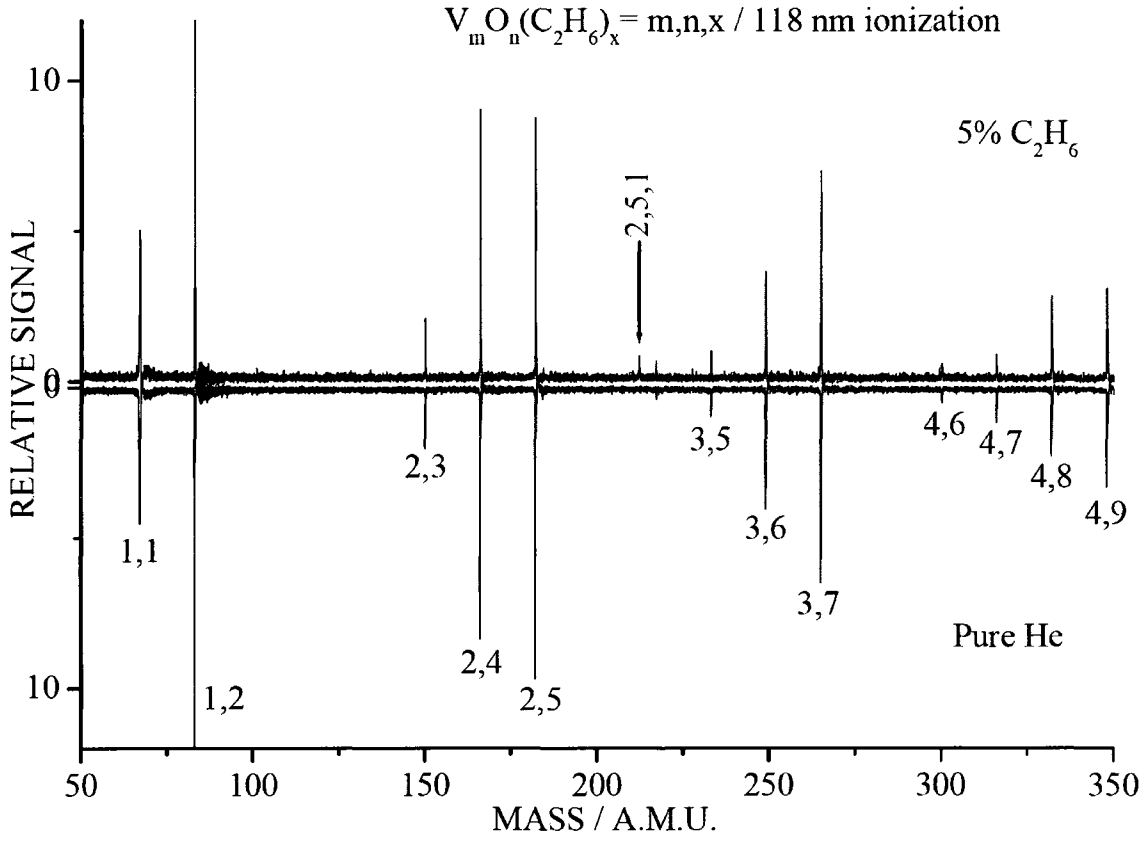


Figure 5.10: TOF mass spectra for interactions of V_mO_n with 5% C_2H_6 seeded in He (top trace) and pure He (bottom trace).

and charged clusters apparently do not influence the neutral cluster chemistry.[5.40,5.41] Possible reason for negligible ion-molecule reaction effect on neutral cluster reactivity is that many more neutral clusters than ionic clusters are present after the cluster growth process, especially in the case that the experimental conditions are optimized to produce the neutral clusters as efficiently possible.[5.39]

Fourth, we can reduce the number of charged particles entering the fast flow reactor by as much as 60% (through an electric field inserted between the cluster generation

channel and fast flow reactor) and find no change in the neutral cluster or product distribution.

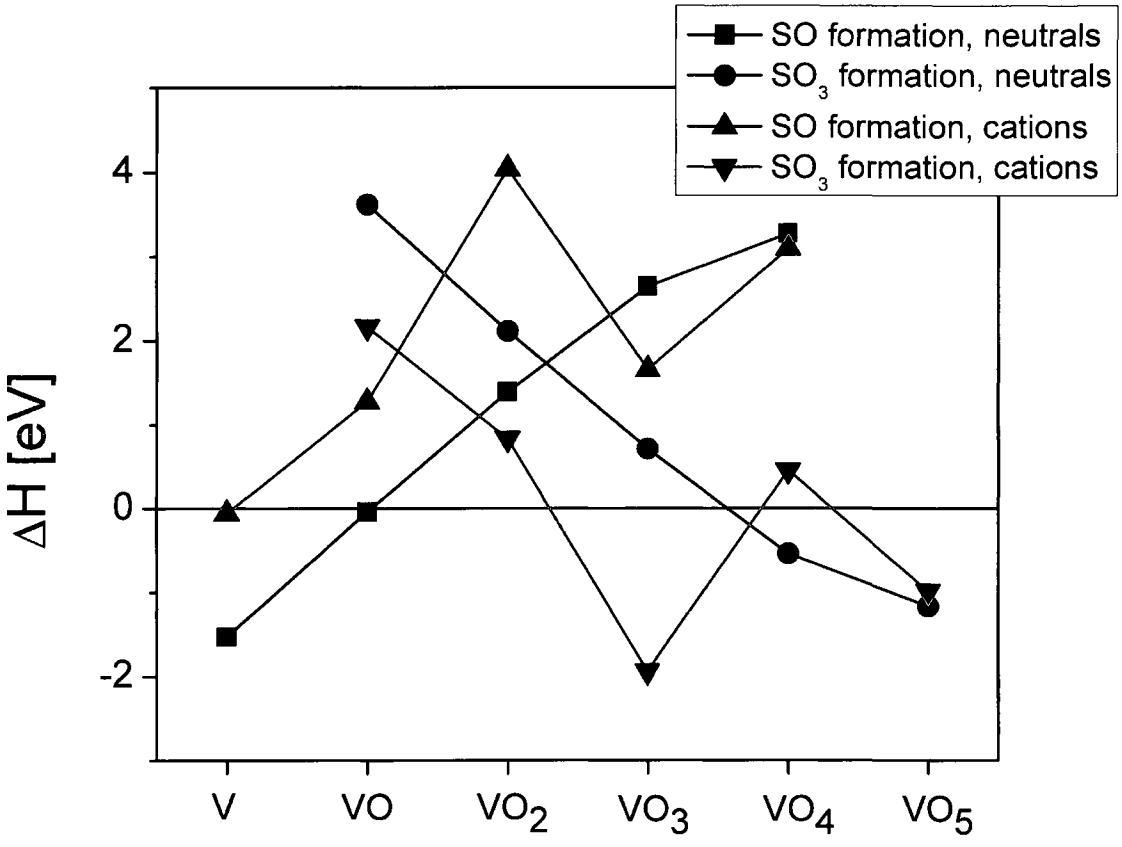


Figure 5.11: Enthalpy (at 298.15 K) for $VO_n^{0/+} + SO_2 \rightarrow VO_{n+1}^{0/+} + SO$ and $VO_n^{0/+} + SO_2 \rightarrow VO_{n-1}^{0/+} + SO_3$ reactions.

Fifth, SO formation on neutral V_mO_n clusters is thermodynamically more favorable than on the related cationic clusters. The reaction enthalpies for $VO_n + SO_2$ and $V_2O_n + SO_2$ are calculated by BPW91/LANL2DZ density functional theory coupled with experimental correction and presented in Figs. 5.11 and 5.12.[2.28] As seen from Figs. 5.11 and 5.12, isolated SO_3 product generation is favorable both on neutral VO_4, VO_5, V_2O_6,

V_2O_7 clusters and ionic VO_3^+, VO_5^+, $V_2O_5^+$, $V_2O_6^+$ clusters; however, SO formation is only favorable on neutral clusters, V, V_2O_2 and V_2O_3. Observation of the isolated SO

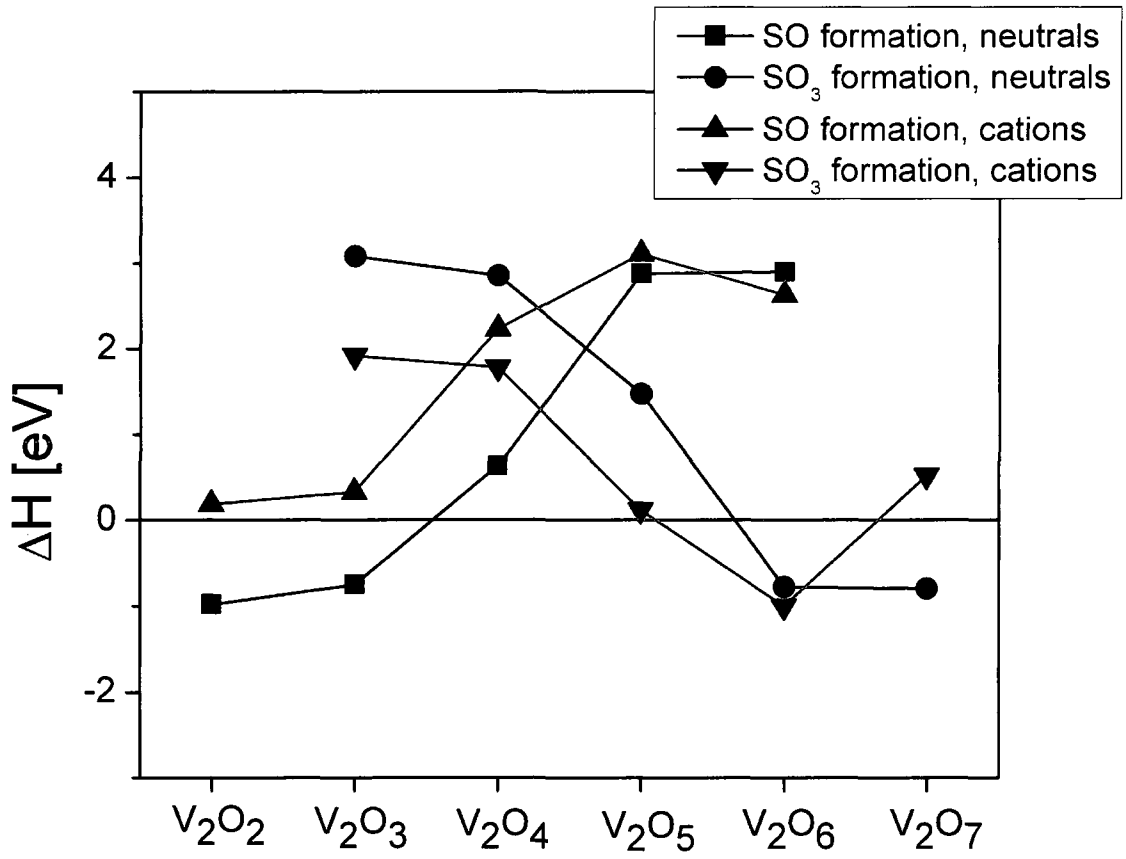


Figure 5.12: Enthalpy (at 298.15 K) for $V_2O_n^{0/+} + SO_2 \rightarrow V_2O_{n+1}^{0/+} + SO$ and $V_2O_n^{0/+} + SO_2 \rightarrow V_2O_{n-1}^{0/+} + SO_3$ reactions.

signal in Figs. 5.2 and 5.7 strongly suggests that contributions from ions in the fast flow reactor experiments are negligible.

5.4.2 Back flow concern in the fast flow reactor

One may argue that a possible problem with the experimental setup shown in Fig. 5.1 to investigate neutral cluster reactivity is the direct coupling of the fast flow reactor to the

cluster formation channel: Such connection might enable back flow of the reactant gases (SO_2, SO_2/O_2) into the cluster formation region, and as a result, the laser ablation generated plasma could react with reactant gases directly and the original cluster distribution could be changed.

To address this concern, saturated hydrocarbons, such as C_2H_6 instead of SO_2, are used as the reactant gas. The result is shown in Fig. 5.10. Considering about 10% experimental uncertainty for mass peak intensities and the weak association reaction between V_2O_5 and C_2H_6, presence of C_2H_6 in the fast flow reactor essentially causes no change of the cluster distribution. We do observe change of selective depletion of V_mO_n clusters and association products if unsaturated hydrocarbons, such as C_2H_2 and C_2H_4 are used. This result can be well interpreted as reactions of V_mO_n with the reactant gas molecules (C_2H_2 and C_2H_4) in the fast flow reactor. The details are presented in a separate publication.[5.33] Hydrocarbons, such as methane and others, are extensively used as carbon sources to produce metal carbides by reaction with laser ablation generated metal (Ti, Zr, V, Nb, ...) plasmas.[5.42] Thus, essentially no change of the V_mO_n distribution caused by C_2H_6 as shown in Fig. 5.10 implies that reactant gas back flow is not a problem in our experiments. If back flow into the cluster formation region were a problem, C_2H_6 would react strongly with vanadium plasma to produce vanadium carbides or at least change the original oxide cluster distribution if C_2H_6 gas spatially overlaps with the plasma. So we conclude that the present reactions arise from pre-formed vanadium oxide clusters with the reactant gases in the fast flow reactor. One may additionally argue that

due to residual SO_2 in the vacuum system, the surface of the used metal (V) foil can absorb SO_2 that eventually results in production and observation of sulfur containing clusters $V_mO_nSO_2$. Because signals of $V_mO_nSO_2$ disappear while signals of V_mO_n increase (due to no scattering) immediately after closing Nozzle II in the experiment, the SO_2 adsorption is not a problem. In other words, the results of the "pure He" spectra in Figs. 5.2, 5.4 and 5.5 can be re-produced no matter when the spectra are recorded; before, in between, or after the recording of the other spectra with SO_2 injected.

5.4.3 Observation of SO_3 by x-ray ionization

In the V_mO_n + SO_2 reaction, a mass peak at 80 amu is detected by 26.5 eV ionization as shown in Fig. 5.6. The intensity of this signal is related to the generation of V_mO_n clusters: when the ablation laser is blocked, meaning no V_mO_n clusters are generated, the 80 amu signal significantly decreases; however, the 80 amu signal is much broader than V_mO_n cluster signals, for example, VO_2, V_2O_4, etc, as well as that for SO. The 80 amu feature could be caused by hot molecules of SO_3, generated from exothermic reactions between V_mO_n and SO_2, or ringing on the MCP's due to a large SO_2 signal generated by 26.5 eV laser ionization. In order to clarify this issue, some experiments are carried out and the assignment of signal of 80 amu is discussed below.

1. "SO_3" (80 amu) signal is not generated from contamination of SO_2 gas.

In the study of neutral V_mO_n clusters reacting with SO_2, pure SO_2 gas is added to the fast flow reactor by a General Valve. If a weak SO_2 pulse is employed by adjusting the pulse duration and pulse intensity of the General Valve, the MCP detector is not saturated by

the SO_2 signal (~ 900 mV). Using the 26.5 eV laser for ionization, an SO_3 signal is not detected while narrow SO and SO_2 signals (35 ns) are observed in the mass spectrum.

2. 80 amu signal is not due to "ringing" of the MCP detector.

The line width of the SO_2 signal (Fig. 5.13a) becomes much broader when the pulse intensity and duration of SO_2 gas is increased as shown in Fig. 5.13b. In addition, two obvious "bumps" are observed on the high mass (right) side of the SO_2 signal. The second bump is located at mass number 80 amu, and coincides with the expected SO_3^+ (amu 80) signal. This feature could be caused by the overload of MCP detector due to too many ions of SO_2^+ generated by 26.5 eV ionization. To avoid the MCP saturation by the SO_2^+ signal, we gate the supplied voltage on the MCP to cut off the SO_2^+ signal. The MCP is gated by simply turning off the bias voltage, and then pulsing it on at a specific time after a large, unwanted signal (SO_2^+, in this case) arrives at the MCP. Nevertheless, the bump at mass number 80 does not disappear while SO_2^+ is completely removed from the mass spectrum; however, the large quantity of ions, generated from the high concentration of reactant in the molecular beam, can adhere to the MCP surface. In other words, the signal species still reaches the detector while the voltage is simply off. The presence of such a large number of ions in a short time on the detector surface may cause a "ringing" response for the detector output because of capacitance issues, arcing, or other reasons, and when the bias voltage is pulsed on, this ringing may be viewed in the mass spectrum and account for the two bumps observed in Fig. 5.6. To address this problem, we use a mass gating technique that does not allow the large number of ions to

reach the MCP; thus, SO_2^+ and other large signals in the mass spectrum, such as He^+, O_2^+, Ar^+, etc. signals, are reduced to just a few mV.

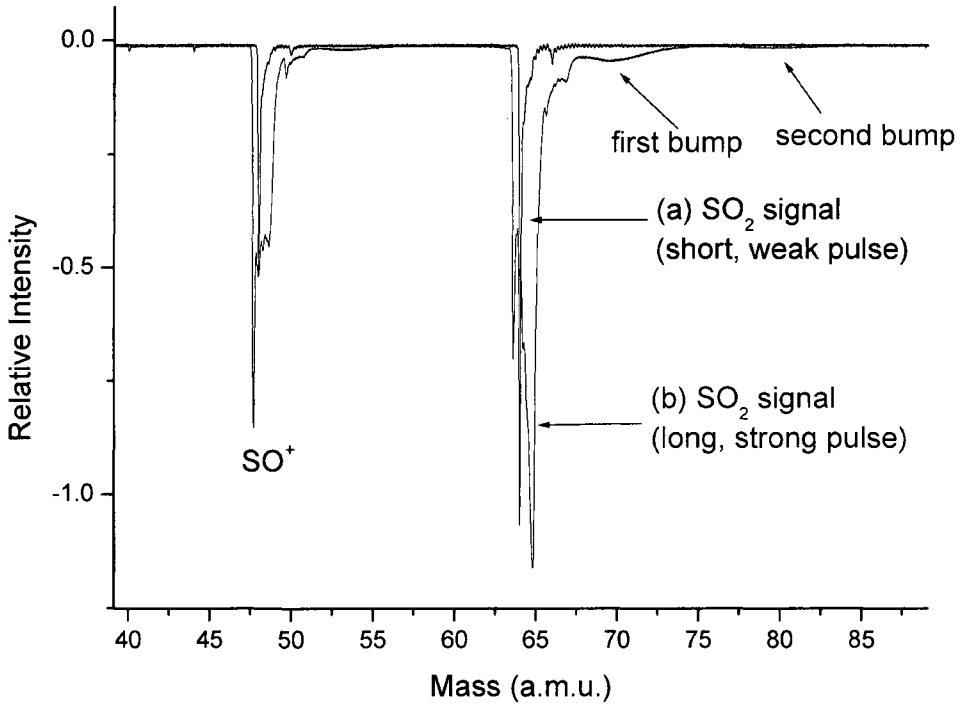


Figure 5.13: TOF mass spectra for SO_2 added in the fast flow reactor.

In the present experiments, a reflectron time of flight mass spectrometer is used to detect ion signals after the neutral clusters, reactants, and reaction products are ionized by the 26.5 eV soft x-ray laser radiation. The acceleration voltages on the three plates in the ionization region are +1000, +700 and 0 V. A mass gate is placed just before the MCP detector to block selected ions from hitting the detector by pulsing a voltage on the mass gate. A schematic drawing of the mass gate is displayed as Fig. 5.14. The three meshes are evenly spaced over approximately 1 cm, and voltages of 0, 1200, and 0 V are applied to the three meshes, respectively. The mass gate is enclosed in an aluminum box that is

held at ground potential in order to preserve the field free region of the flight tube. The middle mesh is used as the gate and is pulsed between 0 and 1200 V with a rise and fall time of 25

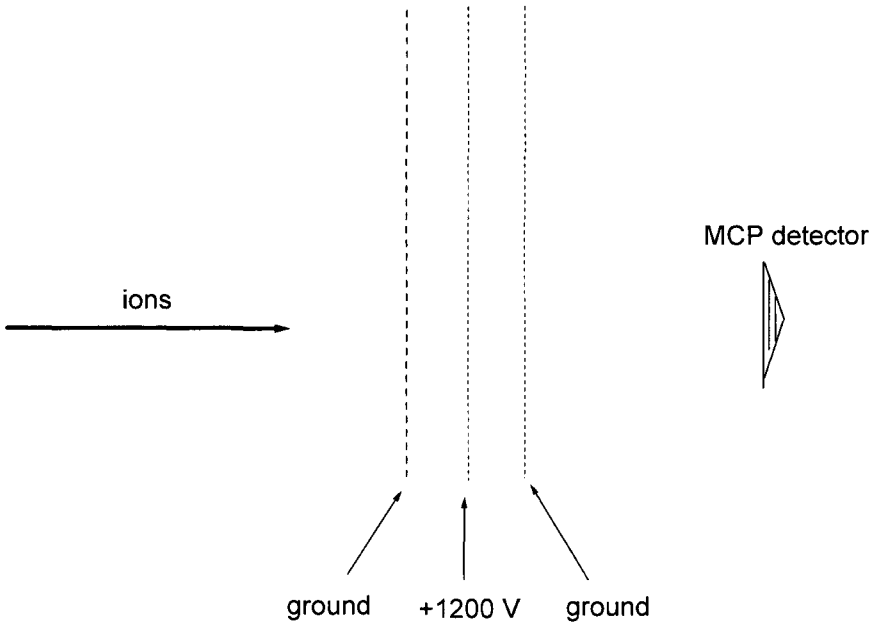


Figure 5.14: Schematic diagram for the mass gate configuration.

ns. Ions that are accelerated by 1000 V from the ionization region can not pass through the mass gate when the voltage of the middle plate is pulsed to 1200 V. The mass gate can block any mass number and any mass region by setting pulse timing and duration parameters for the voltage on the mass gate. Using this design, the shortest pulse duration on the mass gate is measured to be ~ 100 ns; one mass unit up to ~ 200 amu can be selected and blocked from the reacting clusters. In the present experiments, the mass gate is employed to block all the ions less than 70 amu including the large signals of SO_2^+, He^+, O_2^+ Ar^+, etc. The advantage of using a mass gate is that the large quantity of ions

ionized by the 26.5 eV laser are prevented from arriving at the MCP detector. Any issue caused by MCP overload, or the oscillation of the electrical circuit associated with the MCP, is thereby completely eliminated. As shown in Fig. 5.15, ion signals less than 60 amu have

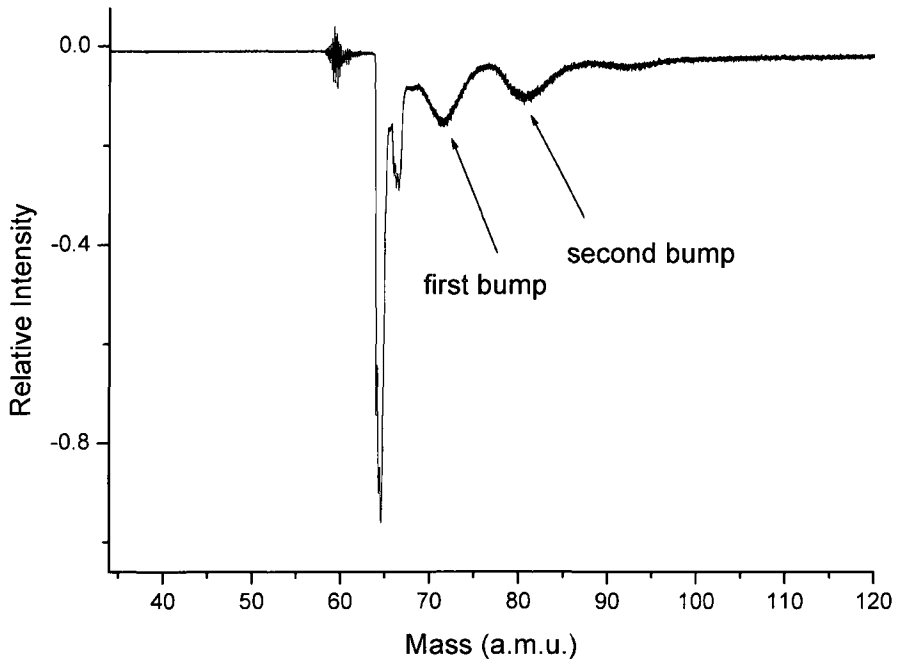


Figure 5.15: TOF mass spectra for SO_2 with the mass gate configuration

been cut by the mass gate; however, bumps on the mass spectrum are still obviously present even under these conditions if SO_2 is in the reaction cell. Therefore, one can conclude that the bumps following large signals are not caused by MCP overload or ringing of the electrical circuit. For the comparison reasons, the reactions of neutral cobalt oxide clusters with SO_2 in the fast flow reactor under the same conditions as discussed above are further investigated: the same features, including a board SO_2 mass

peak and the following bumps, are again observed in the mass spectra. What causes these bumps is not certain at present. They may be caused by a large number of photoelectrons that are generated from the ionization of a large number of neutral species (He, O_2, SO_2, etc) by the 26.5 eV laser. These photoelectrons will have more than 10 eV energy and are energetic enough to ionize most neutral species in the ionization region. Additionally, high concentrations of He, O_2, and SO_2 species create a large probability for ionization by the photoelectrons. Species ionized by photoelectrons will yield broad TOF mass features because photoelectrons generated from ionization of beam species and perhaps others are not as well localized as the focused laser light. We do not observe such features ("bumps") between 66 amu and 82 amu if SO_2 is not present in the beam or fast flow reactor. The photoelectrons may also generate ground potential fluctuations in the apparatus at these weak signal levels (ca. 1 mV).

3. SO_3 product generated from V_mO_n + SO_2 reactions.

On the basis of our calculations, SO_2 can be oxidized by oxygen rich vanadium oxide clusters, such as VO_3, V_2O_6, and V_3O_7, etc., to generate SO_3 product. We expect to detect an SO_3 signal only by 26.5 eV soft x-ray laser ionization since the ionization energy of SO_3 (13.15 eV) is higher than 10.5 eV; however, the "bump" signals after the huge SO_2 signal seriously interface with measurement of SO_3 product signal and confuse the SO_3 assignment. Additionally, only a small amount of SO_3 will be generated in the experiment because oxygen rich clusters are much less prevalent than oxygen deficient (e.g. VO, V_2O_3, V_3O_6, etc.) and the most stable clusters (e.g. VO_2, V_2O_5, V_3O_7, etc.) under the

given experimental conditions. For example, the intensity of the VO_3 signal is about 5% of the intensity of the VO_2 or VO signals in the mass spectrum. Therefore, although the SO product signal generated from oxygen deficient clusters reacting with SO_2 is readily observed in the experiments, the SO_3 product will have a low concentration in the beam and will be much harder to detect. For instance, the ratio of the VO_2SO_2 signal intensity to VO_2 is about 15% as presented in Fig. 6, and if only a 3 mV intensity of the VO_3 signal is observed, the SO_3 signal can be expected to be ca. 3*15% = 0.45 mV. Although an SO_3 product is contributed from oxygen rich clusters in general, the total signal intensity is still expected at ca. 2 mV because oxygen rich clusters are a minor component in the molecular beam even for up to 15% O_2 in the helium carrier gas. Therefore, a small SO_3 signal can be buried by the "bump" (~ 4-5 mV) following the SO_2 signal, as discussed above. Note that the feature at 80 amu is much smaller (~ 1 mV) in the absence of laser ablation. Thus we must conclude that, under the present experimental conditions, an SO_3 signal cannot be definitively identified, although such a signal is not inconsistent with, or ruled out by, the experimental observations.

5.4.4 Pick Up Cell vs. Fast flow Reactor Experiments

The observation of many association products ($V_mO_nSO_2$ in Figs. 5.2, 5.4, and 5.5) at near room temperature conditions indicates that reaction barriers for SO_2 approaching V_mO_n are quite small. Prior to the present high pressure, low temperature fast flow reactor studies, some effort was devoted to finding reactions of SO_2 with V_mO_n in a low pressure, high temperature pick up cell experimental setup, such as that successfully used by us to

study dehydrogenation of unsaturated hydrocarbons (C_2H_2, C_6H_6, ...) on metal clusters (Nb_n and Ta_n).[5.43] In the pick up cell setup, V_mO_n, formed in a supersonic molecular beam, passes through a reaction cell that contains about 1 mTorr pure SO_2 gas. This pressure is continuous and stable compared to the pulsed pressure in the fast flow reactor. In this instance, association products (or SO) are not identified, although some hard to reproduce, relative signal intensity changes for the clusters are observed, at a signal/noise ratio of ca. 1-2. This comparison implies that the collision rate (cooling and kinetics) is important for the reactions. In the fast flow setup, the instantaneous reactant gas pressure (during V_mO_n residence in the tube) is estimated[5.27] to be 14 Torr under our experimental conditions. This ensures that many collisions can occur between the initial association intermediates $V_mO_nSO_2^*$ and the bath (He) or reactant gases, which remove collisional and binding energies from $V_mO_nSO_2^*$. In a pick up cell, no such stabilization or opportunity for reaction occurs. Moreover, collisions in the expansion do not cool V_mO_n clusters (vibrational temperature is $\geq$ 700 K)[5.21] to ca. 300 K before forming $V_mO_nSO_2^*$. As a result, $V_mO_nSO_2^*$ in the pick up cell setup can quickly dissociate to regenerate reactants V_mO_n and SO_2. Another important difference between the fast flow and pick up cell setups is that more collisions between V_mO_n and SO_2 can be achieved in the fast flow reactor than in the pick up cell. Under typical conditions of 5% SO_2 in the fast flow reactor, the partial SO_2 pressure is about 700 mTorr, much higher than the SO_2 pressure (~1 mTorr) in the pick cell. In the pick up cell, the gas pressure has to be low to prevent extensive collisions that will finally destroy the original molecular beam.[5.44] Moreover,

to prevent pressure overload in mass spectrometer, the pressure in the pick up cell cannot be high because the reactant gas is continuously flowing.

By using the partial SO_2 gas pressure (700 mTorr at 5% SO_2) and estimated reaction time (50 μs), the first order depletion rate ($k_1(V_mO_n+SO_2) \equiv k_{m,n}$, in units of $10^{-13}cm^3molecule^{-1}s^{-1}$) of V_mO_n clusters in Fig. 5.4 can be estimated: $k_{2,4}$= 8.8, $k_{2,5}$= 11.6, $k_{3,6}$= 14.1, $k_{3,7}$= 9.5, $k_{4,8}$= 8.8, $k_{4,9}$= 4.0, $k_{5,11}$= 4.3, $k_{5,12}$= 2.1, $k_{6,13}$= 8.8, and $k_{6,14}$= 3.5. Because the depletion due to pure scattering is negligible (see Fig. 5.10), the above listed depletion rates can be taken as true reaction rates between V_mO_n and SO_2 under the adopted experimental conditions. Thus 1 mTorr (density ~ 3×10^{13} molecule/cm^3) SO_2 in the pick up cell (reaction time ~ 100 μs) is not sufficient to cause an observable reaction depletion of V_mO_n. For example, the reaction depletion of V_2O_5 in the pick up experimental conditions is only 0.35% based on the estimated $k_{2,5}$= 11.6×10^{-13} $cm^3molecule^{-1}s^{-1}$. The observed V_mO_n depletion in these experiments is thus mostly due to the SO_2 scattering.

5.4.5 Theoretical Computations

Our preliminary density functional theory (DFT) calculations and those expanded in part I[5.28] also support the experimental results. The calculations are performed using the Gaussian 98[5.45] and Gaussian 03[5.46] programs, the BPW91 functional,[5.47,5.48] and the LANL2DZ[5.49] and TZVP[5.50] basis sets. (see Ref. 5.28, part I for details). Cluster calculations are performed for many spin states and various isomers, typically within 20 eV of the global minimum structure and electronic state.[5.28] Many different intermediate

states for the reaction complexes are also obtained. The calculated binding energies at BPW91/TZVP level of theory between V_mO_n and SO_2 are high (typically around 2-3 eV for most stable $V_mO_nSO_2$ structures). This explains the observation of many association products, because higher binding energies provide more chance for the bath gas (He) to remove collisional and binding energies from the initial association intermediate ($V_mO_nSO_2^*$).[5.43] The Gaussian 98 program is used to investigate the reaction of VO with SO_2. The reaction pathways are followed and no overall barrier for reaction (5.1), which is thermodynamically favored by more than 1 eV according to the calculation, is found.[5.28] Calculations (using Gaussian 03 program) are specifically applied for reaction (5.2) followed by reaction (5.6). The results are schematically shown in Fig. 5.16. A large binding energy is found for VO_2 with SO_2 and the association reaction (5.2) is facile (with

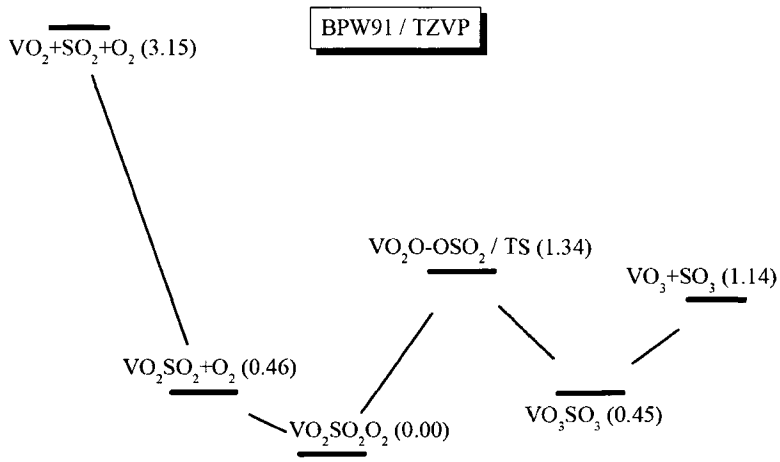


Figure 5.16: A schematic diagram showing SO_3 formation starting from three free gas molecules: VO_2, SO_2, and O_2. The values in parenthesis are relative energies in eV. Note that these calculations are performed with the Gaussian 03 suite of programs and can be different from those of Gaussian 98 by as much as ± 0.05 eV.

no barrier), in agreement with observations. VO_2SO_2 further association with O_2 is also facile, but the association energy is low. A 1.34 eV barrier is determined for the $VO_2SO_2O_2$ rearrangement to VO_3SO_3, which essentially involves the breaking of an O-O bond and the making of O_2V-O and O_2S-O bonds. The SO_3-VO_3 bond strength is 0.7 eV. The overall reaction $VO_2+SO_2+O_2 \rightarrow VO_3+SO_3$ is exothermic by 2 eV, but reaction (5.6) is endothermic by 0.7 eV and has a significant barrier (0.9 eV). Assuming these computed values are relatively accurate, if bath gas collisions do not remove all the collisional and large binding energies present in reaction (5.2), reaction (5.5) is quite possible as suggested by the experiment. Thus, this reaction channel is open if bath gas cooling is slower than reaction (5.6). Note that in general these calculations are probably correct within ±1 eV. Further discussion of additional calculation results is presented in part I.[5.28] Taking account that SO is observed as a isolated product by single photon ionization (Fig. 5.2), these calculational results also indicate that SO formation is thermodynamically favorable on neutral oxygen deficient V_mO_n (m = 1, 2, 3, 4) cluster surfaces[5.28] but unfavorable on all the cationic $V_mO_n^+$ (m = 1, 2) clusters (see Figs. 5.11 and 5.12). These calculations indicate that SO comes from neutral cluster reactions $V_mO_n + SO_2 \rightarrow V_mO_{n+1} + SO$ rather than $V_mO_n^+ + SO_2 \rightarrow V_mO_{n+1}^+ + SO$. Therefore, the theoretical calculations are in good agreement with experimental observations.

5.4.6 Possible Condensed Phase Reaction Mechanisms

The present gas phase studies suggest several molecular level SO_3 formation mechanisms for condensed phase reactions using vanadium oxides as catalysts: (M1) SO may be

formed from oxygen deficient sites by processes similar to reactions (5.1) and (5.4) as suggested by our experiments and calculations - SO_3 is formed from reaction of SO with O_2 (reaction 5.5); (M2) SO_3 may be formed from oxygen rich sites directly, as our calculations suggest that reactions of oxygen rich clusters (such as, V_2O_6, V_3O_8, V_4O_{11}, ...) with SO_2 to form SO_3 are thermodynamically favorable;[5.28] and (M3) SO_3 formation involves SO_2 association with active sites, followed by oxidation with adsorbed or free O_2. (M1) and (M2) do not necessarily address the selectivity of oxidation of SO_2 especially in the presence of vanadium oxide catalysts because any oxygen poor and oxygen rich metal oxides will tend to reduce SO_2 to SO and oxidize SO_2 to SO_3. This arises from a consideration of respective M-O, S-O, and O-O bond strengths. These mechanisms make some sense, however, if one considers that many other supported metal oxides such as Fe_2O_3, Re_2O_7, Nb_2O_5, and WO_3 are also found to be catalytic for oxidation of SO_2, although their performance is not as good as to that found for V_2O_5 catalysts.[5.7,5.51] (M1), (M2), and the catalytic cycles resulting from these mechanisms are studied in greater detail in part I.[5.28] The results indicate that the activity of a catalyst for the SO_2 oxidation to SO_3 is dependent on many issues: bond energies, reaction barriers, reaction rates, etc., not only defect sites on a surface. The (M3) mechanism may address the activity of SO_2 over vanadium oxide catalysts as opposed to other metal oxides, because the present gas phase studies indicate that binding between SO_2 and V_mO_n is strong and further oxidation of the association intermediates only has a medium (~ 1 eV) barrier as shown for the simplest example in Fig. 5.16. We have studied

the reaction of neutral iron oxide clusters (Fe_mO_n) with SO_2 with no observation of any association products, indicating relatively weak binding between Fe_mO_n and SO_2, or a high approaching barrier between them. Below, a catalytic cycle for regeneration will be presented that incorporates these initial reactions.

The apparent activation energy for oxidation of SO_2 over a supported vanadium oxide catalyst is determined to be 21±2 kcal/mol (= 0.91±0.09 eV).[5.8,5.51] Considering the fact that VO_n represents an active site for a supported V_2O_5 catalyst,[5.6,5.8,5.51] the model study shown in Fig. 5.16 may reflect a real mechanism for condensed phase catalysis; however, the activation energy (0.91±0.09 eV) is interpreted as SO_3 desorption energy in the condensed phase studies. The calculated results (Fig. 5.16) indicate that this activation energy may mainly involve O-O bond cleavage for the $VO_2O - OSO_2$ / VO_3SO_3 complex. This gas phase interpretation also agrees with the mechanism for oxidation of CO by O_2 over iron oxides: weakening of the O-O bond is a key step.[5.52]

A "strong support effect" is found for oxidation of SO_2 over supported vanadia catalysts: for example, catalysts supported on a CeO_2 surface are much more reactive than those on a SiO_2 surface.[5.6] The molecular level effect/mechanism of supports is not well understood due to complexity in the condensed phase studies.[5.3,5.6] A support can certainly modify or change the chemical or electronic properties, and even structures of the supported vanadium oxides, and thereby generate "the support effect". Molecule level consideration suggest that even the properties of vanadium oxides are little changed by the support; we may still observe the support effect due to reaction kinetics. As implied in

Fig. 5.16, reactions (5.2) and (5.6) can occur, but bath gas (He) cooling has to be efficient enough to remove energy from the initial association intermediate ($VO_2SO_2^*$). This cooling must be slow enough, however, so that part of the collisional and binding energies between VO_2 and SO_2 remain in the intermediate to overcome the barriers for the processes to form VO_3 and SO_3. In the condensed phase, controlling collisional and binding energies between supported V_mO_n and SO_2 is mediated by both surface phonons and reactant gases (SO_2/O_2). The cooling rate for surface phonons and reactant gases has to be just right so that processes similar to reactions (5.2) and (5.6) can proceed. This provides a new alternative explanation of the support dependence in condensed phase systems, as different supports should provide different molecular level cooling (vibrational energy redistribution) effects. The experiments and calculations firmly indicate that SO_2 association with most of the neutral vanadium oxide clusters is facile; this association indicates that a vanadium oxide catalyst is potentially useful for SO_2 oxidation because a catalyst should be able to coordinate the molecule that is going to be catalyzed.

The effect of energy dissipation on the surface for catalyst reactivity has never been carefully considered; the phenomenon should be considered if one wants to interpret catalysis at a molecular level. The support effect in catalysis can be very complex, such as change/modification of electronic and geometrical structure of the supported catalyst, change/modification of the structural stability, catalyst acidity and basicity, surface mobility of the supported catalyst, the increase/decrease of the number of active sites of

the catalyst, and anything that can change the reaction barriers and yields; however, at a molecular level, energy flow and redistribution within a reaction system has to be considered to interpret mechanisms of a reaction fully, including a catalytic reaction. The major point emphasized by calculations[5.28] and strongly supported by these experimental results is that the catalytic action of V_mO_n is based on the thermodynamics of SO_2/V_mO_n bond strengths and not on reaction barriers modified by special site-specific species.[5.28]

Moreover, oxygen exchange between V_2O_5 catalyst and their supports can supply more defect sites, oxygen rich/oxygen deficient, on the catalyst's surface. In this study, we find that oxidation and reduction of SO_2 can occur on oxygen rich and oxygen deficient sites, respectively, for the overall reaction of SO_2 with V_mO_n clusters.

The above discussed SO_3 formation mechanisms (M1) and (M2) have as a basic idea that both oxidation and reduction occur for generation of SO_3 from SO_2 assisted by a vanadium oxide catalyst. One of the main advantages of this type of mechanism is that it provides a "catalytic cycle" (regeneration) for the reaction. The following reactions are all possible and form three possible catalytic cycles based on (M1), (M2) and (M3) mechanisms of SO_3 formation given above. Note that in the following reactions V_mO_n is used to describe a stable site.

CATALYTIC CYCLE I: SO and SO_3 formation occur on oxygen deficient and oxygen rich sites, respectively.

1. Formation of oxygen deficient and oxygen rich sites

$$2V_mO_n \rightarrow 2V_mO_{n-1} + O_2$$

$2V_mO_n + O_2 \rightarrow 2V_2O_{n+1}$

$V_mO_n \rightarrow V_mO_{n-2} + O_2$

$V_mO_n + O_2 \rightarrow V_mO_{n+2}$

2. Reactions of oxygen deficient and oxygen rich sites with SO_2 and regeneration

$V_mO_{n-2} + SO_2 \rightarrow V_mO_{n-1} + SO$; $SO + O_2 \rightarrow SO_3$

$V_mO_{n-1} + SO_2 \rightarrow V_mO_n + SO$; $SO + O_2 \rightarrow SO_3$

$V_mO_{n+1} + SO_2 \rightarrow V_mO_n + SO_3$

CATALYTIC CYCLE II: SO and SO_3 formation occur on stable sites.

1. Reactions of stable sites with SO_2, formation of oxygen rich and oxygen deficient sites

$V_mO_n + SO_2 \rightarrow V_mO_{n-1} + SO_3$

$V_mO_n + SO_2 \rightarrow V_mO_{n+1} + SO$; $SO + O_2 \rightarrow SO_3$

2. Regeneration of stable sites

$V_mO_{n-1} + SO_2 \rightarrow V_mO_n + SO$; $SO + O_2 \rightarrow SO_3$

$V_mO_{n+1} + V_mO_{n-1} \rightarrow 2V_mO_n$

$V_mO_{n-2} + O_2 \rightarrow V_mO_n$

$2V_mO_{n-1} + O_2 \rightarrow 2V_mO_n$

$V_mO_{n+1} + SO_2 \rightarrow V_mO_n + SO$

CATALYTIC CYCLE III: SO_3 formation occurs on stable sites through oxidation by both O_2 and catalyst.

1. Formation of reaction intermediate from a stable site

$V_mO_n + SO_2 \rightarrow V_mO_nSO_2$

2. Oxidation of a reaction intermediate by O_2 and SO_3 formation

$$V_mO_nSO_2 + O_2 \rightarrow V_mO_{n+1} + SO_3$$

3. Regeneration of a stable site

$$V_mO_{n+1} + SO_2 \rightarrow V_mO_n + SO_3$$

$$2V_mO_{n+1} \rightarrow 2V_mO_n + O_2$$

Thus, even though we do not study the full catalytic cycle of the condensed phase, gas phase cluster chemistry can be employed to suggest such mechanistic processes based on observed cluster behavior and calculated mechanisms. We do not necessarily support or emphasize any one of these above mechanisms in particular: all seem possible and may well be simultaneously active or separately active under experimental conditions.

5.5 CONCLUSIONS

Due to fragmentation found for multi-photon or electron impact ionization processes, *neutral* cluster reactivity has been previously difficult to access and assess. In this work, the technique of single photon ionization is successfully employed to study the reactivity of *neutral* vanadium oxide clusters toward sulfur dioxide in the gas phase. Many association reaction intermediates $V_mO_nSO_2$, as well as reaction products SO and SO_3, are observed. Both experiments and calculations suggest that SO_2 can be reduced and oxidized by oxygen deficient and oxygen rich clusters, respectively. Further reactions of VO_2SO_2, $V_3O_7SO_2$, and $V_5O_{10}SO_2$ with O_2 are positively identified. Three SO_3 formation mechanisms (M1 – M3, see Discussion Section) are proposed. Several condensed phase catalytic cycles are suggested based on these SO_3 formation mechanisms. At the

molecular level, the importance of catalyst supports is considered to be at least associated with cooling of the active site based on observations of gas phase reactivity for pick up cell (high temperature) and fast flow reactor (low temperature) experiments. Gas phase collisions and cooling by surface phonons appear as unavoidable features for these reactions. A full understanding of oxidation of SO_2 over vanadia catalysts needs further studies of both gas and condensed phase systems. Results of the present gas phase study provide new ideas/mechanisms, such as intermediates (SO, $V_mO_nSO_2$) and oxidation of the intermediates, that may be observed and checked in investigations of the condensed phase systems.

REFERENCES

[5.1] G. Ertl, H. Knozinger, and J. Weikamp, *Handbook of Heterogeneous Catalysis* (Wiley-VCH, 1997).

[5.2] I. T. Horvath, *Encyclopedia of Catalysis* (Wiley International, 2003).

[5.3] B. M. Weckhuysen, and D. E. Keller, Catal. Today **78**, 25 (2003).

[5.4] J. L. G. Fierro, *Metal Oxides* (Taylor & Francis Group, LLC, 2006)

[5.5] R. A. van Santen and M. Neurock, *Molecular Heterogeneous Catalysis* (Wiley-VCH, 2006).

[5.6] I. E. Wachs, Catal. Today **100**, 79 (2005).

[5.7] J. P. Dunn, H. G. Stenger, Jr., and I. E. Wachs, J. Catal. **181**, 233 (1999)

[5.8] J. P. Dunn, H. G. Stenger, Jr., and I. E. Wachs, Catal. Today **51**, 301 (1999)

[5.9] I. Giakoumelou, V. Parvulescu, and S. Boghosian, J. Catal. **225**, 337 (2004)

[5.10] J. N. J. van Lingen, O. L. J. Gijzeman, B. M. Weckhuysen, and J. H. van Lenthe, J. Catal. **239**, 34 (2006).

[5.11] D. E. Keller, D. C. Koningsberger, and B. M. Weckhusen, J. Phys. Chem. B **110**, 14313 (2006).

[5.12] E. L. Muetterties, Science **196**, 839 (1977).

[5.13] M. Witko, K. Hermann, and R. Tokarz, J. Electron. Spectrosc. Relat. Phenom. **69**, 89 (1994).

[5.14] X. Lai and D. W. Goodman, J. Mol. Catal. A **162**, 33 (2000).

[5.15] J. M. Thomas, Topics in Catalysis **38**, 3 (2005).

[5.16] D. R. Justes, R. Mitric, N. A. Moore, V. Bonacic-Koutecky, and A. W. Castleman, Jr., J. Am. Chem. Soc. **125**, 6289 (2003).

[5.17] A. Fielicke, R. Mitric, G. Meijer, V. Bonacic-Koutecky, and G. van Helden, J. Am. Chem. Soc. **125**, 15716 (2003).

[5.18] N. A. Moore, R. Mitric, D. R. Justes, V. Bonacic-Koutecky, and A. W. Castleman, Jr., J. Phys. Chem. B. **110**, 3015 (2006).

[5.19] S. Feyel, D. Schroder, X. Rozanska, J. Sauer, and H. Schwarz, Angew. Chem. Int. Ed. **45**, 4677 (2006).

[5.20] S. Feyel, D. Schroder, X. Rozanska, J. Sauer, and H. Schwarz, Angew. Chem. Int. Ed. **45**, 4681 (2006).

[5.21] Y. Matsuda and E. R. Bernstein, J. Phys. Chem. **A 109**, 3803 (2005).

[5.22] Y. Matsuda and E. R. Bernstein, J. Phys. Chem. A **109**, 314 (2005).

[5.23] Y. Matsuda, D. N. Shin, and E. R. Bernstein, J. Chem. Phys. **120**, 4142 (2004).

[5.24] D. N. Shin, Y. Matsuda, and E. R. Bernstein, J. Chem. Phys. **120**, 4157 (2004).

[5.25] Y. Matsuda, D. N. Shin, and E. R. Bernstein, J. Chem. Phys. **120**, 4165 (2004).

[5.26] F. Dong, S. Heinbuch, S.-G. He, Y. Xie, J. J. Rocca, and E. R. Bernstein, J. Chem. Phys. **125**, 164318 (2006).

[5.27] M. E. Geusic, M. D. Morse, S. C. O'Brien, and R. E. Smalley, Rev. Sci. Instrum. 56, 2123 (1985).

[5.28] E. Jakubikova and E. R. Bernstein, J. Phys. Chem. A, 111, 13339 (2007).

[5.29] Y. Xie, S.-G. He, F. Dong, and E. R. Bernstein, J. Chem. Phys. 128, 044306 (2008).

[5.30] D. N. Shin, Y. Matsuda, and E. R. Bernstein, J. Chem. Phys. **120**, 4150 (2004).

[5.31] F. Dong, S. Heinbuch, J. J. Rocca, and E. R. Bernstein, J. Chem. Phys. **124**, 224319 (2006).

[5.32] J. J. Rocca, Rev. Sci. Instrum. 70, 3799 (1999).

[5.33] F. Dong, S. Heinbuch, Y. Xie, J. J. Rocca, E. R. Bernstein, Z. Wang, K. Deng and S.-G. He, J. Am. Soc. Soc. 130, 1932 (2008).

[5.34] K. B. Snow and T. F. Thomas, Int. J. Mass Spectrom. Ion Processes 96, 49 (1990).

[5.35] G. Black, R. L. Sharpless, and T. G. Slanger, Chem. Phys. Lett. **90**, 55 (1982).

[5.36] N. L. Garland, Chem. Phys. Lett. **290**, 385 (1998).

[5.37] R. C. Bell, K. A. Zemski, K. P. Kerns, H. T. Deng and A. W. Castleman Jr, J. Phys. Chem. A, **102**, 1733 (1998)

[5.38] K. A. Zemski, D. R. Justes, and A. W. Castleman Jr, J. Phys. Chem. A, **105**, 10237 (2001).

[5.39] K. Bowen, personal communication to ERB.

[5.40] M. R. Zakin, R. O. brickman, D. M. Cox and A. Kaldor, J. Chem. Phys. **88**, 3555 (1988)

[5.41] M. R. Zakin, R. O. brickman, D. M. Cox and A. Kaldor, J. Chem. Phys. **88**, 6605 (1988)

[5.42] B. D. Leskiw and A. W. Castleman Jr., C. R. Physique **3**, 251 (2002), and references therein.

[5.43] S.-G. He, Y. Xie, and E. R. Bernstein, J. Chem. Phys. **125**, 164306 (2006).

[5.44] M. Andersson, J. L. Persson, and A. Rosén, J. Phys. Chem. **100**, 12222 (1996).

[5.45] M. J. Frisch, G. W. Trucks, H. B. Schlegel, et al.; Gaussian 98, Revision A.11; Gaussian, Inc.: Pittsburgh PA, 2001.

[5.46] M. J. Frisch, G. W. Trucks, H. B. Schlegel, et al.; Gaussian 03, Revision C.02; Gaussian, Inc.: Wallingford CT, 2004.

[5.47] A. D. Becke, Phys. Rev. A **38**, 3098 (1988).

[5.48] J. P. Perdew and Y. Wang, Phys. Rev. B **45**, 13244 (1991).

[5.49] P. J. Hay and W. R. Wadt, J. Chem. Phys. **82**, 270 (1985)

[5.50] A. Schaefer, C. Huber, and R. Ahlrichs, J. Chem. Phys. **100**, 5829 (1994).

[5.51] J. P. Dunn, H. G. Stenger, Jr., I. E. Wachs, Catal. Today **53**, 543 (1999).

[5.52] B. V. Reddy, F. Rasouli, M. R. Hajaligol, and S. N. Khanna, Chem. Phys. Lett. **384**, 242 (2004).

Chapter 6

Reactions of Methanol and Ethanol with Neutral Vanadium Oxide Clusters

6.1 REACTIONS OF NEUTRAL VANADIUM OXIDE CLUSTERS WITH METHANOL AND ETHANOL

Transition metal oxides are important heterogeneous catalysts and their properties and reactions have been the subject of numerous studies.[6.1] The oxidation of methanol is interesting because of its importance in catalytic processes[6.2,6.3]; for example, oxidative reforming of methanol is an important catalytic process in fuel cells.[6.4] Selective oxidation of methanol on supported vanadium oxide catalysts has been considered as a simple probe reaction for a number of other selective oxidation reactions.[6.5,6.6] The major product of methanol oxidation over V_2O_5 is found to be formaldehyde, with minor products of dimethyl ether, etc.[6.7] The mechanism for oxidation of methanol on supported vanadium oxide is suggested to be methanol oxidation by the catalyst, and not by gas phase molecular O_2.[6.8] In this case, O_2 molecules are used to oxidize the reduced V^{+4} or V^{+3} sites back to active V^{+5} sites. In situ Raman and UV-visible measurements reveal that the catalytically active sites are fully oxidized surface VO_4 sites.[6.9,6.10] Three different V-O functionalities, terminal V=O, bridging V-O-V, and bridging V-O-support bonds, are identified for the surface of supported vanadium oxide in the catalytic methanol oxidation process.[6.11-6.13] In some studies, terminal V=O are considered to

be the active sites,[6.14-6.17] and in others, bridging V-O-V are considered to be the active sites.[6.18] Recently, Wachs et al. suggested that the bridging V-O-support bond contributes to methanol oxidation.[6.3,6.19] Although an extensive research effort over last two decades to explore the process of methanol oxidation in the condensed phase has been undertaken, a fundamental understanding of these catalytic reactions at an atomic and molecular level is still lacking. The complicated catalytic surface process is still difficult to interpret fully.

Gas phase metal/metal oxide clusters and their reactions with small molecules are considered to be a model system for active sites of condensed/surface phase chemistry. Clusters generated in gas phase have relatively well defined structures, size dependent properties, and they are relatively accessible by theoretical calculations. A full understanding of reaction behavior of gas phase clusters can, in principle, provide insight into the mechanism of practical catalyst systems. [6.20]

The reactivity of vanadium/niobium/tantalum oxide cluster ions toward methanol has been studied in the gas phase using mass spectrometric techniques.[6.21-6.24] The reactions of mass selected M^+ and MO^+ (M=V, Nb and Ta) with CH_3OH have been studied by Tang and co-workers[6.21] using Fourier transform ion-cyclotron resonance (FT-ICR) mass spectrometry coupled with a laser ablation ion source. In their experiments, $VO_2CH_4^+$, $VOCH_2O^+$ and VO_2^+ are detected as the main products of the reaction VO^+ + CH_3OH; some secondary reaction products $V(OCH_3)_2^+$ and $V(OH)_2^+$ are also observed. Employing a guided ion beam mass spectrometer, Castleman et al. studied the reactions of methanol with $V_mO_n^+$ and $Nb_mO_n^+$ cluster ions.[6.22] The products observed in their experiments are H_2, CH_3, CH_3OH, and C_2H_6O attached to mass selected cluster ions.

Recently, Schwarz's group[6.23a] published a comprehensive study of $V_mO_n^+$ and $V_mO_{n-1}(OH)^+$ (m = 1-4, n = 1-10) cluster ion reactivity toward methanol using a mass spectrometric technique coupled with an electrospray ion source. Several reaction channels are identified in their experiments: abstraction of a hydrogen atom, a methyl radical or a hydroxymethyl radical, elimination of methane, and adduct formation. Formaldehyde is produced via four different pathways. In another experiment, Schwarz et al.[6.23b] studied reactions of methanol with mass selected V^+, VOH^+, VO^+, and VO_2^+ cations by FT-ICR mass spectrometry with an ablation ion source. Oxidation state of the metal is a key factor which determines the reactivity of the cluster. Most experiments in the gas phase explore the reactivities of metal oxide cluster ions with methanol. Additionally, theoretical studies are employed to elucidate the mechanisms of these ion-molecule reactions between metal/metal oxide cluster ions and methanol.[6.21,6.23b,6.25-6.27] Partial charge transfer between metal oxide clusters and support materials (either bulk or surface) may play an important role in catalytic processes in the condensed phase. On the other hand, gas phase studies of neutral clusters can provide useful information that can assist one in the analysis of condensed phase catalysis systems. Neutral clusters generally exhibit significantly different reactivity than ionic clusters.[6.27-6.31]

Recently, our group has employed a new desk-top, 26.5 eV/photon (46.9 nm), soft x-ray laser coupled with time of a flight mass spectrometer (TOFMS) to study gas phase neutral metal oxide clusters and their reactions.[6.32] With this ionization source, all neutral cluster species and their reaction products can be ionized and detected. In the study of vanadium oxide clusters reacting with C_2 hydrocarbons, we found that the double bond of C_2H_4 can be broken by neutral oxygen rich vanadium oxide clusters

($V_xO_{y+1,2,...}$). In the present work, reactions of neutral vanadium oxide clusters with methanol and ethanol are studied. Four kinds of reactions are identified employing CH_3OH and deuterated (CD_3OH) methanol. The mechanisms for the reactions V_mO_n + CH_3OH/CD_3OH are discussed in detailed.

6.2 EXPERIMENTAL PROCEDURES

The reactions of neutral vanadium oxide clusters with methanol/ethanol are investigated using a time of flight mass spectrometer (TOFMS) coupled with single photon ionization by a desk-top 26.5 eV soft x-ray laser. Since the experimental apparatus has been described in detail elsewhere,[6.33] only a general outline of the experimental scheme will be presented in this report. Briefly, neutral vanadium oxide clusters are generated in a conventional laser vaporization/supersonic expansion source. A 532 nm wavelength laser (second harmonic of a Nd/YAG laser, 1064 nm) is employed to ablate a target of vanadium metal foil (99.7%, Aldrich) at 10-20 mJ/pulse. A mixture of 0.5% O_2 and He is used as a carrier/reaction gas at 80 psig for the generation of V_mO_n neutral species. The reactant gas, formed by flowing He (99.9%) through a reservoir containing methanol/ethanol (CH_3OH and C_2H_5OH are spectroscopic grade, deuterated CD_3OH is 99.8 atom % D, Aldrich) at a pressure of 15 psi, is pulsed into the reactor tube located ~ 20 mm downstream from the exit of the expansion channel. The instantaneous reactant gas mixture pressure in the reactor cell is about 1 Torr in this set up. In this design, the flow tube reactor (70 mm length, ∅ 6 mm) is coupled directly to the cluster formation channel (40 mm length, ∅ 1.8 mm). After the flow tube reactor, the ions created in the ablation source and flow tube reactor are removed by an electric field. Vanadium oxide clusters generated from the ablation source react with reactant gases in the flow tube

reactor.[6.34] Neutral clusters and reaction products pass through a 4 mm skimmer into the ionization region of a time of flight mass spectrometer (TOFMS Wiley-McLauran design, R.M. Jordan Co.), where these neutral species are ionized by the focused soft x-ray laser.[6.35]

The soft x-ray laser (26.5 eV/photon energy) emits pulses of about 1 ns duration with an energy/pulse of 10 μJ at a repetition rate of up to 12 Hz. A pair of gold coated mirrors, a torodial and a plane mirror, is placed in a grazing incidence Z-fold configuration just before the ionization region of the TOFMS to provide alignment and focusing capabilities for the laser with respect to the molecular beam at the ionization region. The transmissivity of the Z-fold mirror system is about 40%. Soft x-ray laser light is not tightly focused in the ionization region to avoid multiphoton ionization and a space charge Coulomb effect due to He^+ ions. A large number of He^+ ions can be produced by 26.5 eV ionization of He in the molecular beam, and these could broaden the V_mO_n, etc. mass spectral features. Since a 26.5 eV photon from the EUV laser is able to ionize the He carrier gas employed in the expansion, the microchannel plate (MCP) ion detector voltage is gated to reduce the MCP gain when He^+ arrives at the mass detector, in order to prevent detector circuit overload and saturation. 118 nm laser light is generated by focusing the third harmonic (355 nm, ~30 mJ/pulse) of a Nd:YAG laser in a tripling cell that contains about a 250 Torr argon/xenon (10/1) gas mixture. To separate the generated 118 nm laser beam from the 355 nm fundamental beam, a magnesium fluoride prism (apex angle = 6 deg), which was not employed in our previous studies,[6.36] is inserted into the laser path. In this case, one is quite sure that mass signals are generated by ionization purely through the VUV laser radiation at low power (~1 μJ/pulse, pulse

duration ~5 ns).

6.3 EXPERIMENTAL RESULTS

6.3.1 Reactions of V_mO_n clusters with CH_3OH

Figure 6.1 displays mass spectra, generated by 26.5 eV (46.9 nm) single photon ionization from a soft x-ray laser, of reactants and products for the reaction of V_mO_n clusters with CH_3OH. Neutral vanadium oxide clusters are generated at low oxygen concentration conditions (0.5% O_2/He expansion). In the present paper, the formula V_mO_n is used to represent general vanadium oxide clusters. The predominant signals are identified as reactants VO_2, V_2O_4/V_2O_5, V_3O_7, V_4O_{10}, V_5O_{12}, etc., as shown in the lower spectra of Figures 6.1 (a), (b) and (c), for different cluster size regions. These vanadium

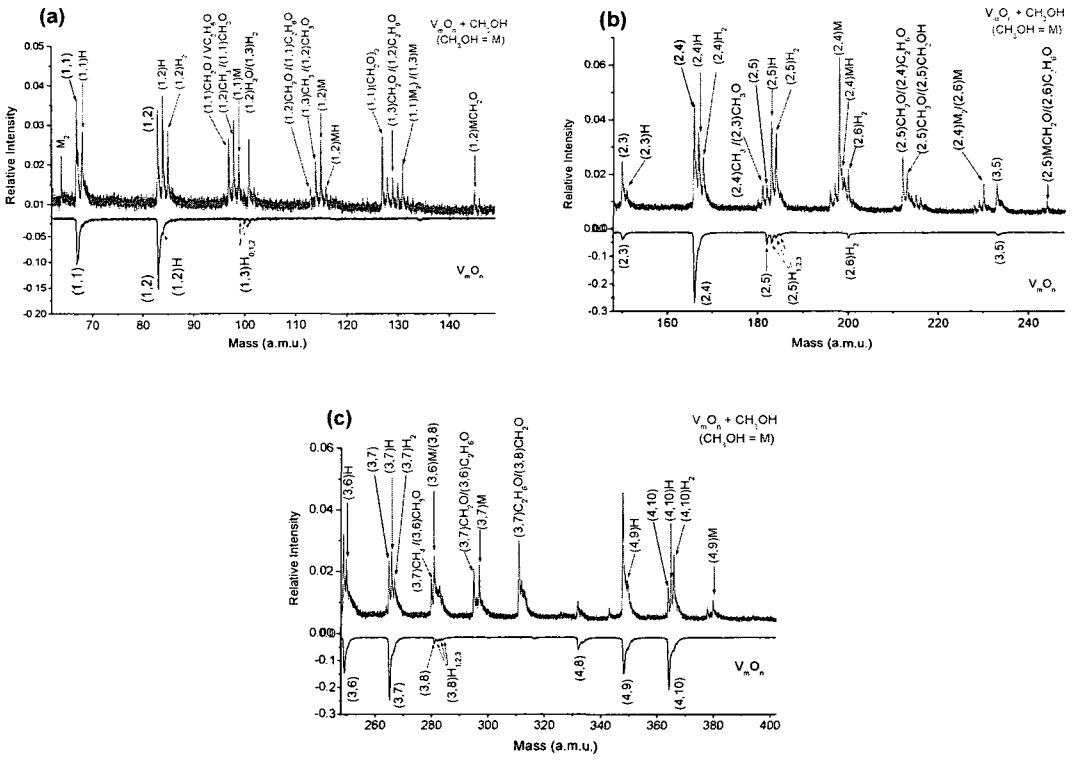


Figure 6.1: Reactions of V_mO_n clusters with CH_3OH studied by 26.5 eV soft x-ray laser ionization. The lower spectrum displays the V_mO_n cluster distribution generated by a 0.5% O_2/He expansion gas; the upper spectrum displays the new cluster distribution and products of the V_mO_n + CH_3OH reaction after CH_3OH/He is added to the flow tube reactor. Expanded mass regions around different size clusters are shown in (a), (b) and (c).

oxide clusters (labeled as V_xO_y) have the most stable stoichiometric structures as demonstrated experimentally and theoretically.[6.33a,6.37,6.38] A number of oxygen deficient vanadium oxide clusters (V_xO_{y-z}: VO, $V_2O_{2,3}$, $V_3O_{5,6}$, $V_4O_{8,9}$, $V_5O_{9,10,11}$, and $V_6O_{13,14}$) are observed in the cluster distribution. They are missing one or two oxygen atoms compared to the most stable clusters, and present a tendency to become the most stable clusters by reacting with O or O_2.[6.38] Some oxygen rich clusters (V_xO_{y+1}: VO_3, V_3O_8, and V_5O_{13}, etc.) are also observed in the mass spectra. They have one or more oxygen atoms compared to the most stable clusters, and present a tendency to lose O or O_2 and become the most stable clusters.[6.38] Additionally, one can find that these oxygen rich neutral vanadium oxide clusters are always present with one or more attached hydrogen atoms, such as VO_3H_2, $V_2O_6H_2$, $V_3O_8H_{1,2}$, etc.[6.33a]

To study reaction of neutral V_mO_n clusters with methanol, mixed CH_3OH/He gas is pulsed into the reactor at a pressure of 10 ~ 15 psi. When the neutral vanadium oxide clusters generated from the ablation/expansion source pass through the reactor cell, collisions will occur between neutral V_mO_n clusters and CH_3OH molecules. The instantaneous reactant gas pressure in the reactor cell (during the time that V_mO_n is in the cell) is estimated to be about 1 Torr. New reaction products and the remnant neutral V_mO_n clusters are detected by a 26.5 eV laser ionization. As shown in Figure 6.1, several kinds of main products are identified for the reactions V_mO_n + CH_3OH.

First, association products, $VO(CH_3OH)_{1,2}$, VO_2CH_3OH, $V_2O_4(CH_3OH)_{1,2}$, $V_3O_6CH_3OH$, and $V_3O_7CH_3OH$ etc, are observed, and they are generated from simple association reactions. Second, a series of products VOH, $VO_2H_{1,2}$, $V_2O_4H_{1,2}$, $V_2O_5H_{1,2}$, V_3O_6H, and $V_3O_7H_{1,2}$ is identified in the mass spectra. They can be generated by the

abstraction of hydrogen from CH_3OH molecules. Note that oxygen deficient clusters (VO, V_2O_3, V_3O_6) can extract only one hydrogen atom from CH_3OH to from VOH, V_2O_3H, V_3O_6H, and V_4O_9H, while the clusters with the most stable stoichiometry (VO_2, V_2O_4, V_2O_5, and V_3O_7) can extract two hydrogen atoms from CH_3OH molecules to form $VO_2H_{1,2}$, $V_2O_4H_{1,2}$, $V_2O_5H_{1,2}$, and $V_3O_7H_{1,2}$. Oxygen rich vanadium oxide clusters (VO_3, V_2O_6, V_3O_8, etc.) can extract more than one hydrogen atom from methanol to form clusters, such as VO_3H_2, $V_2O_6H_2$, and $V_3O_8H_{1,2,3}$ (Figure 6.1). These hydrogen attached oxygen rich clusters also appear in pure unreacted transition metal (V, Nb, and Ta) oxide cluster distributions.[6.33a] Any trace of H_2O, hydrocarbons, H_2, etc. absorbed in or on the metal, or surface OH in the experimental system can be a hydrogen source due to the high reactivity of oxygen rich clusters, in general.

The third variety of products observed in V_mO_n + CH_3OH reactions is $V_mO_n(CH_3OH)_{0,1}CH_2O$; for example, $VOCH_2O$, VO_2CH_2O, $VO_2(CH_3OH)CH_2O$, VO_3CH_2O, $V_2O_5CH_2O$, $V_2O_5(CH_3OH)CH_2O$, $V_3O_6CH_2O$, $V_3O_7CH_2O$, etc. These species can be generated from intramolecular dehydrogenation or intracluster dehydration reactions. The product $V_mO_nCH_2O$ can also be formulated as isomeric $V_mO_{n-1}C_2H_6O$; for example, VO_2CH_2O has the same mass number as VOC_2H_6O, and similar isomeric pairs can be noted for $VO_3CH_2O/VO_2C_2H_6O$, $V_2O_5CH_2O/V_2O_4C_2H_6O$, $V_3O_7CH_2O/V_3O_6C_2H_6O$, etc. (shown in Figure 6.1). They are considered to be the fourth type of product in V_mO_n + CH_3OH reactions. $V_mO_{n-1}C_2H_6O$ may be generated from an intermolecular dehydration reaction; however, it is impossible to distinguish $V_mO_nCH_2O$ from $V_mO_{n-1}C_2H_6O$ in methanol (CH_3OH) experiments. Additionally, some minor products $VO_2CH_3/VOCH_3O$, VO_3CH_3/VO_2CH_3O, $V_2O_4CH_3/V_2O_3CH_3O$, and

$V_3O_7CH_3/V_3O_6CH_3O$ are detected in the mass spectrum of Figure 6.1. We will discuss reaction mechanisms in detail in the Discussion Section.

Methanol clusters are easily formed in the molecular beam, so a weak signal of the $(CH_3OH)_2$ dimer relative to CH_3OH signal is detected (Figure 6.1) when the gas mixture CH_3OH/He is pulsed into the reactor tube. The huge signal for CH_3OH is truncated by adjusting the timing of the MCP detector turn on to prevent detector circuit overload and saturation. One knows that the $(CH_3OH)_2H^+$ signal is always observed after the ionization of the neutral trimer $(CH_3OH)_3$[6.33e], so no observation of protonated $(CH_3OH)_nH^+$ ($n \geq 2$) in the mass spectrum indicates that methanol clusters are not prevalent under these experimental conditions. Therefore, reactions between V_mO_n and methanol clusters can be neglected in our experiments.

The reaction of V_mO_n + CH_3OH is also studied using 118 nm laser ionization. As shown in Figure 6.2, most of the products observed are similar to those detected by 26.5 eV ionization, with the exception of some neutral oxygen rich vanadium oxide clusters and products with high ionization energy, such as $V_2O_6H_2$, that are not present in the 118 nm spectra.

6.3.2 Reactions of V_mO_n clusters with CD_3OH

Isomers as suggested above can not be distinguished in the mass spectra of Figure 6.1: $V_mO_nCH_2O$ have the same mass number as $V_mO_{n-1}C_2H_6O$, and $VO(CH_3OH)_2$ has the same mass number as VO_3CH_3OH since the mass number of CH_3OH is equal to molecular O_2. Therefore, the reaction channels for V_mO_n + CH_3OH reactions can not be completely resolved in the mass spectra of Figure 6.1. In order to distinguish the isomers produced in the reactions of V_mO_n + CH_3OH, deuterated methanol (CD_3OH) is employed

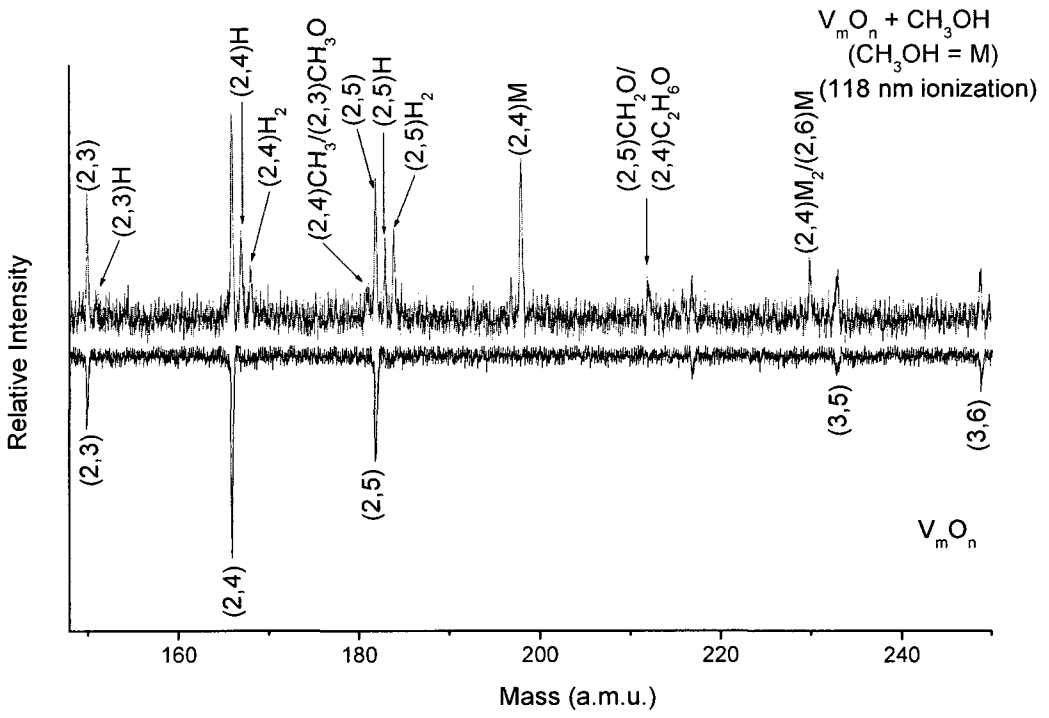


Figure 6.2: Reactions of V_mO_n clusters with CH_3OH studied by 118 nm (10.5 eV) laser ionization. The products detected by 10.5 eV laser are similar to those detected by 26.5 eV soft x-ray laser ionization shown in Figure 6.1(b).

in the reaction mixture instead of CH_3OH. Figures 6.3(a), (b) and (c) present the mass spectra obtained under the same experimental conditions as described above except CD_3OH is substituted for CH_3OH. Products $VOCD_3OH$, VO_2CD_3OH, $V_2O_4CD_3OH$, $V_3O_6CD_3OH$, and $V_3O_7CD_3OH$ are assigned to association products between V_mO_n and CD_3OH. In experiments with CD_3OH, no significant peaks at V_2O_3H, V_3O_5H, and V_3O_6H are observed (see Figure 6.3 (b,c)); VOH is, however, observed. These V_mO_nH signals can be distinguished from their neighbor V_2O_3, V_3O_5, and V_3O_6 signals even though they partly overlap each other. One knows that mass resolution will decrease with increasing mass number; however, one mass unit can readily be resolved between V_2O_4D and V_2O_4DH, V_2O_5H and V_2O_5D/H_2, $V_2O_6H_2$ and $V_2O_4CD_3OH$, etc. Therefore, the signals of

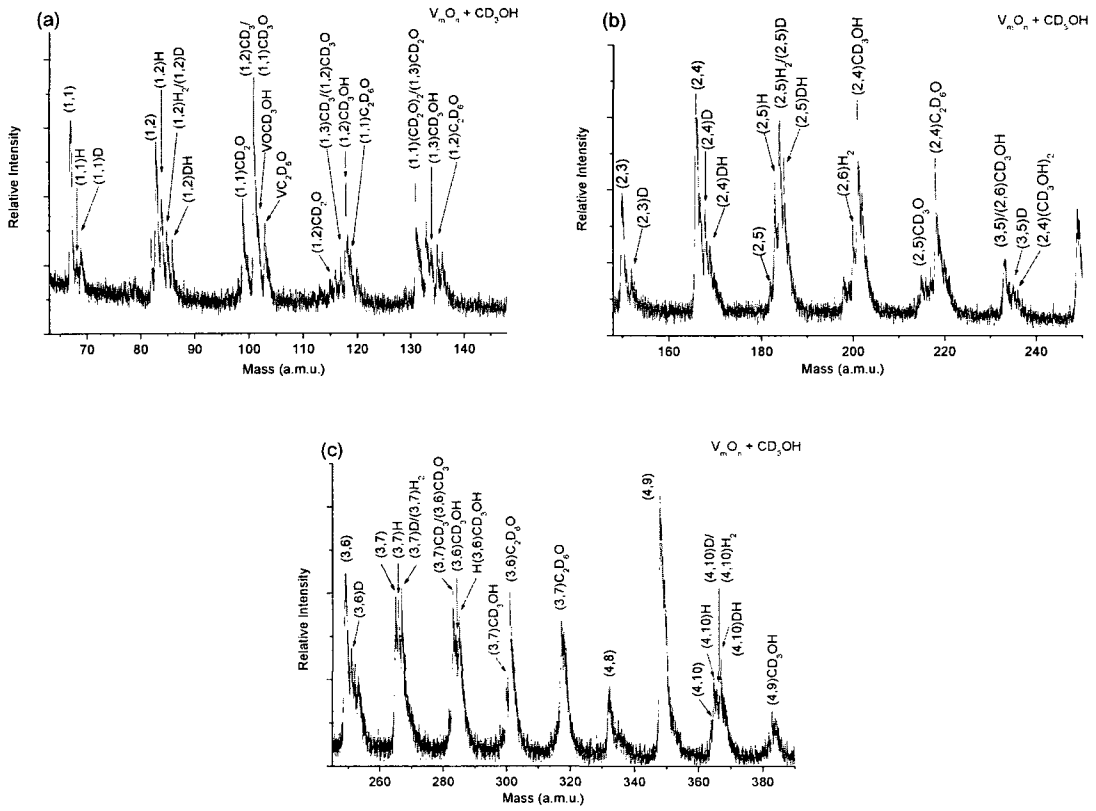


Figure 6.3: Reactions of V_mO_n clusters with CD_3OH studied by 26.5 eV soft x-ray laser ionization. The mass spectrum is obtained under the same experimental conditions as given in Figure 6.1 except that CD_3OH is substituted for CH_3OH. Expanded mass regions around different size clusters are shown in (a), (b) and (c).

VOD, V_2O_3D, V_2O_4D, V_3O_5D, V_3O_6D are identified as the major products of hydrogen abstraction reactions for oxygen deficient vanadium oxide clusters reacting with CD_3OH, while $VO_2H_{0,1}D/VO_2H_{1,2}$, $V_2O_5H_{0,1}D/V_2O_5H_{1,2}$, $V_3O_7H_{0,1}D/V_3O_7H_{1,2}$, $V_4O_{10}H_{0,1}D$ $/V_4O_{10}H_{1,2}$ are identified for stable vanadium oxide clusters reacting with CD_3OH. In the reactions of V_mO_n + CH_3OH, isomeric products $V_mO_nCH_2O$ and $V_mO_{n-1}C_2H_6O$ have the same mass number (in Figure 6.1); however, they are distinguishable as two separated products $V_mO_nCD_2O$ and $V_mO_{n-1}C_2D_6O$ with different mass numbers for V_mO_n + CD_3OH reactions. Both $VOCD_2O$ and VC_2D_6O are observed in Figure 6.3(a), while $V_2O_4C_2D_6O$, $V_3O_6C_2D_6O$, and $V_3O_7C_2D_6O$ are observed in Figures 6.3(b) and (c). Products

$V_2O_4C_2H_6O$, $V_3O_6C_2H_6O$, and $V_3O_7C_2H_6O$ rather than $V_2O_5CH_2O$, $V_3O_7CH_2O$, and $V_3O_7C_2H_6O$ are thus confirmed for the reactions V_mO_n + CH_3OH. Products $V_mO_nCH_2O$ and $V_mO_{n-1}C_2H_6O$ can be generated by a different reaction mechanism that will be discussed below in the next section.

6.3.3 Reactions of V_mO_n clusters with C_2H_5OH

Another alcohol compound, ethanol C_2H_5OH, is also used as a reactant with V_mO_n clusters. When C_2H_5OH/He gas is added to the reactor, many new product signals are observed in the mass spectra associated with reactions between V_mO_n and C_2H_5OH. As shown in Figure 6.4, the major products observed are association adducts $V_mO_n(C_2H_5OH)H_{0,1,2}$. $VOCH_3CHO$ is the only detected signal that is generated from a hydrogen elimination reaction for V_mO_n + C_2H_5OH, implying that different reaction mechanisms must responsible for V_mO_n cluster reacting with CH_3OH and reacting with C_2H_5OH.

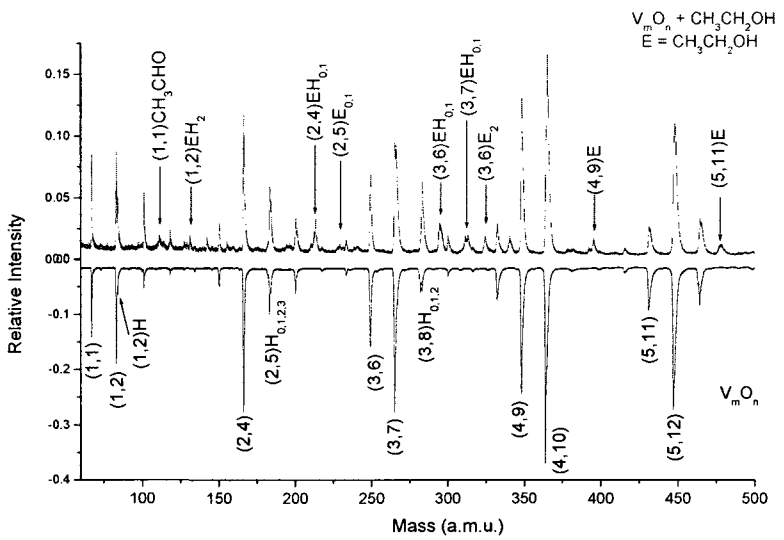


Figure 6.4: Reactions of V_mO_n clusters with C_2H_5OH studied by 26.5 eV soft x-ray laser ionization. The lower spectrum displays the V_mO_n cluster distribution; the upper spectrum displays the new cluster distribution and products for the reaction V_mO_n + C_2H_5OH reaction after C_2H_5OH/He is added to the flow tube reactor.

6.4 DISCUSSION

6.4.1 Comparison between 26.5 eV and 10.5 eV ionization

In the present work, a 26.5 eV (46.9 nm) soft x-ray laser is employed to ionize vanadium oxide clusters and their reaction products with methanol and ethanol. The high photon energy of 26.5 eV radiation might possibly fragment/photodissociate neutral clusters or their reaction products during the ionization process, and thereby confuse the identification of ground state neutral species chemistry. In order to clarify this issue, a comparison experiment is done in which both a 10.5 eV and 26.5 eV laser are used for ionization in the study of V_mO_n cluster reactions with CH_3OH. Near threshold single photon ionization using a 10.5 eV laser photon does not leave enough excess energy in the clusters to fragment any vanadium oxide cluster or break any chemical bond of the reaction products following ionization of the neutral species.[6.33] Comparing Figure 6.1 (b) (26.5 eV ionization) and Figure 6.2 (10.5 eV ionization), one sees that the reaction products present are almost the same. Our conclusion is that the fragmentation or photodissociation of neutral vanadium oxide clusters and their reaction products caused by a single 26.5 eV photon is virtually not present in these experiments, as well documented in ref. 33a for Nb, Ta, and V samples at both 26.5 eV and 10.5 eV ionization energies.

In our previous work, we have found that the distribution of neutral V_mO_n clusters is nearly the same using either method for ionization, except that some oxygen rich clusters with high ionization energies (> 10.5 eV) can not be detected by 10.5 eV photon ionization.[6.33a] The reason we prefer to use 26.5 eV laser as the ionization source is that it can ionize all the neutral metal oxide clusters generated in the expansion/ablation

source and all reaction products generated in the reactor. For example, $V_2O_6H_2$ is detected by 26.5 eV laser as shown in Figure 6.1 (b) but can not be detected by 10.5 eV laser (see Figure 2).

6.4.2 Mechanism of V_mO_n + CH_3OH/CD_3OH reactions

Reactions of neutral vanadium oxide clusters with methanol in a flow tube reactor are investigated by time of flight mass spectroscopy coupled with single photon ionization at 26.5 eV. Several kinds of reaction channels can be identified for V_mO_n + CH_3OH/CD_3OH reactions. The details of these mechanisms are discussed for each type of reaction.

Association reactions

Association reactions are found to be one of the main reaction channels for vanadium oxide clusters reacting with methanol,

$$V_mO_n + CH_3OH \rightarrow V_mO_nCH_3OH \qquad (6.1)$$

This association reaction is surely stabilized by collisions in the reactor, most likely with He gas, but also other species. Reaction equations such as this one, and others presented below, are employed to imply mass balance in the usual manner. More detailed partial mechanisms are discussed in the paragraphs following such equations.

As shown in Figure 6.1, complexes $VOCH_3OH$, VO_2CH_3OH, $V_2O_3CH_3OH$, $V_2O_4CH_3OH$, $V_3O_6CH_3OH$, $V_3O_7CH_3OH$, etc. are observed as products for the reaction of V_mO_n + CH_3OH. In the reaction with unlabeled methanol CH_3OH, the mass difference $\Delta m = 32$ can correspond to CH_3OH or O_2 in the mass spectrum. For example, $V_2O_4CH_3OH$ can also be assigned to V_2O_6; however, they can be distinguished in the reaction of V_mO_n with labeled methanol CD_3OH. Under the present experimental conditions, almost all V_mO_n clusters can associate with methanol to form $V_mO_nCH_3OH$.

In our studies of neutral vanadium oxide clusters reacting with small molecules (H_2O, NO, NO_2, and CO), saturated hydrocarbon (C_2H_6, C_3H_8, and C_4H_{10}), alkenes (C_2H_4, C_3H_6, C_4H_8, C_4H_6), benzene (C_6H_6), toluene ($CH_3C_6H_5$), etc. only a few very weak (at best) association products can be detected. In addition, we also find that methanol molecules do not associate with neutral Zr_mO_n oxide clusters.[6.33f] Moreover, methanol molecules only tend to associate with the most stable and oxygen rich Nb_mO_n and Ta_mO_n clusters, unlike for the present case in which almost all V_mO_n cluster tend to associate with CH_3OH. These experimental results suggest that methanol molecules must be very active toward neutral vanadium oxide clusters. These cluster experimental results imply that, in the condensed phase, methanol molecules will be readily adsorbed onto the surface of a vanadium oxide catalyst and that this behavior is not necessarily universal with respect to all surface and/or molecules.

Hydrogen abstraction reactions

The abstraction of hydrogen atoms from CH_3OH to form $V_mO_nH_{1,2}$, occurs for almost all neutral vanadium oxide clusters as shown in Figure 6.1. Note that products with only one H atom (VOH, V_2O_3H, V_3O_6H, and V_4O_9H) are observed for oxygen deficient clusters V_xO_{y-1}(VO, V_2O_3, V_3O_6, and V_4O_9), while products with one or two H atoms ($VO_2H_{1,2}$, $V_2O_4H_{1,2}$, $V_2O_5H_{1,2}$, $V_3O_7H_{1,2}$, and $V_4O_{10}H_{1,2}$) are observed for the most stable clusters (VO_2, V_2O_4, V_2O_5, V_3O_7, and V_4O_{10}). The hydrogen abstraction reactions can be represented as follows:

$$V_xO_{y-1} + CH_3OH \rightarrow V_xO_{y-1}H + CH_3O/CH_2OH \quad (6.2)$$

$$V_xO_y + CH_3OH \rightarrow V_xO_yH + CH_3O/CH_2OH \quad (6.3a)$$

$$\rightarrow V_xO_yH_2 + CH_2O \quad (6.3b)$$

In reactions (6.2) and (6.3a), abstraction of one H atom from CH_3OH will generate a concomitant product, either CH_3O (methoxy) radical, or the thermochemically more stable CH_2OH (hydroxymethy) radical.[6.39] In reaction (6.3b), abstraction of two H atoms from CH_3OH will lead to a CH_2O (formaldehyde) product. Hydrogen abstraction reactions involve C-H and/or O-H cleavage of CH_3OH. The reaction mechanisms can be revealed in labeling experiments with CD_3OH since the cleavage of C-D or O-H will yield distinguishable products through mass spectroscopy. For the reaction products $V_mO_nH_2$, two hydrogen atoms may be abstracted from one or two methanol molecules. Of course, the same issues arise for mass selected cluster ion reactions in a flow tube reactor. In order to address this issue, DFT calculations at the BPW91/LANL2DZ level are employed to elucidate the VO_2 + CH_3OH reaction. This theory level is used to calculate V_mO_n cluster structures.[6.38] The reaction for VO_2 abstracting two hydrogen atoms from two methanol molecules is not thermodynamically favorable, however:

$$VO_2 + 2CH_3OH \rightarrow VO_2H_2 + 2CH_2OH \qquad \Delta H_{298} = +2.6 \text{ eV} \qquad (6.3c)$$

while abstracting two hydrogen atoms from one methanol is thermodynamically favorable,

$$VO_2 + CH_3OH \rightarrow VO_2H_2 + H_2CO \qquad \Delta H_{298} = -0.03 \text{ eV} \qquad (6.3d)$$

Therefore, for V_mO_n clusters, the abstraction of two hydrogen atoms from two methanol molecules should not be a major concern for the present study.

As shown in Figure 6.3, for oxygen deficient clusters, observed products of hydrogen abstraction reactions are dominated by VOD, V_2O_3D, and V_3O_6D etc., employing CD_3OH in the labeling experiments. This indicates that the abstracted hydrogen is derived from the CD_3 moiety of CD_3OH, and the concomitant product is CD_2OH. The

following reaction will occur:

$$V_xO_{y-1} + CD_3OH \rightarrow V_xO_{y-1}D + CD_2OH \quad (6.4)$$

For the most stable vanadium oxide clusters, the products $VO_2H/D/HD$, $V_2O_4H/D/HD$, $V_2O_5H/D/HD$, $V_3O_7H/D/HD$, and $V_4O_{10}H/D/HD$ are observed in labeling experiments, revealing that abstracted hydrogen atoms come from both CD_3 and OH units of methanol even though the O-H bond (104.4 kcal/mol[6.40]) is stronger than the C-H bond (94 kcal/mol[6.40]). The following reactions can occur:

$$V_xO_y + CD_3OH \rightarrow V_xO_yH + CD_3O \quad (6.5a)$$

$$\rightarrow V_xO_yD + CD_2OH \quad (6.5b)$$

$$\rightarrow V_xO_yDH + CD_2O \quad (6.5c)$$

For the most stable vanadium oxide clusters, both the CH_3O radical and CH_2OH radical can be generated in reaction (6.5a,b). Note that product formaldehyde (CH_2O) is formed in reaction (6.5c).

Oxygen rich vanadium oxide clusters are documented to be are very active in attaching H atoms from any hydrogen source (H_2O, hydrocarbons, etc) in a high vacuum system. Consequently, $V_xO_{y+1}H_{0,1,2}$ clusters are always observed in the distribution of neutral vanadium oxide clusters; as pointed out above, this is not true for all M_mO_n clusters we have studied. The results of the present study indicate that generation of CH_2O (formaldehyde) through the abstraction of two H atoms (dehydrogenation) from one CH_3OH molecule can only occur on oxygen rich and stable vanadium oxide clusters, and not on oxygen deficient clusters. Further, this gas phase study of V_mO_n clusters reacting with methanol suggests the following two possibilities for the condensed phase:

CH_3OH may tend to lose H from its CH_3 moiety on oxygen deficient surfaces of vanadium oxide catalysts; and oxygen rich surfaces may tend to generate a CH_2O product through reactions with both hydrogen containing moieties of CH_3OH. This suggestion is based on the experimental observation that oxygen deficient clusters abstract one D atom from the CD_3 moiety of CD_3OH, while the stable and oxygen rich clusters abstract two hydrogen (H/D) atoms from CD_3OH, one from each hydrogen containing moiety of methanol. Similar results are also found in the studies of vanadium oxide cluster cation reactions with methanol: dehydrogenation of methanol is preferred for the high valent cluster cations, whereas low valent clusters show little or no reactivity with respect to H_2 uptake.[6.23a]

Dehydration and dehydrogenation reactions

As displayed in Figure 6.1, a series of new products is observed in the reactions between V_mO_n with CH_3OH. They correspond to two possible isomeric products: $V_mO_{n+1}CH_2O$ (VO_2CH_2O, VO_3CH_2O, $V_2O_5CH_2O$, and $V_3O_7CH_2O$), and $V_mO_nC_2H_6O$ (VOC_2H_6O, $VO_2C_2H_6O$, $V_2O_4C_2H_6O$, and $V_3O_6C_2H_6O$). These products are distinguished by isotopic labeling experiments ($CD_3 \leftrightarrow CH_3$). As shown in Figure 6.3, $V_mO_nC_2D_6O$ (VC_2D_6O, VOC_2D_6O, $VO_2C_2D_6O$, $V_2O_4C_2D_6O$, $V_3O_6C_2D_6O$, and $V_3O_7C_2D_6O$) are assigned to the dominant products, while only $VOCD_2O$ and VO_2CD_2O are observed at the low mass region. Products $V_mO_nC_2D_6O$ are generated from intermolecular dehydration or dehydrogenation reactions,

$$V_mO_n + 2CD_3OH \rightarrow V_mO_n(CD_3OH)_2 \rightarrow V_mO_nC_2D_6O/V_mO_{n-1}(CD_3O)_2 + H_2O \quad (6.6a)$$

$$V_mO_{n-1} + 2CD_3OH \rightarrow V_mO_{n-1}(CD_3OH)_2 \rightarrow V_mO_nC_2D_6O/V_mO_{n-1}(CD_3O)_2 + H_2 \quad (6.6b)$$

The results of the labeling experiments demonstrate that in reaction (6.6a), the

eliminated H_2O is taken from OH units of two CD_3OH molecules, suggesting that two CD_3OH molecules are first adsorbed on the appropriate vanadium oxide clusters, and then an intermolecular dehydration (6.6a) or dehydrogenation (6.6b) reaction occurs between two CD_3OH molecules. In the study of mass selected $V_mO_n^+$ clusters [6.22,6.23a], products $V_mO_nC_2D_6O/V_mO_{n-1}(CD_3O)_2$ are observed for $V_mO_n^+$ clusters, but not for $V_mO_{n-1}^+$ clusters, reacting with CH_3OH. For example, $V_2O_4C_2H_6O^+$, $V_3O_6C_2H_6O^+$ are observed for $V_2O_4^+/V_3O_6^+ + 2CH_3OH$,[6.22] but not for $V_2O_3^+/V_3O_5^+ + 2CH_3OH$. In addition, if one considers thermodynamics, product H_2O in reaction (6.6a) is more stable than H_2 in reaction (6.6b). Therefore, the product $V_mO_nC_2D_6O$ is most likely generated through reaction (6.6a) rather than through reaction (6.6b).

A secondary reaction, $V_mO_{n-1}CD_2O + CD_3OH \rightarrow V_mO_nC_2D_5HO$, does not occur since products $V_mO_{n-1}C_2D_5HO$ are not observed in the labeling experiments. Product H_2O is obtained from the OH moieties of two CH_3OH molecules, since all deuterium atoms are left on the clusters to generate $V_mO_nC_2D_6O$. Additionally, intermolecular dehydration of CH_3OH on vanadium oxide clusters must be very fast because almost no association products with two CH_3OH/CD_3OH molecules are observed in the mass spectrum, even through dehydration products $V_mO_nC_2D_6O$ are detected for most clusters reacting with CH_3OH. Several conceivable structures can be considered for the C_2D_6O moiety of $V_mO_nC_2D_6O$: dimethyl ether (CH_3OCH_3), ethanol (CH_3CH_2OH), as well as various dissociative adsorption products on V_mO_n clusters. We can not identify these isomers from our experiments. $V_mO_nC_2D_6O$ can also be considered as $V_mO_{n-1}(CD_3O)_2$, in which two methoxy moieties are associated with metal oxide clusters. In condensed phase studies, formaldehyde (H_2CO) is measured to be the main product, while dimethyl ether

is the major byproduct for oxidation of methanol to formaldehyde on a supported vanadium oxide catalysts.[6.41] The structure of the C_2H_6O/C_2D_6O attached to V_mO_n clusters is not known at this time.

Products $VOCD_2O$ ($VOCH_2O$) and VO_2CD_2O (VO_2CH_2O) are also observed in the reactions of V_mO_n clusters with deuterated methanol as shown in Figure 6.3 (Figure 6.1a). Product $VOCD_2O$ may be generated from two possible reactions,

$$VO + CD_3OH \rightarrow VOCD_2O + DH \quad (6.7)$$

$$VO_2 + CD_3OH \rightarrow VOCD_2O + DHO \quad (6.8)$$

Reaction (6.7) is an intramolecular dehydrogenation reaction, and reaction (6.8) is an intramolecular dehydration reaction. In both reactions, a formaldehyde (CH_2O) unit is formed on vanadium oxide clusters after H_2 or H_2O is eliminated from the association intermediate $V_mO_nCH_3OH$. The structure of $VO_2CH_2/VOCH_2O$ is unknown at present; the reaction channel for $V_mO_nCH_2O$ generation can not be identified experimentally. Calculations are required to generate more specific open reaction channels.

6.4.3 Reactions of V_mO_n + CH_3CH_2OH

Ethanol (C_2H_5OH) is also used as a reactant to study the reactivity of V_mO_n clusters toward alcohols in general. As shown in Figure 6.3, association complexes $V_mO_nCH_3CH_2OH$ and $V_mO_n(CH_3CH_2OH)H$ are the major products for V_mO_n + CH_3CH_2OH reactions. $V_mO_n(CH_3CH_2OH)H$ product may be generated from proton transfer reactions between two ethanol molecules following their association with a V_mO_n cluster. Hydrogen abstraction products, such as, VOH, $VO_2H_{1,2}$, V_2O_3H, $V_2O_5H_{1,2}$, etc. observed in V_mO_n + CH_3OH reactions are not observed in V_mO_n + CH_3CH_2OH reactions. Moreover, no obvious product is generated from intermolecular dehydration, or

intramolecular dehydrogenation for V_mO_n and CH_3CH_2OH reactions. A significant difference between CH_3OH and CH_3CH_2OH chemistry in reactions with V_mO_n clusters is apparent.

6.5 CONCLUSIONS

The reactions of neutral vanadium oxide clusters with methanol and ethanol are investigated employing 26.5 eV soft x-ray laser and 10.5 eV nm laser ionization coupled with TOFMS. In the experiments, nearly identical reaction products are detected using 26.5 eV and 10.5 ev laser ionizations. We conclude that neutral vanadium oxide clusters and their reaction products are not fragmented or photodissociated by 26.5 eV photons. Three major reactions are identified for V_mO_n + CH_3OH/CD_3OH:

(1) Association reactions: Association products $V_mO_nCH_3OH$ are observed for most of vanadium oxide clusters in the experiments, indicating that methanol molecules are easily adsorbed on neutral vanadium oxide clusters. In the condensed phase, the surface of a vanadium oxide catalyst should easily adsorb methanol molecules.

(2) Hydrogen abstraction reactions: Oxygen deficient vanadium oxide clusters (VO, V_2O_3, V_3O_6, etc.) can abstract only one hydrogen atom from a CH_3/CD_3 unit of CH_3OH/CD_3OH to form $V_xO_{y-1}D/H$ products. The most stable vanadium oxide clusters (VO_2, V_2O_4, V_2O_5, V_3O_7, V_4O_{10}, etc.), can abstract more than one hydrogen atom from CH_3 and/or OH to form $V_xO_yDH_{0,1,2}$ products. Oxygen rich vanadium oxide clusters (VO_3, V_2O_6, V_3O_8, etc.) can abstract more than one H atom from any kind of hydrogen source in a high vacuum system to form $V_xO_{y+1}H_{0,1,2}$ products. The experimental results indicate that abstraction of two H atoms from CH_3OH to generate CH_2O (formaldehyde) product takes place on oxygen rich and stable vanadium oxide clusters rather than oxygen

deficient vanadium oxide clusters. Experimental results suggest that, in the condensed phase, an oxygen rich surface of a vanadium oxide catalyst will generate CH_2O products.

(3) Intermolecular dehydration reactions: Strong signals of VOC_2D_6O, $VO_2C_2D_6O$, $V_2O_4C_2D_6O$, and $V_3O_7C_2D_6O$ are observed in the experiments, indicating that the intermolecular dehydration reaction, $V_mO_n + 2CH_3OH \rightarrow V_mO_n(CH_3OH)_2 \rightarrow V_mO_nC_2H_6O$, is one of the major reaction channels for the V_mO_n reactions with methanol. A concomitant product H_2O is derived from the OH moieties of two CH_3OH molecules. Intermolecular dehydration of CH_3OH on vanadium oxide clusters must be very fast because almost no association products $V_mO_n(CH_3OH)_2$ are detected in the experiments.

Additionally, products $VOCD_2O$ ($VOCH_2O$) and VO_2CD_2O (VO_2CH_2O) are also observed in the reaction of V_mO_n clusters with CD_3OH (CH_3OH). They can be generated from minor reaction channels of intramolecular dehydrogenation or intramolecular dehydration.

An obviously different behavior is observed for V_mO_n reactions with CH_3CH_2OH compared to CH_3OH. Association reactions are identified as the only major channel for the reaction of V_mO_n with CH_3CH_2OH.

REFERENCES

[6.1] (a) J. L. G. Fierro, Metal Oxides Chemistry and Applications, Taylor & Francis, **2006**; (b) Thomas, Catalytic Processes and Proven Catalysts, Academic Press, New York, **1970**. (c) A. T. Bell, Science, **299**, 1688 (2003). (d) D. Schroder, H. Schwarz, Angew. Chem. Int. Ed. Engl. **34**, 1973 (1995). (e) R. A. J. O'Hair, A. K. Vrkic, P. F. James, J. Am. Chem. Soc. **126**, 12173 (2004).

[6.2] R. G. Herman, Q. Sun, C. Shi, K. Klier, C. Wang, H. Hu, I, E. Wachs, M. M. Bhasin, Catalysis Today, **37**, 1 (1997).

[6.3] I. E. Wachs, Catalysis Today, **100**, 79 (2005).

[6.4] (a) Z. Jusys, R. J. Behm, J Phys. Chem. B **105,** 10874 (2001); (b) K. Drew, G. Girishkumar, K. Vinodgopal, P. V. Kamat, J Phys. Chem. B **109**, 11851 (2005).

[6.5] I. E. Wachs, G. Geo, M. V. Juskelis, B. M. Weckhuysen, Stud. Surf. Sci. Catal. **109**, 305 (1997).

[6.6] B. M. Weckhuysen and D. E. Keller, Catalysis Today, 78, 25 (2003).

[6.7] (a) J. Sambeth, L. Gambaro, H. Thomas, Adsorp. Sci. Technol. **12**, 171 (1995). b) J. Sambeth, M. Centeno, A. Paul, L. Briand, H. Y. Thomas, J. Odriozola, J. Mol. Catal. A **161**, 89 (2000). c) L. Gambaro, J. Mol. Catal. A **214**, 287 (2000).

[6.8] (a) G. Froment, K. B. Bischoff, Chemical Reactor Analysis and Design, Wily, New York, 1979. b) S. Chio, I. E. Wachs, 223rd ACS National Meeting, Orlando, FL, United States, April 7-11, 2002, FUEL-509.

[6.9] T. Feng, J. M. Vohs, J. Catal. **221**, 619 (2004).

[6.10] G. S. Wong, M. R. Concepcion, J. M. Vohs, J. Phys. Chem. B **106**, 6451 (2002).

[6.11] N. Das, H. Eckert, H. Hu, I. E. Washs, J. F. Walzer, F. J. Feher, J. Phys. Chem. **97**, 8240 (1993).

[6.12] T. Oyama, G. T, Went, K. B. Lewis, A. T. Bell, G. A. Somorjai, J. Phys. Chem. **93**, 6786 (1989).

[6.13] L. J. Burcham, G. Deo, X. Gao, I. E. Wachs, Topics in Catalysis, **11/12**, 85 (2000).

[6.14] M. Ai, J. Catal. **77**, 279 (1982)

[6.15] A. Andersson, J. Solid State. Chem. **42**. 279 (1982).

[6.16] C. Louis, J. Tatibouet, M. Che, J. Cata. **109**, 354 (1988).

[6.17] J. Allison, W. Goddard, J. Catal. **92**, 127 (1985).

[6.18] R. Weber, J. Phys. Chem. **98**, 2999 (1994).

[6.19] (a) M. Badlani, I. R. Wachs, Catal. Lett. **75**, 137 (2001). (b) L. E. Briand, J. M. Jehng, L. Cornaglia, A. M. Hirt, I. E. Wachs, Catal. Today, **78**, 257 (2003).

[6.20] (a) Y. Xie, S. G. He, F. Dong, E. R. Bernstein, J. Phys. Chem. A (Accepted). (b) E. Jakubikova, A. K. Rappé, E. R. Bernstein, J. Phys. Chem. A (Accepted).

[6.21] Y. Cao, X. Zhao, B. Xin, S. Xiong, Z. Tang, J. Mol. Struct. **683**, 141 (2004).

[6.22] D. R. Justes, N. A. Moore, A. W. Castleman Jr. J. Phys. Chem. B **108**, 3855 (2004).

[6.23] (a) S. Feyel, L. Scharfenberg, C. Daniel, H. Hartl, D. Schrolder, H. Schwarz, J. Phys. Chem. A, **111**, 3278 (2007). (b) M. Engeser, D. Schroder, H. Schwarz, Chem. Eur. J. **11**, 5975 (2005).

[6.24] P. Jackson, K. J. Fisher, G. D. Willett, Chem. Phys, **262**, 179 (2000).

[6.25] R. Z. K. Khaliullin, A. T. Bell, J. Phys. Chem. **106**, 7832 (2002).

[6.26] P. Boulet, A. Baiker, H. Chermette, F. Gilardoni, J. C. Volta, J. Weber, J. Phys. Chem. B **106**, 9659 (2002).

[6.27] J. Dobler, M. Pritzsche, J. Sauer, J. Am. Chem. Soc. **127**, 10861 (2005).

[6.28] D. R. Justes, R. Mitric, N. A. Moore, V. Bonacic-Koutecky, A.W. Castleman, Jr. J. Am. Chem. Soc. **125**, 6289 (2003).

[6.29] J. H. Futrell, *Gaseous Ion Chemistry and Mass Spectrometry*, Wiley, New York, 1986.

[6.30] K. Eller, H. Schwarz, Chem. Rev. **91**, 1121 (1991).

[6.31] D. K. Bohme, H. Schwarz, Angew. Chem. Int. Ed. **44**, 2336 (2005).

[6.32] F. Dong, S. Heinbuch, J. J. Rocca, E. R. Bernstein, Z. C. Wang, K. Deng, and S. G. He, J. Am. Chem. Soc. (Accepted)

[6.33] (a) F. Dong, S. Heinbuch, J. J. Rocca, E. R. Bernstein, J. Chem. Phys. **125**, 164318 (2006). (b) S. Heinbuch, F. Dong, J. J. Rocca, E. R. Bernstein, J. Chem. Phys. **126**, 244301 (2007). (c) F. Dong, S. Heinbuch, J. J. Rocca, E. R. Bernstein, J. Chem. Phys. **125**, 154317 (2006). (d) S. Heinbuch, F. Dong, J. J. Rocca, E. R. Bernstein, J. Chem. Phys. **125**, 154316 (2006). (e) F. Dong, S. Heinbuch, J. J. Rocca, E. R. Bernstein, J. Chem. Phys. **124**, 224319 (2006). (f) S. Heinbuch, F. Dong, J. J. Rocca, E. R. Bernstein, (Submitted to J. Opt. Soc. Am. B).

[6.34] M. E. Geusic, M. D. Morse, S. C. O'Brien, R. E. Smalley, Rev. Sci. Instrum. **56**, 2123 (1985).

[6.35] (a) S. Heinbuch, M. Grisham, D. Martz, J. J. Rocca, Opt. Express, **13**, 4050 (2005). (b) J. J. Rocca, V. N. Shlyaptsev, F. G. Tomasel, O. D. Cortazar, D.

Hartshorn, J. L. A. Chilla, Phys. Rev. Lett. **73**, 2192 (1994). (c) J. J. Rocca, Rev. Sci. Instrum. **70**, 3799 (1999).

[6.36] (a) Y. Matsuda, E. R. Bernstein, J. Phys. Chem. A **109**, 314 (2005). (b) Y. Matsuda, D. N. Shin, E. R. Bernstein, J. Chem. Phys. **120**, 4142 (2004). (c) D. N. Shin, Y. Matsuda, E. R. Bernstein, J. Chem. Phys. **120**, 4157 (2004). (d) Y. Matsuda, E. R. Bernstein, J. Chem. Phys. **120**, 4165 (2004).

[6.37] M. Calatayud, J. Andres, A. Beltran, J. Phys. Chem. *A*., **105**, 9760 (2001).

[6.38] (a) E. Jakubikova, A. K. Rappé, E. R. Bernstein, J. Phys. Chem. A **111**, 12938, (2007). (b) E. Jakubikova, Ph. D Dissertation (May, **2007**).

[6.39] NIST Standard Reference Database, see http://webbook.nist.gov/chemistry.

[6.40] CRC handbook of Chemistry and Physics, 62nd Edition, F192, 1981-1982.

[6.41] J. M. Miller, L. J. Lakshmi, Appl. Cata. A: Gerneral, 190, 197 (2000).

Chapter 7

C=C Bond Cleavage on Neutral $VO_3(V_2O_5)_n$ Clusters

7.1 C=C BOND CLEAVAGE ON NEUTRAL $VO_3(V_2O_5)_N$ CLUSTERS

The oxidation of alkenes over supported metal oxide catalysts is a very important catalytic process in the chemical industry. For example, catalytic partial oxidation of propylene (CH_2=$CHCH_3$) produces acrolein (CH_2CHCHO), one of the more employed industrial chemical intermediates.[7.1-7.3] A number of bulk metal oxide catalysts has been used for these reactions.[7.3,7.4] Since processes on metal oxide catalytic surfaces are so complex, a fundamental understanding of these catalytic processes is still not available and thus a rational approach to effective catalyst synthesis is difficult. Gas phase studies of metal oxide clusters and their reaction behavior can help to understand the mechanism of elementary reactions in catalytic processes under isolated, controlled, and reproducible conditions.[7.5-7.10]

Great efforts have been made to understand the mechanism of alkene oxidation on condensed phase catalytic surfaces through both experimental[7.11-7.21] and theoretical

studies of transition metal oxide clusters.[7.22-7.27] Using a tandem mass spectrometer equipped with an electrospray ionization (ESI) source, Feyel and co-workers[7.26] studied the oxidation of 1-butene (C_4H_8) with mass selected $V_3O_7^+$ cluster ions. Oxidative dehydrogenation (ODH) of hydrocarbons is identified as a major reaction channel, accompanied by a minor channel involving C-C single bond cleavage to generate a product $V_3O_7(C_2H_4)^+$. The reactions of mass selected $V_mO_n^+$ with ethylene (C_2H_4) were investigated by Castleman and co-workers.[7.15-7.17] Oxygen transfer reactions are observed in their experiments and are determined to be the most energetically favorable channel for $V_2O_5^+/V_4O_{10}^+ + C_2H_4$ reactions based on theoretical calculations.[7.16] In the studies of $V_mO_n^+$ reactions, they found that the clusters $V_2O_{4,5}^+$, $V_3O_7^+$, and $V_5O_{12}^+$ are able to break the C2-C3 (single bond) of 1-butene (C_4H_8) to produce $V_mO_nC_2H_4^+$. In the reaction of $V_mO_n^+$ with 1,3 butadiene (C_4H_6), major association products are identified in addition to some minor reactions, such as, oxygen abstraction, dehydration, etc.[7.18,7.19] No significant reactivity for anionic clusters $V_mO_n^-$ toward 1-butene or 1,3 butadiene is reported in their experiments.[7.19] While the reactions of metal oxide cluster ions with alkenes have been widely investigated in the gas phase, very few studies have been carried out for neutral metal oxide clusters and their reactions, since one must find a valid method to ionize neutral species without fragmentation. Additionally, some highly oxidized (e.g. VO_3, etc.) metal oxide clusters have high ionization energies (IE).[7.28] We believe that the study of neutral metal oxide clusters and their reactions can provide valuable information about active sites of metal oxides employed for catalytic processes.

Recently, we studied the reactions of neutral vanadium oxide clusters with ethane (C_2H_6), ethylene (C_2H_4), and acetylene (C_2H_2) employing a new desk-top, 26.5 eV/photon (46.9 nm), soft x-ray laser for ionization.[7.22] Using this ionization source, all the species of neutral metal oxide clusters and their reaction products can be detected. We found that oxygen rich clusters $VO_3(V_2O_5)_{n=0,1,2}\ldots$, (e.g., VO_3, V_3O_8, and V_5O_{13}) can lead to a cleavage of the C=C bond of C_2H_4 to produce $(V_2O_5)_nVO_2CH_2$ clusters, while association products are observed for reactions V_mO_n + C_2H_6/C_2H_2. Neutral V_mO_n clusters present a significantly different reactivity than $V_mO_n^{+/-}$ cluster ions in reactions with C_2H_4. Since cleavage of C=C/C-C bonds in hydrocarbons is the key step in the decomposition of large hydrocarbons into small molecules, investigation of C=C bond breaking on neutral oxygen rich $VO_3(V_2O_5)_{n=0,1,2}\ldots$clusters takes on special importance.

In the present studies, the reactivity of neutral vanadium oxide clusters toward alkenes C_2H_4 (ethylene), C_3H_6 (propylene), C_4H_8 (1-butene), C_4H_6 (1, 3-butadiene), and C_2F_4 (tetrafluoroethylene) and benzene (C_6H_6), is investigated employing single photon ionization at 26.5 eV (46.9 nm) to analyze reactants and products in a time of flight mass spectrometer (TOFMS). Products generated through C=C bond cleavage of the alkenes are detected in all cases for V_mO_n + $C_2H_4/C_3H_6/C_4H_8/C_4H_6$. Oxygen rich vanadium oxide clusters with structure $VO_3(V_2O_5)_{n=0,1,2}\ldots$ exhibit a specific activity with regard to the C=C bond cleavage of alkenes. In the studies of V_mO_n reacting with C_2F_4 and C_6H_6, different reactions than those observed for alkenes are identified due to the effects of F replacement of H and ring formation. DFT calculations are performed to explore the

mechanisms for the reaction of VO_3 with C_3H_6, C_2F_4 and C_6H_6, and aid in the interpretation and explanation of our experimental observations.

7.2 EXPERIMENTAL AND THEORETICAL METHODS

Experiments performed for this study of neutral cluster reactions involve a time of flight mass spectrometer (TOFMS) coupled with single photon ionization of reactants and products by a desk-top 26.5 eV EUV laser. The experimental apparatus has been described in detail elsewhere.[7.22,7.29] Briefly, the neutral vanadium oxide clusters are generated in a conventional laser vaporization/supersonic expansion cluster source by laser ablation (focused 532 nm laser, 10-20 mJ/pulse) of vanadium foil into a carrier gas of ~ 0.5% O_2/He at 80 psig. The reactant gases (15 psi), pure C_2H_4, C_3H_6, C_3H_8, C_4H_6, C_4H_8, C_4H_{10}, C_6H_6/He, and C_2F_4 are pulsed into the flow tube reactor that is similar to the equipment designed by Smalley et. al.[7.30] The instantaneous reactant gas pressure in the reactor cell is about 20 Torr so that good cooling is achieved for the neutral metal oxide clusters generated in the ablation source. In this design, a flow tube reactor (70 mm length, ∅ 6 mm) is coupled directly to the cluster formation channel (40 mm length, ∅ 1.8 mm). After the flow tube reactor, the ions created in the ablation source and flow tube reactor are removed by an electric field. This method is commonly used in the study of elementary reactions of neutral and ionic metal clusters.[7.30-7.34] The possibility of charge exchange between the ions and much more abundant neutral species can be neglected based on the study of Kaldor et al.[7.32] Additionally, the products observed in our neutral vanadium oxide cluster reactions with alkenes[7.22] are not observed in mass selected

vanadium oxide cluster ion reactions.[7.15-7.17,7.26] So we are confident that the products observed in our experiments are generated from neutral vanadium oxide clusters reacting with C_xH_y, and not from cluster ions. Additionally, in the studies of neutral V_mO_n clusters reacting with C_2H_2, C_2H_4, C_2H_6, cluster distributions and identified reaction products obtained by using 26.5 eV laser and 10.5 eV (118 nm) laser for ionization are nearly identical except for signal intensities.[7.22] Cluster fragmentation cannot occur during near threshold single photon ionization with a 10.5 eV laser.[7.28] Therefore, we assume that fragmentation during the 26.5 eV ionization process can be neglected in the present studies, as well. Since the 26.5 eV laser can ionize He, O_2, and alkenes, C_2F_4 and C_6H_6 reactants, which have high concentrations in the expansion/reaction cell system, we must gate the microchannel plate (MCP) detector voltage to protect it from overload and saturation.

The soft x-ray laser (26.5 eV/photon energy) emits pulses of about 1 ns duration with an energy/pulse of 10 μJ that is reduced to 3 ~ 5 μJ after transversing a z-fold mirror system and is not tightly focused in the ionization region to avoid multiphoton ionization and a space charge Coulomb effect due to He^+ ions produced by 26.5 eV ionization of He in the molecular beam.

DFT calculations are carried out using the Gaussian 03 program.[7.35] The B3LYP functional[7.36-7.38] and TZVP basis set[7.39] are used to study the reactions of VO_3 with C_3H_6, C_2F_4, and C_6H_6. The B3LYP/TZVP level of theory, with moderate computational cost, was tested to give reasonably good results for bond strengths of vanadium

oxides.[7.16,7.40,7.41] The enthalpies of formation for C_2 hydrocarbons are also calculated very well at this level of theory. This method was shown previously to describe the VO_3 + C_2H_4 reaction system in good agreement with experimental results.[7.22] For each reaction channel, the calculation involves geometry optimization of various reaction intermediates and transition states through which the intermediates evolve into one another. Intrinsic reaction coordinate (IRC) calculations[7.42,7.43] are performed so that a transition state connects two appropriate local minima on the reaction pathways. In this method, once a stable state is found, several relaxed potential energy surfaces (PESs) can be scanned for possible internal reaction coordinates.

7.3 RESULTS

In the present experiments, a 26.5 eV laser is employed to ionize neutral clusters and their reaction products. The V_mO_n cluster distribution, generated under low oxygen concentration (0.5% O_2/He expansion gas at 80 psi), is displayed in the mass spectrum of Figure 7.1(a). Three categories of vanadium oxide clusters can be identified. Vanadium oxide clusters VO_2, V_2O_4, V_2O_5, V_3O_7, V_4V_{10}, V_5O_{12}, V_6O_{15}, etc. can be expressed as stoichiometries of the form $(VO_2)_{0,1}(V_2O_5)_n$. These clusters are the most stable clusters (highest intensities for V_mO_n within a given V_m cluster family) in the neutral V_mO_n cluster distribution based on both experiments[7.29a] and theoretical calculations.[7.40,7.41] Oxygen rich clusters VO_3, V_2O_6, V_3O_8, V_5O_{13}, etc. that have one more oxygen atom compared to the most stable clusters. They can be expressed as $(V_2O_5)_nO$ and $VO_3(V_2O_5)_n$ for the clusters containing even and odd number of V atoms, respectively. These oxygen rich

clusters are found to associate one or two hydrogen atoms to make more stable structures. These clusters cannot be ionized by 10.5 eV laser due to high ionization energy. Oxygen deficient clusters VO, V_2O_3, $V_3O_{5,6}$, $V_4O_{8,9}$, etc. can also be observed; they have one or more oxygen atoms fewer than the most stable clusters (see Figure 7.1(a)).

7.3.1 V_mO_n + $C_2H_4/C_3H_6/C_4H_8/C_4H_6$ Reactions

To study neutral V_mO_n cluster reactions with alkenes, reactant gases (pure C_2H_4, C_3H_6, C_4H_8, and C_4H_6) are individually and separately pulsed into the flow tube reactor to interact with neutral vanadium oxide clusters generated from the ablation/expansion source. As shown in Figure 7.1(b), when C_2H_4 ($H_2C{=}CH_2$) is added to the reactor, the products VO_2CH_2, $V_3O_7CH_2$, and $V_5O_{12}CH_2$, generated from V_mO_n + C_2H_4 reactions, can be identified as the main products; several other association products, $VO_2C_2H_4$, $V_2O_5C_2H_4$, and $V_3O_8C_2H_4$, are also observed. In previous studies, we have demonstrated that the V_mO_n cluster distribution and reaction products of V_mO_n + C_2H_4 are almost the same detected through 26.5 eV (46.9 nm) and 10.5 eV (118 nm) laser ionizations, except that some vanadium oxide clusters with high ionization energies are only detected by 26.5 eV laser. This observation indicates that no significant fragment occurs during the ionization process employing 26.5 eV radiation.

As shown in Figure 7.1(c), if the reactant propylene ($H_2C{=}CHCH_3$) is added into the flow cell reactor, a series of new signals is assigned to products $VO_2C_2H_4$, $V_3O_7C_2H_4$, and $V_5O_{12}C_2H_4$ for the reactions V_mO_n + C_3H_6. Additionally, some products (VO_2CH_2,

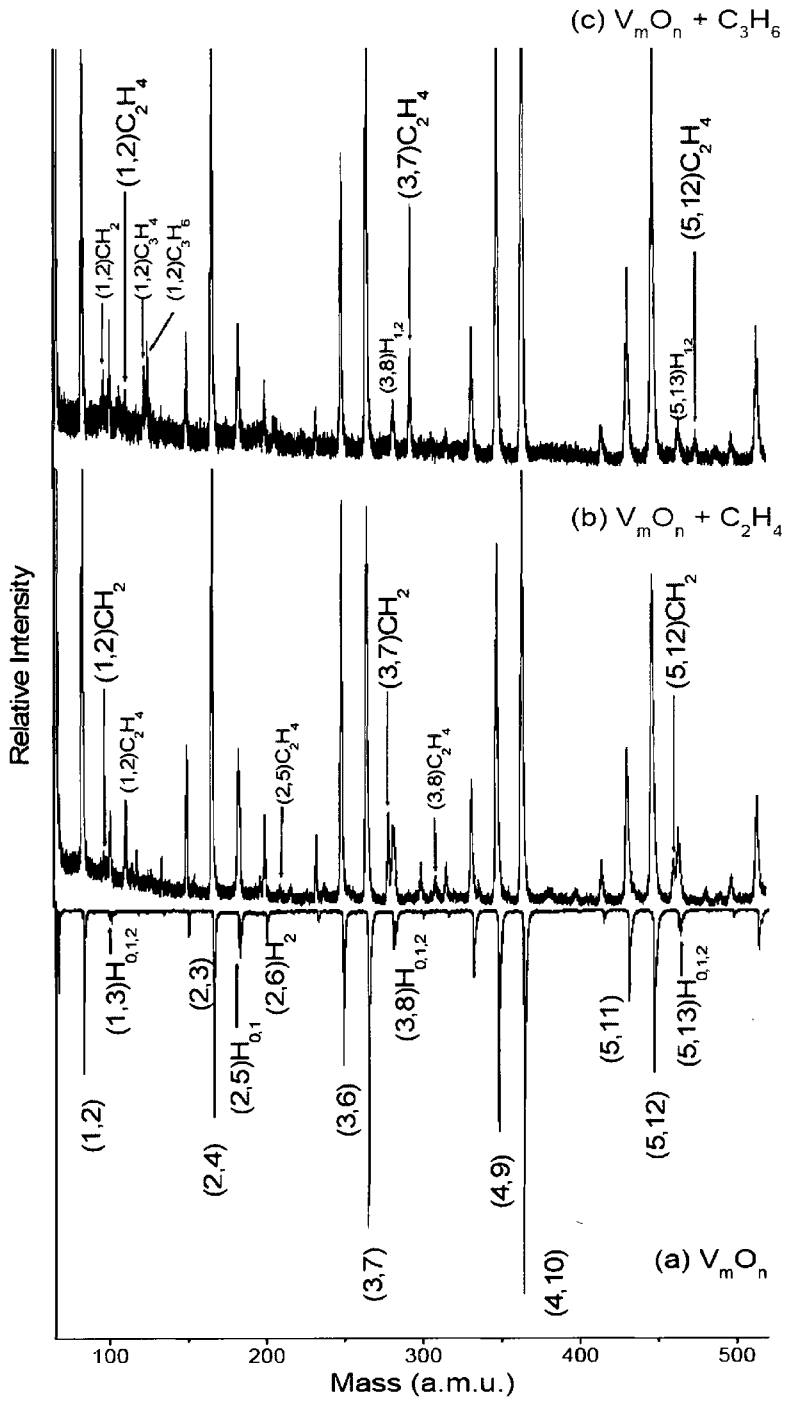


Figure 7.1: Reactions of V_mO_n clusters with pure ethylene (C_2H_4) and propylene (C_3H_6) studied by 26.5 eV soft x-ray laser ionization. (a) V_mO_n cluster distribution generated with 0.5% O_2/He expansion gas at 80 psi. Reactant gases (15 psi), (b) pure C_2H_4 (c) pure C_3H_6, are added to the flow tube reactor. New products of the reactions are detected.

$VO_2C_3H_4$, and $VO_2C_3H_6$) are only detected for small vanadium oxide clusters.

Figure 7.2 displays the mass spectra generated from reactions between V_mO_n and

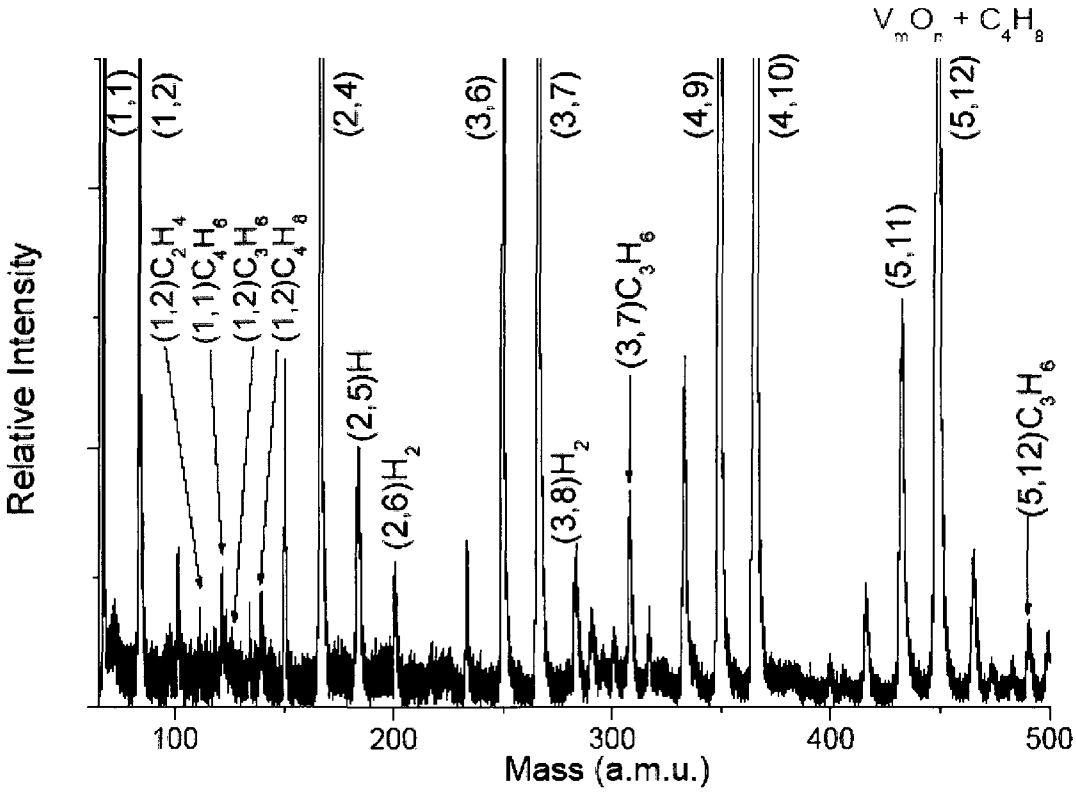


Figure 7.2: Reactions of V_mO_n clusters with pure 1-butadiene (C_4H_8). Reactant gas pure C_4H_8 (15 psi) is added to the flow tube reactor. New reaction products and remaining clusters are detected by 26.5 eV soft x-ray laser ionization.

1-butene (C_4H_8, $H_2C{=}CHCH_2CH_3$). The complexes VOC_3H_6, $V_3O_7C_3H_6$, and $V_5O_{12}C_3H_6$, are identified as the major products, while several small signals corresponding to VOC_4H_6, $VO_2C_2H_4$, and $VO_2C_4H_8$ are also observed. 1,3-butadiene (C_4H_6, $H_2C{=}CH\text{-}CH{=}CH_2$) is another alkene with a C=C double bond used as a reactant. For neutral clusters V_mO_n reacting with 1, 3-butadiene, products VOC_3H_4, $V_3O_7C_3H_4$, and $V_5O_{12}C_3H_4$ are detected along with a few association products, $VO_2C_4H_6$ and $V_2O_4C_4H_6$, as shown in Figure 7.3.

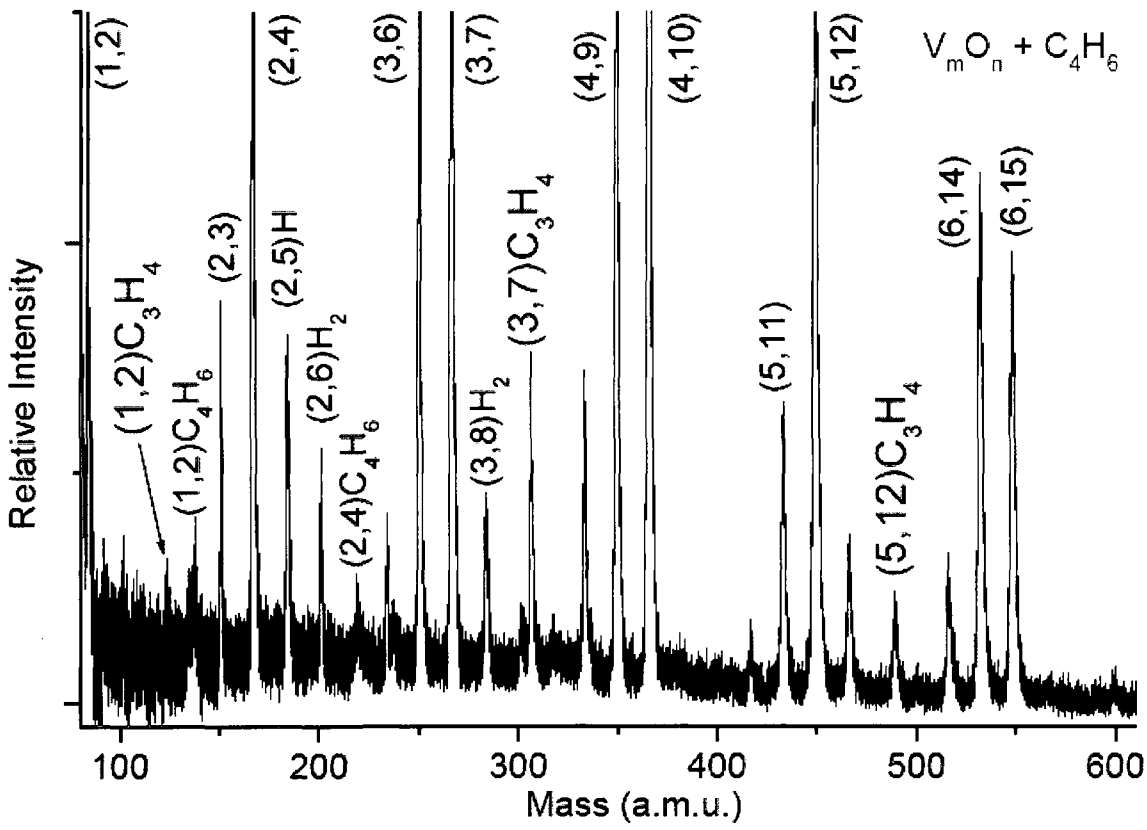


Figure 7.3: Reactions of V_mO_n clusters with 1,3-butadiene (C_4H_6). Reactant gas pure C_4H_6 (15 psi) is added to the flow tube reactor. New reaction products and remaining clusters are detected by 26.5 eV soft x-ray laser ionization.

Additionally, signals of oxygen rich V_mO_n clusters VO_3, V_3O_8, V_5O_{13} disappear in the reactions of V_mO_n clusters with alkenes (C_3H_6, C_4H_8, and C_4H_6), as shown in Figures 7.1, 7.2, and 7.3.

7.3.2 $V_mO_n + C_6H_6/C_2F_4$

As displayed in Figure 7.4, products $VO_2C_6H_4$, $V_2O_4C_6H_4$, $V_3O_7C_6H_4$, and $V_5O_{12}C_6H_4$ are observed for reactions of $V_mO_n + C_6H_6$. These products are different than those generated by the reaction $V_mO_n + C_2H_4/C_3H_6/C_4H_6/C_4H_8$. Reactions between V_mO_n and tetrafluoroethylene ($CF_2=CF_2$), are also investigated; however, no significant product is

detected in the experiments, not even association complexes, using 26.5 eV x-ray laser ionization. The reaction mechanism of V_mO_n clusters with C_2F_4 and C_6H_6 are studied by DFT calculation as discussed in the following section.

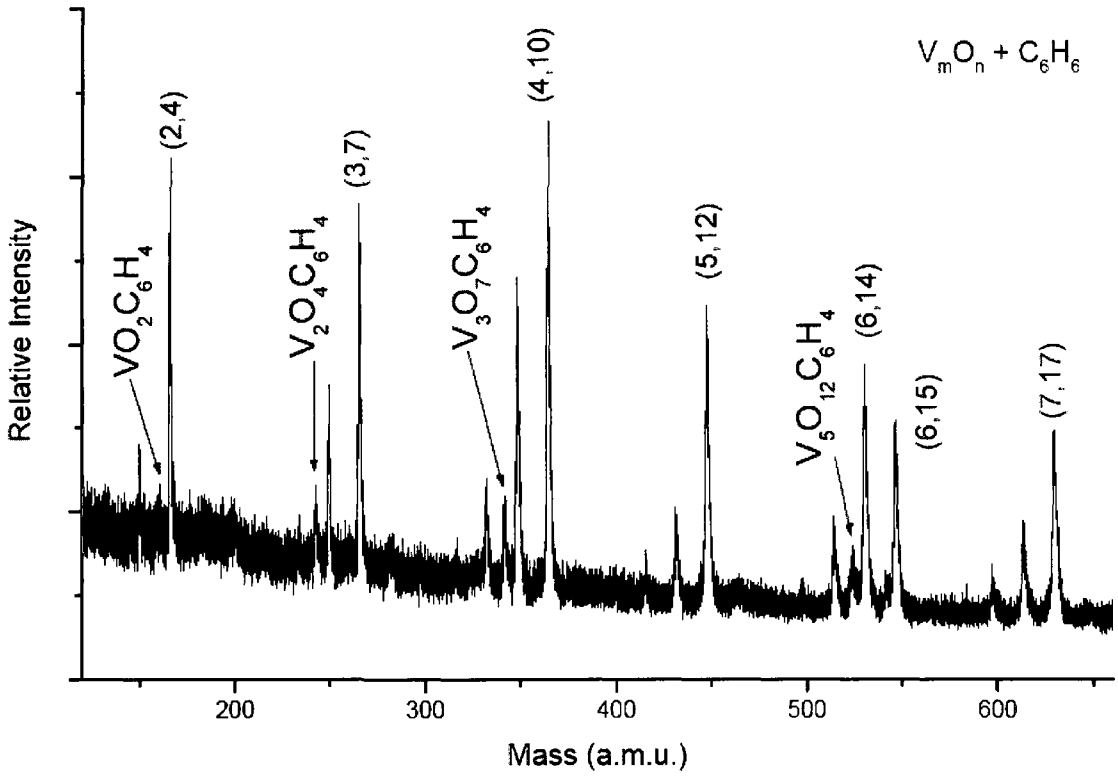


Figure 7.4: Reactions of V_mO_n clusters with benzene (C_6H_6). Reactant gas C_6H_6 /He (15 psi) is added to the flow tube reactor. New reaction products and remaining clusters are detected by 26.5 eV soft x-ray laser ionization.

7.4 DISCUSSION

7.4.1 V_mO_n + Alkenes (C_2H_4, C_3H_6, C_4H_8, C_4H_6)

As shown in Figure 7.1(b), products VO_2CH_2, $V_3O_7CH_2$, and $V_5O_{12}CH_2$ are identified as the main products for the reactions of V_mO_n + C_2H_4, implying that the following reactions occur:

$$(V_2O_5)_nVO_3 + H_2C{=}CH_2 \rightarrow (V_2O_5)_nVO_2CH_2 + CH_2O \quad (7.1)$$

In reaction (7.1), the C=C bond of ethylene (C_2H_4) is broken on specific vanadium oxide clusters, $VO_3(V_2O_5)_n$. Based on DFT calculations,[7.22] the reaction $VO_3 + C_2H_4 \rightarrow VO_2CH_2 + CH_2O$ is thermodynamically favorable by 0.3 eV, and is an overall barrierless reaction at room temperature; therefore, one can deduce that the general reaction (7.1) can also occur to generate products VO_2CH_2, $V_3O_7CH_2$, and $V_5O_{12}CH_2$ expressed as $(V_2O_5)_nVO_2CH_2$. One notes that products, such as $V_2O_5CH_2$ and $V_4O_{10}CH_2$, etc., are not observed in the experiments, indicating that C=C bond breaking for C_2H_4 only occurs on oxygen rich vanadium oxide clusters with $VO_3(V_2O_5)_n$ stoichiometries. Another possible reaction, $VO_2 + C_2H_4 \rightarrow VO_2CH_2 + CH_2$ (ΔH_{298} = + 3.5 eV), corresponding to the observation of product VO_2CH_2, is also considered; however, it is not a thermodynamically available reaction at room temperature. Thus, products $(V_2O_5)_nVO_2CH_2$ do not arise from reaction $(V_2O_5)_nVO_2 + C_2H_4 \rightarrow (V_2O_5)_nVO_2CH_2 + CH_2$, and one can conclude that C=C bond cleavage is not favorable for the most stable neutral vanadium oxide clusters (VO_2, V_2O_4, V_2O_5, V_3O_7...).

We have documented that the products VO_2CH_2 and $V_3O_7CH_2$ detected by the 26.5 eV laser are definitely generated from the neutral vanadium oxide cluster reacting with C_2H_4, and are not generated from fragmentation during the ionization processes since such reaction products are also detected by using 10.5 eV laser ionization. One knows that in this latter instance, insufficient excess energy exist in the clusters to break any bonds during the ionization processes by 118 nm single photon, near threshold ionization.

Therefore, it is reasonable to consider that analogous products detected in the studies of V_mO_n + alkene reactions are not associated with fragmentation due to high photon energy at 26.5 eV.

The above results of $V_mO_n + C_2H_4$ reactions suggest that all C=C bonds of alkenes might be cleaved on vanadium oxide clusters with stoichiometries and structures $VO_3(V_2O_5)_n$. To explore this possibility, other alkene molecules are used instead of ethylene to react with neutral V_mO_n clusters. As shown in Figure 7.1(c), if reactant propylene (H_2C=$CHCH_3$) is added into the reactor, a series of new signals is assigned to products $VO_2C_2H_4$, $V_3O_7C_2H_4$, and $V_5O_{12}C_2H_4$ for the reactions $V_mO_n + C_3H_6$. These products can be generated from the following reactions:

$$(V_2O_5)_nVO_3 + H_2C{=}CHCH_3 \rightarrow (V_2O_5)_nVO_2C_2H_4 + H_2CO \qquad (7.2)$$

In this reaction, C=C bonds of propylene are broken as in the reactions of V_mO_n with ethylene. This chemistry can be considered driven by the formation of the stable product formaldehyde.

Several reaction products identified as VOC_4H_6, $VO_2C_2H_4$, and $VO_2C_4H_8$ are also observed for the reactions between V_mO_n and 1-butene (C_4H_8, H_2C=$CHCH_2CH_3$) as displayed in the mass spectrum of Figure 7.2. These products can be generated from C=C bond cleavage reactions as follows:

$$(V_2O_5)_nVO_3 + H_2C{=}CHCH_2CH_3 \rightarrow (V_2O_5)_nVO_2C_3H_6 + H_2CO \qquad (7.3)$$

1,3-butadiene (C_4H_6, H_2C=CH-CH=CH_2) is an alkene with two C=C double bond used as a reactant. For neutral clusters V_mO_n reacting with 1, 3-butadiene, products VOC_3H_4,

$V_3O_7C_3H_4$, and $V_5O_{12}C_3H_4$ are detected along with a few association products $VO_2C_4H_6$ and $V_2O_4C_4H_6$ (shown in Figure 7.3). A C=C bond of C_4H_6 can be cleaved on V_mO_n clusters as in the reaction,

$$(V_2O_5)_nVO_3 + H_2C{=}CHCH{=}CH_2 \rightarrow (V_2O_5)_nVO_2C_3H_4 + H_2CO \qquad (7.4)$$

Note that in reactions 7.1 – 7.4, the C=C bonds of the alkenes are cleaved in reactions with $(V_2O_5)_nVO_3$ clusters, and H_2CO (formaldehyde) molecules are formed as an additional separated product. Oxygen rich clusters VO_3, V_3O_8, and V_5O_{13} detected in the pure vanadium oxide cluster distribution disappear when alkenes (C_3H_6, C_4H_8, and C_4H_6) are added to the reactor as shown in Figures 7.1, 7.2, and 7.3, indicating the high reactivity of these clusters. Therefore, we conclude that C=C bonds of alkenes are broken in reactions with neutral vanadium oxide clusters (VO_3, V_3O_8, and V_5O_{13}) of the general form $(V_2O_5)_nVO_3$ via reactions 7.1 - 7.4.

The mechanism of C=C bond breaking on $(V_2O_5)_nVO_3$ clusters to generate a H_2CO (formaldehyde) product can be explored through theoretical calculations. Based on the calculation results for the reaction VO_3+C_2H_4, the reaction starts with the O atom of VO_3 attacking a C atom of CH_2=CH_2 molecule to form an association intermediate releasing about 0.67 eV energy, in which the C=C double bond in CH_2=CH_2 is significantly weakened to become a single C-C bond. A stable five membered ring intermediate is then formed via [3+2] cycloaddtion. A large amount of energy (2.12 eV) is then released, leading to C-C bond breaking to generate VO_2CH_2 and H_2CO products. The channel VO_3 + C_2H_4 → VO_2CH_2 + H_2CO is an overall barrierless reaction pathway, and can occur at

room temperature.[7.22]

To understand the reaction mechanisms between V_mO_n with larger alkenes, we apply DFT calculations to VO_3+ C_3H_6 reaction at the B3LPY/TZVP level:

$$VO_3 + H_2C{=}CHCH_3 \rightarrow VO_2C_2H_4 + H_2CO \qquad \Delta H = -0.29 \text{ eV} \quad (7.5)$$

As shown in Figure 7.5, the reaction starts with VO_3 attacking C=C bond of C_3H_6 molecule to form intermediate **1**, in which the C=C double bond in $CH_3CH{=}CH_2$ (bond length = 1.33 Å) is significantly weakened to become a single C-C bond 1.48 Å in intermediate **1** (C-C single bond length = 1.5 Å in C_3H_6). Via transition state **1/2**, a lowest energy intermediate **2** with a five membered ring is formed and releases a large amount of energy about 2.12 eV. Through transition state **2/3**, the C-C bond of intermediate **2** ruptures and yields intermediate **3**, in which CH_2 and C_2H_4 radicals connect with two O atoms of VO_3 by C-O bonds, respectively. In intermediate **4**, the formation of a V-O-C three membered ring weakens and stretches the V-O bond between the H_2CO moiety and the $VO_2C_2H_4$ moiety, and finally results in generating products **P1** ($VO_2C_2H_4$ + H_2CO) with the release of 0.25 eV energy. The pathway is thermodynamically favorable and barrierless for reaction (7.5). Anoter oxygen transfer reaction pathway, **3** → **3/5** → **5** → **P2** (VO_2CH_2 + CH_3CHO), is also thermodynamically available. The reaction product VO_2CH_2 is observed in Figure 7.1(a). The mechanism of C=C breaking for V_mO_n + C_3H_6 is the same as for the V_mO_n + C_2H_4 reaction. The formation of the most stable structures with five membered rings in both reactions are the key steps for C=C bond cleavages. We

believe that the same mechanism will be found for VO_3 reacting with other alkenes, such

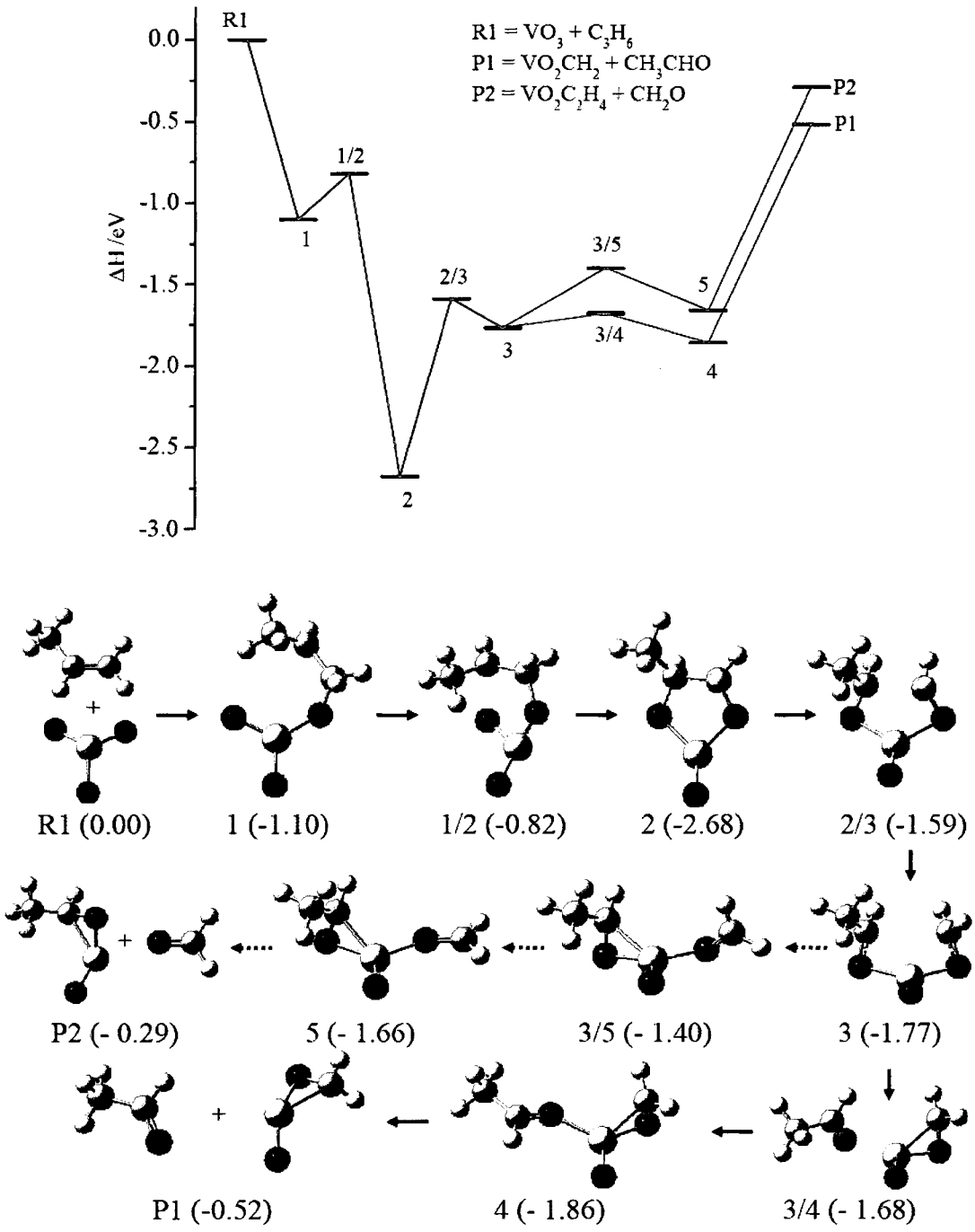


Figure 7.5: DFT calculated potential energy surface for $VO_3 + C_3H_6 \rightarrow VO_2C_2H_4 + H_2CO$ reaction at the theory level B3LYP/TZVP. Structures are the optimized geometries of the reaction intermediates and transition states. Relative energies are in eV. A complete potential surface of $VO_3 + C_3H_6$ reaction can be

found in ref. 7.27.

as C_4H_8 and C_4H_6, since similar reaction products generated from C=C bond cleavage are observed in these experiments. A complete potential surface for the $VO_3 + C_3H_6$ reaction can be found in ref. 7.27.

VO_3 has one more oxygen atom compared to the most stable vanadium oxide VO_2, so it can be considered as an oxygen centered radical. The oxygen rich vanadium oxide clusters VO_3, V_3O_8, V_5O_{13}, etc. can be expressed as $VO_3(V_2O_5)_{n=0,1,2}...$ As shown in Figure 7.6, the V_3O_8 structure can be generated from V_2O_5 bonded to VO_3, and expressed as $(V_2O_5)(VO_3)$. For $V_3O_8 + C_2H_4$ reaction, a five membered ring structure is also found for the stable complex species $V_3O_8C_2H_4$ (Figure 7.6c); this structure is similar to those found for the $VO_3 + C_2H_4/C_3H_6$ reaction (Figure 7.5, intermediate **2**). The double bond of $H_2C=CH_2$ is weaken to a single bond in the five membered ring structure, eventually leading to a broken C-C bond. Recently, Santambrogio et al. studied the structures of $V_mO_n^-$ anion clusters by experimental IRMPD spectra and DFT calculations.[7.15] Closed shell clusters $V_3O_8^-$, $V_5O_{13}^-$, and $V_7O_{18}^-$ can be identified as a $(V_2O_5)_{n=1,2,3}(VO_3)^-$ structure, in which VO_3 and (V_2O_5) moieties are clearly found, similar to that of the neutral cluster V_3O_8, shown in Figure 7.6.

The present gas phase studies of neutral vanadium oxide cluster reactions with alkenes can suggest a possible catalytic model for oxidative cleavage of alkenes on condensed phase surfaces. From this work, we can offer a catalytic model for aldehyde formation through oxidation of alkenes on VO_3. Based on our calculations

(B3LYP/TZVP), reaction $VO_2C_2H_4 + O_2 \rightarrow VO_3 + CH_3CHO$ is also thermodynamically

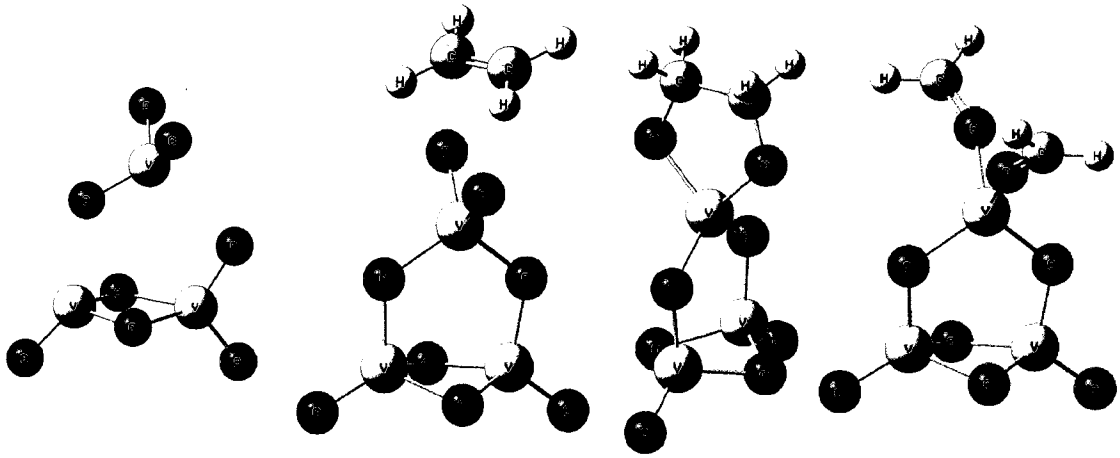


Figure 7.6: DFT calculations (B3LYP/LANL2DZ) of structures: (a) VO_3 and V_2O_5; (b)V_3O_8 and C_2H_4; (c) $V_3O_8C_2H_4$; (d) C=C cleavage on V_3O_8.

available without a barrier. A thermodynamically feasible catalytic cycle can be suggested as follows:

$$VO_3 + H_2C{=}CHCH_3 \rightarrow VO_2C_2H_4 + H_2CO \qquad \Delta H = -0.25 \text{ eV}$$

$$VO_2C_2H_4 + O_2 \rightarrow VO_3 + CH_3CHO \qquad \Delta H = -2.66 \text{ eV}$$

$$H_2C{=}CHCH_3 + O_2 \rightarrow CH_3CHO + H_2CO \qquad \Delta H_{298} = -2.91 \text{ eV} \qquad (7.6)$$

In reaction (7.6), C_3H_6 (propylene) is cleaved at the C=C bond and is oxidized to H_2CO (formaldehyde) and $VO_2C_2H_4$ products. If these reactions take place in an oxygen rich environment, $VO_2C_2H_4$ can be oxidized by O_2 molecules in a second step to generate VO_3 and CH_3CHO. Both steps in this cycle are exothermic and overall barrierless. Theoretical calculations indicate that the VO_3 moiety can be considered as an active site for neutral vanadium oxide clusters:[7.22] V_3O_7, V_5O_{15}, etc. clusters can be considered as V_2O_5 bonded to VO_3, as shown in the general formula $VO_3(V_2O_5)_n$. Therefore, a general

catalytic oxidation reaction of alkenes on vanadium oxide clusters is suggested as:

$$R\text{-}HC{=}CH_2 + O_2 \xrightarrow{VO_3(V_2O_5)_n} R\text{-}CHO + H_2CO \qquad (7.7)$$

In this reaction, alkenes are oxidized by O_2 to produce aldyhydes on vanadium oxide with a structure $VO_3(V_2O_5)_{n=0,1,2}$. In practical catalysis, the selective oxidative cleavage of alkenes is very important. Our study provides useful information for designing catalysts to aid in the oxidation of alkenes.

7.4.2 Mechanism of $V_mO_n + C_2F_4$ Reactions

Substitution of the hydrogen atoms in small hydrocarbons by fluorine has a marked effect on many of their physical and chemical properties. Asymmetric replacement of hydrogen by fluorine can result in a significant increase in the molecular dipole moment, and a C-F bond is also stronger than a C-H bond.[7.44,7.55] In our experiments, we do not detect any reaction product when C_2F_4 gas is used as a reactant added into the flow cell reactor. To explore the effect of fluorine replacement in reactions of V_mO_n + alkenes, we investigate the mechanism of $VO_3 + C_2F_4$ by DFT calculations at the theory level B3LYP/TZVP. As shown in Figure 7.7, the potential surface for the $VO_3 + C_2F_4$ reaction is similar to that of $VO_3 + C_2H_4/C_3H_6$ reactions (Figure 7.5). The O atom of VO_3 attacks C_2F_4 to form intermediate **6**, and then form a lowest energy intermediate **7** with a five membered ring via transition state **6/7**. About 4.43 eV energy is released in this step. Two reaction pathways, (1) oxygen transfer reaction to produce $VO_2 + C_2F_4O$ and (2) C=C cleavage reaction to produce $VO_2CF_2 + CF_2O$, are thermodynamically available without

barriers at room temperature. Note that the reaction potential surface for the VO_2+ C_2F_4 reaction is

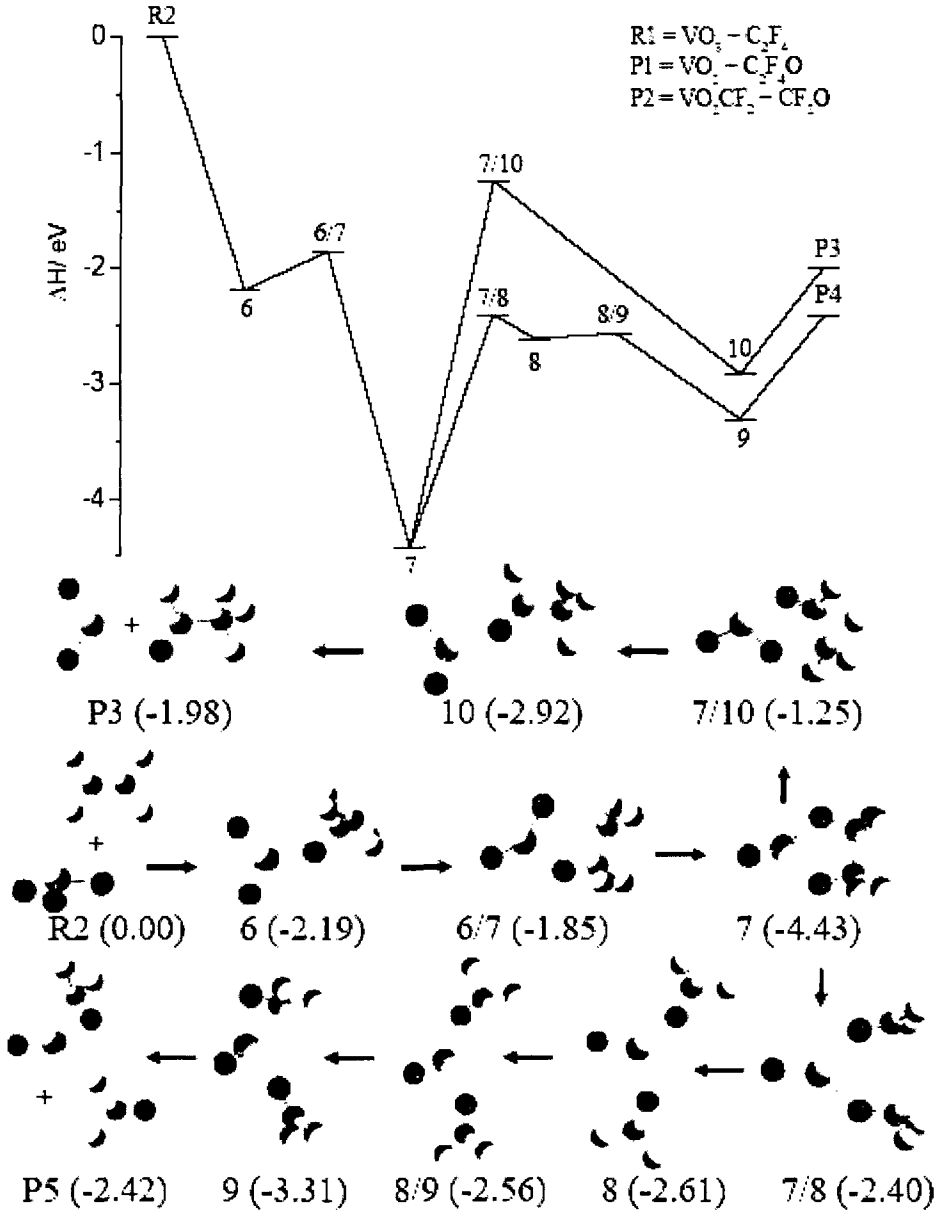


Figure 7.7: DFT calculated potential energy surface for the VO_3 + C_2F_4 reaction at the theory level B3LYP/TZVP. Structures are the optimized geometries of the reaction intermediates and transition states. Relative energies are in eV.

similar to that VO_2+C_2H_4/C_3H_6 reactions; however, no significant reaction product is

detected in the experiments. The theoretical calculational result is then in disagreement with experimental observations.

The effects of fluorine on alkenes, most notably for tetrafluoroethylene, have been investigated by others under different circumstances.[7.45-7.47] The experimental and theoretical studies of $O + C_2F_4 \rightarrow CF_2 + OCF_2$ reaction are undertaken by Nguyen et al.[7.45] They find that the $O + C_2F_4$ reaction is initiated by a chain-addition on the C=C double bond of C_2F_4 to form an intermediate OC_2F_4 without a transition state, at the B3LYP/6-311+G(3df) level of theory. Their calculation results are in conflict with experimental studies; the overall rate constant for $O + C_2F_4$ reaction depends positively on temperature with an Arrhenius activation energy of 0.6 +/- 0.2 kcal/mol.[7.48] To explore this issue, they employ a combination method of using B3LYP, G2M(UCC, MP2), CBS-QB3, and G3, and find a transition state for $O + C_2F_4$ with a barrier of 0.4 kcal/mol. Comparison of the potential surface for the $O + C_2F_4$ reaction[7.45] with that of the $VO_3 + C_2F_4$ reaction (Figure 7.7), suggests a very similar reaction mechanism: the O atom, or O atom of VO_3, attacks C_2F_4 to form $OC_2F_4/VO_3C_2F_4$ without a barrier. Breaking of the C=C double bond then leads to generation of the products, $F_2CO + CF_2$/ $VO_2CF_2 + F_2CO$. Structure of the intermediate OC_2F_4 is similar to that of $VO_3C_2F_4$ if VO_3 is considered to be an oxygen centered radical. Therefore, if we consider a steric effect for VO_3 in place of the O atom reacting with C_2F_4, one can suggest that a transition state with a higher barrier for the $VO_3 + C_2F_4$ reaction than that found for the $O + C_2F_4$ reaction, exists. This barrier cannot be calculated at B3LYP/TZVP level, however This

barrier may slow down the reaction between VO_3 and C_2F_4, resulting in no product detected on the time scale of the present experiment.

7.4.3 Mechanism of $V_mO_n + C_6H_6$ Reactions

Benzene has a delocalized π double bond system with no particular localized single or double bonds; the delocalization of electrons makes benzene more stable typically than alkenes. As displayed in Figure 7.4, products $VO_2C_6H_4$, $V_2O_4C_6H_4$, $V_3O_7C_6H_4$, and $V_5O_{12}C_6H_4$ are observed for reactions $V_mO_n + C_6H_6$. The products may be generated from possible dehydration reactions:

$$V_mO_{n+1} + C_6H_6 \rightarrow V_mO_nC_6H_4 + H_2O \qquad (7.8)$$

The reaction products generated from $V_mO_n + C_6H_6$ reactions are different from those generated by V_mO_n + alkene reactions. The potential surface for the reaction,

$$VO_3 + C_6H_6 \rightarrow VO_2C_6H_4 + H_2O \qquad \Delta H = -0.79 \text{ eV} \qquad (7.9)$$

is calculated at the B3LYP/TZVP level as shown in Figure 7.8. As a first step, the O atom of VO_3 bonds to one C atom of the C_6H_6 molecule to form the structure of intermediate **11**. Through transition state **11/12**, one H atom transfers from a C atom to an O atom of VO_3. Following structural adjustment via transition state **12/13**, intermediate state **13** is formed, and then another H atom is transferred to the same O atom of VO_3 as a second step. In the structure of intermediate **14**, a H_2O moiety is connected to $VO_2C_4H_6$ by a weak bond. Step three, yields final products H_2O and $VO_2C_4H_6$ while releasing energy of 0.79 eV. On the basis of this calculation, a dehydration reaction between VO_3 and C_6H_6 is thermodynamically favorable and overall barrierless. This calculated process is in

agreement with our experimental observation of a $VO_2C_4H_6$ product in the mass spectrum as displayed in Figure 7.4.

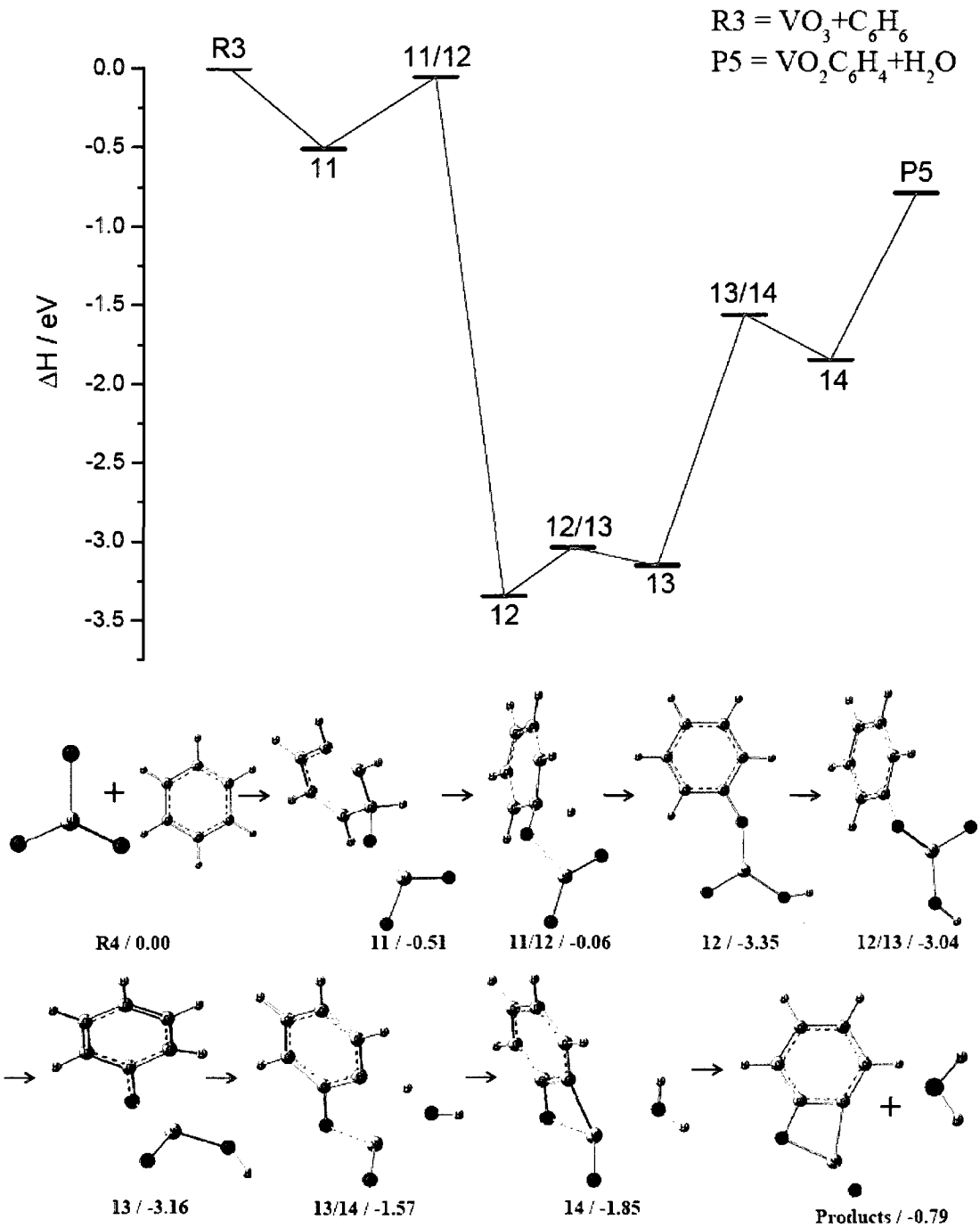


Figure 7.8: DFT calculated potential energy surface for VO_3 + C_6H_6 reaction at the theory level B3LYP/TZVP. Structures are the optimized geometries of the reaction intermediates and transition states. Relative energies are in eV.

7.4.4 Specificity of C=C Bond Cleavage Reactions

C=C bond cleavage of alkenes on neutral V_mO_n clusters is a unique reaction. First, this reaction only occurs on neutral $(V_2O_5)_nVO_3$ clusters. No product is detected with regard to C=C bond scission in the reactions of alkenes with the most stable clusters (VO_2, V_2O_5, V_3O_7, V_4O_{10}...), oxygen deficient clusters (VO, V_2O_3, V_3O_6...), or oxygen rich clusters with an even number of V atoms (V_2O_6, V_4O_{11}...). Second, only C=C double bonds of alkenes cleave on neutral vanadium oxide clusters. The single C-C bond of alkanes and triple C≡C bond of alkynes are not broken on neutral vanadium oxide clusters. In our studies of neutral V_mO_n cluster reactions with saturated hydrocarbons C_2H_6, C_3H_8, and C_4H_{10}, the intensities of V_mO_n cluster signals decrease in roughly the same proportion expect for a few association products. The reactivity of saturated hydrocarbons is lower than that of unsaturated species in reactions with neutral V_mO_n clusters. We also investigate reactions between V_mO_n and tetrafluoroethylene (CF_2=CF_2), and find that C=C bond cleavage does not occur in this case. Third, these reactions only occur on vanadium oxide clusters: reactions of other neutral metal oxide clusters, such as Nb_mO_n, Ta_mO_n, Ti_mO_n, Co_mO_n, Si_mO_n, Fe_mO_n, etc. with alkenes do not generate products corresponding to C=C bond cleavage. Experimental and theoretical results indicate that the activity of metal oxide clusters is dependent on many issues: bond energies, reaction barriers, reaction rates, etc., and not only on the oxygen content of M_mO_n clusters. Fourth, these reactions only occur on neutral clusters. Neutral vanadium oxide clusters behave

differently than do the comparable cluster ions in reactions with alkenes. Oxygen transfer reactions are observed as a major reaction channel for $V_mO_n^+$ cluster ions reacting with C_2H_4;[7.16] for $V_mO_n^+ + C_4H_8$ reactions, $V_mO_nC_2H_4$ products are observed for clusters $V_2O_{4,5}^+$, $V_3O_7^+$, and $V_5O_{12}^+$ due to single bond C2-C3 cleavage.[7.18,7.19] $V_3O_7^+$ is especially efficient in the dehydrogenation of 1,3-butadiene and in the cracking of 1-butene;[7.18,7.19,7.26] however, the products that correspond to double bond breaking are not observed in any $V_mO_n^+$ cluster reaction with alkenes.

7.5 CONCLUSIONS

An experimental and theoretical study of the reaction of neutral V_mO_n clusters with the alkenes, ethylene, propylene, 1-butene, and 1,3-butadiene, and tetrafluoroethylene and benzene are conducted. We find that the C=C bonds of the alkenes C_2H_4, C_3H_6, C_4H_6, and C_4H_8 are cleaved on vanadium oxide oxygen rich clusters of the form $VO_3(V_2O_5)_{n=0,1,2...}$, generating products $(V_2O_5)_nVO_2CH_2$, $(V_2O_5)_nVO_2C_2H_4$, $(V_2O_5)_nVO_2C_3H_4$, and $(V_2O_5)_nVO_2C_3H_6$ for reactions $V_mO_n + C_2H_4/C_3H_6/C_4H_6/C_4H_8$, respectively. Formaldehyde (H_2CO) molecules are formed as another product of these reactions. The cleavage of C=C bonds of alkenes on neutral V_mO_n clusters is a unique reaction. These reactions do not occur for (1) the most stable V_mO_n clusters, (2) oxygen rich V_mO_n clusters with even number of V atoms, (3) other metal oxide clusters, such as Nb_mO_n, Ta_mO_n, Ti_mO_n, Co_mO_n, Si_mO_n, Fe_mO_n, etc., (4) vanadium oxide cluster ions ($V_mO_n^{\pm}$), and (5) for $V_mO_n + C_2F_4$ or C_6H_6. No reaction products are detected for $V_mO_n + C_2F_4$ reactions. For the reactions of $V_mO_n + C_6H_6$ only the dehydration products

$VO_2C_6H_4$, $V_2O_4C_6H_4$, $V_3O_7C_6H_4$, and $V_5O_{12}C_6H_4$ are detected. DFT calculations indicate that the reaction $VO_3+C_3H_6 \rightarrow VO_2C_2H_4 + H_2CO$ is thermodynamically favorable and overall barrierless at room temperature, and that a VO_3 moiety may be considered as an active site for $VO_3(V_2O_5)_{n=0,1,2}\ldots$ structures. Based on experimental data and DFT calculations, a catalytic cycle for oxidation of alkenes to produce formaldehyde and aldehydes on vanadium oxide is suggested. The experimental and theoretical studies of $VO_3+ C_2F_4/C_6H_6$ reactions indicate that C=C bond cleavage does not occur for these two reactions due to fluorine replacement and delocalized π double bond effects.

REFERENCES

[7.1] Valbert, J. R.; Zajacek, J. G.; Orenbuch, D. I. E*ncyclopedia of Chemical Processing and Design*, Marcel Dekker: New York, **1993**, p88.

[7.2] Zhao, C.; Washs, I. E. *Catalysis Today*, **2006**, *118*, 332.

[7.3] Nijhuis, T. A.; Akkee,M. M.; Moulijn, J. A.; Weckuysen, B. M. *Ind. Eng. Chem. Res.* **2006**, *45*, 3447.

[7.4] Grasselli, R. K. *Top. Catal.* **2000**, *21*, 79.

[7.5] Ogliaro, F.; Harris, N.; Cohen, S.; Filatov, M.; Visser, de, S. P.; Shaik, S. *J. Am. Chem. Soc.* **2000**, *122*, 8977.

[7.6] Bohme, D. K.; Schwarz, H. *Angew. Chem. Int. Ed.* **2005**, *44*, 2336.

[7.7] Zemski, K. A.; Justes, D. R.; Bell, R.C.; Castleman, A. W., Jr. *J. Phys. Chem. A* **2001**, *105*, 4410.

[7.8] Schlangen, M.; Schroder, D.; Schwarz, H. *Angew. Chem. Int. Ed.* **2007**, *46*, 1641.

[7.9] de Bruin, B.; Budzelaar, P. H. M.; Wal, A. G.. *Angew. Chem. Int. Ed.* **2004**, *43*, 4142.

[7.10] Asmis, K. R.; Brummer, M.; Kaposta, C.; Santambrogio, G.; von Helden, G.; Meijer, G.; Rademann, K.; Woste, L. *Phys. Chem. Chem. Phys*. **2002**, 4, 1101.

[7.11] Feyel, S.; Schroder, D.; Schwarz, H. *J. Phys. Chem. A* **2006**, *110*, 2647.

[7.12] Feyel, S.; Dobler, J.; Schroder, D.; Sauer, J.; Schwarz, H. *Angew. Chem. Int. Ed.* **2006**, *45*, 4681.

[7.13] Kang, K.; Beauchamp, J. L. *J. Am. Chem. Soc.* **1986**, *108*, 5663.

[7.14] Stevens, A. E.; Beauchamp, J. L. *J. Am. Chem. Soc.* **1979**, *101*, 6449.

[7.15] Santambrogio, G.; Brummer, M.; Woste, L.; Dobler, J.; Sierka, M.; Sauer, J.; Meijer, G.; Asmis, K. R. *Phys. Chem. Chem. Phys.*, **2008**, *10*, 3992.

[7.16] (a) Justes, D. R.; Mitric, R.; Moore, N. A.; Bonacic-Koutecky, V.; Castleman, A. W., Jr. *J. Am. Chem. Soc.* **2003**, *125*, 6289. (b) Moore, N. A.; Mitric, R.; Justes, D. R.; Bonacic-Koutecky, V.; Castleman, A.W., Jr. *J. Phys. Chem. B* **2006**, *110*, 3015.

[7.17] Zemski, K. A.; Justes, D. R.; Castleman, A.W., Jr. *J. Phys. Chem. A* **2001**, *105*, 10237.

[7.18] Bell, R. C.; Zemski, K. A.; Kerns, K. P.; Deng, H. T.; and Castleman, A.W., Jr. *J. Phys. Chem. A* **1998**, *102*, 1733.

[7.19] Bell, R. C.; Castleman, A.W., Jr. *J. Phys. Chem. A* **2002**, *106*, 9893.

[7.20] Zemski, K. A.; Justes, D. R.; Castleman, A.W., Jr. *J. Phys. Chem. A* **2001**, *105*, 4410.

[7.21] Fielicke, A.; Mitric, R.; Meijer, G.; Bonacic-Koutecky, V.; von Helden, G. *J. Am. Chem. Soc.* **2003**, *125*, 15716.

[7.22] Dong, F.; Heinbuch, S.; Xie, Y.; Rocca, J. J.; Bernstein, E. R.; Wang, Z. C. Deng, K.; He, S. G. *J. Am. Chem. Soc.* **2008**, *130*, 1932.

[7.23] Cheng, M. J.; Chenoweth, K.; Oxgaard, J.; van Duin, A. Goddard, III, W. A. *J. Phys. Chem. C* **2007**, *111*, 5115.

[7.24] Gracia, L.; Sambrano, J. R.; Safont, V. S.; Calatayud, M.; Beltran, A.; Andres, J. *J. Phys. Chem. A* **2003**, 107, 3107.

[7.25] Gracia, L.; Sambrano, J. R.; Andres, J.; Beltran, A. *Organometallics*, **2006**, *25*, 1643.

[7.26] Feyel, S.; Schroder, D.; Rozanska, X.; Sauer, J.; Schwarz, H. *Angew. Chem. Int. Ed.* **2006**, *45*, 4677.

[7.27] Wang, Z.; Xue, W.; Ma, Y.; Ding, X.; He, S.; Dong, F.; Heinbuch, S.; Rocca, J. J.; Bernstein, E. R. *J. Phys. Chem. A*, **2008**, *112*, 5984.

[7.28] Matsuda, Y.; Bernstein, E. R. *J. Phys. Chem. A* **2005**, *109*, 3803.

[7.29] (a) Dong,F.; Heinbuch, S.; Rocca, J. J.; Bernstein, E. R. *J. Chem. Phys.* **2006**, *125*, 164318. (b) Dong, F.; Heinbuch, S.; Rocca, J. J.; Bernstein, E. R. *J. Chem. Phys.* **2006**, *124*, 224319. (c) Xie, Y.; He, S. G.; Dong, F.; Bernstein, E. R. *J. Chem. Phys.* **2008**, *128*, 044306.

[7.30] Geusic, M. E.; Morse,M. D.; O'Brien, S. C.; Smalley, R. E. *Rev. Sci. Instrum.* **1985**, *56*, 2123.

[7.31] Xie, Y; He, S. G.; Dong, F. Bernstein, E. R. *J. Chem. Phys*. **2008**, *128*, 044306.

[7.32] Zakin, M. R.; Brickman, R. O.; Cox, D. M.; Kaldor, A. *J. Chem. Phys.* **1988**, *86*, 3555.

[7.33] Morse, M. D.; Geusic, M. E.; Heath, J. R.; Smalley, R. E. *J. Chem. Phys.* **1985**, *83*, 2293.

[7.34] Knickelbein, M. B. *Annu. Rev. Phys. Chem.* **1990**, *50*, 79.

[7.35] M. J. Frisch, et al. *Gaussian 03, Revision C.02, Gaussian*, Inc, Wallingford CT, **2004**.

[7.36] Becke, A. D. *Phys. Rev. A* **1988**, *38*, 3098.

[7.37] Becke, A. D. *J. Chem. Phys.* **1993**, *98*, 5648.

[7.38] Lee, C. T.; Yang, W. T.; Parr, R. G. *Phys. Rev. B* **1988**, *37*, 785.

[7.39] Schafer, A.; Huber, C.; Ahlrichs, R. *J. Chem. Phys.* **1994**, *100*, 5829.

[7.40] (a) Jakubikova, E.; Rappe, A. K.; Bernstein, E. R. *J. Phys. Chem. A* **2007**, *111*, 13339. (b) Jakubikova, E. Ph. D. Dissertation (May, **2007**).

[7.41] Calatayud, M.; Andres, J.; Beltran, A. *J. Phys. Chem. A.* **2001**, *105*, 9760.

[7.42] Gonzalez, C.; Schlegel, H. B. *J. Chem. Phys.* **1989**, *90*, 2154.

[7.43] Gonzalez, C.; Schlegel, H. B. *J. Phys. Chem.* **1990**, *94*, 5523.

[7.44] Muir, M.; Baker, J. *Molecular Physic*, **1996**, *89*, 211.

[7.45] Nguyen, T. L.; Dils, B.; Carl,S. A.; Vereecken, L.; Peeter, J. *J. Phys. Chem. A* **2005**, *109*, 9786.

[7.46] Carter, E. A.; Goddard III, W. A. *J Am. Chem. Soc.* **1988**, *110*, 4077.

[7.47] Yang, S. Y.; Borden, W. T. *J Am. Chem. Soc.* **1989**, *111*, 7282.

[7.48] Cvetanovic, R. J. *J. Phys. Chem. Ref. Data* **1987**, *16*, 261.

Chapter 8

Partial Oxidation of Propylene Catalyzed by VO_3 Clusters: A DFT Study

8.1 INTRODUCTION

Vanadium oxides are an important class of heterogeneous catalysts used both in industry and in the laboratory.[8.1-8.3] The well-known industrial processes facilitated by vanadium oxide based catalysts include oxidation of SO_2 to SO_3 in the production of sulfuric acid, selective reduction of NO_x with NH_3 for pollution control, selective oxidation of hydrocarbons in the production of more expensive and useful chemicals, and so forth. In order to interpret these important processes at a molecular, mechanistic level, efforts have been devoted to investigate the chemistry (bonding, structural, and reactivity properties, etc.) of vanadium oxide clusters in the gas phase by both experimental[8.4-8.8] and theorical[8.7-8.12] means. On the other hand, discovery of new and interesting chemistry of vanadium oxide clusters would finally shed light on design, synthesis, and more effective use of practical catalysts.

The chemistry of neutral vanadium oxide clusters in the gas phase is not well studied experimentally due to difficulties in detection of these neutral metal oxide clusters without fragmentation during multi-photon or electron-impact ionization processes. Single photon ionization through radiation of vacuum ultra-violet and soft x-ray lasers

has been effectively employed recently to detect neutral transition metal oxide and sulfide clusters without fragmentation,[8.13] and the reactivity of neutral vanadium oxide clusters toward C_2 hydrocarbons has been successfully studied.[8.14] One of the interesting chemistries identified is that $(V_2O_5)_nVO_3 + C_2H_4 \rightarrow (V_2O_5)_nVO_2CH_2 + CH_2O$ occurs under near room temperature conditions, for n = 0, 1, and 2. This C=C double bond cleavage reaction is not found in the reaction of cationic vanadium oxide clusters with ethylene. In contrast, a set of oxygen transfer reactions are identified for cationic species: $(V_2O_5)_n^+ + C_2H_4 \rightarrow (V_2O_5)_{n-1}V_2O_4^+ + CH_3CHO$, where n = 1, 2, and 3.[8.6,8.7] Based on density functional theory (DFT) calculations for the neutral VO_3, cluster the oxygen transfer reaction channel ($VO_3 + C_2H_4 \rightarrow VO_2 + CH_3CHO$) is thermodynamically more favorable than the C=C bond cleavage channel; however, formation of CH_3CHO is kinetically less favorable at room temperature than formation of HCHO due to a higher overall reaction barrier.

The mechanism of the reaction of $(V_2O_5)_nVO_3$ with C_2H_4 is interesting in that the reaction kinetics and the reaction dynamics play opposite roles. This is generally of fundamental importance in selective oxidation of hydrocarbons because formation of unwanted CO_2 and H_2O are usually thermodynamically most favorable. In this work, DFT calculations are employed to investigate the reaction of VO_3 with propylene (C_3H_6), in order to explore the generality of double bond cleavage of alkenes over VO_3. We anticipate that the additional methyl group of propylene will result in different chemistry for $VO_3 + C_3H_6$ than that found for $VO_3 + C_2H_4$. Moreover, to generate a complete model catalytic cycle, reactions of O_2 with some kinetically allowed products will be considered to regenerate VO_3.

In the chemical industry, selective oxidation of propylene is particularly

important.[8.15,8.16] The selective oxidation of propylene over vanadium oxide catalysts supported (Al_2O_3, SiO_2, TiO_2, and Nb_2O_5, etc.)[8.16-8.18] or unsupported[8.19] has been extensively investigated. Products formed with high selectivity are acrolein (CH_2CHCHO) over V_2O_5/Nb_2O_5,[8.17] acetone ($(CH_3)_2CO$) over V_2O_5/TiO_2,[8.16] acetaldehyde (CH_3CHO) over V_2O_5/SiO_2,[8.18] acetaldehyde and acetic acid (CH_3COOH) over V_2O_5-MoO_3,[8.19] and others. The mechanisms for the formation of C=C bond scission products, such as acetaldehyde is not well explored. Ruszel et. al.[8.18] suggest that partial degradation of propylene over supported vanadium oxide catalysts may be considered as an electrophilic surface oxygen species O_2- or O- adding to a C=C double bond through the formation of peroxo or oxo intermediates which can decompose by breaking a C-C bond.

To address catalytic mechanisms involving vanadium oxides, considerable efforts have been devoted to determining the structures of catalytically active sites on the supports. Surface mono-vanadium species are generally accepted to have the structure O=V-(O-*X*)$_3$ (pyramid model), in which *X* is an atom (such as Si, Ti, ...) in the support;[8.3,8.20] however, some recent experimental and theoretical studies suggest that the species should have the structure O=V(=O_2)-O-*X* (umbrella model).[8.21] The structures of the mono-vanadium sites will be more complicated if surface acidity (hydrogen species) is considered.[8.22] Evidence indicates that structures of catalytically active sites are dynamic and some reactive intermediates do not live long enough to be captured by available experimental (mainly spectroscopic) techniques.[8.17] VO_3 has structure similar to the umbrella model surface mono-vanadium species. VO_3 may also serve as a model for a reactive surface intermediate. Thus irradiated VO_3 clusters can serve as a model catalyst to interpret possible surface chemistry and reactive species.

8.2 COMPUTATIONAL DETAILS

DFT calculations using the Gaussian 03 program[8.23] are employed to study reactions of VO_3 with C_3H_6 and reactions of the kinetically allowed products from VO_3+C_3H_6 with O_2 to regenerate VO_3. The DFT calculations involve geometry optimization of various reaction intermediates and transition states. Transition state optimizations are performed by using either the Berny algorithm[8.24] or the synchronous transit-guided quasi-Newton (STQN) method.[8.25,8.26] For most cases, initial guess structure of the transition state is obtained through relaxed potential energy surface (PES) scans using an appropriate internal coordinate. For a few complicated cases, the initial structure is obtained by using the multi-coordinate driven method[8.27] that determines the relaxed PES in terms of more than one active internal coordinate. Vibrational frequencies are calculated to check that the reaction intermediates have all positive frequencies and species in the transition states have only one imaginary frequency. Intrinsic reaction coordinate (IRC) calculations[8.28,8.29] are also performed so that a transition state connects two appropriate local minima in the reaction paths. The hybrid B3LYP exchange-correlation functional[8.30] is adopted. A contracted Gaussian basis set of triple zeta valence quality[8.31] plus one *p* function for H and V atoms and one *d* function for C and O atoms is used. This basis set is denoted as TZVP in Gaussian 03 program. This functional and basis set are tested to predict reasonably good energetics for vanadium oxides and hydrocarbons at moderate computational costs in several theoretical investigations.[8.7,8.8] Test calculations indicate that basis set superposition error (BSSE)[8.32,8.33] is negligible, so the BSSE is not taken into consideration in this study. The zero-point vibration corrected energies ($\Delta H_{0\,K}$) and the Gibbs free energies at 298 K ($\Delta G_{298\,K}$) are reported in this study. Cartesian coordinates, electronic energies, and vibrational frequencies for all of the optimized structures are

available upon request.

8.3 RESULTS

8.3.1 Reaction of VO_3 with C_3H_6

The following reaction channels are followed for the reaction of VO_3 with C_3H_6.

$VO_3 + C_3H_6 \rightarrow VO_2CHCH_3 + HCHO$ (formaldehyde), $\Delta H_{298\,K} = -0.29$ eV (8.1)

$VO_3 + C_3H_6 \rightarrow VO_2CH_2 + CH_3CHO$ (acetaldehyde), $\Delta H_{298\,K} = -0.53$ eV (8.2)

$VO_3 + C_3H_6 \rightarrow VO_2 + CH_3CH_2CHO$ (propaldehyde), $\Delta H_{298\,K} = -0.65$ eV (8.3)

$VO_3 + C_3H_6 \rightarrow VO_2 + CH_3COCH_3$ (acetone), $\Delta H_{298\,K} = -0.99$ eV (8.4)

$VO_3 + C_3H_6 \rightarrow VO_2 + C_3H_6O$ (propylene oxide), $\Delta H_{298\,K} = +0.39$ eV (8.5)

$VO_3 + C_3H_6 \rightarrow VO_2H_2 + CH_2{=}CHCHO$ (acrolein), $\Delta H_{298\,K} = -1.67$ eV (8.6)

$VO_3 + C_3H_6 \rightarrow VO_2C_3H_4 + H_2O$ (water), $\Delta H_{298\,K} = -1.00$ eV (8.7)

The DFT calculated enthalpy of reaction at 298 K ($\Delta H_{298\,K}$) is listed after each reaction. The potential energy profiles for reactions (8.1)-(8.7) are plotted in Figure 8.1. The structures and energies of the reaction intermediates and transition states are given in Figure 8.2. The vanadium species VO_3, VO_2, VO_2CH_2, VO_2CHCH_3, and $VO_2C_3H_4$ have doublet ground states. (Figure S1). For simplicity, crossing of spin doublet and quartet potential energy surfaces (spin conversion[8.35]) is not considered for reactions (8.1)-(8.5) and (8.7). The product VO_2H_2 has a quartet ground state, and its lowest doublet state is higher in energy by 1.41 eV (defined by $\Delta H_{0\,K}$). Spin conversion is thus possible in later stages of reaction (8.6). As shown in Figure 8.1, doublet-quartet conversion is not required because formation of doublet VO_2H_2 is also thermodynamically favorable.

The formation of various partial oxidation products (HCHO, CH_3CHO, CH_3CH_2CHO, CH_3COCH_3, and $CH_2{=}CHCHO$) in the reaction $VO_3 + C_3H_6$ is thermodynamically favorable. The formation of HCHO and CH_3CHO involves C=C bond

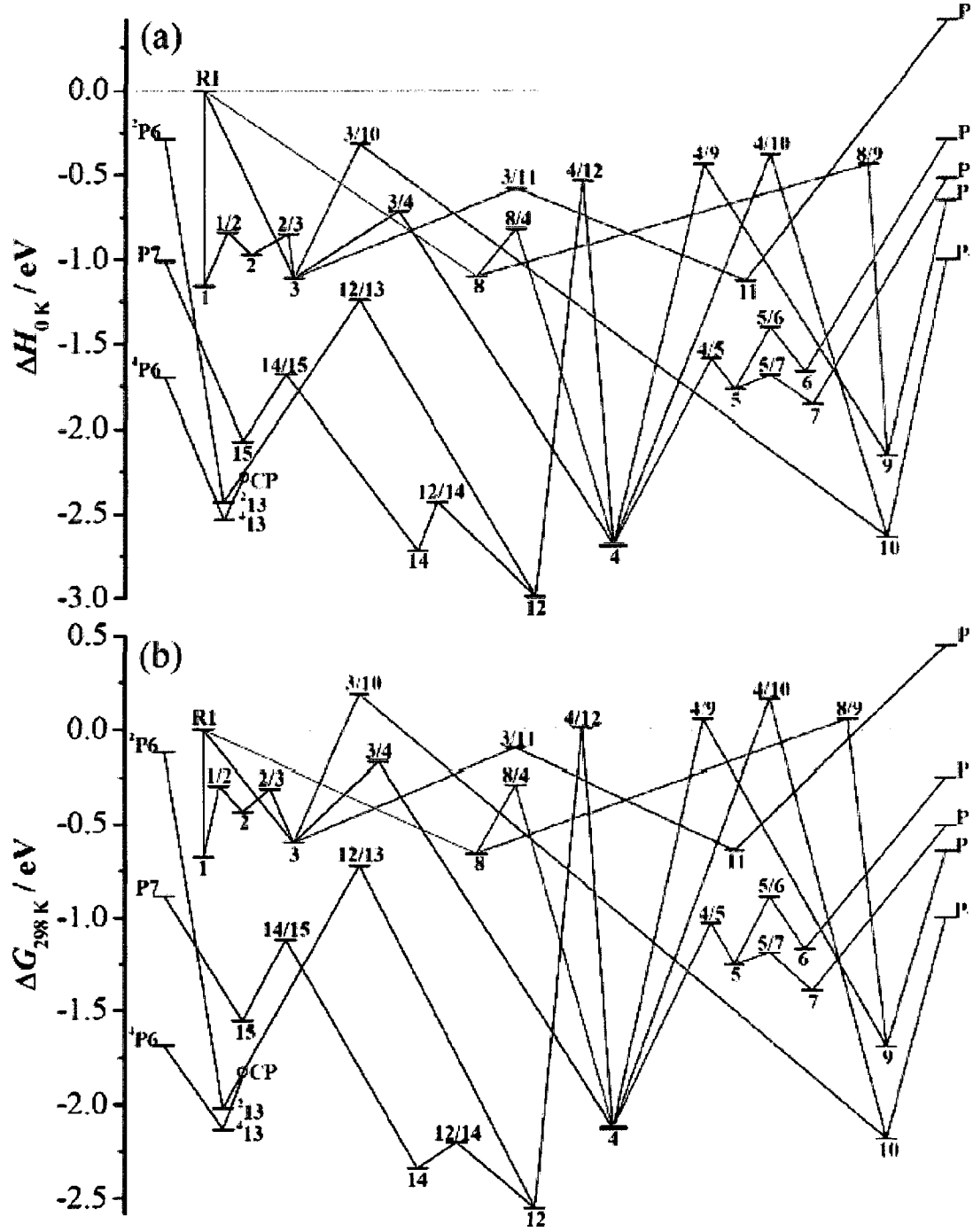


Figure 8.1: Potential energy profiles for the reaction of VO_3 with propylene. The profiles are plotted for zero-point vibration corrected energies (a) and Gibbs free energies at 298 K (b) relative to the separated reactants VO_3 + C_3H_6. The reaction intermediates and transition states are denoted as n and n_1/n_2, respectively. In the figure, **R1** = VO_3 + C_3H_6, **P1** = VO_2CHCH_3 + HCHO, **P2** = VO_2CH_2 + CH_3CHO, **P3** = VO_2 + CH_3CH_2CHO, **P4** = VO_2 + CH_3COCH_3, **P5** = VO_2 + C_3H_6O, **P6** = VO_2H_2 + CH_2=CHCHO, and **P7**= $VO_2C_3H_4$ + H_2O. Superscripts 2 and 4 denote species in doublet and quartet spin states, respectively. "CP" denotes a possible spin conversion points for reaction **R1** → **P6** (see text for details).

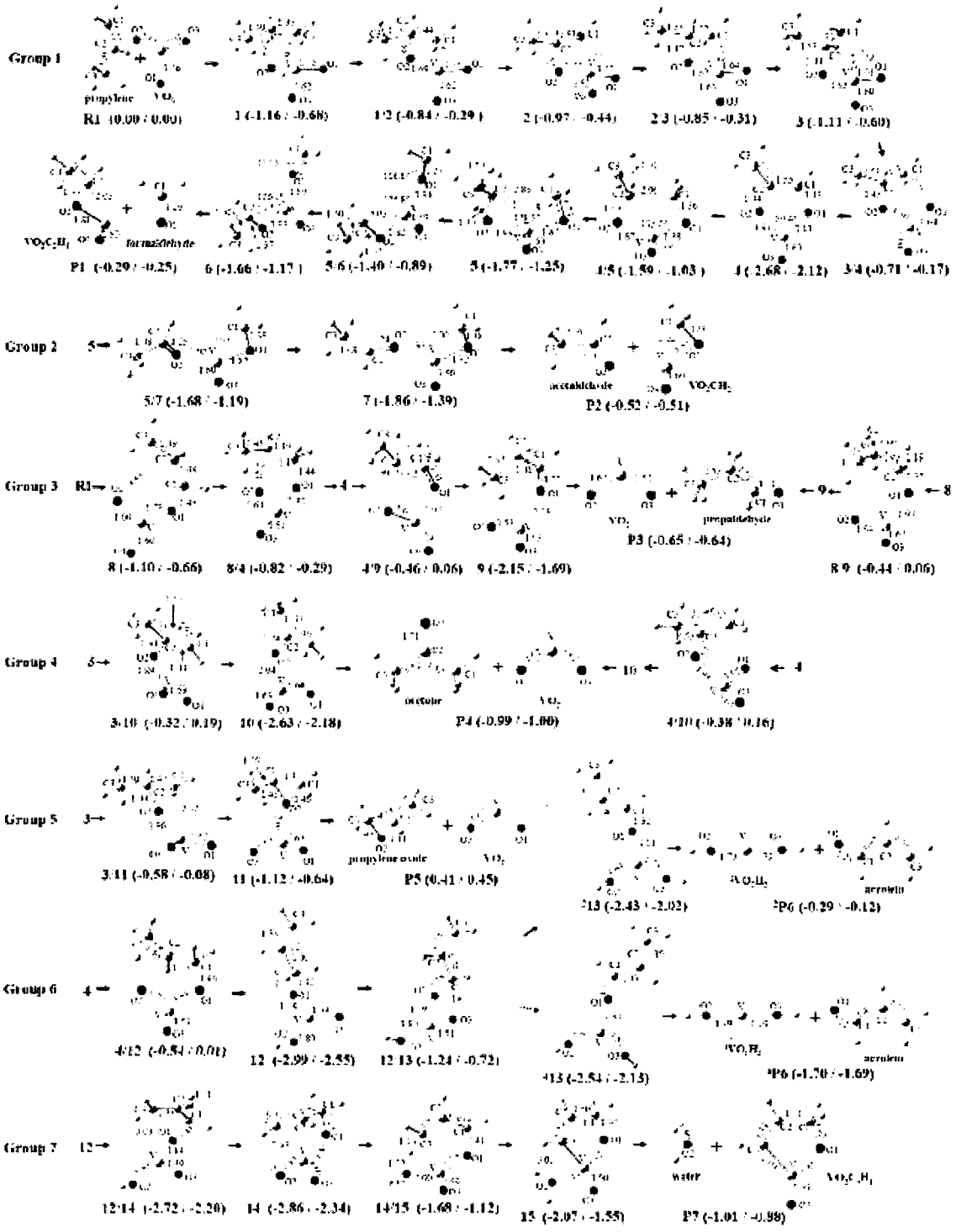


Figure 8.2: Optimized structures and energies of the species in Figure 8.1. The energies (in eV) are given as ($\Delta H_{0\,K}$ / $\Delta G_{298\,K}$) below each geometry. The bond lengths in 0.1 nm and some bond angles in degrees are given. The structures are grouped according to reactions (8.1)-(8.7) in the text.

cleavage, while formation of other products involves hydrogen transfers. Reactions (8.1)-(8.4) and (8.6)-(8.7) indicate that less heat of reaction (0.29 and 0.53 eV versus 0.65, 0.99, 1.00, and 1.67 eV) is released in the formation of the C=C bond cleavage products than in the formation of hydrogen transfer products, including $VO_2C_3H_4 + H_2O$. Figure 8.1(a) indicates that all of the thermodynamically allowed reactions are also kinetically favorable at 0 K; however, considering an equilibrium reaction at $T = 298$ K, Figure 8.1(b) indicates that all of the hydrogen transfer processes are subject to some overall free energy barriers: $\Delta G_{298\ K} = +0.01$ eV (Figure 8.2, Group 6, **4/12**, formation of H_2O and CH_2=CHCHO), +0.06 eV (Group 3, **8/9**, CH_3CH_2CHO), and +0.19 eV (Group 4, **3/10**, CH_3COCH_3). This is due to the entropy loss ($\Delta S < 0$) in the formation of reaction intermediates from the separated reactants VO_3 and C_3H_6. The entropy contribution ($-\Delta S \times T > 0$) puts the relative free energy above the relative enthalpy by about 0.5 eV for the reaction intermediates, while the relative energy positions of the separated products (P1-P7) do not change significantly. Because of relatively low barriers, the overall free energy barriers in the C=C bond cleavage process are still negative ($\Delta G_{298\ K} =$ -0.29 eV, see Figure 2/Group 3 for **8/4**).

The critical reaction intermediate in the C=C bond cleavage process has a five-membered ring structure (**4** in Figure 8.2/Group 1) that is formed through a [3+2] cycloaddition. The cycloaddition processes ($VO_3 + C_3H_6 \rightarrow$ **1** $\rightarrow$ **1/2** $\rightarrow$ **2** $\rightarrow$ **2/3** $\rightarrow$ **3** $\rightarrow$ **3/4** $\rightarrow$ **4,** or $VO_3 + C_3H_6 \rightarrow$ **8** $\rightarrow$ **8/4** $\rightarrow$ **4**) are overall barrierless. Formation of **4** results in a net energy release of 2.68 eV ($\Delta H_{0\ K}$). The C=C bond in the C_3H_6 moiety becomes a single bond that is reflected by the lengthening of the C1-C2 bond length (0.155 nm in **4** vs 0.133 nm in free C_3H_6). The amount of energy released is sufficient to overcome the

barrier (1.09 eV) in the C=C bond cleavage process (**4** → **4/5** → **5**). HCHO and CH_3CHO moieties are almost formed in **5** after this process. Two parallel processes **5** → **5/6** → **6** → **P1** and **5** → **5/7** → **7** → **P2** with no overall barriers cause formation of formaldehyde (H_2CO) and acetaldehyde, respectively.

Starting from the cycloaddition intermediate **4**, a hydrogen transfer from the methyl group to a ring oxygen atom (O2) results in intermediate **12** (**4** → **4/12** → **12**). This process is subject to a high-energy barrier (2.14 eV) because **4** with the ring structure is energetically quite stable; however, the high energy (2.68 eV) released in the formation of **4** is sufficient to overcome this barrier. Considering entropy contribution ($-\Delta S \times T$), this hydrogen process is subject to a tiny positive (0.01 eV, Figure 8.2) overall free energy barrier at room temperature. Because **12** is even lower in energy than **4**, the subsequent processes that mainly involve transfer of a second hydrogen atom are overall barrierless. Acrolein (**P6**) and water (**P7**) can be formed starting from **12**: **12** → **12/13** → **13** → **P6**; **12** → **12/14** → **14** → **14/15** → **15** → **P7**.

Other critical reaction intermediates in the reaction of VO_3 with C_3H_6 are **3** and **8** (see Figures 8.1 and 8.2) that are formed through bonding between C1 or C2 with the single bonded oxygen atom (O3) in VO_3. Transfer of one hydrogen atom starting from these intermediates results in formation of propylaldehyde (**8** → **8/9** → **9** → **P3**) and acetone (**3** → **3/10** → **10** → **P4**). Open structures **3** and **8** are not as stable as the ring structure **4**. Hydrogen transfers starting from open structures **3** and **8** are thus subject to lower barriers than they are starting from ring structure **4** (0.79 and 0.66 eV vs 2.30 and 2.22 eV, defined by $\Delta H_{0\ K}$). As a result, net overall hydrogen transfer barriers are determined by a balance between energy release and consumption. The overall barriers to

the formation of propylaldehyde (**P3**) and acetone (**P4**) are similar (compare **4/9** with **8/9** and **4/10** with **3/10**).

Propylene oxide can be formed overall barrierlessly starting from intermediate **3** (**3** → **3/11** → **11**); however, a high binding energy (1.53 eV, see Figure 8.2) between propylene oxide and VO_2 prevents formation of separated products (VO_2 + propylene oxide) under room temperature conditions.

8.3.2 Reactions of VO_2CH_2, VO_2CHCH_3, and VO_3C with O_2

The following reaction channels are explored for the reaction of O_2 with VO_2CH_2 and $VO_2C_2H_4$ produced in reactions (8.2) and (8.1), respectively:

$$VO_2CH_2 + O_2 \rightarrow VO_3 + HCHO, \qquad \Delta H_{298\,K} = -2.36 \text{ eV} \quad (8.8)$$

$$VO_2CH_2 + O_2 \rightarrow VO_3C + H_2O, \qquad \Delta H_{298\,K} = -3.31 \text{ eV} \quad (8.9)$$

$$VO_2CHCH_3 + O_2 \rightarrow VO_3 + CH_3CHO, \qquad \Delta H_{298\,K} = -2.60\text{eV} \quad (8.10)$$

$$VO_2CHCH_3 + O_2 \rightarrow VO_3C + CH_3OH, \qquad \Delta H_{298K} = -2.65 \text{ eV} \quad (8.11)$$

The reaction pathway of O_2 with VO_3C, produced in reaction (9) or (11), is also followed:

$$VO_3C + O_2 \rightarrow VO_3 + CO_2, \qquad \Delta H_{298} = -4.08 \text{ eV} \quad (8.12)$$

The potential energy profiles and intermediate structures for the reaction $VO_2CH_2 + O_2$ are plotted in Figures 8.3 and 8.4, respectively. Similar results are given in Figures S2 and S3 (see Supporting Information) for $VO_2CHCH_3 + O_2$. Results for reaction of O_2 with VO_3C are given in Figure 8.5. The listed enthalpies of reaction indicate that reactions of O_2 with hydrocarbons and carbon containing vanadium oxide species (VO_2CH_2, VO_2CHCH_3, and VO_3C) are very exothermic. Barrierless reaction pathways are determined for all the reactions.

Figure 8.3 shows that formaldehyde + VO_3 and water + VO_3C can be formed with no overall barriers in the reaction of VO_2CH_2 with O_2. The O-O bond cleavage (**18** → **18/19**

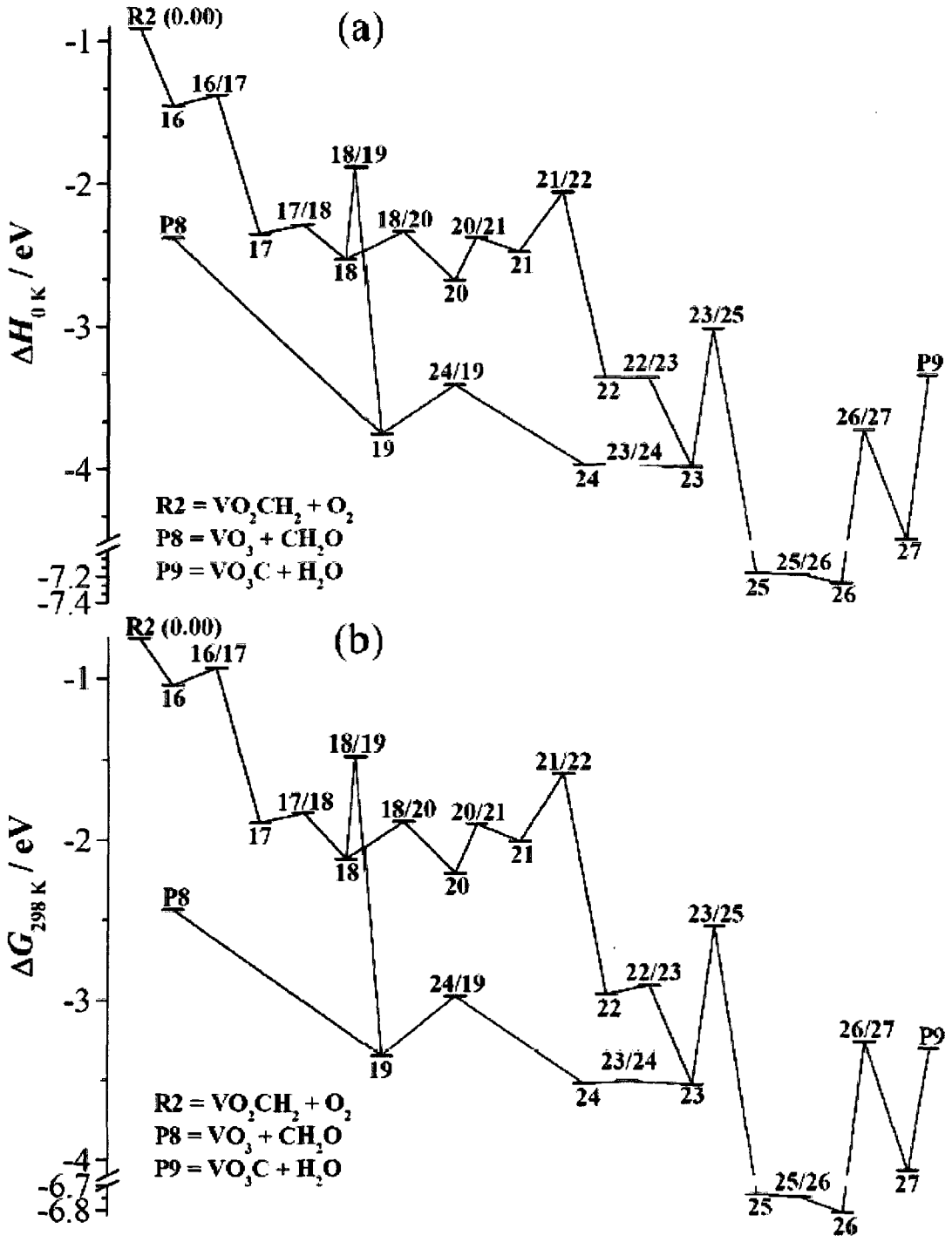


Figure 8.3: Potential energy profiles for the reaction of VO_2CH_2 with O_2. The profiles are plotted for zero-point vibration corrected energies (a) and Gibbs free energies at 298 K (b) relative to the separated reactants $VO_2CH_2 + O_2$. The reaction intermediates and transition states are denoted as n and n_1/n_2, respectively.

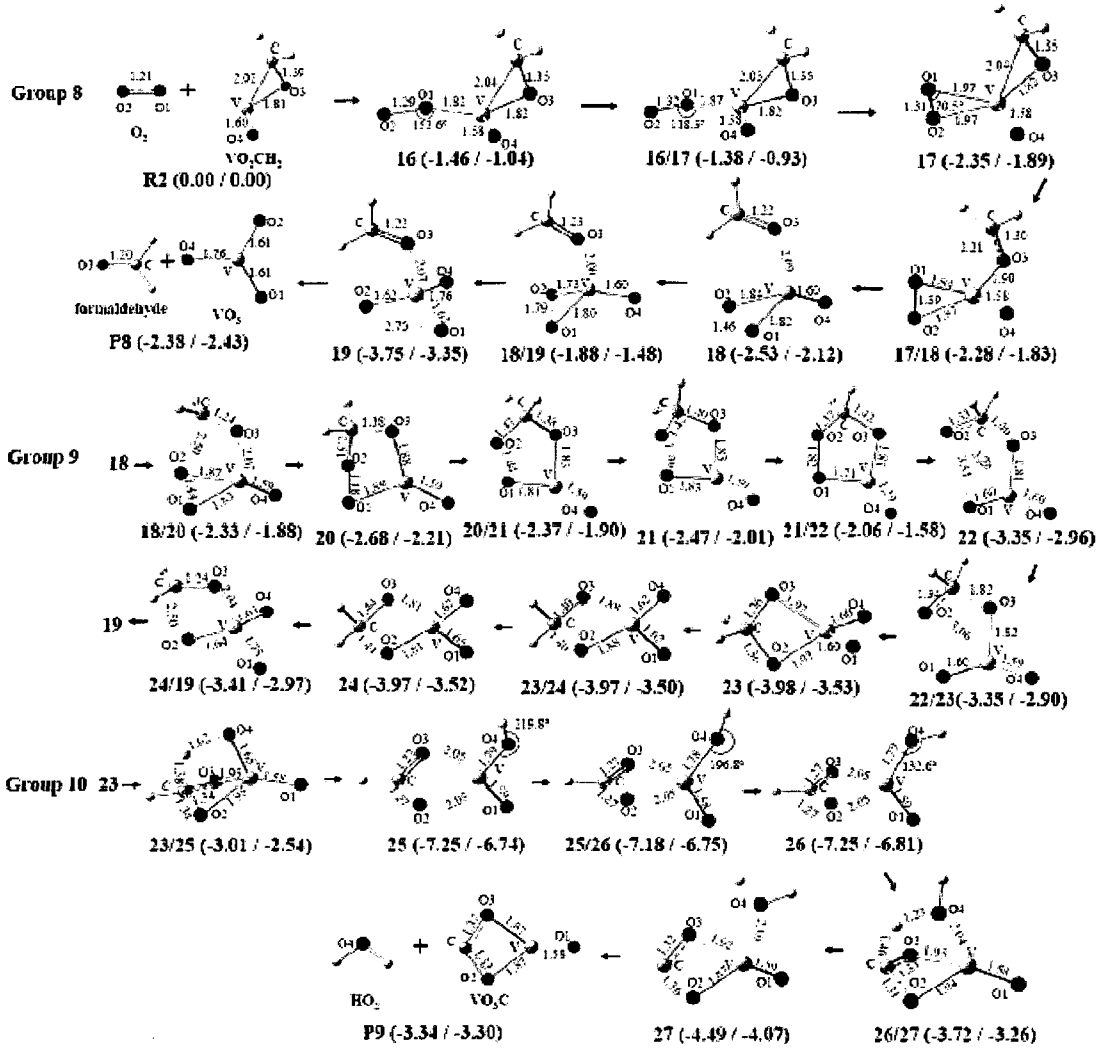


Figure 8.4: Optimized structures and energies of the species in Figure 8.3. The energies (in eV) are given as ($\Delta H_{0\,K}$ / $\Delta G_{298\,K}$) below each geometry. The bond lengths in 0.1 nm and some bond angles in degrees are given.

→ **19** and **21** → **21/22** → **22**, see Figure 8.4) is a critical part of the reaction. Cleavage occurs after rearrangement of the O_2 moiety over VO_2CH_2 that forms appropriate peroxo-species **18** and **21**. After O-O bond cleavage, the large amount of heat of formation (3.75 eV and 3.35 eV) can be used to evaporate the formaldehyde molecule (**19** → VO_3 + HCHO) or to rearrange the reaction complex further to cause water formation (**22** → **22/23** → **23** → **23/25** → **25** → **25/26** → **26** → **26/27** → **27** → VO_3C + H_2O). Figures S2

and S3 show similar reaction processes for the reaction $VO_2CHCH_3 + O_2$; this reaction can be considered as the same as the previous one, except that one of the hydrogen atoms of VO_2CH_2 is changed to a methyl group. Acetaldehyde + VO_3 and methanol + VO_3C can also be formed overall barrierlessly in the reaction. For methanol formation, the methyl group cannot transfer as a hydrogen atom does. As a result, the hydrogen transfers in $VO_2CHCH_3 + O_2$ and those in $VO_2CH_2 + O_2$ are not similar. The details can be seen by comparing Figure 8.4 with Figure S3 for the last group of the structures connected by arrows.

Figure 8.5 shows that the model catalyst VO_3 can also be regenerated overall barrierlessly by reaction of a second O_2 molecule with carbonized vanadium oxide species VO_3C produced in reactions (8.9) and (8.11). Similar to reactions (8.8)-(8.11), O-O bond cleavage can be considered as a critical part of the reaction.

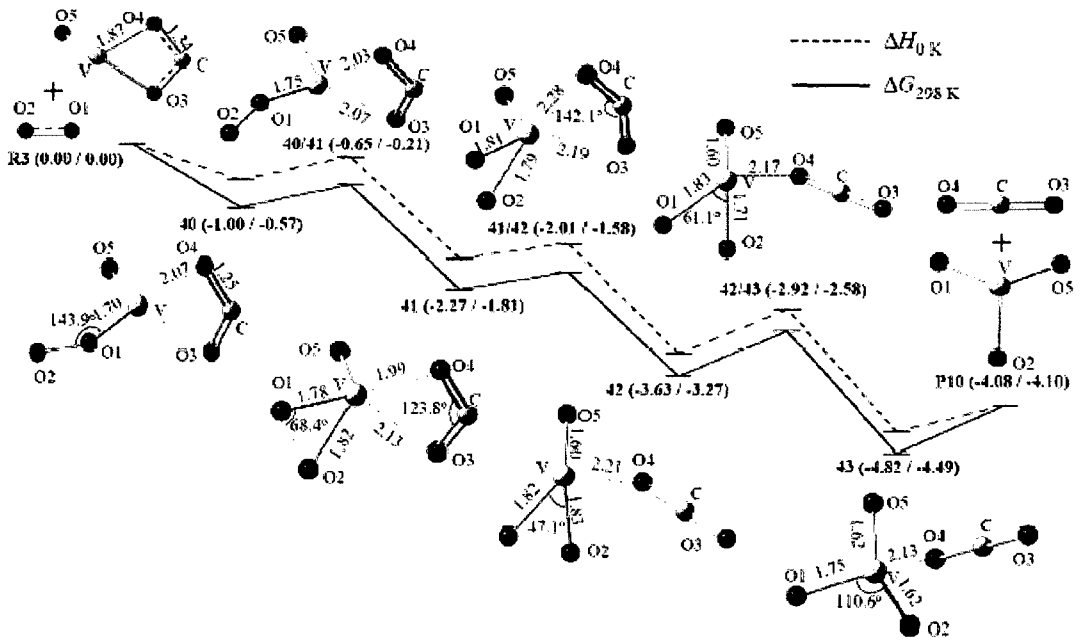


Figure 8.5: Potential energy profiles and optimized structures of reaction intermediates (n) and transition states (n_1/n_2) for $VO_3C + O_2$. The zero-point vibration corrected energy ($\Delta H_{0\,K}$) profile is above the Gibbs free energy ($\Delta G_{298\,K}$) profile. The energies (in eV) are given as ($\Delta H_{0\,K}$ / $\Delta G_{298\,K}$) for each structure. The bond lengths in 0.1 nm and some bond angles in degrees are given.

8.4 DISCUSSION

8.4.1 Comparison of the DFT Results with Gas Phase Experimental Observations

An experimental study employing single photon ionization through radiation generated by a soft x-ray laser and mass detection through a time of flight (TOF) spectrometer has been recently carried out on the reaction of neutral vanadium oxide clusters with propylene in the gas phase, under near room temperature conditions. Figure 8.6 plots the TOF mass spectrum in the mass range of 60-160 a.m.u. for the reactions of neutral V_mO_n clusters with C_3H_6. The experimental conditions are similar to those used for $V_mO_n + C_2H_4$ in ref. 8.14 and complete results, including those with several other unsaturated hydrocarbons,

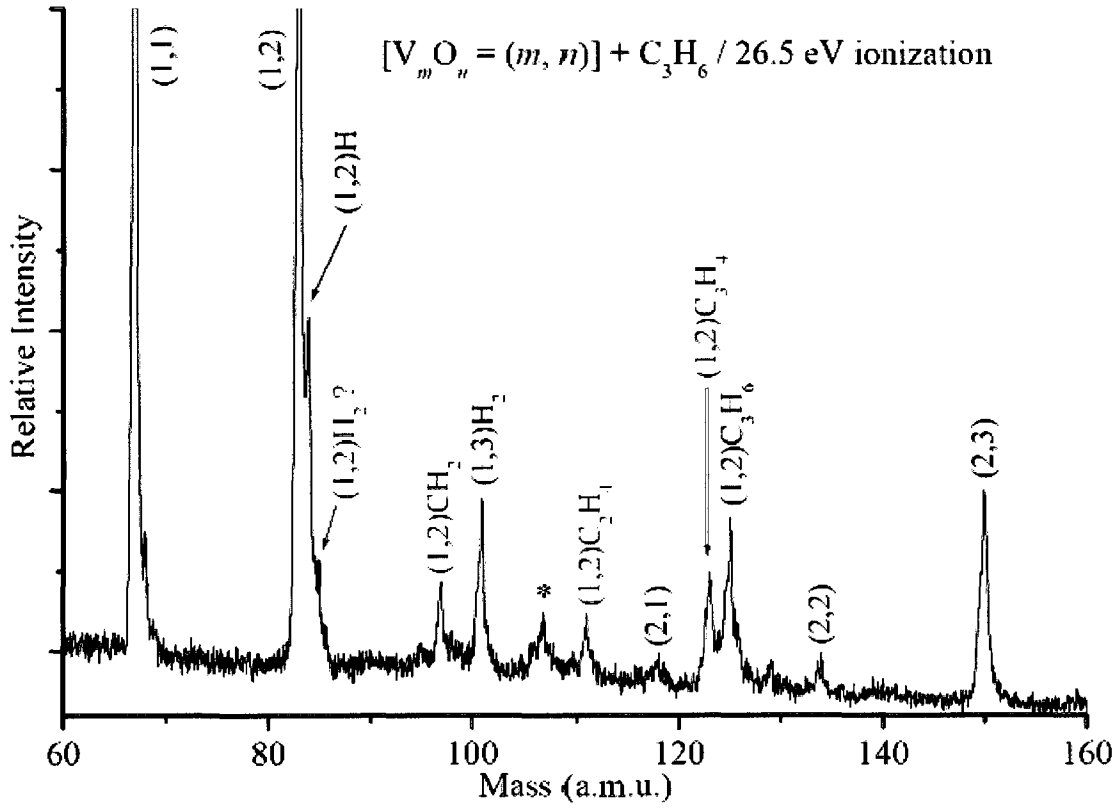


Figure 8.6: TOF mass spectrum in the mass range of 60-160 a.m.u. for the reactions of neutral V_mO_n clusters with C_3H_6. The symbol (m, n) denotes V_mO_n. The four carbon containing clusters VO_2CH_2, $VO_2C_2H_4$, $VO_2C_3H_4$, and $VO_2C_3H_6$ are new species (products) after the reactions/collisions with C_3H_6. An asterisk marks a peak with mass of 107 a.m.u. that can be assigned as VOC_3H_4 ($VO_2 + C_3H_6 \rightarrow VOC_3H_4 + H_2O$?).

will be presented in a separate paper.[8.34] The reaction products VO_2CH_2, $VO_2C_2H_4$, $VO_2C_3H_4$, and possibly VO_2H_2 (the signal of which is overlapped with the shoulder of the unreacted VO_2 feature) are observed. The current DFT study (Figure 8.1 and 8.2) suggests that the observed VO_2CH_2 and $VO_2C_2H_4$ products are formed from VO_3 + C_3H_6, as reactions (8.1) and (8.2) have negative overall free energy barriers at room temperature. Figures 8.1(a) and 8.2 show that the $\Delta H_{0\,K}$ value of **4/12** (critical transition state leading to $VO_2C_3H_4$ formation) is -0.54 eV which is lower than those of P1 ($VO_2C_2H_4$ + HCHO, -0.29 eV) and P2 (VO_2CH_2 + CH_3CHO, -0.52 eV). These results indicate that the experimentally observed $VO_2C_3H_4$ is also generated from the reaction VO_3 + C_3H_6, given that the reaction intermediates are not fully at thermal equilibrium due to the relatively low pressure (~ 1 Torr) of the gas phase flow cell experiments.[8.14,8.34] The formation of VO_2 + CH_3CH_2CHO and VO_2 + CH_3COCH_3 is also possible considering the negative $\Delta H_{0\,K}$ values for the critical transition states (**8/9** and **3/10**) for the reactions (8.3) and (8.4); however, one cannot easily differentiate the product VO_2 from the unreacted VO_2 in the neutral cluster reactivity study.

In Figure 8.1, **4** is a common intermediate involved in the formation of P1-P4, P6, and P7. Based on the Rice-Ramsberger-Kassel-Markus (RRKM) theory, one can expect that product formation with lower barriers will (with some allowance for dynamical considerations) always dominate. The $\Delta H_{0\,K}$ values [see Figures 8.1(a) and 8.2] of the critical barriers are -0.54 eV (**4/12**), -0.52 eV (**P2**), -0.46 eV (**4/9**), -0.38 eV (**4/10**), and -0.29 eV (**P1**). As a result, $VO_2C_3H_4$ (+H_2O) and VO_2CH_2 (+CH_3CHO) will be the dominant products coming from intermediate **4** in the experiment. Figure 8.6 does show that the mass signals of $VO_2C_3H_4$ and VO_2CH_2 are relatively strong with respect to that of

$VO_2C_2H_4$. The $\Delta H_{0\,K}$ value of **P1** (-0.29 eV) is the highest among the five listed barriers. Given that the ionization efficiencies of the vanadium species are similar, observation of comparable mass signals for $VO_2C_2H_4$, $VO_2C_3H_4$, and VO_2CH_2 implies that the entropy [**4** → **4/5** → **5** → **5/6** → **P1**] is more favorable than that for [**4** → **4/12** → **12**] (Figure 8.1(b)), and other dynamical issues, such as state locations and densities of a specific vibration, may influence formation of $VO_2C_2H_4$. Although the current DFT study cannot provide an accurate quantitative prediction for the product abundances in the $VO_3 + C_3H_6$ reaction, the calculated predictions are in qualitative agreement with the experimental observations for VO_2CH_2, $VO_2C_2H_4$, and $VO_2C_3H_4$.

8.4.2 Complexity of the Reactions

The DFT results reported in this study represent reaction channels with negative or small positive overall free energy barriers. The choice of reaction channels is guided by formation of stable products with low reaction barriers. We have not attempted to determine all the possible reaction intermediates and channels, which is hard to achieve for a 13 atom reaction system such as $VO_3 + C_3H_6$. Figure 8.7 gives an example of the challenge involved in investigating all the possible reaction channels in the sub-reaction $VO_3 + C_3H_6 \rightarrow VO_2C_2H_4 + HCHO$. Four isomers are determined for $VO_2C_2H_4$ (a-d in Figure 8.7). VO_2CHCH_3 in reaction (8.1) has highest energy among the four isomers. In following the reaction pathway, a good deal of effort has been devoted to finding allowed pathways to produce $VO_2C_2H_4$ isomers other than VO_2CHCH_3. This involves transfer of a hydrogen atom from the methyl group starting from an appropriate reaction intermediate. Two attempts (TS1 and TS2 in Figure 8.6) are made for this transfer and the two hydrogen transfers are subject to overall barriers 0.81 and 0.23 eV (defined by $\Delta H_{0\,K}$) that are significantly higher than the energy of the separated reactants ($VO_3 + C_3H_6$).

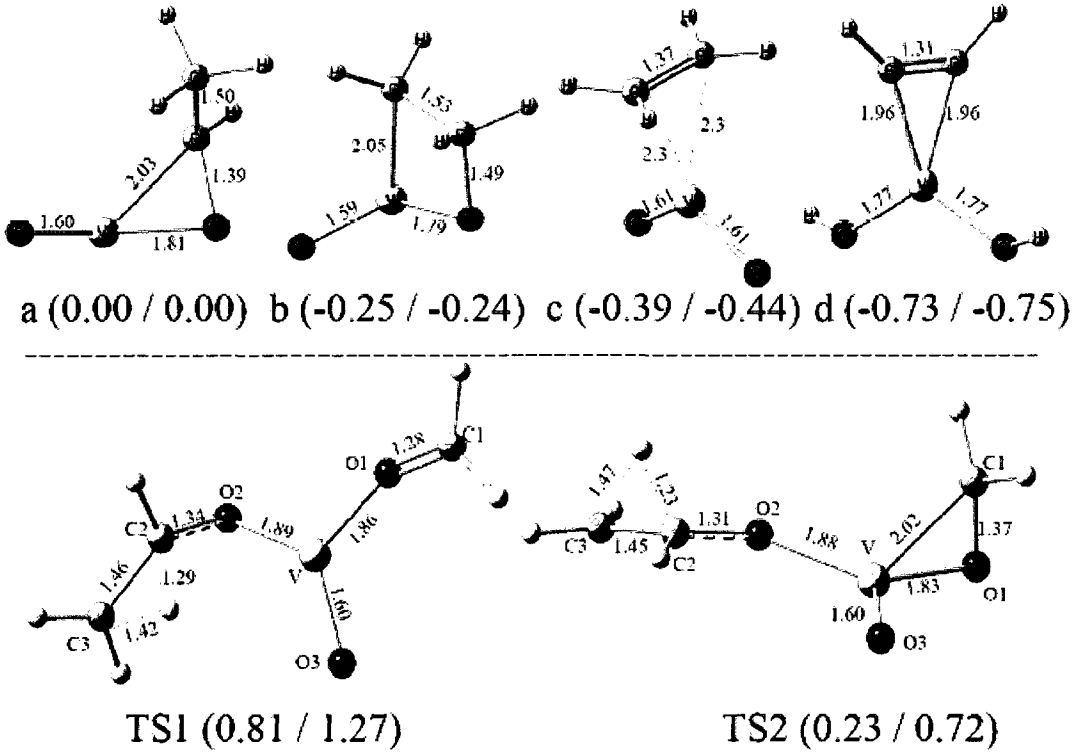


Figure 8.7: Optimized structures and energies of four isomers (a-d) of $VO_2C_2H_4$ (upper panel); optimized structures and energies of two transition states (TS1 and TS2) in reaction $VO_3 + C_3H_6$ to form the CH_2CH_2 moiety (lower panel). The energies (in eV) relative to VO_2CHCH_3 (for isomers a-d) or relative to reactants $VO_3 + C_3H_6$ (for TS1 and TS2) are given as ($\Delta H_{0\,K}$ / $\Delta G_{298\,K}$) below each geometry. The bond lengths in 0.1 nm are given.

8.4.3 Comparison of $VO_3 + C_3H_6$ with $VO_3 + C_2H_4$ and Other Related Reactions

In a previous DFT study,[8.14] we showed that the reaction of $VO_3 + C_2H_4$ produces $VO_2CH_2 + HCHO$ barrierlessly. The results are supported by experimental observations: disappearance of reactants VO_3 accompanied by the appearance of product species VO_2CH_2 in the reaction of neutral vanadium oxide clusters with C_2H_4. The HCHO and CH_3CHO product formation in the reaction of $VO_3 + C_3H_6$ is thus expected. This has been verified in the present study. The generality of the cleavage of C=C bonds in the reaction of alkenes with VO_3 can be summarized as: the large amount of energy released in the [3+2] cycloaddition process is sufficient to break the weakened C=C bond (such as C1-C2 of **4** in Figure 8.2) and evaporate an aldehyde fragment. In addition to the above

similarity between the reactions of $VO_3 + C_3H_6$ and $VO_3 + C_2H_4$, the added methyl group in C_3H_6 results in reaction channels (8.7) and possibly (8.6). Such a mechanism is supported by experiment, as shown in Figure 8.6. As in the C=C bond cleavage process, reaction channels (8.6) and (8.7) take advantage of the large heat of reaction in the [3+2] cycloaddition to overcome the reaction barrier for hydrogen transfer from the methyl group to one oxygen atom (**4** → **4/12** → **12** in Figure 8.1). A detailed comparison shows that direct C_x aldehyde formation ($VO_3 + C_xH_{2x} \rightarrow VO_2 + C_xH_{2x}O$) is subject to lower free energy barriers for $x = 3$ than for $x = 2$ (0.06 eV vs 0.18 eV).

Harvey et al. investigated the reaction of $VO_2^+ + C_2H_4$ nearly ten years ago by both experiment and theory.[8.5] Gracia et al. recently studied the same reaction,[8.11] as well as the reaction $VO_2^+ + C_3H_6$,[8.12] by DFT calculations. By a spin conversion mechanism,[8.5,8.11,8.35] acetaldehyde can be formed overall barrierlessly in $VO_2^+ + C_2H_4$, in agreement with the experimental results.[8.5] The reaction of VO_2^+ with C_3H_6 is predicted to form acetone, propylaldehyde, allene, and propyne as thermodynamically and kinetically allowed products. Reactions of $V_2O_5^+$ and $V_4O_{10}^+$ with C_2H_4 have also been investigated by DFT calculations.[8.7,8.9] Formation of acetaldehyde in both reactions is highly favorable and supports the experimental observations of $V_2O_4^+$ and $V_4O_9^+$ as reaction products.[8.7] Because the [3 (OVO) +2 (C=C)] cycloaddition structure may not be stable in the VO_2^+ + alkene reactions, no reaction involving C=C bond cleavage is discussed. In the reaction $V_2O_5^+ + C_2H_4$, a [3+2] cycloaddition species is predicted to be lower in energy than the separated reactants by 4.44 eV. As can be seen from the results in Figures 8.1 and 8.2, this high energy should be able to cleave the C=C bond and evaporate formaldehyde fragment(s). The authors did suggest a side reaction channel,

$V_2O_5^+ + C_2H_4 \rightarrow V_2O_3^+ + 2HCHO$ (ΔE = -0.65 eV)[8.9], to explain observation of $V_2O_3^+$ as minor product in the experiments.

In addition to the C=C bond cleavage reactions, exothermic processes are predicted for direct oxygenation reactions $VO_3 + C_xH_{2x} \rightarrow VO_2 + C_xH_{2x}O$ and $VO_2^+/V_2O_5^+/V_4O_{10}^+ + C_xH_{2x} \rightarrow VO^+/V_2O_4^+/V_4O_9^+ + C_xH_{2x}O$, in which $C_xH_{2x}O$ is acetaldehyde (x = 2), propylaldehyde (x = 3), or acetone (x = 3). These reaction processes can be divided into three phases: (1) formation of species with structure V-O-C_xH_{2x}, in which the O atom is single-bonded with the C1 (or C2) atom or bridge-bonded with both C1 and C2 atoms; (2) transfer of a hydrogen atom from an O bonded C atom to form species V...O=C_xH_{2x}, in which the O atom is nearly double-bonded with one carbon atom; (3) evaporation of an O=C_xH_{2x} fragment from the vanadium oxide cluster. Phases (1) and (3) proceed with no overall free energy barrier in all of the DFT studied reactions. Phase (2) in the reactions involving the cationic species ($VO_2^+/V_2O_5^+/V_4O_{10}^+ + C_xH_{2x}$) also proceeds with no overall barriers. In contrast, phase (2) of neutral species reactions ($VO_3 + C_xH_{2x}$) are subject to overall free energy barriers (0.06-0.19 eV) according to the DFT calculations. Another major difference between neutral and cationic reaction systems is that in phase (3) more free energy (1.99-2.66 eV versus 1.05-1.18 eV, defined by $\Delta G_{298\ K}$) is needed to evaporate O=C_xH_{2x} from the cationic $VO^+/V_2O_4^+/V_4O_9^+$ structure than from neutral VO_2.

8.4.4 Gas Phase Catalytic Cycles

Figure 8.8 summarizes the barrierless reaction channels that form catalytic cycles for C_3H_6 partial oxidation by O_2 facilitated by the model catalyst VO_3 under gas phase, room temperature conditions. In Figures 8.1 and 8.2, **5/6** and **P1** (VO_2CHCH_3 + HCHO) are higher in energy than **5/7** and **P2** (VO_2CH_2 + CH_3CHO), respectively, so the formation of CH_3CHO is more favorable than that of HCHO for the VO_3 + C_3H_6 reaction. In the

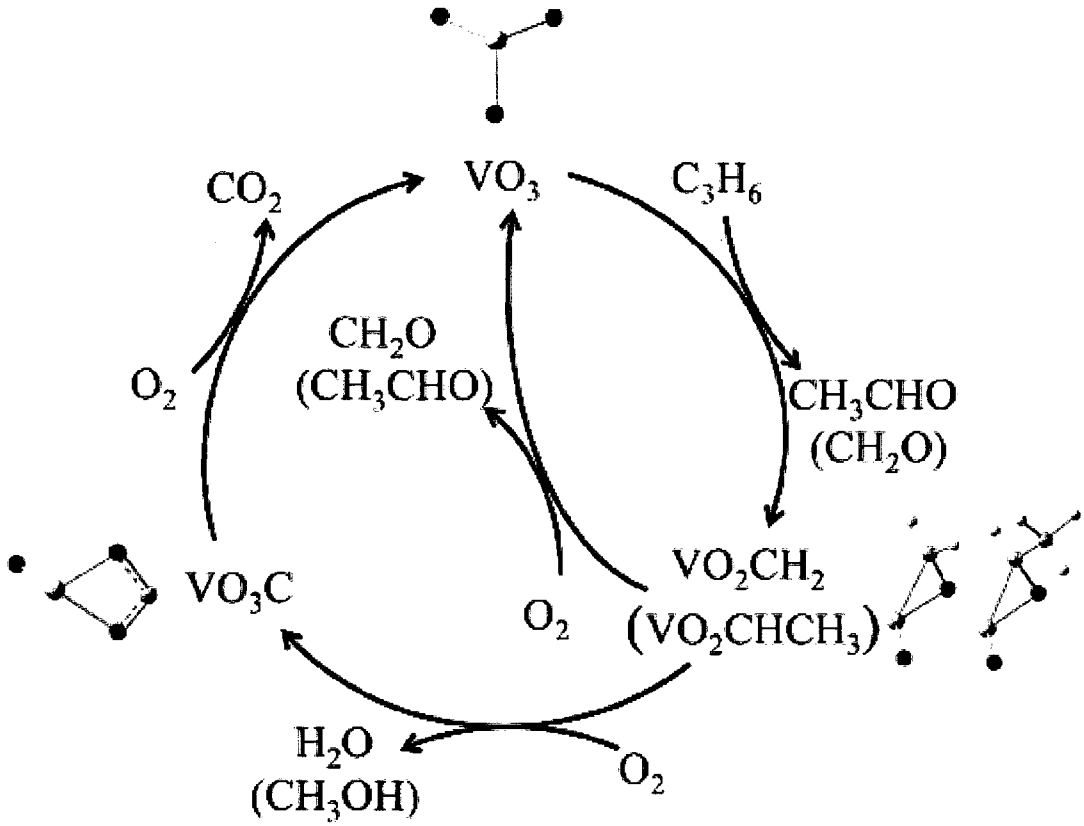


Figure 8.8: Schematic diagram showing barrierless reaction channels that form catalytic cycles for propylene (C_3H_6) partial oxidation over the VO_3 cluster under gas phase, room temperature conditions.

reaction $VO_2CH_2 + O_2$ (Figures 8.3 and 8.4), the product $VO_3C + H_2O$ is thermodynamically and kinetically more favorable than the product $VO_3 + HCHO$. We thus conclude that CH_3CHO (with H_2O and CO_2) will be selectively more abundant among the partial oxidation products (CH_3CHO, HCHO, and CH_3OH) in the reaction of $C_3H_6 + O_2$ catalyzed by VO_3 at room temperature.

The current DFT calculations predict that the C=C bond cleavage products VO_2CHCH_3 and VO_2CH_2 are readily oxidized by O_2 at room temperature to reproduce the VO_3. In the gas phase experimental study of neutral vanadium oxide clusters reacting with C_2H_4 and C_3H_6, HCHO/CH_3CHO are derived as part of the bond cleavage products in reactions such as $VO_3 + C_3H_6 \rightarrow VO_2CH_2 + CH_3CHO$; however, these aldehydes are

not observed probably due to their low concentrations. These products could perhaps be observed by taking advantage of the catalytic cycles in Figure 8.8, because the concentration of products such as CH_3CHO will be increased if a mixed gas of O_2 and C_3H_6, rather than pure C_3H_6, were used as the reactant.

8.5.5 Consideration of Condensed Phase Catalysis

Molecular level reaction mechanisms in complex condensed phase heterogeneous catalysis are difficult to establish by model catalytic studies using a single vanadium cluster; nonetheless, various reaction channels in this study do parallel similar behavior in propylene selective oxidation over various vanadium oxide catalysts.[8.16-8.19] The current study indicates that the formation of various useful product aldehydes (propylaldehyde, acetaldehyde, formaldehyde), acrolein, and acetone can be generated with negative or small positive overall barriers in the reaction of VO_3 with propylene. Moreover, VO_3 can be regenerated easily in selected reactions. In the selective oxidation of propylene over vanadium oxide catalysts, highly selective formation of acetaldehyde,[8.18,8.19] acrolein,[8.17] and acetone[8.16] are observed depending on the specific catalysts used. The DFT study in this work gives molecular level insight in to how these products may be formed. It is interesting to note that acetaldehyde and carbon dioxide are the major products in propylene selective oxidation over V_2O_5/SiO_2.[8.18] The DFT calculations predict that formation of these two products is also the most favorable in model catalytic cycles (Figure 8.8). To explain formation of acetaldehyde from propylene oxidation in heterogeneous catalysis, Ruszel et al., suggest that electrophilic surface oxygen species O_2^- or O^- add to a C=C double bond with formation of peroxo or oxo intermediates that can decompose with breaking of a C-C bond.[8.18] The mechanism of surface O_2^- species adding to the C=C double bond is similar to the [3+2] cycloaddition found for the

reaction of VO_3 with C_3H_6.

The above mentioned comparison between condensed phase and gas phase investigations raises the following interesting question: how realistic is the VO_3 cluster for modeling condensed phase vanadium oxide chemistry? In cluster chemistry, both open-shell (e.g., $V_2O_5^+$ and $V_4O_{10}^+$,[8.7,8.8b] and VO_3 in this study) and closed-shell (e.g., VO_2^+ and $V_3O_7^+$)[8.5,8.8a] clusters are used as prototypes for identification of active centers of bulk or supported vanadium oxides. Different clusters usually possess different reactivities and the open-shell clusters are typically more reactive.[8.5] From the point view of thermodynamics, one does not expect that a stable oxide surface is covered with active centers that can be fully modeled by open-shell radical clusters; however, the radical clusters may serve as (1) models of oxygen-rich or oxygen-poor surface defects, and (2) intermediate reactive centers during catalytic processes. (Note that some surface oxygen species have extremely short lifetimes.[8.17]) In this study, although the oxygen-rich cluster VO_3 is very oxidative and thus unstable in a reducing environment, it can be recycled (Figure 8.8) through the reaction of O_2 with the oxygen-poor intermediates (VO_2CH_2, VO_2CHCH_3, and VO_3C with the vanadium being in +4 oxidation state). As mentioned above, the C_3H_6 partial oxidation products over specific condensed phase vanadium oxides (V_2O_5/SiO_2)[8.18] and over the VO_3 cluster are similar. Thus, we suggest the use of surface characterization techniques to identify some possible new surface species in the selective oxidation of C_3H_6 over vanadium oxide catalysts. A candidate for this species is the one with a five-membered ring structure (similar to **4** in Figure 8.2) that can be formed with no overall barrier and is energetically quite stable. The vanadium is in a +4 oxidation state in this ring structure.

8.5 CONCLUSIONS

The reaction of neutral VO_3 with propylene produces acetaldehyde ($VO_2CH_2 + CH_3CHO$) or formaldehyde ($VO_2CHCH_3 + HCHO$) overall barrierlessly under room temperature conditions. With previous findings of formaldehyde formation ($VO_2CH_2 + HCHO$) in the reaction of VO_3 with ethylene, a general mechanism of C=C bond cleavage of alkenes over VO_3 may be concluded: the heat of reaction in the barrierless [3+2] cycloaddition is sufficient to break the C=C bond and to evaporate an aldehyde fragment. The hydrogen transfer barrier from the methyl group to one oxygen atom can be overcome by using the heat of reaction in the [3+2] cycloaddition, which finally leads to formation of water ($VO_2C_3H_4 + H_2O$) or acrolein ($VO_2H_2 + CH_2=CHCHO$) in the reaction $VO_3 + C_3H_6$. Formation of acetone and propanaldehyde is subject to small overall free energy barriers for the reaction $VO_3 + C_3H_6$. Gas phase catalytic cycles are provided by studying reactions of O_2 with C=C bond cleavage products (VO_2CH_2 and VO_2CHCH_3). These reactions are facile under room temperature conditions and can recycle the VO_3. The DFT predictions of several reaction channels (formation of CH_3CHO, HCHO, and H_2O in the $VO_3 + C_3H_6$ reaction) have been supported by recent gas phase experimental observations. Other DFT results, such as the gas phase catalytic cycles and involvement of the [3+2] cycloaddition intermediates in related reactions, may be verified by further experiments.

Supporting Information Available

Optimized structures and relative free energies of VO_3, VO_2CH_2, VO_2CHCH_3, and $VO_2C_3H_4$ in the doublet and quartet spin multiplicities (Figure S1); Potential energy profiles for the reaction $VO_2CHCH_3 + O_2$ (Figure S2); Optimized structures and relative energies of the species in the reaction channel of $VO_2CHCH_3 + O_2$ (Figure S3). These materials are available free of charge via the Internet at http://pubs.acs.org.

REFERENCES

[8.1] Ertl, G.; Knozinger, H. and Weikamp, J. *Handbook of Heterogeneous Catalysis* ; Wiley-VCH, **1997**.

[8.2] Weckhuysen, B. M. and Keller, D. E. *Catal. Today* **2003**, *78*, 25.

[8.3] Fierro, J. L. G. *Metal Oxides*; Taylor & Francis Group, LLC, **2006**.

[8.4] (a) Zemski, K. A.; Justes, D. R.; Castleman, A. W. *J. Phys. Chem. B* **2002**, *106*, 6136, and references therein. (b) Foltin, M.; Stueber, G. J.; Bernstein, E. R. *J. Chem. Phys.* **1999**, *111*, 9577. (c) Fielicke, A.; Rademann, K. *Phys. Chem. Chem. Phys.* **2002**, *4*, 2621. (d) Schröder, D.; Engeser, M.; Bronstrup, M.; Daniel, C.; Spandl, J.; Hartl, H. *Int. J. Mass Spectrom.* **2003**, *228*, 743. (e) Schröder, D.; Loos, J.; Engeser, M.; Schwarz, H.; Jankowiak, H.C.; Berger, R.; Thissen, R.; Dutuit, O.; Dobler, J.; Sauer, J. *Inorg. Chem.* **2004**, *43*, 1976. (f) Asmis, K. R.; Meijer, G.; Brümmer, M.; Kaposta, C.; Santambrogio, G.; L., W.; Sauer, J. *J. Chem. Phys.* **2004**, *120*, 6461. (g) Molek, K. S.; Jaeger, T. D.; Duncan, M. A. *J. Chem. Phys.* **2005**, *123*, 144313. (h) Feyel, S.; Schröder, D.; Schwarz, H. *J. Phys. Chem. A* **2006**, *110*, 2647. (i) Feyel, S.; Scharfenberg, L.; Daniel, C.; Hartl, H.; Schröder, D.; Schwarz, H. *J. Phys. Chem. A* **2007**, *111*, 3278. (j) Fielicke, A.; Mitric, R.; Meijer, G.; Bonacic-Koutecky, V.; Helde G. *J. Am. Chem. Soc.* **2003**, *125*, 15716. (k) Engeser, M.; Schlangen, M.; Schröder, D.; Schwarz, H.; Yumura, T.; Yoshizawa, K. *Organometallics* **2003**, *22*, 3933-3943. (l) Asmis, K. R.; Brümmer, M.; Kaposta, C.; Santambrogio, G.; Von Helden, G.; Meijer, G.; Rademann, K.; Wöste, L. *Phys. Chem. Chem. Phys.* **2002**, *4*, 1101. (m) Zhai, H. J.; Wang, L. S. *J. Chem. Phys.* **2002**, *117*, 7882. (n) Zhai, H. J.; Döbler, J.; Sauer, J.; Wang, L. S. *J. Am. Chem. Soc.* **2007**, *129*, 13270. (o) Waters, T.; Wedd, A. G.; O'Hair, R. A. J.

Chem. Eur. J. **2007**, *13*, 8818. (p) Wang, W. -G.; Wang, Z. -C.; Yin, S.; He, S. -G.; Ge, M. -F. *Chin. J. Chem. Phys.* **2007**, *20*, 4, 412, and references therein.

[8.5] Harvey, J. N.; Diefenbach, J. N.; Schröder, D.; Schwarz, H. *Int. J. Mass Spectrom.* **1999**, *182/183*, 85.

[8.6] Zemski, K. A.; Justes, D. R.; Castleman, Jr., A. W. *J. Phys. Chem. A* **2001**, *105*, 10237.

[8.7] Justes, D. R.; Mitric, R.; Moore, N. A.; Bonacic-Koutecky, V.; Castleman, A. W., Jr. *J. Am. Chem. Soc.* **2003**, *125*, 6289.

[8.8] (a) Feyel, S.; Schröder, D.; Rozanska, X.; Sauer, J.; Schwarz, H. *Angew. Chem. Int. Ed.* **2006**, *45*, 4677. (b) Feyel, S.; Dobler, J.; Schröder, D.; Sauer, J.; Schwarz, H. *Angew. Chem. Int. Ed.* **2006**, *45*, 4681.

[8.9] Justes, D. R.; Castleman, A. W.; Mitric, R.; Bonacic-Koutecky, V. *Eur. Phys. J. D* **2003**, *24*, 331.

[8.10] (a) Vyboishchikov, S. F.; Sauer, J. *J. Phys. Chem. A* **2000**, *104*, 10913. (b) Vyboishchikov, S. F.; Sauer, J. *J. Phys. Chem. A* **2001**, *105*, 8588. (c) Calatayud, M.; Silvi, B.; Andres, J.; Beltran, A. *Chem. Phys. Lett.* **2001**, *333*, 493. (d) Calatayud, M.; Andres, J.; Beltran, A. *J. Phys. Chem. A* **2001**, *105*, 9760. (e) Calatayud, M.; Andres, J.; Beltran, A.; Silvi, B. *Theor. Chem. Acc.* **2001**, *105*, 299. (f) Calatayud, M.; Andres, J.; Beltran, A. *J. Phys. Chem. A* **2001**, *105*, 9760. (g) Calatayud, M.; Berski, S.; Beltran, A.; Andres, J. *Theor. Chem. Acc.* **2002**, *108*, 12. (h) Pykavy, M.; van Wullen, C. *J. Phys. Chem. A* **2003**, *107*, 5566. (i) Gracia, L.; Sambrano, J. R.; Safont, V. S.; Calatayud, M.; Beltran, A.; Andres, J. *J. Phys. Chem. A* **2003**, *107*, 3107. (j) Cheng, M. J.; Chenoweth, K.; Oxgaard, J.; Duin, A.; Goddard, W. A. *J. Phys. Chem. C* **2007**, *111*, 5115.

[8.11] Gracia, L.; Andres, J.; Safont, V. S.; Beltran, A. *Organometallics* **2004**, *23*, 730-739.

[8.12] Gracia, L.; Sambrano, J. R.; Andres, J.; Beltran, A. *Organometallics* **2006**, *25*, 1643-1653.

[8.13] (a) Matsuda, Y.; Bernstein, E. R. *J. Phys. Chem. A* **2005**, *109*, 314. (b) Matsuda, Y.; Bernstein, E. R. *J. Phys. Chem. A* **2005**, *109*, 3803. (c) Matsuda, Y.; Shin, D. N.; Bernstein, E. R. *J. Chem. Phys.* **2004**, *120*, 4142. (d) Shin, D. N.; Matsuda, Y.; Bernstein, E. R. *J. Chem. Phys.* **2004**, *120*, 4157. (e) Matsuda, Y.; Shin, D. N.; Bernstein, E. R. *J. Chem. Phys.* **2004**, *120*, 4165. (f) Dong, F.; Heinbuch, S.; He, S.-G.; Xie, Y.; Rocca, J. J.; Bernstein, E. R. *J. Chem. Phys.* **2006**, *125*, 164318. (g) He, S.-G.; Xie, Y.; Guo, Y.; Bernstein, E. R. *J. Chem. Phys.* **2007**, *126*, 194315.

[8.14] Dong, F.; Heinbuch, S.; Xie, Y.; Rocca, J. J.; Bernstein, E. R.; Wang, Z. C.; Deng, K.; He, S. G. *J. Am. Chem. Soc.* **2008**, *130*, 1932.

[8.15] (a) Xu, X.; Friend, C. M. *J. Am. Chem. Soc.* **1991**, *113*, 6779. (b) Stangland, E.E.; Stevens, K.B.; Andres, R.P.; W. Delgass, N. *J. Catal.* **2000**, *191*, 332. (c) Xie, J.; Zhang, Q.; Chuang, K. T. *J. Catal.* **2000**, *191*, 86. (d) Berkessel, A.; Brandenburg, M. *Org. Lett.* **2006**, *8*, 20, 4401. (e) Amano, F.; Yamaguchi, T.; Tanaka, T. *J. Phys. Chem. B* **2006**, *110*, 281. (f) Su, Z.; Borho, N.; Xu, Y. *J. Am. Chem. Soc.* **2006**, *128*, 17127. (g) Moens, B.; Winne, H.D.; Corthals, S.; Poelman, H.; Gryse, R.D.; Meynen, V.; Cool, P.; Sels, B.F.; Jacobs, P.A. *J. Catal.* **2007**, *247*, 86.

[8.16] Li, M.; Shen, J. *J. Catal.* **2002**, *205*, 248.

[8.17] Zhao, C.; Wachs, I. E. *Catal. Today* **2006**, *118*, 332.

[8.18] Ruszel, M.; Grzybowska, B.; Gasior, M.; Samson, K.; Gressel, I.; Stoch, *J. Catal. Today* **2005**, *99*, 151.

[8.19] Seiyama, T.; Nita, K.; Maehara, T.; Yamazoe, N.; Takita, Y.; *J. Catal.* **1997**, *49*, 164.

[8.20] (a) Deo, G.; Wachs, I. E.; Haber, J.; *Crit. Rev. Surf. Chem.* **1994**, *4*, 141. (b) Weckhuysen, B. M.; Wachs, I. E.; in: Nalwa, H.S. (Ed.); *Handbook of Surface and Interfaces of Materials Vol.1*, Academic Press, San Diego, **2001**, P. 613. (c) Wachs, I. E.; Weckhuysen, B. M.; *Appl. Catal. A: Gen.* **1997**, *157*, 67.

[8.21] (a) Gijzeman, O. L. J.; van Lingen, J. N. J.; van Lenthe, J. H.; Tinnemans, S. J.; Keller, D. E.; Weckhuysen B. M. *Chem. Phys. Lett.* **2004**, *397*, 277. (b) Keller, D. E.; de Groot F. M. F.; Koningsberger, D. C.; Weckhuysen B. M. *J. Phys. Chem. B* **2005**, *109*, 10223. (c) Keller, D. E.; Koningsberger, D. C.; Weckhuysen B. M. *J. Phys. Chem. B* **2006**, *110*, 14313. (d) Lingen, J. N. J.; Gijzeman, O. L. J.; Weckhuysen B. M.; van Lenthe, J. H.; *J. Catal.* **2006**, *239*, 34.

[8.22] Keller, D. E.; Visser, T.; Soulimani, F.; Koningsberger, D. C.; Weckhuysen, B. M.; *Vib. Spectrosc.***2007**, *43*, 140-151.

[8.23] Frisch, M. J.; Trucks, G. W.; Schlegel, H. B.; Scuseria, G. E.; Robb, M. A.; Cheeseman, J. R.; Montgomery, J. A.; Vreven, T.; Kudin, K. N.; Burant, J. C.; Millam, J. M.; Iyengar, S. S.; Tomasi, J.; Barone, V.; Mennucci, B.; Cossi, M.; Scalmani, G.; Rega, N.; Petersson, G. A.; Nakatsuji, H.; Hada, M.; Ehara, M.; Toyota, K.; Fukuda, R.; Hasegawa, J.; Ishida, M.; Nakajima, T.; Honda, Y.; Kitao, O.; Nakai, H.; Klene, M.; Li,X.; Knox, J. E.; Hratchian, H. P.; Cross, J. B.; Adamo, C.; Jaramillo, J.; Gomperts, R.; Stratmann, R. E.; Yazyev, O.; Austin, A. J.; Cammi, R.; Pomelli, C.; Ochterski, J. W.; Ayala, P. Y.; Morokuma, K.; Voth, G. A.; Salvador, P.; Dannenberg, J. J.; Zakrzewski, V. G.; Dapprich, S.; Daniels, A. D.; Strain, M. C.; Farkas, O.; Malick, D. K.; Rabuck, A. D.; Raghavachari, K.;

Foresman, J. B.; Ortiz, J. V.; Cui, Q.; Baboul, A. G.; Clifford, S.; Cioslowski, J.; Stefanov, B. B.; Liu, G.; Liashenko, A.; Piskorz,P.; Komaromi, I.; Martin, R. L.; Fox, D. J.; Keith, T.; Al-Laham, M. A.; Peng, C. Y.; Nanayakkara, A.; Challacombe, M.; Gill, P. M. W.; Johnson, B.; Chen, W.; Wong, M. W.; Gonzalez, C.; Pople, J. A. Gaussian03(Revision B.04); Gaussian, Inc.: Pittsburgh, PA, 2003.

[8.24] Schlegel, H. B. *J. Comput. Chem.* **1982**, *3*, 214.

[8.25] Peng, C.; Schlegel, H. B. *Israel J. Chem* . **1994**, *33*, 449.

[8.26] Peng, C.; Ayala, P. Y.; Schlegel, H. B.; Frisch, M. J. *J. Comput. Chem.* **1996**, *17*, 49.

[8.27] Berente, I.; Naray-Szabo, G. *J. Phys. Chem. A* **2006**, *110*, 772-778.

[8.28] Gonzalez, C.; Schlegel, H. B. *J. Chem. Phys.* **1989**, *90*, 2154.

[8.29] Gonzalez, C.; Schlegel, H. B. *J. Phys. Chem.* **1990**, *94*, 5523.

[8.30] (a) Becke, A. D. *Phys. Rev. A* **1988**, *38*, 3098. (b) Becke, A. D. *J. Chem. Phys.***1993**, *98,* 5648. (c) Lee, C.; Yang, W.; Parr, R. G. *Phys. Rev. B* **1988**, *37*, 785.

[8.31] Schafer, A.; Huber, C.; Ahlrichs, R. *J. Chem. Phys.* **1994**, *100*, 5829.

[8.32] Boys, S. F.; Bernardi, F. *Mol. Phys.* **1970**, *19*, 553.

[8.33] Simon, S.; Duran, M.; Dannenberg, J. J. *J. Chem. Phys.* **1996**, 105, 11024.

[8.34] Dong, F.; Heinbuch, S.; Rocca, J. J.; Bernstein, E. R. *to be published.*

[8.35] Schröder, D.; Shaik, S.; Schwarz, H. *Acc. Chem. Res.* **2000**, *33*, 139.

Chapter 9

Gas phase study of the reactivity of optical coating materials with hydrocarbons using a desk-top size EUV laser

9.3 INTRODUCTION

The implementation of EUV lithography as a manufacturing tool for the fabrication of the future generations of computer chips requires a solution to the problem of the degradation of the reflectivity of EUV mirrors and masks caused by carbon deposition in the presence of EUV light. This motivates the study of the reaction of prospective metal oxide capping layer materials with hydrocarbons. An increased understanding of these reactions could lead to the development of thin capping layers that might protect EUV optics from carbon build-up. Metal oxide nanoparticles are widely used in chemical reactions for industrial processes, and as of yet, there is not a proper understanding of these chemical reaction processes due to very complicated environments on condensed phase surfaces. Clusters provide a path to the elucidation of chemical activity under isolated, controlled, and reproducible conditions through a detailed mechanistic model for condensed phase and surface reactivity and reactions.

In general, two primary reactive threats contribute to a loss of EUV mirror reflectivity: (1) growth of a carbonaceous layer on the mirror surface caused by the EUV

induced dissociation of adsorbed hydrocarbons; and (2) oxidation of the mirror surface by the radiative dissociation of adsorbed water.[9.1-9.4] Whether an optic is oxidized or carbonized in a given environment depends in part on the relative amounts of H_2O and hydrocarbon in the gas-phase environment. The surface chemistry is presently not well understood. A better understanding could result from studies of nanoclusters in the gas phase, where the clusters can serve as general models for multilayer mirror coatings under ideal reproducible conditions.

Silicon is a material that is widely used as the top layer in multilayer EUV optics that easily oxidizes on the surface leading to the growth of oxide layers upon EUV radiation.[9.2-9.4] During the oxidation process, adsorbed water molecules are dissociated by secondary electrons from the incident EUV radiation and the oxygen atoms react with the Si surface to create SiO_2.[9.7-9.9] This is considered to be an irreversible process causing reflection loss. However, Meiling *et. al.* have shown that the oxidation process can be slowed by up to a factor of 6 by using "smart gas blends" during exposure, such as ethanol.[9.3] Similarly, carbon contamination occurs when EUV-induced photoelectrons crack hydrocarbon molecules that are adsorbed on the mirror surface causing reflection loss[9.4,9.10,9.11]. Meiling *et. al.* found that carbon growth can be suppressed by a factor of up to 50 by admitting O_2 in the vacuum system during exposure.[9.3] Carbon contamination is a reversible process in which adding O_2 to the system increases time between cleanings of the optics.[9.2,9.12]

In order to reduce these reflection loss processes, researchers are searching for materials that are robust to oxidation and carbon deposition in the presence of EUV light and that will extend multilayer mirror lifetimes using capping layers consisting of, but not

limited to, materials such as SiC, SiN, Pt, Ru, Pd, and Rh.[9.6] Of these materials, ruthenium has emerged as the most promising.[9.13] Reportedly, a 5 nm Ru capping layer on a Si surface can increase mirror lifetime by a factor of ~40 while exhibiting minimal reflection loss of the MoSi multilayer structure.[9.6] Nonetheless, while Ru reduces oxidation effects, it does not show the same promise in the reduction of carbon contamination. Other potential candidates to protect the reactive Si surface are thin coatings of titanium/hafnium/zirconium oxide to help reduce the effect of hydrocarbon growth. This report will focus on the reactivity of Si_mO_n, Ti_mO_n, Hf_mO_n, Zr_mO_n, and Ru_mO_n clusters in the gas phase. The conclusions drawn from these studies can help elucidate reactions on optical surfaces.

We have recently completed a series of studies that constitute the first demonstration of the use of EUV lasers in photophysics and photochemistry.[9.14-9.19] These studies have primarily focused on finding active catalysts for the improvement of industrial processes. The experiments were based on the use of a compact capillary discharge EUV laser in the study of nanoclusters and nanocluster reactions. The EUV laser was used to provide single photon ionization of the neutral clusters for mass spectroscopy studies, with the significant advantage of reduced cluster fragmentation with respect to multi-photon or electron ionization sources. In the present study, we are searching for materials that are not active, in the presence of common vacuum system contaminants (e.g., water, carbon oxides, nitrogen oxides, hydrocarbons…) and EUV light, in the process of oxidation of or carbon deposition on optical surfaces. For this purpose, Si/Ti/Hf/Zr/Ru oxide neutral clusters are generated in a conventional laser vaporization/supersonic expansion cluster source by laser ablation of the appropriate metal wafer/foil into a He carrier gas mixed

with 5% OB_{2B} at 80 psig. Neutral clusters pass through a reactor cell into which a reaction gas is input by a pulsed valve. Single photon ionization of the neutral clusters and reaction products takes place using a 46.9 nm (26.5 eV) laser[9.20,9.21] in the ionization region of a time of flight mass spectrometer (TOFMS). The capillary discharge EUV emits pulses of about 1.5 ns duration with an energy/pulse of ~10 μJ at a repetition rate of up to 12 Hz.[9.20,9.21] A time of flight (linear/reflectron) mass spectrometer is employed for mass analysis.

9.3.1 TOFMS Experimental Setup

The experiments were carried out in a flow tube reactor that is similar to the one adopted by Smalley et. al[9.22] (Figure 9.1). A short summary of our flow tube experimental equipment is given below.

M_mO_n (M = Si, Ti, Hf, or Zr) clusters are generated by laser ablation with a focused 532 nm laser (Nd^{3+}: YAG, 10 Hz, 5-8 mJ/cm^2, 8 ns duration) onto a 12 mm diameter spring loaded metal disk in the presence of a pulsed helium carrier gas mixed with 5% O_2, controlled by a R.M. Jordan supersonic nozzle. A translational and rotational (spiral) motion of the disk is managed by a single motor (Maxon) that is powered by a home-made controller with a wide range of speed adjustment. Metal oxide clusters are formed in an adjustable length gas channel with a "waiting room" upstream. Typical dimensions used in this system are 3 mm diameter by 5 mm length for the waiting room and 1.8 mm diameter by 44 mm length for the rest of the channel. The gas channel is coupled directly to a tube/reactor (stainless steel, 6.3 mm inner diameter by 76 mm length). The reactant gases, C_2H_2, C_2H_4, water, etc. are injected into the reactor by a second pulsed valve (General Valve, Series 9) with a pulse duration of about 1 ms. The delay time between

the two valve openings is optimized to yield best product signals. Pressure in the flow tube reactor is estimated to be about 1 Torr in the presence of a reactant gas pulse. After reaction of M_mO_n with hydrocarbons, or other constituents in the reactor, reactants, products, and the buffer gases are expanded into vacuum (ca. 2 x 10^{-7} Torr) to form a molecular beam. The beam enters the detection region of a mass spectrometer chamber (ca. 10^{-6} – 10^{-7} Torr) through a 4 mm diameter skimmer. The clusters and products in the beam are ionized by a 46.9 nm EUV laser that is described in detail in the literature via ref. 9.20, and 9.21.

The EUV laser pulse energy is ~10 μJ at the output of the laser, but is reduced to ~3-5 μJ at the output of a z-fold mirror system placed just before the ionization region with the purpose of providing alignment capability of the beam with respect to the nanocluster setup. The z-fold consists of two gold coated mirrors at grazing incidence: a toroidal mirror with a 50 cm focal length that focuses the incoming beam, and a planar mirror that directs the beam into the ionization region. The cluster ions produced are extracted perpendicularly to the molecular beam and enter 1.0-m-long flight tube in which they are separated in arrival time according to their mass. At the end of the flight tube, the ions are reflected back down the flight tube by reflector plates, refocused and detected by a microchannel plate (MCP) detector operating with a pulsed bias voltage in order to gate large He signals and prevent saturation of the detector. Signals from the detector are fed to a digital oscilloscope through a 50 Ω MHV connector. Time delays between pulsed valve opening, firing the ablation laser, injecting the reaction gas, firing the ionization laser, and gating the MCP's are generated by three programmable digital delay generators. All timings can be adjusted in order to maximize the spectral signal strength.

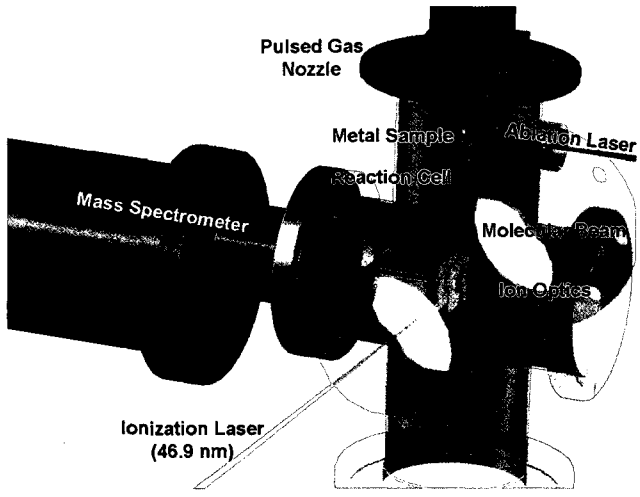


Figure 9.1: Schematic representation of TOFMS experiment. MmOn metal oxide clusters are generated by 532 nm laser ablation of a metal target and the clusters are passed through a reaction cell. The products, reactants, and buffer gasses are ionized by a 46.9 nm laser and detected by TOFMS.

In conventional nanocluster spectroscopy systems that make use of visible or UV wavelength laser photoionization, multi-photon absorptions cause fragmentation of the clusters. During the multiphoton ionization process by a nanosecond light pulse, at least two processes can be responsible for cluster ionization: (1) a cluster can absorb a photon through low-lying electronic states and relax back to the ground electronic state many times, thus heating the cluster until thermionic emission occurs; and (2) vertical absorption of two or more photons can occur without rapid relaxation between absorption steps for both neutral and/or ionic species. In either case, fragmentation of the cluster is likely.[9.23] The EUV laser source drastically changes the ionization process so that multi-photon effects are eliminated. For example, SiO has an ionization energy of ~11.5 eV. Ionization using and ArF excimer laser at 193 nm (6.4 eV) requires multiple photons whereas ionization at 46.9 nm (26.5 eV) has more than enough photon energy to ionize SiO with a single photon. The photoelectron carries away the remaining excess energy above the vertical ionization energy, resulting in almost no fragmentation of the clusters[9.14-9.19] and neutral parent cluster information is retained.

The high energy per pulse (~ 10 μJ) and repetition rate of several Hz of the capillary discharge 46.9 nm laser developed for this purpose is well matched with the repetition rate of the cluster source that utilizes a commercial 10 Hz Nd-YAG laser for sample ablation. The EUV laser is especially important for the study of metal oxide clusters because it ionizes the clusters by single photon transitions and thereby prevents subsequent cluster fragmentation and loss of parent cluster mass information.

9.3 RESULTS

Water and hydrocarbon contaminants are a major problem in EUV optic environments because they are extremely difficult to remove even in very high vacuum enclosures and they readily adsorb onto surfaces. Secondary electrons generated by the incident EUV flux, and to a lesser extent the EUV radiation itself, dissociate the water and hydrocarbons, and are believed to contaminate optics surfaces.[9.5]

9.3.1 Silicon oxide nanocluster (Si_mO_n) reactions

Figure 9.2 depicts mass spectra of the Si_mO_n cluster distribution with no reactant present (Fig. 9.2a), and reaction products with water (H_2O – Fig. 9.2b), acetylene (C_2H_2 – Fig. 9.2c), ethylene (C_2H_4 – Fig. 9.2d), and ethane (C_2H_6 – Fig. 9.2e). In Figure 9.2a, the cluster distribution, with no reactant, is dominated by oxygen deficient clusters such as $Si_2O_{2,3}$, and $Si_3O_{4,5}$. No oxygen rich clusters such as Si_2O_5, or Si_3O_7 are observed. These respective clusters are labeled oxygen rich/deficient because the most stable cluster configuration is of the nature $(SiO_2)_n$; for example, Si_2O_4, and Si_3O_6. Silicon oxide clusters tend to lose 1 or more oxygen atoms upon EUV radiation.

To study neutral Si_mO_n cluster reactions with water, the reactant is pulsed into the reactor in its vapor phase. When the neutral clusters generated from the

ablation/expansion source pass through the reactor cell, collisions will occur between neutral Si_mO_n clusters and the water. A new distribution of neutral clusters and reaction products is obtained by using 26.5 eV laser ionization. As shown in Fig. 9.2b, when water is added to the reactor,

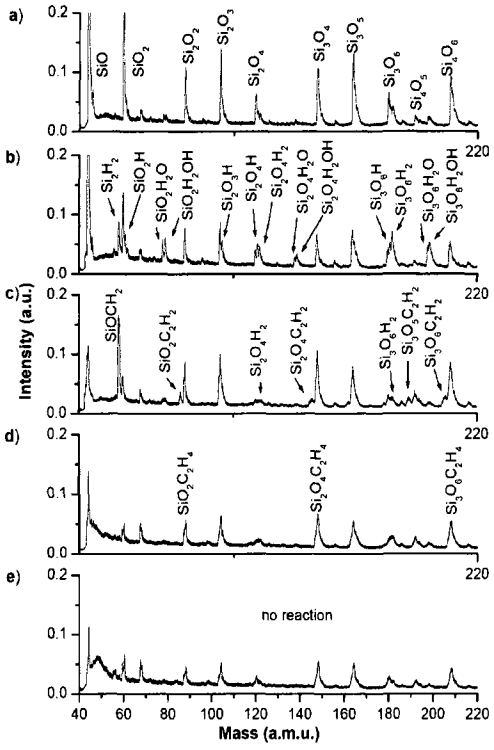


Figure 9.2: (a) Si_mO_n cluster distribution with no reactant in the reaction cell, (b) with water in the reaction cell, (c) with acetylene (C_2H_2) in the reaction cell, (d) with ethylene (C_2H_4) in the reaction cell, and (e) with ethane (C_2H_6) in the reaction cell.

products from the reaction $Si_mO_n + H_2O$ are generated through an association channel,

$$Si_mO_n + H_2O \rightarrow Si_mO_nH_2O \tag{9.1}$$

forming products SiO_2H_2O, $Si_2O_4H_2O$, and $Si_3O_6H_2O$. Generally, the most stable silicon clusters of the form $(SiO_2)_n$, are more active with water than oxygen deficient clusters. The most stable silicon oxide clusters are also observed to take hydrogen atoms from water to form SiO_2H, $Si_2O_4H_{1,2}$, and $Si_3O_6H_{1,2}$ through reaction channels,

$$Si_mO_n + H_2O \rightarrow Si_mO_nH + OH \tag{9.2}$$

$$Si_mO_n + H_2O \rightarrow Si_mO_nH_2 + O \quad (9.3)$$

Hydrocarbons are also commonly present in vacuum enclosures, largely originating from the enclosed system components – e.g., photoresist, outgassing products – and these are similarly adsorbed and dissociated.[9.5] To study neutral Si_mO_n cluster reactions with hydrocarbons, the reactants acetylene (C_2H_2), ethylene (C_2H_4), and ethane (C_2H_6) gases are individually and separately pulsed into the reactor consequently causing collisions between neutral Si_mO_n clusters and the reactants.

When C_2H_2 gas is added to the reactor, many new product signals, formed in the reaction of $Si_mO_n + C_2H_2$, are observed in the mass spectra, as shown in Fig. 9.2(c). The major products, $SiO_2C_2H_2$, $Si_2O_4C_2H_2$, $Si_3O_6C_2H_2$, etc., are generated from the association reactions,

$$Si_mO_n + C_2H_2 \rightarrow Si_mO_nC_2H_2 \quad (9.4)$$

Additionally, new products, $SiOCH_2$, $Si_2O_4H_2$, and $Si_3O_6H_2$, are found. In general, the most stable silicon oxide clusters are more active with acetylene than oxygen deficient clusters.

As shown in Fig. 9.2d, the major products of the reaction $Si_mO_n + C_2H_4$ are assigned as $SiO_2C_2H_4$, $Si_2O_4C_2H_4$, and $Si_3O_6C_2H_4$ generated from an association reaction channel,

$$Si_mO_n + C_2H_4 \rightarrow Si_mO_nC_2H_4 \quad (9.5)$$

Fig. 9.2e illustrates that all cluster signals decrease in roughly the same proportion when the saturated hydrocarbon C_2H_6 gas is added to the reactor cell. A similar result is also observed when inert gases are added to the reactor cell. Therefore, the decrease of cluster signals is due to scattering by the C_2H_6 gas pulsed into the reactor. No major reaction channel is observed.

The reactivity of Si_mO_n clusters is not limited solely to water and these 3 hydrocarbon species. In fact, we find that Si_mO_n clusters are highly reactive with many unsaturated hydrocarbons, formic acid, and alcohols, suggesting that the oxidized Si surface in the condensed phase will easily be contaminated by these and a number of other reactants.

9.3.2 Titanium oxide nanocluster (Ti_mO_n) reactions

The photocatalytic activity of titanium oxide results in thin coatings of the material exhibiting self cleaning and disinfecting properties under exposure to UV radiation.[9.24] These properties make the material a candidate for applications such as protective capping layers on EUV mirrors.

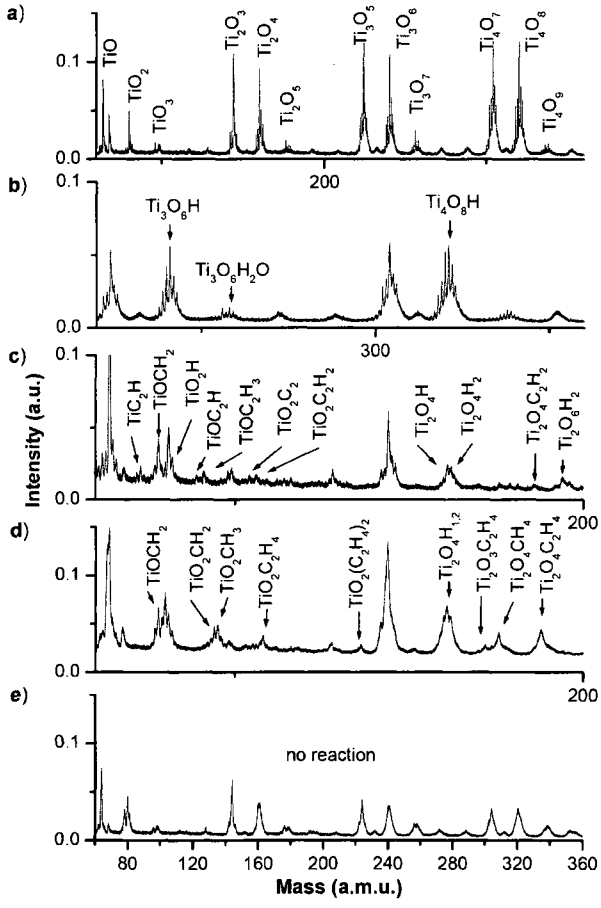


Figure 9.3: (Note that the scales on each section are different in order to better display the data.) (a) Ti_mO_n cluster distribution with no reactant in the reaction cell, (b) with water in the reaction cell, (c) with acetylene (C_2H_2) in the reaction cell, (d) with ethylene (C_2H4) in the reaction cell, and (e) with ethane (C_2H_6) in the reaction cell.

The reactivity of titanium oxide clusters is explored in the gas phase and an example is shown in Figure 9.3 that depicts mass spectra of the Ti_mO_n cluster distribution (Figure 9.3a), and reaction products with H_2O (Fig. 9.3b), C_2H_2 (Fig. 9.3c), C_2H_4 (Fig. 9.3d), and C_2H_6 (Fig. 9.3e). The cluster distribution is once again dominated by oxygen deficient clusters such as TiO, and Ti_2O_3. Contrary to the Si_mO_n cluster distribution, oxygen rich clusters such as TiO_3, or Ti_2O_5 are observed although the signals are weak. Also, the mass resolution of our experimental setup allows us to observe the isotopic structure of the Ti_mO_n clusters.

To study neutral Ti_mO_n cluster reactions with water or hydrocarbons, the experimental method is exactly the same as for Si_mO_n cluster reactions where the reactant gases are individually and separately pulsed into the reactor. As shown in Fig. 9.3b, when water is added to the reactor, products from the reaction Ti_mO_n + H_2O are generated through an association channel to form $Ti_3O_4H_2O$, and products where Ti_mO_n clusters take H atoms from water to form Ti_3O_4H, and Ti_4O_8H are generated.

When acetylene gas is added to the reactor, many new product signals, formed in the reaction of Ti_mO_n + C_2H_2, are observed in the mass spectra, as shown in Fig. 9.3c. Generally, the most stable titanium clusters of the form $(TiO_2)_n$, are more active with acetylene than oxygen deficient clusters generating association products such as $TiO_2C_2H_2$, and $Ti_2O_4C_2H_2$. Although, some reactions occur involving oxygen deficient clusters to form products $TiOCH_2$, $TiOC_2H$, and $TiOC_2H_2$. Additionally, oxygen stable and rich clusters generate new products, TiO_2H, TiO_2C_2, $Ti_2O_4H_{1,2}$, and $Ti_2O_6H_2$.

When ethylene is added to the reactor, we observe association products generated from Ti_mO_n + C_2H_4 (Figure 9.3d). Generally, the most stable titanium clusters of the form

$(TiO_2)_n$, are more active with ethylene than oxygen deficient clusters generating products such as $TiO_2C_2H_{2,3,4}$, and $Ti_2O_4C_2H_4$. A few reactions involving oxygen deficient clusters are also observed to generate $TiOCH_2$, and $Ti_2O_3C_2H_4$. The most stable titanium clusters are also observed to take hydrogen atoms from ethylene and break apart ethylene to form products such as TiO_2CH_2, TiO_2CH_3, and $Ti_2O_4H_{1,2}$.

Figure 9.3e illustrates that all the cluster signals decrease in roughly the same proportion when the saturated hydrocarbon C_2H_6 gas is added to the reactor cell. Again, the decreased cluster signal is due to scattering by the C_2H_6 gas pulsed into the reactor. No major reaction channel is observed.

In a similar fashion to Si_mO_n metal oxide clusters, the reactivity of Ti_mO_n metal oxide clusters is not limited in any way to any one reactant. We find that Ti_mO_n clusters are highly reactive with many unsaturated hydrocarbons, formic acid, water, and alcohols, suggesting that the oxidized Ti surface is similar to the oxidized Si surface, and in the condensed phase will also easily be contaminated by these reactants.

9.3.3 Hafnium oxide nanocluster (Hf_mO_n) reactions

HfO_2 is characterized by a good chemical, thermal and mechanical stability which facilitates its use even under severe conditions[9.25] making it another good candidate for a protective capping layer. The reactivity of hafnium oxide clusters is explored in the gas phase and an example is shown in Figure 9.4 that depicts mass spectra of the Hf_mO_n cluster distribution (Figure 9.4a), and reaction products with H_2O (Fig. 9.4b), C_2H_2 (Fig. 9.4c), C_2H_4 (Fig. 9.4d), and C_2H_6 (Fig. 9.4e). The cluster distribution dominance is shared by both oxygen deficient, and oxygen stable clusters of the type $(Hf_nO_{2n-1})_n$ and

$(HfO_2)_n$, respectively. Oxygen rich clusters, $(Hf_nO_{2n+1})_n$ are observed although the signals are smaller than the oxygen deficient and oxygen stable clusters.

The experimental method is exactly the same as for Si_m/Ti_mO_n cluster reactions in which case the reactant gases are individually and separately pulsed into the reactor. As shown in Fig. 9.4b, when water is added to the reactor, products from the reaction Hf_mO_n + H_2O are generated through an association channel,

$$Hf_mO_n + H_2O \rightarrow Hf_mO_nH_2O \qquad (9.6)$$

Only association reactions involving oxygen stable and rich clusters are observed for $Hf_mO_n + H_2O$.

When acetylene gas is added to the reactor, very few new product signals, formed in the reaction of $Hf_mO_n + C_2H_2$, are observed in the mass spectra, as shown in Fig. 9.4c. Only the most stable hafnium clusters and oxygen rich hafnium clusters are active with acetylene generating association products such as $Hf_2O_4C_2H_2$, $Hf_2O_5C_2H_2$, and $Hf_4O_8C_2H_2$. No reactions occur involving oxygen deficient clusters.

When ethylene, or ethane, shown in Figure 9.4d and 9.4e respectively are added to the reactor, the cluster signals decrease in roughly the same proportion as when inert gases are added to the reactor cell. Therefore, the decrease of cluster signals is due to scattering by the C_2H_4, and C_2H_6 gas pulsed into the reactor in the presence of Hf_mO_n clusters. No major reaction channel is observed.

In contrast to the behavior of Si_mO_n, and Ti_mO_n metal oxide clusters, the reactivity of Hf_mO_n metal oxide clusters is limited to few reactants. We find that Hf_mO_n clusters are highly unreactive with many unsaturated hydrocarbons and alcohols. Even when Hf_mO_n clusters react, the reaction products are few and only involve oxygen stable and rich

structures through association channels. No significant chemistry is observed. These data suggest that the oxidized Hf surface is less reactive than the oxidized Si and Ti surfaces, and in the condensed phase will be contaminated to a much lesser extent by these reactants.

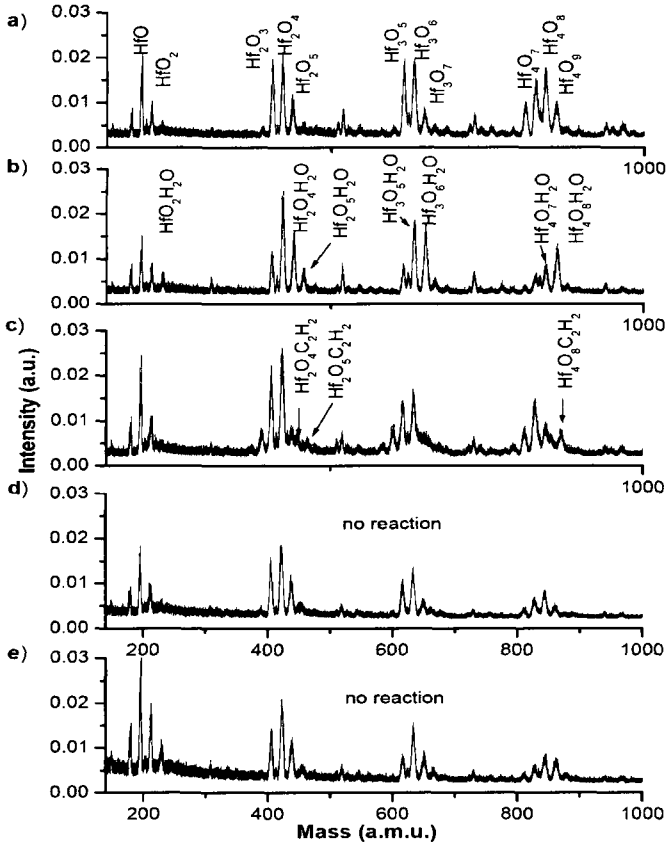


Figure 9.4: (a) Hf_mO_n cluster distribution with no reactant in the reaction cell, (b) with water in the reaction cell, (c) with acetylene (C_2H_2) in the reaction cell, (d) with ethylene (C_2H4) in the reaction cell, and (e) with ethane (C_2H_6) in the reaction cell.

9.3.4 Zirconium oxide nanocluster (Zr_mO_n) reactions

ZrO_2 is characterized by extreme thermal, chemical and mechanical stability which gives rise to a wide range of technical applications for ZrO_2 thin films and coatings, especially in optics[9.26], and protective applications[9.27] making the material a candidate protective capping layers on EUV mirrors.

The reactivity of zirconium oxide clusters is explored in the gas phase and an example is shown in Figure 9.5 that depicts mass spectra of the Zr_mO_n cluster distribution (Figure 9.5a), and reaction products with H_2O (Fig. 9.5b), C_2H_2 (Fig. 9.5c), C_2H_4 (Fig. 9.5d), and C_2H_6 (Fig. 9.5e). The cluster distribution dominance, much like Hf_mO_n, is shared by both oxygen deficient, and oxygen stable clusters of the type $(Zr_nO_{2n-1})_n$ and $(ZrO_2)_n$, respectively. Oxygen rich clusters, $(Zr_nO_{2n+1})_n$, are observed although the signals are smaller than the oxygen deficient and oxygen stable clusters.

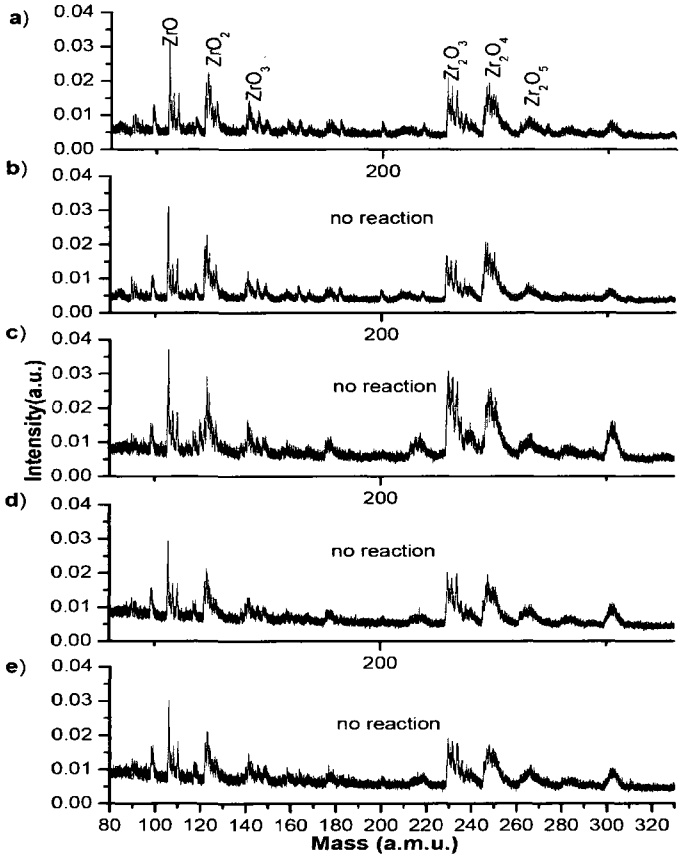


Figure 9.5: (a) Zr_mO_n cluster distribution with no reactant in the reaction cell, (b) with water in the reaction cell, (c) with acetylene (C_2H_2) in the reaction cell, (d) with ethylene (C_2H_4) in the reaction cell, and (e) with ethane (C_2H_6) in the reaction cell.

The experimental method is the same as for $Si_m/Ti_m/Hf_mO_n$ cluster reactions in which case the reactant gases are individually and separately pulsed into the reactor. We find

that Zr_mO_n clusters are highly unreactive with any reactant that we introduce into the system. These data suggest that the oxidized Zr_mO_n surface is less reactive than the oxidized Si, Ti, and even Hf oxide surfaces. The results suggest that a zirconium oxide film will be contaminated to a much lesser extent by these reactants.

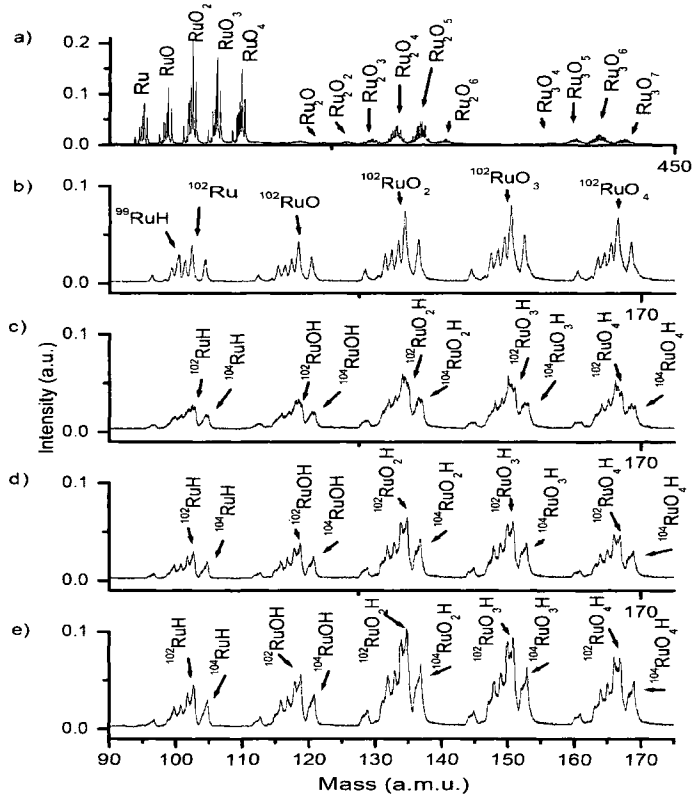


Figure 9.6: (a) Ru_mO_n cluster distribution with no reactant in the reaction cell, (b) with water, (c) with acetylene (C_2H_2) in the reaction cell, (d) with ethylene (C_2H_4) in the reaction cell, and (e) with ethane (C_2H_6) in the reaction cell.

9.3.5 Ruthenium oxide nanocluster (Ru_mO_n) reactions

Ruthenium is amongst metals known for their oxidation resistance along with gold, platinum, and palladium. Ruthenium metal was a natural first choice for a capping layer due to its minimal EUV absorption.[9.1] It is understood by the authors that Ru capping layers proposed in the literature[9.1,9.5,9.6] are pure metal layers and not oxide layers. The

fact remains that pure metal clusters are difficult to detect with the 46.9 nm laser because of crossection/laser energy issues. Nonetheless, experiments for pure Ru_m clusters and their reactivity are currently underway. Ru_mO_n clusters did provide different and interesting chemistry and will almost certainly be a component of any Ru attempted film.

The reactivity of ruthenium oxide clusters is explored in the gas phase and an example is shown in Figure 9.6 that depicts mass spectra of the Ru_mO_n cluster distribution (Figure 9.6a), and reaction products with H_2O (Fig. 9.6b), C_2H_2 (Fig. 9.6c), C_2H_4 (Fig. 9.6d), and C_2H_6 (Fig. 9.6e). The cluster distribution dominance, unlike any of the other metal oxides in this study, is shared by both oxygen stable, and oxygen rich clusters of the type $(RuO_2)_n$, and $(Ru_nO_{2n+1})_n$ respectively. Although many oxygen deficient clusters, $(Ru_nO_{2n-1})_n$, are also present.

The reactivity of the ruthenium oxide cluster is difficult to assess due to the abundance of isotopes present in the spectra. However, when water is added to the system (Fig. 9.6b), one observes and intensity switch at mass number 100 and a decrease at mass number 99 due to a reaction in pure Ru metal as follows,

$$Ru + H_2O \rightarrow RuH + OH \tag{9.7}$$

This was the only observable reaction for Ru_mO_n clusters with water.

When acetylene gas is added to the reactor, new product signals, formed in the reaction of Ru_mO_n + C_2H_2, are observed in the mass spectra, as shown in Fig. 9.6c. Contrary to the other metal oxides in this study, oxygen deficient, stable, and rich ruthenium clusters are active with acetylene generating hydrogen abstraction products such as $^{102}RuOH$, and $^{104}Ru_2O_4H_2$. Generally the reaction can be written,

$$RuO_n + C_2H_2 \rightarrow RuO_nH + C_2H \tag{9.8}$$

The reactions are not isotopically dependant, i.e., they happen for all isotopes. The reactions will only be discussed from what one can see in the spectra which predominantly involve isotopes 102, and 104. Reactions involving other isotopes may be hidden in the background or broadening of the signal from collisions.

When ethylene is added to the reactor, we observe the same hydrogen abstraction products generated from equation 9.8 (Figure 9.6d). Again, the oxygen deficient, stable, and rich ruthenium clusters are active with ethylene generating hydrogen abstraction products.

When the saturated hydrocarbon C_2H_6 gas is added to the reactor cell, once again one can observe the same hydrogen abstraction products generated from equation 9.8 (Figure 9.6e). This is a different from Si, Ti, Hf, and Zr in that none of them react with saturated hydrocarbons.

In a similar fashion to Si_mO_n and Ti_mO_n metal oxide clusters, the reactivity of Ru_mO_n metal oxide clusters is not limited in any way to any one reactant. We find that Ru_mO_n clusters are reactive with many unsaturated and saturated hydrocarbons, while they remain relatively inactive with water, and alcohols, suggesting that the oxidized Ru surface is sensitive to hydrocarbon contamination, but relatively inactive with water and alcohols that are present in any vacuum system. In fact, the only Ru clusters observed to react with water/alcohols were pure Ru with no oxygen. There are no observed association reactions present in the Ru_mO_n spectra.

9.4 CONCLUSIONS

In general, two primary reactive threats contribute to a loss of EUV mirror reflectivity: (1) the growth of a carbonaceous layer on the mirror surface caused by the EUV induced

dissociation of adsorbed hydrocarbons; and (2) the oxidation of the mirror surface by the radiative dissociation of adsorbed water. We have studied five different materials in the gas phase with the intention of relating our data and observations to the application of protective coatings for EUV mirror surfaces. Silicon mirror surfaces are readily oxidized and contaminated upon EUV irradiation.[9.2-9.4] Our spectra involving Si_mO_n metal oxide nanoclusters and their reactions with many unsaturated hydrocarbons, water, and alcohols, show that Si_mO_n clusters are reactive in the gas phase. This suggests that an oxidized Si surface in the condensed phase will be highly reactive. Titanium oxide photocatalytic activity has demonstrated thin coatings of the material exhibiting self cleaning and disinfecting properties under exposure to UV radiation that would be desirable for protecting EUV optic surfaces. Nonetheless, our spectra involving Ti_mO_n metal oxide nanoclusters and their reaction with many unsaturated hydrocarbons, water, and alcohols, show that Ti_mO_n clusters are reactive in the gas phase. The data show that silicon and titanium oxide capping layers in optical coatings may be contaminated easily by residual gasses in vacuum and should be avoided/protected in the presence of EUV irradiation.

Conversely, our spectra involving zirconium and hafnium metal oxide nanoclusters and their reaction with many unsaturated hydrocarbons, water, and alcohols, show that they are unreactive in the gas phase. These data suggest that oxidized hafnium and zirconium surfaces in the condensed phase are much less reactive than Ti or Si oxide surfaces. Zirconium oxide is less reactive than hafnium oxide. Hf and Zr oxides should make good protective coatings for EUV optical surfaces and extend optical lifetimes upon EUV irradiation.

Ruthenium oxide clusters turned out to have different and interesting chemistry. They show almost no reactivity with water and alcohols, where as they are fairly active with saturated and unsaturated hydrocarbons. These data suggest that if there are vacuum systems that have extremely low partial pressures of hydrocarbons[9.1], Ru_mO_n protective capping layers may be of great importance.

Also, it is observed that oxygen deficient clusters in the five cases of $Si_m/Ti_m/Hf_m/Zr_m/Ru_mO_n$ are less reactive than oxygen rich and stable clusters. This result suggests that if a surface is tailored to be oxygen poor, this condition could also help to protect an EUV optic surface from carbon contamination and help to increase lifetime of EUV optics.

Currently, we are undergoing studies that involve the contamination of pure Ru_m clusters to provide a broader knowledge base of protective capping layers that are being examined in other laboratories.

REFERENCES

[9.1] J. Hollenshead, and L. Klebanoff, "Modeling extreme ultraviolet/H_2O oxidation of ruthemium optic coatings," J. Vac. Sci. Technol. B **24(1)**, 118 (2006).

[9.2] B. Mertens, M. Weiss, H. Meiling, R. Klein, E. Louis, R. Kurt, M. Wedowski, H. Trenkler, B. Wolschrijn, R. Jansen, A. Runstraat, R. Moors, K. Spee, S. Pl€oger, R. Kruijs, "Progress in EUV optics lifetime expectations," Microelec. Eng. **73-74**, 16 (2004).

[9.3] H. Meiling, B. Mertens, F. Stietz, M. Wedowski, R. Klein, R. Kurt, E. Loius, and A. Yakshin, "Prevention of MoSi multilayer reflection loss in EUVL tools," SPIE **4506**, 93 (2001).

[9.4] K. Boller, R.-P. Haelbich, H. Hogrefe, W. Jark, and C. Kunz, "Investigation of carbon contamination of mirror surfaces exposed to synchrotron radiation," Nucl. Inst. Meth. **208**, 273 (1983).

[9.5] T.E. Madey, N.S. Faradzhev, B.V. Yakshinskiy, and N.V. Edwards, "Surface phenomena related to mirror degradation in extreme ultraviolet (EUV) lithography," Applied Surface Science **253**, 1691 (2006).

[9.6] G. Kyriakou, D.J. Davis, R.B. Grant, D.J. Watson, A. Keen, M.S. Tikhov, and R.M. Lambert, "Electron Impact-Assisted Carbon Film Growth on Ru(0001): Implications for Next-Generation EUV Lithography," J. Phys. Chem. C **111**, 4491 (2007).

[9.7] T. Engel, "The interaction of molecular and atomic oxygen with Si(100) and Si(111)," Surf. Sci. Rep. 18, 91(1993).

[9.8] G.Y. Mcdaniel, S.T. Fenstermaker, D.E. Walker Jr., W.V. Lampert, S.M. Mukhopadhyay, and P.H. Holloway, " Electron-stimulated oxidation of silicon carbide," Surf. Sci. **445**, 159 (2000).

[9.9] T. Miyake, S. Soeki, H. Kato, A. Namiki, H. Kamba, and T. Suzaki, "Molecular-beam study of sticking of oxygen on Si(100)," Phys. Rev. B **42**, 11801 (1990).

[9.10] R. Roseberg et. al., "Deposition of carbon on gold using synchrotron radiation," Nucl. Inst. and Meth. in Phys. Research A 291, 101 (1990).

[9.11] T. Koide et. al., "Investigation of carbon contamination of synchrotron radiation mirrors," Nucl. Inst. and Meth. in Phys. Research A 246, 215 (1986).

[9.12] M.E. Malinowski, P. Grunow, C. Steinhaus, W.M. Clift, and L.E. Klebanoff, "Use of molecular oxygen to reduce EUV-induced carbon contamination of optics," SPIE **4343**, 347 (2001).

[9.13] C. Tarrio, and S. Grantham, "Synchrotron beamline for extreme-ultraviolet multilayer mirror endurance testing," Rev. Sci. Instrum. **76**, 056101 (2005).

[9.14] F. Dong, S. Heinbuch, J.J. Rocca, and E.R. Bernstein, "Dynamics and fragmentation of van der Waals clusters: $(H_2O)_n$, $(CH_3OH)_n$, and $(NH_3)_n$ upon ionization by a 26.5 eV soft x-ray laser," J. Chem. Phys. **124**, 224319 (2006).

[9.15] S. Heinbuch, F. Dong, J.J. Rocca, and E.R. Bernstein, "Single photon ionization of van der Waals clusters with a soft x-ray laser: $(CO_2)_n$ and $(CO_2)_n(H_2O)_m$," J. Chem. Phys. **125**, 154316 (2006).

[9.16] F. Dong, S. Heinbuch, J.J. Rocca, and E.R. Bernstein, "Single photon ionization of van der Waals clusters with a soft x-ray laser: $(SO_2)_n$ and $(SO_2)_n(H_2O)_m$," J. Chem. Phys. **125**, 154317 (2006).

[9.17] F. Dong, S. Heinbuch, J.J. Rocca, and E.R. Bernstein, "Formation and distribution of neutral vanadium, niobium, and tantalum oxide clusters: Single photon ionization at 26.5 eV," J. Chem. Phys. **125**, 164318 (2006).

[9.18] S. Heinbuch, F. Dong, J.J. Rocca, and E.R. Bernstein, "Single photon ionization of hydrogen bonded clusters with a soft x-ray laser: (HCOOH)x and (HCOOH)y(H2O)z," J. Chem. Phys. **126**, 244301 (2007).

[9.19] F. Dong, S. Heinbuch, Y. Xie, J.J. Rocca, Z. Wang, K. Deng, S. He, and E.R. Bernstein, "Experimental and theoretical study of the reactions between neutral vanadium oxide clusters and ethane, ethylene, and acetylene," J. Am. Chem. Soc. **130**, 1932 (2008).

[9.20] S. Heinbuch, M. Grisham, D. Martz, and J.J. Rocca, "Demonstration of a desk-top size high repetition rate soft x-ray laser," Opt. Exp. **13**, 4050-4055 (2005).

[9.21] S. Heinbuch, M. Grisham, D. Martz, F. Dong, E. R. Bernstein, and J. J. Rocca, " Desk-top size high repetition rate 46.9 nm capillary discharge laser as photoionization source for photochemistry applications," SPIE **5919**, 591907 (2005).

[9.22] M. E. Geusic, M. D. Morse, S. C. O'Brien, R. E. Smalley, "Surface reactions of metal clusters I: The fast flow cluster reactor," Rev. Sci. Instrum. **56**, 2123 (1985).

[9.23] Y. Matsuda and E.R. Bernstein, "On the Titanium Oxide Neutral Cluster Distribution in the Gas Phase: Detection through 118 nm Single-Photon and 193 nm Multiphoton Ionization," J. Phys. Chem. A, **109 (2)**, 314 -319 (2005).

[9.24] Z. Luo, H.Cai, X. Ren, J. Liu, W. Hong, and P. Zhang, "Hydrophilicity of titanium oxide coatings with the addition of silica," Materials Science and Eng. B **138**, 151 (2007).

[9.25] M. Ritala, M. Leskelä, L. Niinistö, T. Prohaska, G. Friedbacher and M. Grasserbauer, "Development of crystallinity and morphology in hafnium dioxide thin films grown by atomic layer epitaxy," Thin Solid Films **250**, 72 (1994).

[9.26] M. Ritala and M. Leskelä, "Zirconium dioxide thin films deposited by ALE using zirconium tetrachloride as precursor," Appl. Surf. Sci. **75**, 333 (1994).

[9.27] M. Atik and M.A. Aegerter, "Corrosion resistant sol-gel ZrO_2 coatings on stainless steel," J. Non-Cryst. Solids **147/148**, 813 (1992).

Chapter 10

Experimental and theoretical studies of Reactions of neutral vanadium and tantalum oxide clusters with NO and NH_3

10.1. INTRODUCTION

Selective catalytic reduction (SCR) of nitric oxide by ammonia over V_2O_5/TiO_2 based catalysts is the most advanced and widely used technology capable of reducing NO_x emissions to the low levels mandated in many areas of the world.[10.1] The overall catalytically promoted reactions are,

$$6NO + 4NH_3 \rightarrow 5N_2 + 6H_2O \qquad (10.1a)$$

$$6NO_2 + 8NH_3 \rightarrow 7N_2 + 12H_2O, \text{ etc.} \qquad (10.1b)$$

In the condensed phase, a vanadium oxide catalyst is loaded on an anatase support as a monolayer, and the active VO_x species is suggested to have monomeric or dimeric structures.[10.2] These VO_x structures are considered to be preferable as active sites rather than bulk V_2O_5. They are proposed to consist of terminal oxygen atoms that can be saturated by

molecules like ammonia or water.[10.3-10.5] Catalyst development for this process aims to improve efficiency, avoid parallel reactions, and to reach lower working temperatures.

Although numerous experimental surface studies have been carried out on the NO SCR reaction over vanadium-based catalysts, a complete elucidation of the reaction mechanism has not been achieved, and very few, if any, gas phase experiments have been conducted. The reaction is generally believed to occur through an Eley-Rideal type mechanism in which ammonia is adsorbed on the vanadium-based catalyst in the first step, and then the reaction proceeds with the activation of nitric oxide from the gas phase;[10.6-10.24] however, the adsorption mode of ammonia on the catalytic surface is still unclear.

Using temperature programmed desorption (TPD) and IR studies, Inomata et al.[10.6,10.7] suggest that the active site for the ammonia activation is the Brønsted acidic V–OH site adjacent to a $V^{5+}O$ site. Because of an additional H, ammonia is suggested to be adsorbed on this site as NH_4^+. Topsøe,[10.10-10.12] and Gasior *et* al.[10.13] both suggest that predominantly Brønsted acid sites (V–OH) are present and active on the surface of oxidized V_2O_5 for the ammonia activation reaction. Following this idea, Ozkan et al.[10.14,10.15] conclude that ammonia adsorbs on pairs of V–OH groups, leading to the formation of surface ammonium ion species. Gilardoni et al.[10.25,10.26] propose that after nitric oxide interaction with pre-adsorbed NH_4^+ species, NH_2NO species form in the gas phase, which then undergo a series of isomerization reactions to give reaction products nitrogen and water. Similarly, Anstrom et al.[10.27,10.28] investigated the role of V_2O_5 in the

reaction of adsorbed NH_4^+ with nitric oxide by using a vanadium oxide cluster containing four vanadium atoms with a Brønsted acidic V–OH site. According to density function theory (DFT) calculations by Yin et al.[10.29] for the mechanism of SCR of NO by NH_3 over a V_2O_5 surface, two hydroxyl groups (V–OH) are responsible for the formation of NH_4^+ species, and a VO group is required for activation of NH_4^+. Aside from adsorption as NH_4^+, a different approach to the SCR of NO by NH_3 suggests that NH_3 adsorbs and dissociates into NH_2 and H, and that the formation of the ammonium ion is a stable intermediate.[10.19,10.30,10.31]

Zhanpeisov et al.[10.31] find that the NH_4^+ species is not favorable from an energetic point of view, and report an energy gain of 47.7 kcal/mol for the NH_3 dissociation on a reactive O site. Janssen et al.,[10.8,10.9] employing isotopic transient studies, consider the VO species to be the active site that is easily reduced. According to this study, ammonia is adsorbed on this site as $V–ONH_2$ by reducing the adjacent VO site to V–OH. Ramis et al.[10.16-10.19] suggest that Brønsted acidity is not a necessary requirement for SCR activity and ammonia is activated for SCR by coordination over Lewis acidic sites on TiO_2 as well and this activated ammonia is easily transformed to the amide NH_2 species by hydrogen abstraction. Besides the examples given above, additional theoretical studies employing the cluster approach to vanadia/titania models have been reported.[10.19,10.32-10.36]

Recently, single-photon ionization (SPI) through soft x-ray (SXR) laser radiation has been successfully implemented by our group to study a series of neutral metal oxide cluster distributions without fragmentation.[10.37-10.47] The SXR laser is demonstrated to

be essential in the detection of all neutral clusters and their products by time of flight mass spectrometry.

In the present work, a fast flow reactor is employed to study the reactivity of neutral vanadium and tantalum oxide clusters toward NO, NH_3, and an NO/NH_3 mixture. The motivation is to generate possible molecular level mechanisms for the SCR of NO by NH_3 in condensed phase catalytic reactions. In the present report, the experimental results are presented and discussed based on DFT calculations. The DFT calculation results occupy a unique position in the analysis of our experimental results because, without them, one can incorrectly conclude that the lack of observed intermediate species for V_mO_n clusters compared to Ta_mO_n clusters, signals an inactivity of V_mO_n clusters to generate and model the condensed phase behavior. Based on the DFT calculations, such a conclusion is incorrect; in fact, quite the opposite is true. Additionally, these calculations demonstrate that an $HOV_mO_{n-1}NH_2$ mechanism is appropriate for the SCR of NO with NH_3 on a V_mO_n catalytic cluster.

10.2 EXPERIMENTAL PROCEDURES

M_mO_n (M = V or Ta) clusters are generated by laser ablation with a focused 532 nm laser (Nd^{3+}: YAG, 10 Hz, 5-8 mJ/cm^2, 8 ns duration) onto a 12 mm diameter spring loaded metal disk in the presence of a pulsed helium carrier gas mixed with 0.5% O_2, controlled by an R.M. Jordan supersonic nozzle. A translational and rotational (spiral) motion of the disk is managed by a single motor (Maxon) that is powered by a home-made controller with a wide range of speed adjustment. Metal oxide clusters are formed in an adjustable length

gas channel with a "waiting room" upstream. Typical dimensions used in this system are 3 mm diameter by 5 mm length for the waiting room and 1.8 mm diameter by 44 mm length for the rest of the channel. The gas channel is coupled directly to a tube/reactor (stainless steel, 6.3 mm inner diameter by 76 mm length). The reactant gases, NO, NH_3, or NO:NH_3 mixture (9:1) are injected into the reactor by a second pulsed valve (General Valve, Series 9) with a pulse duration of about 1 ms. The delay time between the two valve openings is optimized to yield the best product signals. Pressure in the fast flow reactor is estimated to be about 1 Torr in the presence of a reactant gas pulse. After the reaction of M_mO_n with NO, NH_3, or NO:NH_3 in the reactor, reactants, products, and the buffer gases are expanded into vacuum (ca. 2 x 10^{-7} Torr) to form a molecular beam. The beam enters the detection region of a mass spectrometer chamber (ca. 10^{-6} – 10^{-7} Torr) through a 4 mm diameter skimmer. The clusters and products in the beam are ionized by a 46.9 nm SXR laser that is described in detail in the literature.[10.48,10.49]

The SXR laser pulse energy is ~10 μJ at the output of the laser, but is reduced to ~3-5 μJ at the output of a z-fold mirror system placed just before the ionization region with the purpose of providing alignment capability of the beam with respect to the cluster setup. The z-fold consists of two gold coated mirrors at grazing incidence: a toroidal mirror with a 50 cm focal length that focuses the incoming beam, and a planar mirror that directs the beam into the ionization region. The cluster ions produced are extracted perpendicularly to the molecular beam and enter 1.0 m long flight tube in which they are separated in arrival time according to their mass. At the end of the flight tube, the ions are reflected back down

the flight tube by reflector plates, refocused and detected by a microchannel plate (MCP) detector operating with a pulsed bias voltage in order to gate large He signals and prevent saturation of the detector. Signals from the detector are fed to a digital oscilloscope through a 50 Ω MHV connector. Time delays between pulsed valve opening, firing the ablation laser, injecting the reaction gas, firing the ionization laser, and gating the MCP's are generated by three programmable digital delay generators. All timings can be adjusted in order to maximize the spectral signal strength.

The high energy per pulse (~ 10 μJ) and repetition rate of several Hz of the capillary discharge 46.9 nm laser developed for this purpose are well matched with the repetition rate of the cluster source that utilizes a commercial 10 Hz Nd-YAG laser for sample ablation. The SXR laser is especially important for the study of metal oxide clusters because it ionizes the clusters by single photon transitions and thereby prevents subsequent cluster fragmentation and loss of parent neutral cluster mass information. Issues dealing with back flow gas from the reaction flow tube, ions present in the beam that interfere with neutral cluster chemistry, and ionization by the SXR laser photons are extensively discussed and dealt with in our previous publications.[10.37-10.47]

10.3 COMPUTATIONAL DETAILS

DFT calculations using the Gaussian 03 program[10.50] are employed to study reactions of neutral V_mO_n and Ta_mO_n clusters with NO, NH_3, and NO/NH_3. The DFT calculations involve geometry optimization of various reaction intermediates and transition states. Transition state optimizations are performed by using the synchronous transit-guided

quasi-Newton (STQN) method.[10.51,10.52] Vibrational frequencies are calculated to check that the reaction intermediates have all positive frequencies and species in the transition states have only one imaginary frequency. Intrinsic reaction coordinate (IRC) calculations[10.53,10.54] are also performed so that a transition state connects two appropriate local minima in the reaction paths. The hybrid B3LYP exchange-correlation functional[10.55] is adopted. A contracted gaussian basis set of triple zeta valence (TZVP) quality[10.56] for H, N, and O atoms is used and the LANL2TZ[10.57] basis set with the corresponding effective core potentials is used for all metal atoms. Test calculations indicate that basis set superposition error (BSSE)[10.58,10.59] corrections are negligible (~ 1-2 kcal/mol), so the BSSE correction is not taken into consideration in this study.

10.4 RESULTS AND DISCUSSION

In the ensuing presentation, the formula M_mO_n (M = V, Ta) is used for a general representation of the corresponding metal oxide clusters. To study reactions of neutral M_mO_n clusters with NO_x, NH_3, or NO/NH_3 (9:1), mixed reactant/He gas is pulsed into the reactor at a pressure of ~ 10 - 15 psi. When the neutral metal oxide clusters generated from the ablation/expansion source pass through the reactor cell, collisions will occur between neutral M_mO_n clusters and reactant molecules. The instantaneous reactant gas pressure in the reactor cell (during the time that M_mO_n is in the cell) is estimated to be about 1 Torr. New reaction products and the remnant neutral M_mO_n clusters are detected by 26.5 eV, SXR laser single photon ionization.

The high photon energy of 26.5 eV radiation might possibly

fragment/photodissociate neutral clusters or their reaction products during the ionization process, and thereby confuse the identification of ground state neutral species chemistry. In order to clarify this issue, a comparison experiment is conducted in which both a 10.5 eV and 26.5 eV laser are used for ionization in the study of V_mO_n cluster reactions with NO, and NH_3. Near threshold, single photon ionization using a 10.5 eV laser photon does not leave enough excess energy in the clusters to fragment any vanadium oxide cluster or break any chemical bond of the reaction products following ionization of the neutral species.[10.37-10.47] Comparing the resulting spectra from both ionization methods, we found that the reaction products present were almost the same. Our conclusion is that the fragmentation or photodissociation of neutral vanadium oxide clusters and their reaction products caused by a single 26.5 eV photon is virtually not present in these experiments, as well documented in ref. 10.45 for V_mO_n, Nb_mO_n, and Ta_mO_n samples at both 26.5 eV and 10.5 eV ionization energies.

In our previous work, we have found that the distribution of neutral V_mO_n clusters is nearly the same using either method for ionization, except that some oxygen rich clusters with high ionization energies (> 10.5 eV) cannot be detected by 10.5 eV photon ionization.[10.45] The reason we prefer to use 26.5 eV laser as the ionization source is that it can ionize all the neutral metal oxide clusters generated in the expansion/ablation source and all reaction products generated in the reactor.

10.4.1. Structure and Reaction Mechanism for Neutral $M_mO_n + NO_x$

10.4.1.1 Experimental Results

Figure 10.1 displays mass spectra of reactants and products for the reaction of V_mO_n clusters with NO_x. The predominant signals are identified as reactants VO_2, V_2O_4/V_2O_5, V_3O_7, V_4O_{10}, V_5O_{12}, etc., as shown in the lower spectra of Figures 10.1(a), and (b), for different cluster size regions. These vanadium oxide clusters have the most stable stoichiometric structures (labeled as V_xO_y to differentiate between the stable and the general V_mO_n label) as demonstrated experimentally and theoretically.[10.45,10.60,10.61] A number of oxygen deficient vanadium oxide clusters ($V_xO_{y-1,2}$: VO, $V_2O_{2,3}$, $V_3O_{5,6}$, $V_4O_{8,9}$, $V_5O_{9,10,11}$, and $V_6O_{13,14}$) are observed in the cluster distribution. They are missing one or two oxygen atoms compared to the most stable clusters, and present a tendency to become the most stable clusters by reacting with O or O_2.[10.61] Some oxygen rich clusters (V_xO_{y+1}: VO_3, V_3O_8, and V_5O_{13}, etc.) are also observed in the mass spectra. They have one or more oxygen atoms compared to the most stable clusters, and present a tendency to lose O or O_2 and become the most stable clusters.[10.61] Additionally, one can find that these oxygen rich neutral vanadium oxide clusters are almost always present with one or more attached hydrogen atoms, such as VO_3H_2, $V_2O_6H_2$, $V_3O_8H_{1,2}$, etc.[10.45]

Very few products are identified for the reactions V_mO_n + NO_x. First, in Figure 10.1(a), two association products, VO_3NO, and V_2O_5NO, are observed when NO is added to the fast flow reactor. They are generated from simple association reactions,

$$M_mO_n + NO \rightarrow M_mO_nNO \qquad (10.2)$$

and probably stabilized (cooled) by a third body collision.

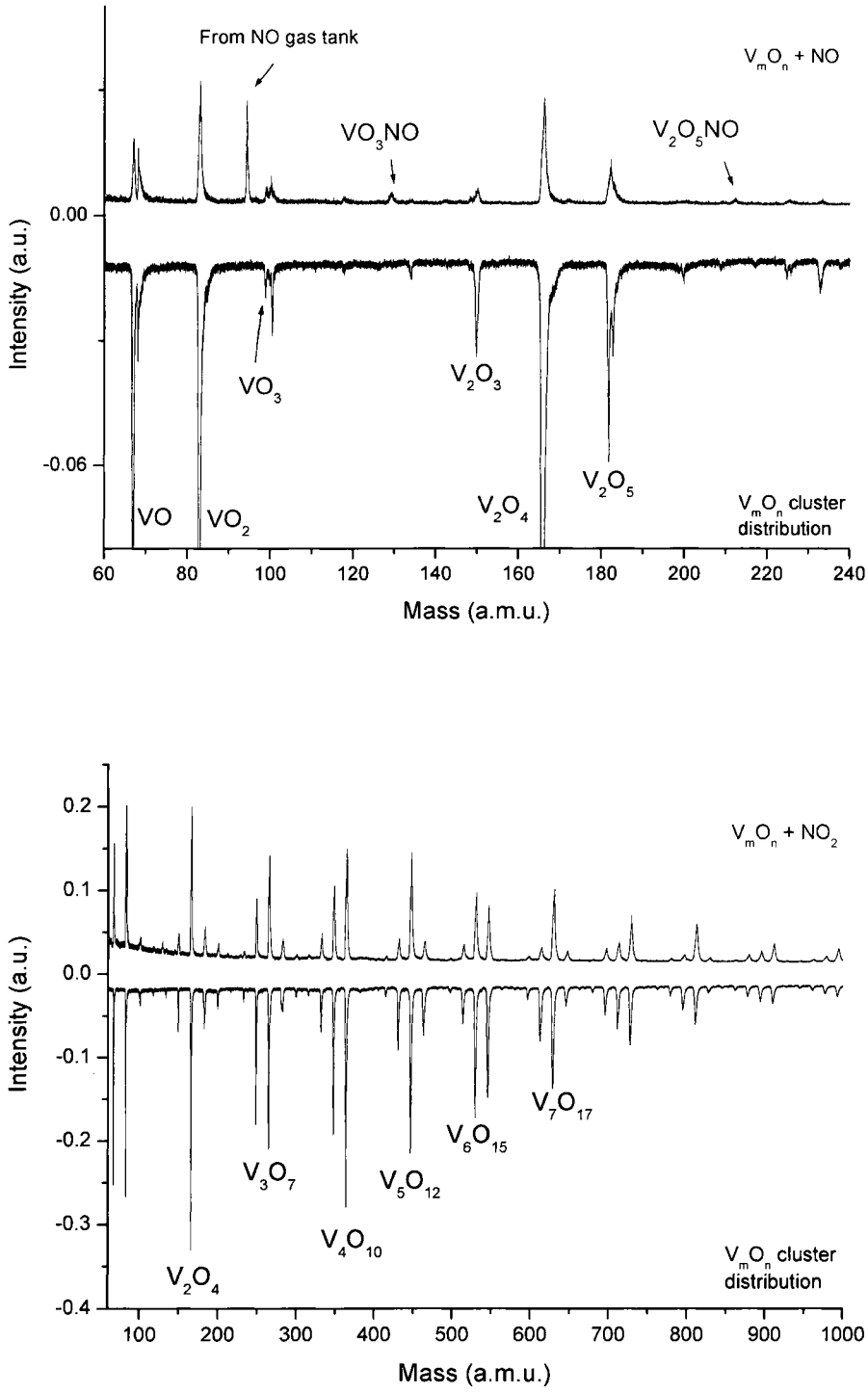


Figure 10.1: Reactions of V_mO_n clusters with (a) NO and (b) NO_2 ionized by a 26.5 eV SXR laser. The reactant gases (15 psi) are added to the flow tube reactor. Very few new products of the reactions are detected.

Only oxygen rich clusters are involved in the association products. The peak present at mass 94 is found to be a contaminant from the NO gas tank. Second, Figure 10.1(b) illustrates that all cluster signals decrease in roughly the same proportion when the NO_2 gas is added to the reactor cell. A similar result is also observed when inert gases are added.[10.37] Therefore, the decrease of cluster signals is due to scattering by NO_2 gas pulsed into the reactor. No major reaction channel is observed.

Figure 10.2 displays mass spectra, generated by 26.5 eV (46.9 nm) single photon ionization from a SXR laser, of reactants and products for the reaction of Ta_mO_n clusters with NO_x. The predominant signals are identified as TaO_2, Ta_2O_4/V_2O_5, Ta_3O_7, etc., as shown in the lower spectra of Figures 10.2(a), and (b). These tantalum oxide clusters have the most stable stoichiometric structures (labeled as Ta_xO_y to differentiate between the stable and the general Ta_mO_n label) as previously demonstrated experimentally.[45] A number of oxygen deficient tantalum oxide clusters ($Ta_xO_{y-1,2}$: TaO, $Ta_2O_{2,3}$, and $Ta_3O_{5,6}$) are observed in the cluster distribution. Some oxygen rich clusters ($Ta_xO_{y+1,2}$: $TaO_{3,4}$, Ta_2O_6, and Ta_3O_8) are also observed in the mass spectra. Additionally, one can find that these oxygen rich, neutral tantalum oxide clusters are almost always present with one or more attached hydrogen atoms, such as TaO_4H, $Ta_2O_6H_2$, etc.:[45] note the doublet or triplet features of these mass signals.

Contrary to the observations for V_mO_n clusters, many new products are identified for the reactions Ta_mO_n + NO_x. In Figure 2(a), association products, $TaO_3(NO)_{1,2}$, $TaO_4(NO)_{1,2}$, Ta_2O_5NO, Ta_2O_6NO, $Ta_2O_6(NO)_{1,2,3}$, and $Ta_3O_8(NO)_{1,2}$ are observed when

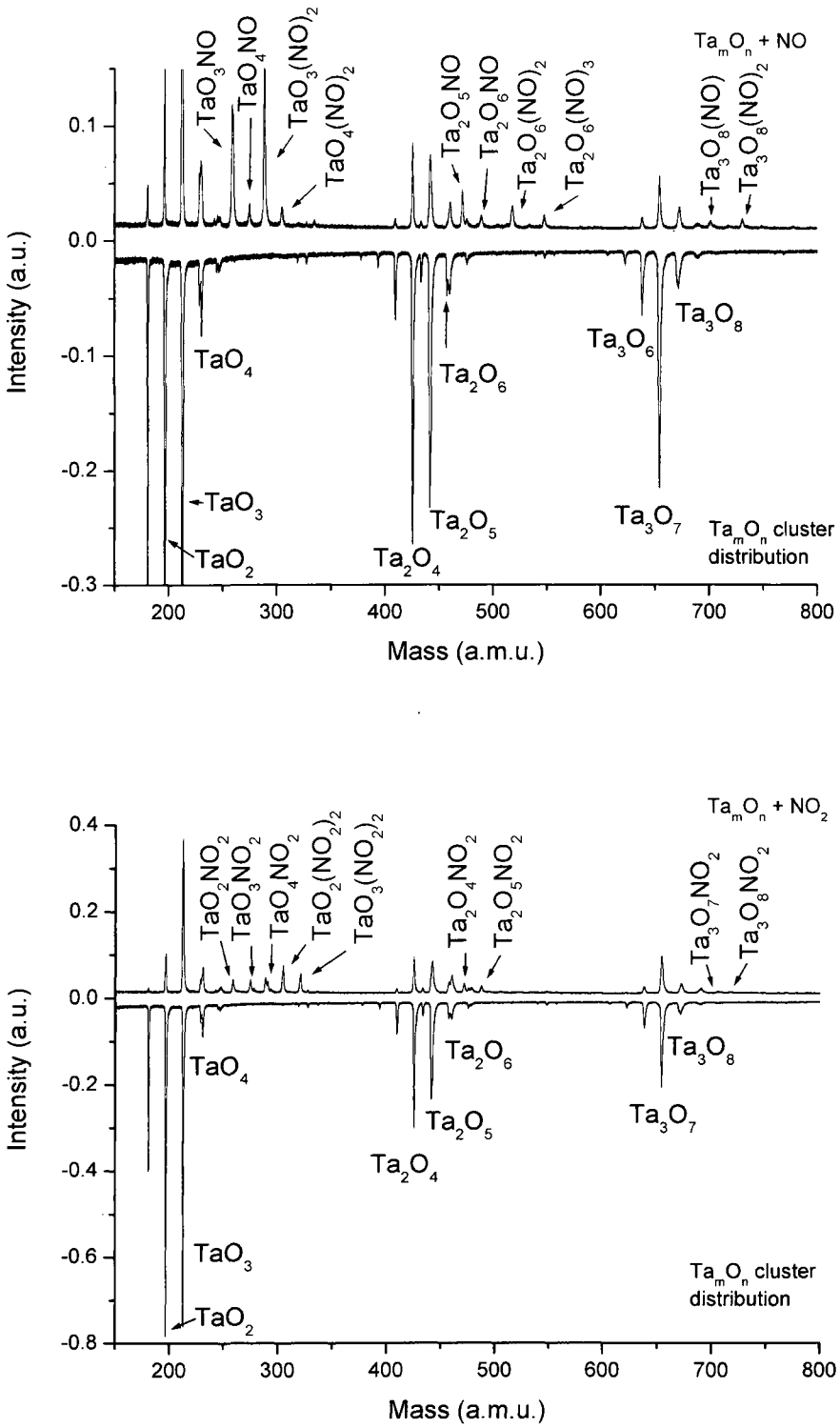


Figure 10.2: Reactions of Ta_mO_n clusters with (a) NO and (b) NO_2 ionized by a 26.5 eV SXR laser. The reactant gases (15 psi) are added to the flow tube reactor. Many new products of the reactions are detected.

NO is added to the reactor. They are generated from simple association reactions (eq. 2). Figure 10.2(b) illustrates a very similar product distribution for NO_2 added to the reaction cell. Association products, $TaO_2(NO_2)_{1,2}$, $TaO_3(NO_2)_{1,2}$, TaO_4NO_2, $Ta_2O_4NO_2$, $Ta_2O_5NO_2$, $Ta_3O_7NO_2$, and $Ta_3O_8NO_2$ are observed. Oxygen stable, and oxygen rich clusters both contribute to the association products. No oxygen deficient clusters are involved in the reaction. The product signals for Ta_mO_n + NO are more abundant, and more intense, than type for V_mO_n indicating that experimentally, Ta_mO_n clusters form more stable intermediate complexes.

In the condensed phase, the interaction of NO with the V_mO_n catalyst is found to be very weak. The conventional SCR process on V_2O_5/anatase (TiO_2) support proceeds according to an Eley-Rideal type mechanism in which ammonia is adsorbed on the vanadium-based catalyst in the first step, and the reaction then proceeds with the activation of nitric oxide from the gas phase.[10.6-10.24] One supporting argument for this type of reaction is that vanadia-based catalysts do not appear as efficient as other catalysts for NO decomposition or oxidation.[10.18] A second argument is found through isotopic labeling experiments.[10.9,10.14] The oxygen atom of the NO molecule is exchanged for the oxygen atom of a vanadyl V=O group. Through isotopic labeling experiments, one demonstrates that NO interacts actively with the V_2O_5/TiO_2 surface implying stronger interaction than usually postulated; however, the exchange is fast and the data suggests[10.9,10.14] that NO does not reside on the surface to react with ammonia. The SCR proceeds via NH_3 adsorption and interaction with a gaseous NO species. Experimentally, our gas phase

results are consistent with condensed phase experiments in that we also observe only a weak interaction between neutral V_mO_n clusters and NO.

10.4.1.2 Theoretical Results

In order to elucidate the interaction of V_mO_n with respect to NO, DFT calculations at the B3LYP level using the TZVP basis set for N, and O atoms, and the LANL2TZ basis set for V atoms are employed. This level of theory level is first used to verify V_mO_n cluster structures calculated in ref. 10.61. Starting with the most stable structure for VO_3, and V_2O_5, geometry optimizations are performed for the association products VO_3NO, and V_2O_5NO and the results are presented in Figures 10.3 (a) and (b), respectively. The interaction can apparently take two forms. For VO_3NO, the most stable structure depicts that NO binds to the V atom and forms an NO_2 molecule bound to a VO_2 moiety with ΔH_{298} = -46.22 kcal/mol (Figure 10.3(a), ΔH_{298} is calculated for the reaction V_mO_n + NO $\rightarrow$ V_mO_nNO). In the reaction, an oxygen transfers from the VO_3 molecule to the NO moiety. The calculated V-N bond length is 2.01 Å. For V_2O_5NO, starting from an OVO_2VO_2 structure similar to ref. 10.19 and 10.61 and adding NO, a bicyclic isomer (shown in Figure 10.3(b)) for which the two vanadium atoms are in a tetrahedral environment is found. This is the most stable compound with ΔH_{298} = -43.21 kcal/mol compared to -62.8 kcal/mol found by ref. 10.19. Similar calculations are performed for the tantalum series in an attempt to discern the difference between NO adsorption on neutral V_mO_n and Ta_mO_n clusters. The resulting lowest energy structures for the products of tantalum clusters in reaction with NO are found loosely to follow the results for

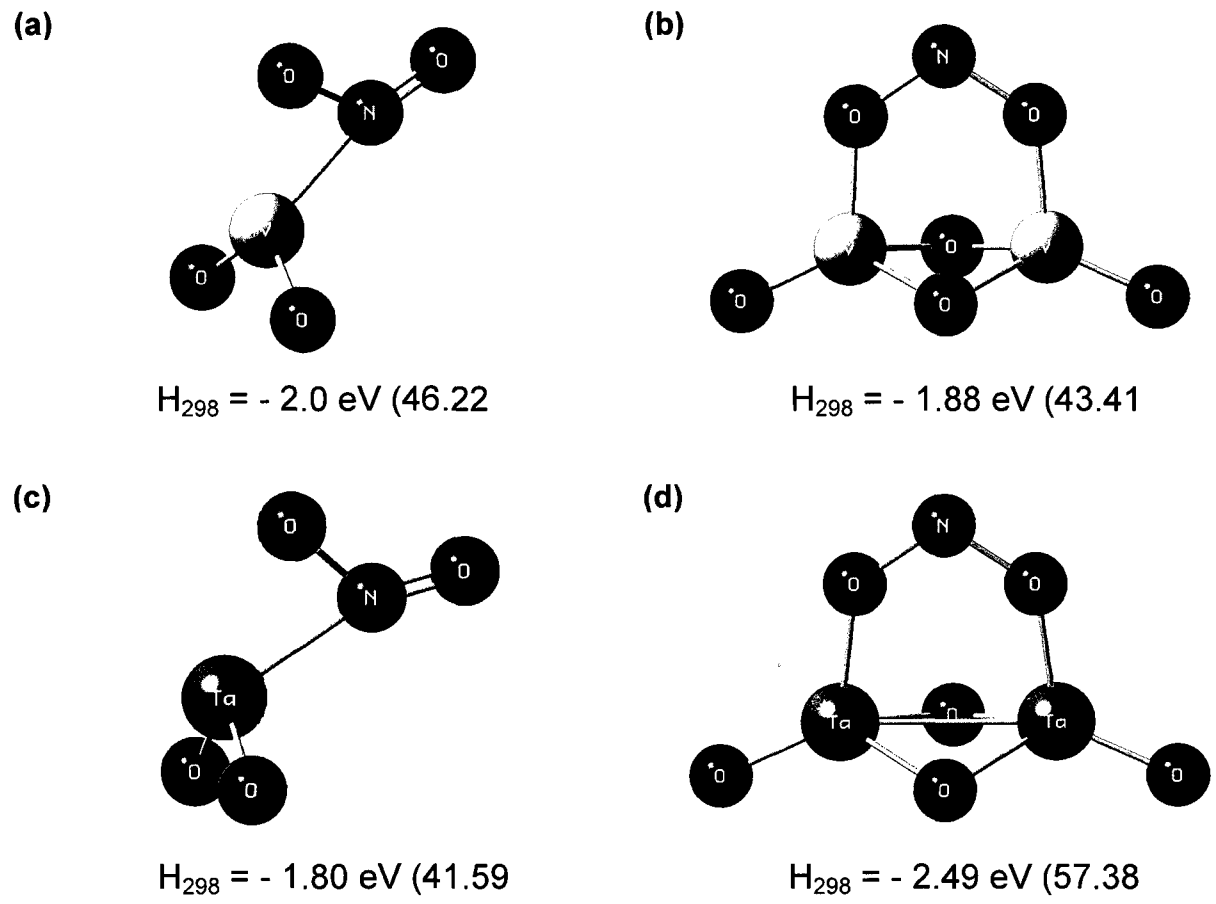


Figure 10.3: DFT results showing the most stable structures for reaction products (a)VO_3NO, (b) V_2O_5NO, (c) TaO_3NO, and (d) Ta_2O_5NO. ΔH_{298} is calculated for the reaction $V_mO_n + NO \rightarrow V_mO_nNO$.

vanadium oxide clusters with no significant difference found for the adsorption energies (Figure 10.3(c), and (d)). The reaction and binding between the MO_3 cluster and NO is through a transfer of an O atom to the NO moiety and the formation of an M-N bond. Both Ta and V species have roughly equal enthalpies of formation. In the case of the larger M_2O_5 cluster NO can attach to the cluster through an O-O bond forming an M-O-N-O-M bridge. For this latter complex, the Ta_2O_5 binding is about 30% larger than the V_2O_5 interaction. Calculations are performed for many other cluster stoichiometries, but are, in general, unsuccessful in demonstrating a different mechanism or structure for

NO adsorption for the two metal oxides. Potential energy surface (PES) scans were also implemented for this reaction and no significant barriers are found in any case.

The gas phase cluster experimental results imply that, in the condensed phase, NO molecules *are not* readily adsorbed onto the surface of a vanadium oxide catalyst, and *are* readily adsorbed onto the tantalum oxide surface. This non-adsorbing characteristic of V_mO_n clusters is desirable from a standpoint that the SCR reaction begins with NH_3 adsorption as a first step and then proceeds with a gas phase interaction with NO. If the catalyst doest not have a strong interaction with NO, as V_mO_n clusters demonstrate, there will be more adsorption sites available for ammonia to begin the SCR process. Our DFT calculations are, in general, unsuccessful in demonstrating a different mechanism or structure for NO adsorption for the two metal oxides. A different theoretical method may be required to explore the reaction of M_mO_n + NO.

10.4.2 Structure and Reaction Mechanism for Neutral M_mO_n + NH_3

10.4.2.1 Experimental Results

Figure 10.4 displays the mass spectrum of reactants and products for the reaction of V_mO_n clusters with NH_3, generated by 26.5 eV single photon ionization. V_mO_n clusters are much more reactive with NH_3 than they are with NO_x. Many association products are observed when NH_3 is added to the reactor. Products $VONH_3$, $VO_2(NH_3)_{1,2}$, $VO_2(NH_3)H$, $VO_3(NH_3)H_2$, $V_2O_4NH_3$, $V_2O_5NH_3$, $V_2O_5(NH_3)H$, and $V_2O_6(NH_3)H_2$ are readily detected. They are generated from association reactions,

$$M_mO_nH_{0,1,2} + NH_3 \rightarrow M_mO_nH_{0,1,2}NH_3 \qquad (10.3)$$

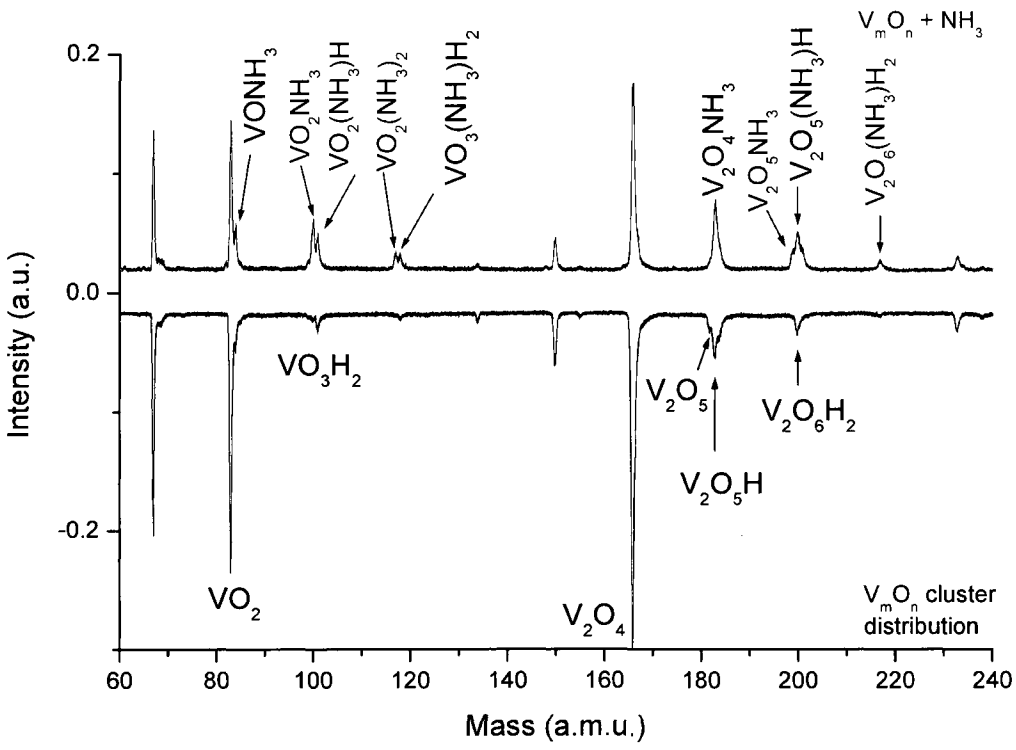


Figure 10.4: Reactions of V_mO_n clusters with NH_3 ionized by a 26.5 eV SXR laser. The reactant gas (15 psi) is added to the flow tube reactor. Many new association products of the reaction is detected.

and are stabilized by collisions with third bodies.

Only oxygen stable and oxygen rich clusters are involved in these association reactions. An additional hydrogen(s) is observed in some of the products (e.g. $VO_3(NH_3)H_2$, $V_2O_5(NH_3)H$, etc.). These clusters arise from the association of ammonia with a corresponding V_mO_n cluster that is already present with one or more attached hydrogen (e.g. VO_3H_2, V_2O_5H, etc., see lower spectrum of Figure 10.4). The additional hydrogen atom may come from the dissociation of NH_3 molecules and attachment of the corresponding clusters, for example in the reaction $VO_3 + NH_3 \rightarrow VO_3NH_3 + H_2 \rightarrow VO_3(NH_3)H_2$. Since the relative intensity of the peaks in the reaction system spectrum

(top of Figure 10.4) does not change from the unreacted spectrum (bottom of Figure 10.4), we label them as association reactions of the corresponding hydrogenated cluster.

In the presence of NH_3, Ta_mO_n clusters behave in a similar fashion to V_mO_n for the reaction $Ta_mO_n + NH_3$. Figure 10.5 displays the Ta_mO_n cluster distribution (lower spectrum) and reaction products (upper spectrum) when NH_3 is added to the reaction cell. Association products, $TaONH_3$, TaO_2NH_3, $TaO_3(NH_3)H_2$, $Ta_2O_4NH_3$, $Ta_2O_5(NH_3)H$, and $Ta_2O_6(NH_3)_{1,2}H_2$ are observed. These products are also generated from association

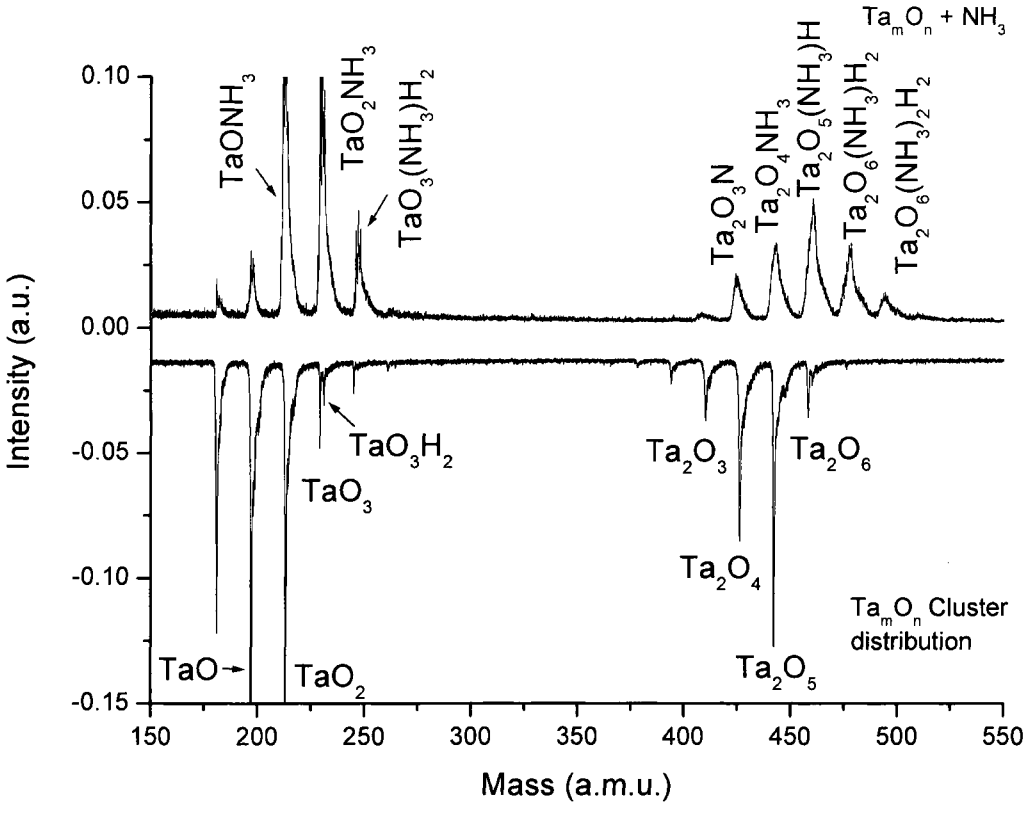


Figure 10.5: Reactions of Ta_mO_n clusters with NH_3 ionized by a 26.5 eV SXR laser. The reactant gas (15 psi) is added to the flow tube reactor. Ta_mO_n clusters behave similarly to V_mO_n clusters and many new association products of the reaction is detected.

reactions (eq. 10.3). Only oxygen stable and oxygen rich clusters are involved in the association products. Additional hydrogen(s) is observed in some of the products (e.g. $TaO_3(NH_3)H_2$, $Ta_2O_5(NH_3)H$, etc.). Similar to $V_mO_n(NH_3)_yH_x$ clusters, $Ta_mO_n(NH_3)_yH_x$ clusters arise from association of ammonia with a corresponding Ta_mO_n cluster that is already present with one or more attached hydrogen atoms (e.g. TaO_3H_2, Ta_2O_5H, etc., see lower spectrum of Figure 10.5).

When comparing Figures 10.4 and 10.5, one notices that the adsorption products are very nearly the same for both V_mO_n and Ta_mO_n clusters. The adsorption energies for the V_mO_n and Ta_mO_n products are similar as well. The values for NH_3 adsorption on Ta_mO_n clusters fall within ± 15% of the calculated results for V_mO_n presented in Figure 10.6.

10.4.2.2 Theoretical Results

Figure 10.6 displays the results of DFT calculations for the lowest energy structures of the reaction products for $V_mO_n + NH_3$. In each case, the addition of NH_3 to any cluster is followed by a hydrogen transfer to form $H(V_mO_n)$ (see Figures 10.6(a-g)) and a V-NH_2 moiety in intermediate structures. Such structures and mechanisms are consistent with those proposed by many authors,[10.8,10.14,10.18,10.19,10.35] based on condensed phase experiments and DFT calculations. Further dissociation of ammonia is found to be less favorable. The NH_2 moiety preferentially binds to the vanadium atom via a V-N bond, except for $V_2O_6H_2$ (Figure 10.6(h) of the systems calculated). Here NH_3 transfers an H atom to a singly bonded O atom and forms an ONH_2 moiety on a terminal oxygen. The V atoms in $V_2O_6H_2$ are saturated by V-O bonds leaving only terminal O atoms for potential

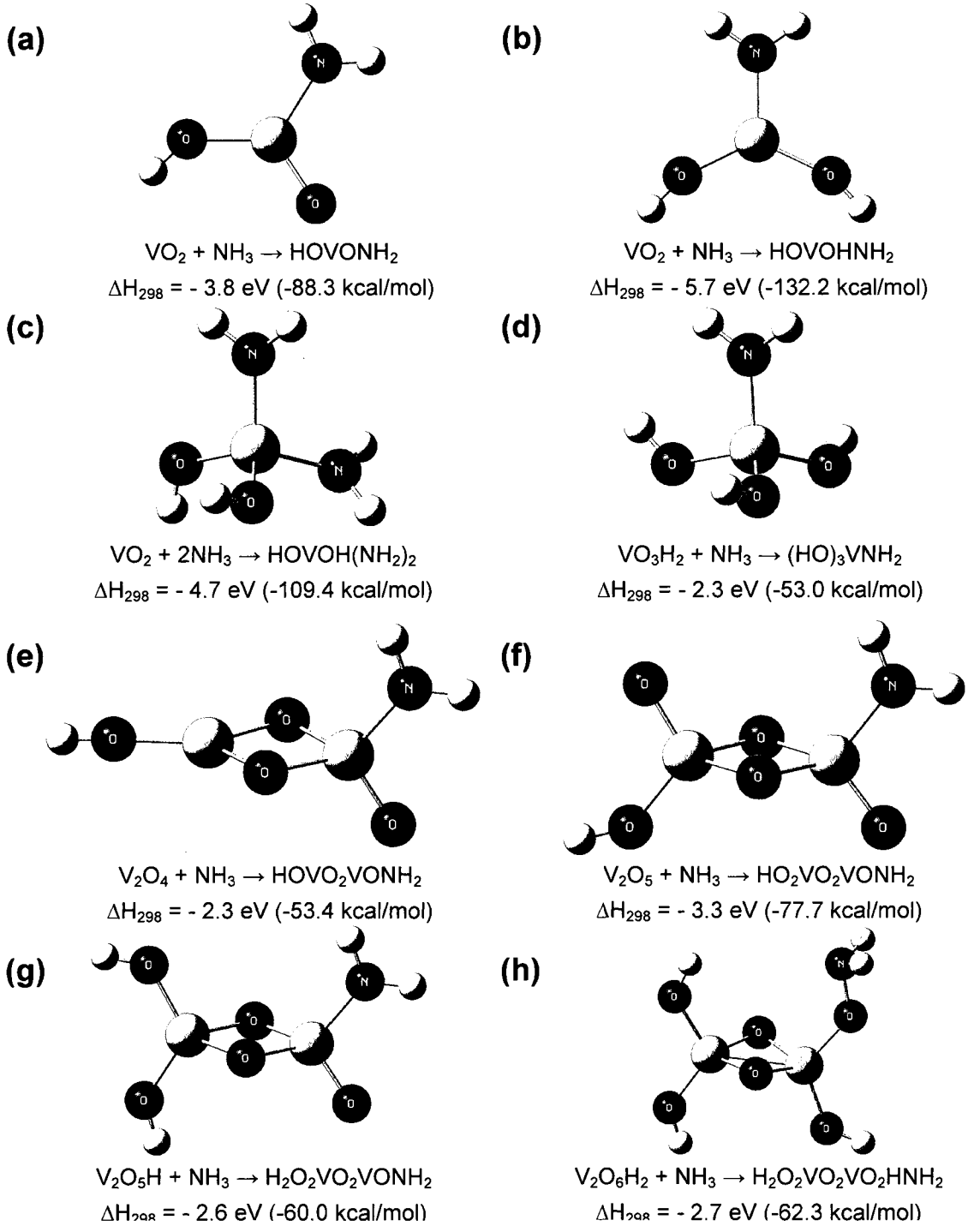


Figure 10.6: DFT results showing the most stable structures for reaction products (a)VO_2NH_3, (b) $VO_2(NH_3)H$, (c) $VO_2(NH_3)_2$, (d) $VO_2(NH_3)H_2$, (e) $V_2O_4NH_3$, (f) $V_2O_5NH_3$, (g) $V_2O_5(NH_3)H$, and (h) $V_2O_6(NH_3)H_2$. DFT calculations for Ta_mO_n clusters revealed similar structures.

reaction sites. This form of interaction between NH_3 and oxygen rich, hydrogen containing $M_xO_yH_z$ may be typical.

Anstrom et al. calculate NH_3 adsorption forming a stabilized NH_4^+ unit which corresponds to the ammonia molecule interaction with a VOH site.[10.27] These theoretical results find an adsorption energy between 7 and 30 kcal/mol for molecular NH_3 on V_2O_5 (0 0 1).[10.27,10.28] In our experiment, VOH sites are found with the presence of VO_2H, VO_3H_2, V_2O_5H, and $V_2O_6H_2$ in the mass spectrum. We calculate adsorption and formation of an NH_4 species for all appropriate hydrogen containing vanadium oxide clusters present in our experiments and we find that adsorption of NH_3 as an NH_4 species is less favorable (on the order of ~ 1 eV for the structures shown in Figures 10.6(a-g) and by about 0.2 eV than the NH_2 structure shown in Figure 10.6(h)).

Experimentally, the abundance of products in the reaction M_mO_n + NH_3 suggests that the interaction of M_mO_n with ammonia is much stronger than the interaction of M_mO_n with NO_x. These experimental results imply that in the condensed phase, the SCR proceeds according to an Eley-Rideal type mechanism in which ammonia is adsorbed on the catalyst in the first step. DFT calculations suggest that the adsorption energy of NH_3 on M_mO_n is stronger than that for adsorption of NO. The heat of adsorption for NO is unexpectedly large, smaller than that for ammonia, but not significantly. Still, in a competetive environment, ammonia will be preferentially adsorbed as the first step in the SCR process. DFT calculations also imply that ammonia adsorbs and then dissociates to form an NH_2 moiety. With regard to the SCR reaction, if an N atom from an adsorbed NO_x

be present at the V_mO_n cluster or site, the NH_2 moiety could bind to it instead of to an O atom; this would generate an N–N bond as required to produce N_2 as a final product. The addition of an $NO:NH_3$ (9:1) mixture is examined in the next section.

10.4.3 Structure and Reaction Mechanism for Neutral M_mO_n + $NO:NH_3$ (9:1)

10.4.3.1 Experimental Results

To study the reactions of M_mO_n clusters in the presence of NO and NH_3, a mixture of $NO:NH_3$ is added to the reaction cell with a ratio of 9:1. Figure 10.7 displays the mass spectrum of reactants and products for the reaction of V_mO_n clusters with $NO:NH_3$ added

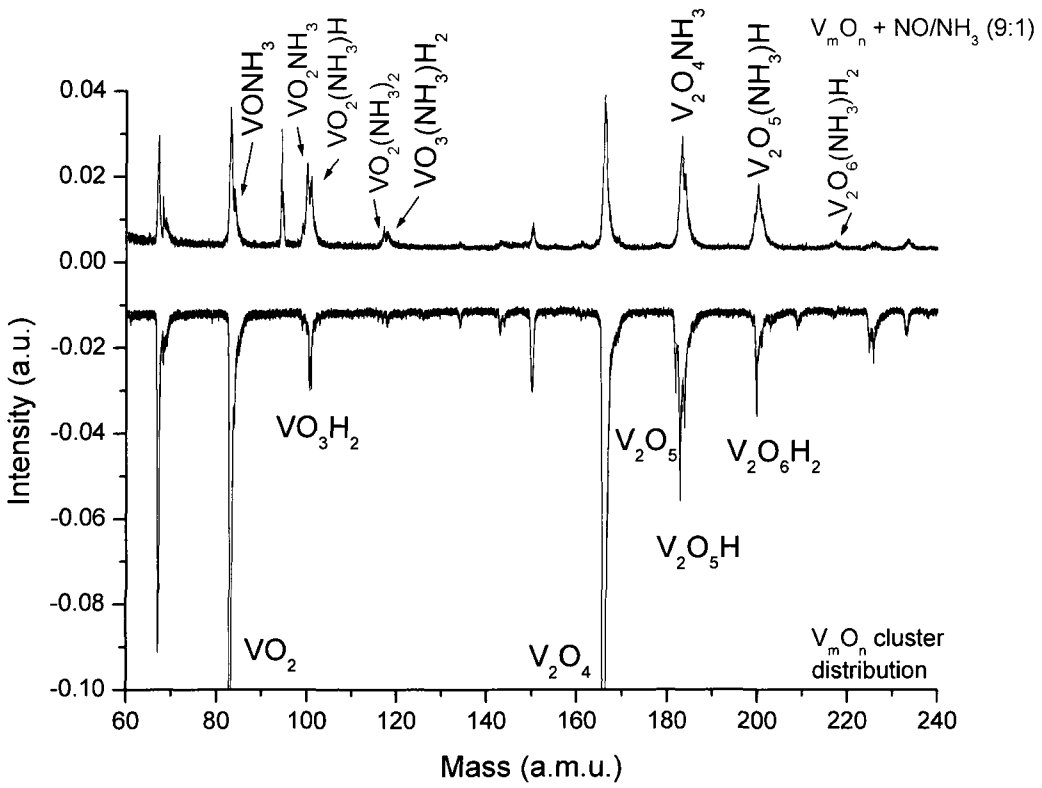


Figure 10.7: Reactions of V_mO_n clusters with $NO:NH_3$ (9:1) ionized by a 26.5 eV SXR laser. The spectrum looks similar to Figure 10.3 where only NH_3 is added to the reactor.

to the reaction cell, as generated by 26.5 eV single photon ionization. When compared to Figure 10.4, one finds that the two mass spectra are nearly identical. The V_mO_n cluster system behaves as if only NH_3 were present in the reactor; in other words, no combined V_mO_n + NH_3/NO adduct or reaction products are detected in the mass spectra. The intensity of the products in Figure 10.7 is slightly less than in Figure 10.4 due to the reduced concentration of NH_3.

Figure 10.8 displays the mass spectra of Ta_mO_n clusters and their products when the same 9:1 ratio of NO:NH_3 is added to the reactor. Figure 10.8(a) shows the mass spectrum for TaO_n clusters with n = 1-3. In this region one can observe that the products strongly mimic the cluster distribution in Figure 10.5 with only NH_3 added to the reactor, with the exception that a new cluster series is found that contains the adduct of both an NO and an NH_3 molecule to form the products $TaO_2(NH_3)NO$, and $TaO_3(NH_3)NO$. The general reaction is,

$$Ta_mO_n + NO{:}NH_3(9{:}1) \rightarrow Ta_mO_n(NH_3)NO \qquad (4)$$

Similarly, Figure 10.8(b) illustrates the mass region for Ta_2O_n clusters with n = 3-6 when NO:NH_3 is added to the reactor. Note that the reaction products of these clusters with NH_3 dominates the mass spectrum. A weak feature (Ta_2O_5NO) is observed for the adduct of only NO and a new cluster series is found that contains the adduct of both an NO and NH_3 molecule to form the products $Ta_2O_5(NH_3)NO$, and $Ta_2O_6(NH_3)NO$.

These reactions are also explored with different NO:NH_3 ratios beginning at 1:1. The concentration of NO proved to be insufficient to compete with the strong reactivity of

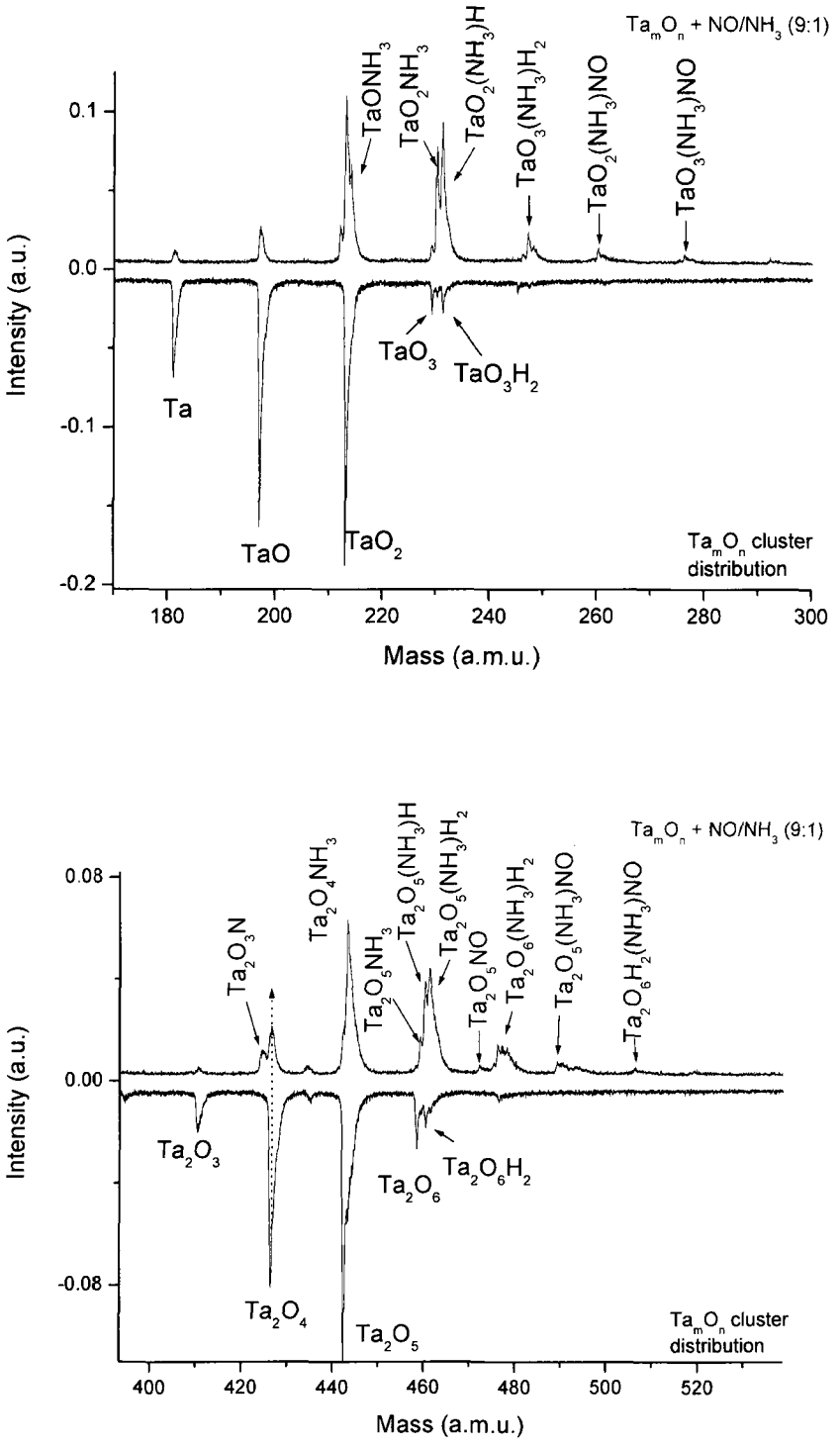


Figure 10.8: Reactions of Ta_mO_n clusters with NO:NH_3 (9:1) ionized by a 26.5 eV SXR laser. Different mass regions are displayed for (a) m = 0, n = 1-3, and (b) m = 1, n = 3-6. A new cluster series emerges involving the coadsorption of NO and NH_3.

NH_3, and the mass spectra display very weak, if any, product intensity that involves both NO and NH_3 reacting with a single Ta_mO_n cluster. As the concentration of NO is increased, a reaction involving both NO and NH_3 is finally observed at a ca. 9:1 NO:NH_3 concentration ratio.

Based on the experimental results and the different behavior for the vanadium and tantalum cluster series, one might conclude from these results that tantalum oxide clusters are more active with the gas mixture and might be a better catalyst for the SCR of NO using ammonia. In order to elucidate this interpretation, the reaction mechanism and potential energy surface is explored via the DFT methods described above.

10.4.3.2 Theoretical Results

To calculate the structures, mechanisms, and surfaces for coadsorption of NO and ammonia on both V_mO_n and Ta_mO_n clusters, we start from the lowest energy structure for one ammonia molecule on an MO_3 cluster (M = V, and Ta) and add an NO molecule to the system. The lowest energy structures calculated favor the placement of NO and NH_3 in the same region. Based on the calculation results for the reaction VO_3 + NO:NH_3 (9:1), the reaction begins with the optimized structure of VO_3 + NH_3 (**R** $HOVO_2NH_2$) as shown in Figure 10.9. The reaction starts by introducing an NO molecule to form intermediate **1** for which the N from the NH_2 radical and the N from the NO are weakly bound. Via transition structure **1/2**, a lowest energy intermediate **2** with two moieties, $ONNH_2$, and $HOVO_2$ is formed. The two moieties can then separate and proceed to product **3** consisting of two separate molecules. A free $ONNH_2$ molecule now exists; production of

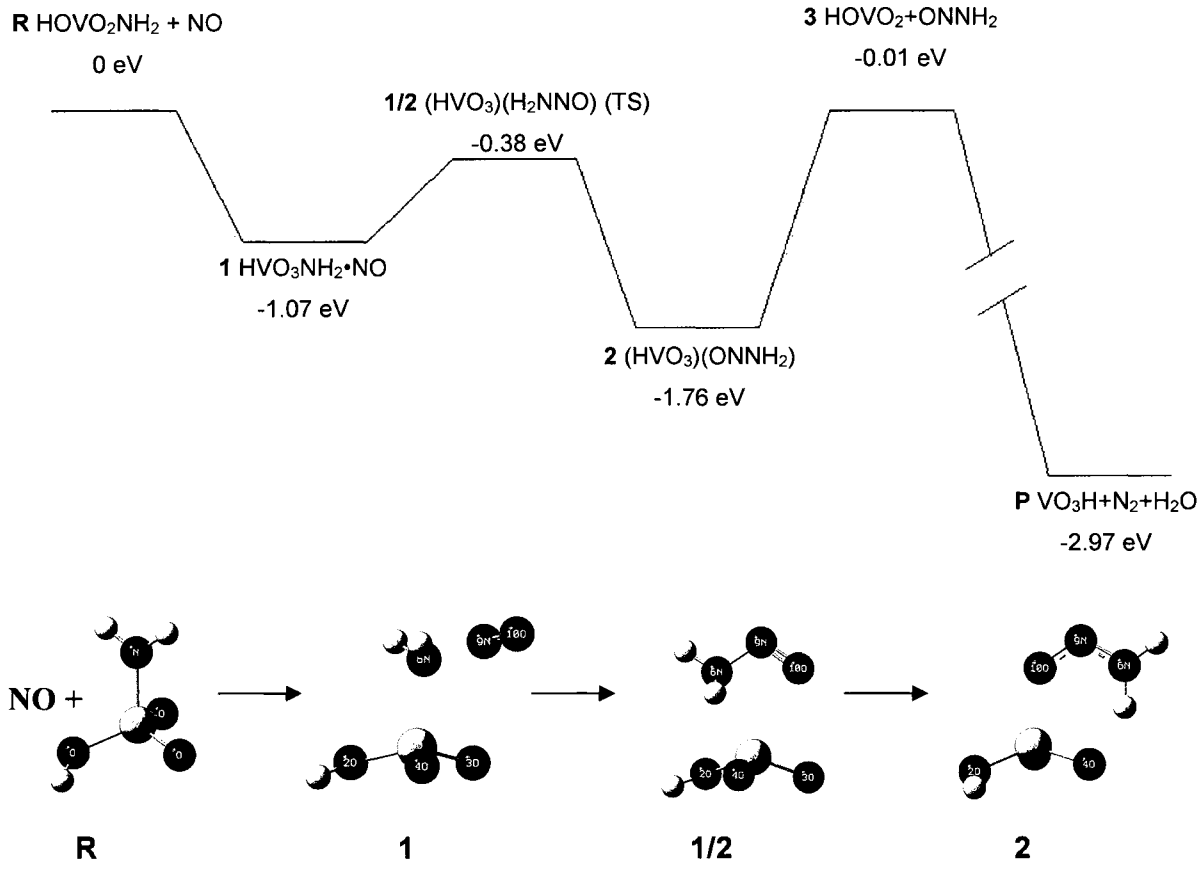


Figure 10.9: DFT calculated potential energy surface for VO_3 + NO:NH_3 reaction. Structures are the optimized geometries of the reaction intermediates and transition states. Relative energies are in eV.

$N_2 + H_2O$ involves a complex mechanism, which, however, has no barrier with respect to the reaction $ONNH_2 \rightarrow N_2 + H_2O$.[10.1,10.62,10.63] This pathway is exothermic by 124.5 kcal/mol.[10.63] Our calculations show that vanadium oxide clusters form a weakly bound intermediate **2** that can separate into **3** $HOVO_2 + ONNH_2$ and can then follow the reaction pathway to form products **P** $N_2 + H_2O$ in an overall barrierless reaction. We suggest that this latter step is the reason that no products involving both NO and ammonia molecules are observed in the mass spectrum (Figure 10.7). Thus, V_mO_n clusters do react with NO and NH_3 to generate N_2 and H_2O. These are properties of a good catalyst that does not

form stable intermediates, but forms weakly bound complexes available for further reaction.

The same calculations for tantalum oxide clusters are conducted. The reaction between NO and ammonia supported by Ta_mO_n clusters starts with the optimized structure of the model system $TaO_3 + NH_3$ (**R** $HOTaO_2NH_2$) as shown in Figure 10.10. The reaction proceeds in a very similar way to vanadium oxide clusters up to transition structure **1/2**: adding an NO molecule forms intermediate **1** in which the N of the NH_2 radical and the N from the NO are weakly bound. The difference between the V and Ta reactions occurs via transition structure **1/2**, leading to a very stable lowest energy intermediate **2** ($HOTaO_2ONNH$) for the Ta species. Here, the vanadium oxide intermediate **2** (Figure 10.9) partitions into two separate radicals whereas the tantalum oxide intermediate **2** (Figure 10.10) forms a stable complex via hydrogen transfer. Generation of product **3** $HOTaO_2 + ONNH_2$ is thermodynamically unavailable for the tantalum oxide reaction to proceed. The calculation results suggest that the reaction should not proceed to form the final products $N_2 + H_2O$. This formation of a stable intermediate for tantalum oxide clusters implies that tantalum oxide clusters should not be a good catalyst for the SCR of NO with ammonia in the condensed phase. The formation of ionic intermediate species of the form $(NH_4^+)(M_mO_n^-)$ is a higher energy pathway than the formation of the radical like species $(HOM_mO_{n-1})(NH_2)(NO)$.

Our experimental results, taken at face value and based on our previous experience with neutral cluster chemistry,[10.37-10.47] would suggest that the observed cluster

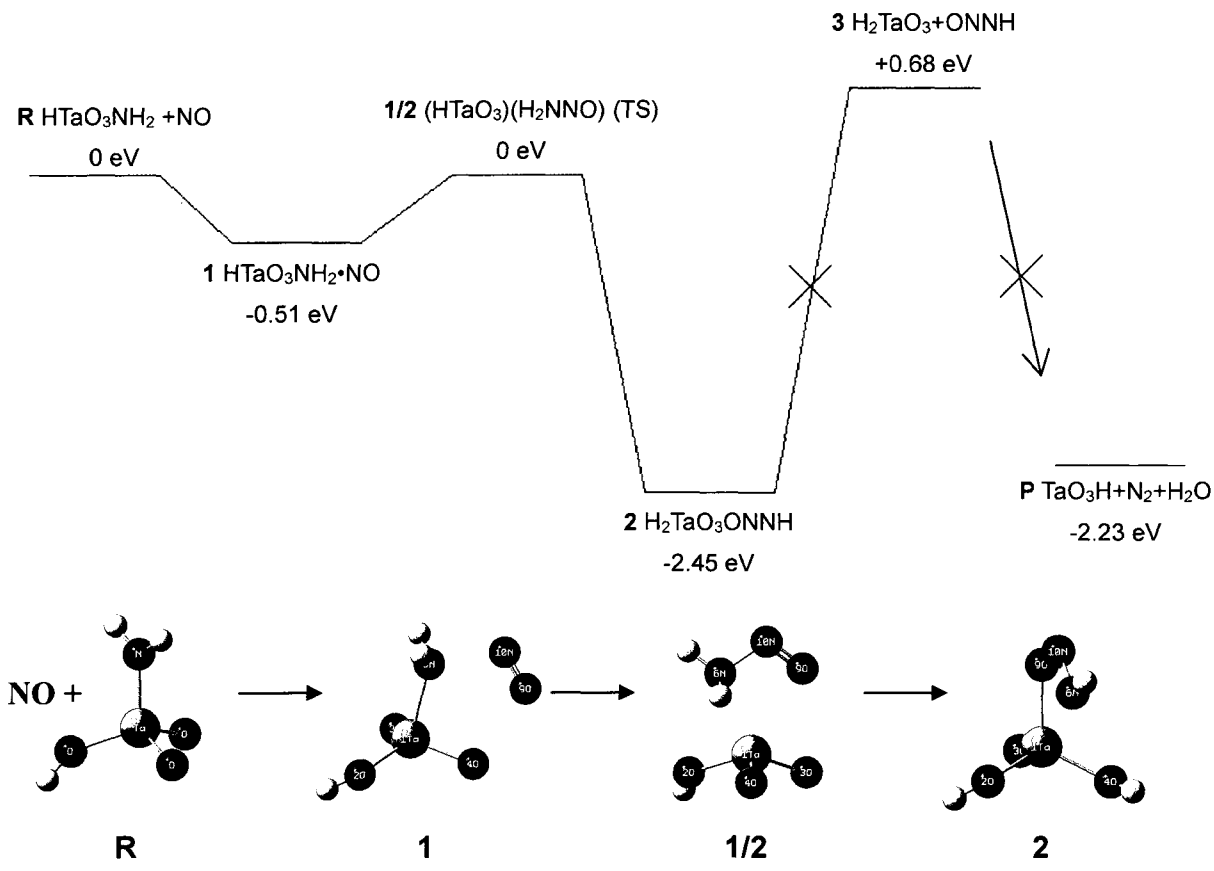


Figure 10.10: DFT calculated potential energy surface for TaO_3 + NO:NH_3 reaction. Structures are the optimized geometries of the reaction intermediates and transition states. Relative energies are in eV.

chemistry for V_mO_n, and Ta_mO_n does not correlate to that observed for condensed phase reactions. In particular, previous observations of reaction intermediates and products are consistent with the reactivity of the clusters and the condensed phase behavior of the modeled catalyst. What we have discussed shows that the DFT reaction potential energy surface and structure calculations do indeed indicate that the V_mO_n cluster system is the reactive one, and does model the condensed phase vanadium oxide promoted reaction as stated in the Introduction. Also, based on the DFT results, the Ta_mO_n system is not catalytically active as the intermediates do not readily yield products due to kinetic

effects, i.e., reaction barriers.

It should also be mentioned that experiments were conducted using neutral Nb_mO_n clusters and the results matched those obtained for V_mO_n clusters. Results involving Nb_mO_n clusters can be extrapolated from the discussion involving V_mO_n clusters.

10.5 CONCLUSIONS

In the present work, the reactivity of neutral vanadium and tantalum oxide clusters toward NO, NH_3, and an NO/NH_3 mixture is explored experimentally and theoretically. Our motivation is to understand possible molecular level mechanisms for the SCR of NO by NH_3 in condensed phase catalytic reactions. We find that V_mO_n clusters react weakly with NO_x in the gas phase whereas Ta_mO_n form many reaction products. If ammonia is added to the reactor in place of NO_x, both V_mO_n, and Ta_mO_n clusters behave in a similar manner and form many association products in the observed mass spectra. If a gas mixture of NO:NH_3 (9:1) is added to the reactor, the two cluster systems behave differently. The mass spectrum of V_mO_n clusters reveals no new products for the coadsorption of NO. Ta_mO_n clusters, on the other hand, form a new cluster series that does involve coadsorption of NO and NH_3. DFT calculations suggest that Ta_mO_n clusters form stable cluster complexes based on the coadsorption of NO and ammonia and that these products are thermodynamically and kinetically stable. V_mO_n clusters form weakly bound complexes that can follow the reaction path toward end products N_2 + H_2O. Thus, cluster intermediates involving NO + NH_3 are not observed in the mass spectrum. Overall, our results suggest that vanadium oxide should make a better catalyst for the SCR of NO

with NH_3 than tantalum oxide clusters. Both our theoretical and experimental results support a radical reaction mechanism in which NH_2 is the important moiety for the V_mO_n based catalytic conversion of NO and NH_3 to N_2 and H_2O.

REFERENCES

[10.1] S. Soyer, A. Uzun, S. Senkan, and I. Onal, Catal. Today **118,** 268 (2006).

[10.2] M.L. Ferreira and M. Volpe, J. Mol. Catal. A: Chem. **164**, 281 (2000).

[10.3] L. Pinaeva, A.P. Suknev, A.A. Budneva, E.A. Paukshtis, and B.S. Balzhinimaev, J. Mol. Catal. **112**, 115 (1996).

[10.4] G.C. Bond and S. Flamertz, Appl. Catal. **71**, 1 (1991).

[10.5] G.T. Went, L.J. Leu, S.J. Lombardo, and A.T. Bell, J. Phys. Chem. **96**, 2235 (1992).

[10.6] 2 M. Inomata, A. Miyamoto, Y. Murakami, J. Catal. **62,** 140 (1980).

[10.7] M. Inomata, A. Miyamoto, Y. Murakami, J. Phys. Chem. **85,** 2372 (1981).

[10.8] F.J.J.G. Janssen, F.M.G. van den Kerkhof, H. Bosch, J.R.H. Ross, J. Phys. Chem. **91**, 5921 (1987).

[10.9] F.J.J.G. Janssen, F.M.G. van den Kerkhof, J. Phys. Chem. **91**, 6633 (1987).

[10.10] N.-Y. Topsøe, J. Catal. **128**, 499 (1991).

[10.11] N.-Y. Topsøe, H. Topsøe, and J.A. Dumesic, J. Catal. **151**, 226 (1995).

[10.12] N.-Y. Topsøe, H. Topsøe, and J.A. Dumesic, J. Catal. **151**, 241 (1995).

[10.13] M.G. Gasior, J. Haber, T. Machej, and T. Czeppe, J. Mol. Catal. **43**, 359 (1988).

[10.14] U.S. Ozkan, Y. Cai, and M.W. Kumthekar, J. Catal. **149**, 375 (1994).

[10.15] U.S. Ozkan, Y. Cai, and M.W. Kumthekar, J. Catal. **149**, 390 (1994).

[10.16] G. Ramis, L. Yi, G. Busca, M. Turco, E. Kotur, and R.J. Willey, J. Catal. **157**, 523 (1995).

[10.17] G. Ramis, L. Yi, and G. Busca, Catal. Today **28**, 373 (1996).

[10.18] G. Busca, L. Lietti, G. Ramis, and F. Berti, Appl. Catal. B **18**, 1 (1998).

[10.19] M. Calatayud, B. Mguig, and C. Minot, Surf. Sci. Reports **55**, 169 (2004).

[10.20] G. Deo and I.E. Wachs, J. Catal. **146**, 323 (1992).

[10.21] H. Schneider, S. Tschudin, M. Schneider, A. Wokaun, and A. Baiker, J. Catal. **147**, 5 (1993).

[10.22] M.A. Centeno, I. Carrizosa, and J.A. Odriozola, Appl. Catal. B: Environ. **19**, 67 (1998).

[10.23] M. Farber and S.P. Harris, J. Phys. Chem. **88**, 680 (1984).

[10.24] T. Komatsu, M. Nunokawa, S. Moon, T. Takahara, D. Namba, and T. Yashima, J. Catal. **148**, 427 (1994).

[10.25] F. Gilardoni, J. Weber, and A. Baiker, Inter. J. Quan. Chem. **61**, 683 (1997).

[10.26] F. Gilardoni, J. Weber, and A. Baiker, J. Phys. Chem. A **101**, 6069 (1997).

[10.27] M. Anstrom, N.-Y. Topsøe, and J.A. Dumesic, Catal. Lett. **78**, 281 (2002).

[10.28] M. Anstrom, N.-Y. Topsøe, and J.A. Dumesic, J. Catal. **213**, 115 (2003).

[10.29] X. Yin, H. Han, and A. Miyamoto, Phys. Chem. Chem. Phys. **2**, 4243 (2000).

[10.30] K. Jug, T. Homann, and T. Bredow, J. Phys. Chem. A **108**, 2966 (2004).

[10.31] N.U. Zhanpeisov, S. Higashimoto, and M. Anpo, Inter. J. Quan. Chem. **84**, 677 (2001).

[10.32] N.A. Kachurovskaya, E.P. Mikheeva, and G.M. Zhidomirov, J. Mol. Catal. A **178**, 191 (2002).

[10.33] E.P. Mikheeva, N.A. Kachurovskaya, and G.M. Zhidomirov, Kin. Catal. **43,** 223 (2002).

[10.34] Y. Izumi, F. Kiyotaki, H. Yoshitake, K. Aika, T. Sugihara, T. Tatsumi, Y. Tanizawa, T. Shido, and Y. Iwasawa, Chem. Commun. **175,** 2402 (2002).

[10.35] K. Jug, T. Homann, and T. Bredow, J. Phys. Chem. A **108,** 2966 (2004).

[10.36] T. Homann, T. Bredow, K. Jug, Surf. Sci. **515**, 205 (2002).

[10.37] S. Heinbuch, F. Dong, J.J. Rocca, and E.R. Bernstein, JOSA B **25**, B85 (2008).

[10.38] S. Heinbuch, F. Dong, J.J. Rocca, and E.R. Bernstein, J. Chem. Phys. **126**, 244301 (2007).

[10.39] S. Heinbuch, F. Dong, J.J. Rocca, and E.R. Bernstein, J. Chem. Phys. **125**, 154316 (2006).

[10.40] S. Heinbuch, F. Dong, J.J. Rocca, and E.R. Bernstein, J. Chem. Phys. **125**, 154316 (2006).

[10.41] F. Dong, S. Heinbuch, Y. Xie, J.J. Rocca, Z. Wang, K. Deng, S. He, and E.R. Bernstein, JACS (accepted).

[10.42] F. Dong, S. Heinbuch, Y. Xie, J.J. Rocca, Z. Wang, K. Deng, S. He, and E.R. Bernstein, JACS **130(6)**, 1932 (2008).

[10.43] F. Dong, S. Heinbuch, J.J. Rocca, and E.R. Bernstein, J. Chem. Phys. **124,** 224319 (2006).

[10.44] F. Dong, S. Heinbuch, J.J. Rocca, and E.R. Bernstein, J. Chem. Phys. **125**, 154317 (2006).

[10.45] F. Dong, S. Heinbuch, J.J. Rocca, and E.R. Bernstein, J. Chem. Phys. **125**, 164318 (2006).

[10.46] Z. Wang, W. Xue, Y. Ma, X. Ding, S. He, F. Dong, S. Heinbuch, J.J. Rocca, and E.R. Bernstein, J. Phys. Chem. **112(26)**, 5984 (2008).

[10.47] S.-G. He, Y. Xie, F. Dong, S. Heinbuch, E. Jakubikova, J.J. Rocca, and E.R. Bernstein, J. Phys. Chem. A **112**, 44 (2008).

[10.48] S. Heinbuch, M. Grisham, D. Martz, and J. J. Rocca, Optics Express **13**, 4050 (2005).

[10.49] S. Heinbuch, M. Grisham, D. Martz, F. Dong, E.R. Bernstein, and J. J. Rocca, SPIE **5919**, 591907 (2005).

[10.50] Frisch, M. J.; Trucks, G. W.; Schlegel, H. B.; Scuseria, G. E.; Robb, M. A.; Cheeseman, J. R.; Montgomery, J. A.; Vreven, T.; Kudin, K. N.; Burant, J. C.; Millam, J. M.; Iyengar, S. S.; Tomasi, J.; Barone, V.; Mennucci, B.; Cossi, M.; Scalmani, G.; Rega, N.; Petersson, G. A.; Nakatsuji, H.; Hada, M.; Ehara, M.; Toyota, K.; Fukuda, R.; Hasegawa, J.; Ishida, M.; Nakajima, T.; Honda, Y.; Kitao, O.; Nakai, H.; Klene, M.; Li,X.; Knox, J. E.; Hratchian, H. P.; Cross, J. B.; Adamo, C.; Jaramillo, J.; Gomperts, R.; Stratmann, R. E.; Yazyev, O.; Austin, A. J.; Cammi, R.; Pomelli, C.; Ochterski, J. W.; Ayala, P. Y.; Morokuma, K.; Voth, G. A.; Salvador, P.; Dannenberg, J. J.; Zakrzewski, V. G.; Dapprich, S.; Daniels, A. D.; Strain, M. C.; Farkas, O.; Malick, D. K.; Rabuck, A. D.; Raghavachari, K.; Foresman, J. B.; Ortiz, J. V.; Cui, Q.; Baboul, A. G.; Clifford, S.; Cioslowski, J.; Stefanov, B. B.; Liu, G.; Liashenko, A.; Piskorz,P.; Komaromi, I.; Martin, R. L.; Fox, D. J.; Keith, T.; Al-Laham, M. A.; Peng, C. Y.; Nanayakkara, A.; Challacombe, M.; Gill, P. M. W.; Johnson, B.; Chen, W.;

Wong, M. W.; Gonzalez, C.; Pople, J. A. Gaussian03(Revision B.04); Gaussian, Inc.: Pittsburgh, PA, 2003.

[10.51] Peng, C.; Schlegel, H. B. *Israel J. Chem* . **1994**, *33*, 449.

[10.52] Peng, C.; Ayala, P. Y.; Schlegel, H. B.; Frisch, M. J. *J. Comput. Chem.* **1996**, *17*, 49.

[10.53] Gonzalez, C.; Schlegel, H. B. *J. Chem. Phys.* **1989**, *90*, 2154.

[10.54] Gonzalez, C.; Schlegel, H. B. *J. Phys. Chem.* **1990**, *94*, 5523.

[10.55] (a) Becke, A. D. *Phys. Rev. A* **1988**, *38*, 3098. (b) Becke, A. D. *J. Chem. Phys.***1993**, *98,* 5648. (c) Lee, C.; Yang, W.; Parr, R. G. *Phys. Rev. B* **1988**, *37*, 785.

[10.56] Schafer, A.; Huber, C.; Ahlrichs, R. *J. Chem. Phys.* **1994**, *100*, 5829.

[10.57] L.E. Roy, P.J. Hay, and R.L. Martin, J. Chem. Theory Comp. **4**, 1029 (2008).

[10.58] S.F. Boys and F. Bernardi, Mol. Phys. **19**, 553 (1970).

[10.59] S. Simon, M. Duran, and J.J. Dannenberg, J. Chem. Phys. **105**, 11024 (1996).

[10.60] M. Calatayud, J. Andres, A. Beltran, J. Phys. Chem. *A*., **105**, 9760 (2001).

[10.61] (a) E. Jakubikova, A. K. Rappé, and E. R. Bernstein, J. Phys. Chem. A **111**, 12938, (2007). (b) E. Jakubikova, Ph. D Dissertation (May, **2007**).

[10.62] X. Duan and M. Page, J. Mol. Struct. **333**, 233 (1995).

[10.63] S.P. Walch, J. Chem. Phys. **99**, 5295 (1993).

Chapter 11

Experimental and Theoretical Study of Neutral Al_mC_n and $Al_mC_nH_x$ Clusters

11.1 INTRODUCTION

Metal carbide clusters have been extensively studied as a new class of materials for semiconductors, ceramics, hydrogen storage, and catalysis. In 1992, Castleman and coworkers discovered the metallocarbonbohedrene (Met-car, M_8C_{12}) class of transition metal carbides.[11.1] Such species are identified as a "magic" peak, dominant in the distribution of metal carbide cluster cations in a mass spectrometer. Met-cars are made up of 8 metal and 12 carbon atoms, and are found to be particularly stable cage structure. Met-cars can be formed by the early transition metals including Ti, V, Nb, Ta, Zr, Mo, Fe, Mo, etc.,[11.2,11.3] but not by later transition metals such as Ni, Co, Cu, etc.[11.3-11.5] In order to elucidate the growth mechanisms for these special structures, geometric structures of metal carbide clusters have been investigated through both experimental[11.3-11.10] and theoretical studies.[11.11-11.13] Tono et al.[11.4] studied divanadium ($V_2C_n^-$) and dicobalt ($Co_2C_n^-$) anions as representative of dimetallic carbides of the early and late 3d transition metals, respectively. They found that the geometric structures of $Co_2C_n^-$ clusters exhibit a tendency of carbon atoms to aggregate and form a C_n substructure, while $V_2C_n^-$ clusters form a vanadium carbide network with VC_2 building blocks. The structures of Mo_nC_{4n}

are described as planar clusters of two, three, or four molybdenum atoms surrounded by carbon dimers.[11.8] Wang's group observed new prominent peaks in the $Ti_xC_y^-$ anion mass spectra derived from laser vaporization experiments, suggesting that C_2 dimers, cubic framework, and layered structures play essential roles in the determining the structures and chemical bonding of titanium carbide clusters.[11.14,11.15] Recently, Duncan et al. studied noble metal carbide cluster cations (MC_n^+, n = Cu, Au), and found that copper favors the formation of carbides with an odd number of carbon atoms, while gold shows marked decrease in ion intensity after clusters with 3, 6, 9, and 12 carbons.[11.16] The structures of metal carbide clusters are highly dependent on the valence electronic configurations of the metals.

Aluminum carbide clusters, considered as non-classical and non-stoichiometric structures,[11.17-11.24] are different from the most metal carbide clusters with cubic frameworks and layered structures.[11.7,11.12,11.13] Wang and co-workers studied small negative ion $Al_mC_n^-$ clusters by photoelectron spectroscopy and *ab initio* calculations. They report that Al_4C[11.18] and Al_5C[11.22] clusters have tetracoordinate planar structures, an Al_2C_2 cluster has a quasilinear (acetylenic) structure,[11.19] and an Al_3C_2 cluster is formed by attaching a third aluminum on one side of Al_2C_2.[11.20] Recently, Naumkin[11.23] calculated the structures of small $Al_{2m}C_n$ clusters, and concluded that all systems beyond C_2Al_2 are structurally different from their stoichiometric hydrocarbon counterparts due to ionic bonding of Al atoms to carbon molecular centers. To date, no report is found for the experimental study of neutral aluminum carbide clusters. The distribution, definitive structures, and formation mechanisms for neutral Al_mC_n clusters are still not well known. $Al_mC_nH_x$ clusters can be a potential material for hydrogen storage as complex aluminum

hydrides;[11.24] however, no experimental or theoretical study is carried out on $Al_mC_nH_x$ clusters.

In the present work, neutral aluminum carbide clusters (Al_mC_n) and aluminum carbon hydride clusters ($Al_mC_nH_x$) are studied by time of flight mass spectrometry coupled with single photon ionization (SPI) by 193 (6.4 eV, UV), 118 (10.5 eV, VUV), and 49.6 (26.5 eV soft x-ray) nm lasers. Neutral Al_mC_n clusters are generated by laser ablation of mixed aluminum/carbon targets into a carrier gas of pure helium gas. Only some Al_mC_n clusters can be detected by SPI with 193 nm photons; however, all Al_mC_n clusters can be detected by 26.5 eV, soft x-ray laser ionization. A significant alternating behavior is found for the ionization energies of neutral Al_mC_n clusters. Neutral $Al_mC_nH_x$ clusters are generated by ablating pure aluminum metal into mixed hydrocarbon/He carrier gases or ablating Al/C disk into a H_2 carrier gas. The hydrocarbon plasma reaction method is successfully used to generate pure metal carbide clusters for reactive early transition metals (Ti, V, Zr, Nb, Hf, Cr, Mo, and Fe). A series of $Al_mC_nH_x$ clusters are thereby observed by mass spectrometry, implying that a different mechanism is operative for $Al_mC_nH_x$ cluster formation than for early transition metal carbides. Ionization energies of $Al_mC_nH_x$ clusters change systematically with the numbers of H atoms in the clusters. Theoretical calculations are carried out to investigate the structures, molecular orbitals, and vertical ionization energies (VIEs) of neutral Al_mC_n and $Al_mC_nH_x$ clusters.

11.2 EXPERIMENTAL AND THEORETICAL METHODS

The experimental studies of neutral Al_mC_n and $Al_mC_nH_x$ clusters involve a time of flight mass spectrometer (TOFMS) coupled with SPI at 193 nm, 118 nm, and 46.9 nm. The experimental apparatus and laser sources have been described in previous publications

from this laboratory,[11.25] and therefore only a general outline of the experimental scheme will be presented in this report. Briefly, the neutral aluminum carbide clusters are generated in a conventional laser ablation/expansion source through laser ablation (focused 532 nm laser, 10-20 mJ/pulse) of an mixed Al/C target into a carrier gas of pure helium gas (99.9995%) at 80 psi. The target is made by pressing a mixture of carbon and aluminum powders. To generate aluminum carbon hydride clusters, three methods are used: (1) a pure aluminum foil (99.7%, Aldrich) target is used for laser ablation and a mixture of 5% hydrocarbon (CH_4, C_2H_4, or C_2H_6) and helium is used for the expansion gas; (2) a mixed Al/C target is used for laser ablation, and pure hydrogen is used for expansion gas; and (3) neutral aluminum carbide clusters are generated by ablation of an Al/C target, and then reacted with pure hydrogen gas in a fast flow reactor (70 mm length, ∅ 6 mm), which is coupled directly to the cluster formation channel (40 mm length, ∅ 1.8 mm). The ions created in the ablation source and fast flow reactor are removed by an electric field before entering the ionization region. The instantaneous reactant gas mixture pressure in the reactor cell is about 1~2 Torr in this set up. In order to distinguish isomeric clusters $Al_mC_nH_x$ in the mass spectra, methane-d_4 (99 atom % D, Aldrich) and methane-^{13}C (99 atom % ^{13}C, Aldrich) are also used as reactants in the experiments.

The soft x-ray laser (26.5 eV/photon energy)[11.26] emits pulses of about 1 ns duration with an energy/pulse of 10 μJ that is reduced to 3 ~ 5 μJ after the light transverses a z-fold mirror system, and is not tightly focused in the ionization region to avoid multiphoton ionization and a Coulomb space charge effect due to He^+ ions produced by 26.5 eV ionization of He in the molecular beam. Since the 26.5 eV laser can ionize He, H_2, CH_4, C_2H_4, C_2H_6 molecules, which have high concentrations in the

expansion/fast flow reactor system, we must gate the microchannel plate (MCP) detector voltage to protect it from overload and saturation. 118 nm laser light is generated by focusing the third harmonic (355 nm, ~30 mJ/pulse) of a Nd:YAG laser in a tripling cell that contains about a 250 Torr argon/xenon (10/1) gas mixture. To separate the generated 118 nm laser beam from the 355 nm fundamental beam, a magnesium fluoride prism (apex angle = 6 deg) is inserted into the laser light path. In this case, one is quite sure that mass signals are generated by ionization purely through the VUV laser radiation at low power (~1 μJ/pulse, pulse duration ~5 ns). In the experiments, the fluence of an unfocused 193 nm laser is set to about 80 μJ/cm^2/pulse to avoid mutiphoton ionization of neutral clusters.

All the calculations reported in the present work are performed with the Gaussian03 program package.[11.27] The structures of neutral Al_mC_n and $Al_mC_nH_x$ clusters are initially optimized using a hybrid method including a mixture of Hartree–Fock exchange with density functional exchange-correlation (B3LYP)[11.28] and a polarized split-valence basis set (6-311+G*).[11.29] The structures and ionization energies of the lowest energy structures for some Al_mC_n and $Al_mC_nH_x$ clusters are refined using the second order Moller-Plesset perturbation theory (MP2)[11.30] with the same basis set. The vertical ionization energy (VIE) is the difference in energy between the ground state of the neutral cluster and the ionized cluster that has the same geometry as the neutral cluster. The B3LYP/6-311+G* and MP2/6-311+G* methods have been used by Wang and Boldyrev et al.[11.18-11.20] to calculate the structures of aluminum carbide clusters. The electronic configuration of Al_mC_n clusters alternate between open and closed shell with the even-odd number of Al atoms because the aluminum atom has an odd number electrons. Spin

restricted (RHF) and spin unrestricted (UHF) wave functions are used for all closed shell and open shell systems, respectively. The molecular orbitals (MOs) for Al_mC_n and $Al_mC_nH_x$ clusters are calculated at the B3LYP/6-311+G* level. Wave function spin contamination is not a serious problem for these cases at the B3LYP theory level because $<S^2>$ (S(S+1)) values are uniform and deviate only slightly from the pure spin values 0.75. B3LYP wave functions have also been used to calculated MOs of $AlC_n/AlC_n^-/AlC_n^+$ clusters by Largo[11.31] and Li et al.[11.32] We also calculate MO of these clusters at the MP2/6-311+G* level; however, serious spin contamination is found for some of the open shell clusters. For example, using the MP2/6-311+G* level of theory, the $<S^2>$ values for Al_3C_3 and Al_5C_2 clusters are 0.893689 and 0.951627, respectively, which are much larger than 0.75 for a spin pure function as is appropriate. Using the B3LYP/6-311+G* theory level, the $<S^2>$ values for Al_3C_3 and Al_5C_2 clusters are 0.765272 and 0.767105, respectively, which are very closed to the expected pure spin $<S^2>$ valve. The highest occupied molecular orbitals of some Al_mC_n and $Al_mC_nH_x$ clusters are analyzed and plotted for the B3LYP orbitals by using the Chemcraft program.

11.3 EXPERIMENTAL RESULTS

11.3.1 Al_mC_n Clusters

Neutral Al_mC_n clusters are generated in the ablation/expansion source in our experiments through laser ablation of an Al/C target into the pure helium expansion gas. Figure 11.1(a) displays the distribution of neutral Al_mC_n clusters ionized by SPI of 193 nm light. Several series of the Al_mC_n clusters are identified in the mass spectrum; for example, Al_3C_2, Al_3C_4, Al_3C_6, Al_3C_8, and Al_3C_{10}, Al_5C, Al_5C_3, and Al_5C_5, and Al_7C_2 and Al_7C_4. Under the same experimental conditions, using the 26.5 eV soft x-ray laser for ionization, many more

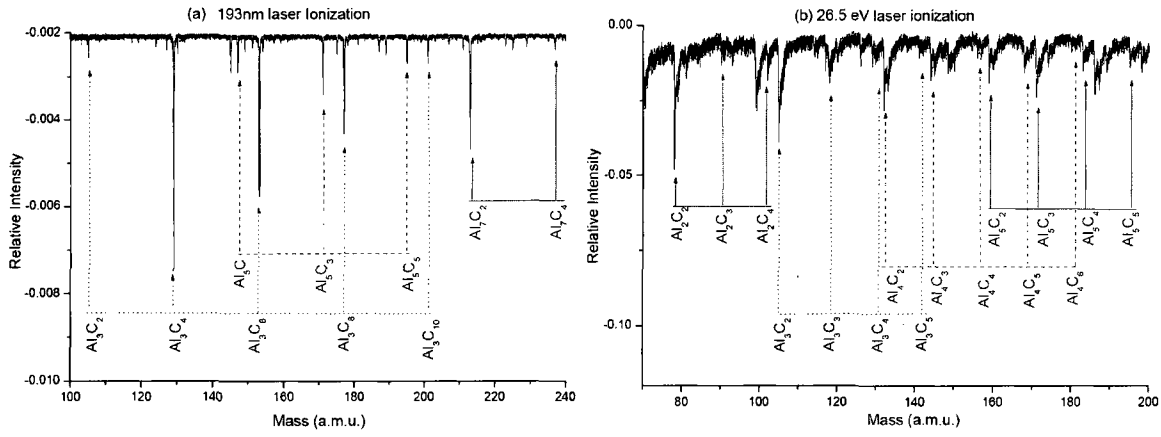


Figure 11.1: Mass spectra of Al_mC_n clusters ionized by (a) a 193 nm (6.4 eV) UV laser and (b) a 46.9 nm (26.5 eV) soft X-ray laser. Clusters are generated by laser ablation of a mixed Al-C target into a pure He expansion gas at 80 psi backing pressure.

aluminum carbide clusters including $Al_2C_{2\text{-}4}$, $Al_3C_{2\text{-}5}$, $Al_4C_{2\text{-}6}$, and $Al_5C_{2\text{-}5}$ are detected as shown in Figure 11.1(b). Since the intensity of the soft x-ray laser is much lower than that of the 193 nm laser, the signal intensities in the experiments with soft x-ray laser ionization are much weaker than those derived by the 193 nm laser ionization; however, the distribution of neutral Al_mC_n clusters can still be identified.

11.3.2 $Al_mC_nH_x$ Clusters

Three methods are used to generate the $Al_mC_nH_x$ clusters in the experiments. For method (1), pure aluminum foil is used as the ablation target, and mixtures of a hydrocarbon (CH_4, C_2H_4 or C_2H_6) and He are used as the expansion gas. As shown in Figure 11.2, an abundance of aluminum carbon hydride clusters are observed in the mass spectrum by using a 193 nm laser for SPI. For example, mass numbers 69 (Al_2CH_3), 79 (Al_2C_2H), 85 ($Al_2C_2H_5/Al_3H_4$), 93 ($Al_2C_3H_3$), 105 (Al_2C4H_3/Al_3C_2), 119 ($Al_3C_3H_2/Al_2C_5H_5$), 129 ($Al_3C_4/Al_2C_6H_3$), 145 ($Al_4C_3H/Al_3C_5H_4$), 161 ($Al_4C_4H_5/Al_5CH_2$), 171 ($Al_4C_5H_3/Al_5C_3$), 185 ($Al_5C_4H_2/Al_4C_6H_5$) amu, etc. are detected. Similar distributions of $Al_mC_nH_x$ clusters

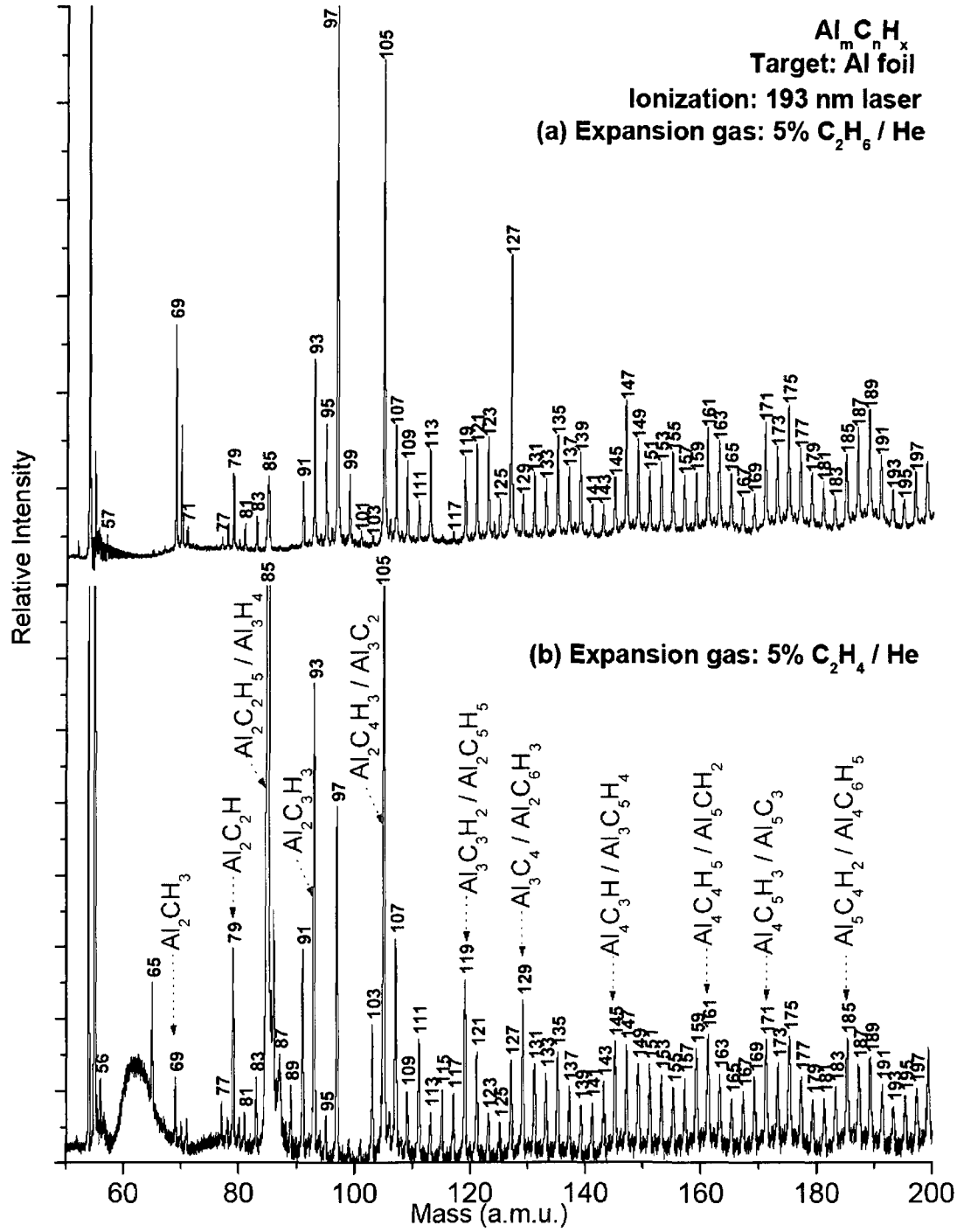


Figure 11.2: Mass spectrum of $Al_mC_nH_x$ clusters ionized by a 193 nm laser. Clusters are generated by laser ablation of pure Al foil into a mixture of (a) 5% C_2H_6/He and (b) 5% C_2H_4/He expansion gases at 80 psi backing pressure.

are observed in Figure 11.3 if the clusters are generated by using method (2), in which a mixed Al/C target is used for ablation, and pure H_2 gas is used for expansion gas. For

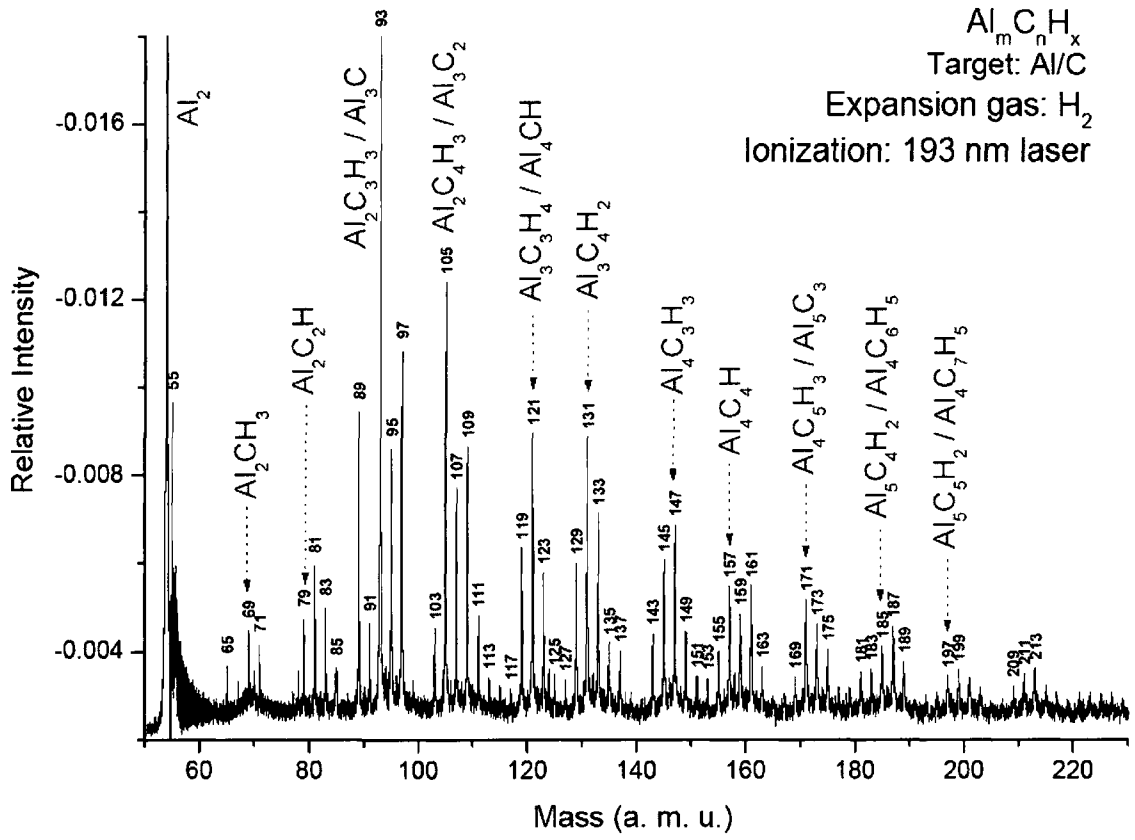


Figure 11.3: Mass spectrum of $Al_mC_nH_x$ clusters ionized by a 193 nm laser. Clusters are generated by laser ablation of a mixed Al-C target into an H_2 expansion gas at 80 psi backing pressure.

method (3), neutral Al_mC_n clusters are generated by ablation of a mixed Al/C target first, and then react with H_2 molecules in a fast flow reactor after the expansion and cooling processes. As shown in Figure 11.4, many new species are detected such as Al_2CH_3, $Al_2C_3H_3$, $Al_3C_3H_2$, $Al_3C_4H_2$, Al_4C_3H, Al_4C_4H, etc. which are generated from the reactions of $Al_mC_n + H_2$ in the fast flow reactor. Note that all signals identified for $Al_mC_nH_x$ clusters in the 193 nm SPI experiments are found for odd mass numbers (Figures 11.2-11.4). In the present studies, $Al_mC_nH_x$ clusters are also detected by 118 nm laser SPI. As shown in Figure 11.5, many signals are identified as $Al_mC_nH_x$ clusters with both odd and even mass numbers, for example, $Al_2C_2H_{1\text{-}12}$, $Al_2C_3H_{1\text{-}12}$, $Al_3C_2H_{1\text{-}12}$, $Al_3C_3H_{1\text{-}12}$, and etc. This experimental observation must involve the ionization energies of the $Al_mC_nH_x$ clusters.

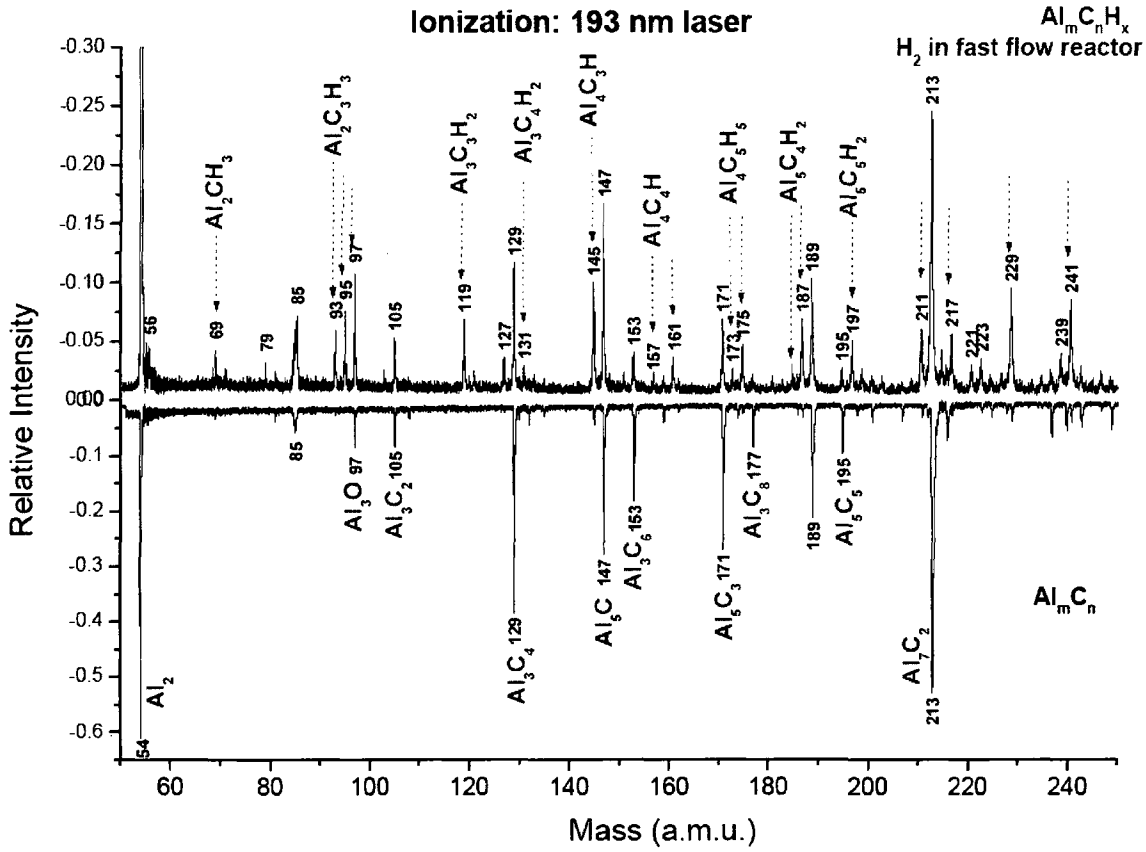


Figure 11.4: $Al_mC_nH_x$ clusters generated through reactions of Al_mC_n clusters with H_2 gas in a fast flow tube reactor. The Al_mC_n clusters are generated by ablation of a mixed Al-C target into an He expansion gas. Reactant gas H_2 (15 psi) is added to the fast flow reactor. New reaction products and remaining clusters are detected by 193 nm laser ionization.

We investigate this issue through theoretical calculations of the structure, ionization energy, and highest occupied molecular orbital (HOMO) energy of $Al_mC_nH_x$ clusters in the Discussion Section.

In the studies of Al_mC_n and $Al_mC_nH_x$ clusters, we take full advantage of the available three laser sources (193 nm, 118 nm, and 46.9 nm). In the experiment, relatively high power can be provided by the 193 nm laser (unfocused, ~ 80 μJ), and a good signal to noise ratio can be obtained in the mass spectra; however, a single photon of 193 nm light cannot ionize all neutral clusters generated in the ablation/expansion source as

shown in Figure 11.1-11.4. A single photon (10.5 eV) of the 118 nm laser can ionize most of the neutral Al_mC_n and $Al_mC_nH_x$ clusters with high resolution to distinguish one mass number difference at ca. 500 amu. The 118 nm, 10.5 eV laser is a good ionization source to detect $Al_mC_nH_x$ clusters, as presented in Figure 11.5; however, when a 118 nm laser is used to study Al_mC_n clusters, very weak signals are observed because the method of

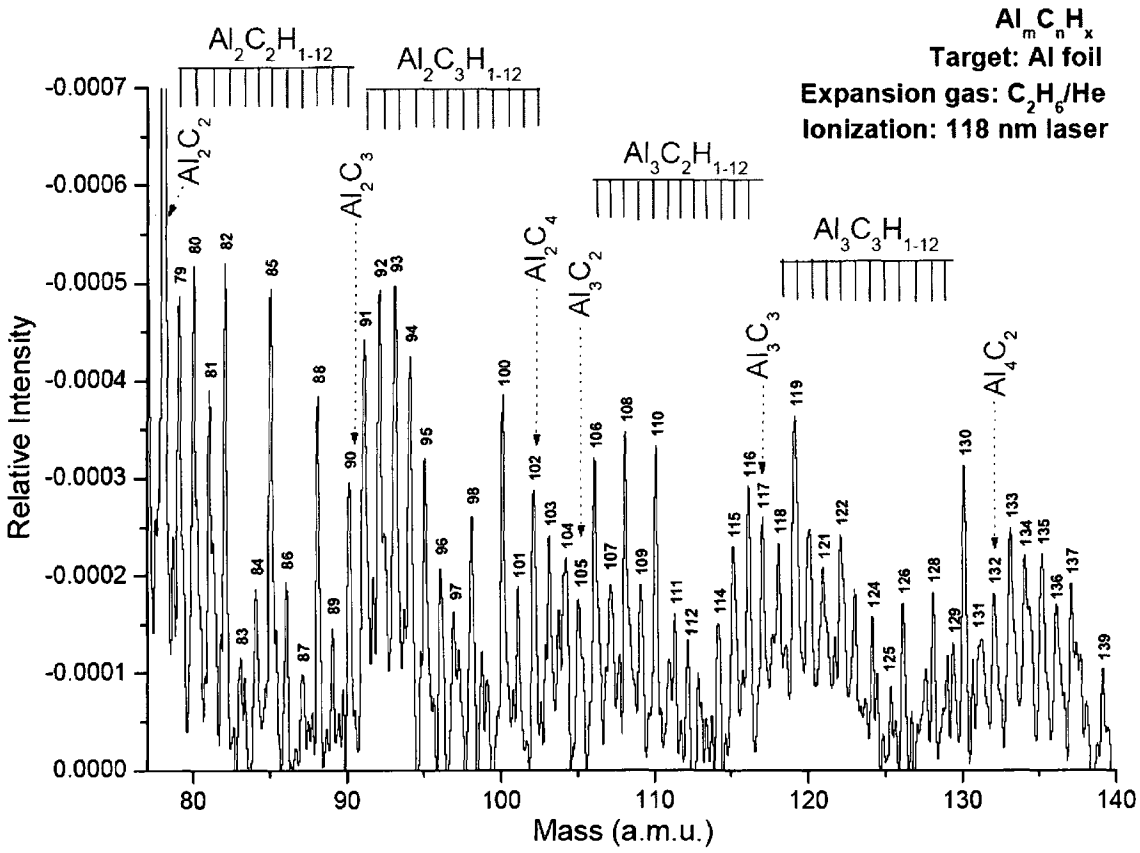


Figure 11.5: Mass spectrum of $Al_mC_nH_x$ clusters ionized by a 118 nm laser. Clusters are generated by laser ablation of Al foil into a mixture of 5% C_2H_6/He expansion gas at 80 psi backing pressure.

ablating the mixed Al/C target does not generate very many Al_mC_n clusters. The 46.9 nm soft x-ray lasers is a unique ionization source that can ionize any neutral species generated in the molecular beam. Nonetheless, the resolution of mass spectrum obtained using 46.9 nm soft x-ray laser ionization is not as good as that observed with the 118 nm laser ionization to detect $Al_mC_nH_x$ clusters; the 46.9 nm soft x-ray laser is defocused in

order to avoid multiphoton ionization and a space charge Coulomb effect due to He^+ ions produced by 26.5 eV ionization of He (carrier gas) in the molecular beam. Additionally, amplified spontaneous emission (ASE) generated with the 46.9 nm laser degrades mass resolution for the detection of weak signals. Therefore, in the present experiments, we use 46.9 nm soft x-ray laser to detect Al_mC_n clusters (Figure 11.1b), and use 118 nm laser to detect $Al_mC_nH_x$ clusters in order to detect all neutral clusters generated in the cluster synthesis processes. Both ionization laser sources are essential components of these overall studies.

11.3.3 Isotopic Substitution Experiments

The detected $Al_mC_nH_x$ clusters can not be uniquely distinguished in the mass spectra (Figures 11.2, 11.3 and 11.4) due to mass degeneracy (isobars) for some of clusters; for example, $Al_2C_3H_3$ and Al_3C have the same mass number (93 amu), $Al_2C_4H_3$ and Al_3C_2 have the same mass number (105 amu), etc. Many possible isomers cannot be simply labeled in the mass spectra. In order to distinguish the isomers, isotopic CD_4/He and $^{13}CH_4$/He instead of CH_4/He mixtures are employed as the expansion gas to generate neutral $Al_mC_nH_x$ clusters (see method 1). As displayed in Figure 11.6, the clusters Al_2CH_3 (69), Al_2C_2H (79), $Al_2C_3H_3$ (93), $Al_2C_4H_3/Al_3C_2$ (105), $Al_3C_3H_2$ (119), etc. are distinguished and assigned to the main products of $Al_mC_nH_x$ clusters. Note that the signal at mass number 105 amu (Figure 11.6c) consists of two compounds ($Al_2C_4H_3$ and Al_3C_2). In the CD_4/He experiment (Figure 11.6b), one identifies two peaks of 105 (Al_3C_2) and 108 ($Al_2C_4D_3$), which correspond to the peak of mass number 105 amu in the CH_4/He experiment (Figure 11.6c). In the $^{13}CH_4$/He experiment, this peak is divided into the 107 ($Al_3{}^{13}C_2$) and 109 ($Al_2{}^{13}C_4H_3$) amu peaks as shown in Figure 11.6a. Several series of

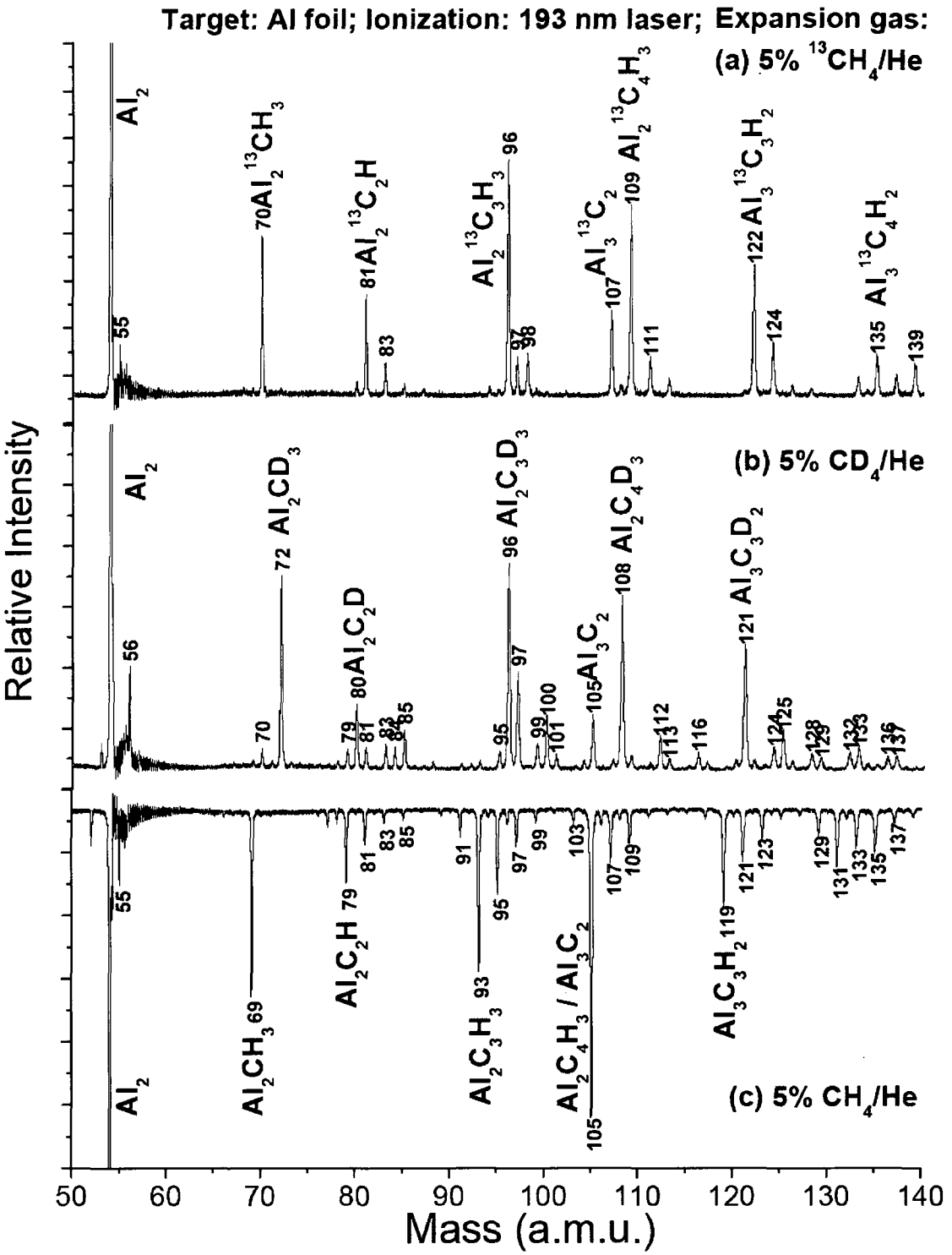


Figure 11.6: Mass spectra of $Al_mC_nH_x$ clusters ionized by 193 nm laser. Clusters are generated by laser ablation of Al foil into a mixture of (a) 5% $^{13}CH_4$/He, (b) 5% CD_4/He, and (c) 5%CH_4/He expansion gas at 80 psi backing pressure.

$Al_mC_nH_x$ clusters observed in Figures 11.2-11.4 are identified as $Al_2CH_{3,5}$, $Al_2C_2H_{1,3,5,7,9,11}$, $Al_2C_3H_{1,3,5,7,9}$, $Al_2C_4H_{3,5,7,9,11}$, $Al_3C_2H_{2,4,6,8,10}$, $Al_3C_3H_{2,4,6}$, $Al_3C_4H_{2,4,6,8,10}$, $Al_4C_3H_{1,3,5,7,9}$, $Al_4C_4H_{1,3,5,7,9}$, $Al_4C_5H_{1,3,5,7}$, $Al_5C_4H_{2,4,6,8,10}$, etc.

11.4 THEORETICAL CALCULATION RESULTS

11.4.1 Neutral Al_mC_n clusters

Structures: Possible structures for small neutral Al_mC_n clusters are calculated at the B3LYP/6-311+G* level of theory and the lowest energy structures for these clusters are refined using an MP2 theory with the same basis set. The optimized isomers for the neutral Al_2C_2 clusters are displayed in Figure 11.7. The lowest energy isomer Al_2C_2_**a** is a linear symmetric Al-C-C-Al structure like acetylene with two H atoms replaced by two

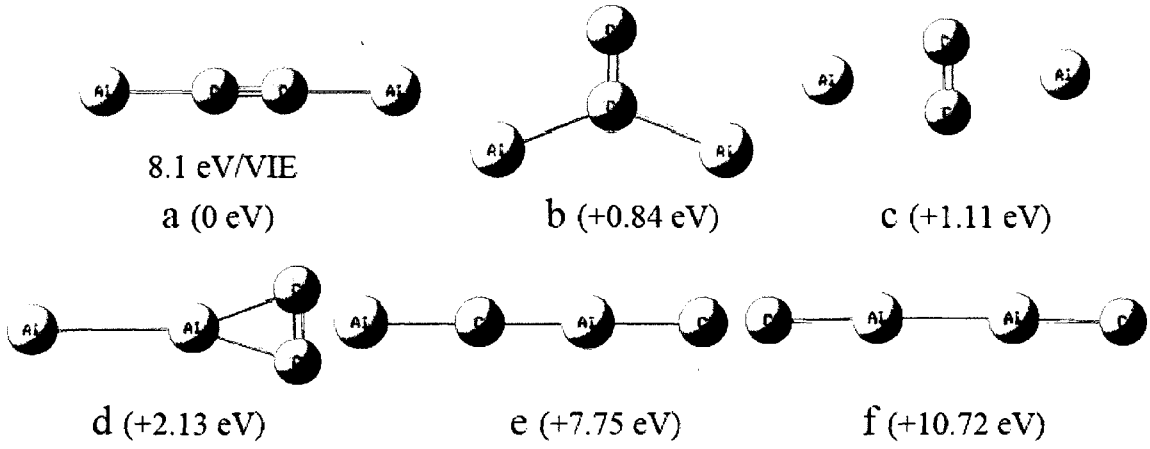


Figure 11.7: DFT optimized geometries for the Al_2C_2 cluster at the B3lYP/6-311+G* theory level. Values (in eV) in parentheses below each geometry are isomer energies relative to lowest energy isomer **a**.

Al atoms. Isomer Al_2C_2_**b** is 0.84 eV higher in energy than the lowest energy isomer Al_2C_2_**a** and has a T-shaped structure in which two Al atoms connect with one C atom. Isomers **c** and **d** are planar structures with one or two Al atoms bridged by C=C bonds, and they have higher energies than isomer Al_2C_2_**a** by 1.09 and 2.08 eV, respectively. The other two isomers **e** (Al-C-Al-C) and **f** (C-Al-Al-C) have linear structures without C-C

bonds. These latter two isomers have significantly higher energies than the lowest energy isomer Al_2C_2_**a**.

The optimized lowest energy structures of clusters Al_3C_2, Al_4C_2, Al_5C_2, Al_6C_2, Al_2C_4 and Al_3C_3 are presented in Figure 11.8. The lowest energy structure for Al_3C_2 is found to be a planar structure that can be described as adding one Al atom on one side of the Al_2C_2_**a** cluster. The lowest energy structure of the Al_4C_2 cluster is also a planar structure, described as adding two Al atoms on either side of the Al_2C_2_**a** cluster. For the Al_5C_2 cluster, the lowest energy structure has a nonplanar pentagonal shape, and for the Al_6C_2 cluster, the lowest energy structure can be considered as adding two Al atoms on

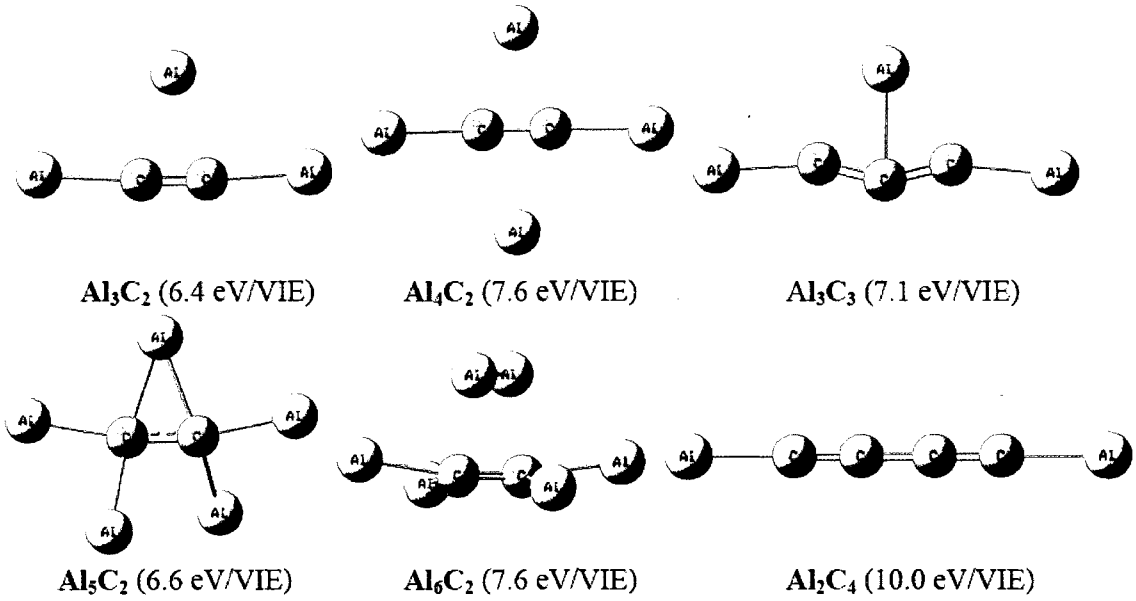


Figure 11.8: Lowest energy structures of small Al_mC_n cluster optimized at the MP2/6-311+G* theory level. Values (in eV) in parentheses below each geometry are VIEs for the clusters calculated at the same theory level.

the top of a distorted Al_4C_2 structure. The C-C bond lengths in these clusters are 1.26, 1.29, 1.34, 1.40, and 1.37 Å for Al_2C_2, Al_3C_2, Al_4C_2, Al_5C_2, and Al_6C_2 clusters, respectively. Additionally, the lowest energy structures for the Al_3C_3 and Al_2C_4 clusters can be formed from Al_3C_2 and Al_2C_2 by extending the C-C chain. All of the lowest energy

structures of these neutral Al_mC_n clusters are found to be in singlet states.

VIEs: We calculated VIEs for Al_mC_n clusters with the lowest energy structures at the MP2/6-311+G* level of theory. Based on calculation, VIEs for Al_mC_2 clusters are Al_2C_2 (8.1 eV), Al_4C_2 (7.6 eV), Al_6C_2 (7.6 eV), Al_3C_2 (6.4 eV), and Al_5C_2 (6.6 eV), respectively. In Figure 11.9, VIEs of neutral Al_mC_2 clusters are plotted against the number of Al atoms in the clusters. Additionally, the VIEs for Al_3C_3 and Al_2C_4 cluster are calculated to be 7.1 and 10.0 eV, respectively.

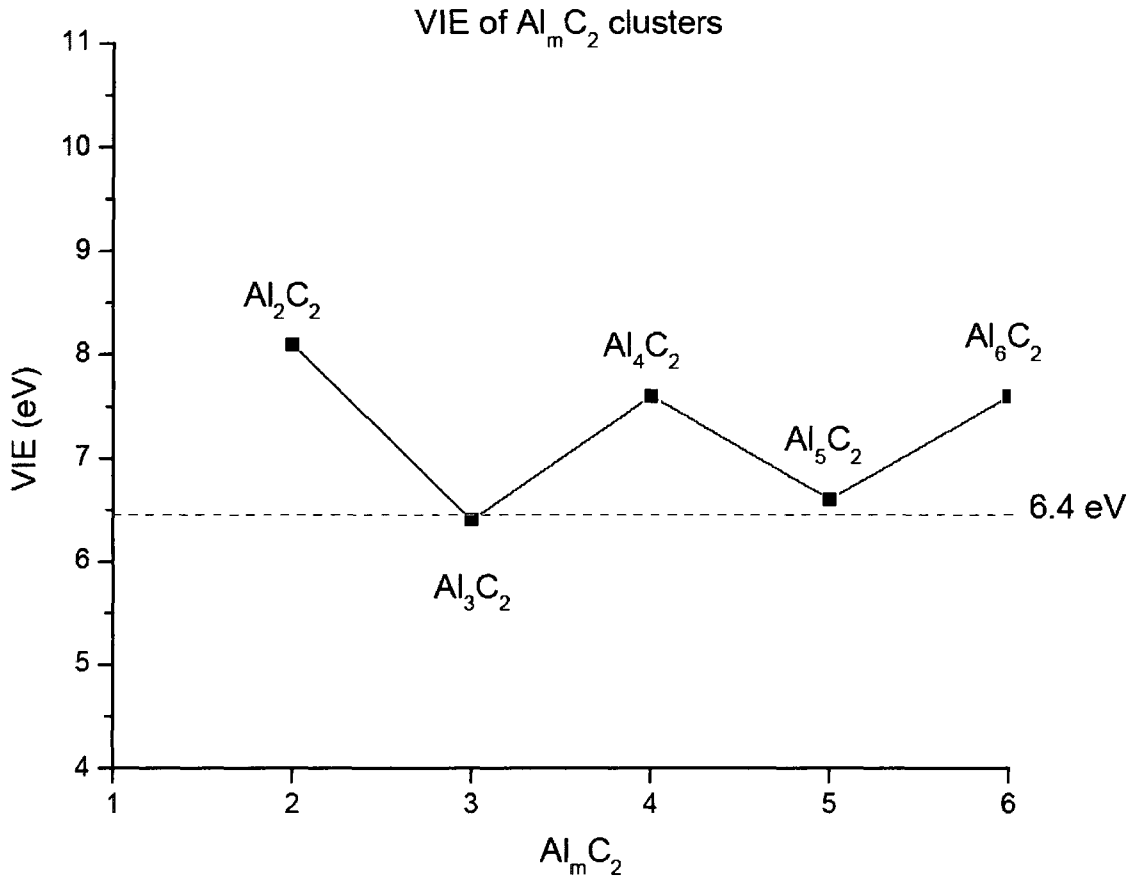


Figure 11.9: The VIEs of Al_mC_2 clusters plotted against the number of Al atoms m in the clusters. (Calculated at the MP2/6-311+G* theory level)

Molecular orbitals: We also perform DFT calculations to explore the highest occupied molecular orbitals (HOMOs) for neutral Al_mC_n clusters (lowest energy

structures) at the B3LYP/6-311+G* level of theory. As shown in Figure 11.10, the HOMO of the Al_2C_2 cluster is primarily a combination of two lone pair Al orbitals interacting with a C-C σ bonding orbital. The HOMO of the Al_3C_2 cluster is obviously a combination of a C-C antibonding π orbital and σ bonding C-Al and Al-Al orbitals. The HOMO of the Al_4C_2 cluster can be characterized by a C-C π orbital with contributions

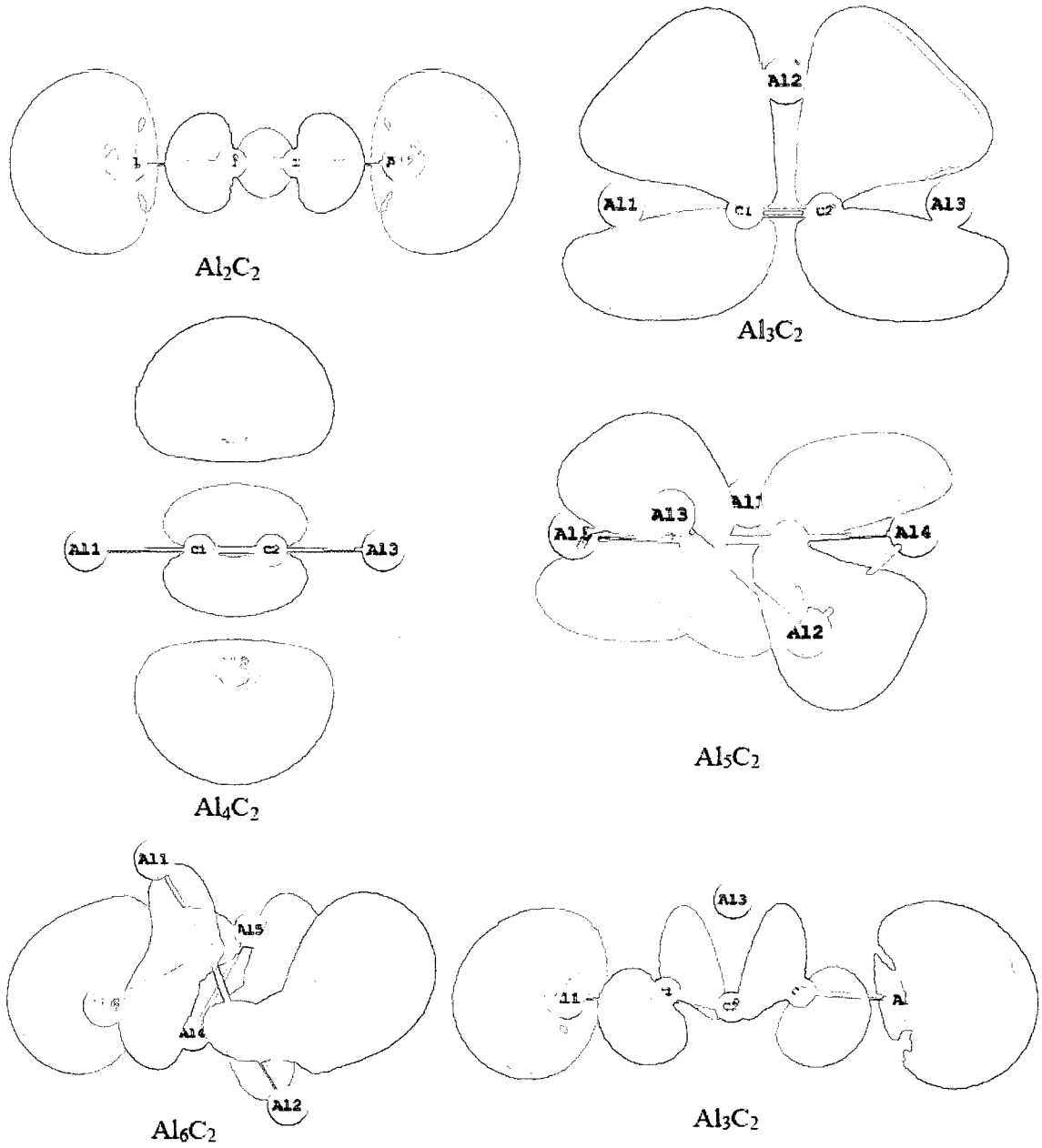


Figure 11.10: HOMOs for the lowest energy Al_mC_n structures calculated at the B3LYP/6-311+G* level.

from the lone pair orbitals of two bridging Al atoms. For the Al_5C_2 cluster, a C-C antibonding π orbital and a bonding σ orbital of Al-Al contribute to the cluster's HOMO. The HOMO for the Al_6C_2 cluster can be described as σ bonds formed between Al and C atoms with a very slight contribution from a C-C antibbonding π orbital. Additionally, the HOMO of the Al_3C_3 cluster is composed of a C-C-C antibonding π orbital and the lone pair orbitals of two end Al atoms. In the Discussion Section, we will interpret the relationship between the ionization energy and molecular orbitals for Al_mC_n clusters.

11.4.2 Neutral $Al_mC_nH_x$ Clusters

Structures: Stable structures for $Al_2C_2H_x$ clusters are optimized at the B3LYP/6-311+G* level of theory and are shown in Figure 11.11. For clusters containing one H atom (Al_2C_2H), the isomer Al_2C_2H_**a** is the lowest energy structure, in which the H atom bonds to a C atom and Al_2C_2 moiety is changed from linear to planar. If the H atom connects with an Al atom to form isomer Al_2C_2H_**b**, the energy increases 0.07 eV relative to the lowest energy isomer Al_2C_2H_**a**. For clusters containing two H atoms ($Al_2C_2H_2$), the lowest energy isomer is $Al_2C_2H_2$_**a** formed by adding two H atoms on one Al atom of the Al-C=C-Al cluster. The second lowest energy isomer is found to be $Al_2C_2H_2$_**b**, in which two H atoms are bonded to the two different C atoms joined by a C=C bond. The isomer $Al_2C_2H_2$_**b** is 0.43 eV higher in energy than the isomer $Al_2C_2H_2$_**a**. If the two H atoms bond to different Al atoms to form isomer $Al_2C_2H_2$_**c**, the energy of the structure (2.25 eV) will be much higher than the lowest energy isomer $Al_2C_2H_2$_**a**. In the lowest energy structure $Al_2C_2H_3$_**a**, two H atoms bond to one Al atom and the other H atom bonds to a C atom of the C=C bond. $Al_2C_2H_3$_**b** and **c** are formed by connecting all three H atoms to two Al or C atoms. Their energy is slightly higher than that of $Al_2C_2H_3$_**a** **by** 0.05 and

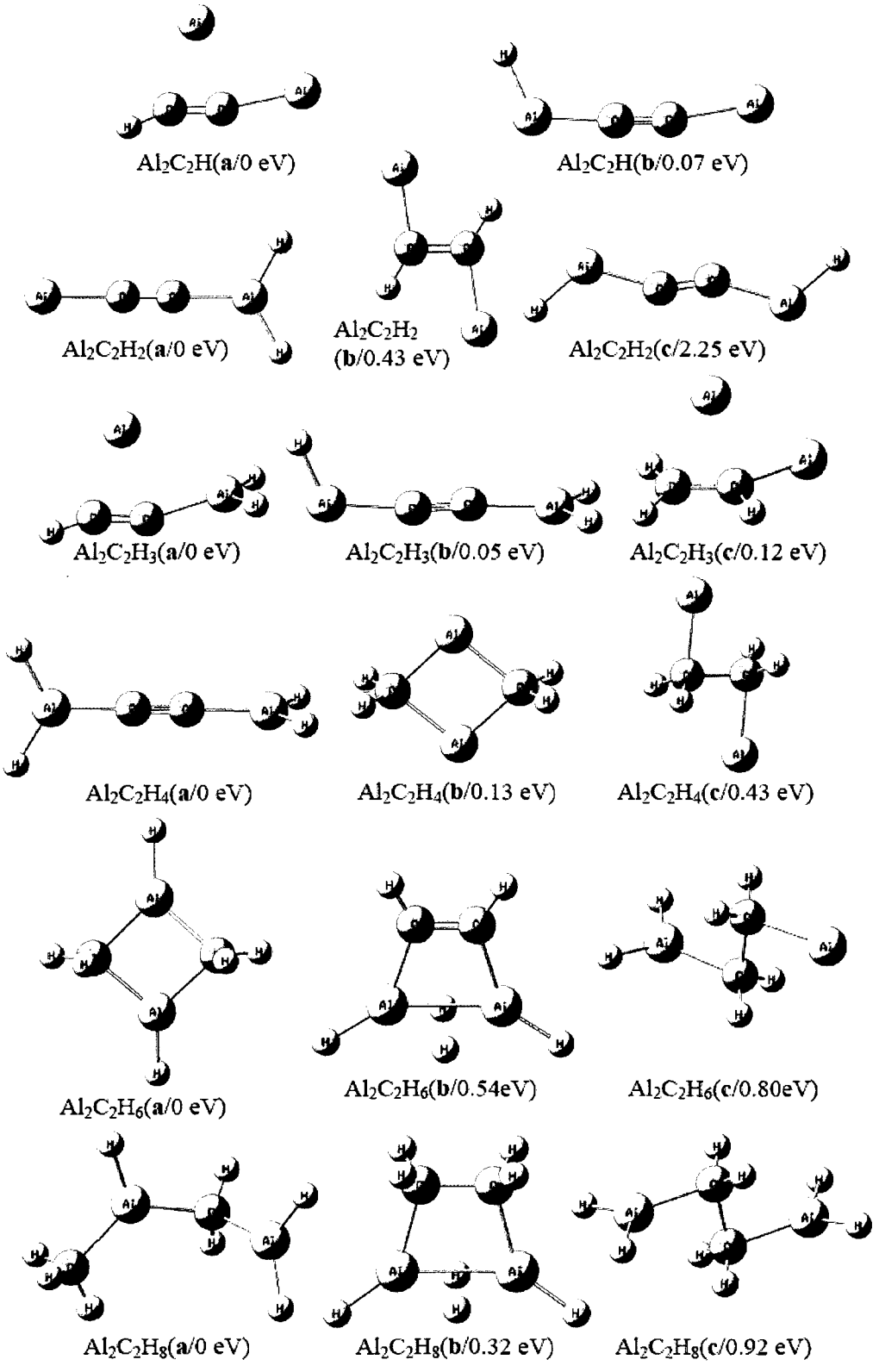


Figure 11.11: Optimized geometries for $Al_2C_2H_x$ cluster at the B3lYP/6-311+G* theory level. Values (in eV) in parentheses below each geometry are the isomer energies relative to lowest energy isomer a.

0.12 eV, respectively. For the $Al_2C_2H_4$ cluster, the lowest energy structure isomer $Al_2C_2H_4$_**a** can be formed by adding four H atoms to the Al atoms of the Al-C=C-Al cluster. An Al-C-Al-C four-memerbered ring structure is found as isomer $Al_2C_2H_4$_**b**, in which the four H atoms are connected to the two C atoms. The structure energies for isomers $Al_2C_2H_4$_**b** is 0.13 eV higher than isomer $Al_2C_2H_4$_**a**. If the four H atoms are connected to the C atoms, the isomer $Al_2C_2H_4$_**c** is formed with energy higher than the lowest energy isomer $Al_2C_2H_4$_**a** by 0.43 eV.

Some possible isomers for the clusters containing 6 and 8 H atoms are also investigated. The lowest energy isomer for $Al_2C_2H_6$ cluster is an Al-C-Al-C four-membered ring structure like $Al_2C_2H_6$_**a**, and the second lowest energy structure is a $Al_2C_2H_6$_**b**, a four-membered ring structure with a C=C double bond in which two H atoms are in a bridge position relative to the Al-Al moiety, and the other four H atoms bond with two Al and two C atoms. The isomer $Al_2C_2H_6$_**c** can be formed by adding six H atoms to a distorted Al-C=C-Al cluster. Isomers $Al_2C_2H_6$_**b** and $Al_2C_2H_6$_**c** have higher energies than isomer $Al_2C_2H_6$_**a** by 0.54 and 0.80 eV, respectively. For the cluster $Al_2C_2H_8$, the lowest energy molecule is $Al_2C_2H_8$_**a**, a chain structure of C-Al-C-Al saturated by H atoms similar to an alkane structure. Additionally, a four-membered ring (Al-C-C-Al) structure ($Al_2C_2H_8$_**b**) and another chain Al-C-C-Al ($Al_2C_2H_8$_**c**) structure are also found. They have higher energy than $Al_2C_2H_8$_**a** by 0.32 and 0.92 eV, respectively.

VIEs: The lowest energy structures for the $Al_2C_2H_{1\text{-}4}$ and $Al_3C_2H_{1,2}$ clusters are refined at the MP2/6-311+G* theory level, and VIEs for these clusters are calculated at

the same level. The VIEs for Al_2C_2, Al_2C_2H, $Al_2C_2H_2$, $Al_2C_2H_3$, and $Al_2C_2H_4$ clusters are 8.1, 6.3, 8.7, 7.0, and 10.3 eV, respectively. The VIEs of $Al_2C_2H_x$ clusters are plotted against the number of H atoms in the clusters as shown in Figure 11.12. Additionally, the VIEs of $Al_3C_2H_1$ and $Al_3C_2H_2$ clusters are calculated as 7.5 and 6.9 eV, respectively.

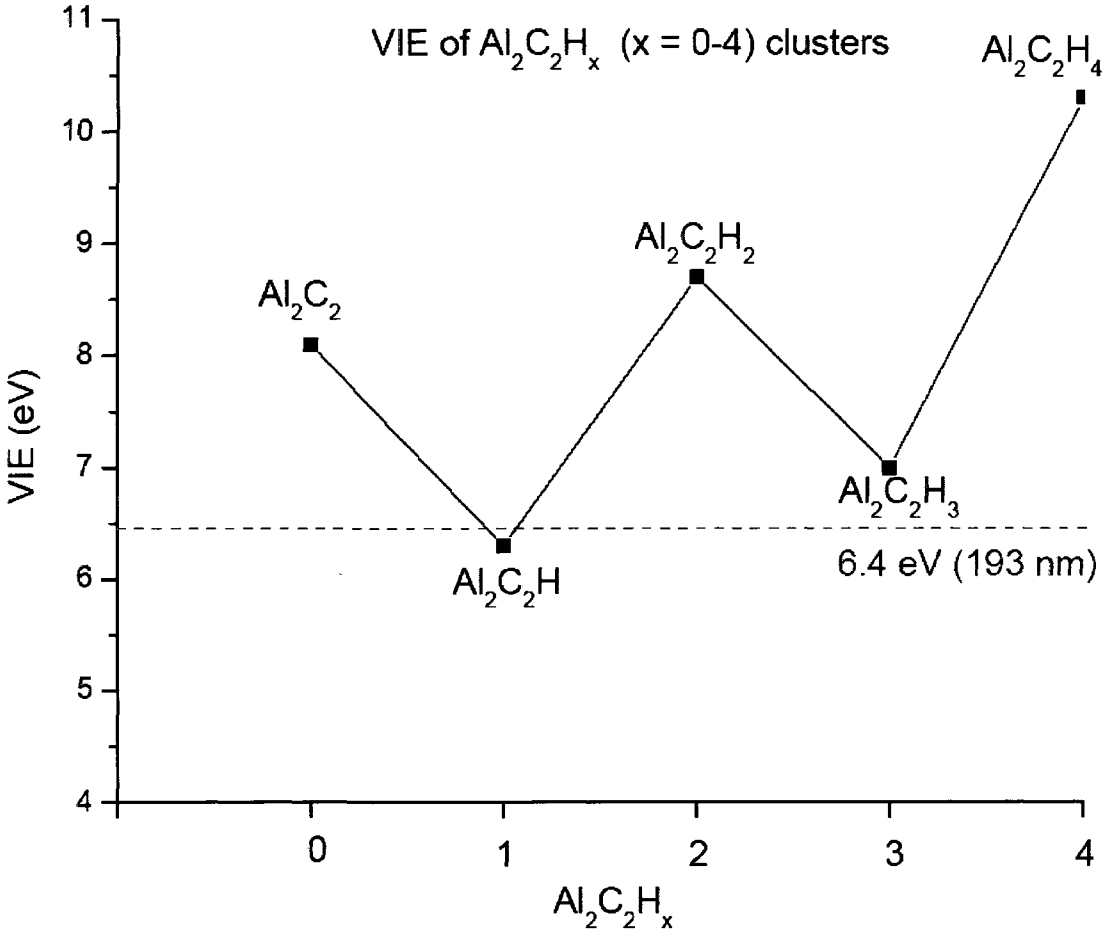


Figure 11.12: VIEs of $Al_2C_2H_x$ clusters plotted against the number of H atoms x in the clusters. (Calculated at the MP2/6-311+G* theory level)

HOMOs: The HOMOs for the $Al_2C_2H_{1\text{-}4}$ and $Al_3C_2H_{1,2}$ clusters calculated at the B3LYP/6-311+G* level of theory are plotted in Figure 11.13. HOMOs for the Al_2C_2H and $Al_2C_2H_3$ clusters are primarily C=C antibonding π in character, interacting with H and Al atoms. The HOMO of the $Al_2C_2H_2$ cluster is mainly composed of a lone pair orbital of an Al atom. For the $Al_2C_2H_4$ cluster, the HOMO is characterized by a bonding

C=C π orbital. The HOMO for the $Al_3C_2H_1$ cluster is a distorted antibonding π C=C orbital interacting with the non bonding orbital of Al and σ orbital of H. And the HOMO of $Al_3C_2H_2$ cluster is primarily C=C antibonding π in character, similar to the HOMO of Al_3C_2.

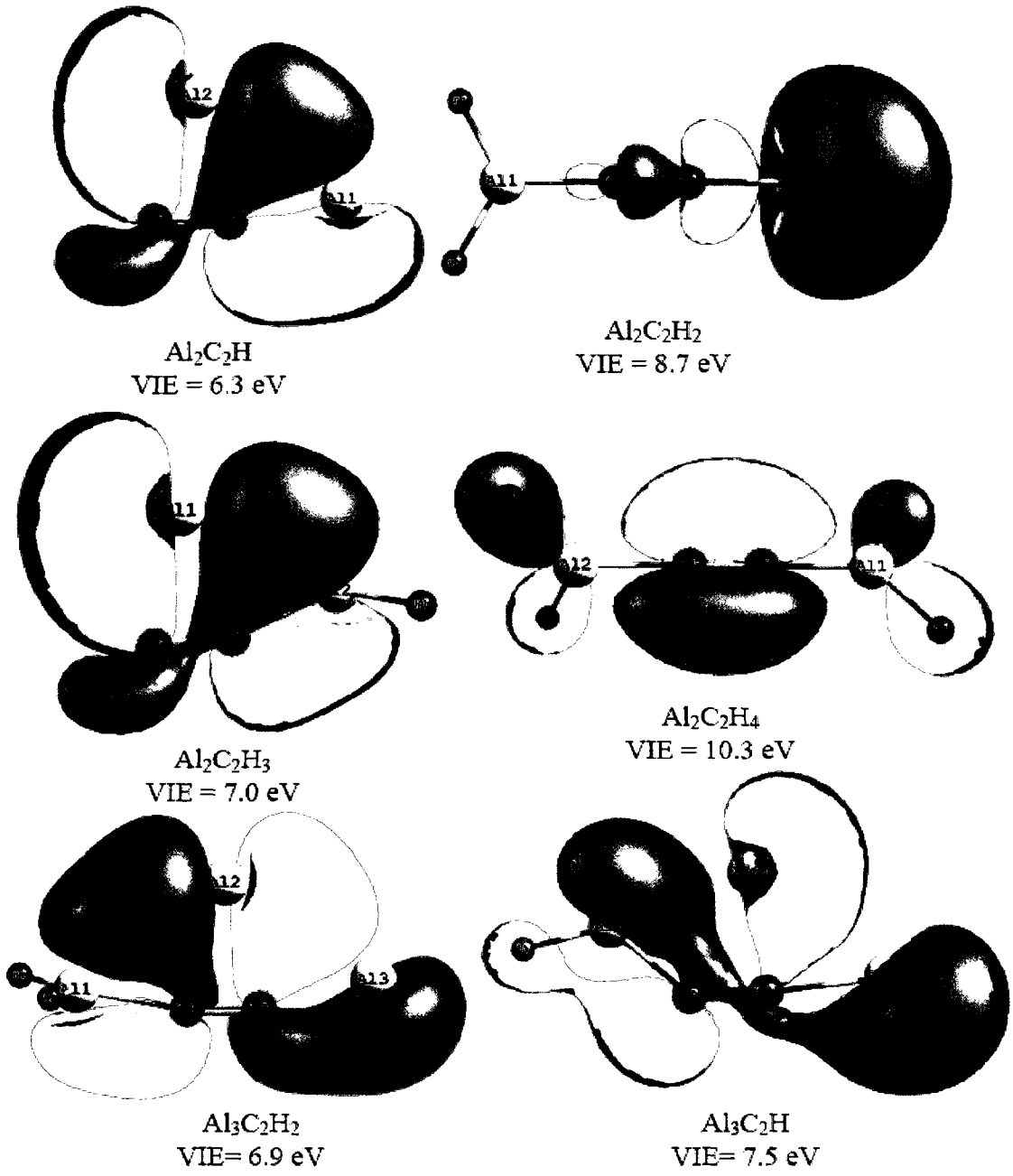


Figure 11.13: HOMOs for the lowest energy $Al_2C_2H_{1\text{-}4}$ and $Al_3C_2H_{1,2}$ cluster structures calculated at the B3LYP/6-311+G* theory level. Values (in eV) in parentheses below each cluster are the VIEs for the clusters calculated at the MP2/6-311+G* theory level.

A detailed discussion about the relationship between molecular orbital, VIE, and experimental results for $Al_mC_nH_x$ clusters can be found in the following section.

11.5 DISCUSSION

11.5.1 Al_mC_n clusters

Neutral Al_mC_n clusters are generated through the ablation of a mixed Al-C target into pure He expansion gas. As shown in Figure 11.1a, several series of Al_mC_n clusters are detected by SPI at 193 nm: Al_3C_{2n} (n = 1-5), Al_5C_{2n+1} (n = 0 - 2), and Al_7C_{2n} (n =1, 2). These clusters should have lower ionization energies than 6.4 eV. Note that these the signals identified for Al_mC_n clusters have odd mass numbers in the mass spectrum. Under the same experimental conditions, all Al_mC_n clusters are detected by SPI of the 26.5 eV soft X-ray laser: Al_2C_n (n = 2-4), Al_3C_n (n = 2-4), Al_4C_n (n=2-5), and Al_5C_n (n=2-5) cluster series (see Figure 11.1b). One knows that the photon energy of the soft X-ray laser is high enough to ionize all neutral species. This experimental observation indicates that all aluminum carbide clusters Al_mC_n ($m \leq 7$, $n \leq 10$) are generated in the experiment. We have previously, on the basis of our studies on metal and metal oxide clusters[11.25] and van der Waals clusters,[11.33] proved that fragmentation caused by the high photon energy of the soft X-ray laser can be neglected. Through comparison of the 193 nm and soft X-ray experimental results, we find that the following Al_mC_n clusters are not detected by 193nm SPI due to their high ionization energies: (1) Al_mC_n clusters with an even number of aluminum atoms, such as Al_2C_n, Al_4C_n, Al_6C_n etc; (2) the Al_3 family with odd numbers of C atoms (Al_3C_{2n+1}); (3) the Al_5 family with even an number of C atoms (Al_5C_{2n}); and (4) the Al_7 family with odd an number of C atoms (Al_7C_{2n+1}). Experimental observation indicates that the ionization energies of the Al_mC_n clusters systematically change with

both the number of Al atoms and C atoms.

Theoretical calculations are performed to study the structures of Al_mC_n clusters. As presented in Figure 11.7, the lowest energy structure Al_2C_2_**a** can be described as an acetylene geometry considering Al substituted for H atoms. The isomers without C-C bond (Al_2C_2_**e** and Al_2C_2_**f**) have significantly higher energies than the isomers with C-C bond (Al_2C_2_**a**, **b** and **c**), indicating that C-C bond formation stabilizes neutral Al_2C_n clusters. Based on the calculations, a C-C bond is also formed in the lowest energy structures of other Al_mC_2 clusters, such as Al_3C_2, Al_4C_2, Al_5C_2, and Al_6C_2, as shown in Figure 11.8. The bond length for the C-C moiety for the lowest energy structure of Al_2C_2 (1.26 Å) and Al_3C_2 (1.29 Å) are longer than the triple bond of acetylene (1.22 Å), but shorter than the double bond of ethylene (1.34 Å). The C-C bond for the Al_4C_2 (1.34 Å) clusters is close to that of a C=C hydrocarbon double bond, and slightly shorter than the C=C double bonds for Al_5C_2 (1.40 Å) and Al_6C_2 (1.37 Å) clusters. The C-C bond lengths in these clusters increase with the number of Al atoms with the exception of Al_6C_2. Additionally, C=C chains are also formed in the lowest energy structures of Al_3C_3 and the Al_2C_4 clusters, further indicating that structures with C=C bonds are energetically favorable for small neutral Al_mC_n clusters. The structures of aluminum carbide clusters are quite different from most other metal carbide clusters; these latter species tend to form cubic frame structures due to relatively strong ionic bonds between the metal and carbon atoms.[11.7,11.12,11.13] The bond strengths of the metal-carbon bonds apparently strongly influence and eventually decide the structures of metal carbides. The strength of Al-C bond is 3.51 eV,[11.24] much weaker than for transition metal-carbon bonds for example, Ti-C (4.5 eV), V-C (4.9 eV).[11.34]

A significant even-odd alternation is found for VIEs of neutral Al_mC_n clusters as plotted in Figure 11.9, in which the clusters with an odd number of Al atoms (Al_3C_2 and Al_5C_2) have lower VIEs than clusters with an even number of Al atoms (Al_2C_2, Al_4C_2, and Al_6C_2). The calculational results are in very good agreement with experimental observation, in that the Al_3C_2 (VIE=6.4 eV) cluster is detected by SPI at 193 nm (Figure 11.1a), and clusters Al_5C_2 (VIE=6.6 eV), Al_2C_2 (VIE=8.1 eV), Al_4C_2 (VIE=7.5 eV), and Al_6C_2 (VIE=7.6 eV) are not detected since they have higher VIEs than 6.4 eV based on the calculations. The same trend of VIEs for Al_mC_n clusters found through theoretical calculations is observed in the experiment; this indicates that the predicted structures of the calculated clusters can be believable, and further, that their calculated formation mechanisms and chemical reactivity can be realistically explored through a similar level of theory. Thus, the experimental data yield not only which clusters are observed, but also present an observed parameter (VIE) to be compared to theory for its validation.

Aluminum and carbon atoms have 13 and 6 electrons, respectively. The valence electron configurations of neutral Al_mC_n clusters thus change from closed to open shell with even and odd number of Al atoms in the clusters. In general, closed shell clusters (Al_2C_2, Al_4C_2, and Al_6C_2) have higher ionization energies than open shell clusters (Al_3C_2 and Al_5C_2). This is a reasonable explanation for the VIE variation with the number of Al atoms in neutral Al_mC_2 (m = 2, 3, 4, 5, 6) clusters (Figure 11.9), and for no detection of all neutral Al_mC_n clusters with an even number of Al atoms ($Al_{2m}C_n$ - Al_2C_n, Al_4C_n, Al_6C_n) by 193 nm laser SPI. On the other hand, not all of the open shell clusters $Al_{2m+1}C_n$ are detected in the experiments with 193 nm laser SPI. For example, we detect $Al_3C_{2,4...}$ but not $Al_3C_{1\ 3...}$ clusters, and detected $Al_5C_{1,3...,}$ but not $Al_5C_{2,4...}$clusters. Thereby, the

ionization energies of the Al_mC_n clusters do not simply depend on open or closed shell valence electron configurations, but VIEs also depend on the electric structure details of the clusters.

In order to understand the properties of neutral Al_mC_n clusters, we carry out DFT calculations to investigate the highest occupied molecular orbitals for a series of Al_mC_2 (m = 2, 3, 4, 5, 6) clusters. Through analysis of the molecular orbitals of the clusters (Figure 11.10), one can find that the HOMOs for open shell clusters Al_3C_2, Al_3C_3, and Al_5C_2 with relative lower ionization energies process an antibonding π orbital character, and the HOMOs for closed shell clusters Al_2C_2, Al_4C_2, and Al_6C_2 with high ionization energies are characterized by σ or π bonding orbitals. Antibonding orbitals have relatively high orbital energy in general, and more easily lose an electron compared to a comparable bonding orbital. The calculatoional results are in good agreement with our experimental observations that Al_2C_2, Al_2C_4, and Al_2C_6 clusters cannot be detected by SPI of 193nm laser. Additionally, Al_3C_2, Al_3C_3, and Al_5C_2 are both open shell systems, but only Al_3C_2 is detected by the 193 nm laser. If one compares the HOMOs of Al_5C_2 and Al_3C_3 with that of Al_3C_2 (Figure 11.10), one finds that the HOMOs for Al_5C_2 and Al_3C_3 clusters are described not only by a C=C antibonding π orbital but also by a lone pair orbital from Al atoms, while a pure C=C antibonding π orbital is the major component of the Al_3C_2 cluster HOMO. This is why the Al_5C_2 and Al_3C_3 cluster have slightly higher VIEs than the Al_3C_2 cluster and cannot be detected by 193 nm SPI (Figure 11.1).

11.5.2 $Al_mC_nH_x$ clusters

$Al_mC_nH_x$ clusters are generated by ablation of pure Al foil into a mixture of hydrocarbon/He expansion gas. Under this condition, aluminum metal vapor created by

laser ablation reacts with hydrocarbon compounds in the ablation source, and then $Al_mC_nH_x$ clusters are formed during a supersonic expansion and cooling processes. This method is used to generated pure metal carbide clusters for less reactive, later transition metals or main group metals (Ni, Co, W, Ag, Cu, Bi, Sb).[11.35,11.36] The distribution of the $Al_mC_nH_x$ clusters detected by the 193 nm laser is presented in the mass spectra of Figure 11.2. Only clusters with odd mass numbers are observed, for example, $Al_2C_2H_{1,3,5...}$, $Al_2C_3H_{1,3,5...}$, $Al_2C_4H_{1,3,5...}$, $Al_4C_3H_{1,3,5...}$, $Al_3C_2H_{2,4,6}$, $Al_3C_3H_{2,4,6}$, $Al_3C_4H_{2,4,6...}$, etc. Single photon energy of a 118 nm, 10.5 eV laser is sufficient to ionize most neutral metal compound clusters near threshold without leaving enough excess energy in the clusters to fragment the original neutral clusters.[11.25] If a 118 nm laser is used for ionization, all $Al_mC_nH_x$ clusters with even and odd mass numbers are detected as shown in Figure 11.5, indicating that all $Al_mC_nH_x$ clusters are generated under the present experimental conditions. Therefore, some $Al_mC_nH_x$ clusters must have higher ionization energies than the single photon energy of 193 nm light, resulting in the absence of these clusters in the 193 nm generated mass spectra. As we discussed above, the closed shell Al_mC_n clusters, such as Al_2C_m, Al_4C_m, etc. have high ionization energies, and they cannot be ionized by 193 nm SPI (Figure 11.1). The hydrogen containing clusters $Al_2C_2H_{1,3,5...}$, $Al_2C_3H_{1,3,5...}$ and $Al_4C_3H_{1,3,5...}$with an odd number of H atoms are detected, while clusters $Al_2C_2H_{2,4,6...}$, $Al_2C_3H_{2,4,6...}$ and $Al_4C_3H_{2,4,6...}$with an even number of H atoms are not detected by 193 nm SPI (Figure 11.2-11.5). Adding an odd number of H atoms to closed shell $Al_{2m}C_n$ clusters changes these clusters from closed shell to open shell electronic configurations, and thereby the ionization energies of these clusters can be below 6.4 eV. Open shell clusters $Al_3C_{2,4,6...}$ are detected by 193 nm SPI, $Al_3C_2H_{1,3,5}$ and $Al_3C_4H_{1,3,5}$ clusters with

odd number of H atoms are not detected at this ionization energy, while $Al_3C_2H_{2,4,6...}$ and $Al_3C_4H_{2,4,6...}$ clusters are detected. Adding an odd number of H atoms to the open shell clusters $Al_3C_{2,4,6...}$, changes their electronic structure from open shell to closed shell configurations, increasing the ionization energies of these clusters above 6.4 eV. Additionally, the open shell cluster Al_3C_3 (VIE=7.1 eV) is not detected by 6.4 eV SPI, but hydrogen containing open shell clusters $Al_3C_3H_{2,4,8...}$ are detected by 6.4 eV SPI (see Figure 11.2-11.5): adding an even number of H atoms to these open shell clusters must change their electronic structures sufficiently to lower their VIEs below 6.4 eV.

Theoretical calculations are preformed to investigate the structures of $Al_2C_2H_x$ clusters at the B3LYP/6-311+G* theory level. As shown in Figure 11.11, the hydrogen containing clusters $Al_2C_2H_{1-4}$ are not saturated by H atoms, and the lowest energy isomers for these clusters are similar to unsaturated hydrocarbons. In these structures, H atoms bond to either C or Al atoms with little difference in energy. For example, the lowest energy isomer Al_2C_2H**_a**, in which the H atom binds to a C atom, is 0.07 eV lower in energy than isomer Al_2C_2H**_b**, in which the H atom binds to an Al atom. The lowest energy isomer $Al_2C_2H_3$ **_a** formed by two H atoms binding to one Al atom and one H binding to a C atom is 0.05 eV lower in energy than isomer $Al_2C_2H_2$**_b** formed by binding three H atoms to two Al atoms. Isomer $Al_2C_2H_4$ **_a** and $Al_2C_2H_4$ **_b** have almost the same energy for the four H atoms bonded to either Al or C. This fact can account for the general richness of different structures for these $Al_mC_nH_x$ clusters. Clusters $Al_2C_2H_8$ have a saturated structure, like hydrocarbons C_nH_{2n+2}, for hydrogen containing $Al_mC_nH_x$ clusters with classical Al-H and C-H bonds.

Experiments show that clusters containing more than 8 hydrogen atoms, such as

$Al_2C_2H_{9,11}$ (193 nm ionization experiment, Figures 11.2 and 11.3) and $Al_2C_2H_{9\text{-}12}$ (118 nm ionization experiment, Figure 11.5) are readily identified in the mass spectra, indicating that hydrogen containing clusters $Al_2C_2H_{9\text{-}12}$ are generated under the present experimental condition. This observation suggests that H_2 molecules can possibly be adsorbed on $Al_mC_n/Al_mC_nH_x$ clusters through chemisorptions, causing more hydrogen to be associated with the clusters than can be accounted for by a saturated classical chemical bond structure. Recently, Durgun et al.[11.37-11.39] calculated H_2 adsorption on a transition metal-ethylene $C_2H_4M_2$ (TM-ethylene) complex, in which two metal atoms are bonded to a C=C through a bridge structures. They found that, based on calculation, up to 12 H_2 molecules can be adsorbed around the $C_2H_4Ti_2$ complex: up to ~ 14% hydrogen storage for this complex. We can not identify $Al_mC_nH_x$ clusters containing more than 12 H atoms in the mass spectra, since the mass number of carbon is 12.

To understand the effect of H atoms on the ionization energies of aluminum carbon hydride clusters, we perform *ab inito* calculations to study the VIEs at the MP2/6-311+G* theory level. As plotted in Figure 11.12, the VIEs of $Al_2C_2H_x$ clusters change with the number of H atoms. The Al_2C_2H (VIE = 6.3 eV) and $Al_2C_2H_3$ (VIE = 7.0 eV) clusters, detected in the 193 nm ionization experiment, have low ionization energies (ca. 6.4 eV), based on the calculations, while the clusters Al_2C_2 (VIE = 8.1 eV), $Al_2C_2H_2$ (VIE = 8.7 eV), and $Al_2C_2H_4$ (VIE = 10.3 eV) have obviously higher ionization energies than 6.4 eV. These calculational results are in a good agreement with the experimental observations, indicating that predicted structures of the calculated $Al_mC_nH_x$ clusters are quite reasonable.

The HOMOs for $Al_2C_2H_x$ clusters are calculated at the B3LYP/6-311+G* level, as

shown in Figure 11.13. HOMOs for open shell clusters Al_2C_2H and $Al_2C_2H_3$ are antibonding π orbitals characteristic of a C=C moiety interacting with H and Al atoms, HOMOs for the closed shell clusters Al_2C_2, $Al_2C_2H_2$, and $Al_2C_2H_4$ are characterized as either bonding σ and lone pair orbitals of the Al atom or bonding π orbitals of the C=C atoms. The number of H atoms in the clusters switches the HOMOs of the $Al_2C_2H_x$ between closed shell and open shell systems, leading to VIE alternation with even-odd numbers of H atoms in the clusters. Additionally, open shell Al_3C_2 cluster (VIE = 6.4 eV) are detected in the SPI of 193 nm experiment due to them relatively low VIE. Adding one H to the Al_3C_2 cluster yields closed shell cluster (Al_3C_2H) with VIE about 7.5 eV, add two H atoms to Al_3C_2 yields $Al_2C_2H_2$ with a VIE of 7.5 eV. The HOMOs of $Al_3C_2H_{0,1,2}$ change with the number of H atoms as shown in Figure 11.13. The calculational results of HOMOs of the $Al_mC_nH_x$ cluster give us in-depth understanding of our experimental observations.

11.5.3 Synthetic Reaction Mechanisms for Al_mC_n and $Al_mC_nH_x$

The mechanism for $Al_mC_nH_x$ cluster formation is very complicated in the ablation/expansion source. As discussed in the experimental section, by using method (1), Al atoms generated from ablation of Al foil can react with hydrocarbons in the expansion gas to form $Al_mC_nH_x$ clusters in the ablation/expansion source. This hydrocarbon plasma reaction synthetic method is also the most efficient source for generation of pure metal carbide clusters for reactive early transition metals (Ti, V, Zr, Nb, Hf, Cr, Mo, Fe).[11.1-11.3,11.40] A mechanism can be suggested for M_mC_n cluster generation: the ablated M_m species and ensuing plasma can interact with (and heat) C_xH_y molecules to form C_z and H species which can react with M_m species in the plasma. Metal carbide clusters M_mC_n are

formed by the reaction of metal and carbon atoms/carbon clusters during the expansion and cooling processes.[11.40] In the present experiments, many hydrogen containing aluminum carbon clusters are generated by using the hydrocarbon plasma reaction synthetic method. These experimental observations of $Al_mC_nH_x$ cluster generation are different from those for most transition metals reacting with hydrocarbon under similar experimental conditions. Only M_mC_n clusters are generated for these other transition metals.[11.1-11.3,11.40] For $Al_mC_nH_x$ cluster generation, we suggest that Al_mC_n clusters are formed through reactions between Al atoms/clusters and C atoms/clusters first, and then Al_mC_n clusters react with H atoms/molecules to form $Al_mC_nH_x$ clusters during the ablation, expansion, and cooling processes. H atoms and H_2 molecules are generated from dehydrogenation of hydrocarbons by aluminum metal vapor and plasma at high temperature, in the ablation source. (See blow for more discussion of Al_mC_n reacting with H_2).

In another experiment using method (2) above, Al and C atoms and clusters are generated by ablation of a mixed Al/C target to form Al_mC_n clusters that then react with H_2 expansion gas in the ablation source. A similar distribution of $Al_mC_nH_x$ clusters to that formed for hydrocarbon plasma reaction method (1) is observed as shown in Figure 11.3. This similarity for final $Al_mC_nH_x$ distribution substantiates the mechanism for $Al_mC_nH_x$ cluster formation suggested above.

One can additionally argue another possible mechanism: Al atoms generated from the ablation of pure Al foil or mixed Al-C target react with H atoms/molecules to form the Al_mH_n clusters for a first step, and then the Al_mH_n clusters react with C or C_m to form $Al_mC_nH_x$ clusters. In order to explore this mechanism, we use pure Al foil as the ablation

target and pure H_2 or mixed H_2/He gas as the expansion gas to generate Al_mH_x clusters; however, only pure Al_n clusters are observed in the mass spectrum by using 193nm laser SPI, except for a very few signals of aluminum hydride clusters such as $Al_3H_{1\text{-}3}$ and $Al_8H_{1,2}$. Pure aluminum clusters can also be generated through ablating pure Al foil into pure He expansion gas. The distributions of Al_n clusters generated with the two expansion gases methods are almost the same, indicating that H_2 molecules are stable in reactions with Al atoms and clusters, even at the high temperature conditions in the ablation source. Recently, Bowen and co-workers studied aluminum hydride clusters by using a pulsed arc cluster ionization source (PACIS).[11.41,11.42] A broader series of Al_mH_x clusters are generated in their experiments. They found that H_2 molecules are not very reactive toward Al atoms and clusters in a traditional ablation/expansion source, in agreement with our experimental observations. Therefore, the reaction mechanism forming Al_mH_x clusters first in the ablation source and then $Al_mC_nH_x$ clusters is not a reasonable one for $Al_mC_nH_x$ cluster formation under our experimental conditions.

To explore the mechanism for $Al_mC_nH_x$ cluster formation further, we design another experiment in which Al_mC_n clusters are generated by ablating a mixed Al/C target into He expansion gas first (method 3), and then react with H_2 molecules in a fast flow reactor. As shown in Figure 11.4, many new hydrogen containing clusters, $Al_mC_nH_x$, are observed if H_2 gas is added into the reactor. One finds $Al_mC_nH_x$ clusters with fewer hydrogen atoms generated by using method (3) compared to those generated by using methods (1) and (2). The reason is that in the fast flow reactor, the reactions occur at lower temperature, and fewer collisions occur between Al_mC_n and H_2 molecules relative to the reactions occurring in the ablation/expansion source. On the basis of our calculations,

hydrogenation reactions for Al_2C_2 and H_2 molecules are thermodynamically favorable without barrier. For example,

$$Al_2C_2 + H_2 \rightarrow Al_2C_2H_2 \text{ (isomer } \mathbf{a}) \qquad \Delta H = -0.94 \text{ eV} \qquad (11.1)$$

$$Al_2C_2H_2 + H_2 \rightarrow Al_2C_2H_4 \text{ (isomer } \mathbf{a}) \qquad \Delta H = -1.0 \text{ eV} \qquad (11.2)$$

Therefore, $Al_mC_nH_x$ clusters can be generated by reactions between Al_mC_n clusters and H_2 molecules. On the other hand, energies required for dehydrogenation reactions of $Al_mC_nH_x$ are about 1.0 and 2.0 eV for removing one and two H_2 molecules, respectively, for covalently bonded H atoms in the clusters. Note that the most stable structures for small Al_mC_n clusters have linear geometries with unsaturated C-C bonds and not cubic frame structures (Figures 11.7 and 11.8) based on our calculational results. These linear, multiple C-C bonded structures enable Al_mC_n cluster reactions with hydrogens to form $Al_mC_nH_x$ clusters.

Based on the present studies, $Al_mC_nH_x$ clusters can be a potential material for hydrogen storage. Hydrogen is an ideal clean fuel for storage, transport, and conversion of energy. A design target for automobile fueling has been set by the U. S. Department of Energy at 6.5 % hydrogen by weight. Recently, intensive research has been initiated on complex aluminum hydrides $M_mAl_nH_x$ (M=Li, Na, Mg, B, Ti, Zr) for hydrogen storage since these compounds have high hydrogen storage capacity (10.54% wt H for $LiAlH_4$, 7.41% wt H for $NaAlH_4$), low cost, and availability in bulk.[11.24,11.43-11.47] $Al_mC_nH_x$ clusters also have a high percentage of hydrogen by weight: for example, 13.3% H for a $Al_2C_2H_{12}$ cluster and 10.25% H for an $Al_3C_2H_{12}$ cluster. Additionally, H atoms can bond with either Al or C atoms in these clusters with little energy difference for the various possible cluster isomers. Hydrocarbons have high hydrogen content, but they are not

good materials for hydrogen fuel storage since high energy is required to release H_2 from them due to their C-H bond strength (104 kcal/mol for CH_4, and 125 kcal/mol for C_2H_4). The Al-H bond strength (68 kcal/mol[11.34,11.48]) is much weaker than the C-H bond strength and thus less energy is required for dehydrogenation of $Al_mC_nH_x$ clusters than for C_xH_y molecules. Additionally, through the reaction $Al_m + C_nH_y \rightarrow Al_mC_nH_y \rightarrow y/2\ H_2 + Al_mC_n$, H_2 fuel is non polluting compare to a C_xH_y fuel.

11.6 CONCLUSIONS

Neutral aluminum carbide clusters Al_mC_n are generated in an ablation/expansion source through ablating a mixed Al-C target. In the experiments, we find that only some Al_mC_n clusters with odd mass numbers can be ionized by a 193 nm laser through single photon ionization, while all neutral Al_mC_n clusters are detected using a 46.9 nm laser for single photon ionization. Based on our DFT calculations, the VIEs of Al_mC_2 (m=2, 3, 4, 5, 6) clusters change with odd-even numbers of Al atoms because the electronic structures of the clusters change from open shell to closed shell configurations, respectively. The open shell clusters Al_3C_2 (6.3 eV) and Al_5C_2 (6.6 eV) have lower ionization energies (near the photon energy 6.4 eV), while closed shell clusters Al_2C_2 (VIE = 8.1 eV), Al_4C_2 (VIE = 7.6 eV), Al_6C_2 (VIE = 7.6 eV) have higher ionization energies. The calculation results are in good agreement with experimental observation in that Al_2C_2, Al_4C_2, and Al_6C_2 are not detected in the 193 nm ionization experiment. Theory and experiment agree on the major observation, indicating that predicted geometrical and orbital structures for the calculated Al_mC_n and $Al_mC_nH_x$ clusters are most likely correct. HOMOs for the closed shell clusters Al_2C_2, Al_4C_2, and Al_6C_2 are characterized as bonding π or σ orbitals, and HOMOs for the open shell clusters Al_3C_2, Al_3C_3, and Al_5C_2 are composed of antibonding π orbitials.

Additionally, in contrast with other transition metal carbides, the lowest energy structures of small neutral Al_mC_n clusters are characterized by the formation of C=C bonds, due to the relatively low energy of the Al-C bond.

Neutral aluminum carbon hydride clusters $Al_mC_nH_x$ can be generated through hydrocarbon plasma reactions, in which pure Al is used for the ablation target and hydrocarbons CH_4, C_2H_4 and C_2H_6 are used for the expansion gas. In the experiments, only clusters with odd mass numbers are observed in the mass spectrum using a 193 nm laser for SPI, while all $Al_mC_nH_x$ clusters are detected in the 118 nm laser SPI experiment. Based on calculations for neutral $Al_2C_2H_x$ (x = 0, 1, 2, 3, 4) clusters, the cluster VIEs change with the number of H atoms, because adding an H atom changes the electronic configuration of the clusters from open shell to closed shell or vice versa. HOMOs for open shell clusters Al_2C_2H and $Al_2C_2H_3$, with low ionization energies, are obviously antibonding π orbitals, and HOMOs for closed shell clusters Al_2C_2, $Al_2C_2H_2$, $Al_2C_2H_4$, with high ionization energies, are bonding π or σ orbitals. These calculation results are in good agreement with experimental observations that Al_2C_2H and $Al_2C_2H_3$ clusters, but not Al_2C_2, $Al_2C_2H_2$, $Al_2C_2H_4$ clusters, can be ionized and detected by 193 nm laser SPI. Based on experimental and theoretical studies, the formation mechanism for aluminum carbon hydride clusters is suggested to be that Al_mC_n clusters are formed first, and then react with H atoms or H_2 molecules to form $Al_mC_nH_x$ clusters in the ablation/expansion source. Calculations indicate that the lowest energy structures for $Al_2C_2H_x$ clusters can be formed by bonding H atoms either to C or Al atoms without a large difference in energy.

REFERENCES

[11.1] (a) Guo, B. C.; Kerns, K. P.; Castleman, A. W., Jr. *Science*, **1992**, *255*, 1411. (b) Guo, B. C.; Wei, S.; Purnell, J.; Buzza, S.; Castleman, A. W., Jr. *Science*, **1992**, *256*, 515. (c) Wei, S.; Guo, B. C.; Purnell, J.; Buzza, S., Castleman, A. W., Jr. *Science*, **1992**, *256*, 818.

[11.2] (a) Cartier, S. F.; May, B. D.; Castleman, A. W., Jr. *J. Am. Chem. Soc.* **1994**, *116*, 5295. (b) Cartier, S. F.; May, B. D.; Castleman, A. W., Jr. *J. Chem. Phys.* **1994**, *100*, 5384. (c) Wei, S.; Guo, B. C.; Deng, H. T.; Kerns, K.; Purnell, J.; Buzza, S.; Castleman, A. W., Jr. *J. Am. Chem. Soc.* **1994**, *116*, 4475-4476. (d) Pilgrim, J. S.; Duncan, M.A. *J. Am. Chem. Soc.* **1993**, *115*, 9724. (e) Yeh, C. S.; Byun, Y. G.; Afzaal, S.; Kan, S. Z.; Lee, S.; Freiser, B. S.; Hay, P. J. *J. Am. Chem. Soc.* **1995**, *117*, 4042-4048. (f) Pilgrim, J. S.; Duncan, M. A. *J. Am. Chem. Soc.* **1993**, *115*, 6958-6961. (f) Li, S.; Wu, H.; Wang, L.-S. *J. Am. Chem. Soc.* **1997**, *119*, 7417-7422.

[11.3] Rohmer, M. M.; Benard, M. Poblet, J. M. *Chem. Rev.* **2000**, *100*, 495.

[11.4] (a) Tono, K.; Terasaki, A.; Ohta, T.; Kondow, T. *J. Chem. Phys.* **2002**, *117*, 7010. (b)Yamada, Y.; Castleman, A. W., Jr. *Chem. Phys. Lett.* **1993**, *204*, 133-138.

[11.5] Reddic, J. E.; Duncan, M. A. *Chem. Phys. Lett.* **1997**, *264*, 157.

[11.6] Boldyrev, A. I.; Sinons, J. *J. Phys. Chem. A* **1997**, *101*, 2215.

[11.7] Knappenberger, K. L. Jr.; Jones, C. E. Jr.; Sobny, M. A.; Iordanov, I.; Sofo, J. Castleman, A. W. Jr. *J. Phys. Chem. A* **2006**, *110*, 12814.

[11.8] Jin, C.; Haufler, R. E.; Hettich, R. L., Barshick, C. M.; Compton, R. N.; Puretzky, A. A.; Demyanenko, A. V.; Tuinman, A. A. *Science*, **1994**, *263*, 68.

[11.9] He, S. G.; Xie, Y.; Dong, F.; Bernstein, E. R. *J. Chem. Phys.* **2006**, *125*, 164306.

[11.10] Brock, L. R.; Duncan, M. A. *J. Phys. Chem.* **1996**, *100*, 5654.

[11.11] Pacheco, J. M.; Gueorguiev, G. V. *Phys. Rev. B.* **2003**, *68*, 241401(R).

[11.12] Heaven, M. W.; Stewart, G. M.; Buntine, M. A.; Metha, G. F. *J. Phys. Chem. A* **2000**, *104*, 3308.

[11.13] (a) Dryza, V.; Addicoat, M. A.; Gascooke, J. R.; Buntine, M. A.; Metha, G. F. *J. Phys. Chem. A* **2008**, *112*, 5582. (b) Dryza, V.; Addicoat, M. A.; Gascooke, J. R.; Buntine, M. A.; Metha, G. F. *J. Phys. Chem. A* **2005**, *109*, 11180.

[11.14] Wang, L. S.; Cheng, H. S. *Phys. Rev. Lett.* **1997**, *78*, 2983.

[11.15] Wang, L. S.; Wang, X. B.; Wu, H. B.; Cheng, H. *J. Am. Chem. Soc.* **1998**, *120*, 6556.

[11.16] Ticknor, B. W.; Bandyopadhyay, B.; Duncan, M. A. *J. Phys. Chem. A* **2008**, published on web.

[11.17] Boldyrev, A. I.; Simons, J.; Li, X.; Wang, L. S. J. *Am. Chem. Soc.* **1999**, *121*, 10193.

[11.18] Li, X.; Wang, L. S.; Boldyrev, A. I.; Simons, J. *J. Am. Chem. Soc.* **1999**, *121*, 6033.

[11.19] Cannon, N.; Boldyrev, A. I.; Li, X.; Wang, L. S. *J. Chem. Phys.* **2000**, *113*, 2671.

[11.20] Li, X.; Wang, L. S.; Cannon, N.; Boldyrev, A. I. *J. Chem. Phys.* **2002**, *116*, 1330.

[11.21] (a) Boldyrev, A. I.; Simons, J.; Li, X.; Chen, W.; Wang, L. S. *J. Chem. Phys.* **1999**, *110*, 8980. (b) Zubarev, D. Y.; Boldyrev, A. I. *J. Chem. Phys.* **2005**, *122*, 144322.

[11.22] Boldyrev, A. I.; Simons, J.; Li, X.; Wang, L. S. *J. Chem. Phys.* **1999**, *111*, 4993.

[11.23] Naumkin, F. Y. *J. Phys. Chem. A* **2008**, *112*, 4660.

[11.24] Zhao, Ji-Cheng; Knight, D. A;. Brown, G. M.; Kim, C.; Hwang, Son-Jong; Reiter J. W.; Bowman, R. C. Jr; Zan, J. A.; Kulleck, J. G. *J. Phys. Chem. C*, **2009**, *113*, 2. (b) Zuttel, A. *Naturwissenschaffen*, **2004**, *91*, 157.

[11.25] (a) Dong, F.; Heinbuch, S.; Xie, Y.; Bernstein, E. R.; Rocca, J. J.; Wang, Z. C. Ding, X. L.; He, S. G. *J. Am. Chem. Soc.* **2009**, *131*, 1507. (b) Dong, F.; Heinbuch, S.; Xie, Y.; Rocca, J. J.; Bernstein, E. R.; Wang, Z. C. Deng, K.; He, S. G. *J. Am. Chem. Soc.* **2008**, *130*, 1932. (b) (c) Dong,F.; Heinbuch, S.; Rocca, J. J.; Bernstein, E. R. *J. Chem. Phys.* **2006**, *125*, 164318.

[11.26] (a) Heinbuch, S.; Grisham, M.; Martz, D.; Rocca, J. *J. Opt. Express*, **2005**, *13*, 4050.; (b) Rocca, J. J.; Shlyaptsev, V. N.; Tomasel, F. G.; Cortazar, O. D.; Hartshorn, D.; Chilla, J. L. A.; *Phys. Rev. Lett.* **1994**, *73*, 2192; (c) Rocca, J. J. *Rev. Sci. Instrum.* **1999**, *70*, 3799.

[11.27] Frisch, M. J.; et al. *Gaussian 03, Revision C.02, Gaussian*, Inc, Wallingford CT, **2004**.

[11.28] (a) Becke, A. D. *Phys. Rev. A* **1988**, *38*, 3098. (b) Becke, A. D. *J. Chem. Phys.***1993**, *98,* 5648. (c) Lee, C. T.; Yang, W. T.; Parr, R. G. *Phys. Rev. B* **1988**, *37*, 785.

[11.29] (a) McLean, A. D.; Chandler, G. S. *J. Chem. Phys.* **1980**, *72*, 5639. (b) Clark, T.; Chandrasekhar, J.; Spitznagel, G. W.; Schleyer, P. v. R. *J. Comput. Chem.* **1983**, *4*, 294. (c) Frisch, M. J.; Pople, J. A.; Binkley, J. S. *J. Chem. Phys.* **1984**, *80*, 3265 1984.

[11.30] Krishnan, R.; Binkley, J. S.; Seeger, R.; Pople, J. A. *J. Chem. Phys.* **1980**, *72*,

650.

[11.31] Largo, A.; Redondo, P.; Barrientos, C. *J. Phys. Chem. A* **2002**, *106*, 4217.

[11.32] Li, G. L.; Tang, Z. *J. Phys. Chem. A* **2003**, *107*, 5317.

[11.33] (a) Dong,F.; Heinbuch, S.; Rocca, J. J.; Bernstein, E. R. *J. Chem. Phys.* **2006**, *124*, 224319. (b) Dong,F.; Heinbuch, S.; Rocca, J. J.; Bernstein, E. R. *J. Chem. Phys*. **2006**, *125*, 154317. (c) Heinbuch, S.; Dong,F.; Rocca, J. J.; Bernstein, E. R. *J. Chem. Phys*. **2006**, *125*, 154316. (d) Heinbuch, S.; Dong,F.; Rocca, J. J.; Bernstein, E. R. *J. Chem. Phys*. **2007**, *126*, 244301.

[11.34] Robert, C. W.; Melvin J. A. CRC hand book of chemistry and Physics 62nd, CRC Press, Inc. **1981-1982**.

[11.35] Reddic, J. E.; Duncan, M. A. *Chem. Phys. Lett.* **1997**, *264*, 157.

[11.36] Schultz, N. E.; Staszewska, G.; Staszewski, P.; Truhlar, D. J. *J. Phys. Chem. B* **2004**, *108*, 4850.

[11.37] Durgun, E.; Ciraci, S.; Zhou, W.; Yildirim, T. *Phys. Rev. Lett.* **2006**, *97*, 226102.

[11.38] Zhou, W.; Yildirim, T.; Durgun, E.; Ciraci, S. *Phys. Rev. B* **2007**, *76*, 085434.

[11.39] Akman, N. Durgun, E.; Yildirim, T.; Ciraci, S. *J. Phys: Condens. Matter* **2006**, *18*, 9509.

[11.40] Guo, B. C.; Wei, S.; Chen, Z.; Kerns, K. P.; Purnell, J.; Buzza, S.; Castleman, A. W., Jr. *J. Chem. Phys.* **1992**, *97*, 5243.

[11.41] Li, X.; Grubisic, A.; Stoker, S. T.; Cordes, J.; Gantefor, G. F.; Bowen, K, H.; Kiran, B.; Willis, M.; Jena, P.; Burgert, R.; Schnockel, H. *Science* **2007**, *315*, 356.

[11.42] Grubisic, A.; Li, X.; Stoker, S. T.; Cordes, J.; Gantefor, G. F.; Bowen, K, H.;

Kiran, B.; Jena, P.; Burgert, R.; Schnockel, H. *J. Am. Chem. Soc.* **2007**, *129*, 5969.

[11.43] Felderhoff, M.; Weidenthaler, C.; von Helmolt, R.; Rberle, U. *Phys Chem Chem Phys*, **2007**, *9*, 2643.

[11.44] Orimo, S.; Nakamori, N.; Rliseo, J.; R. Zuttel, A.; Jensen, C. M. *Chem. Rev.* **2007**, *107*, 4111.

[11.45] Sakintuna, B.; Lamari-Darkrim, F. Hirscher, M. *Internal J. Hydrogen Energy* **2007**, *32*, 1121.

[11.46] van den Berg, A. W. C.; Arean, C. O. *Chem. Commun.* **2008**, *668*.

[11.47] Fichtner, M.; Engel, J.; Fuhr, O.; Kircher, O.; Rubner, O. M*aterials Science and Engineering B* **2004**, *108*, 42.

[11.48] Chase, M. W., Jr., NIST-JANAF Themochemical Tables, Fourth Edition, J. *Phys. Chem. Ref. Data*, Monograph 9, **1998**, 1-1951.

Chapter 12

Conclusions

We have employed single photon ionization mass spectrometry to study several cluster systems and their products. To conduct this work we developed a new type of photoionization source consisting of a desk-top size capillary discharge laser that emits 10 μJ pulses of 26.5 eV photons. The work made use of this experimental technique and DFT calculations to discover cluster geometries and properties. The research was in part motivated by the need for a better understanding of molecular level mechanisms for catalytic reactions.

The cluster mass spectrometry setup made use, for the first time, of a single-photon ionization source consisting of a desk-top size soft x-ray (SXR) laser excited by a capillary discharge. The high photon energy of the SXR laser allows access to study clusters with high ionization energies. The 46.9 nm (26.5 eV/photon) laser ionizes clusters by single photon transitions preventing multi-photon absorption and subsequent cluster fragmentation. Also, the SXR laser aids us with the detection of small molecule reaction products with high ionization energies.

Single photon ionization with 26.5 eV photons is shown to be an excellent diagnostic for neutral cluster distribution in general, including all varieties of clusters from van der

Waals, to hydrogen bonded, metal, and covalent metal oxide systems. During the ionization process(es) nearly all the excess energy above the VIE of the cluster is removed by the exiting photoelectron. Where possible a comparison between 10.5 and 26.5 eV ionization is made to show that the results of both methods of ionization are nearly identical, except, the 26.5 eV ionization is capable of finding all species present in the sample with ionization energies above 10.5 eV. Most importantly this ionization approach has found oxygen rich clusters and oxygen rich clusters with added hydrogen that have not previously been identified for laser ablation metal oxide clusters.

In more advanced experiments, many association reaction intermediates as well as catalytic reaction products have been observed. At the molecular level, the importance of catalyst supports is considered to be at least associated with cooling of the active site based on observations of gas phase reactivity for pick up cell (high temperature) and fast flow reactor (low temperature) experiments. Results of the present gas phase studies provide new ideas/mechanisms, such as intermediates (SO, $V_mO_nSO_2$) and oxidation of the intermediates, that may be observed and checked in investigations of the condensed phase systems. Similarly, results involving the SCR (Selective Catalytic Reduction) of NO using NH_3, nonreactive species for use as capping layers for EUV optics, and cluster structures for suggested hydrogen storage materials have been achieved.

A long term goal of the project is to develop a quantum mechanical (potential energy surface), mechanistic, atomic level understanding of heterogeneous reaction rate enhancement of gas phase reactions by the bulk and surface condensed phase for many other systems. The versatility of the experimental approach demonstrated here allows for

new studies to be conducted by simply changing the sample or reactant, leaving a great number of possibilities for the experimenter to explore.

Future work involving new systems and the use of photoelectron spectroscopy can result in a more detailed understanding of the mechanism for removal of the excess ionization energy (26.5 – VIE) eV from the cluster by photoelectron emission. Photoelectron spectroscopy studies can also further increase the understanding of the ionization mechanisms and dynamics of clusters.

Appendix A

Design and operation characteristics of a high repetition rate desk-top size 46.9 nm capillary discharge laser

In this Appendix, the design and demonstration of a desk-top size high repetition rate capillary discharge-pumped soft x-ray laser is covered. The laser was developed with the objective of realizing a high repetition rate single-photon photoionization source for photochemistry applications, an application discussed in Dissertation. The first section focuses mainly on the compact desk-top design and the discharge parameters required for operation of the laser. The remaining sections will present the measurements taken to characterize the operation of the laser at repetition rates up to 12 Hz. Observations on the lifetime of the capillary will also be discussed.

A.1 DESIGN CHARACTERISTICS OF A DESK-TOP SIZE HIGH REPETITION RATE CAPILLARY DISCHARGE-PUMPED SOFT X-RAY LASER

We describe a capillary discharge laser that is significantly more compact and less costly than its predecessors. It is to our knowledge the first soft x-ray laser to fit onto a small desk, and to be easily transportable (Fig. A.1b), and also the first such laser to be installed in a photochemistry lab and used as a photoionization source in time of flight mass spectroscopy (TOFMS) systems. The laser emits >10 μJ pulses of λ= 46.9 nm light at up to 12 Hz repetition rate. It occupies a table area of approximately 0.4 × 0.4 m^2 (0.4 x 0.8 m^2 including

the vacuum pump), smaller than that occupied by many widely used ultraviolet gas lasers. The power supplies and gas handling system can be accommodated in two small racks that

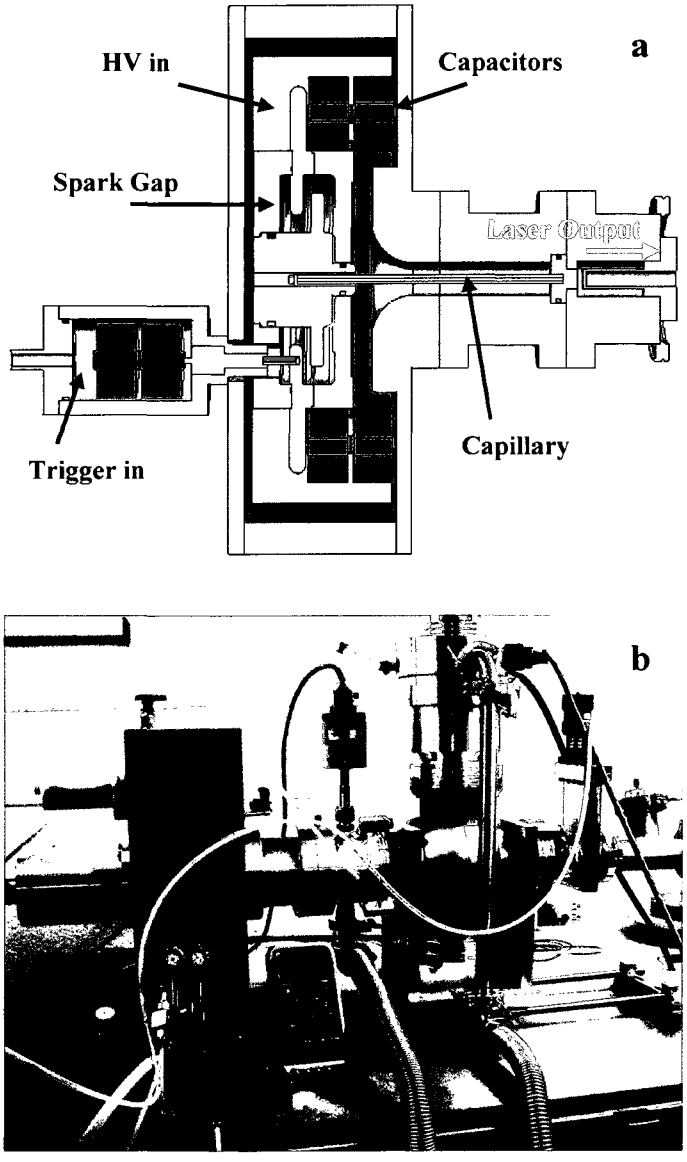


Figure A.1. (a) Schematic representation of the 46.9nm capillary discharge laser. (b) photograph of the laser device. A handheld multimeter is shown to provide a reference of scale.

fit under a standard optical table. The reduced size of this capillary discharge device is achieved making use of a very low inductance co-axial discharge configuration (Fig. A.1a) that decreases the voltage necessary to generate the peak current required for laser

excitation. This allows the excitation of the capillary discharge channel utilizing strontium titanate capacitors, which are charged to moderate voltages (< 90 kV). The reduced voltage eliminates the need of a Marx generator. As a result the volume of the pulsed power unit is ~ 9 times smaller (figure A.2) than that of previous capillary discharge lasers[A.1] and can be accommodated in a small rack under a regular optical table. The result is an extremely compact high repetition rate laser that is easily transportable (Fig. A.1b).

As in the case of the larger size Ne-like Ar 46.9 nm capillary discharge lasers previously demonstrated[A.2, A.7-A.11], laser amplification is generated by fast discharge excitation of an Ar-filled capillary tube. The magnetic force of the current pulse and large thermal pressure gradients near the wall rapidly compress the plasma to form a dense and hot column with a large density of Ne-like ions, with a very high axial uniformity and a length to diameter ratio of the order of 1000:1. Collisional electron impact excitation of the ground state Ne-like ions produces a population inversion between the $3p\ ^1S_0$ and $3s\ ^1P_1$ levels, resulting in amplification at 46.9 nm.[A.6]

Laser amplification is obtained in a plasma column generated in an aluminum-oxide capillary 3.2 mm inside diameter and 21 cm in length filled with pre-ionized Ar gas at an optimized pressure of 700 mTorr. The plasma column is excited by current pulses of $\approx$ 22 kA peak amplitude that are monitored with a Rogowski coil. The excitation current pulse is produced by discharging a set of strontium titanate capacitors with a combined capacitance of 27 nF through a high voltage spark-gap switch pressurized by air (main spark-gap) that is connected in series with the capillary load. The capacitors, which are placed in a ring configuration surrounding the main spark-gap, are pulse-charged to 80-90 kV by a pulsed power unit that is enclosed in a separate box and connected to the laser head with a high

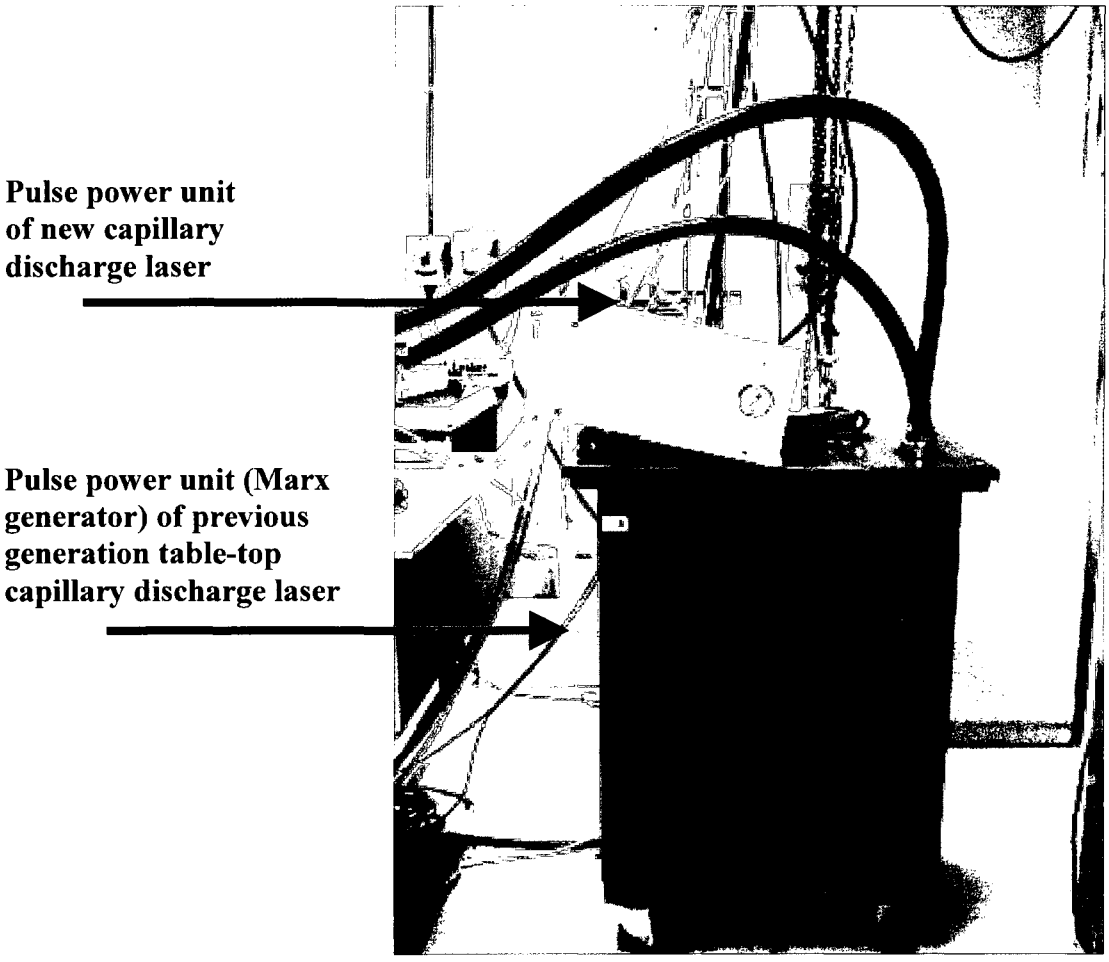


Figure A.2: Size comparison of pulsed power units for new and old capillary discharge lasers. The new pulse power unit is ~ 9 times smaller than the Marx generator.

voltage coaxial cable. A preionization current that is directly applied to the capillary load filled with Ar gas. This current creates a lowly ionized state of the Ar gas and helps to create uniform initial plasma conditions necessary for a stable compression

The main excitation that creates the Ne-like Ar plasma is achieved when the spark-gap shown in Figure A.1a is closed and discharges the ring of ceramic capacitors sending a large current pulse through the capillary load. This main current pulse is initiated by triggering the main spark-gap with a ~ -50 kV pulse applied to the trigger input also shown in Figure A.1a. This allows the synchronization of the laser output with external events with a jitter of

several ns, as required in our specific application to photochemistry experiments. Sub-nanosecond jitter can also be obtained using laser triggering of the spark-gap.[A.12]

A typical current pulse is shown in Fig. 2.4. The pulse has a 0% to 70% rise time of approximately 30 ns, and a first half cycle duration of 165 ns. A pronounced kink in the current is observed to occur about 38 ns after the beginning of the current pulse. This local minima of the current occurs at the time the plasma column reaches its minimum diameter of 200-300 μm, and is caused by the significant increase in the plasma column inductance that accompanies the reduction of the plasma column diameter. The laser pulse of approximately 1.5 ns FWHM duration occurs shortly before the time of maximum plasma compression.

The capillary, the strontium titanate capacitors, and spark-gap are all contained in an Al enclosure that helps to shield the electromagnetic noise produced by the fast discharge. Biodegradable transformer oil is circulated for electrical insulation and also for cooling using a commercially available chiller unit. The laser light exits the cathode electrode that has a hole on axis and that is maintained at ground potential. Argon is continuously flown at the cathode end of the discharge, and is differentially pumped on one side of a 2 mm pinhole by a scroll pump and on the other side of the pinhole by a 360 l/s turbomolecular pump to avoid significant attenuation of the laser beam by photoionization of Ar atoms.

A.2 LASER OUTPUT PULSE ENERGY AND TIMING JITTER MEASUREMENTS

The laser output pulse energy was measured using a vacuum photodiode placed at 80 cm from the exit of the laser and the data were recorded and stored by a 5 Gs/s digitizing oscilloscope. The quantum efficiency of the Al photocathode was previously calibrated with respect to a silicon photodiode of known quantum yield.[A.7] The laser output was attenuated

with several stainless steel meshes of measured transmissivity to avoid saturation of the photodiode. The laser was successfully operated at repetition rates up to 12 Hz. Figure A.5a shows the shot to shot variation of the peak of the excitation current pulse for 1500 consecutive shots at 12 Hz repetition rate. Figure A.5b and Fig A.5c illustrate the corresponding shot to shot variation of the laser output pulse energy as a function of the shot number and its statistical distribution respectively. The average pulse energy is 13 μJ and the standard deviation is 1.3 μJ, corresponding to an average power of about 0.15 mW. The

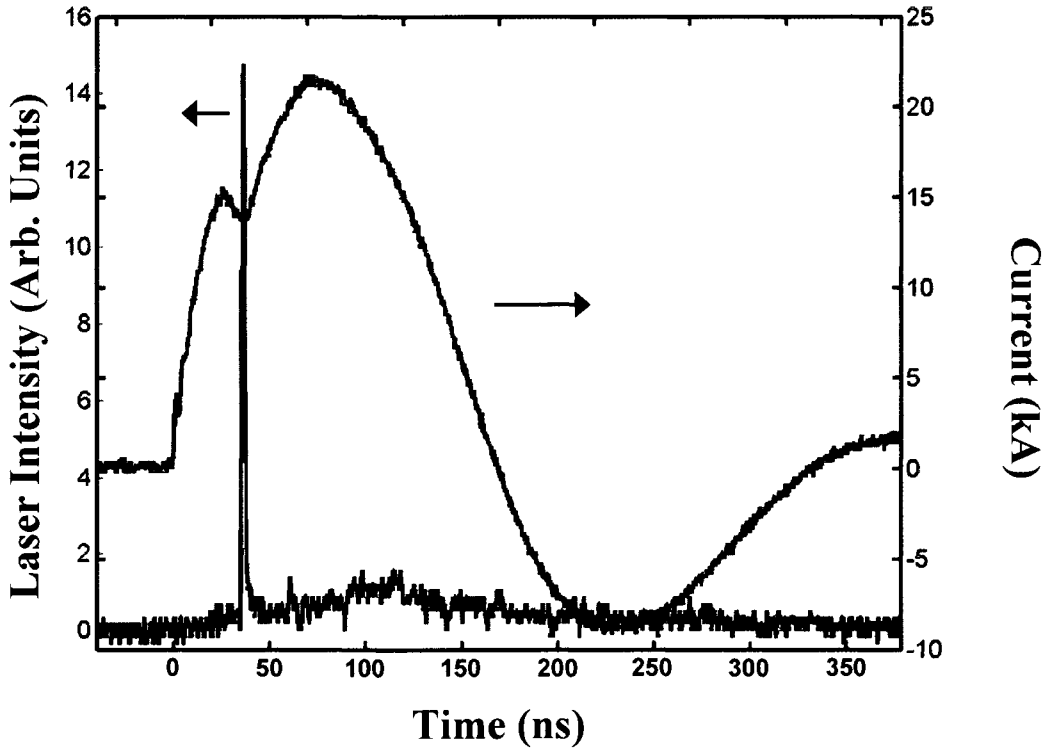


Figure A.4. Discharge current pulse and laser output pulse. The kink in the current trace is caused by the abrupt increase of the plasma column inductance at the time of the pinch.

A.3 OBSERVATIONS ABOUT THE CAPILLARY LIFETIME

Ablation of the capillary walls by the powerful discharge over a large number of shots increases their roughness, ultimately leading to the deterioration of the uniformity of the

plasma column and to a consequent decrease of the laser output energy. Capillary lifetime tests were conducted at 12 Hz repetition rate recording the laser output energy for a large number of shots. The laser output pulse energy was measured to decay by a factor of 2 after about 2 10^4- 3 10^4 shots (Fig. A.6). This is to our knowledge the longest series of soft x-ray laser shots achieved to date. The full output pulse energy can be recovered by replacing the used capillary discharge tube by a new one, an operation that demands 30- 40 minutes including the pumping time required to evacuate the system to a pressure of $< 1\times10^{-5}$ Torr.

A.4 FAR FIELD LASER OUTPUT

The far field laser output intensity distribution (Fig. A.7a) was measured using a microchannelplate/phosphor screen read by a CCD array detector of 1024 X 1024 pixels placed at 157.5 cm from the exit of the laser. The microchannel plate was gated with a ~ 5 ns voltage pulse to be able to discriminate the laser light from the long lasting spontaneous emission by the plasma in hundreds of extreme ultraviolet transitions. The beam profile was observed to have an annular shape that is the result of refraction of the amplified rays by radial electron density gradients in the plasma column. [2.13-2.14] Figure A.7b shows a cross section of an output intensity pattern acquired in a single shot. The peak-to-peak divergence is about 5.2 mrad.

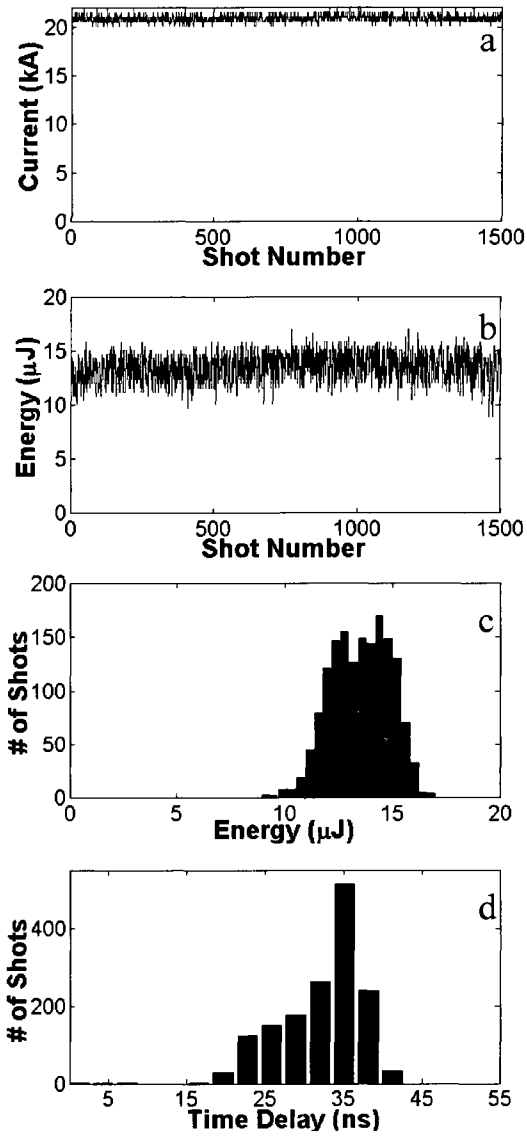


Figure A.5: Data corresponding to 1500 shots of continuous12 Hz repetition rate laser operation. (a) peak current; (b) measured laser output pulse energy; (c) distribution of the laser output pulse energy. The average pulse energy is 13 μJ; (d) statistics of the time delay between the laser pulse and the TTL signal into the high voltage trigger unit.

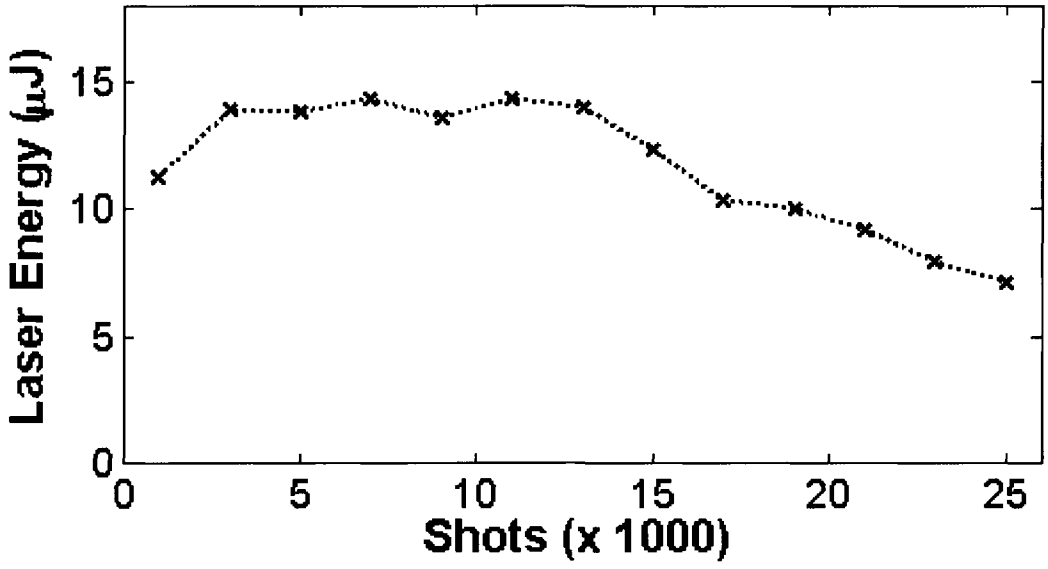


Figure A.6: Variation of the laser output pulse energy as a function of the number of shots. The data was obtained operating the laser at 12 Hz repetition rate. The output energy is observed to degrade to half of the maximum value in about 2-3 10^4 discharge shots

A.5 SUMMARY

In summary we have demonstrated high repetition rate (12 Hz) operation of a desk-top 46.9 nm lasers that is easily transportable and has a relatively low timing jitter. To the authors knowledge this is the first demonstration of a soft x-ray laser that can maintain an output energy of > 10μJ at repetition rates up to 12 Hz with a total lifetime of 2 10^4- 3 10^4 shots and the first to be installed in a photochemistry lab. The laser is electrically triggered to allow synchronization with external events. This new type of portable short wavelength laser is of interest for numerous applications including experiments in photochemistry, materials characterization and patterning, and high resolution imaging. The next chapter discusses the result of the use of this laser in nanocluster spectroscopy experiments.

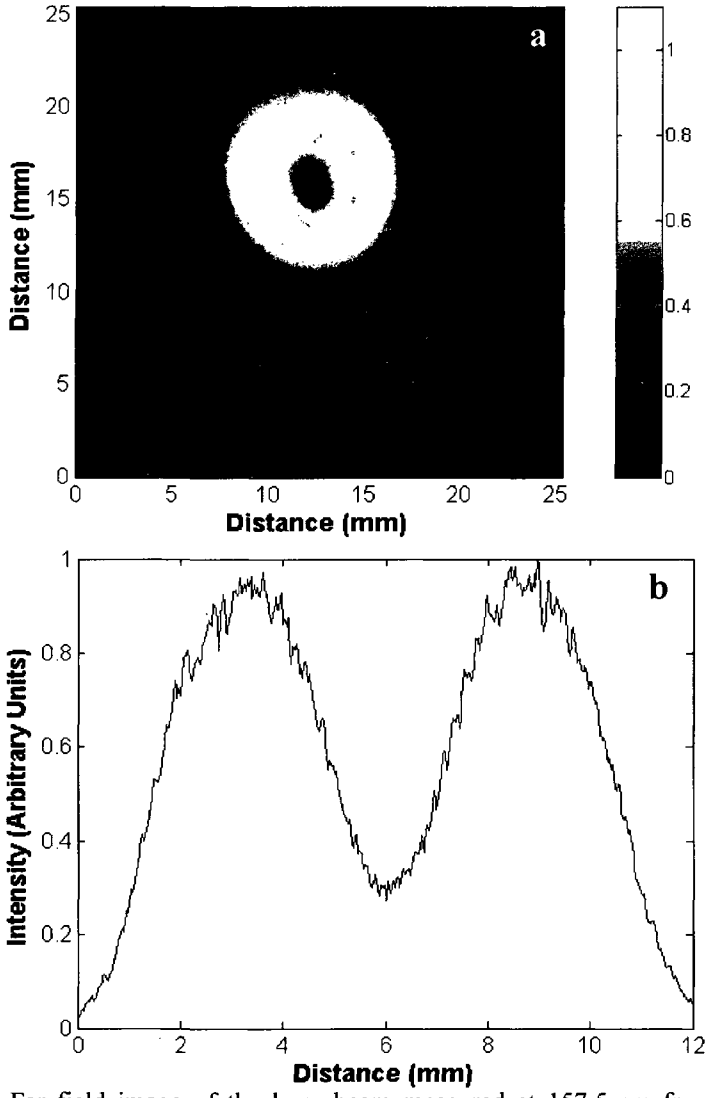


Figure A.7: (a) Far field image of the laser beam measured at 157.5 cm from the capillary exit. (b) corresponding intensity lineout. The peak-to-peak beam divergence is ~ 5 mrad.

REFERENCES

[A.1] B. R. Benware, C. D. Macchietto, C. H. Moreno, and J. J. Rocca, "Demonstration of a high average power table top soft x-ray laser," Phys. Rev. Lett. **81**, 5804 (1998).

[A.2] J. J. Rocca, V. Shlyaptsev, F.G. Tomasel, O.D. Cortazar, D. Hartshorn, J.L.A. Chilla, "Demonstration of a discharge pumped table-top soft x-ray laser," Phys. Rev. Lett. **73**, 2192, (1994).

[A.3] J. Dunn, Y. Li, A. L. Osterheld, J. Nilsen, J. R. Hunter, V. N. Shlyaptsev, "Gain Saturation Regime for Laser-Driven Tabletop, Transient Ni-Like Ion X-Ray Lasers," Phys. Rev. Lett. **84**, 4834 (2000).

[A.4] S. Sebban,. R. Haroutunian, Ph. Balcou, et al., Phys. Rev. Lett. **86**, 3004 (2001) and S. Sebban, T. Mocek, D. Ross, et al., "Demonstration of a Ni-Like Kr Optical-Field-Ionization Collisional Soft X-Ray Laser at 32.8 nm," Phys. Rev. Lett. **89**, 253901 (2002).

[A.5] K.A. Jenulewicz, A. Lucianetti, G. Pruebe, W. Sadner and P.V. Nickles, "Saturated Ni-like Ag x-ray laser at 13.9 nm pumped by a single picosecond laser pulse," Phys. Rev. A **68,** 051802 (2003).

[A.6] A. Butler, A.J. Gonsalves, C.M. McKenna, D.J. Spence, S.M. Hooker, S. Sebban, T. Mocek, I. Betttaibi and B. Cros, "41.8-nm Xe^{8+} laser driven in a plasma waveguide," Phys. Rev. A **70**, 023821 (2004).

[A.7] J. J. Rocca, D. P. Clark, J. L. A. Chilla, V. N. Shlyaptsev, "Energy Extraction and Achievement of the Saturation Limit in a Discharge-Pumped Table-Top Soft X-Ray Amplifier," Phys. Rev. Lett. **77**, 1476 (1996).

[A.8] B. R. Benware, C. D. Macchietto, C. H. Moreno, and J. J. Rocca, "Demonstration of a high average power table top soft x-ray laser," Phys. Rev. Lett. **81**, 5804 (1998).

[A.9] C. D. Macchietto, B. R. Benware, and J. J. Rocca, "Generation of millijoule-level soft-x-ray laser pulses at a 4-Hz repetition rate in a highly saturated tabletop capillary discharge amplifier," Opt. Lett. **24**, 1115 (1999).

[A.10] A. Ben-Kish, M. Shuker, R.A. Nemirowsky, A. Ron, and J.L. Schwob, "Plasma Dynamics in Capillary Discharge Soft X-Ray Lasers," Phys. Rev. Lett. **87**, 1 (2001).

[A.11] A. Ritucci, G. Tomassetti, A. Reale, L. Palladino, L. Reale, F. Flora, L. Mezi, S.V. Kukhlevsky., A. Faenov, T. Pikuz, "Investigation of a highly saturated soft X-ray amplification in a capillary discharge plasma waveguide," Applied Phys. B **78**, 965 (2004).

[A.12] B. Luther, L. Furfaro, A. Klix, and J.J. Rocca, "Femtosecond laser triggering of a sub-100 picosecond jitter high-voltage spark gap," Appl. Phys. Lett. **79**, 3248-3250 (2001).

[A.13] C.H. Moreno, M.C. Marconi, V.N. Shlyaptsev, B. Benware, C. Macchietto, J.L.A. Chilla, J.J. Rocca, "Two-dimensional near-field and far-field imaging of a Ne-like Ar capillary discharge table-top soft-x-ray laser," Phys. Rev. A **58**, 1509 (1998).

[A.14] J.L.A. Chilla and J.J. Rocca, "Beam optics of gain-guided soft-x-ray lasers in cylindrical plasmas," J. Opt. Soc. Am. B **13**, 2841 (1996).